EPRI

Guidelines for Determining Design Basis Ground Motions

Volume 1: Method and Guidelines for Estimating Earthquake Ground Motion in Eastern North America

WARNING:
Please read the Export Control Agreement on the back cover.

Technical Report

Guidelines for Determining Design Basis Ground Motions

Volume 1: Method and Guidelines for Estimating Earthquake Ground Motion in Eastern North America

Procedures currently used to assess the nature of earthquake ground motion in Eastern North America introduce considerable uncertainty to the design parameters of nuclear power plants and other critical facilities. This report examines that issue in-depth and provides an engineering model and guideline for selecting a site and assessing its seismic suitability.

INTEREST CATEGORIES

Nuclear seismic risk, design, and qualification
Advanced light water reactors
Risk analysis; management and assessment
Nuclear plant life extension

KEYWORDS

Earthquakes
Site characterization
Hazard assessment
Seismic engineering
Seismology
Geotechnical engineering

BACKGROUND Eastern North America has sparse earthquake activity with rare occurrences of large earthquakes; thus, little data exists to empirically quantify the characteristics of ground motions. Procedures currently used to estimate ground motion effects in this region introduce considerable uncertainty into the process of developing seismic designs, either due to the procedure's subjectivity or the lack of physical calibration.

OBJECTIVES To develop generic relations for estimating ground motion appropriate for site screening; to develop a guideline for conducting a thorough site investigation needed to define the seismic design basis.

APPROACH The project team specifically considered ground motions resulting from earthquakes with magnitudes from 5 to 8, fault distances from 0 to 500 km, and frequencies from 1 to 35 Hz. To develop generic ground motion relations for Eastern North America, they used theoretical models calibrated against data from earthquakes throughout North America and the world. In these models, the contributions to ground motion, including its variability, were evaluated using physical representations of earthquake processes. Earthquake processes involve the initial generation of seismic energy or waves at the earthquake fault ("source effects"), followed by the propagation of seismic waves through the earth's crust ("path effects"), and finally the modification of seismic waves as they travel through soils near the earth's surface ("site effects"). The team also collected and analyzed extensive geotechnical data at three reference sites. This information provided the basis for developing a guideline to help assess site suitability.

RESULTS This project resulted in an engineering model for estimating earthquake ground motions in Eastern North America. The model considers a wide range of earthquake sizes and site conditions and may be used directly for site screening purposes.

The work also resulted in a guideline for conducting geotechnical and seismic engineering investigations needed to determine the design basis for a site. This guideline is appropriate for investigating a wide range of site conditions and soil depths within and outside Eastern North America.

EPRI PERSPECTIVE Cost-effective seismic regulation of nuclear power plants requires site-specific definition of seismic ground motions. The development of engineering procedures for estimating earthquake ground motion can thus benefit both

to define the safe shutdown earthquake (SSE). The regulatory guidance found in Section 2.5 of the Standard Review Plan (NUREG 0800) is quite limited in scope and does not reflect the current state of knowledge on earthquake phenomena. With no accepted generic procedures in place, utilities constantly face uncertainty associated with site-specific developments and applications. These factors result in seismic design bases that are excessively conservative and/or contribute to licensing delays, regulatory instability, and high utility costs in the licensing process.

In 1988, EPRI completed a seismic hazard model for the central and eastern United States (NP-4726), including a ground motion model (NP-6074). The present work directly complements NP-4726, while replacing and going significantly beyond the results of NP-6074. The engineering ground-motion model can be used for screening potential sites before conducting extensive site investigations. The guideline provides needed background information to conduct an appropriate geotechnical and seismic engineering investigation of a site for licensing purposes. Additional EPRI reports that provide a basis for the current report include: NP-5577, NP-5875, NP-6304, TR-100409, TR-100410, TR-102261, and TR-102262.

This report is presented in five volumes. Essential background, approach and results are given mainly in Volume 1. Volumes 2, 3, and 4 are appendices containing detailed analyses. Volume 5 (licensed material) contains *Quantification of Seismic Source Effects*, which is summarized in Volume 1, Section 4.

PROJECT

RP3302

EPRI Project Manager: J. F. Schneider

Nuclear Power Division

For further information on EPRI research programs, call
EPRI Technical Information Specialists (415) 855-2411.

Guidelines for Determining Design Basis Ground Motions

Volume 1:
Method and Guidelines for Estimating Earthquake Ground Motion in Eastern North America

TR-102293
Research Project 3302

Final Report, November 1993

Prepared by
ELECTRIC POWER RESEARCH INSTITUTE
in cooperation with the Joint Contractors
(Southern Electric International, Commonwealth Research Corporation,
and Public Service Corporation of New Jersey),
the Nuclear Management and Resources Council,
the U.S. Department of Energy and Sandia National Laboratories.

Prepared for
Electric Power Research Institute
3412 Hillview Avenue
Palo Alto, California 94304

EPRI Project Manager
J. F. Schneider

Advanced Reactors Development
Nuclear Power Division

DISCLAIMER OF WARRANTIES AND LIMITATION OF LIABILITIES

ORGANIZATION(S) THAT PREPARED THIS REPORT:
ELECTRIC POWER RESEARCH INSTITUTE

ORDERING INFORMATION

Requests for copies of this report should be directed to the EPRI Distribution Center, 207 Coggins Drive, P.O. Box 23205, Pleasant Hill, CA 94523, (510) 934-4212. There is no charge for reports requested by EPRI member utilities.

LIST OF COSPONSORS

Early Site Permit Demonstration Program (ESPDP) Participants

Southern Electric International
42 Inverness Center Parkway
Birmingham, AL 25242

Commonwealth Research Corporation
1400 Opus Place
Downers Grove, IL 60515

Public Service Corporation of New Jersey
80 Park Plaza, 11-A
Newark, NJ 07101

Electric Power Research Institute
3412 Hillview Ave.
Palo Alto, CA 94303

Nuclear Management and Resources Council
1776 Eye Street, Suite 300
Washington, DC 2006

Department of Energy
Office of Nuclear Energy
19901 Germantown, MD 20874

Sandia National Laboratories
1515 Eubank Boulevard Southeast
Albuquerque, NM 87123

PROGRAM PARTICIPANTS

Participants	Affiliation
Project Manager	
Dr. John Schneider	Electric Power Research Institute
Principal Participants	
Dr. Norman Abrahamson	Consultant
Dr. Donald Anderson	CH2M Hill, Inc.
Dr. Gail Atkinson	Consultant
Prof. Carl Costantino	City University of New York
Prof. I.M. Idriss	University of California at Davis
Dr. Robin K. McGuire	Risk Engineering, Inc.
Dr. Robert Nigbor	Agbabian Associates
Dr. Robert Pyke	Consultant
Dr. Walter Silva	Pacific Engineering & Analysis
Dr. Paul Somerville	Woodward-Clyde Consultants—Pasadena
Dr. J. Carl Stepp	Electric Power Research Institute
Prof. Kenneth Stokoe	University of Texas at Austin
Prof. M. Nafi Toksoz	Massachusetts Institute of Technology
Dr. Gabriel Toro	Risk Engineering, Inc.
Dr. Robert Youngs	Geomatrix Consultants
Contributors	
Prof. Keiiti Aki	Consultant
Dr. C. T. Chin	Moh & Associates, Taiwan
Dr. James Chin	University of Southern California
Dr. Shyh-Jeng Chiou	Geomatrix Consultants
Mr. Mark Fuhriman	University of Texas at Austin
Dr. Robert Graves	Woodward-Clyde Consultants
Prof. Robert Herrmann	St. Louis University
Mr. Seon-Keun Hwang	University of Texas at Austin
Mr. Athar Khwaja	University of Texas at Austin
Mr. Joseph Laird	University of Texas at Austin
Mr. David Lapp	Geomatrix Consultants
Mr. Ben T. Lin	Moh & Associates, Taiwan
Mr. Mihalis Madianos	Geomatrix Consultants

Contributors

Dr. Batakrishna Mandal	Massachusetts Institute of Technology
Mr. James McLaren	Woodward-Clyde Consultants
Mr. Bruce Redpath	Redpath Geophysics
Ms. Nancy Smith	Woodward-Clyde Consultants
Ms. Cathy Stark	Pacific Engineering & Analysis
Mr. Robert Steller	Agbabian Associates
Dr. Joseph Sun	Woodward-Clyde Consultants
Dr. Y. T. Gu	City University of New York
Mr. Ernest Heymsfield	City University of New York
Dr. Xiao-ming Tang	Massachusetts Institute of Technology
Mr. Chris Volksen	University of California at Davis
Mr. Donald Wells	Geomatrix Consultants
Mr. Doug Wright	Pacific Engineering & Analysis
Dr. Shen-Chyun Wu	Risk Engineering, Inc.
Ms. Joanne Yoshimura	Consultant

LIST OF CONTRACTORS

Guidelines for Determining Design Basis Ground Motions

TR-102293

Contract	Contractor
RP3302-02	Professor M. Nafi Toksoz Consultant 15 Walsingham St. Newton, MA 02162
RP3302-04	Professor Kenneth Stokoe Consultant 4602 Laurel Canyon Dr. Austin, TX 78731
RP3302-05	Professor I.M. Idriss Consultant P.O. Box 330 Davis, CA 95617-0330
RP3302-06	Dr. Gail Atkinson Consultant 125 Dunbar Road South Waterloo, Ontario N2L 2E8 CANADA
RP3302-07	Dr. Norman Abrahamson Consultant 5319 Camino Alta Mora Castro Valley, CA 94546

Contract	Contractor
RP3302-08	Dr. Paul Somerville Woodward-Clyde Consultants 566 El Dorado St. Pasadena, CA 91101
RP3302-09	Dr. Robin K. McGuire Risk Engineering, Inc. 5255 Pine Ridge Road Golden, CO 80403
RP3302-10	Dr. Walter Silva Pacific Engineering and Analysis 311 Pomona Avenue El Cerrito, CA 94530
RP3302-11	Dr. Robert Pyke Consultant 1076 Carol Lane #136 Lafayette, CA 94549
RP3302-12	Dr. Robert Youngs Geomatrix Consultants 100 Pine Street—10th Floor San Francisco, CA 94111
RP3302-13	Dr. Donald Anderson CH2M Hill, Inc. P.O. Box 91500 Bellevue, WA 98009-2050
RP3302-14	Professor Keiiti Aki Consultant 622 Paseo de la Playa Redondo Beach, CA 90277
RP3302-15	Dr. Joseph Sun Woodward-Clyde Consultants 500 12th Street, Suite 100 Oakland, CA 94607-4014
RP3302-16	Dr. Robert Nigbor Agbabian Associates 1111 South Arroyo Parkway Suite 405 Pasadena, CA 91105
RP3302-18	Prof. Carl Costantino Consultant 4 Rockingham Rd. Spring Valley, NY 10977

ABSTRACT

This report develops and applies a method for estimating strong earthquake ground motion. The emphasis of this study is on ground motion estimation in Eastern North America (east of the Rocky Mountains), with particular emphasis on the Eastern United States and southeastern Canada. Specifically considered are ground motions resulting from earthquakes with magnitudes from 5 to 8, fault distances from 0 to 500 km, and frequencies from 1 to 35 Hz. The two main objectives were: (1) to develop generic relations for estimating ground motion appropriate for site screening; and (2) to develop a guideline for conducting a thorough site investigation needed to define the seismic design basis. For the first objective, an engineering model was developed to predict the expected ground motion on rock sites, with an additional set of amplification factors to account for the response of the soil column over rock at soil sites. The results incorporate best estimates of ground motion as well as the randomness and uncertainty associated with those estimates. For the second objective, guidelines were developed for gathering geotechnical information at a site and using this information in calculating site response. As a part of this development, an extensive set of geotechnical and seismic investigations was conducted at three reference sites. Together, the engineering model and guidelines provide the means to select and assess the seismic suitability of a site.

ACKNOWLEDGMENTS

This project was made possible through extensive support from a great number of institutions and individuals.

For review of draft copies of the report, conducted under an extremely tight schedule, we much appreciate the thoughtful comments by the following individuals: Dr. Michael Bohn, Sandia National Laboratory; Prof. Ricardo Dobry, Rensselaer Polytechnic Institute; Mr. Jeff Kimball, Department of Energy; Dr. Takeji Kokusho, Central Research Institute of Electric Power Industry, Japan; and Dr. Scott Slezak, Sandia National Laboratory.

Field measurements at the reference sites at Treasure Island and Gilroy 2 in California and at Lotung, Taiwan, required considerable logistical coordination and cooperation between institutions and individuals. Major contributions to seismic and other geophysical measurements at Treasure Island and Gilroy 2 were made by Mr. Takashi Kanamori and Mr. Finn Michelson of Oyo Geospace, Mr. Kenji Tanaka of Oyo Corporation, and Mr. Ed Steller of Agbabian Associates. Extensive seismic measurements at Treasure Island and Gilroy 2 were also made by Dr. Ronald Andrus, Mr. Marwan Aouad, and Mr. James Bay of the University of Texas at Austin. Generous support from Mr. Thomas Fumal and Mr. James Gibbs of the U.S. Geological Survey is also acknowledged for their contribution to geologic and seismic logging, respectively, of boreholes at the Gilroy 2 and Treasure Island sites. The following companies assisted the project by providing special equipment used in the measurements: ANCO Engineers, Kinemetrics, Inc., Oyo Corporation, and Redpath Geophysics.

For making arrangements or generously providing access to the reference sites, we are grateful to numerous individuals. We thank Ms. Susan Chang and Dr. Lelio Mejia of Woodward-Clyde Associates for assistance in logistics of drilling at Gilroy 2. Special thanks to Mr. Richard Lake and Mr. Roger Kostenko of Pitcher Drilling Co. for their excellence in drilling and sampling at the Gilroy 2 and Treasure Island sites. Drilling at Lotung, Taiwan, was coordinated expertly by Moh & Associates. We thank Mr. Y. H. Cheng, Deputy Director of the Nuclear Engineering Department at Taiwan Power Co., for helping with access to drilling at the Lotung site owned by Taiwan Power Co. For access to Gilroy 2, we thank Mr. John Belleau, site owner, and Mr. Roger and Ms. Marie Ellissondo, site managers (National 9 Inn). For Treasure Island site access, we thank Mr. Thomas Cuckler and Mr. Donald Brown of the Civil Engineering Department of the Treasure Island Naval Air Station.

Additional data were also generously provided by many individuals and institutions from complementary field measurements at various field test sites. Prof. Pedro de Alba of the University of New Hampshire, Mr. John Egan of Geomatrix Consultants, Prof. Roman Hryciw of the University of Michigan, and Prof. Kyle Rollins of Brigham Young University all generously provided data for our use from other geotechnical studies at Treasure Island. Sponsors of studies that produced these data were the U.S. Naval Air Station and the National Science Foundation. Prof. Pedro de Alba also provided access to boreholes drilled for several of these studies, also sponsored by the National

Science Foundation. Mr. Jeff Kimball of the Department of Energy made it possible to use a collection of geotechnical data from a site at the Savannah River site, South Carolina.

All of the laboratory measurements of dynamic properties of soil samples from the reference sites were performed at the Geotechnical Engineering Center of the University of Texas at Austin (GEC-UT). The large-scale chamber tests used to study field damping measurements were also performed at the GEC-UT. We thank Mr. Ngarkok Lee and Mr. Mark Twede of that institution for their assistance in this work. Further, the assistance of Ms. Teresa Tice-Boggs of the Geotechnical Engineering Center contributed significantly to the success of this work.

Several people assisted in providing and assembling data for the earthquake database used in this project. We appreciate the help of Mr. Phillip Munro of the Geological Survey of Canada for information regarding characteristics of strong-motion instrument sites for data recorded during the 1988 Saguenay, Quebec, earthquake and aftershocks.

Dr. David Boore of the U. S. Geological Survey provided an analysis of the distribution of selected ground motion data recorded on Wood-Anderson seismographs in southern California. Dr. Gail Atkinson provided seismic data and site descriptions from the Eastern Canada Telemetered Seismic Network.

We would like to thank the following people for their participation in various workshops held during the course of the project: Dr. David Boore, Dr. Jon Fletcher, Mr. Thomas Fumal, Mr. James Gibbs, Dr. William Joyner, and Dr. John Vidale of the U.S. Geological Survey; Mr. Scott Ashford, University of California at Berkeley; Ms. Ornella Bonamassa, University of California at Santa Cruz; Dr. David Rodgers, Rogers Pacific Consultants; Mr. Takashi Kanamori and Mr. Finn Michelson of Oyo Geospace; Dr. Clifford Roblee, California Department of Transportation; and Dr. Richard Lee, Westinghouse Savannah River Co. These individuals participated in numerous stimulating discussions that greatly contributed to the final product.

Finally, it is with great appreciation for the financial and managerial support, and, equally important the trust and confidence provided us, that we thank various individuals within and associated with the Department of Energy and utility industry for making the project possible. Special thanks to Ms. Susan Gray, Mr. Murv Little, and Mr. Joseph Santucci of the EPRI Advanced Reactor Program for their generous support, and especially to Ms. Gray for her direction as project manager of the Early Site Permit Demonstration Program. Thanks to Mr. Walter Pasedag of the Department of Energy and Mr. Ajoy Moonka of Sandia National Laboratory; to the Industry Siting Group, especially Mr. Louis Long; to the Nuclear Management and Resources Council (NUMARC), especially Mr. John Ronafalvy; to the Joint Contractors comprised of Southern Electric International, Commonwealth Research Corporation, and Public Service Company of New Jersey, especially Dr. Ninu Kaushal (Commonwealth Edison Co.).

CONTENTS

Volume 1: Method and Guidelines for Estimating Earthquake Ground Motion in Eastern North America

Section Page

LIST OF FIGURES

Figures **Page**

Figures **Page**

Figures **Page**

Figures **Page**

Figures **Page**

Figures **Page**

Figures **Page**

Figures **Page**

Figures **Page**

Figures **Page**

Figures **Page**

LIST OF TABLES

Figures **Page**

Tables **Page**

EXECUTIVE SUMMARY

Introduction

This report develops and applies a method for estimating strong earthquake ground motion. The motivation for this development was the need for a systematic, physically based, empirically calibrated method that can be used to estimate ground motions for input to the design of nuclear power plants and other critical facilities. These ground motions are a function of the earthquake's magnitude and the physical properties of the earth through which the seismic waves travel from the earthquake fault to the site of interest. Procedures currently used to account for these effects introduce considerable uncertainty into the ground motion determination, either due to subjectivity of the procedure or the lack of physical calibration.

The emphasis of this study is on ground motion estimation in Eastern North America (east of the Rocky Mountains), with particular emphasis on the Eastern United States and southeastern Canada. Eastern North America is a stable continental region, having sparse earthquake activity with rare occurrences of large earthquakes. In the absence of large earthquakes within the region of interest, little data exist to empirically quantify the characteristics of ground motions associated with these events. While methods developed in more seismically active areas such as Western North America can be applied to Eastern North America, fundamental differences in the regional geology can lead to variations in ground motion characteristics. Therefore, empirically based approaches that are applicable for other regions, such as Western North America, do not appear to be appropriate for Eastern North America.

Recent advances in science and technology have now made it possible to combine theoretical and empirical methods to develop new procedures and models for estimating ground motion within Eastern North America. Specifically considered are ground motions resulting from earthquakes with magnitudes from 5 to 8, fault distances from 0 to 500 km, and frequencies from 1 to 35 Hz. The results of this report can be used to determine seismic hazards, provided the magnitudes and distances of potential earthquakes are predetermined. In particular, this report is intended for use in site screening as well as detailed characterization of ground motion at a site, such as may be required for structural design.

This study was conducted by a team of experts in seismology, geotechnical engineering, and seismic engineering. The investigations were carried out over a period of approximately 18 months from September 1991 to March 1993. Work included a series of focused workshops with project participants to help achieve consensus recommendations. The project was sponsored by the U. S. Department of Energy (DOE), Sandia National Laboratories, Southern Electric International, Commonwealth Research Corporation, Public Service Company of New Jersey, and the Electric Power Research Institute as part of the DOE's Early Site Permit Demonstration Program. The project was managed by the Electric Power Research Institute.

Objectives

There were two central objectives of the project: (1) to develop generic relations for estimating ground motion

appropriate for site screening; and (2) to develop a guideline for conducting a thorough site investigation needed to define the seismic design basis. For the first objective, a set of relations was needed that could be used to predict the expected ground motion on rock or on soil for a future earthquake. The approach was to develop an engineering model consisting of relations appropriate for rock sites and an additional set of amplification factors to account for the response of the soil column over rock at soil sites. For the second objective, a guideline was developed for gathering geotechnical information at a site and using this information in calculating site response. Together, the engineering model and guideline provide the means to select and assess the seismic suitability of a site.

Approach

The method that was used to develop generic ground motion relations in this effort is markedly different from the approach of previous studies. In this study, theoretical models, which have been calibrated against data from earthquakes throughout North America and the world, are used to characterize earthquake ground motion in Eastern North America. In these models, the contributions to ground motion, including its variability, are evaluated using physical representations of earthquake processes. These processes involve the initial generation of seismic energy or waves at the earthquake fault ("source effects"), followed by the propagation of seismic waves through the earth's crust ("path effects"), and finally the modification of seismic waves as they travel through soils near the earth's surface ("site effects"). For a given earthquake magnitude and distance, the source, path, and site each contribute to the observed ground motion, as follows:

- The source controls both the seismic energy generated by rupture of an earthquake fault as well as the accompanying dynamic characteristics.
- The seismic path contributes to ground motion through reflection, refraction, and damping of seismic waves within the earth's crust in response to the various physical properties along the wave path.
- The site contributes to the evolution of seismic waves in much the same way as the path, though on a smaller scale. Site effects are a function primarily of soil depth and type.

The characteristics of the seismic source, path, and site effects form the basis for the parameters in the theoretical models.

The ground motion relations for rock sites were developed using a physically based, empirically calibrated ground motion model. In the model, a wide range of values was assigned to the ground motion parameters. Using the combination of all model parameters and their ranges of values, computer simulations produced hundreds of records of earthquake ground motion for each magnitude and distance considered. While each earthquake simulation represents a possible future earthquake, each earthquake is not equally likely to occur. Therefore, based upon extensive analyses of past earthquakes and comparisons to model predictions, distributions were assigned to the values for all model parameters. The parameter value distributions were based on partitioning their variability into two types: uncertainty, which is due to the lack of knowledge of earthquake characteristics; and randomness, which is due to the inherent variability of those characteristics. Finally, individual parameter weights were combined for each earthquake simulation to produce the appropriate "distribution" of earthquake ground motion for every magnitude, distance, and frequency considered. Together, these distributions constitute a family of functional relations that define the final engineering ground motion model for rock sites. In turn, the engineering model defines ground motion for median levels and associated variability.

To accommodate sites with soil overlying rock (referred to as local site effects), site amplification factors were developed for a range of soil types and depths representative of soil conditions in Eastern North America. The factors were derived by first accumulating data that describe the behavior of various soils during seismic loading. These data were then used to assess the variability in seismic properties, especially the wave velocity as it changes with depth. In addition, seismic velocity and material damping data were gathered from three reference sites using a variety of field and laboratory techniques. The reference site data were used (1) to improve physical understanding of the dynamic processes of soil response and (2) to assess procedures for measuring the physical properties needed to estimate site effects. The estimation problem is particularly difficult because the seismic properties of soils change depending upon the

level of shaking. The resulting "nonlinear" effects generally cause the ratio of soil-to-rock motions (i.e., soil amplification) to decrease as the corresponding rock motion increases. The quantification of these effects through theoretical modeling and comparisons to empirical data resulted in factors that describe the amplification of soils relative to rock for several soil categories. The amplification factors were developed for a wide range of rock motions and are given as median values with variability.

Finally, based upon extensive geotechnical data that were collected at the three reference sites and analyzed as part of this program, a guideline was developed for assessing soil characteristics and site response. This guideline applies to planning and conducting a systematic and thorough geotechnical investigation of soil properties at a potential site. Guidance is also provided for performing dynamic analyses required to determine the response of the soil column to earthquake shaking at (and beyond) the levels of motion of interest to the seismic design.

Conclusions

The engineering ground motion model developed in this study can be used for screening potential sites in Eastern North America before conducting extensive site investigations. However, the application of these procedures to site screening requires information regarding earthquake magnitudes and distances as well as certain site properties such as soil depth and site geology. Magnitudes and distances of potential earthquakes may be derived either probabilistically or deterministically.

The guideline—together with the results of investigations of the three reference sites—provides the means to conduct an appropriate geotechnical and seismic engineering site investigation. In all, this guideline is appropriate for use given a wide range of site conditions and soil depths. While there are certain soil types (e.g., those with liquefaction potential) for which this guideline may not be directly applicable, it may be used widely both within and outside Eastern North America.

The information compiled in this report represents a comprehensive assessment of the nature of earthquake ground motion in Eastern North America. The results incorporate best estimates of ground motion as well as the randomness and uncertainty associated with those estimates for a wide range of earthquake magnitudes, distances, and frequencies. Overall, the results of this study will be useful in performing seismic hazard evaluations and establishing seismic design standards for many years to come.

Organization

The results of this study are presented in five volumes. *Volume I: Methodology and Guidelines for Estimating Earthquake Ground Motion in Eastern North America*, represents the main body of the report, presents the model development and summarizes the key results and conclusions of the study. *Volume II: Appendices for Ground Motion Estimation*, presents the appendices to Sections 2 to 7 of Volume I, and consists primarily of data and details of analyses used to develop the engineering ground motion model and geotechnical guidelines. *Volume III: Appendices for Field Investigations*, and *Volume IV: Appendices for Laboratory Investigations*, present the details of field and laboratory investigations of reference sites; Section 8 of Volume 1 constitutes a summary of these appendices. *Volume V: Seismic Source Effects*, presents separately (as a licensed report) the analyses of the seismic source performed for input to the engineering ground motion model; a summary of this volume is given as Section 4 of Volume 1.

1

INTRODUCTION

1.1 Background[1]

This report summarizes work to investigate earthquake ground motions in eastern North America (ENA), east of longitude 105°W. The general purpose is to develop engineering estimates of earthquake ground motions for application in the eastern United States (EUS) based on a physical understanding of how the earth behaves, explicitly expressing uncertainties in estimates caused by lack of knowledge both about properties of the earth and about physical processes that govern the generation and transmission of seismic energy.

In the assessment of suitability for future nuclear power plant siting evaluations there is a need for both a generic ground motion model for site screening and a set of procedures for site characterization for development of a site-specific design basis. The generic model yields the first-order estimate to the suitability of a site and is manifested by a set of equations with a limited number of parameters appropriate to the source, path and site combination. The equations are conditional on a measure of earthquake size (generally a magnitude measure) and distance from the energy release to the site. The earthquake size measure (typically body-wave magnitude determined from Lg waves, m_{Lg}, in the EUS) must be an appropriate measure of energy released in the engineering band of interest. The function of distance must account for the interaction of seismic waves (both body and surface waves) with the structure of the earth, and must account for intrinsic attenuation of energy in the earth, both along the entire travel path and in the near surface crustal layers where attenuation may be especially prominent.

Next, for development of a site-specific design basis, the site applicant is generally required to obtain site-specific data. In particular, local geological and geotechnical data need to be obtained and analyzed to determine the appropriate site response. The site response is generally considered to be the evolution of the seismic wave field from bedrock below the site to the top of the soil column, or free surface of the earth. In the past 10 years there has been a significant evolution in methods to acquire site-specific data—particularly the definition of soil properties—and methods to calculate site response, especially for large seismic inputs.

It is anticipated that the current recommendations for earthquake ground motions will be robust with respect to changes in our understanding of ground motion in the EUS. The field of strong-motion seismology changes slowly, most often as the result of new information gained from earthquake observations; and given that earthquakes are sufficiently rare events in the EUS, significant advances in our understanding of the earthquake ground motion process are unlikely in a short time frame. This is not to say that the field is stagnant, or that we know all we need to know to estimate the shaking during future earthquakes with precision. On the contrary, there is much to be learned, both about the transmission of seismic waves in the earth and about properties of the earth in many locations that affect that wave transmission. Rather our knowledge about processes and properties of the earth is unlikely to change greatly in the next few years, over most of the EUS. In addition, the specific focus of this project is on quantifying the variability in earthquake motions that may be

1. Refer to Appendix 1.A for the Glossary of Seismological and Geotechnical Terms.

anticipated given today's information base and physical understanding of earthquake motion generation and transmission. We therefore expect that additional information will allow us to reduce the estimation uncertainty and provide more precise ground-motion estimates.

Thus there is great value in the collection of data in a region or at a site, to reduce uncertainties on the values of parameters used in ground motion estimation. The procedure developed in this project allows for the reduction of uncertainties if data of certain types are collected. The power of the recommended method is that it allows ground motion estimation with different amounts of available data, so the method can be used for screening sites (when little or no site- or vicinity-specific data are available), for ranking candidate sites (when some data may be available), and for final analysis and design at a specific site (when very detailed, site- and regional-specific data have been collected). This flexibility means that designers and regulators can proceed with decisions with a knowledge of how uncertainty in ground motion estimates might change as new data are collected and incorporated into the estimation process. This will bring stability and efficiency to the design and licensing process. Thus the procedure recommended here for estimating strong shaking should be evaluated as a method applied for the next few years in the eastern US. We simply do not see any development that would change these recommendations, other than the unlikely occurrence of several moderate to large EUS earthquakes that are well recorded from near-source to teleseismic distances on a variety of soil conditions.

The procedures for estimating strong shaking have been developed using multiple interpretations and assumptions. Each of these interpretations and assumptions might be applicable over all of the EUS, or several might apply, each to a specific region. The incorporation of multiple assumptions is made explicitly to give stability to the estimation process; it is unlikely that any one of these assumptions will be proven to be "correct" during the next few years. This procedure is preferred over a model that adopts a single set of assumptions, where that set of assumptions must be updated following every data set collected from an EUS earthquake.

This methodology follows the philosophy that it is best to make mean-centered estimates of ground shaking, taking all uncertainties into account. There is no general attempt to be "conservative" in the sense of adopting higher-than-average assumptions as best estimates. This philosophy allows more quantitative, explicit statements of safety than if conservatisms are introduced during several steps of the process and compounded resulting in an unknown degree of seismic safety.

Engineering interest in seismic ground motions for nuclear power plants (NPPs) is in the frequency range 1 to 25 Hz, so this procedure estimates response spectra amplitudes for those frequencies, plus peak ground acceleration (PGA). The last parameter is included for historical reasons, so that this procedure can be compared to others that have been published, but is not necessary for the estimation of response spectra, as spectral amplitudes are estimated directly.

1.2 Previous Models of Eastern United States Ground Motions

Previous procedures used to estimate earthquake shaking in the EUS span a range of methods. The earliest methods, used prior to the 1980s, relied on estimating the attenuation of Modified Mercalli intensity (MMI) from observations of historical earthquakes (e.g., Gupta and Nuttli, 1976; Bollinger, 1977) and converting MMI estimated at the site to peak motion parameters such as PGA (e.g., Trifunac and Brady, 1975; Murphy and O'Brien, 1977). Spectra were then estimated by scaling a standard spectral shape by the peak parameters (Newmark et al., 1973).

The first method of estimating ground motion in the EUS on a physical basis was developed by Nuttli (1979). He estimated the Fourier spectrum of motion as a function of earthquake magnitude and distance based on seismological theory, and used a simple theoretical scaling to estimate peak time-domain amplitudes from the Fourier spectrum. Inherent in this method were relations that scaled the corner frequency of the motion by the seismic moment of the earthquake.

Atkinson (1984) applied random vibration theory (RVT) to estimate earthquake motions in ENA in 1984. This was followed by more detailed applications (Boore and Atkinson, 1987; Toro and McGuire, 1987) that included detailed comparisons of estimates with data. RVT allows a complete estimate of ground motion characteristics, including frequency content, duration, peak time-domain amplitudes, and seismograph response (from which measures of earthquake size on different magnitude

scales can be derived) (see, for example Hanks and McGuire, 1981, and Boore, 1983). The RVT method has been verified in California over a wide range of magnitudes and distances (e.g., McGuire et al., 1984), and its adoption for predictions in the EUS was a natural extension of the success of the method in estimating earthquake ground motions in California.

All of the aforementioned studies presented single models for estimating EUS ground motions. Two major efforts to quantify *uncertainties* in predicted ground motion amplitudes were undertaken by EPRI/SOG (1988) and Lawrence Livermore National Laboratory (Bernreuter et al., 1985) in their respective projects to characterize earthquake hazards at NPP sites. The EPRI/SOG study quantified uncertainties by making predictions for three sets of assumptions, including two based on RVT and one based on the Nuttli approach of predicting peak motion parameters and scaling a standard spectral shape. For site amplification, the EPRI/SOG study developed soil categories representative of the range of site conditions of operating nuclear power plant sites in the eastern US, as appropriate for one-dimensional site response analyses using RVT. The soil categories developed were based primarily on shear-wave velocities as a function of depth appropriate for the dominantly stiff-soil sites encountered at NPPs in the EUS. The uncertainties associated with site amplification factors were not well-constrained, because of poor constraints on dynamic soil properties and on analysis methods. The LLNL study polled and quantified the opinions of five ground motion consultants on the range of estimates of EUS ground motions, and quantified ground motion uncertainty using the weights ascribed to those methods by the participants. For site amplification the LLNL study calculated soil response for several categories of sites using one-dimensional shear wave models with random input motions. Figures 1-1 and 1-2 show comparisons of the mean ground motion estimates for rock outcrops from the equations developed by the EPRI/SOG study and those adopted by the LLNL study; these ground motion estimates generally show similar amplitudes and ranges of uncertainty.

As broad as the EPRI/SOG and LLNL studies were, both had deficiencies. Neither made a detailed study of the physical processes driving ground motion characteristics but adopted methods that were readily available at the time. The EPRI/SOG study did not use a wide range of expert opinion, but relied on one group to make judgments and interpretations, and included one model that scales spectral amplitudes from peak motion parameters using California spectral shapes, which are deficient in the high-frequency content typical of EUS ground motions. This is now judged to be an obsolete method. Some of the LLNL participants used this method. Some also gave significant weight to methods that estimate ground motion by predicting a site MMI and converting that site MMI to a response spectrum using correlations from California, a procedure that is also obsolete. The obsolescence of methods that scale California spectral shapes, and of those that convert estimated site MMI, comes from two recent advances. First was the recognition in recent years (e.g., Atkinson, 1984; Boore and Atkinson, 1987; Toro and McGuire, 1987) that a stochastic model based on the band-limited, white noise representation of ground motion and RVT is an accurate, quantitative method to characterize shaking in the EUS. Second was the collection of digital seismograph data over a range of earthquake magnitudes and distances, which could be used to estimate parameters in a stochastic model. These advances came subsequent to the EPRI/SOG and LLNL efforts, so neither study is satisfactory as a fundamental basis on which to license NPPs over the next five to ten years. Further, studies of ground motion in the EUS since these two studies were published (e.g., Burger et al., 1987; Barker et al., 1989; Somerville et al., 1990; Atkinson and Mereu, 1992) have focused on specific characteristics of shaking in a subregion, not on a broad methodology of ground motion estimation that encompasses all major uncertainties and that is applicable throughout the EUS. Finally, recent studies following recorded earthquake ground motions in California have emphasized the need to separate site effects from source and path effects, when predicting earthquake shaking.

In summary, a study of the type undertaken here has never been performed for the EUS. Previous studies either have concentrated on specific physical characteristics of ground shaking, or have quantified uncertainties but have included methods and equations that are now obsolete and not based on a physical understanding of how seismic energy is transmitted through the earth.

More recent research has provided new data on many of the input assumptions to the ground motion model, including those concerning attenuation (Atkinson and

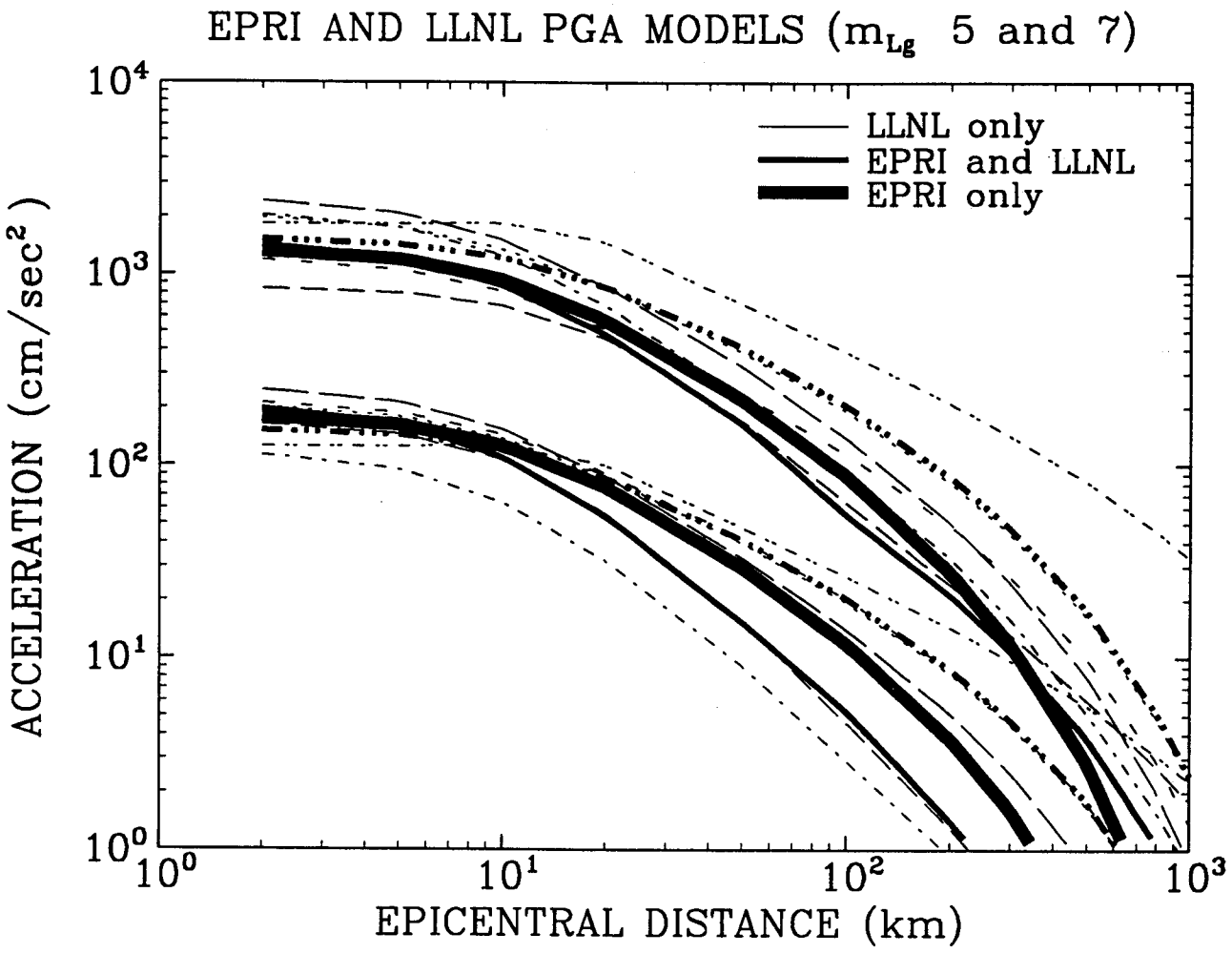

Figure 1-1. Comparison of predicted peak acceleration vs. distance for the EPRI/SOG study (the thick and medium lines) and the LLNL study (the medium and thin lines). Predictions are shown for m_{Lg} 5 and 7.

Mereu, 1992), duration (Atkinson, 1993) and, most significantly, the source (Atkinson, 1993). The implications of the new data in these areas is considered in the current study.

1.3 Seismic Hazard Perspective

The EUS is an area of generally low historical seismicity, with a few moderate-to-large earthquakes that, if they recurred today in a populated area, would cause significant damage. Among these are the earthquakes in 1811–1812 near New Madrid, Missouri (magnitudes estimated around 8), the 1886 Charleston, South Carolina earthquake (magnitude estimated around 7), the 1929 Grand Banks earthquake (magnitude m_b = 7) and the 1925 Charlevoix earthquake (m_b = 6.5) (see, for example, Hanks and Johnston, 1992). These events, and the more numerous earthquakes with magnitudes in the 5 to 6 range, are sufficient cause for taking precautions against seismic motions in the design of NPPs. There are large uncertainties in the causes and characteristics of earthquakes in the EUS, and the situation is complicated because earthquakes may have several causes in one region, and several other causes in another region. Thus what we learn in one region about earthquake mechanisms and source dynamics may or may not apply to other regions of the EUS. Much effort has therefore gone

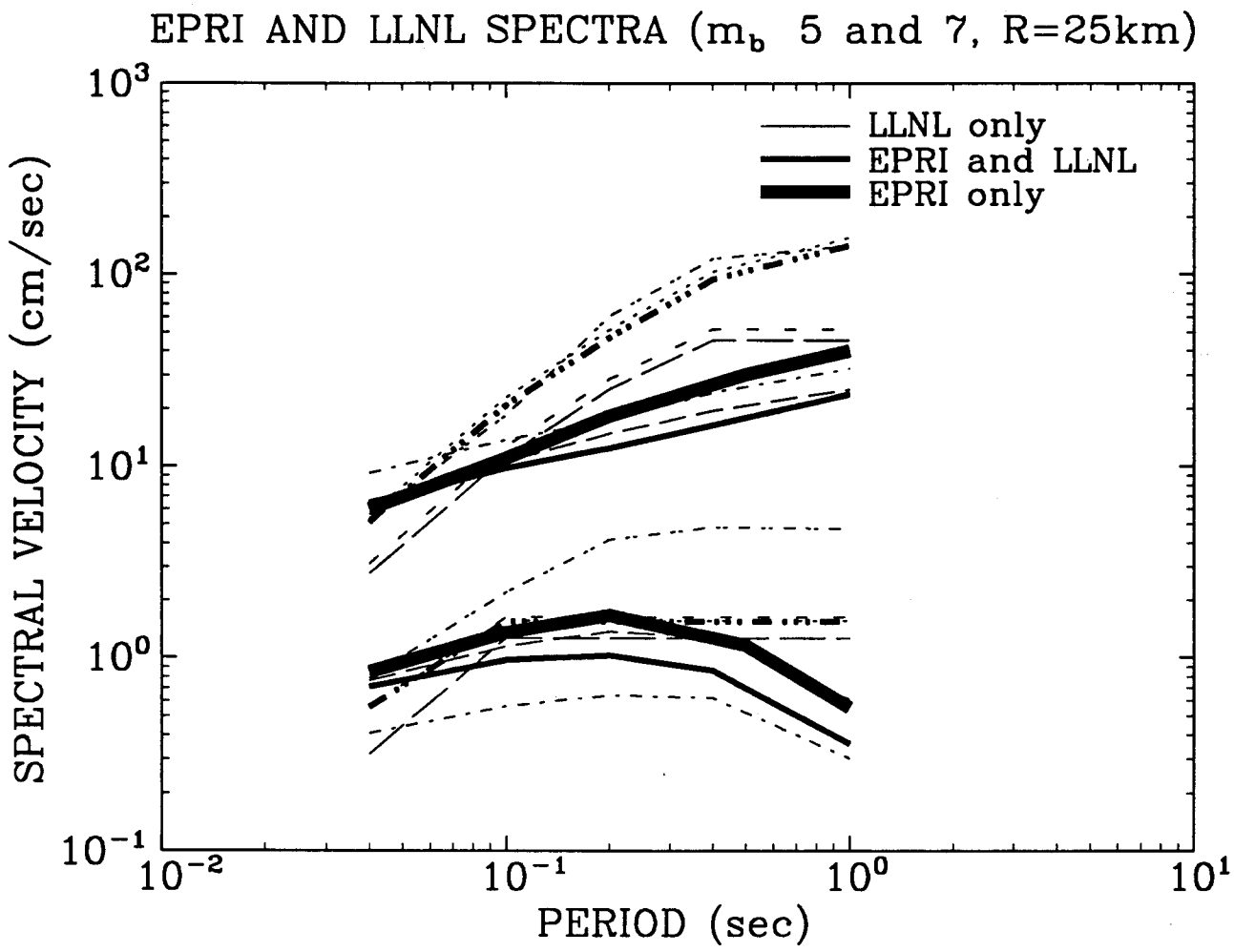

Figure 1-2. Comparison of response data predicted by the EPRI/SOG study (thick and medium lines) and the LLNL study (medium and thin lines). Predictions are shown for m_{Lg} 5 and 7 and a distance of 25 km.

into documenting these uncertainties as we understand them today (e.g. in the EPRI/SOG and LLNL studies).

Because of these significant uncertainties on the causes and characteristics of earthquakes, the concept of a deterministic "design earthquake," in the sense of a worst-case event, is lost. The largest, closest earthquake can only be defined in the context of a tectonic hypothesis, which itself may have high, or low, or exceedingly low credibility. Thus the worst-case earthquake may only have meaning in the context of a probabilistic statement. Further, the worst-case earthquake may be different for high frequencies of the ground motion than it is for low frequencies. Finally, even when earthquake source properties (e.g. magnitude, location, stress drop, and style of faulting) are specified, there is considerable variation of ground motions from site to site at the same distance, so the concept of a maximum earthquake only makes quantitative sense in a probabilistic context.

A probabilistic seismic hazard assessment (PSHA) is intended to integrate over all possible earthquakes in a region, accounting for their relative probabilities of occurrence, to derive probabilities of various levels of ground shaking occurring at a site in a future time interval. Modern PSHAs account explicitly for uncertainties

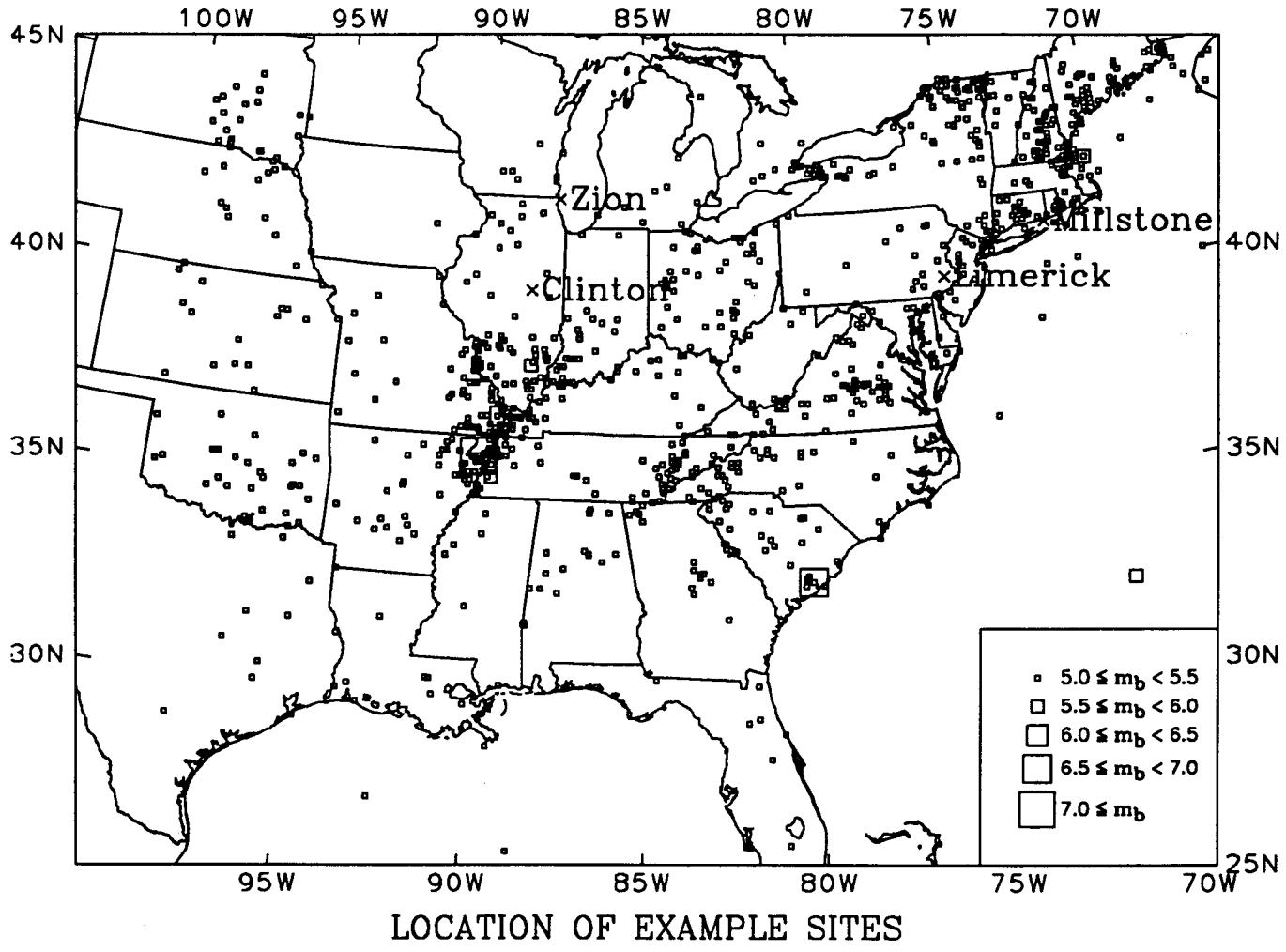

Figure 1-3. Map showing four nuclear-plant sites used to investigate the contribution of various magnitudes and distances to seismic hazard. Also shown is the seismicity in the EPRI catalog.

in earthquake characteristics and in ground motion characteristics, so the deliberate evaluation of ground motion uncertainties and their effects on ground motion prediction is critical. With such information, PSHA can indicate which earthquake magnitudes and distances dominate the hazard at a site for a given frequency and probability level. This can help to focus on ground motion prediction for the right characteristics, and also to help design engineering facilities for the most likely characteristics of earthquake shaking at any probability level.

It is useful to illustrate this point for typical sites in the central and eastern United States and for various measures of ground motion. Figure 1-3 shows the location of four nuclear-plant sites selected for this analysis. Calculations were performed using the EPRI/SOG seismicity interpretations and attenuation functions (for the sake of expediency only the median EPRI/SOG attenuation equation was used). The Millstone and Limerick sites are located in areas of moderate local seismicity, with maximum magnitudes typically lower then m_{Lg} 6.5. These sites are typical of the eastern seaboard. The

Clinton and Zion sites are located in areas of relatively low seismicity and low maximum magnitudes, at distances of 300 to 600 km from the New Madrid seismic zone. These sites are typical of midwestern sites within a 600 km radius from the New Madrid zone, which has the highest rate of seismicity in the United States Stable Continental Region.

Figures 1-4 and 1-5 show the contribution to the hazard for peak ground acceleration (PGA), by magnitude and distance, for the Millstone and Clinton sites. Most of the hazard comes from magnitudes lower than 6.5 and distances smaller than 50 km.

Figures 1-6 and 1-7 show the same type of results for 1-Hz spectral velocity. This relatively low-frequency measure of ground motion differs from PGA in that it has a stronger dependence on magnitude and a somewhat weaker dependence on distance. Also, the results are very different between the two sites. For Millstone, the contributions to the hazard are shifted to somewhat higher magnitudes and longer distances. For Clinton, nearly all the hazard comes from large earthquakes in the New Madrid seismic zone.

These results are useful for identifying which parameters in ground-motion models deserve the most attention from an engineering standpoint. Because high-frequency (>5Hz) ground motions are most important for nuclear-plant structures and equipment, the most effort should go into refining ground-motion estimates for magnitudes 5.0 to 6.5 and distances less than 50 km. Issues such as stress drop variability and site response are important in this magnitude-distance range.

Though somewhat less critical than high-frequency ground motions, ground motions at frequencies of 1 to 5 Hz are still important for certain nuclear-plant structures (and for equipment mounted on those structures, see Toro et al., 1988). Significant effort should go into refining low-frequency ground-motion estimates from large earthquakes at distances up to several hundred kilometers. Issues such as source scaling, Lg wave propagation, and anelastic attenuation (for frequencies near 1 Hz only) are important in this magnitude-distance range.

Considerable emphasis is placed in this study on the development of well-quantified soil amplification factors and in the development of guidelines for geotechnical site characterization. Because of significant advances in methodologies in this area, it is evident that large benefits in reducing conservatism in ground motion estimation are gained through investigation of site properties.

1.4 Regulatory Perspective

The Standard Review Plan of the USNRC (1990) for vibratory ground motion identifies a hierarchy of approaches considered appropriate for the estimation of seismic ground motion at a site:

1. The direct use of recorded ground motions to develop a statistical basis for estimation of design response spectra from multiple records of similar magnitudes, distances, and site conditions.
2. The use of scaled, recorded ground motions that have been adjusted to account for differences in magnitude, distance, and site conditions from those to be used for design.
3. Estimation of peak motion parameters (peak acceleration, velocity, and displacement) using *state-of-the-art* relationships appropriate for the region of study, and development of response spectra using standard spectral shapes scaled to those peak parameter values. Estimating motions by using correlations between ground motion parameters and MMI is discouraged because of the lack of data at the higher intensities.
4. The use of theoretical-empirical modeling of ground motion, when the input parameters and the appropriateness of the model are well-documented.

The development of this hierarchy was based on the underlying assumption that earthquake ground motions in the EUS and in California are similar, at least in the near field. Recent recordings however have shown that motions in the two regions differ, so it is not appropriate to use empirical data from California to represent EUS ground motions. Further, the direct empirical observations in the EUS at high levels of ground motion are too sparse to justify a data-based approach in that region.

For these reasons, it is necessary to use the theoretical-empirical modeling method in the EUS. This approach uses a theoretical model to estimate ground motion amplitudes in the frequency band of interest to engineering analysis and design, a model that has been validated using data largely from California where instrumental

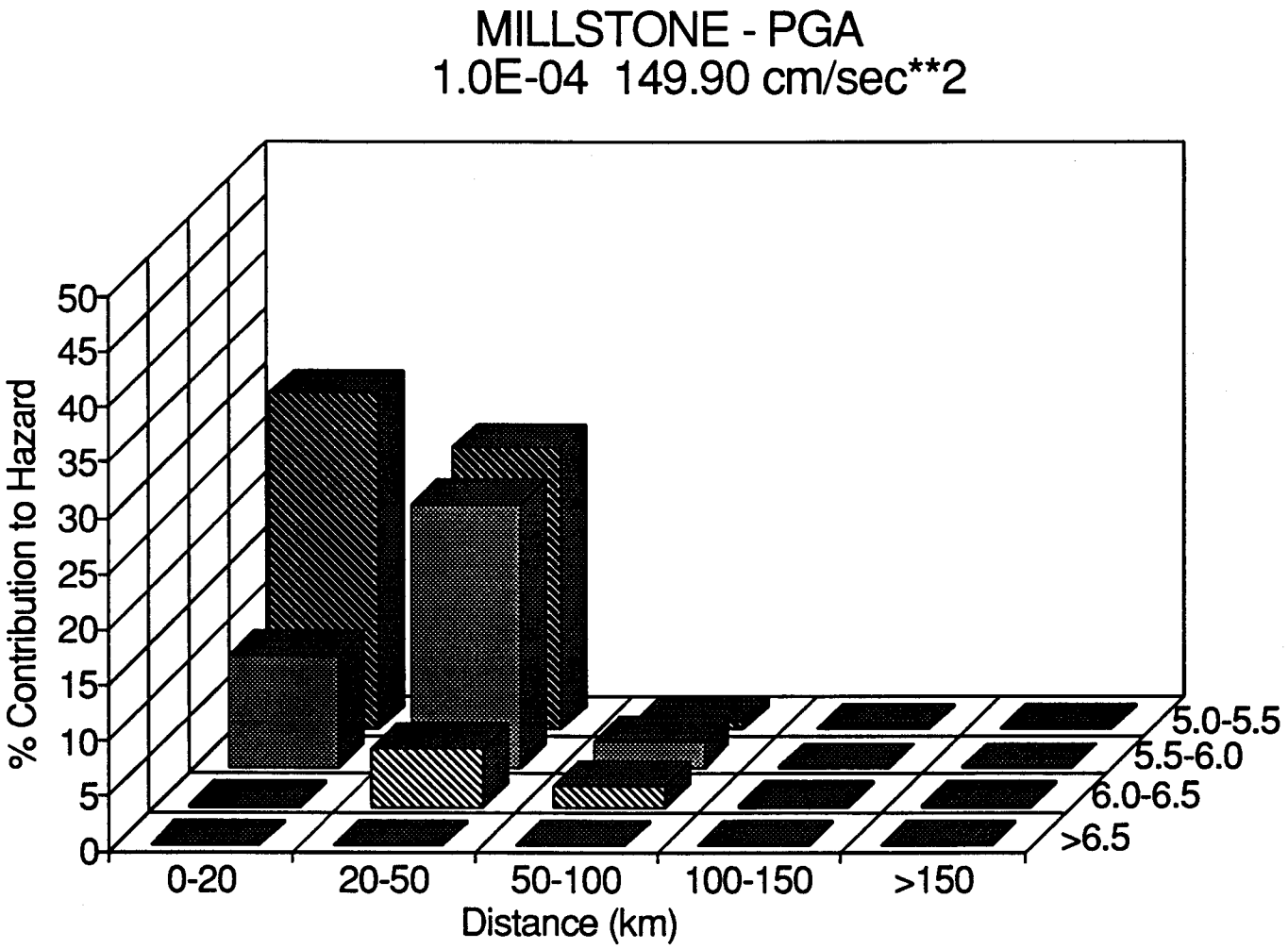

	Distance					
Magnitude	0-20	20-50	50-100	100-150	>150	All Dists.
5.0-5.5	30.3	25.3	0.7	0.0	0.0	56.3
5.5-6.0	10.2	23.7	2.4	0.0	0.0	36.3
6.0-6.5	0.0	5.3	2.0	0.1	0.0	7.3
<6.5	0.0	0.0	0.1	0.1	0.0	0.2
All Mags.	40.5	54.2	5.1	0.1	0.0	

Figure 1-4. Contribution to hazard at 10^{-4} annual exceedance probability, by magnitude and distance: PGA at the Millstone site.

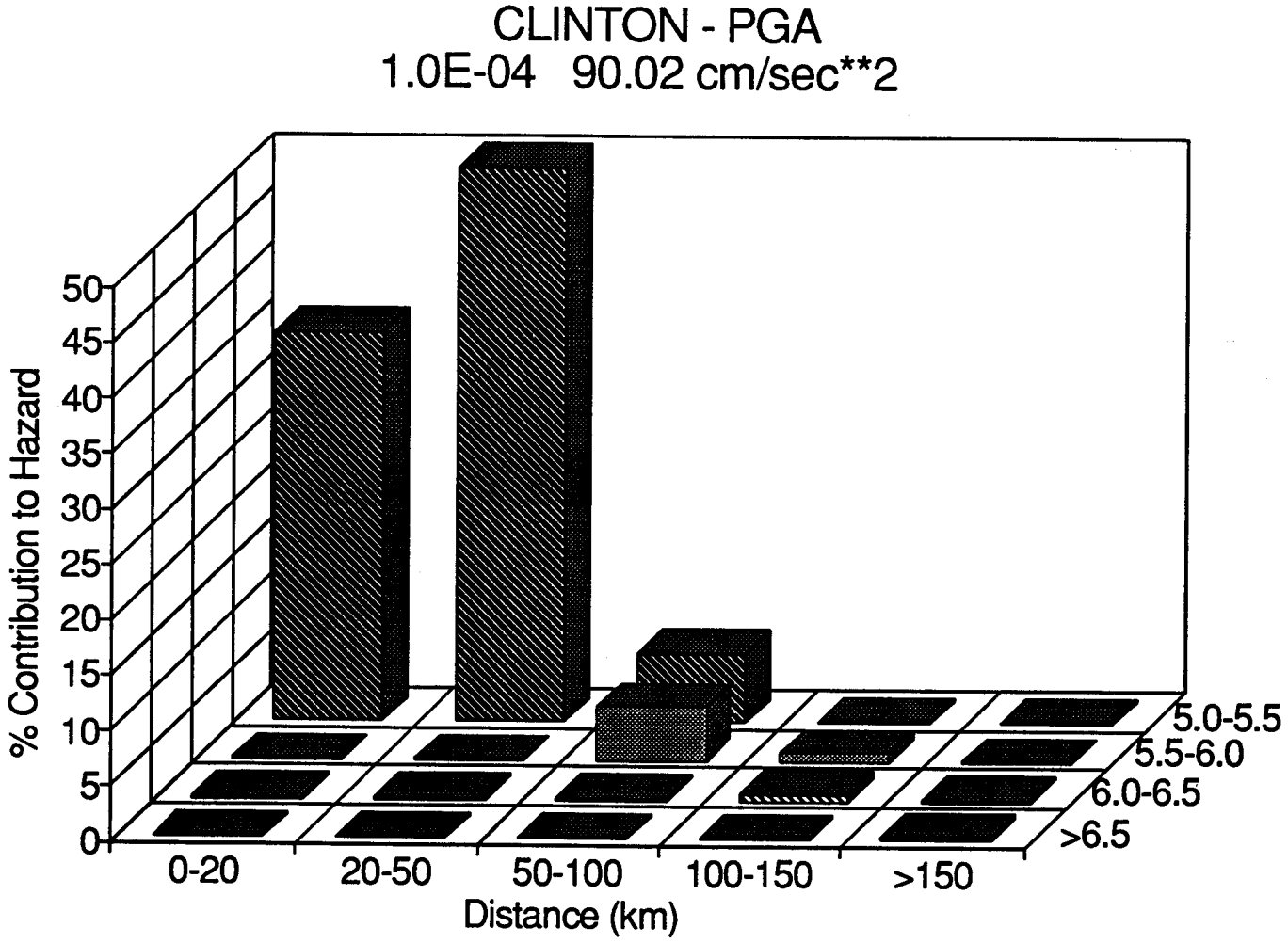

	Distance (km)					
Magnitude	0-20	20-50	50-100	100-150	>150	All Dists.
5.0-5.5	35.0	52.0	6.2	0.1	0.0	93.2
5.5-6.0	0.0	0.0	4.9	0.8	0.0	5.7
6.0-6.5	0.0	0.0	0.0	0.5	0.2	0.7
<6.5	0.0	0.0	0.0	0.0	0.3	0.3
All Mags.	35.0	52.0	11.0	1.5	0.5	

Figure 1-5. Contribution to hazard at 10^{-4} annual exceedance probability, by magnitude and distance: PGA at the Clinton site.

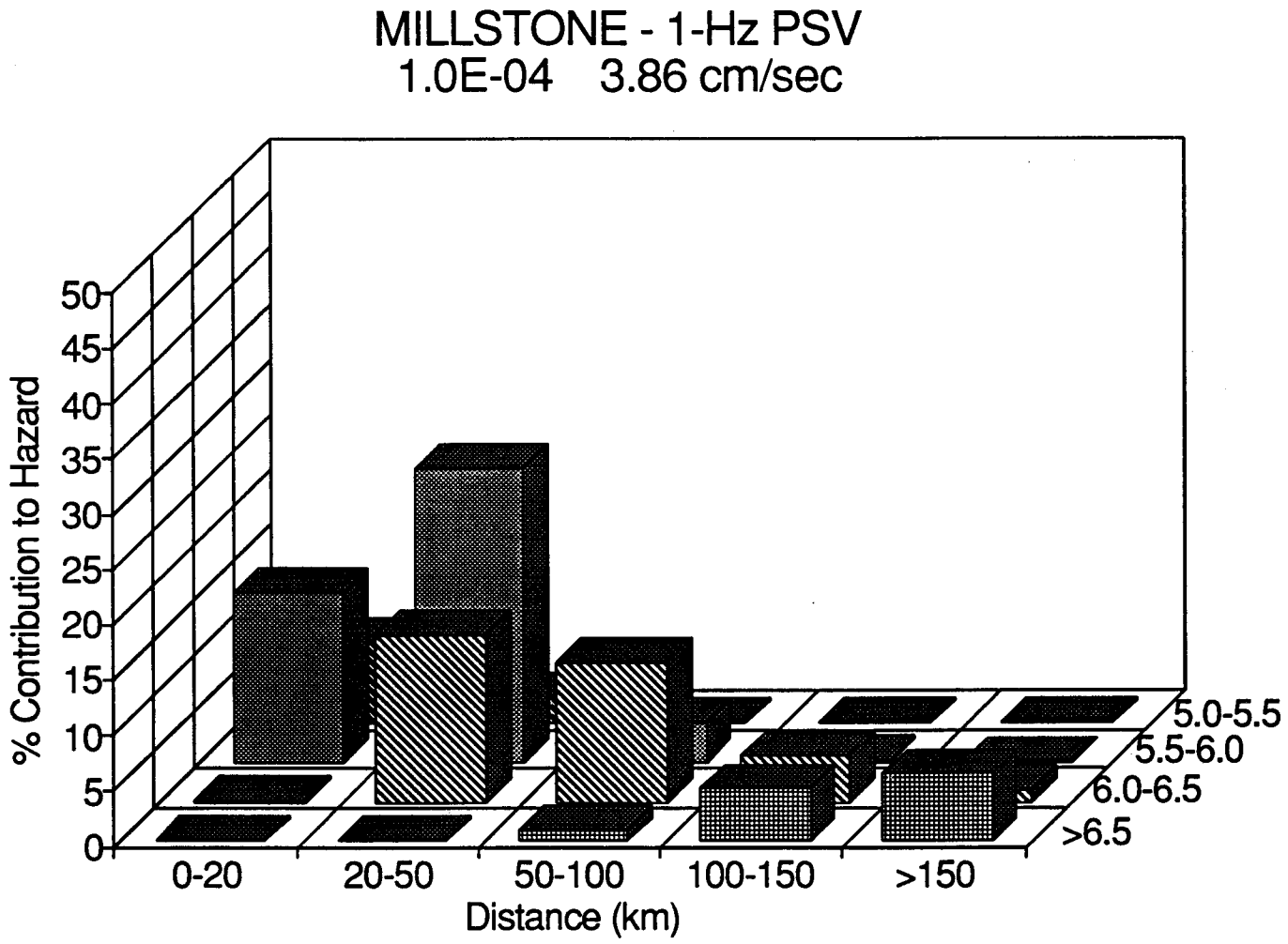

	Distance					
Magnitude	0-20	20-50	50-100	100-150	>150	All Dists.
5.0-5.5	7.4	2.4	0.0	0.0	0.0	9.9
5.5-6.0	15.4	26.7	3.6	0.2	0.0	45.9
6.0-6.5	0.0	15.0	12.5	4.1	1.0	32.6
<6.5	0.0	0.0	1.0	4.7	6.0	11.7
All Mags.	22.8	44.2	17.1	8.9	7.0	

Figure 1-6. Contribution to hazard at 10^{-4} annual exceedance probability, by magnitude and distance: 1-Hz spectral velocity at the Millstone site.

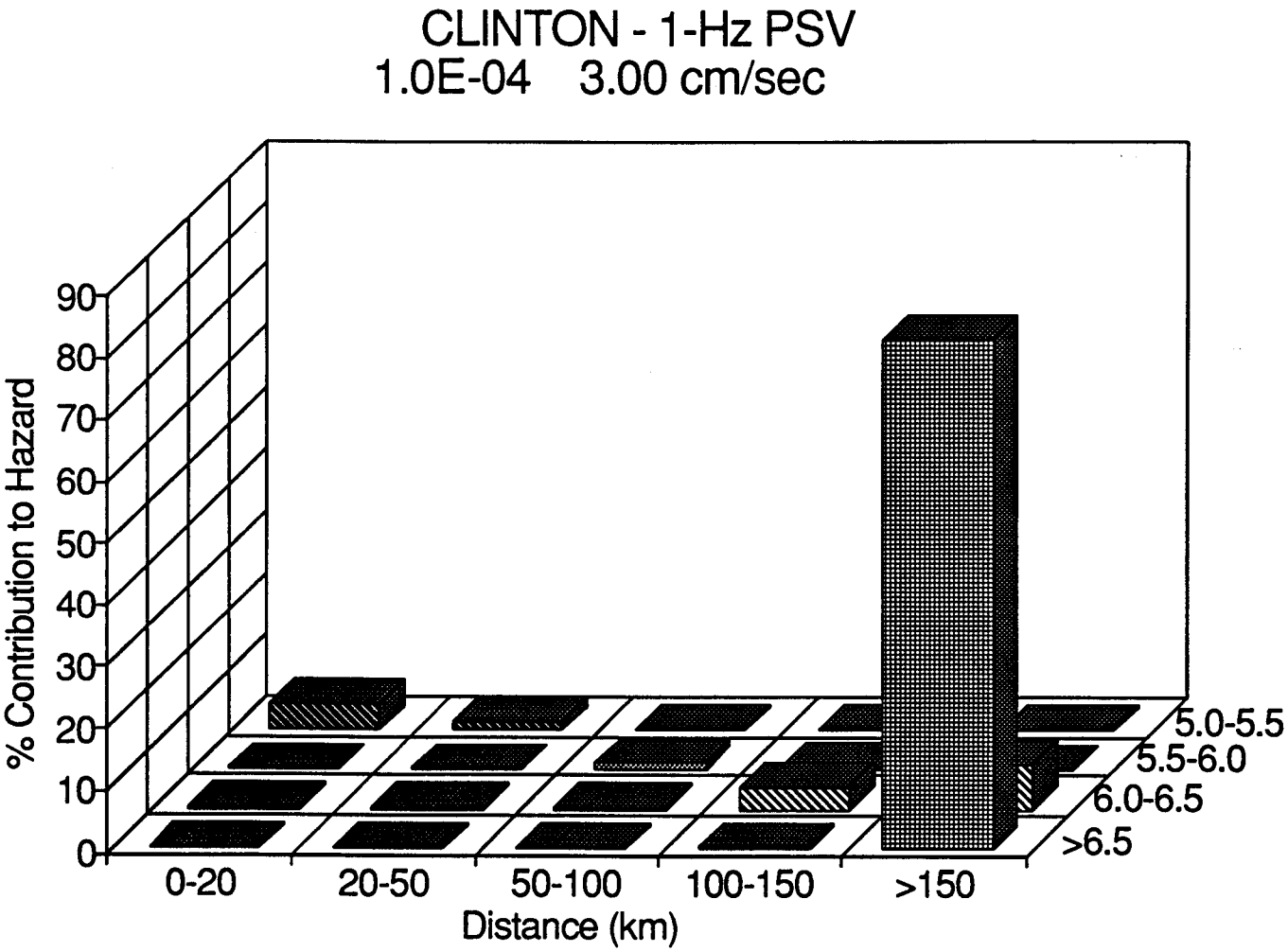

	Distance (km)					
Magnitude	0-20	20-50	50-100	100-150	>150	All Dists.
5.0-5.5	4.0	1.2	0.0	0.0	0.0	5.2
5.5-6.0	0.0	0.0	0.9	0.4	0.1	1.4
6.0-6.5	0.0	0.0	0.0	3.7	7.2	10.9
<6.5	0.0	0.0	0.0	0.3	82.2	82.5
All Mags.	4.0	1.2	1.0	4.5	89.4	

Figure 1-7. Contribution to hazard at 10^{-4} annual exceedance probability, by magnitude and distance: 1-Hz spectral velocity at the Clinton site.

records are available over a wide range of magnitudes and distances. The model is adjusted to reflect properties of the earth in the EUS, and is checked to verify that it is accurate at low levels of shaking in the EUS where instrumental records are abundant. Thus there is confidence that the extrapolation to higher levels of ground motion is reasonable, within the uncertainties documented by the model. In fact, there is no other defendable way to estimate ground motions for the region; the use of MMI introduces uncertainties that can be neither quantified nor resolved because of the observational, subjective, regionally-dependent nature of the scale, and the use of peak motion parameters requires adopting spectral shapes from California that may be deficient at certain frequencies. Moreover, peak motion parameters reduce information about the ground motion (such as duration and frequency content) to one or two values, thus greatly restricting the information available.

The theoretical-empirical approach adopted here is the most appropriate method to estimate earthquake shaking in the EUS. It corresponds to points 2 and 4 in the above hierarchy, where for point 2 the scaling is accomplished by theoretical methods that have been shown to be accurate by comparison to data. The theoretical-empirical method is preferred because there are no direct instrumental records of ground motion in the EUS at the damaging levels of shaking corresponding to typical NPP seismic design levels, i.e. point 1 in the hierarchy cannot be followed. Also, point 3 is not preferred, because spectral and duration differences between California ground motions and those of the EUS mean that standard spectral shapes based on empirical, California data should not scaled for use in the EUS.

In addition to the hierarchy on preferred approaches, the Standard Review Plan (1990) identifies attributes that are judged to be important to any ground motion model, with the highest acceptability given to the model with the most attributes.

These are:

1. ability to describe the full response spectrum,
2. ability to provide a full description of the uncertainty (median, mean, and fractiles),
3. ability to account for site effects,
4. ability to estimate time histories of motion,
5. ability to estimate duration of shaking and number of strong motion cycles,
6. ability to define ground motion at different elevations, and
7. ability to incorporate effects of material property variations.

The model developed here has all of the above attributes, and in fact goes further than any previous model in its ability to provide a complete description of seismic ground motion and its uncertainty for analysis and design.

Currently, the only regulatory guidance for geotechnical site characterization is given in R.G. 1.132 (USNRC, 1977), "Site Investigations for Foundations of Nuclear Power Plants." This guidance is limited to a general description of the types of geotechnical investigations that are recommended for assessment of foundation stability. First, considerable advances have been made in these methods in the past 15 years that warrant including in new guidance criteria. Second, R.G. 1.132 does not bridge the gap from site geotechnical issues in foundation engineering to seismological issues in determining the design basis ground motion. A coordinated effort is needed to generate optimally a set of geotechnical data (a) for input to a dynamic analysis of site response, and (b) for estimation of the design basis ground motion. Therefore, this study develops a complete guideline for consideration as a new regulatory guide on site response analysis and geotechnical site characterization. The guideline draws extensively on lessons learned from the development of test cases as well as on extensive review of recent literature.

1.5 Significant Ground Motion Issues

Several issues are perceived as significant to the estimation of seismic shaking in the EUS. They may or may not be significant in the estimation of seismic hazard at a particular site, depending on the areal sources, magnitudes, and distances affecting that site, and depending on the frequency range of engineering interest.

1.5.1 Source Issues

Information about seismic source characteristics of eastern North American earthquakes is available from teleseismic and regional seismograms of all of the larger events that have occurred since the 1920s. The information available at longer periods (1 second and longer) is

sufficient to make comparisons of this set of earthquakes with those of other stable continental regions and with those of tectonically active regions. Recent analyses indicate that the Brune stress drop (Brune, 1970, 1971) of these events, which reflects the overall duration of the source rupture and the average rate of release of seismic moment, is about 100 bars on average (Somerville et al., 1987; Boatwright and Choy, 1992). These stress-drop estimates are largely constrained by teleseismic recordings that are deficient in high-frequency energy. However, when we wish to prescribe source characteristics at frequencies above 1 Hz, which are relevant to the seismic design of nuclear power plants, our data base is much more sparse because we have few nearby, on-scale seismograms that are rich in high frequencies. To extrapolate our teleseismic Brune stress drop estimates for these larger earthquakes to higher frequencies, we need a model of the spectral shape. There is evidence that a spectral model having two corners (Atkinson, 1993) may be more appropriate than a Brune model having a single corner. We would like to resolve which model is more appropriate, and if this cannot be clearly resolved then we need to know whether these different spectral models could produce significant differences in predicted ground motion amplitudes. Some further constraint on spectral amplitudes at high frequencies comes from data from smaller magnitude earthquakes, but to extrapolate to the larger earthquakes of interest requires knowledge of spectral scaling with magnitude.

Strong ground motions are influenced by a large number of aspects of source finiteness in addition to the Brune stress drop. As the size of the fault rupture increases, we expect that the rate of attenuation of strong ground motion as a function of closest distance to the rupture will tend to decrease at close distances, producing a magnitude-dependent shape. Also, the finiteness of the fault will produce azimuthal variation of ground motion amplitudes at a given closest distance due to the orientation of the fault (e.g. foot wall/hanging wall differences), and the geometry of rupture initiation and evolution on the fault plane (rupture directivity). Additional sources of variation are the geometry of the fault and the focal mechanism of the earthquake, which determine its radiation pattern. In order to fully incorporate the uncertainty in predicted ground motions, the site-to-site and event-to-event variations must be considered. Site-to-site variations are incorporated in this study in the modeling variability (Section 3), and event-to-event variations are incorporated through variations in source parameters such as effective stress drop.

The size of the earthquake is characterized by seismic moment in source models used to predict ground motion attenuation. However, in the earthquake catalog for the eastern United States, seismic moments are generally not known for the older and smaller events. In this situation, we need either to convert Lg magnitude (m_{Lg}) estimates to seismic moment, or to develop a procedure for characterizing source size in terms of m_{Lg} in the ground motion model. Empirical relationships between seismic moment and m_{Lg} have been developed, but are subject to some uncertainty due to the small numbers of events that constrain the relationship at large magnitudes, and large uncertainties in some seismic moment estimates, especially those derived from spectral analysis. Relationships have been developed between seismic moment and m_{Lg} based on ground motion models, but it is necessary to demonstrate that relationships derived solely from the model are compatible with empirical data.

1.5.2 Path Issues

Traditionally, ground motion attenuation relations have been developed using regression of recorded ground motion data. In this approach, the only parameters relating to the path between the seismic source and the recording site have been the length of the path and in some instances the focal depth, and it has not been necessary to inquire into the physics of wave propagation in the earth's crust. Recorded ground motions in the EUS show that there are clear differences in path effects in this region from path effects in California. This is illustrated in Figure 1-8, which compares recorded ground motions from the Whittier, California earthquake and the Saguenay, Ontario earthquake, both about magnitude 5.8. While there are no close data for Saguenay, recordings in the distance range 50 to 100 km clearly indicate differences in amplitudes for the high frequencies. Unfortunately the EUS ground motion data set is not large enough for the empirical approach to be effective in resolving regional variations, effects of focal depth, near-surface effects, and other factors, so it is necessary to use physical models of seismic wave propagation to guide the development of attenuation relations.

In the simplest wave propagation models, in which crustal structure is modeled by a plane layered medium, the gross crustal structure controls the geometrical spreading of waves from the source and hence the shape of the attenuation curve. At close distances, ground motions are dominated by the direct shear wave, whose geometrical spreading is controlled by the velocity gradient above the source. At larger distances, ground motions are dominated by diving rays, and the depths and velocity gradients in the lower crust control the geometrical spreading of these diving rays that are critically reflected back to the surface. We therefore expect the attenuation of ground motion in the distance range of several tens of kilometers to 200 km from the source to be primarily controlled by the earthquake source depth and by the seismic velocity and attenuation structure of the crust. Ground motion attenuation in this distance range is expected to vary with regional variations in plane layered crustal structure models. However, the lateral variations in crustal structure implied by these regional variations may cause departures from the predictions of plane layered models. Also, the scattering that is evident in recorded data is not incorporated in simple wave propagation models, other than by the use of models with quality factor Q, which accounts for both intrinsic absorption and scattering. The presence of scattering in recorded data will also cause departures from the calculations of simple wave propagation models.

Before we use seismic wave propagation models to develop attenuation relations, we need to establish whether there is evidence that wave propagation models provide an adequate explanation of observed ground motion attenuation. This issue can be addressed by the modeling of recorded data and the use of quantitative comparisons between recorded and model results. Since model calculations of ground motion attenuation will result in parametric dependencies on crustal structure (including Q) and focal depth, and perhaps source parameters, further confirmation of the model can be obtained by testing whether these dependencies are observed in recorded data.

Since the effects of geometrical spreading, anelastic absorption, and scattering all contribute to the shape of the attenuation curve, there are tradeoffs involved in the estimation of each from a set of empirical data. Since the effect of anelastic attenuation is relatively small inside 100 km, this tradeoff should not result in a great deal of uncertainty in the major effects of geometrical spreading, such as the effect of critical reflections from the lower crust. However, at distances beyond 100 km, the effects of geometrical spreading and anelastic absorption become comparable to geometrical effects and therefore more difficult to separate. In this situation, it is usually necessary to make certain assumptions about the form of the anelastic absorption function or the rate of geometrical spreading at large distances or both in order to estimate the parameters describing these two effects (Atkinson and Mereu, 1992).

A variety of computational procedures are available for representing the effects of wave propagation in a layered crust on ground motion attenuation, most of which require some simplifying assumptions and approximations. These include the frequency-wave number integration method, the generalized ray theory method, and the geometrical ray theory method. We would like to select a method that is relatively simple to use but that avoids approximations and simplifying assumptions that could cause significant bias and uncertainty in predicted ground motion attenuation.

For practical application, we need to identify those regional variations in crustal structure and focal depth that can have a significant effect on ground motion attenuation, especially those for which additional modeling or data can reduce the uncertainty, or change the mean estimate, from those of previous models.

1.5.3 Site Issues

In the development of an integrated site-response methodology, the task is to account for the most significant dynamic properties and geometrical wave propagation effects in a generic procedure. This procedure needs to be complex enough to provide realistic mean estimates and uncertainties of site response, yet simple enough to be used efficiently and effectively in a wide variety of applications. In this context, there are a number of important site effects issues that need to be addressed. These are: 1) the adequacy of a vertically propagating wave model; 2) the applicability of equivalent-linear and nonlinear dynamic soil computational models; 3) the comparison of *in situ* versus laboratory-derived dynamic properties; 4) measurements of damping and the effects of high confining pressures (at deep soil sites); and 5) the extension of site response models from horizontally polarized S waves to vertical motions.

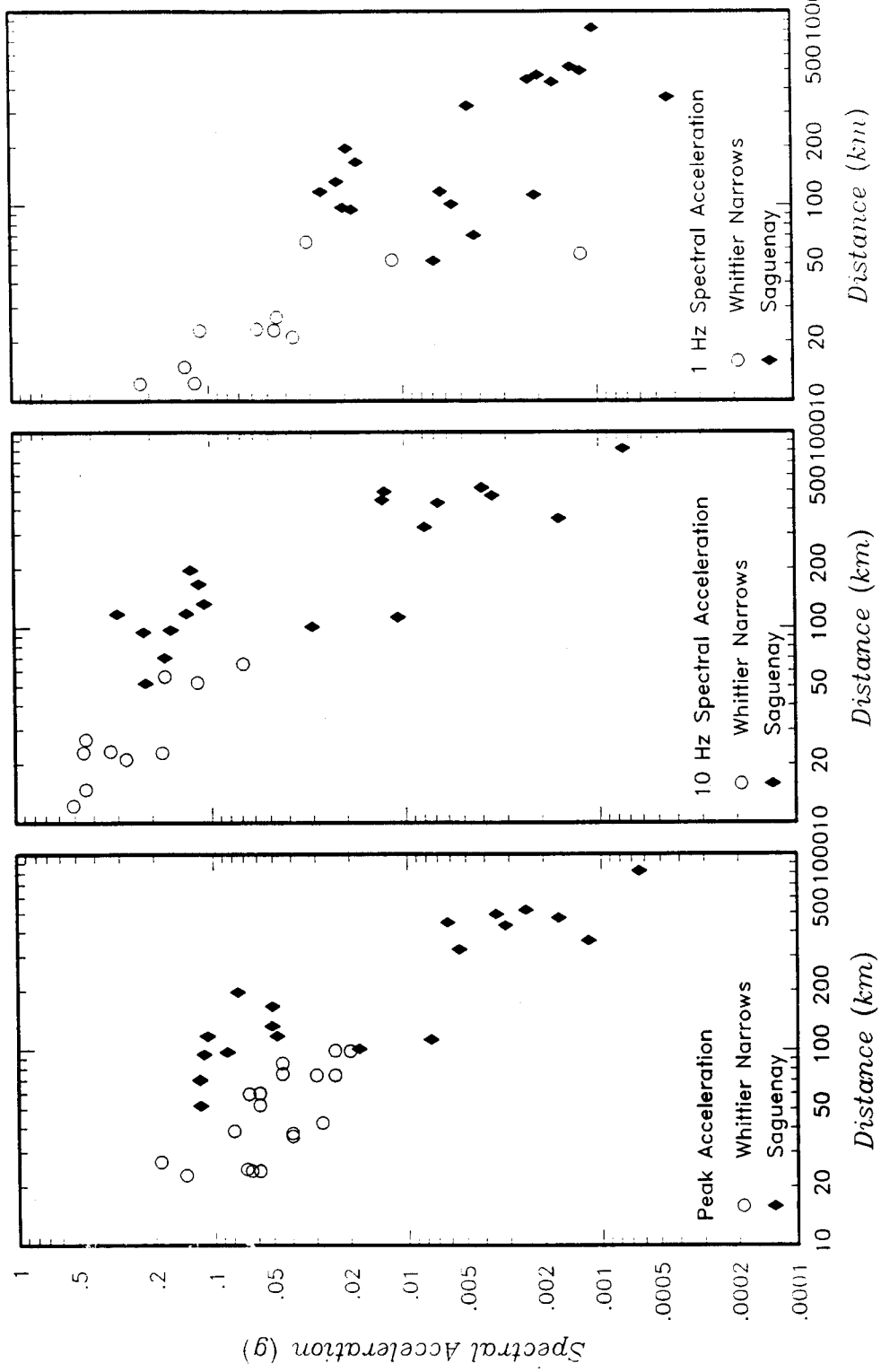

Figure 1-8. Recorded ground motions during Whittier Narrows, California, and Saguenay, Ontario, earthquakes, for peak acceleration and spectral acceleration at 10 and 1 Hz (5% damping).

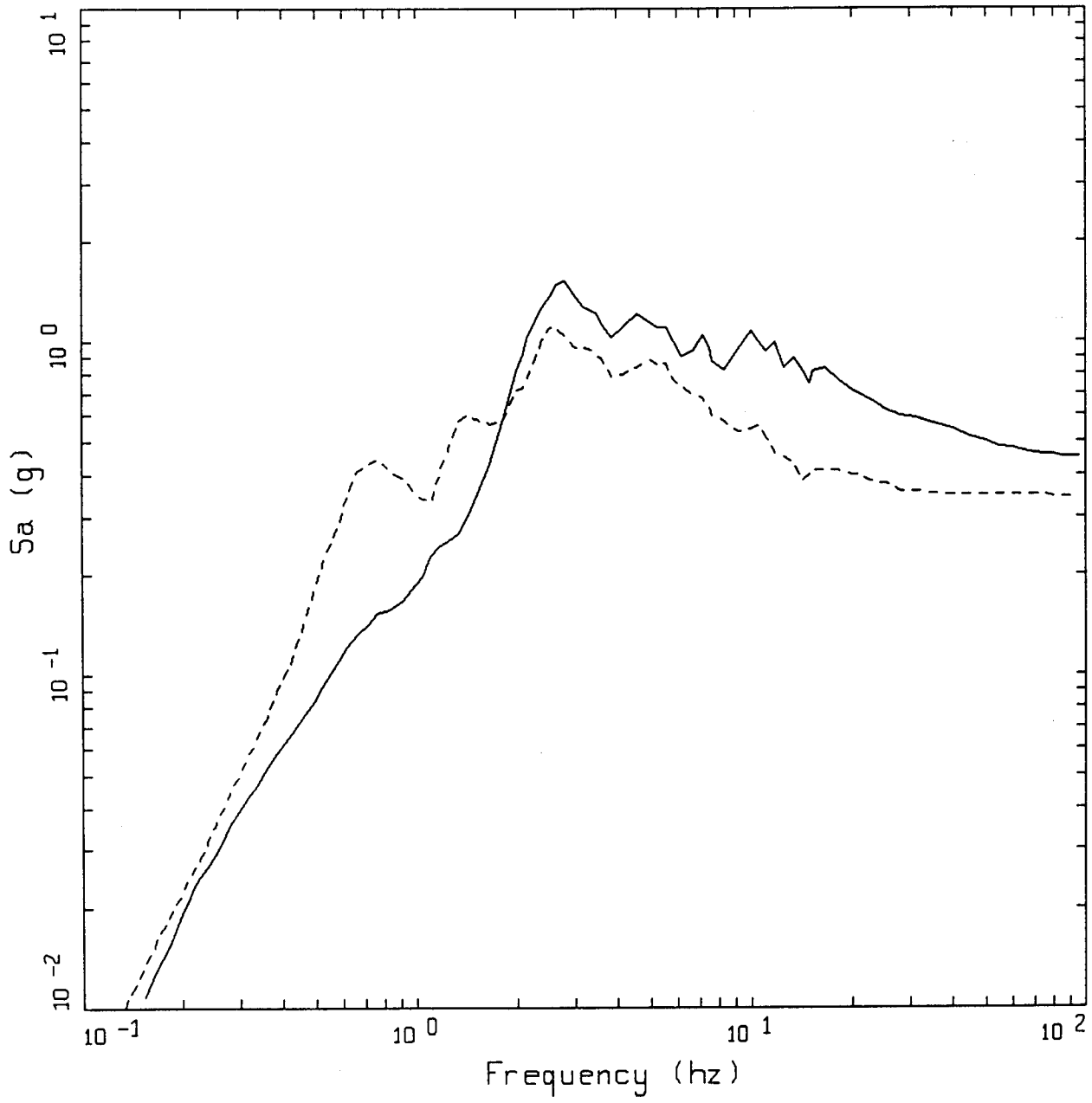

Figure 1-9. Response spectra (5% damped) recorded at Gilroy 1 (rock: solid line) and Gilroy 2 (soil: dashed line) during the 1979 Loma Prieta earthquake (the log average of two horizontal components is plotted).

The difference in spectral content resulting from soil-site effects is dramatic, as illustrated in Figure 1-9. This figure compares response spectra recorded at rock and soil accelerograph stations at Gilroy, California, during the 1979 Loma Prieta earthquake, and illustrates the degree to which near-surface variations in dynamic material properties affect strong ground motions. These effects are dominated by 1-D (i.e. vertical) variations, upon which are superimposed the effects of lateral heterogeneities. Such laterally varying structures as surface

topography, dipping interfaces, and changes in material properties contribute to two- and three-dimensional (2-D and 3-D) aspects of ground motion estimation. These non-homogeneous effects, resulting from scattering, focusing, and mode conversions are present to some extent at all sites. In some cases, such effects can significantly alter the spectral content of ground motions as well as increase the duration of strong shaking. Results of a previous EPRI study have shown that in the bandwidth from several seconds to about 15 Hz approximately 75% of the power that is observed at the surface of sites can be modeled as vertically propagating shear waves (Silva et al., 1988). The remainder must be essentially accounted for in the effects mentioned above. The ground motion model presented in this report is based on a 1-D model of wave propagation. This means that the remainder of the ground motion effects must be treated as random, that is, they contribute to variability but are not explicitly modeled.

As levels of strain increase in soils, the constant relationship between applied stress and resulting strain is no longer valid, resulting in nonlinear soil response. While the effects of nonlinear soil response are reasonably well understood, and different modeling approaches are well calibrated in the range of strong motion observations, models can differ substantially in predicted behavior where well-calibrated data are sparse. A simplified approach to treating this condition is to approximate the response in an equivalent-linear fashion, whereby the equivalent shear modulus and damping are approximated at each strain level and the final response is determined in an iterative fashion. Nonlinear and equivalent-linear codes need to be tested to determine their ranges of applicability and sensitivities to various assumptions of material properties.

In the absence of permanent deformations, the estimation of site response is controlled primarily by the shear modulus and damping of the soil column. These parameters may be constrained by a combination of direct measurements of earthquake motions together with *in situ* and laboratory testing. All have limitations which must be considered in the analysis of data for site response modeling. In particular, dynamic properties needed to predict nonlinear effects are extremely difficult to obtain *in situ*; therefore laboratory procedures have been developed to measure properties from intact borehole samples. Due to unquantified effects of sample disturbance and the physical limitations of extrapolating from small samples to an entire site, the results of these measurements must be treated cautiously. Where possible it is essential to make comparisons between more direct *in situ* measurements and analyses of strong motion records. To this end, this report considers several test cases where strong motion data and *in situ* and laboratory measurements are compared through a variety of analyses.

A significant source of uncertainty in dynamic analyses is the effect of confining pressure on damping; this is extremely important in dynamic analyses of deep soil sites (depths greater than a few hundred ft), where the effects of damping dominate the estimation of amplification (or deamplification). An important contribution of this report is the estimation of damping at high confining pressure. This is accomplished by measuring the effects of confining pressure directly in the laboratory and comparing the low-strain results to damping analyses of bore hole seismic data. Corroboration of these data provides the needed constraints for extending the results to high strain using strong motion data and nonlinear or equivalent-linear models.

The discussion above has focused entirely on horizontal motions generated primarily by S waves. Extension of the methodology to vertical motions is needed, especially at near-source distances. It is commonly assumed that vertical motions are approximately 2/3 horizontal at all source-receiver distances. Growing evidence suggests, however, that vertical motions often exceed horizontal motions at near-source distances (e.g., Niazi and Bozorgnia, 1992). This phenomenon is probably due to non-vertically incident S-wave energy being converted to P waves, which then propagate through the soil column with much lower damping than S waves, particularly at large strains. Under these circumstances, the extent to which vertical motions depart from the 2/3 vertical/horizontal ratio needs to be considered in the design basis. Therefore, in the site response methodology are developed site amplification factors appropriate for vertical motions.

Finally, the conduct of site investigations and site-response analysis for the establishment of a seismic design basis requires careful guidance. Thus, in addition to each of these site issues considered above, this study develops general guidelines for site-specific applications to the siting of critical facilities.

1.6 Organization of this Report

This report summarizes work undertaken to understand and estimate strong earthquake shaking and its uncertainty in the EUS. The report is divided into 10 sections, many of which have extensive supportive data, theory, and analyses contained in appendices. Section 2 describes data available from the region with which to test and calibrate models of shaking. This is a very general model that has been shown to be applicable to a wide range of earthquake ground-motion estimation problems. Most of these data are for small magnitudes or large distances and do not fall under the category of "strong shaking," but they provide a basis to assess the credibility of the models being proposed, for the ranges of magnitudes and distances where data are available. Section 3 describes the theoretical ground motion model including wave propagation, which is based on RVT, and the model used to predict the effects of surficial soils, which is based on a vertically-propagating shear wave representation of the shaking. Volume 5, summarized in Section 4, describes how the seismic source is quantified for the purposes of this methodology. The representation of the energy content of the source, and how the source spectrum (stress drop and corner frequencies) changes with magnitude, are addressed here. Section 5 describes how crustal path effects are incorporated into the ground motion model, including possible reflections of seismic energy from deep layers and contributions from surface waves. Both Sections 4 and 5 describe what uncertainties are important in the estimation process and how they are handled by the recommended procedure. Sections 6, 7, and 8 represent the site effects portion of the report. Section 6 quantifies the effects of local soils in modifying the characteristics of ground shaking, again describing the critical uncertainties and how they are treated. Section 7 presents a geotechnical guideline for acquiring site-specific data and for conducting a site response analysis. Section 8 describes the development of *in situ* and laboratory data and analysis methods from specific test sites examined in detail in the course of this project. The results of this section are used extensively to develop the geotechnical guidelines in Section 7 and the site amplification model in Section 6. The final recommended procedures for generic application developed primarily in Sections 4, 5, and 6 are integrated in Section 9, which summarizes the recommendations as the "Engineering Model of Strong Ground Motion," including treatment of uncertainty. This section also includes comparisons of predictions to data and to other estimates of ground motion in the EUS. Finally, Section 10 draws conclusions from the study on the physical processes that are active, how these are treated by the recommended model, and how uncertainties are handled by the procedure.

References

Algermissen, S.T., D.M. Perkins, P.C. Thenhaus, S.L. Hanson, and B.L. Bender (1982). Probabilistic estimates of maximum acceleration and velocity in rock in the contiguous United States, US Geol. Survey Open-File Rept. 82-1033, 99p.

Atkinson, G.M. (1984). Attenuation of strong ground motion in Canada from a random vibrations approach, *Bull. Seis. Soc. Am.*, 74:2629–2653.

Atkinson, G.M. and R.F. Mereu (1992). The shape of ground motion attenuation curves in southeastern Canada, *Bull. Seis. Soc. Am.*, 82:2104–2032.

Atkinson, G.M. (1993). Earthquake ground motion studies in eastern North America, in preparation.

Barker, J.S., P.G. Somerville and J.P. McLaren (1989). Modeling ground motion attenuation in eastern North America, *Tectonophysics*, 167:139–149.

Bernreuter, D.L, J.B. Savy, R.W. Mensing, and D.H. Chung (1987). Development of eastern United States ground motion models, Rept. NUREG/CR-3756, US Nuclear Reg. Comm.

Bernreuter, D.L., J.B. Savy, R.W. Mensing, J.C. Chen, and B.C. Davis (1985). Seismic hazard characterization of the eastern United States, Tech. Rept. LLNL UCID-20421, Lawrence Livermore Nat. Lab., 2 vol.

Boatwright, J., and G.L. Choy (1992). Acceleration source spectra anticipated for large earthquakes in northeastern North America, *Bull. Seis. Soc. Amer.*, 82:660–682.

Bollinger, G.A. (1977). Reinterpretation of the intensity data for the 1886 Charleston, South Carolina earthquake, US Geol. Survey Prof. Paper 1028.

Boore, D.M., and G.M. Atkinson (1987). Stochastic prediction of ground motion and spectral response parameters at hard-rock sites in eastern North America, *Bull. Seis. Soc. Am.*, 7:440–467.

Boore, D.M. (1983). Stochastic Simulation of High-Frequency Ground Motions Based on Seismological Models of the Radiated Spectra, *Bull. of Seism. Soc. of Amer.*, 73:1865–1984.

Brune, J.N. (1970). Tectonic stress and the spectra of seismic shear waves from earthquakes, *Jour. Geophys. Res.*, 75:4997–5002.

Brune, J.N. (1971). Correction. *Jour. Geophys. Res.*, 76:5002.

Burger, R.W., P.G. Somerville, J.S. Barker, R.B. Herrmann, and D.V. Helmberger (1987). The effects of crustal structure on strong ground motion attenuation relations in eastern North America, *Bull. Seism. Soc. of Amer.*, 77:420–439.

EPRI/SOG (1988). *Seismic hazard methodology for the central and eastern United States, Revised, Elect. Power Res. Inst. and Seismicity Owners Group*, Report NP-4726A, Elec. Power Res. Inst., Palo Alto, 10 vol.

Gupta, I.N. and O.W. Nuttli (1976). Spatial attenuation of intensities for central US earthquakes, *Bull. Seis. Soc. Am.*, 66:743–751.

Hanks, T.C. and A.C. Johnston (1992). Common features of the excitation and propagation of strong ground motion for North American earthquakes, *Bull. Seis. Soc. Am.*, 82:1 January 1–23.

Hanks, T.C. and R.K. McGuire (1981). The Character of High-Frequency Strong Ground Motion, *Bull. Seism. Soc. of Amer.*, 71:2071–2095.

McGuire, R.K., A.M. Becker, and N.C. Donovan (1984). Spectral Estimates of Seismic Shear Waves. *Bull. Seism. Soc. of Amer.*, 74:1427–1440.

McGuire, R.K., G.R. Toro, and W.J. Silva (1988). *Engineering model of earthquake ground motion for eastern North America*, Rept. NP-6074, Elec. Power Res. Inst., Palo Alto.

Murphy, J.R., and L.J. O'Brien (1977). The correlation of peak ground acceleration amplitude with seismic intensity and other physical parameters, *Bull. Seis. Soc. Am.*, 67:877–915.

Newmark, N.M., J.A. Blume, and K.K. Kapur (1973). Seismic design spectra for nuclear power plants, *Jour. Power Div.*, Amer. Soc. Civil Engrs., 287–303.

Niazi, M. and Y. Bozorgnia (1992). Behavior of near-source vertical and horizontal response spectra at Smart-1 array, Taiwan, *Earthq. Eng. Struc. Dyn.*, 21:37–50.

Nuttli, O.W. (1979). The relation of sustained maximum ground acceleration and velocity to earthquake intensity and magnitude, *State of the art for assessing earthquake hazards in the United States, Report 16*, Misc. Paper S-73-1, US Army Eng. Waterways Exp. Station, Vicksburg, MS.

Silva, W., T. Turcotte, and Y. Moriwaki (1988). *Soil response to earthquake ground motion*, Elec. Power Res. Inst., Report NP-5747, Palo Alto.

Silva, Walter J. (1991). *Site geometry and global characteristics, in Proc.: NSF/EPRI Workshop on Dynamic Soil Properties and Site Characterization*, Elec. Power Res. Inst., Rept NP-7337, 1, p. 6-1 to 6-80.

Somerville, P.G., J.P. McLaren, L.V. LeFevre, R.W. Burger, and D.V. Helmberger (1987). Comparison of source scaling relations of eastern and western North American earthquakes, *Bull. Seis. Soc. Am.*, 77:1, April, 322–346.

Somerville, P.G., J.P. McLaren, C.K. Saikia, and D.V. Helmberger (1990). The November 25, 1988 Saguenay, Quebec earthquake: source parameters and the attenuation of strong ground motion, *Bull. Seism. Soc. of Amer.*, 80:1118–1143.

Taylor, J.M. (1991). Conclusions of the probabilistic seismic hazard studies conducted for nuclear power plants in the eastern United States, US Nuclear Reg. Comm. Policy Issue SECY-91-135, May 14.

Toro, G.R., and R.K. McGuire (1987). An investigation into earthquake ground motion characteristics in eastern North America, *Bull. Seis. Soc. Am.*, 77:468–489.

Toro, G.R., R.K. McGuire, and W.J. Silva (1988). *Engineering model of earthquake ground motion for eastern North America, Elec. Power Res. Inst.*, Report NP-6074, Palo Alto, Oct.

Trifunac, M.D., and G.A. Brady (1975). On the correlation of seismic intensity scales with the peaks of recorded strong ground motion, *Bull. Seis. Soc. Am.*, 65:139–162.

US Nuclear Regulatory Commission (1977). Site investigations for foundations of nuclear power plants, Reg. Guide 1.132.

US Nuclear Regulatory Commission (1990). Standard review plan 2.5.2 for vibratory ground motion, NUREG-0800, Rev. 2.

2

EMPIRICAL GROUND MOTION DATA IN EASTERN NORTH AMERICA

Analyses of empirical strong motion data have provided the bases for most of the ground motion models used in engineering evaluations of earthquake hazards throughout the world. In regions with infrequent earthquakes, such as ENA, empirical models based on recorded strong motion data must be replaced by models based on other shaking measures or by models based on calibrated theoretical/numerical techniques; the latter being the focus of the study presented in this report. What recorded ground motion data that is available for a region then provides a means of evaluating the appropriateness of the developed models. It is therefore important to collect and categorize the available earthquake ground motion data in order to make it useful for evaluating ground motion models.

This section describes the data base of ground motion recordings for ENA earthquakes compiled for this project. The compilation and categorization of the data are discussed first. The data are then examined with regression models to identify the constraints implied by the data on magnitude and distance scaling and ground motion variability. The examination of the variance in the recorded motions provides one measure of the uncertainty in estimating the ground motions from individual events in the ENA. In addition, statistical analysis of strong motion data from active technical environments (e.g., California) were provided to aid in evaluating modeling scaling results. These analyses are presented in Appendix 2C.

2.1 Data Sources and Data Characterization

The earthquake recordings compiled for this project consist of all ground motion recordings obtained on strong ground motion instruments in eastern North America and all seismographic network data from magnitude ~m_b 5.0 and greater earthquakes recorded at distances of 500 km or less. A few smaller events recorded by the Eastern Canadian Telemetered Network (ECTN) that were used to evaluate various numerical modeling studies were also included in the data base. The data bases of the National Center for Earthquake Engineering Research (NCEER) and the National Earthquake Information Center (NEIC) were searched to identify potential ground motion recordings. All identified ground motion records were then entered into a structured data base format described in Appendix 2A. The data base contains information on the earthquake sources (origin time, location, depth, size measures, and focal mechanism), the recording stations (location, instrument housing, site geology), and the recordings (source-to-site distance, record processing parameters, peak accelerations, and 5%-damped spectral accelerations).

Figure 2-1 shows the spatial distributions of earthquakes and recording stations contained in the data base and Figure 2-2 shows the distribution of the horizontal and vertical component data in terms of earthquake magnitude, source-to-site distance, and general site classification. The compiled data base consists of 191 records recorded during 51 earthquakes at 95 sites. Approximately half of the earthquakes are aftershocks or secondary events in earthquake sequences. One hundred five of the records are multicomponent acceleration or velocity recordings and the remainder are vertical component velocity recordings that have been converted to accelerograms. Figures 2-3 through 2-10 show peak 5-percent damped spectral response for selected frequencies plotted versus hypocentral distance for four magnitude intervals.

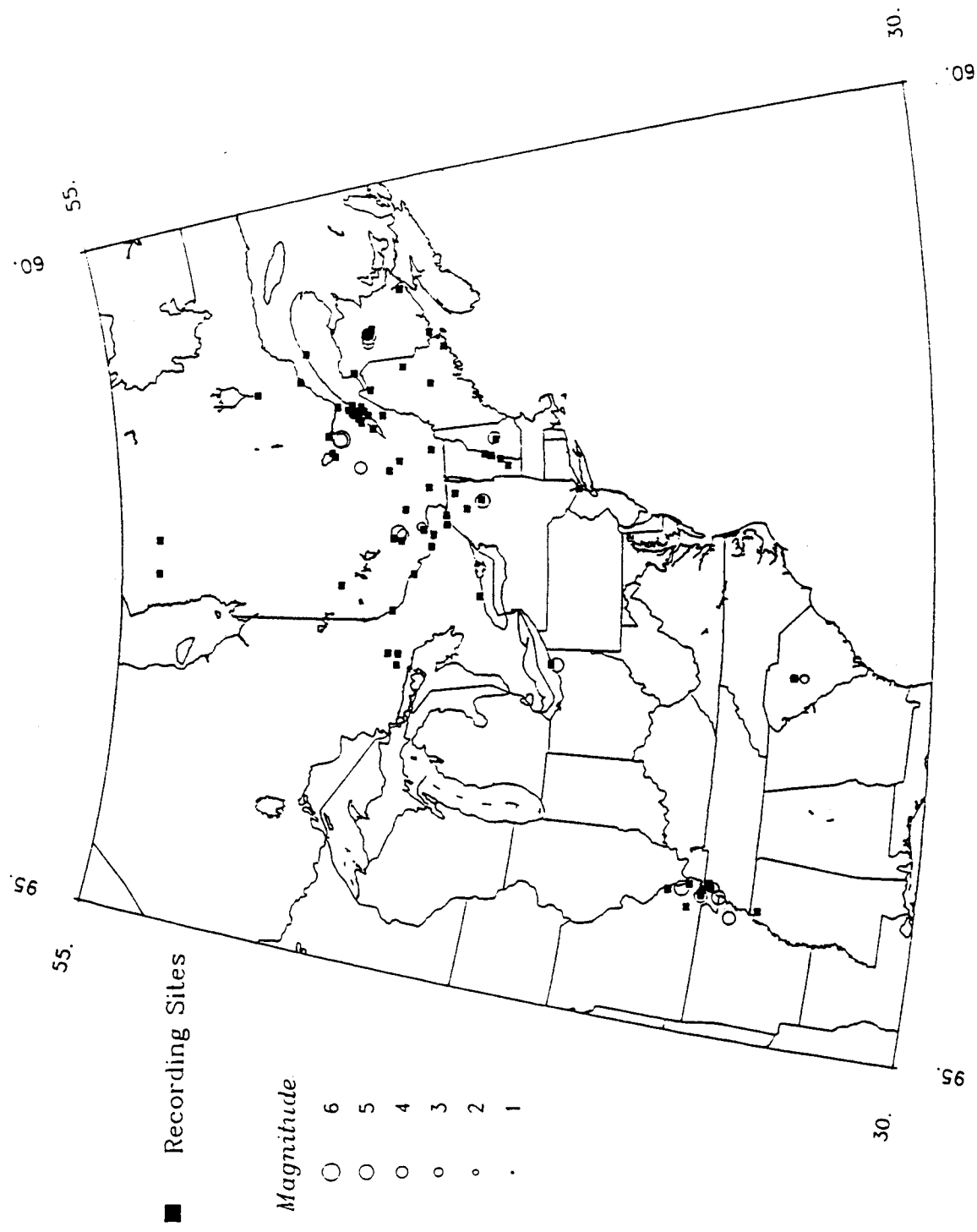

Figure 2-1. Distribution of earthquake epicenters for ground motion data in ENA data base. Earthquake size is indicated by symbol size following the indicated scale. Map scale is 1:20,000,000. Note the Nahanni event is not shown as it lies well to the northwest of the map.

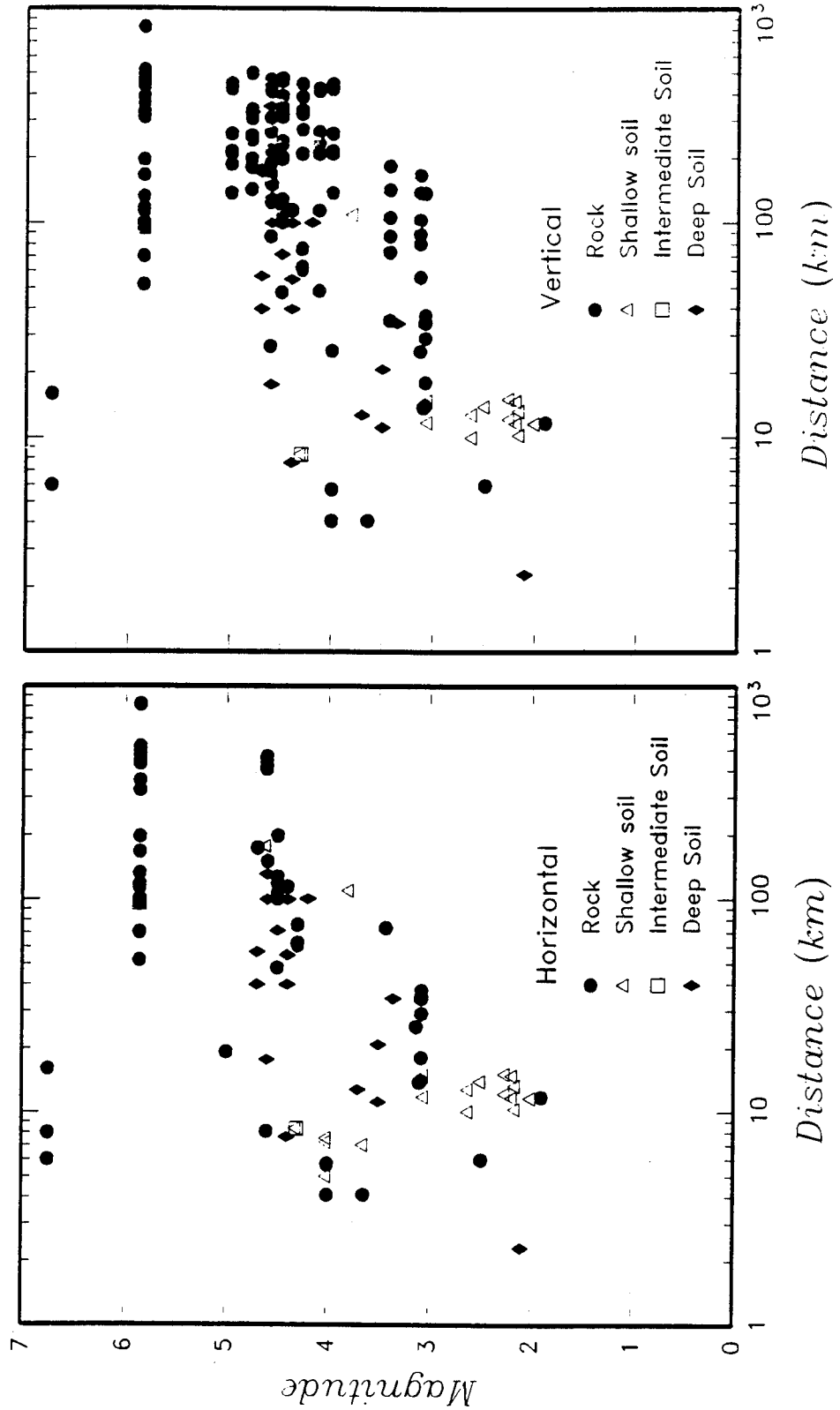

Figure 2-2. Magnitude-distance scatter plot of ENA ground motion data base.

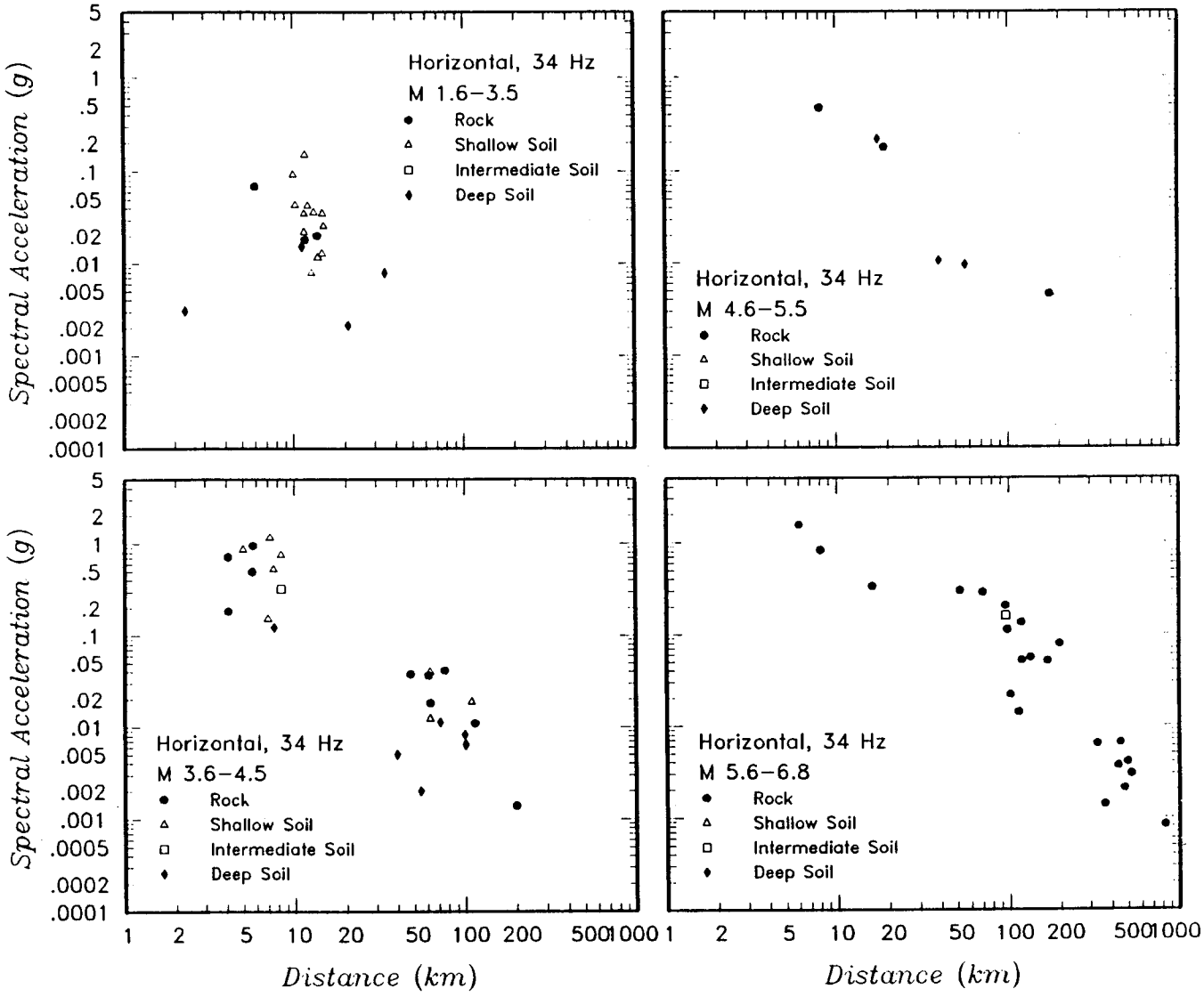

Figure 2-3. Peak horizontal spectral acceleration data for 34 Hz frequency from ENA ground motion data base.

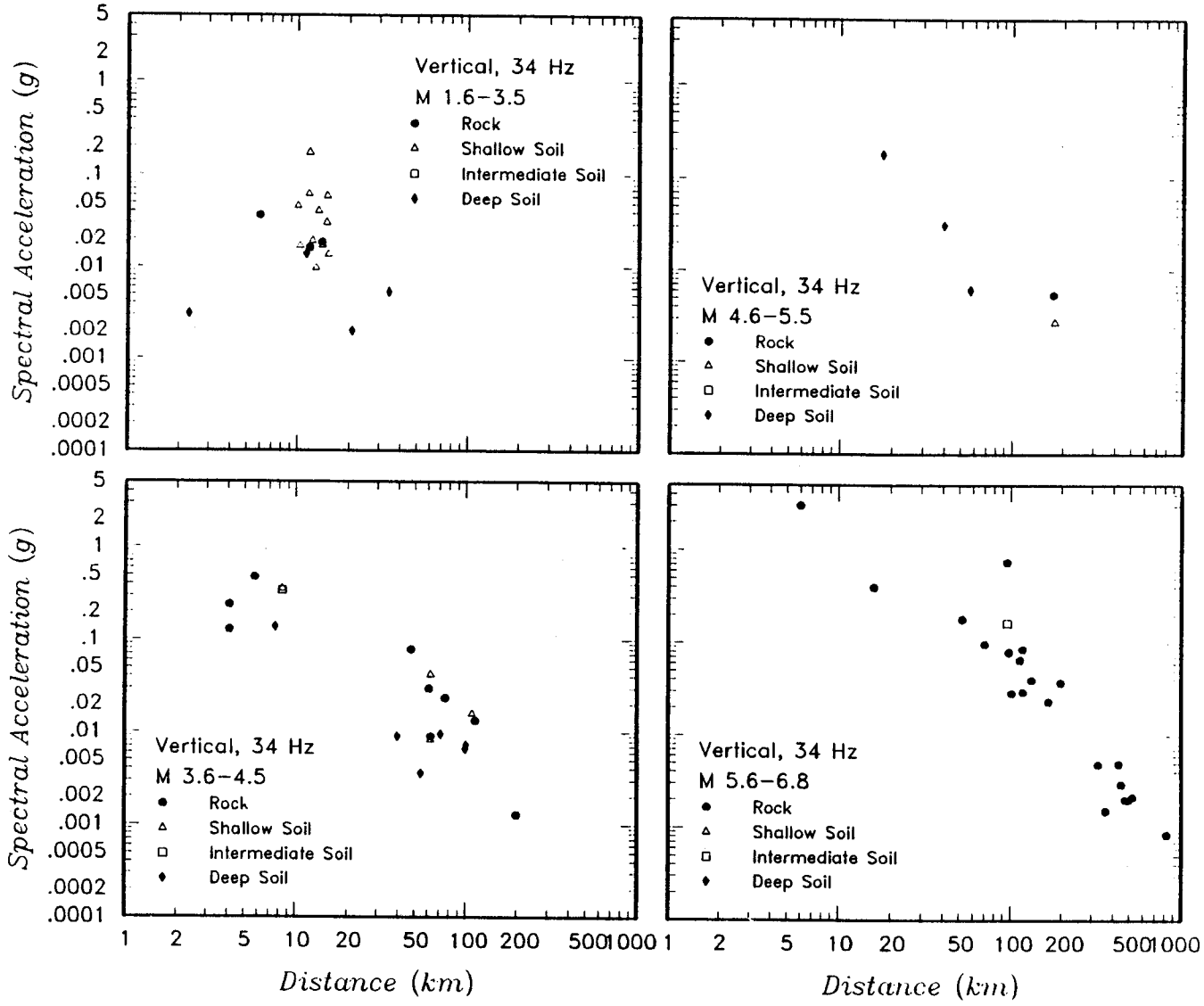

Figure 2-4. Peak vertical spectral acceleration data for 34 Hz frequency from ENA ground motion data base.

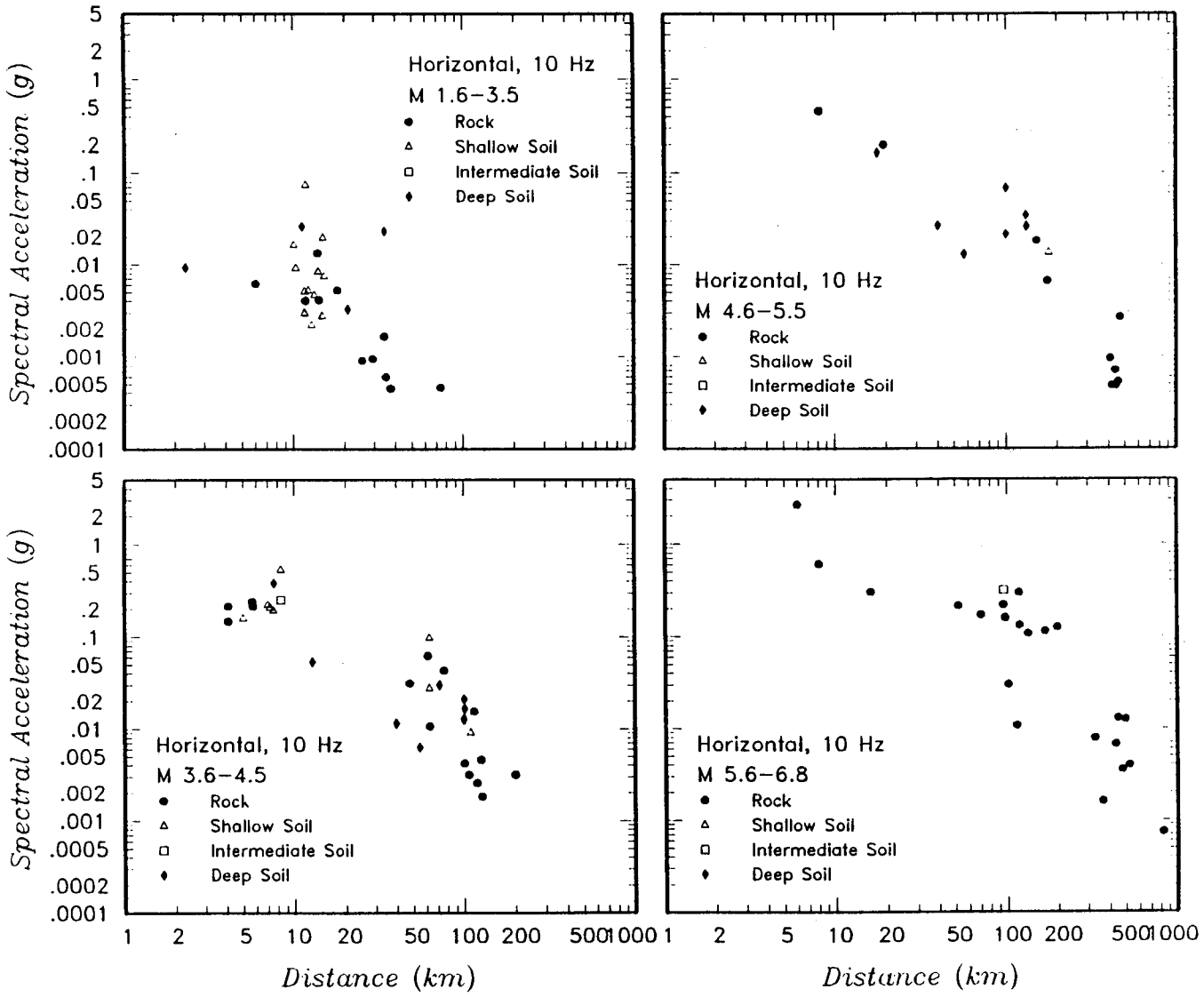

Figure 2-5. Peak horizontal spectral acceleration data for 10 Hz frequency from ENA ground motion data base.

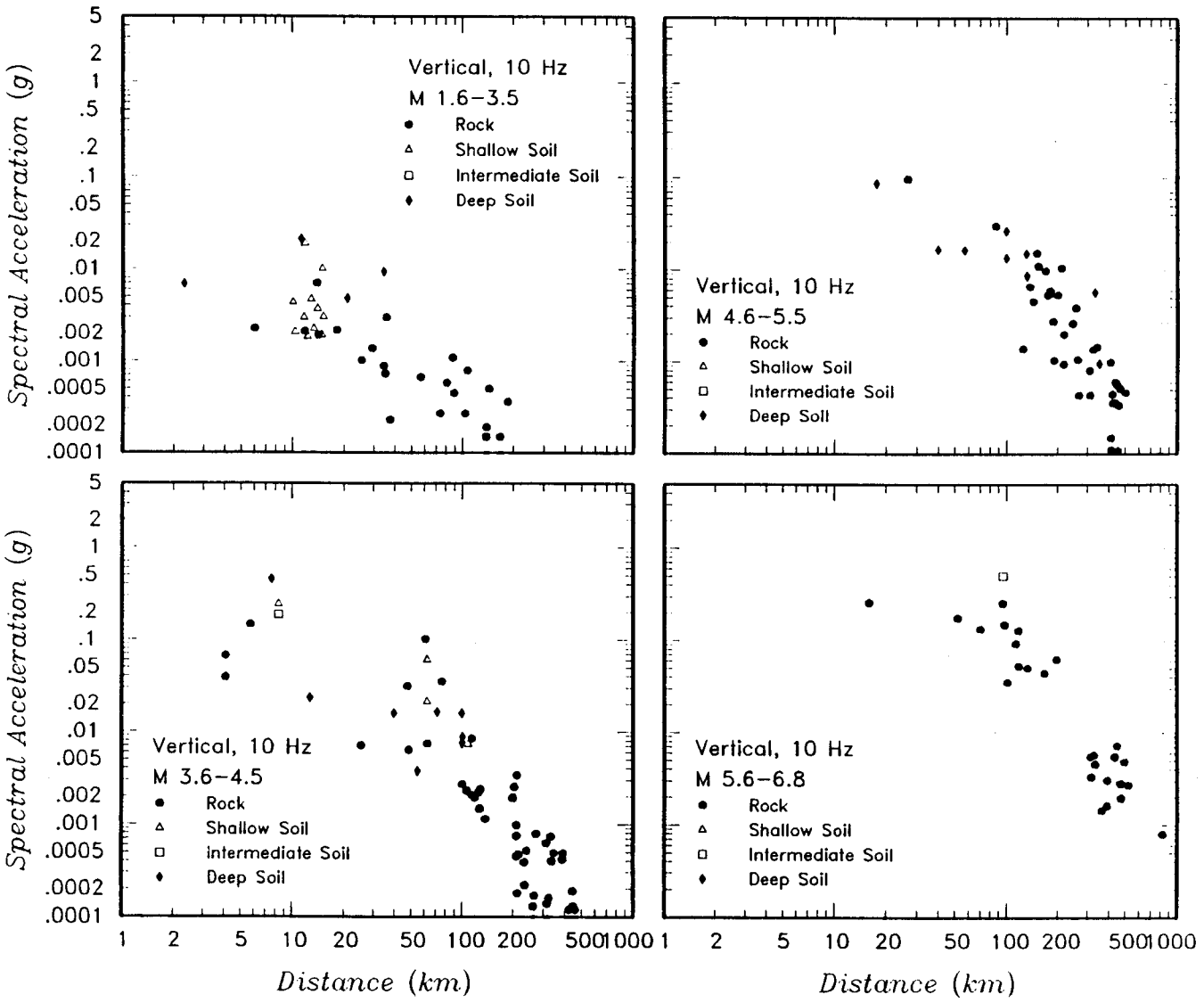

Figure 2-6. Peak vertical spectral acceleration data for 10 Hz frequency from ENA ground motion data base.

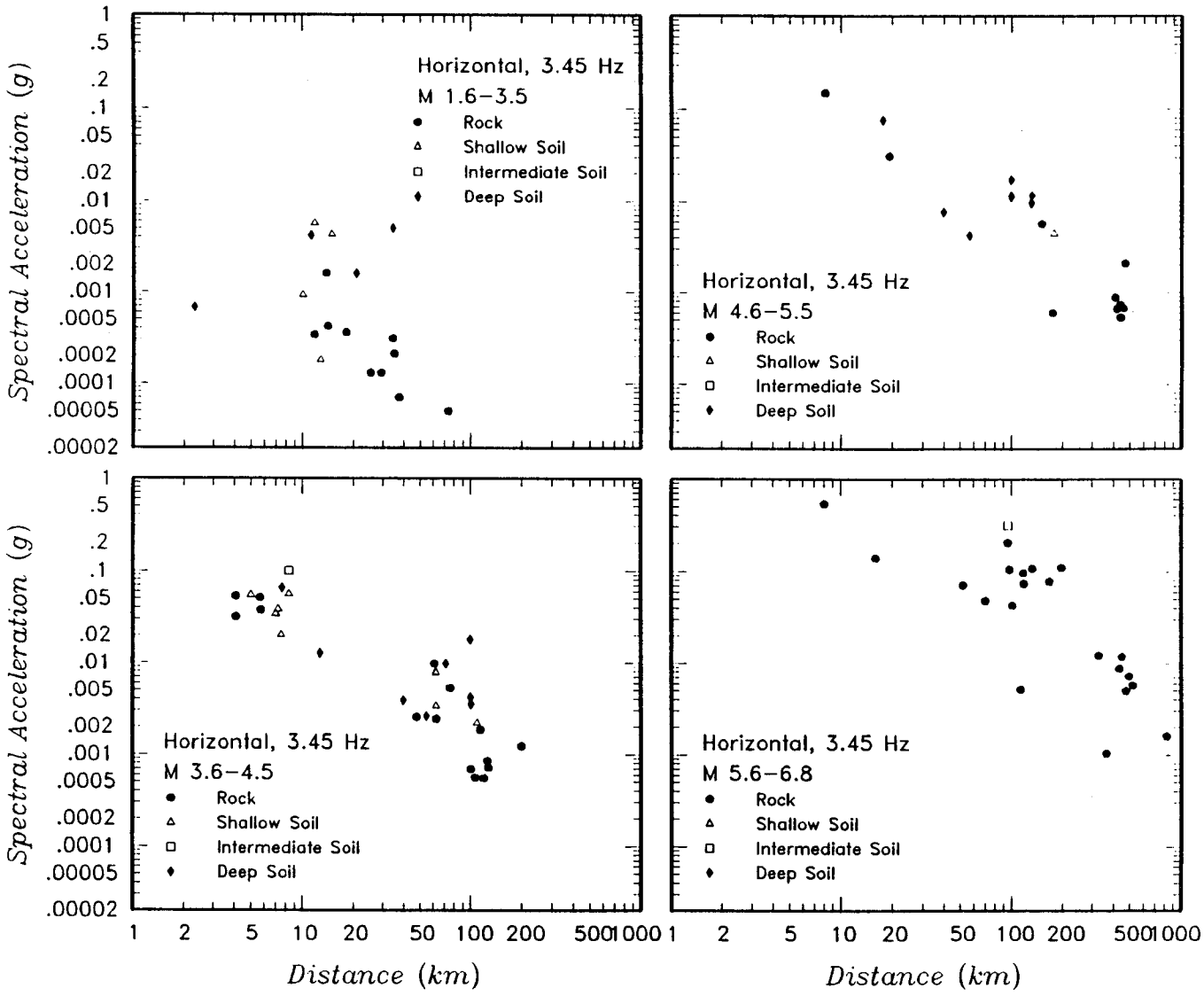

Figure 2-7. Peak horizontal spectral acceleration data for 3.45 Hz frequency from ENA ground motion data base.

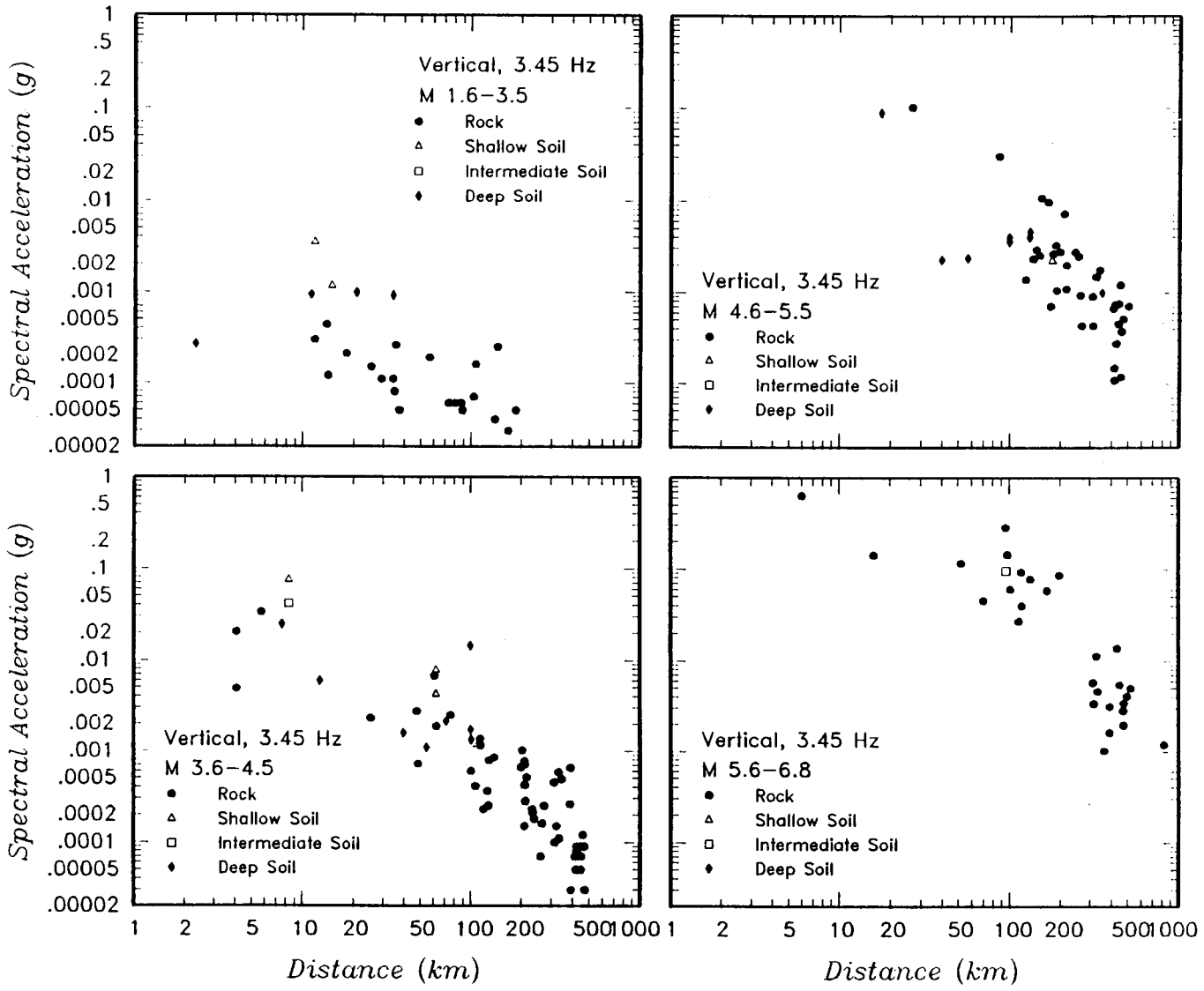

Figure 2-8. Peak vertical spectral acceleration data for 3.45 Hz frequency from ENA ground motion data base.

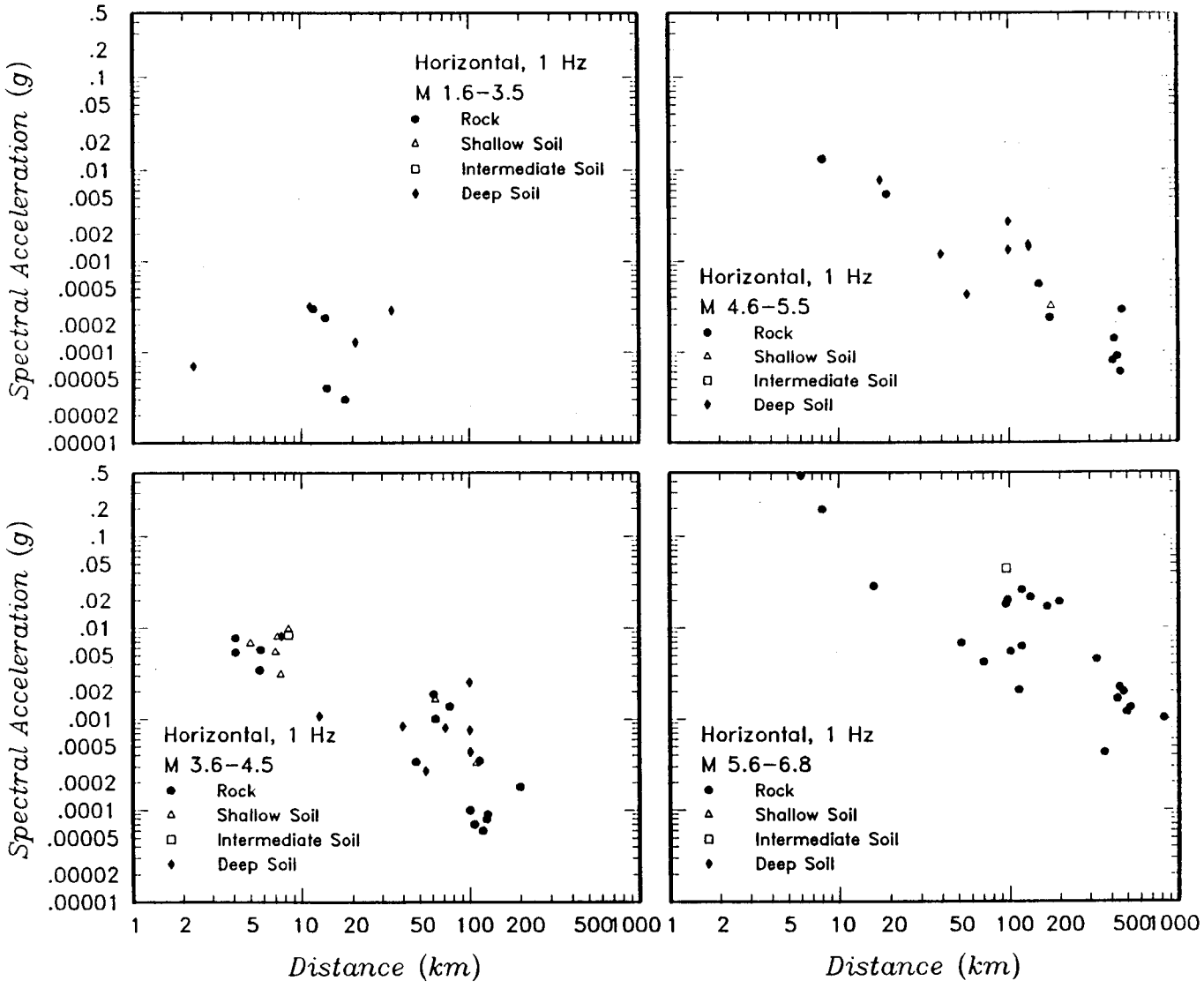

Figure 2-9. Peak horizontal spectral acceleration data for 1 Hz frequency from ENA ground motion data base.

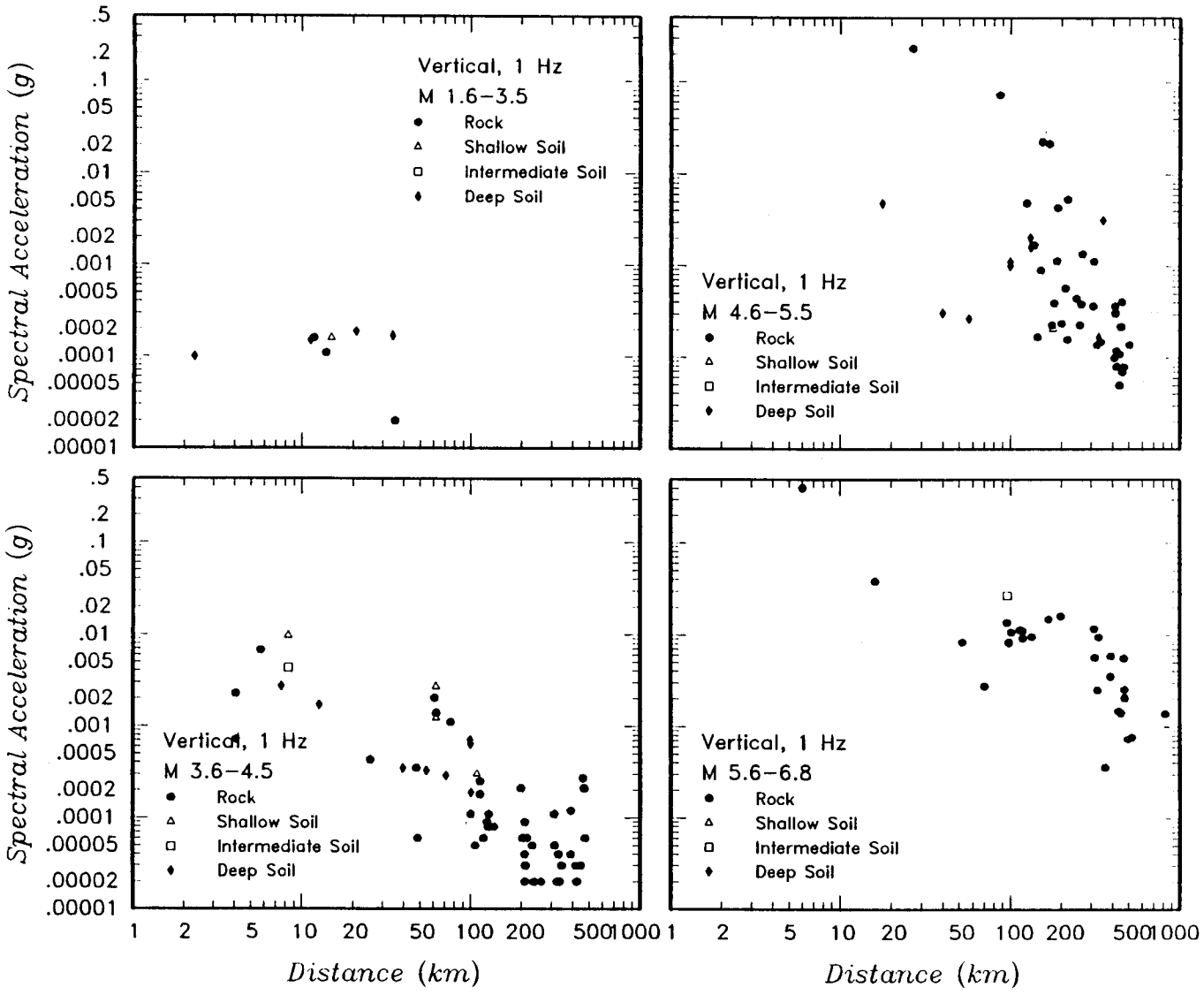

Figure 2-10. Peak vertical spectral acceleration data for 1 Hz frequency from ENA ground motion data base.

2.2 Examination of Empirical Ground Motion Data

2.2.1 Approach

The ground motion data compiled in this study provides a means of examining magnitude and distance scaling relationships and the components of variability of peak amplitude data. The data were examined by regression analyses utilizing simple attenuation models of the form used by Joyner and Boore (1982)

$$\ln[y(f)_{ij}] = C_1 + C_2(M_i - 6) + C_3(M_i - 6)^2 + C_4 \ln(R_j) + C_5 R_j + \sum_k C_k \cdot Z^{k_j} + \eta_i + \varepsilon_{ij} \quad \text{(Eq. 2-1)}$$

where M_i is the magnitude of the i^{th} earthquake (either m_{Lg} or **M**), R_j is the hypocentral distance (or fault distance for near-source recordings of large events) to the j^{th} site, the Z^k terms are a set of dummy variables to account for various classification effects in the data, and C_1 through C_k are coefficients fit to the data. The analyses were conducted utilizing a *random effects* regression formulation (Brillinger and Preisler, 1985; Abrahamson and Youngs, 1992) which partitions the total error in Equation 2-1 into an inter-event (earthquake-to-earthquake) component, η_i and an intra-event (within earthquake) component, ε_{ij}. The random effects model is somewhat similar in concept to the two-stage regression technique employed by Joyner and Boore (1982) in that it separates the estimation of distance scaling of ground motion from the estimation of magnitude scaling. The method also requires that possible parametric effects will usually need to be observed in data from multiple events for their effect to be statistically significant. Brillinger and Preisler (1985) have shown that the random effects model yields essentially identical results to the two-staged regression approach in fitting the Joyner and Boore (1982) data set.

2.2.2 Examination of Scaling Relationships

Regression analyses were performed to evaluate the magnitude and distance scaling parameters of Equation 2-1. Because the focus of this study is on the development of ground motion models to evaluate the hazard from moderate-to-large earthquakes, the data used in the analysis was limited to recordings from magnitude 4 and larger earthquakes. The resulting ground motion data sets consist of 66 horizontal recordings and 132 vertical recordings. The geometric mean of the peak spectral ordinates at each frequency was used in the analysis to avoid having to account for correlation between the two components in estimating the uncertainties in the fitted parameters. The specific form of Equation 2-1 used was

$$\ln[y(f)] = C_1 + C_2(M-6) + C_3(M-6)^2 + C_4 \ln(R) + C_5 R + C_6 \cdot Z_{SS} + C_7 \cdot Z_{IS} + C_8 \cdot Z_{DS} \quad \text{(Eq. 2-2)}$$

where the terms Z_{SS}, Z_{IS}, and Z_{DS} denote site classification codes B, C, and D described in Appendix 2A, Table 2A-2. Parameter Z_{SS} takes on the value 1 for shallow soil sites (depth to rock < 20 m) and zero for all other site conditions; Z_{IS} takes on the value 1 for intermediate depth soil sites (depth to rock 20 to 100 m) and zero for all other site conditions; and Z_{DS} takes on the value 1 for deep soil sites and zero for all other site conditions. Table 2A-2 also classifies the rock underlying the soil deposits at the recording sites into four categories: hard crystalline rock; hard sedimentary rock; softer, weathered rock; and soft rock over hard rock. Unfortunately, the only sites in the data base underlain by other than crystalline rock are those underlain by deep soil deposits while the sites underlain by shallow and intermediate depth soils are all underlain by hard crystalline rocks. Thus the effect of deep soil could not be separated from the effect of rock type in examination of the data.

Figure 2-11 shows the fitted values of the linear and quadratic magnitude scaling terms C_2 and C_3 as a function of frequency for horizontal and vertical motions. Shown are fits using Lg magnitude, m_{Lg}, and moment magnitude, **M**. The linear magnitude scaling term increases with decreasing frequency, as one would expect, and exhibits values at high frequency near the theoretical value of 0.6 that one would obtain from use of the stochastic model (see Section 3). Scaling with m_{Lg} appears to be slightly more linear than with **M** (smaller values of C_3). The large error bars indicate that the limited empirical data does not provide a tight constraint on magnitude scaling parameters.

Figure 2-12 shows the fitted values of the geometric and absorption distance scaling parameters C_4 and C_5 as a function of frequency for horizontal and vertical motions.

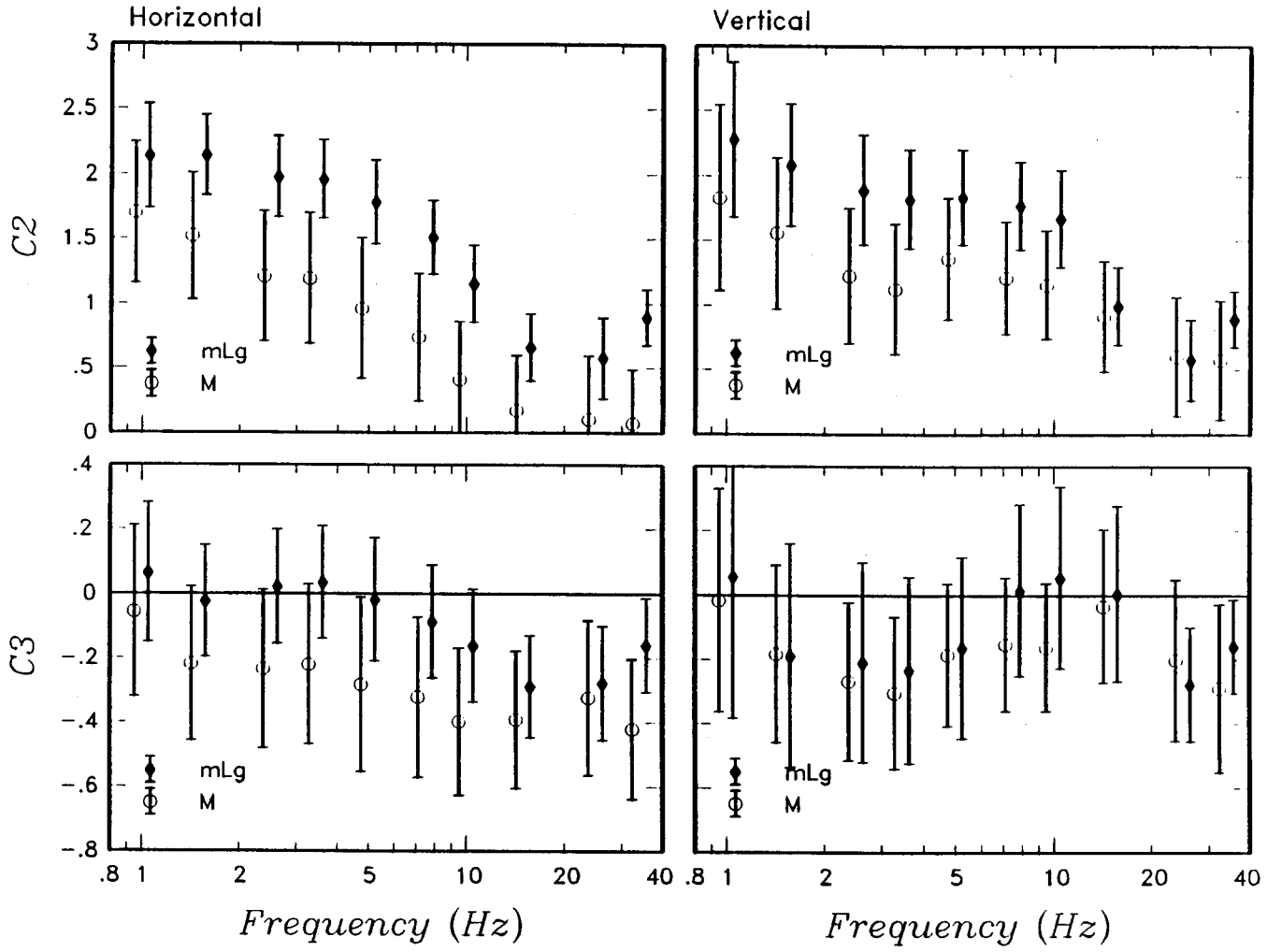

Figure 2-11. Magnitude scaling terms from fit of Equation 2-2 to horizontal and vertical spectral accelerations for magnitude 4 and greater events. Error bars represent plus-or-minus one standard error confidence limits on parameter value.

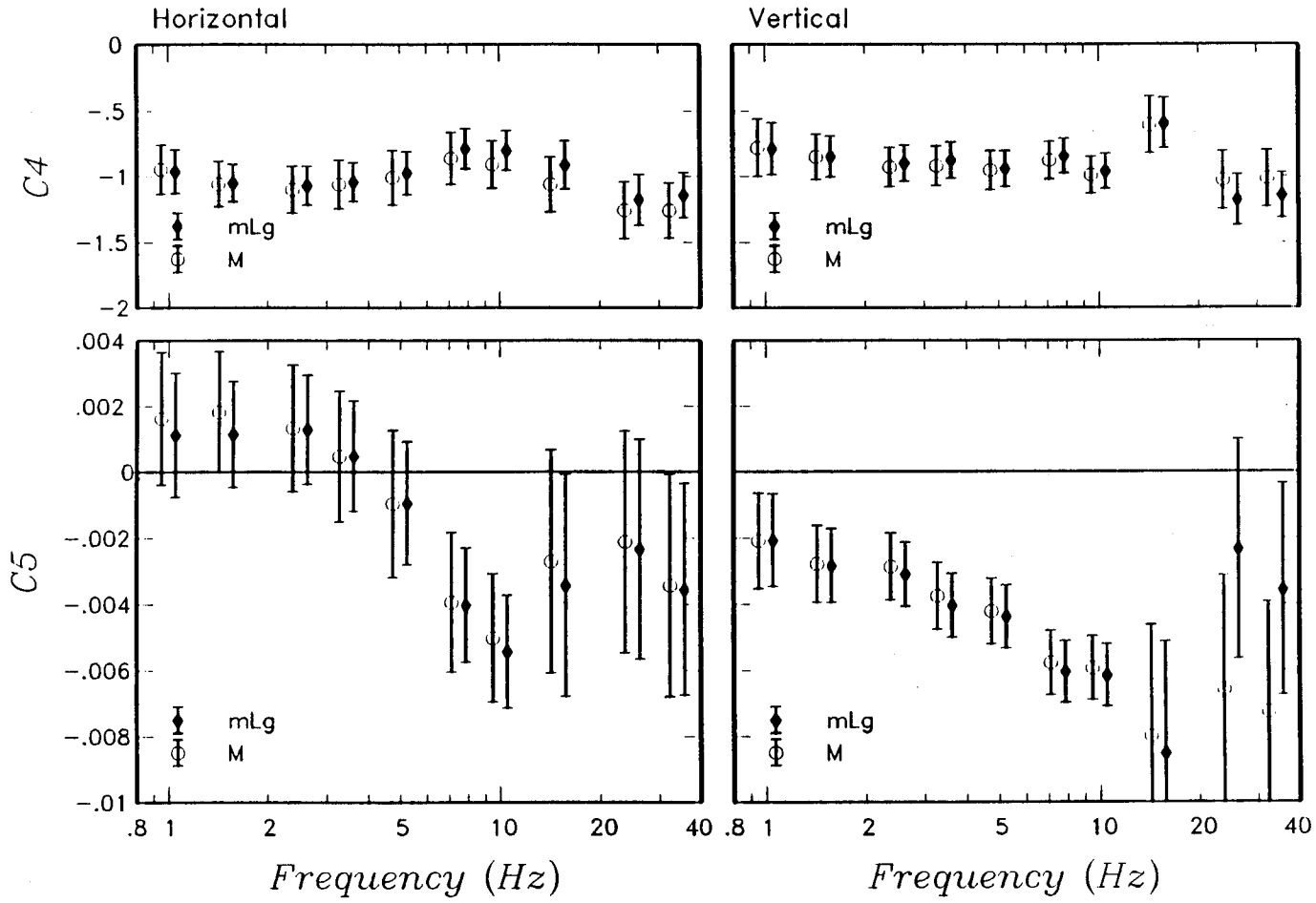

Figure 2-12. Distance scaling terms from fit of Equation 2-2 to horizontal and vertical spectral accelerations for magnitude 4 and greater events. Error bars represent plus-or-minus one standard error confidence limits on parameter value.

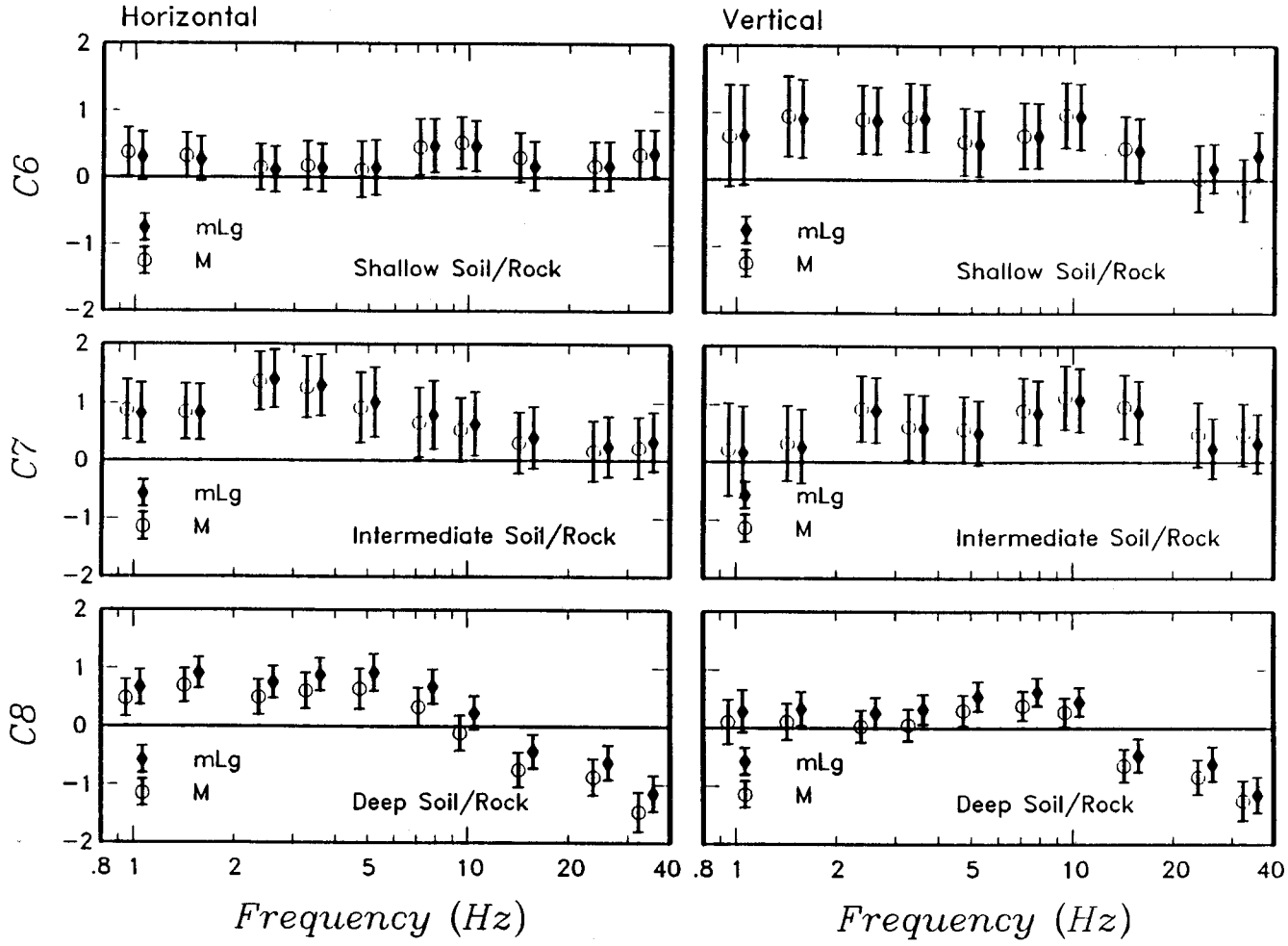

Figure 2-13. Site classification terms from fit of Equation 2-2 to horizontal and vertical spectral accelerations for magnitude 4 and greater events. Error bars represent plus-or-minus one standard error confidence limits on parameter value.

Again, fits using m_{Lg} and **M** are presented, with the two magnitude scales yielding very similar distance scaling parameters. The geometric attenuation parameter lies near the theoretical value of –1 for body waves in a whole space and shows somewhat higher values for vertical motions than for horizontal motions. The absolute value of the absorption parameter tends to increase in value with increasing frequency, consistent with most representations of the frequency dependence of Q. Again, the large error bars indicate that the limited data do not provide a tight constraint on attenuation parameters.

Figure 2-13 shows the fitted values of the site classification terms C_6, C_7, and C_8. The shallow and intermediate depth terms indicate fairly uniform amplification throughout the frequency range with greater amplification for the intermediate depth deposits. It should be noted that the intermediate depth results are based on very limited data. The deep soil deposits, parameter C_8, indicates de-amplification of high frequencies and amplification of low frequencies. As discussed above, the deep soil sites are also underlain by sedimentary rock, as opposed to crystalline rock for the other site types, and

the values for scaling parameter C_8 shown on Figure 2-12 represent a combination of these two effects. The de-amplification at high frequencies may result from soil damping in deeper, presumably somewhat softer soil deposits and/or an increased high frequency absorption factor, κ, for sedimentary rocks. The fact that the low frequency amplification in deep soils is similar or slightly less than that for intermediate depth soils may reflect the effect of a lower soil/rock velocity contrast for the deep soil sites.

Figure 2-14 compares the site amplification functions computed from coefficients C_6, C_7, and C_8 with those computed from the analysis of strong motion data from active tectonic regions, principally WNA, described in Appendix 2C. In general, the site amplifications computed from the two data sets are similar. The largest differences between the ENA and WNA results are for frequencies of 2 to 5 Hz for intermediate depth soils and for frequencies above 10 Hz for deep soils. The soil/rock spectral ratios shown on Figure 2-14 for the WNA data do not differentiate between intermediate depth and deep soil deposits. The majority of the WNA data are from deeper soil deposits and should conform more closely with the deep soil site amplification functions computed for ENA, although analyses of soil site strong ground motion data have shown that soil depth is not a statistically significant factor in predicting ground motions for frequencies of 1 Hz and higher (Campbell, 1989). As discussed above, the de-amplification at higher frequencies for ENA deep sites may be due to differences in the rock properties between the deep soil and rock sites that are not present in the WNA data set.

The results presented in Figures 2-10 through 2-12 are generally consistent with the trends that one would expect for ground motion amplitudes based on theoretical models and examination of large sets of empirical ground motion data. Because of the generally large error of estimation of the ENA scaling parameters, the effect at any one frequency is only marginally statistically significant. But taken over a wide frequency band, the results present a consistent pattern that provide broad constraints on ground motion scaling parameters.

2.2.3 Examination of Variance of Peak Motion Parameters

The variance in the peak ground motion parameters is estimated by finding the corresponding variances of the error terms η_i and ε_{ij}, denoted by τ^2 and σ^2, respectively. Assuming independence between the two error terms, the total variance, σ_T^2 is then obtained by the sum of the two variance components ($\sigma_T^2 = \tau^2 + \sigma^2$).

Figures 2-15 through 2-19 show the values of τ, σ, and σ_T obtained from fits of Equation 2-2 to the horizontal and vertical spectral ordinates. Smaller values of the inter-event standard error were obtained when fitting to m_{Lg} magnitude than when fitting to moment magnitude M (Figure 2-15). This is coincident with a more linear scaling with magnitude found for m_{Lg}. Similar intra-event standard errors were found for both magnitude scales (Figures 2-17 and 2-18), consistent with the similar distance scaling terms obtained. The combined total error is somewhat smaller for scaling with m_{Lg} and exhibits an decrease in variance with increasing frequency, especially for vertical motions (Figure 2-17). The total standard error is somewhat larger than that reported for WNA strong ground motion data (e.g., Joyner and Boore, 1982; Sadigh and others, 1989; Campbell, 1989, 1991). The larger values may reflect the impact of larger distances and/or smaller magnitudes in the ENA data set compared to that of the WNA, or may be inherent to ENA ground motions. These issues will be explored below.

Figures 2-18 and 2-19 show the results of two sensitivity studies. Figure 2-18 shows the effect of the number of classification parameters included in the model on the computed total standard error. The 8-parameter model is the model defined in Equation 2-2. The 5-parameter model includes only the magnitude and distance scaling terms from Equation 2-2, thus assuming no difference among site categories in spectral acceleration. Inclusion of the site classification terms results in a reduction in the computed total standard error. The statistical significance of the reduction in error was checked by using the likelihood ratio test (eg. Seber and Wild, 1989, p. 196). The likelihood ratio test statistic, LR, is given by

$$LR = 2\,[LL(\theta) - LL(\theta_o)] \qquad \text{(Eq. 2-3)}$$

where $LL(\theta)$ is the log-likelihood computed for the fit of a specified set of parameters, θ, to the data and the test is of the hypothesis that θ equals a specified vector θ_0. In this case, the test is that coefficients C_6, C_7, and C_8 are all zero. The LR statistic is approximately distributed as chi-squared when the hypothesis is true (Seber and Wild,

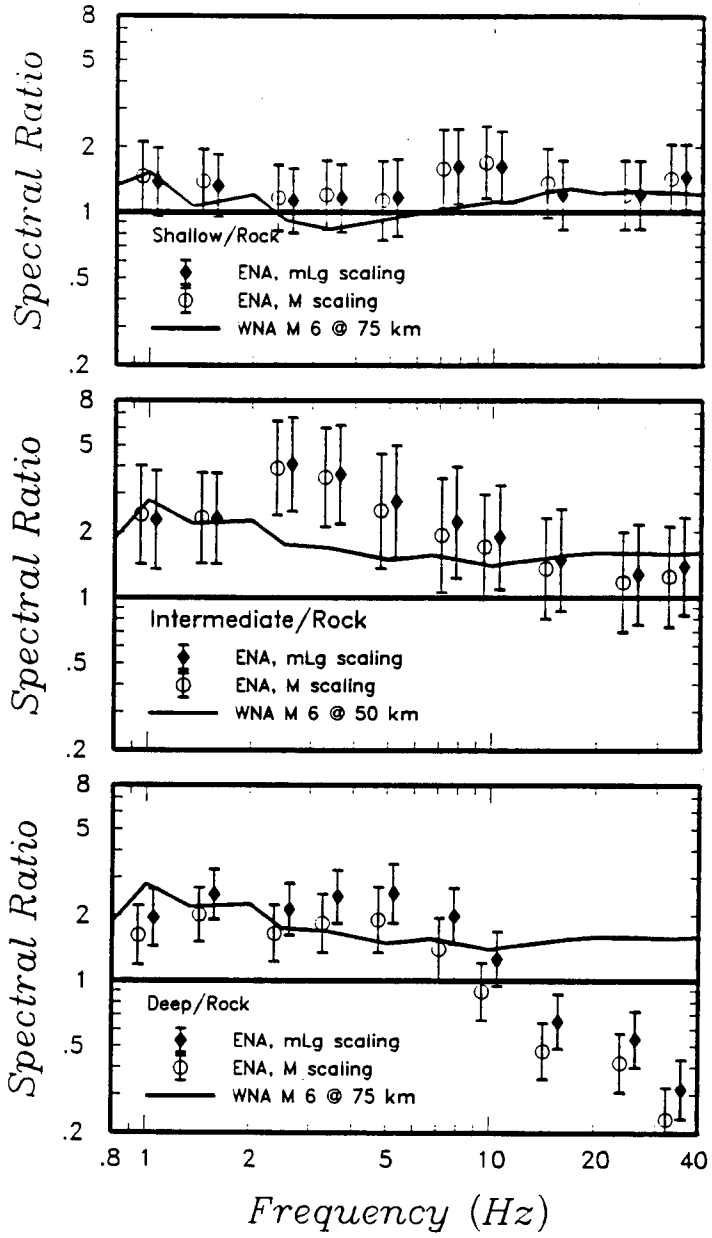

Figure 2-14. Comparison of soil/rock spectral ratios computed from site amplification factors shown in Figure 2-13 for ENA data with spectral ratios obtained from analyses of strong motion data from WNA.

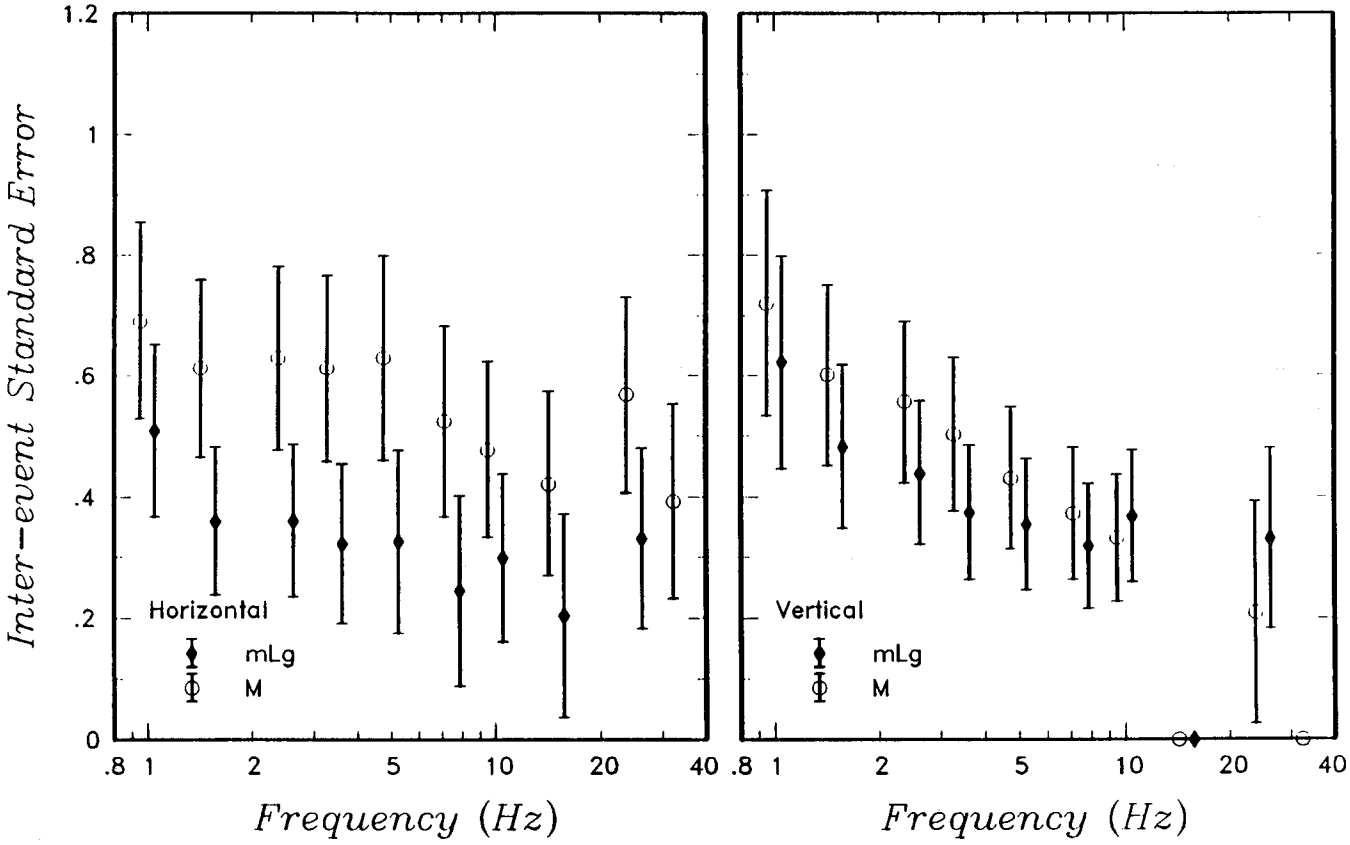

Figure 2-15. Inter-event standard error, τ, for horizontal and spectral accelerations from fit of Equation 2-2 to ground motion data for magnitude 4 and greater events. Error bars represent plus-or-minus one standard error confidence limits on parameter value.

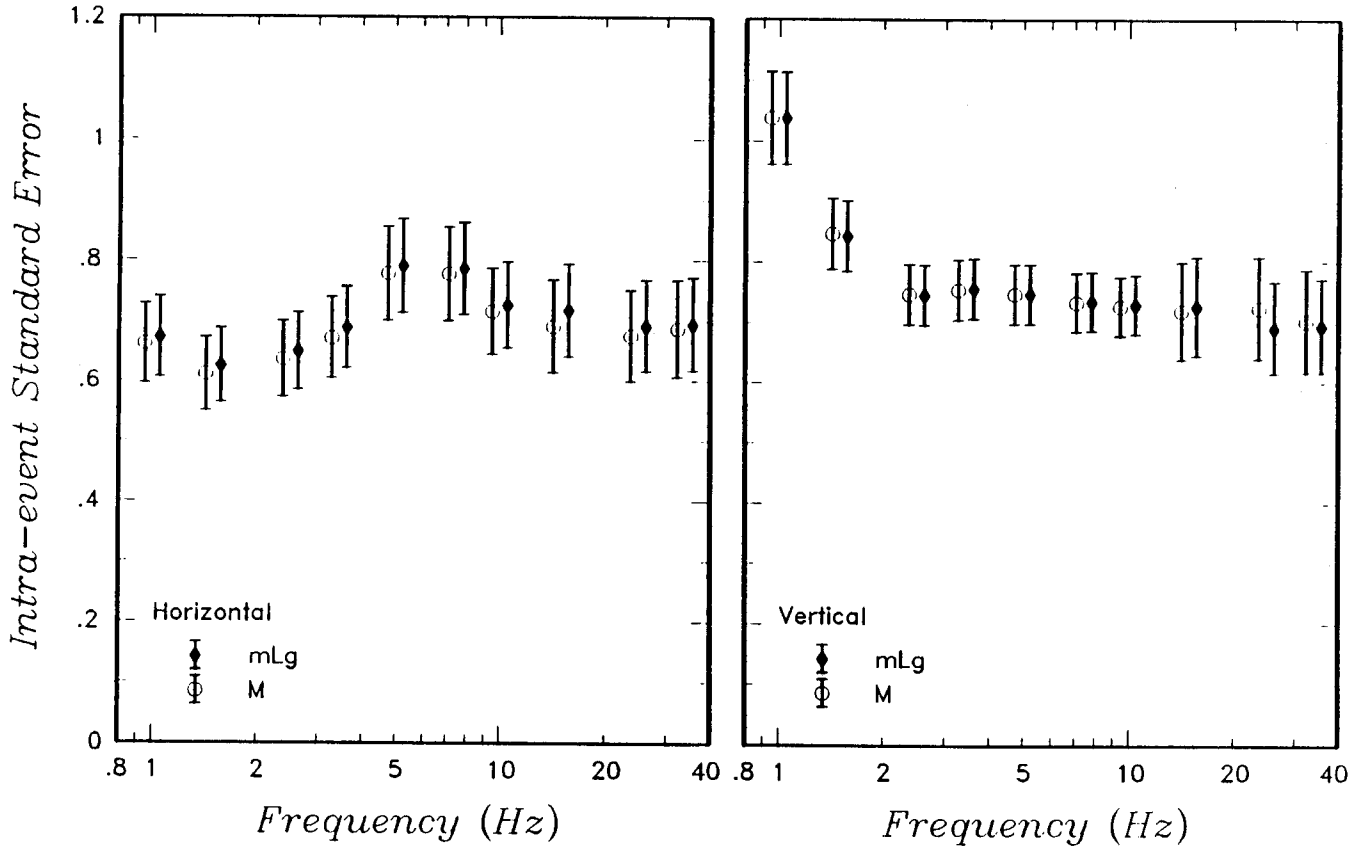

Figure 2-16. Intra-event standard error, σ, for horizontal and vertical spectral accelerations from fit of Equation 2-2 to ground motion data for magnitude 4 and greater events. Error bars represent plus-or-minus one standard error confidence limits on parameter value.

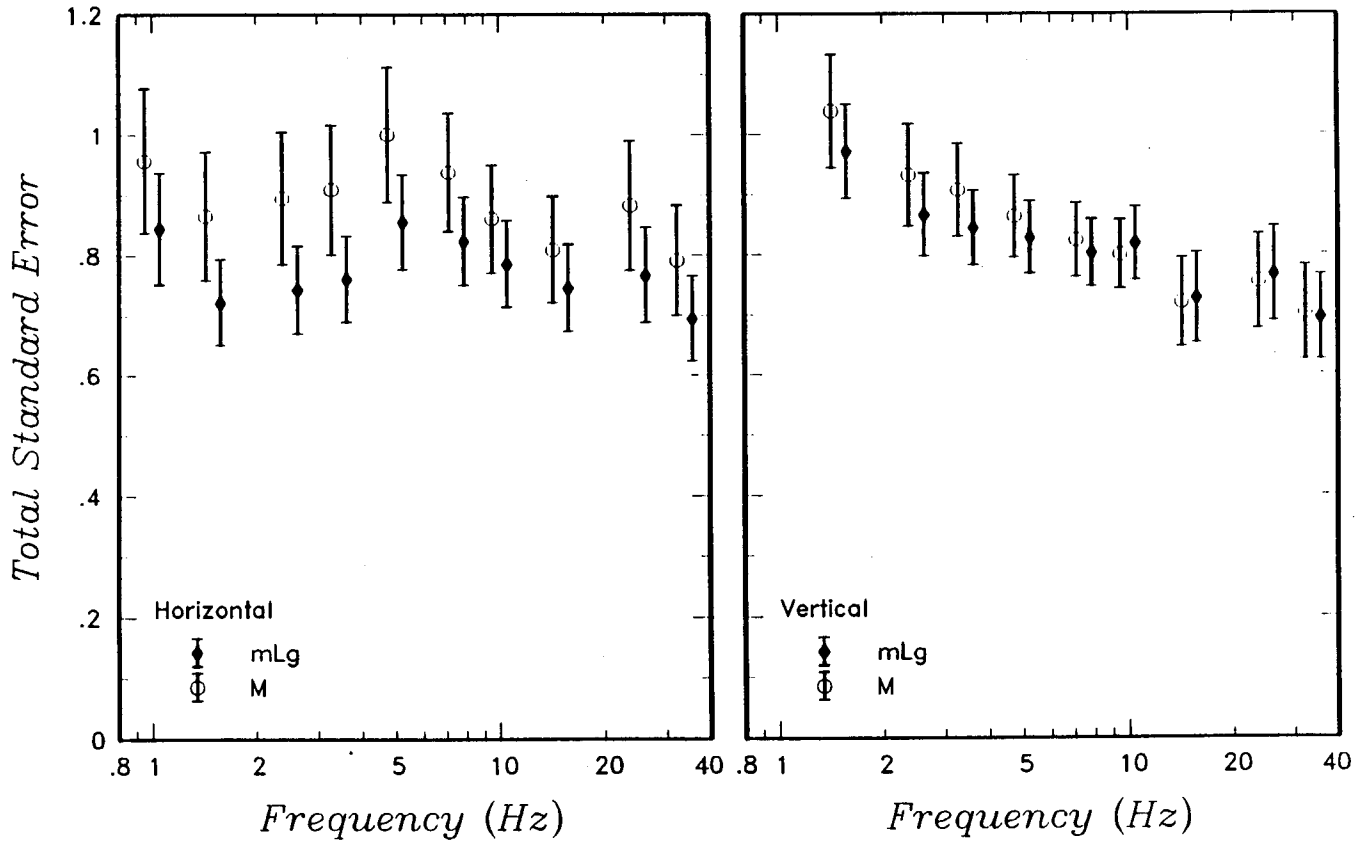

Figure 2-17. Total standard error, σ_T, for horizontal and vertical spectral accelerations from fit of Equation 2-2 to ground motion data for magnitude 4 and greater events. Error bars represent plus-or-minus one standard error confidence limits on parameter value.

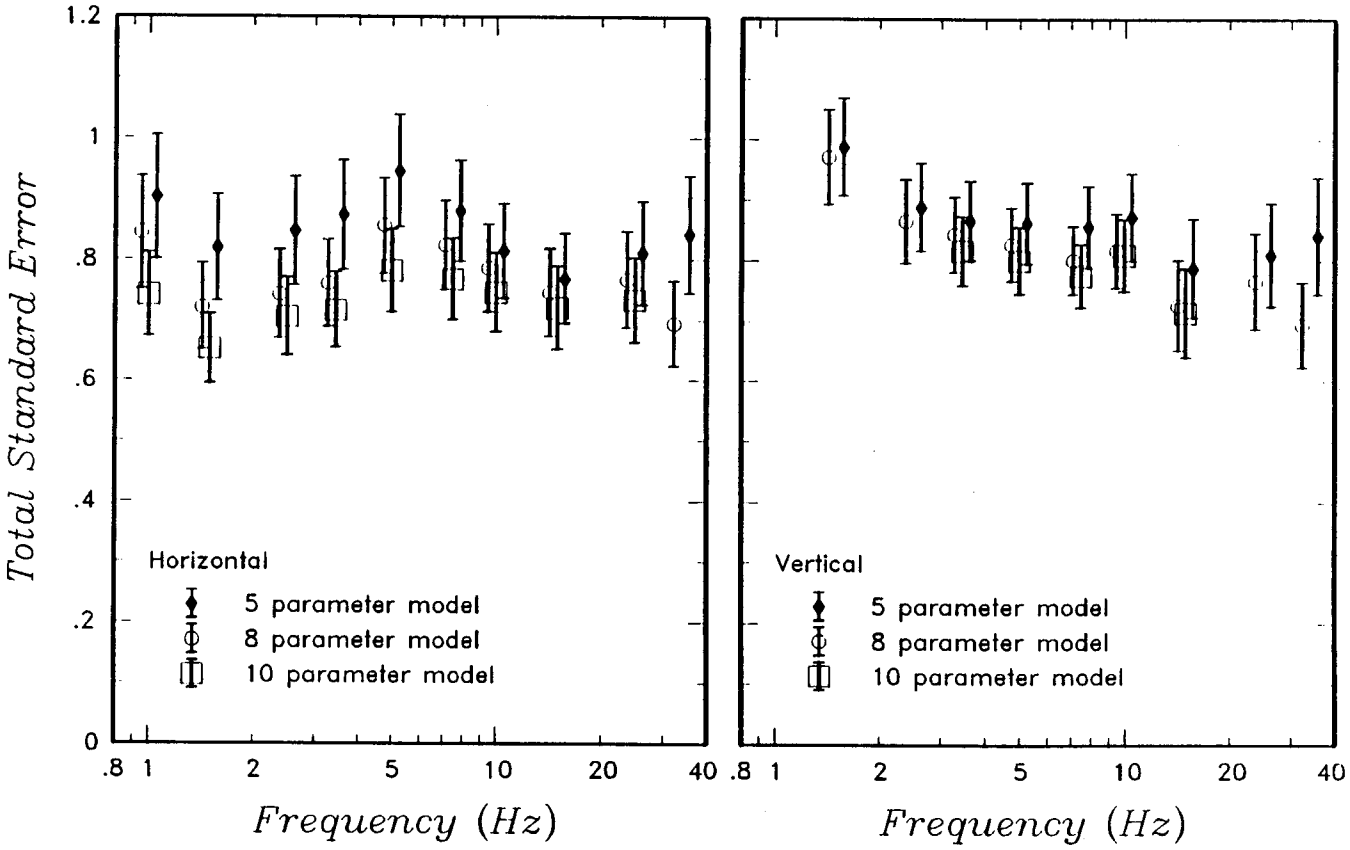

Figure 2-18. Effect of inclusion of classification parameters on computed total standard error for horizontal and vertical spectral accelerations (m_{Lg} scaling). The five parameter model does not include any classification terms and the 10 parameter model includes two additional terms to account for crustal structure regionalization.

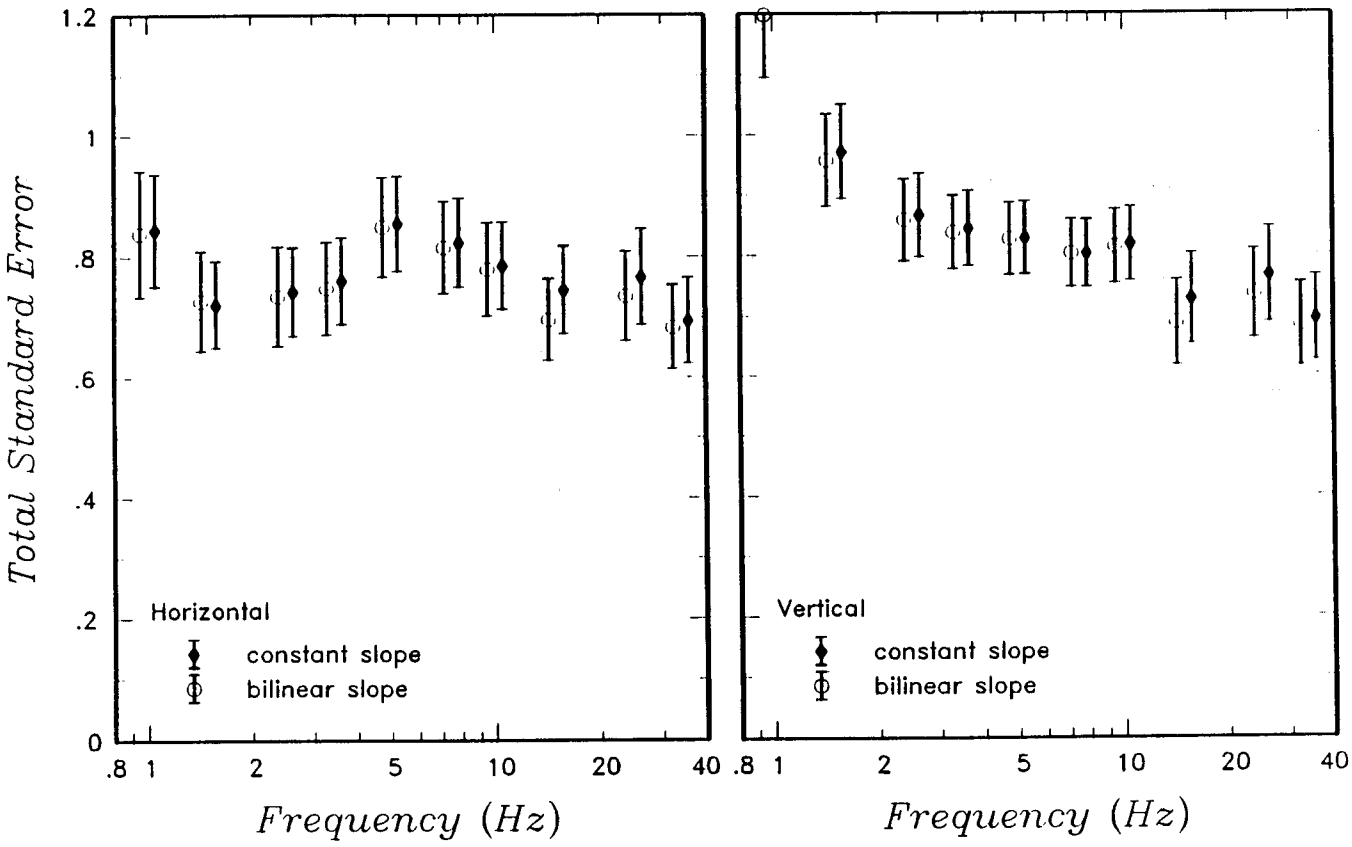

Figure 2-19. Effect of use of bilinear distance attenuation function on computed total standard error for horizontal and vertical spectral accelerations (m_{Lg} scaling). The bilinear model has a break in slope at 60 km.

1989). Using the likelihood ratio test, the hypothesis that the site classification coefficients are zero cannot be rejected at any individual frequency.

The 10 parameter model included the eight parameters for Equation 2-2 plus two parameters to account for effects due to site location within the various crustal regionalization zones described in Section 5. As described in Section 5, the ENA was divided into two primary crustal regions on the basis of differences in wave propagation characteristics: a primary region consisting of the majority of ENA, and the gulf coast. A third subregion was defined as part of the primary region which may have marginally different attenuation characteristics. The empirical data analyzed come from two of these zones, the primary zone and the subregion zone. A dummy variable was added that took on a value of 0 for sites in the primary zone and 1 for sites in the subregion. A second dummy variable was added to test for effects on amplitude for cases where the earthquakes and recording sites were located in different zones. Because of the limited, scattered data, the slight reduction in total variance resulting from inclusion of these two additional parameters was found to be not statistically significant.

Figure 2-19 shows the effect of fitting a bilinear form for the geometric spreading term to the data. Atkinson and Mereu (1992) have shown that the bilinear form with a slope break at 60 km provides an adequate representation of the effects of crustal reflections and changes in attenuation rates observed in the ECTN network data. As indicated by the results shown on Figure 2-19, the use of a bilinear distance attenuation function results in minimal reduction in computed standard error. This may result from the consideration of data from multiple regions with different crustal effects, or may be due to the limited data being too scattered to define a clear trend.

The empirical estimates of the variability in ENA ground motion amplitudes is derived from a data set that contains a large portion of seismographic network recordings obtained at regional distances, rather than strong motion recordings at distances usually of interest in evaluating seismic hazards from moderate size events. Appendix 2B discusses an examination of the variability in regional seismographic network peak amplitude data from ENA and WNA and a comparison with the variability of strong motion peak amplitude data. The results indicate that there does not appear to be a significant difference between the variability in network and strong motion peak amplitude data and the level of variability in peak amplitudes from network data is similar in ENA and WNA.

It has been noted that the standard error in peak ground motion data recorded in WNA decreases with increasing earthquake magnitude (e.g., Sadigh, 1983, Idriss, 1985; Abrahamson, 1988; Youngs and others, 1990). The mean magnitude for the ENA data set analyzed in this study is approximately magnitude 5, significantly lower than that of typical ground motion data sets used to develop attenuation relationships for WNA. Figure 2-20 compares the standard errors of peak horizontal spectral accelerations shown in Figure 2-17 with values computed from WNA ground motion data by Sadigh and others (in preparation) for specific magnitude intervals. The comparison indicates that the values computed for the ENA data fall within the range of values computed from smaller-magnitude WNA data.

2.2.4 Summary

The analyses of the ENA ground motion data set indicate similar trends to that observed in WUS evaluations of ground motion attenuation. The peak spectral acceleration scaling parameters estimated from the data follow expected trends and have values that one would expect from evaluations of WUS data or from the predictions of theoretical models. Because of the limited extent of the data set, it provides only very broad constraints on the form and parameters of appropriate attenuation relationships for evaluating seismic hazard in the ENA. The examinations of both strong ground motion and seismographic network amplitude data indicate comparable levels of standard error for ENA and WNA data when the effects of earthquake size on ground motion variability are taken into account.

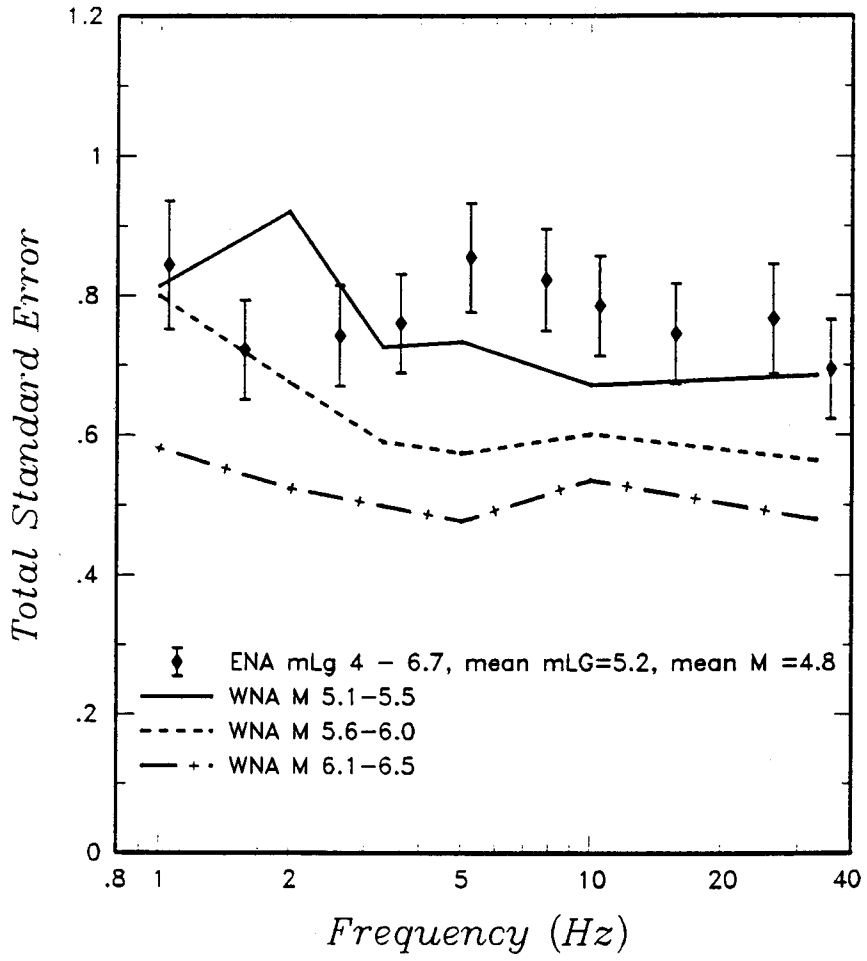

Figure 2-20. Comparison of total standard error for fit of (2-2) to horizontal spectral acceleration data with standard errors for spectral ordinates for WNA strong motion data in various magnitude bands (from Sadigh and others, in preparation).

References

Abrahamson, N.A. (1988). Statistical properties of peak ground accelerations recorded by the SMART1 array: *Bull. Seism. Soc. Am.*, 78, 26–41.

Abrahamson, N.A., and R.R. Youngs (1992). A stable algorithm for regression analysis using the random effects model: *Bull. Seism. Soc. Am.*, 82, 505–510.

Atkinson, G.M., and R.F. Mereu (1992). The shape of ground motion attenuation curves in southeastern Canada: *Bull. Seism. Soc. Am.*, 82, 2014–2031.

Brillinger, D.R., and H.K. Preisler (1985). Further analysis of the Joyner-Boore attenuation data: *Bull. Seism. Soc. Am.*, 75, 611–614.

Campbell, K.W. (1989). Empirical prediction of near-source ground motion for the Diablo Canyon Power Plant Site, San Luis Obispo County, California: U.S. Geological Survey Open-File Report 89-484, 115 p.

Campbell, K. W. (1991). A random effects analysis of near source ground motions for the Diablo Canyon Power Plant site, San Luis Obispo County, California: a report prepared for Lawrence Livermore National Laboratory by Dames & Moore, July 25, 1991.

Idriss, I.M. (1985). Evaluating seismic risk in engineering practice: Proceedings of the Eleventh International Conference on Soil Mechanics and Foundation Engineering, San Francisco, August 12–16, pp. 255–320.

Joyner, W.B., and D.M. Boore (1982). Prediction of earthquake response spectra: U.S. Geological Survey Open File Report 82-977.

Sadigh, K. (1983). Considerations in the development of site-specific spectra, in Proceedings of Conference XXII, Site-Specific Effects of Soil and Rock on Ground Motions and the Implications for Earthquake Resistant Design: U.S. Geological Survey Open-File Report 83-845, pp. 423–458.

Sadigh, K., C.-Y. Chang, F. Makdisi, and J.A. Egan (1989). Attenuation relationships for horizontal peak ground acceleration and response spectral acceleration for rock sites: *Seism. Res. Ltrs.*, 60, 19.

Sadigh, K., F. Makdisi, R.R. Youngs, C.-Y. Chang, and D. Rosidi (in preparation). Attenuation relationships for horizontal peak ground acceleration and response spectral ordinates: paper being prepared for submittal to Earthquake Spectra.

Seber, G.A.F., and C.J. Wild (1989). *Nonlinear Regression*, John Wiley and Sons, New York.

Youngs, R.R., F. Makdisi, K. Sadigh, and N.A. Abrahamson (1990). The case for magnitude dependent dispersion in peak ground acceleration (abs.): *Seism. Res. Ltrs.*, 61, 1, p. 30.

3

THEORETICAL GROUND MOTION MODELING

3.1 Introduction

This section presents the tools that are needed to assess the contributions to ground motion variability from seismic source and path effects, and that are needed for development of the ground motion attenuation relations. In this process, two approaches to modeling ground motion are used. The first, referred to as the stochastic ground motion model, is a simple and computationally efficient approach. The stochastic model was selected to make many thousands of earthquake simulations incorporating a wide range of parameters for source, site, and path effects. The results of these simulations were used to build the engineering ground motion model in Section 9. The second modeling approach, referred to as the semi-empirical ground motion model, is less computationally efficient, but more rigorous in its treatment of wave propagation effects for individual source-path combinations. The semi-empirical model was used to test the significance of crustal path effects in estimating ground motion and to assess the associated path uncertainty (see Section 5).

The two modeling methods are outlined below, including validations of the methods against strong motion recordings from several large earthquakes. These validations provide the bases for their use in modeling eastern North American ground motion.

3.2 The Stochastic Ground Motion Model

The engineering ground motion model presented in Section 9 is based on a simple physical model of the earthquake source and crustal wave propagation. The model characterizes strong ground motions as stochastic in time, with a Fourier amplitude spectrum specified by a fundamentally simple and deterministic seismological model of the source, path, and site (Hanks and McGuire, 1981; Boore, 1983, 1986; Silva, 1991). An essential and significant aspect of the model is that, while being extremely simple, it also provides estimates of strong ground motions with reasonable accuracy. Additional, but important, side benefits arising from the model's simplicity are the natural separation of source, path, and site effects and the accompanying computational efficiency. As a result, an accurate appraisal of the effects of variability in source, path, and site parameters as well as model bias can be readily quantified.

3.2.1 Model Description

The stochastic ground motion model (sometimes referred to as the Band-Limited-White-Noise or BLWN model), in which the energy is distributed randomly over the duration of the source, has proven to be very effective in modeling a wide range of ground motion observations. Time-domain measures such as peak acceleration, peak particle velocity, Wood-Anderson magnitude, and short-period P- and S-wave amplitudes as well as frequency-domain measures such as response spectra and Fourier amplitude spectra, have been predicted with reasonable accuracy (Hanks and McGuire, 1981; Boore, 1983, 1986; Boore and Atkinson, 1987; Silva and Lee, 1987; Toro and McGuire, 1987; Silva et al., 1990; Silva and Darragh, 1993).

The ground motion model employed here uses an omega-squared (ω^2) Brune source model (Brune, 1970; 1971) with a single corner frequency and a constant stress drop (Boore, 1983; Atkinson, 1984) (Figure 3-1). The ω^2 model has become a seismological standard because of its simplicity and ability to predict spectral amplitudes and shapes over an extremely broad range of magnitudes,

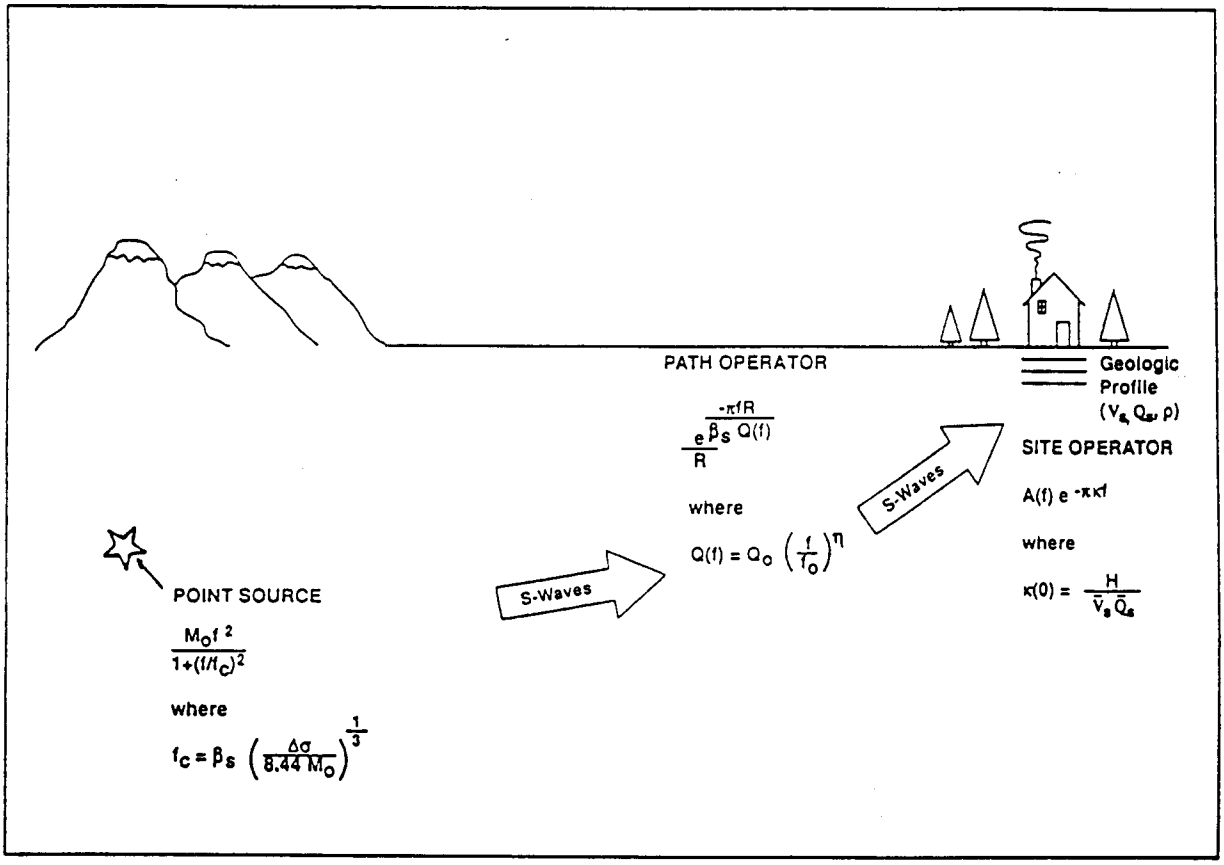

Figure 3-1. Schematic of the stochastic ground motion model. To include crustal propagation effects the 1/R in the path operator is replaced by a geometrical attenuation term which includes the effects of direct and both sub- and post-critical reflected phases (Appendix 3A).

distances and frequencies, as well as tectonic regions worldwide. In particular, the ω^2 model has been used to satisfactorily predict spectral shapes for earthquake magnitudes from M –2 (Fehler and Phillips, 1991) to M 8-1/4 (Hartzell and Heaton, 1988), and high-frequency amplitudes and duration up to M 9.5 (Boore, 1986). It is the only source model that has demonstrably predicted ground motion amplitudes of interest to engineering applications over the entire magnitude range of the observational record.

Ground motion is assumed to emanate from the source at a point, thus ignoring effects associated with the finite spatial-temporal extent of the rupture process. In its simplest form, the model assumes waves propagate in a homogeneous, uniform half space. The model is first described for this simple case, followed by a discussion of additional wave propagation effects that are incorporated into the complete modeling procedure. In a homogeneous, uniform half space, the acceleration Fourier amplitude spectrum, a(f), where f is frequency, is given by:

$$a(f) = C \frac{f^2}{1+(f/f_c)^2} \frac{M_o}{R} P(f)\, A(f)\, e^{-\frac{\pi f R}{\beta_o Q(f)}} \qquad \text{(Eq. 3-1)}$$

where

M_o = Seismic moment

R = Distance to the equivalent point source

β_0 = Shear-wave velocity at the source

$Q(f)$ = $Q_0(f)^\eta$, frequency-dependent quality factor model where Q_0 and η are model parameters

$A(f)$ = Amplification factors

$P(f)$ = High-frequency truncation filter

f_c = Source corner frequency and

$C = (1/\rho_0\beta_0^3) \times (2) \times (0.55) \times (1/\sqrt{2}) \times \pi$

The effects of a velocity gradient in the crust or near-surface are accommodated through the $A(f)$ amplification factors or transfer function. C is a constant which contains source-region density ρ_0 and shear-wave velocity β_0 terms and accounts for the free-surface effect (factor of 2), the source radiation pattern averaged over a sphere (0.55) (Boore, 1986), and the partition of energy into two horizontal components $(1/\sqrt{2})$. The product of these factors is a single constant factor 0.78.

Source scaling is provided by specifying two independent parameters, the seismic moment (M_0) and the stress drop ($\Delta\sigma$) (Figure 3-1). The seismic moment is related to magnitude through the definition of moment magnitude M by the relation

$\log M_0 = 1.5\,M + 16.1$ (Hanks and Kanamori, 1979) (Eq. 3-2)

The stress drop $\Delta\sigma$ relates the corner frequency f_c to M_0 through the relation

$f_c = \beta_0 (\Delta\sigma / 8.44\, M_0)^{1/3}$ (Brune, 1970; 1971) (Eq. 3-3)

The spectral shape of the single-corner-frequency ω-square source model is then described by the two free parameters M_0 and $\Delta\sigma$. The corner frequency increases with the source area shear-wave velocity and with increasing stress drop, both of which may be region dependent.

In order to compute peak time-domain values, i.e. peak acceleration, peak particle velocity, and peak oscillator response, random vibration theory (RVT) is used to relate RMS calculations to peak value estimates (Boore, 1983; Boore and Joyner, 1984).

3.2.1.1 Point Source Model Parameters for Rock Sites

In a half-space model, the near-surface amplification factors, $A(f)$, account for the increase in amplitude as the seismic energy travels through lower-velocity crustal materials near the earth's surface (Figure 3-1) (Boore, 1986; Silva and Darragh, 1993). These factors depend on average crustal and near-surface shear-wave velocity and density. In applications to hard rock environments, which exist principally in eastern North America (ENA), the near surface (1–2 km) velocity gradients are small and this effect is neglected (Boore and Atkinson, 1987).

The $P(f)$ filter models the observation that acceleration spectral density appears to fall off rapidly beyond some region-dependent maximum frequency. This observed phenomenon truncates the high-frequency portion of the spectrum and is responsible for the band-limited nature of the stochastic model. This spectral fall-off has been attributed to near-site attenuation (Hanks, 1982; Anderson and Hough, 1984) or to source processes (Papageorgiou and Aki, 1983) or perhaps to both effects. Hanks (1982) termed the phrase f_{max} to describe this site-dependent corner frequency. In the Anderson and Hough (1984) attenuation model, which is adopted in this study, the form of the $P(f)$ filter is taken as

$$P(f) = e^{-\pi\kappa(0)f} \quad \text{(Eq. 3-4)}$$

$\kappa(0)$ is a site- and distance-dependent parameter that represents the effect of intrinsic attenuation on the seismic waves as they propagate through the crust from source to receiver (Figure 3-1). Kappa depends on epicentral distance (r) and on both the shear-wave velocity (β_R) and quality factor (Q_s) averaged over a depth of H beneath the receiver or site. At zero epicentral distance, κ is given by

$$\kappa(0) = \frac{H}{\overline{\beta}_R \overline{Q}_s} \quad \text{(Eq. 3-5)}$$

The value of $\kappa(0)$ is attributed to attenuation in the very shallow crust directly beneath the site (Hough et al., 1988). Silva and Darragh (1993) suggest that the predominant kappa effects extend from the surface down to several hundred meters and possibly as deep as 1 to 2 km. The intrinsic attenuation along this part of the path is thought to be frequency-independent, but site-dependent, i.e., dependent on site geology (Hough et al., 1988). In this study, $\kappa(0)$ is assumed to be distance independent and is simply referred to as kappa. (Any distance-dependent attenuation or damping effects are absorbed in $Q(f)$ (Equation 3-1).) Kappa has been determined for several rock and soil sites representative of western North America (WNA) (Anderson and Hough, 1984; Anderson, 1986). For an average WNA rock site, a value between 0.02 and 0.06 sec is appropriate (Boore, 1986; Silva and Darragh, 1993). For eastern North America, a stable continental region with generally older and stronger crustal rocks, average kappa values range from about 0.004 sec to about 0.01 sec (Silva and Darragh, 1993). Similar models have been applied previously to the ENA (e.g., Silva and Green, 1989; Silva et al., 1989; Silva and Darragh, 1993).

The crustal anelastic attenuation from the source to just below the site is modeled with the frequency-dependent quality factors Q_f. In previous studies, the geometrical attenuation was taken as $1/R$ (or $1/\sqrt{R}$ for distances greater than about 100 km). In order to accommodate the effects of direct and supercritically-reflected waves in a crustal structure, this simple geometrical attenuation is replaced by a formulation due to Ou and Herrmann (1990) and later refined by Herrmann (Appendix 3A). The later extension represents an effort to increase the accuracy of the formulation, making it compatible with asymptotic ray theory for plane layered earth models. This method explicitly accounts for reflection, transmission, and free surface coefficients as well as some subcritical and all post-critical shear-wave arrivals. As a result, the numerical constants in the C term (Equation 3-1) are modified to accommodate the effects of a horizontally layered crust (Appendix 3A). With this technique, the geometrical attenuation and duration for direct plus post-critically reflected waves may be computed in a manner appropriate for the BLWN-RVT model.

In application, the plane-wave propagators of Silva (1976) are used to propagate SH or P-SV motion through the layered structure. To model an average horizontal component, the computed Fourier amplitude spectrum (Equation 3-1) is input as outcrop motion at the top of the source layer using the SH or P-SV propagators. Normal (SH for horizontal motion) or inclined (P-SV for vertical motion) incidence is assumed and the crust is taken as elastic with damping accommodated in the $Q(f)$ and kappa terms.

For fixed magnitude and distance, specific source, path, and site parameters are: stress drop ($\Delta\sigma$), crustal damping ($Q(f)$), crustal shear-wave velocity profile, and kappa (κ). These represent the point-source ground-motion parameters for a rock site.

3.2.1.2 Treatment of Site Effects

The parameters that influence the computed site response include the shear-wave velocity profile and strain dependent shear modulus and shear-wave damping. In order to accommodate the effects of surficial soils in eastern, central, and southeastern North America, generic site amplification factors are developed relative to hard rock conditions (Section 6) using the equivalent-linear approach described below.

To model soil response, an RVT-based equivalent-linear approach is used to propagate the point-source outcrop power spectral density through a one-dimensional soil column. RVT is used to predict peak time domain values of shear-strain based upon the shear-strain power spectrum. In this sense, the procedure is analogous to the program SHAKE (Schnabel et al., 1972) except that peak shear strains in SHAKE are measured in the time domain. The purely frequency-domain approach obviates a time domain control motion and, perhaps just as significantly, eliminates the need for a suite of analyses based on different input motions. This arises because each time domain analysis may be viewed as one realization of a random process. In this case, several realizations of the random process must be sampled to obtain a statistically stable estimate of site response. The realizations are usually performed by employing different control motions with approximately the same level of peak acceleration. In the frequency-domain approach, the estimates of peak shear strain as well as oscillator response are, as a result of the RVT, fundamentally probabilistic in nature. Stable estimates of site response can then be rapidly computed, permitting statistically significant estimates of uncertainties based on parametric variations.

3.2.1.3 Model Parameters

The source and path parameters used in the stochastic point-source model include source region shear-wave velocity and density, stress drop ($\Delta\sigma$), $Q(f)$ model, kappa, and crustal structure. Source region velocity and density are taken from the appropriate crustal model (Midcontinent or Gulf Coast, Section 5.5) for the given source depth. The median stress drop and kappa values, uncertainties, and distributions are shown in Table 3-1. The rationale for the median and uncertainty values is presented in Section 4 for stress drop and Section 5 for kappa.

Table 3-1

Model Parameters and Distributions for the Stochastic Ground Motion Model

Parameter	Median	Sigma	Distribution
$\Delta\sigma$	120 bars	0.70	log-normal
κ	0.006 sec	0.40	log-normal
Q(f) Models			
Midcontinent	**Q_0**		**η**
mean	670		0.33
upper-range	1000		0.30
lower-range	400		0.40
Gulf Coast			
mean	300		0.30
upper-range	500		0.30
lower-range	200		0.30

Table 3-1 also shows the $Q(f)$ models for the Midcontinent and Gulf Coast crustal structures. To accommodate uncertainty in the Q_0 and η values for each regional $Q(f)$ model (mean values in Table 3-1), upper-range and lower-range $Q(f)$ models are defined (Section 5). This was done as an alternative to placing distributions on Q_0 and η and varying them independently. The mean values for the model parameters given in Table 3-1 are used to generate a set of ground motions for each crustal region as a function of distance for any specified magnitude and source depth. Dispersion about the median ground motion predictions are computed by varying the model parameters according to the distributions shown in Table 3-1. This "parametric" variability of ground motion is discussed in Section 9.

3.2.2 Model Validation

An essential aspect of any numerical modeling approach is a demonstration of the model's ability to predict recorded strong ground motions. In this section, ground motions are modeled and compared to actual recordings for the 1989 Loma Prieta, 1987 Whittier Narrows, 1985 Nahanni, and 1988 Saguenay earthquakes. (Section 3.2.4 presents a statistical analysis of these results.) These events were chosen because they are relatively well-recorded large events (M 5.8 to 6.9, Table 3-2), and either there are numerous strong motion records available at close distances (i.e., < 100 km) (Whittier Narrows and Loma Prieta) or the events are from ENA and were recorded at a few close-in sites (Nahanni) or a wide range of distances (Saguenay). It is important to note that while the model results are best constrained by the more numerous close-in stations available from the Whittier Narrows and Loma Prieta events, data from the Nahanni and Saguenay events yield an essential calibration of the model for application to ENA.

Table 3-2

Model Parameters for Variability Calculations for the Stochastic Ground Motion Model

Earthquake	M	$\Delta\sigma$ (bars)	Q_0	η	κ (sec)	σ_{ln}	$e^{\sigma^2/2}$	N
Loma Prieta	6.9*	171	150*	0.60*	0.052	0.35	1.18	23
Whittier Narrows	5.9	165	150*	0.60*	0.038	0.43	1.15	12
Nahanni	6.8*	86	670*	0.33*	0.011	0.60	1.12	3
Saguenay	5.8*	655	361	0.87	0.026	0.87	1.19	20

* Fixed

An important initial step in the validation process is the selection of stations and associated seismic. For the stochastic model, site-specific effects for soil sites are incorporated into the computations separately (Section 3.2.1.2), with nonlinear response of soils treated explicitly in Section 6. Therefore, the emphasis in the validation is on maximizing the number of rock sites, particularly for the Loma Prieta earthquake. For rock sites, the determination of kappa values is more straightforward, and the effects of nonlinear soil response at high levels of motion are largely avoided. On the other hand, for the semi-empirical ground motion model (Section 3.3), the site-specific effects are not directly modeled so the emphasis was placed on including as many sites as is practical. The result is that for the stochastic model 61 sites were selected for the four events, while for the semi-empirical model, 104 sites were selected (Section 3.3.2). 39 of these sites are common to the two validation exercises; the comparison of validations using only the sites in common is discussed in Section 3.4.

Appropriate values for the model parameters stress drop, $Q(f)$, and kappa were estimated for each earthquake by fitting Equation 3-1 to the log Fourier amplitude spectra computed from recorded motions (Section 4.2). The use of log spectra is appropriate since short period ground motions are generally considered to be log normally distributed. Fitting on log amplitudes, however, results in model parameters that are appropriate for median Fourier amplitude predictions. Since Parseval's relation, used in the RVT process to relate power spectra to RMS time domain values, is based on a mean spectrum, the model prediction should be corrected by the mean/median ratio of the Fourier amplitude. This ratio is given by

$$mean\ /\ median = e^{\frac{\sigma^2}{2}} \qquad \text{(Eq. 3-6)}$$

where σ^2 is estimated from the residuals of the fit of Equation 3-1 to the Fourier amplitude spectrum.

Not all of the model parameters could be determined for each earthquake, depending upon number of stations and distance distribution of stations. In particular, due to the limited number of stations and distances for the Nahanni and Whittier Narrows earthquakes as well as limited bandwidth for the Saguenay earthquake, magnitudes could not be resolved for these events. In order to provide more stable inversions, magnitudes were fixed to published values based upon teleseismic data. For consistency, the magnitude was held fixed for the Loma Prieta earthquake as well. In addition, a constant multiplicative term, D, was added to Equation 3-1 for each site. This term was included to reduce the coupling of unmodeled broad-band local crustal as well as site effects into the kappa values. If the assigned magnitudes are inconsistent with the data sets being analyzed, as is sometimes the case when comparing long period spectral levels from strong motion data to teleseismically determined seismic moments, the D terms provide a mechanism for adjustment. This reduces the tendency for the inversion process to place the effect of magnitude inconsistencies in the corner frequency or stress drop. The variability of the D terms is included as modeling uncertainty in the total modeling variability.

The model parameter estimation and subsequent forward modeling used both the simple $1/R$ ($1/\sqrt{R}$, R)$100km$) and refined Herrmann (Appendix 3A) geometrical attenuation models for the Loma Prieta and Saguenay earthquakes. Since the models produced similar parameter values, the simple $1/R$ model is used for all four earthquakes to estimate the model parameter values and modeling variability.

3.2.2.1 Loma Prieta Model

The resulting parameters for the Loma Prieta earthquake are shown in Table 3-2. For crustal amplification, the velocity model given in Wald et al. (1991) was used. For the soil sites, GL2, PVA, and TRI site specific soil profiles were available and were placed on top of the Wald et al. (1991) crust. The soil sites were not used in estimating the model parameter values, as a sufficient number of rock sites were available. In the forward modeling for the variability calculation, the nonlinear response of the soils is accommodated using an RVT based equivalent-linear technique (Section 6). At these sites, the log average kappa value for the rock sites of 0.052 sec (Table 3-2) is used for the shallow crustal damping. The moment magnitude was fixed at 6.9 resulting in a stress drop of 171 bars. The $Q(f)$ model was also fixed with a Q_0 of 150 and an η of 0.60, values appropriate for western North America (Boore, 1983). Table 3-3 lists the sites used, individual kappa values, D terms, and point source distances. The distances are the closest distance to the surface projection of the top of the rupture assuming a depth of 12 km, the location of the largest asperity (Wald et al., 1991).

Table 3-3

Loma Prieta Earthquake: Seismic Stations Used in Validation of Stochastic Model

Label	Number	Organization	Station Name	κ(sec)**	D	R(km)
COR‡	57007	CSMIP	Corralitos	0.067	0.79	12.0
LGPC‡	–	UCSC	Los Gatos	0.046	1.04	12.4
BRAN‡	–	UCSC	Branciforte Dr.	0.032	0.87	15.6
GL1‡	47379	CSMIP	Gilroy 1	0.038	0.80	19.2
GL2*‡	47380	CSMIP	Gilroy 2	0.052	1.00	20.0
UCS‡	58135	CSMIP	UCSC-Lick Lab	0.032	0.82	20.0
UCSC‡	–	UCSC	UCSC-Seismic Lab	0.025	0.71	23.3
GL6‡	57383	CSMIP	Gilroy 6	0.060	0.77	26.8
PAV*‡	1227	USGS	Palo Alto VA	0.052	1.00	26.8
SLA‡	1601	USGS	SLAC	0.069	1.26	30.5
RDC‡	58263	CSMIP	Redwood City-Cañada	0.065	0.63	39.9
SAS‡	47189	CSMIP	SAGO South	0.080	0.76	40.8
A07	58378	CSMIP	APEEL 7	0.065	1.10	45.6
A10‡	58373	CSMIP	APEEL 10	0.087	1.18	45.6
MON‡	47377	CSMIP	Monterrey City Hall	0.042	0.47	45.6
BEL	58262	CSMIP	Belmont-2 story	0.072	1.01	47.5
A2E‡	58219	CSMIP	APEEL 2E, CUSH	0.059	0.75	54.3
SSP‡	58539	CSMIP	Sierra Point	0.036	0.93	66.1
SFD‡	58130	CSMIP	SF Diamond Height	0.052	1.16	74.0
PHS‡	58338	CSMIP	Piedmont J.H.	0.051	0.98	75.0
SFR‡	58151	CSMIP	SF Rincon	0.029	1.04	76.9
YBI‡	58163	CSMIP	Yerba Buena Island	0.073	1.03	77.9
SFH‡	58131	CSMIP	SF Pacific Heights	0.069	1.14	78.9
SFT‡	58133	CSMIP	SF Telegraph Hill	0.059	1.00	78.9
TRI*	58117	CSMIP	Treasure Island	0.052	1.00	79.9
SFC‡	58132	CSMIP	SF Cliff House	0.065	1.31	80.9

* Soil sites.

** Kappa values are relative to the fixed Q(f) of $150\,f^{0.6}$. For distances exceeding about 50 km, the kappa values are strongly coupled to the Q(f) model.

‡ Also modeled using semi-empirical method, see Sections 3.3 and 3.4.

A comparison between the computed 5% damped acceleration response spectra using the parameters listed in Table 3-2 and the log average of the two horizontal components at each site is shown in Figure 3-2. In general, the simple point-source provides a good match to the spectra computed from the recorded motions both close-in and at large distances. A feature of interest is the overprediction by the point source model at low frequencies, particularly at close sites. These high levels of motion impact the uncertainty as well as model bias at low frequencies.

3.2.2.2 Whittier Narrows Model

For the Whittier Narrows earthquake, the magnitude and $Q(f)$ model were constrained to M 5.9 and $150 f^{0.6}$ respectively (Table 3-2). The crustal model used is from Wald et al. (1988). For the soil sites, since site specific profiles were not available, a generic profile appropriate for sandy soils was used in place of the top layer of Wald et al. (1988a) crustal model. Recordings from both rock and soil sites are used in estimating the model parameter values with the response of soil sites treated as linear. The resulting stress drop is 165 bars (Table 3-2) with an average kappa value of 0.038 sec. Kappa values would, to first order, account for possible nonlinear effects through increased damping and higher values than would apply for linear response. Stations, distances, D terms, and site kappa values are listed in Table 3-4. Distances are closest distance to the surface projection of the rupture surface down to the depth of the largest asperity at 15.2 km (Hartzell and Iida, 1990).

Figure 3-3 shows comparisons between predicted and recorded motions in terms of response spectra for the Whittier Narrows earthquake. As with the Loma Prieta earthquake, the match is generally good at most of the sites. Again there is a tendency for the point source model to overpredict at low frequencies at rock sites (GVR and MTW).

3.2.2.3 Nahanni Earthquake

The Nahanni earthquake analyzed here is the mainshock, the only Nahanni event recorded on all three strong motion instruments. The moment magnitude was fixed at 6.9 with Q_0 and η fixed at the mean Midcontinent $Q(f)$ model (Table 3-2). A crustal structure was not used, as little amplification is expected in propagating from the source region to the surface in this predominately cratonic crustal environment. Assuming a source region shear-wave velocity and density of 3.5 km/sec and 2.7 cgs, appropriate for the Midcontinent crustal model layer 1 (Section 5), the resulting stress drop is 86 bars. The average kappa value is 0.011 sec. Table 3-5 lists the sites, inversion parameters and distances. Approximate point-source distances are taken as closest distance to the surface projection of the top of the rupture plane to a depth of 9 km. The site D values vary from 0.61 to 1.34, possibly reflecting a large uncertainty in the appropriate distance for the point source.

Figure 3-4 shows the comparison of recorded motions to model predictions for the three sites. Site 1 shows an underprediction for frequencies exceeding about 2 Hz with an average zero period spectral acceleration over 1g for the recorded motions. These very high levels of motion occur approximately 8 seconds into the record and may be associated with local effects. This short burst of energy does not appear at the other sites, lending support to a localized cause. It is not surprising then that this simple model predicts lower short-period motions. If the response spectra are computed using the first 7.5 seconds, the model and recorded motions show much closer agreement.

3.2.2.4 Saguenay Earthquake

For the Saguenay earthquake only the moment magnitude, 5.8, was held fixed. Although a large number of stations are available out to nearly 500 km (Table 3-6), permitting resolution of both $Q(f)$ and kappa values, the determination of magnitude (seismic moment), based upon the single-corner-frequency-omega-square model (Equation 3-1) is not reliable due to the limited bandwidth. Additionally, the mainshock exhibits strongly non-ω^2 characteristics having much more high frequency (>1 Hz) energy content relative to intermediate frequencies than is compatible with a simple ω^2 source model (Section 4), Boore and Atkinson (1992). The resulting high stress drop, 655 bars, (Table 3-2) reflects this model inconsistency. The resulting $Q(f)$ model is $361 f^{0.87}$ and represents paths in both the Grenville and Appalachian crustal structures. The average kappa value is 0.026 sec, but this value is ill-constrained because many of the ECTN data used have limited bandwidth or H/V ratio assumptions that limit the data (Table 3-6). Also, kappa determined from stations beyond 100 km tend to have some correlation with $Q(f)$, so that the relatively higher kappa values at these distances might also reflect the fact

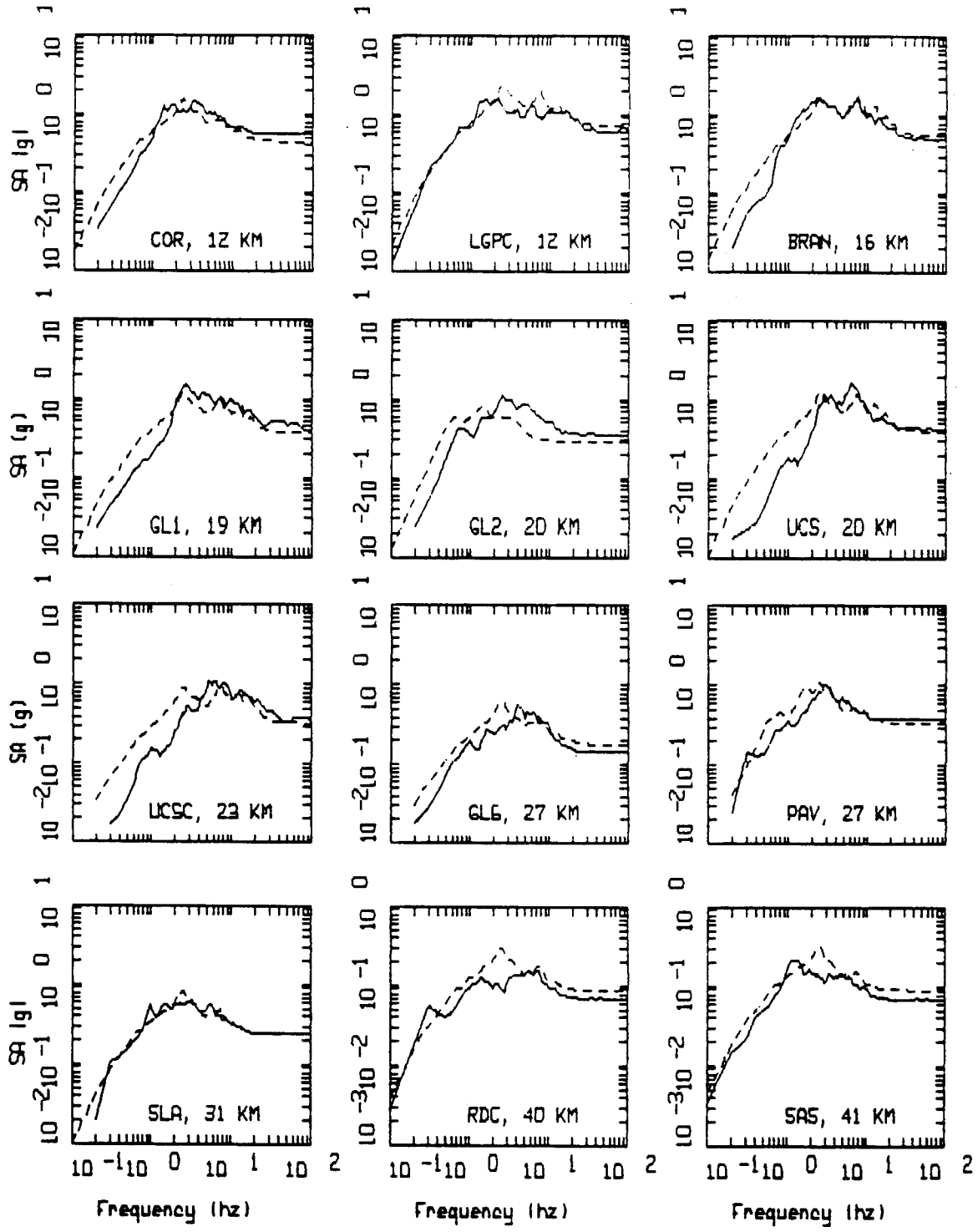

Figure 3-2. Comparison of observed and modeled 5% damped acceleration response spectra for the 1989 Loma Prieta earthquake. Model results are from the stochastic ground motion model. (Solid line — average of two horizontal spectra; dashed line - - - model.)

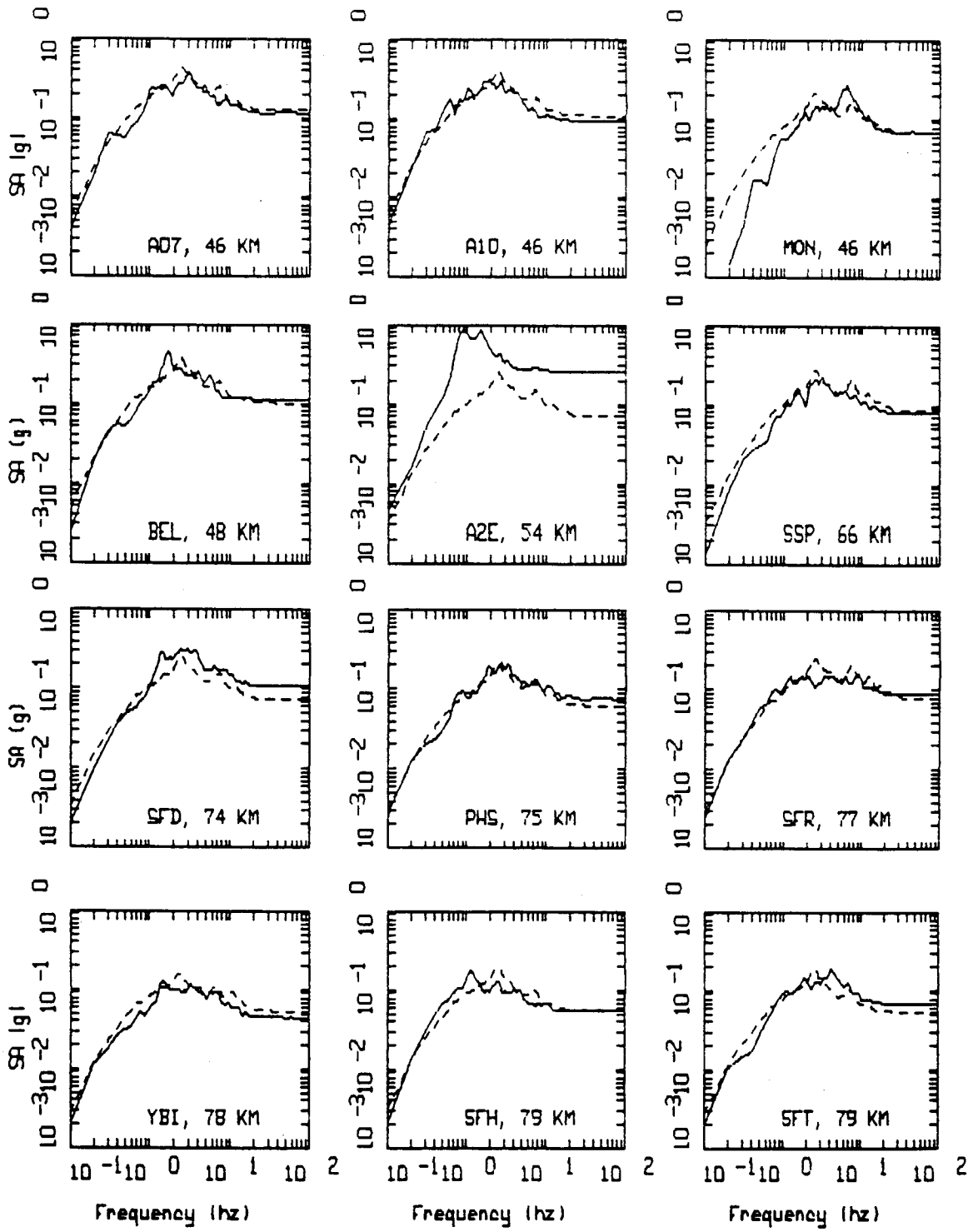

Figure 3-2 (Continued). Comparison of observed and modeled 5% damped acceleration response spectra for the 1989 Loma Prieta earthquake. Model results are from the stochastic ground motion model. (Solid line — average of two horizontal spectra; dashed line - - - model.)

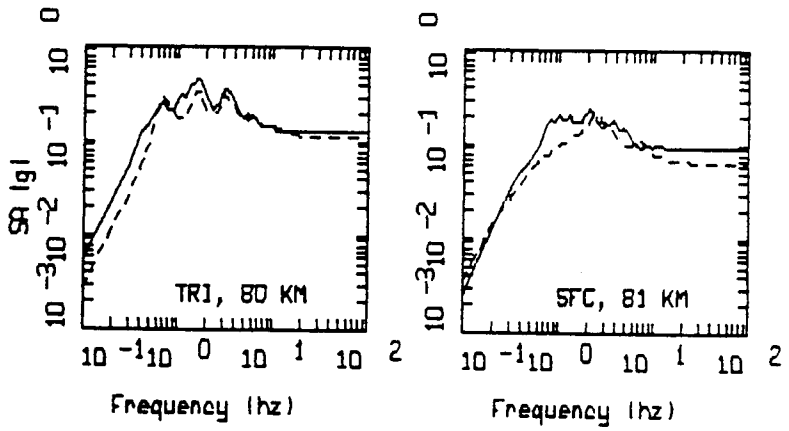

Figure 3-2 (Continued). Comparison of observed and modeled 5% damped acceleration response spectra for the 1989 Loma Prieta earthquake. Model results are from the stochastic ground motion model. (Solid line — average of two horizontal spectra; dashed line - - - model.)

Table 3-4

Whittier Narrows Earthquake: Seismic Stations Used in Validation of Stochastic Model

Label	Number	Organization	Station Name	κ(sec)	D	R(km)
GVR‡	709	USGS	Garvey Reservoir-abut.	0.035	1.08	15.6
WND*‡	289	USGS	Whittier Narrows Dam-upst.	0.026	0.54	15.9
ALH*‡	482	USGS	Alhambra-900 S. Fremont	0.044	0.84	16.8
SNM*‡	24401	CSMIP	San Marino	0.048	0.53	17.1
OBG*‡	24400	CSMIP	LA-Obregon Park	0.039	0.96	18.1
WHB*‡	804	USGS	Whittier-Bright	0.039	0.87	18.3
LBM*‡	5129	USGS	LA-Bulk Mail	0.047	1.11	18.9
VRN*	288	USGS	Vernon CMD	0.069	1.26	20.3
NWK*	634	USGS	Norwalk-Imperial South	0.048	0.68	21.9
DOW*‡	14368	CSMIP	Downey-Co. Maint.	0.061	1.09	23.1
MTW‡	24399	CSMIP	Mt. Wilson	0.012	0.29	23.8
HSL*‡	24303	CSMIP	LA Hollywood Storage Lot	0.029	0.58	28.8

* Soil sites.
‡ Also modeled using semi-empirical method, see Sections 3.3 and 3.4.

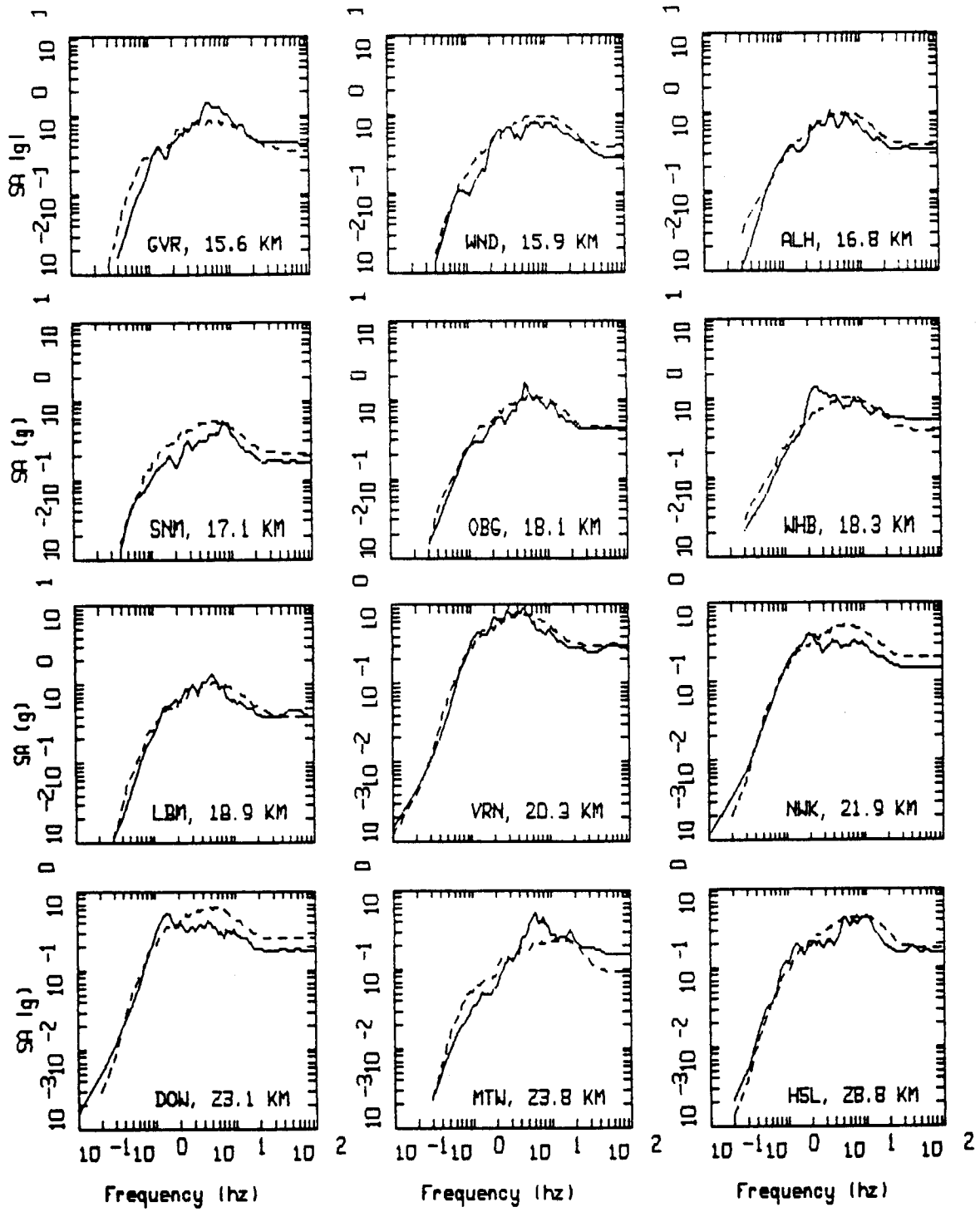

Figure 3-3. Comparison of observed and modeled 5% damped acceleration response spectra for the 1987 Whittier Narrows earthquake. Model results are from the stochastic ground motion model. (Solid line — average of two horizontal spectra; dashed line - - - model.)

Table 3-5

Nahanni Earthquakes: Seismic Stations Used in Validation of Stochastic Model

Label	Number	Organization	Station Name	κ(sec)	D	R(km)
S2‡	2	GSC	Site 2	0.012	0.61	9.2
S1‡	1	GSC	Site 1	0.021	1.34	9.6
S3‡	3	GSC	Site 3	0.005	0.61	21.1

‡ Also modeled using semi-empirical method, see Sections 3.3 and 3.4.

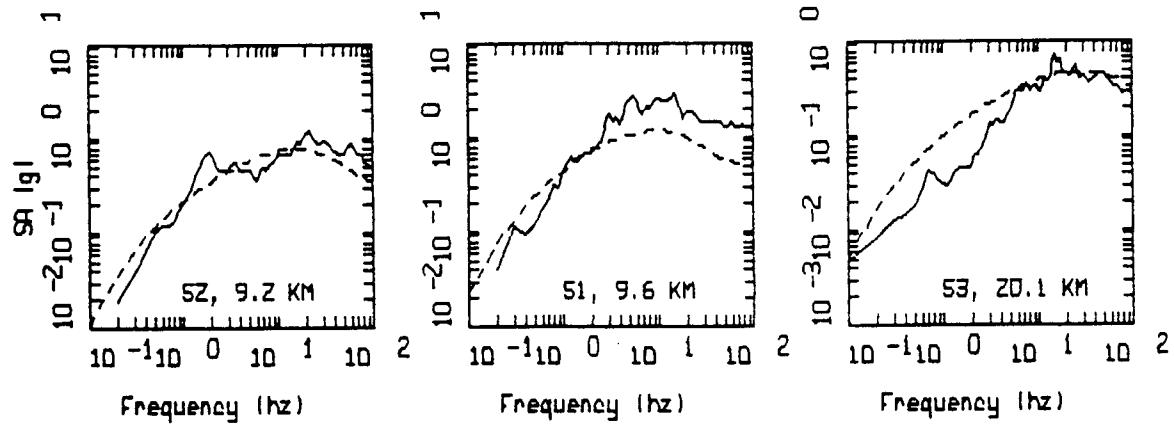

Figure 3-4. Comparison of observed and modeled 5% damped acceleration response spectra for the 1985 Nahanni earthquake. Model results are from the stochastic ground motion model. (Solid line — average of two horizontal spectra; dashed line - - - model.)

Table 3-6

Saguenay Earthquake: Seismic Stations Used in Validation of Stochastic Modeling

Label	Number	Organization	Station Name	κ(sec)**	D***	R(km)
S16‡	16	GSC	Chicoutimi-Nord	0.006	1.0	52.0
S17‡	17	GSC	St-André-du-Lac-St-Jean	0.003	1.0	69.9
S20‡	20	GSC	Les Eboulements	0.002	1.0	94.9
S08‡	8	GSC	La Malbaie	0.010	1.0	97.4
A54	—	ECTN	A54	0.025	1.0	97.9
A61	—	ECTN	A61	0.022	1.0	98.6
A64	—	ECTN	A64	0.024	1.0	105.5
A16	—	ECTN	A16	0.029	1.0	117.4
S10‡	10	GSC	Riviere-Ouelle	0.020	1.0	118.0
A21	—	ECTN	A21	0.025	1.0	124.2
A11	—	ECTN	A11	0.038	1.0	125.6
EBN*	–	ECTN	Edmundston, N.B.	0.035	1.0	231.3
SBQ*	–	ECTN	Sherbrooke, Que	0.038	1.0	311.0
GSQ*	–	ECTN	Grosses Roches, Que.	0.045	1.0	315.0
TRQ*	–	ECTN	Mont Tremblant, Que.	0.015	1.0	332.5
MNT*	–	ECTN	Montreal, Que.	0.031	1.0	346.4
KLN*	–	ECTN	McKendrick L., N.B.	0.059	1.0	390.5
GRQ*	–	ECTN	Grand Remous, Que.	0.025	1.0	392.2
OTT*	–	ECTN	Ottawa, Ont.	0.036	1.0	460.8
WBO*	–	ECTN	Williamsburg, Ont.	0.032	1.0	468.3

* ECTN vertical component, H/V of 1.4 used to convert vertical records to horizontal.

** Kappa values for the horizontal component ECTN sites ANN may not be reliable due to the limited bandwidth. The vertical component sites also have a limited bandwidth and neglect any frequency dependence in the H/V ratio.

*** Fixed.

‡ Also modeled using semi-empirical method, see Sections 3.3 and 3.4.

that paths to these stations have lower $Q(f)$ values appropriate for the dominantly Appalachian structure they traverse. Table 3-6 lists the sites, kappa values, D terms, and hypocentral distances. For this earthquake, the initial inversion resulted in D terms that were all very close to 1. An additional inversion was then performed with D fixed to 1 at all sites. The nine most distant sites are vertical component ECTN stations. For these records, an H/V ratio of 1.4 was used.

In Figure 3-5 are shown the comparisons between computed and recorded motions, expressed as 5% damped response spectra. For most of the sites, the model provides a good match to the recorded motions at high frequencies due to the high stress drop. At low frequencies, the systematic departure of the recorded motions from the model predictions is evident at the sites with horizontal components. At the vertical component sites, labeled Z in Figure 3-5, the model overprediction is less pronounced. This may be a result of using a frequency independent H/V ratio. Over all of the sites, in general, the simple point-source model provides a reasonably good match to the recorded motions at high frequencies and is generally conservative at low frequencies.

3.2.3 Modeling Variability and Bias

For strong ground motions predicted from numerical modeling to be accepted for use in engineering design, it is necessary to demonstrate that the numerical modeling procedure can accurately predict recorded strong ground motions. In addition, an estimate of the variability in ground motion estimates derived from numerical modeling is needed, analogous to the variability given for empirical attenuation models. A quantitative assessment of the modeling or residual variability (Abrahamson et al., 1990) associated with the stochastic point-source model is computed here for the four events modeled in the previous section.

The total variability of the predicted strong ground motion should include all sources of variability: modeling variability, which is due to factors not accounted for in the source or wave propagation models; and parametric variability, which is due to variability in the values of source parameters for future earthquakes. Procedures are described by Abrahamson et al. (1990) for quantifying the goodness-of-fit between simulated and recorded ground motions, and for estimating the total variability of predicted ground motions for future earthquakes by combining modeling variability and parametric variability. The partitioning of the total variability into modeling and parametric components may be different for different simulation procedures. Any model parameters that are estimated on an earthquake-specific or site-specific basis need to be considered in the parametric variations; whereas model parameters that remain fixed for all events and sites are not considered in the parametric variations. The parametric variability for the stochastic model is estimated in Section 9; the modeling variability is discussed below.

The modeling variability is derived from the comparison of observed and modeled (or predicted) response spectra. These spectra are shown in Figures 3-2 to 3-5 for the stochastic model comparisons. The modeling variability is defined as the standard error of the residuals of the log of the average horizontal component response spectra. The residual is defined as the difference of the logarithms of the observed average 5% damped acceleration response spectra and the predicted response spectra. At each period, the residuals are squared, and summed over the total number of sites (61) for all four earthquakes. Dividing the resultant sum by the number of sites results in an estimate of the model variance or residual variance. Any model bias that exists may be estimated in the process (Abrahamson et al., 1990) and used to correct (lower) the residual variance.

Figure 3-6a shows the model bias versus frequency. The computed model bias is essentially zero at the 90% confidence level for frequencies above about 3 Hz. The negative model bias for lower frequencies is primarily due to the point-source tendency for overprediction at low frequencies at close sites (shown in the Loma Prieta and Whittier Narrows earthquakes response spectra) and the large overprediction at intermediate-to-low frequencies for the Saguenay earthquake response spectra.

As discussed in Section 9, the variability of ground motion can be separated into randomness and uncertainty. Randomness represents intrinsic variability and uncertainty represents variability due to our lack of knowledge. The modeling variability can also be separated into uncertainty and randomness terms. The residual standard error corrected for model uncertainty represents modeling randomness. In this case, both the model bias and the D (site) terms are uncertain because they represent systematic misfits between modeled and recorded

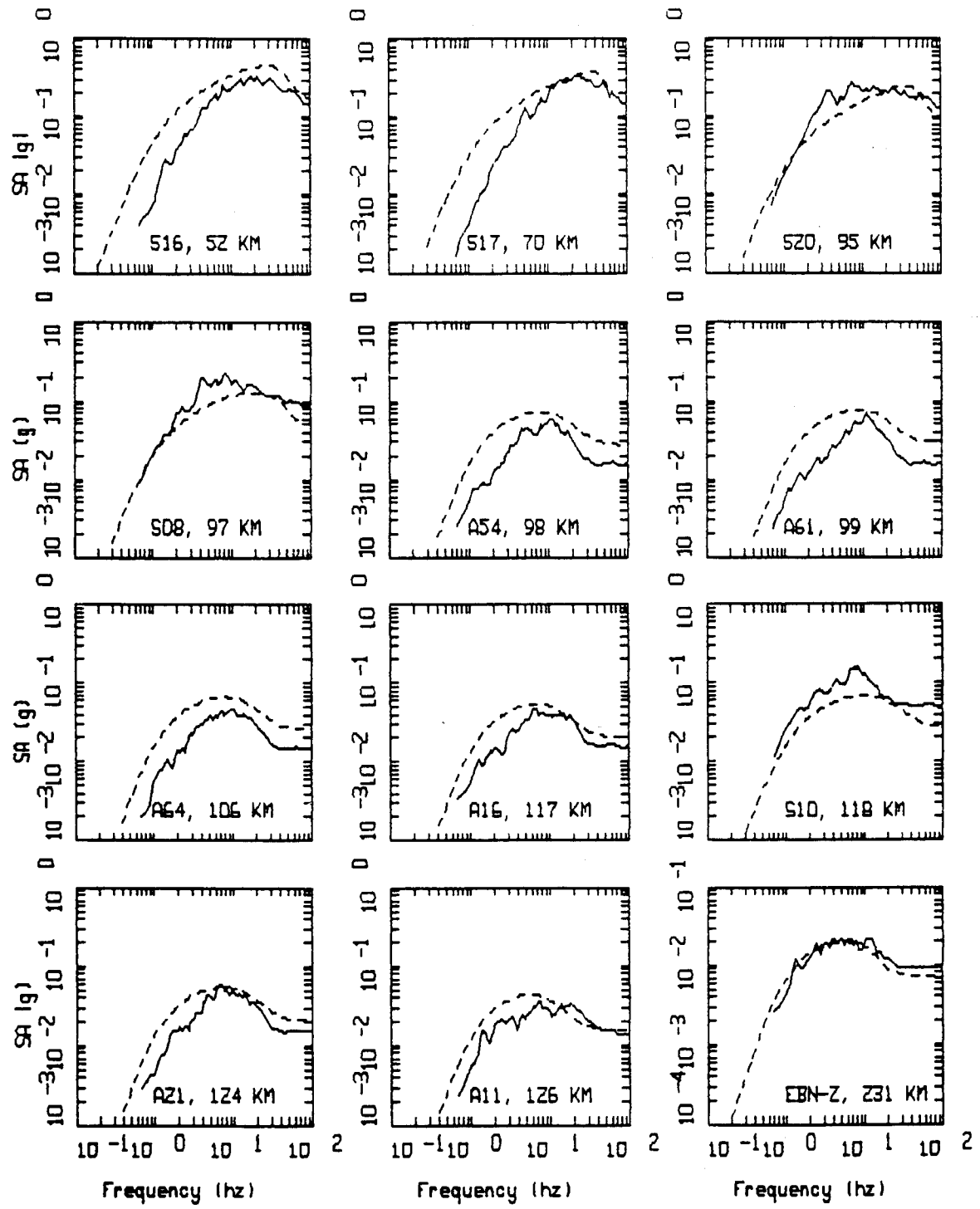

Figure 3-5. Comparison of observed and modeled 5% damped acceleration response spectra for the 1988 Saguenay earthquake. Model results are from the stochastic ground motion model. (Solid line — average of two horizontal spectra or vertical spectrum : 1.4. Dashed line - - - model.)

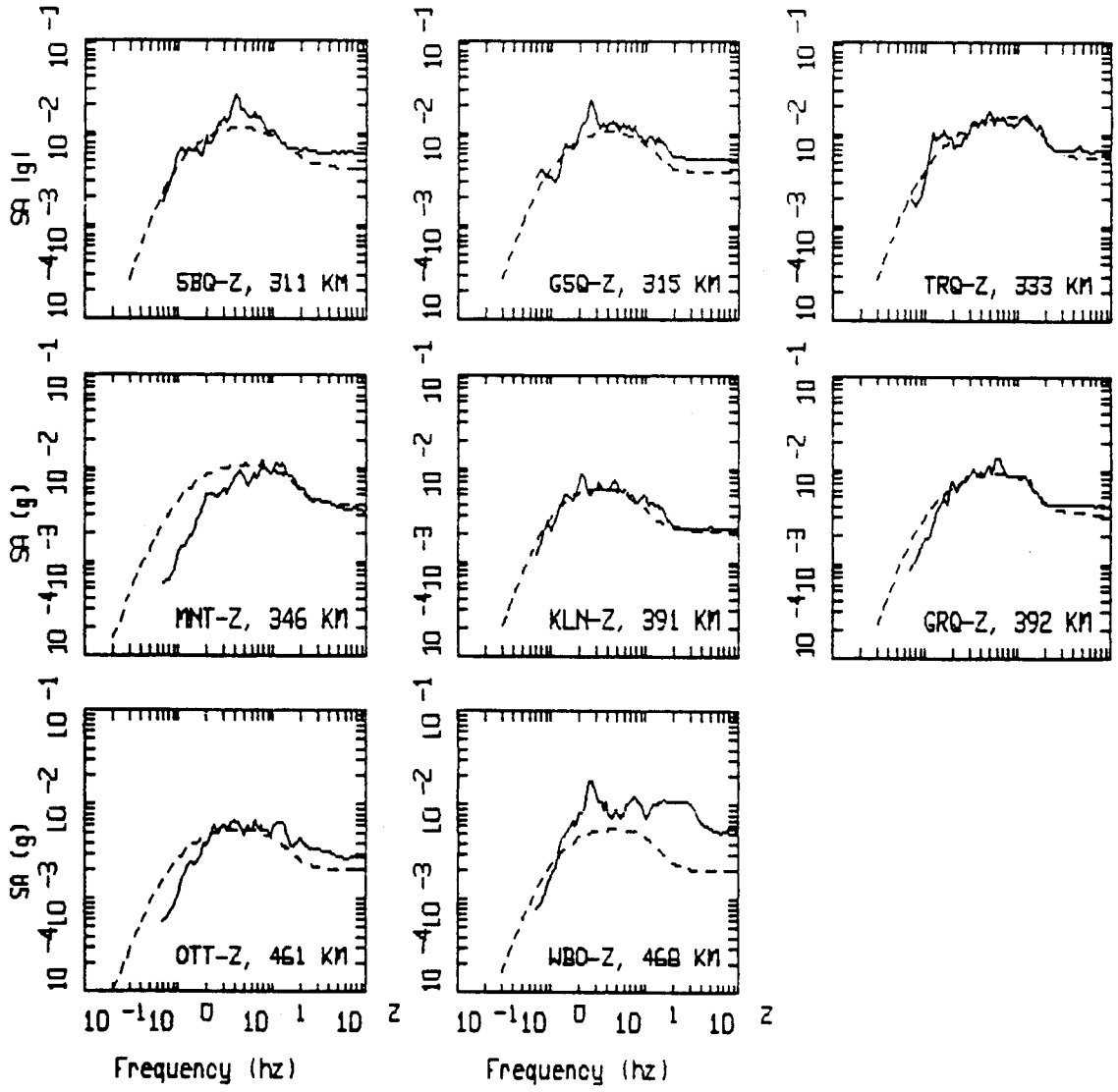

Figure 3-5 (Continued). Comparison of observed and modeled 5% damped acceleration response spectra for the 1988 Saguenay earthquake. Model results are from the stochastic ground motion model. (Solid line — average of two horizontal spectra or vertical spectrum : 1.4. Dashed line - - - model.)

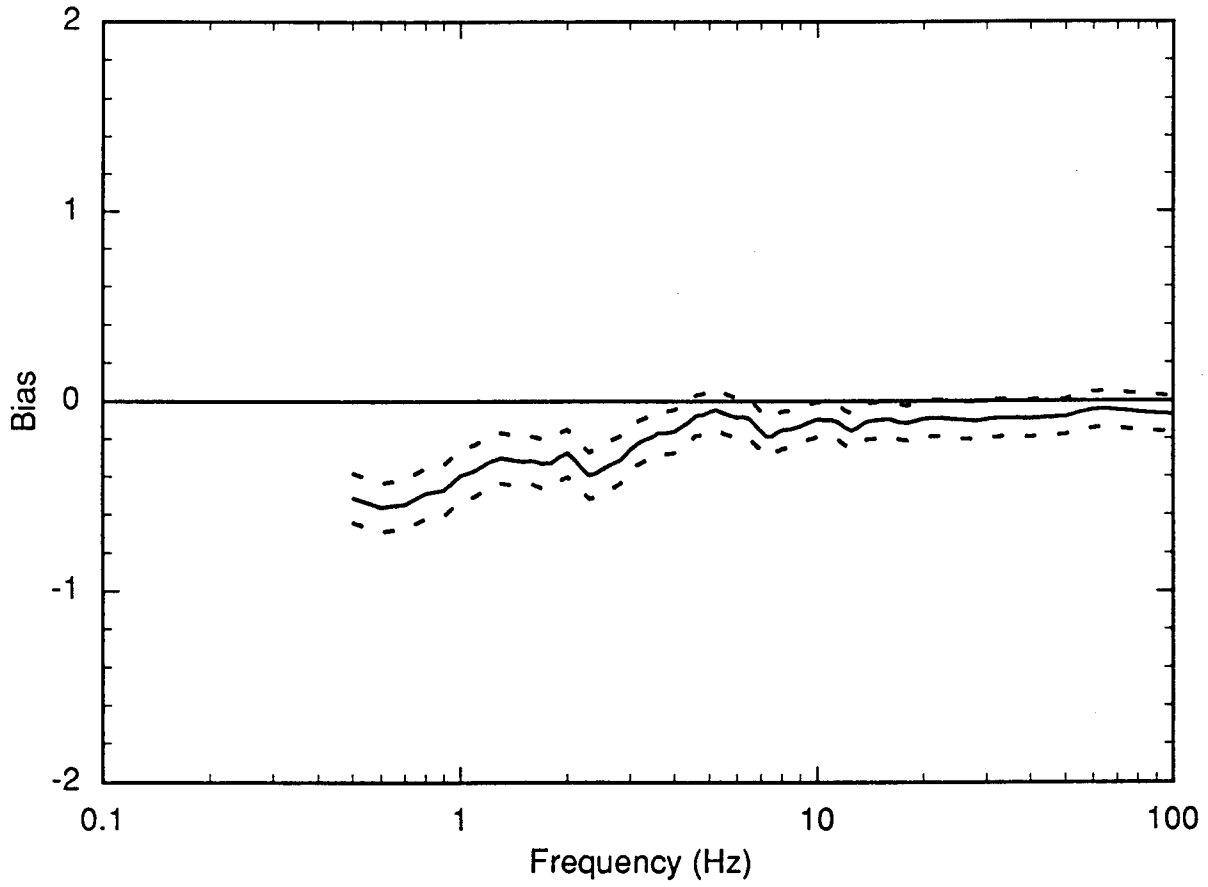

Figure 3-6a. Modeling bias computed from recordings at 61 stations for the Loma Prieta, Whittier Narrows, Nahanni, and Saguenay earthquakes using the stochastic ground motion model. Dashed lines represent 90% confidence limits.

ground motions. Since it may be possible to reduce these systematic variations by refining the model, the effects of the bias and the variability of the D terms represent modeling uncertainty. The modeling randomness and the combined modeling randomness and uncertainty are shown in Figure 3-6b.

The overall low levels of the standard error and small bias at frequencies above about 3 Hz indicate the ability of the simple point-source stochastic model to accurately predict strong ground motions in a variety of crustal regions and site conditions. Additionally, any significant model bias exists only at low frequencies and reflects an overprediction of ground motions. These overpredictions are largely driven by the Saguenay earthquake.

3.3 Semi-Empirical Ground Motion Model

At frequencies below about 2 Hz, the principal features of strong ground motions can be modeled using deterministic models of the earthquake source. The ability of synthetic seismograms to match recorded strong ground motions at low frequencies has been clearly demonstrated during the past decade; a summary of events studied is given in Mendoza and Hartzell (1988) and Heaton (1990). However, at the higher frequencies of interest for this study, strong ground motions are highly affected by stochastic processes. The modeling procedure described below combines empirical and theoretical approaches to modeling ground motion effects in order to capture the essence of both deterministic and stochastic elements of ground motion. The combined semi-empirical model is

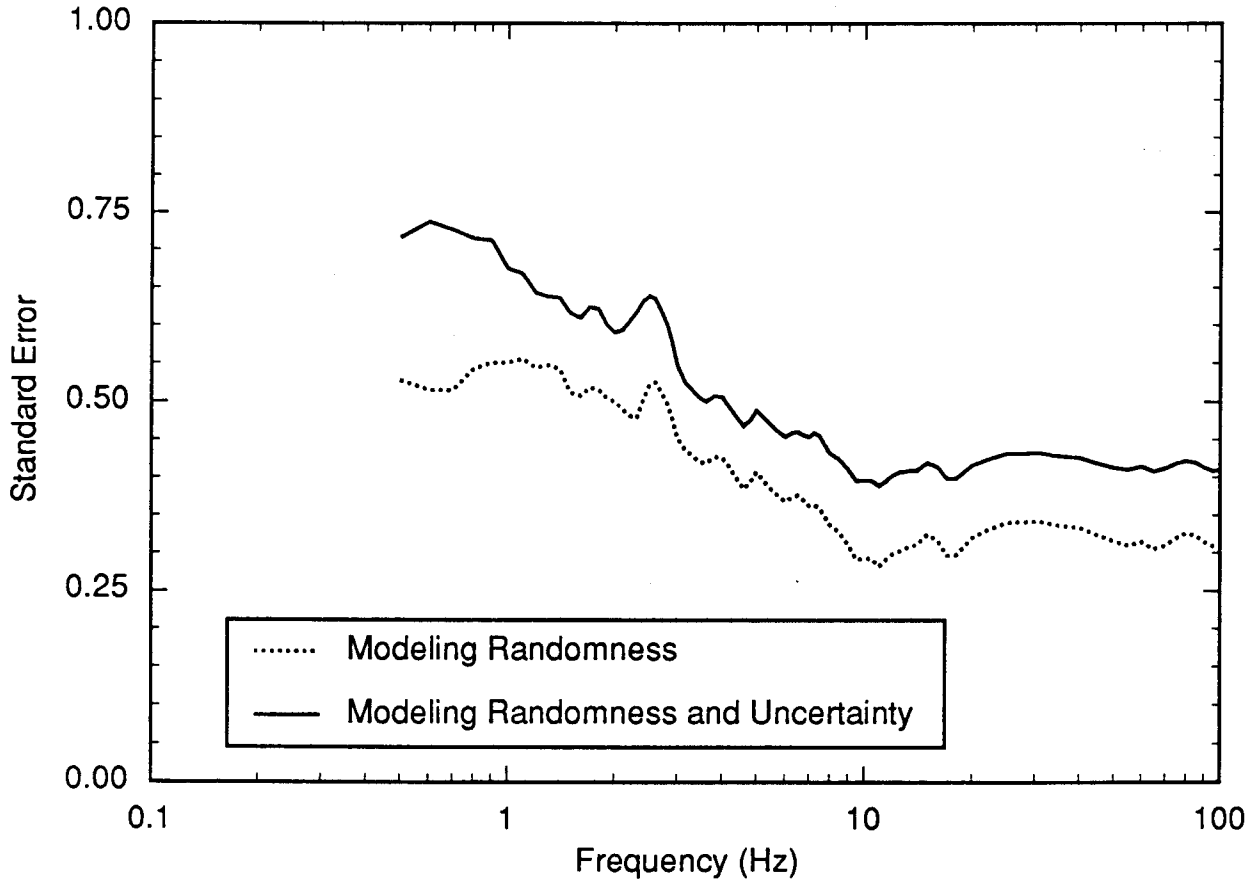

Figure 3-6b. Standard error of modeling or modeling variability (natural log) computed from recordings at 61 stations for the Loma Prieta, Whittier Narrows, Nahanni, and Saguenay earthquakes using the stochastic ground motion model. Solid line, total variability (modeling uncertainty plus randomness); dashed line, corrected for model bias and site term D.

used in this study to quantify path effects or, more precisely, contributions to ground motion variability made by wave propagation in the earth's crust (Section 5).

3.3.1 Model Description

In the semi-empirical ground motion modeling approach, near-source recordings of small earthquakes are used as empirical source functions to provide a realistic representation of effects such as source radiation that are difficult to deterministically model at high frequencies due to their stochastic behavior. Wave propagation effects are modeled using simplified transfer functions or Green's functions that are designed to transfer empirical source functions from their recording sites to those required for use in simulations at a specific site. The details of the simulation procedure are described by Wald et al. (1988a) and Somerville et al. (1991), and are summarized in Appendix 3.B.

The procedure is illustrated schematically in Figure 3-7. The fault is divided into discrete elements, and the motions from these elements are lagged and summed across the fault to simulate the propagation of rupture over the fault surface. A stochastic component is included in the speeds of fault slip and rupture propagation to simulate heterogeneity in rupture dynamics. Large scale asperities (areas of concentrated slip and high-frequency radiation) are introduced by varying the slip distribution over the fault surface.

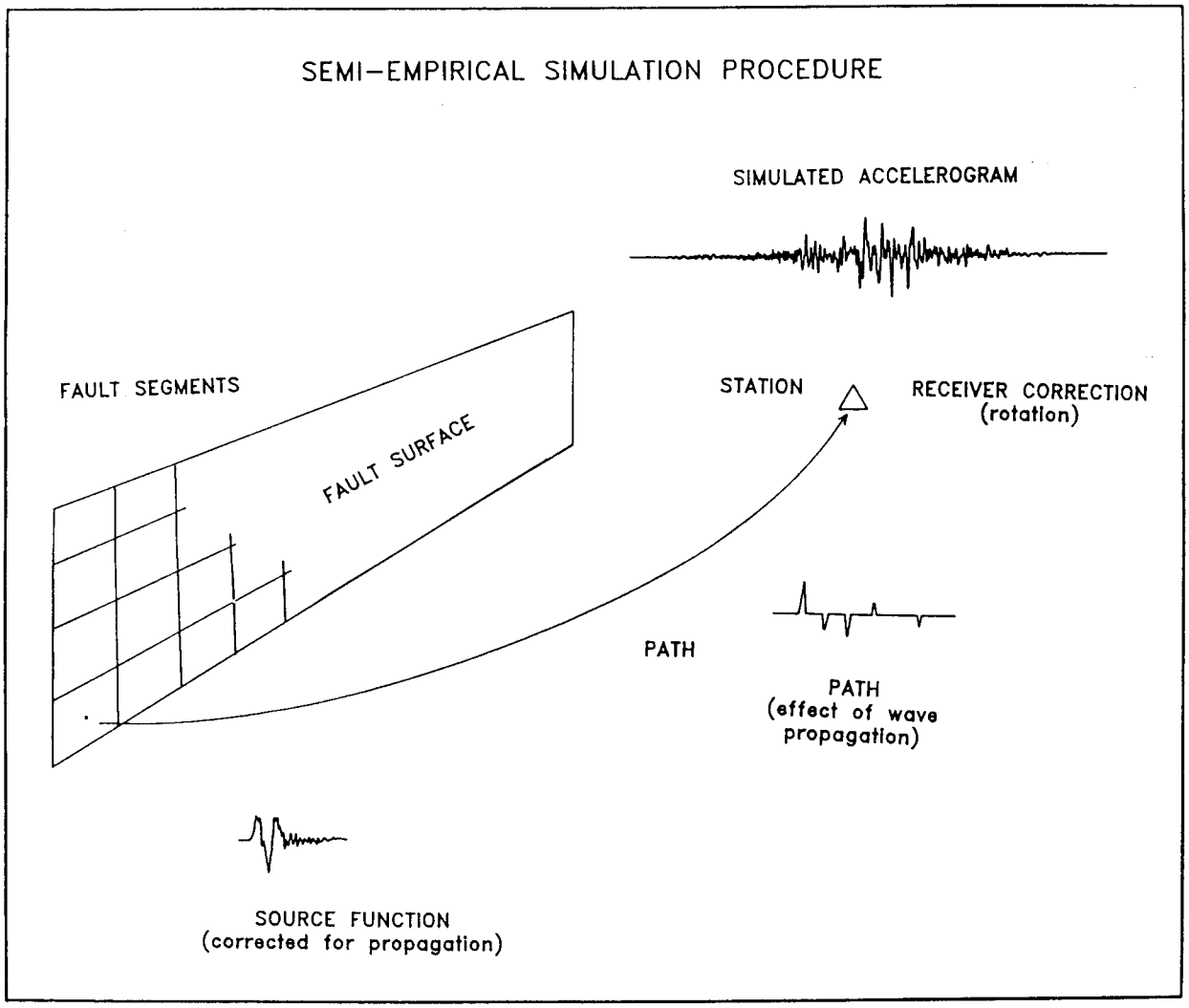

Figure 3-7. Schematic diagram of the ground motion simulation procedure. Source: Somerville et al., 1990.

The Green's functions are calculated using the method of generalized rays (Helmberger and Harkrider, 1978). Rays corresponding to the direct P and S waves and to the primary reflection (and head wave beyond critical angle) from each interface below the source are included, as shown schematically in Figure 3-8. The overall seismogram is produced by summing these various rays, which generally arrive at the site at different times. The amplitude and time relationships between these arrivals change with distance, producing seismograms whose amplitudes and durations change with distance. In a homogeneous half space, the rate at which ground motion decays with distance is the inverse source distance, 1/R. At source-site distances less than the critical distance (the distance beyond which all seismic energy is reflected back to the surface from a given boundary), the interference between the upgoing wave and waves reflected due to the velocity gradient below the source causes attenuation more rapid than 1/R. Beyond the critical distance, however, critical reflections cause the

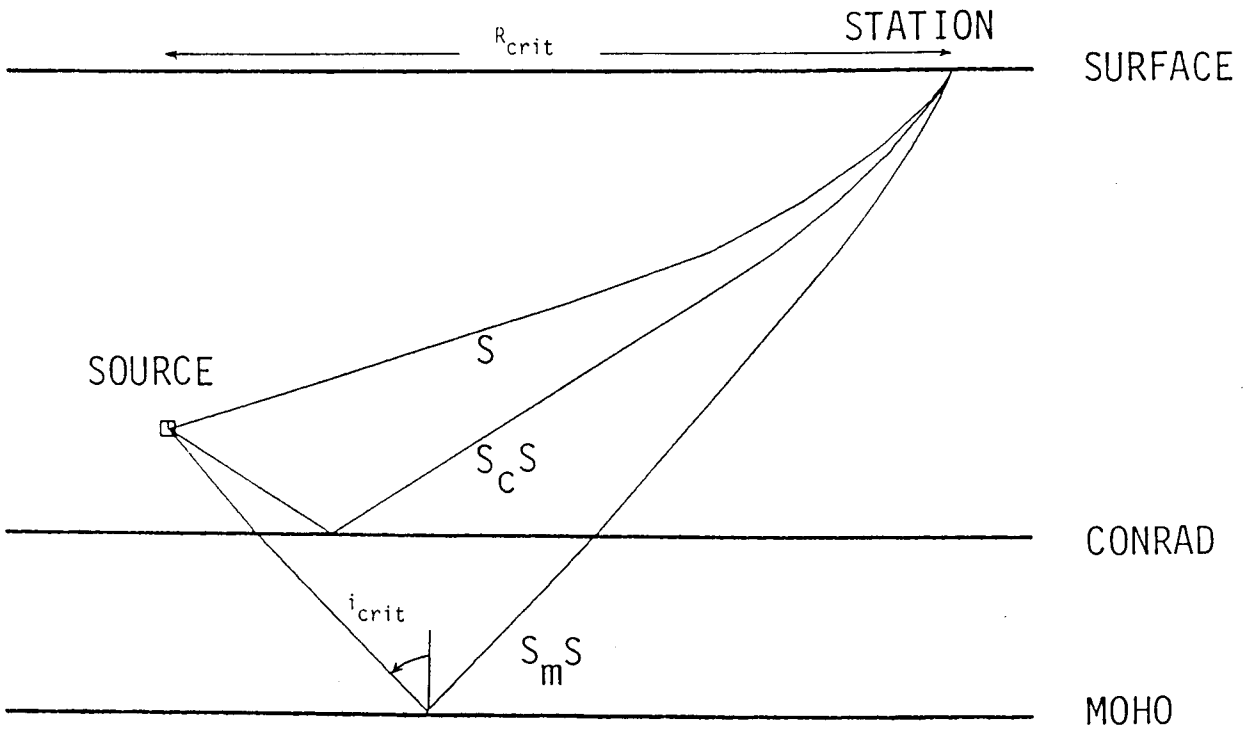

Figure 3-8. Schematic diagram of the wave propagation model, with direct waves (S) and waves S_cS and S_mS reflected from the Conrad and Moho layers. At the critical angle (i_{crit}), the incident wave is totally reflected back to the surface at distances starting at the critical distance R_{crit}.

attenuation to be less rapid than 1/R. Thus the peak amplitudes and duration of the seismogram are a function of the crustal structure and focal depth.

The simplified Green's functions that are used, described further by Somerville et al. (1991), are the response of the crust for P, SV and SH potentials. The receiver function is represented empirically, as described below, and the radiation pattern is assigned an average value. At high frequencies, the small set of rays that used are expected to contain most of the important arrivals out to distances of 200 km. To realistically model the wave propagation at greater distances, it would be necessary to include a much larger set of rays, or use the frequency-wavenumber integration method in place of the generalized ray method. In this application, then, ground motion modeling is not extended beyond 200 km distance.

3.3.2 Model Validation

The semi-empirical ground motion model has been validated against strong motion records of several earthquakes. These include the 1979 Imperial Valley earthquake (Wald et al., 1988a); the 1987 Whittier Narrows earthquake ((Wald et al., 1988b); Saikia, 1992), the 1988 Nahanni earthquake (Somerville et al., 1990); the 1989 Loma Prieta earthquake (Somerville et al., 1992a,b), and the 1985 Michoacan, Mexico and Valparaiso, Chile earthquakes (Somerville et al., 1991).

For the purposes of this study, a validation of the method was performed using a standard set of procedures for four earthquakes: the 1989 Loma Prieta earthquake (55 stations); the 1987 Whittier Narrows earthquake (37 stations); the 1988 Nahanni earthquake (3 stations); and the

Table 3-7

Source Parameters of Earthquakes Used in Validation of Semi-Empirical Simulation Method

Earthquake	Seismic Moment (x 10^{25} dyne cm)	Depth to Top Center (km)	Fault Length (km)	Fault Width (km)	Strike	Dip	Rake	Rupture Velocity (km/sec)	Rise Time (sec)
1985 Nahanni	17.6	3.56	32	15	180	22	110	2.7	0.96
1987 Whittier Narrows	1.0	12.35	12	9	280	30	110	2.5	0.40
1988 Saguenay	0.5	23.14	4	6	323	65	78	3.0	0.40
1989 Loma Prieta	29.5	3.38	40	18	128	70	140	2.7	1.14

1988 Saguenay earthquake (9 stations), for a total of 104 recordings. All available digital strong motion data at source-site distances of less than about 200 km were used in the validation, regardless of site conditions. The simulation method is described in Section 3.3.1 and Appendix 3.B. The standard procedures were as follows. For each event, published slip models were used to characterize the source, and published crustal structure models were used to characterize the wave propagation path. The source and path models are described by Hartzell and Iida (190) and Wald et al. (1989) respectively for the Whittier Narrows earthquake; Somerville et al. (1990) for the Saguenay earthquake; EPRI (1992) for the Nahanni earthquake; and Wald et al. (1992) for the Loma Prieta earthquake. Where these slip models included multiple time windows, a slip model was derived having a single time window. The source models of the four events are summarized in Table 3-7. The stations used in the validation of the four events are listed in Tables 3-8 through 3-11.

The empirical source functions were derived from the October 15, 1979 Imperial Valley aftershock. These empirical source functions represent a seismic moment of 0.6×10^{24} dyne-cm and a fault element size of 4km x 3km. For the Saguenay and Nahanni events, these source functions were modified for eastern North American source conditions to have a kappa value of 0.006 sec, while for the Whittier Narrows and Loma Prieta events the source functions were unmodified and retained an average kappa value of 0.055 sec. Unlike the stochastic model, the semi-empirical model does not include the Brune stress-drop as a specified parameter (from which the corner frequency and high-frequency spectral level are derived). Instead, the stress drop and ground motion levels at high frequencies are a function of the high-frequency ground motion levels embodied in the empirical source functions and the source duration of the finite rupture.

Comparisons of predicted and observed 5% damped response spectra are shown in Figures 3-9 to 3-12 for the four events modeled. Generally, the predicted spectra provide a good match to the observed spectra, especially at frequencies greater than 1 Hz. For the Loma Prieta earthquake, (Figure 3-9), there is a systematic underprediction of low frequencies, mainly below 1–2 Hz, but very good correspondence between predictions and observations at higher frequencies. For the Whittier Narrows event (Figure 3-10), which is a smaller event, deficient in low-frequency energy, there is a good match between predicted and observed spectra at all frequencies. While few data were available for the Nahanni event (Figure 3-11), the predicted spectra correspond well with the observed, but not quite as well as for the Loma Prieta and Whittier Narrows events. For the Saguenay event, not much energy is present at low frequency (Figure 3-12), and the model generally underpredicts the data above 1 Hz. This underprediction of high frequencies is probably due to the complexity and richness of high frequency radiation from this event.

3.3.3 Modeling Variability and Bias

The residuals between the recorded and simulated response spectra are used to estimate the variability associated with the simulation procedure. The bias and

Table 3-8
Loma Prieta Earthquake: Seismic Stations Used in Validation of Semi-Empirical Model

Code	Number	Org	Station Name	Closest Distance
agnw	57066	CSMIP	Agnews State Hospital	24.33
andd	1652	USGS	Anderson Dam—Downstream (DMD)	19.64
andl	1652	USGS	Anderson Dam—Left Abutment	19.98
bran*		UCSC	Branciforte Drive	10.80
capi	47125	CSMIP	Capitola	15.11
cldd	57504	CSMIP	Coyote Lake Dam—Downstream	20.53
cor*	57007	CSMIP	Corralitos	3.40
csuh*	58219	CSMIP	CSUH-Stadium (ap3e)	52.37
frem	1686	USGS	Fremont—Emerson Court	39.61
gav	47006	CSMIP	Gavilan College Physical Science	9.50
gil1*	47379	CSMIP	Gilroy #1—Gavilan Water Tower	9.17
gil2*	47380	CSMIP	Gilroy #2—Hwy101/Bolsa Road	10.63
gil3	47381	CSMIP	Gilroy #3—Sewage Plant	12.40
gil4	57382	CSMIP	Gilroy #4—San Ysidro School	14.08
gil6*	57383	CSMIP	Gilroy #6—San Ysidro	17.97
gil7	57425	CSMIP	Gilroy #7—Mantelli Ranch	22.35
gilb	57476	CSMIP	Gilroy Historic Building (FH)	10.56
hall	57191	CSMIP	Hall's Valley, Grant Park	30.19
hol	47524	CSMIP	Hollister—South & Pine	27.58
holc	1575	USGS	Hollister—City Hall Annex	27.03
lbl	58471	CSMIP	Berkeley—Lawrence Berkeley Lab	79.12
lex1	57180	CSMIP	Lexington Dam—left abutment	6.25
lgpc*		UCSC	Los Gatos Presentation Center	3.45
lick*	58135	CSMIP	UCSC—Lick Observatory	18.45
mont	47377	CSMIP	Monterey City Hall	44.20
mpva	1230	USGS	Menlo Park VA Hospital	33.57
mssj	57064	CSMIP	Fremont, Mission San Jose	39.27
muir*	58393	CSMIP	Hayward—Muir School	52.53
oako	58224	CSMIP	Oakland—2 story office bldg	72.11
olem	68003	CSMIP	Olema, Point Reyes	117.14
pavb*	1227	USGS	Palo Alto VA Hospital—Bsmt	26.08
pijh*	58338	CSMIP	Piedmont Jr HS Grounds	73.09

Table 3-8 (Continued)
Loma Prieta Earthquake: Seismic Stations Used in Validation of Semi-Empirical Model

Code	Number	Org	Station Name	Closest Distance
pres	58222	CSMIP	SF—Presidio	77.46
ptba	58043	CSMIP	Point Bonita	82.99
pulg	58378	CSMIP	Pulgas—Upper Crystal Springs Res.	42.35
rdwd*	58263	CSMIP	Redwood City school office bldg.	36.26
rich	58505	CSMIP	Richmond—City Hall Parking Lot	87.76
sago*	47189	CSMIP	SAGO-Hollister	33.92
sali	47179	CSMIP	Salinas	32.48
sfch*	58132	CSMIP	SF—Cliff House	78.78
sfdh*	58130	CSMIP	SF—Diamond Heights	71.29
sfgg	1678	USGS	SF—Golden Gate Bridge	79.46
sfph*	58131	CSMIP	SF—Pacific Heights	76.11
sfrh*	58151	CSMIP	SF—Rincon Hill	74.50
sfth*	58133	CSMIP	SF—Telegraph Hill	76.28
sftt	1239	USGS	SF—Transamerica Title	75.88
skyl*	58373	CSMIP	Skyline—Upper Crystal Springs Res.	42.12
slac*	1601	USGS	Stanford—SLAC Test Lab	30.63
snj	57563	CSMIP	San Jose—Santa Teresa Hill	14.35
srtg	58065	CSMIP	Saratoga—Aloha Avenue	8.29
ssfs*	58539	CSMIP	So SF—Sierra Point	63.11
sunc	1695	USGS	Sunnyvale—Colton Ave	24.09
waho		UCSC	Santa Cruz, Walter's House	17.71
wats	47459	CSMIP	Watsonville	10.34
yerb*	58163	CSMIP	Yerba Buena Island	75.41

* Common to stations modeled by stochastic method.

Table 3-9
Nahanni Earthquake: Seismic Stations Used in Validation of Semi-Empirical Model

Code	Station Name	Closest Distance
Sta1*	Station 1	7.99
Sta2*	Station 2	3.98
Sta3*	Station 3	16.28

* Common to stations modeled by stochastic method.

Table 3-10

Whittier Narrows Earthquake: Seismic Stations Used in Validation of Semi-Empirical Model

Codes	Number	Org	Station Name	Closest Distance
alhc	24461	CSMIP	Alhambra, Fremont School	13.35
alhu*	482	USGS	Alhambra,900 S Fremont, basement	14.34
alta	24402	CSMIP	Altadena: Eaton Canyon	19.47
bulk*	5129	USGS	LA: Bulk Mail Facility	12.95
cast	24278	CSMIP	Castaic: Old Ridge Route	71.90
down*	14368	CSMIP	Downey—County Maint Building	16.68
dume	24396	CSMIP	Malibu: Point Dume School	61.44
feat	13122	CSMIP	Featherly Park Maintenance Bldg	35.02
garv*	709	USGS	Garvey Reservoir	12.83
hadb	14395	CSMIP	Long Beach: Harbor Admin FF	32.72
hasl	24277	CSMIP	Castaic: Hasley Canyon	64.52
hbfs	13197	CSMIP	Huntington Beach: Fire Station	40.13
hemt	12331	CSMIP	Hemet: Stetson Ave Fire Station	120.48
hsbf*	24303	CSMIP	LA: Hollywood Storage FF	22.49
ingl	14196	CSMIP	Inglewood—Union Oil Yard	21.61
kagc	24088	CSMIP	Pacoima: Kagel Canyon	35.10
lacn	24389	CSMIP	Century Cty: LA Country Club N	27.88
lanc	24526	CSMIP	Lancaster: Medical Office Bldg	68.08
lbrp	14241	CSMIP	Long Beach—Recreation Park	29.34
leo5	24055	CSMIP	Leona Valley #5	59.44
leo6	24309	CSMIP	Leona Valley #6	59.90
moor	24283	CSMIP	Moorpark, Ventura Co. Fire Station	73.87
mtwi*	24399	CSMIP	Mt Wilson—CIT Seismic Station	22.91
newh	24279	CSMIP	Newhall: LA Cnty Fire Station	51.75
nord	24087	CSMIP	Arleta: Nordhoff Fire Station	36.20
obre*	24400	CSMIP	LA: Obregon Park	12.67
pomo	23525	CSMIP	Pomona—4th & Locust FF	28.71
rair	13123	CSMIP	Riverside Airport	55.09
ranc	23497	CSMIP	Rancho Cucamonga L&J FF	43.62
rosa	24274	CSMIP	Rosamond, Goode Ranch	83.92
schl	14403	CSMIP	LA: 116th Street School	19.11

Table 3-10 (Continued)

Whittier Narrows Earthquake: Seismic Stations Used in Validation of Semi-Empirical Model

Codes	Number	Org	Station Name	Closest Distance
snmr*	24401	CSMIP	San Marino: Southwest Academy	15.82
sylm	24514	CSMIP	Sylmar: Olive View	41.85
tarz	24436	CSMIP	Tarzana: Cedar Hill Nursery	40.30
vasq	24047	CSMIP	Vasquez Rocks Park	50.03
wdup*	289	USGS	Whittier Narrows Dam—Upstream	12.55
whit*	804	USGS	Whittier: 7215 Bright Avenue	12.79

* Common to stations modeled by stochasitc method.

Table 3-11

Saguenay Earthquake: Stations Used in Validation of Semi-Empirical Method

Codes	Station Name	Closest Distance
SM01	St.-Ferreol, Quebec	114.33
SM02	Quebec, Quebec	149.57
SM05	Tadoussac, Quebec	110.10
SM08*	La Malbaie, Quebec	94.01
SM09	St-Pascal, Quebec	123.03
SM10*	Riviere-Quelle, Quebec	114.82
SM16*	Chicoutimi-Nord, Quebec	48.02
SM17*	St-Andre-du-Lac-St-Jean	66.09
SM20*	Les Eboulements, Quebec	91.40

* Common to stations modeled by stochastic method.

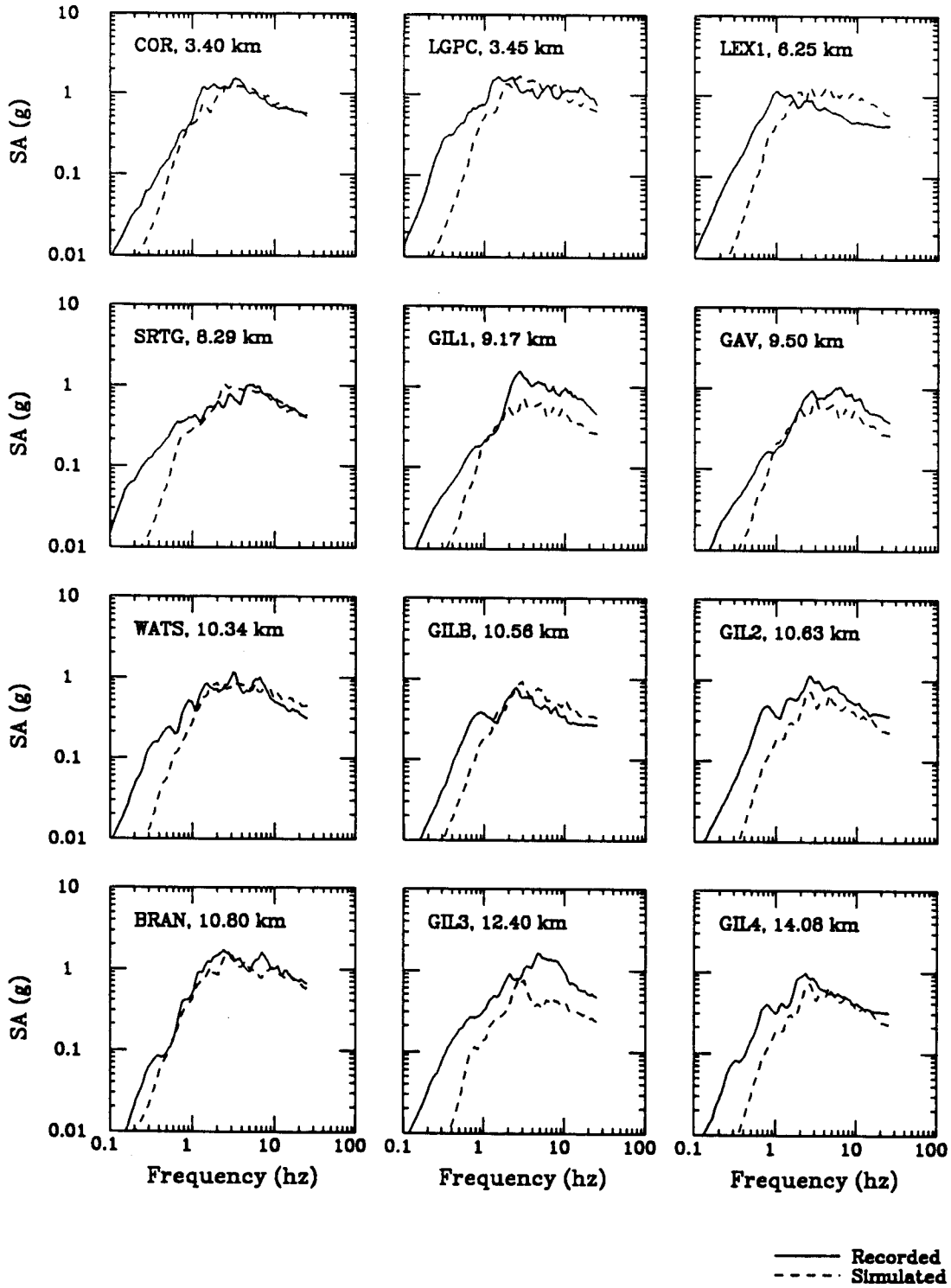

Figure 3-9. Comparison of observed and modeled 5% damped acceleration response spectra for the 1989 Loma Prieta earthquake. Model results are from the semi-empirical ground motion model.

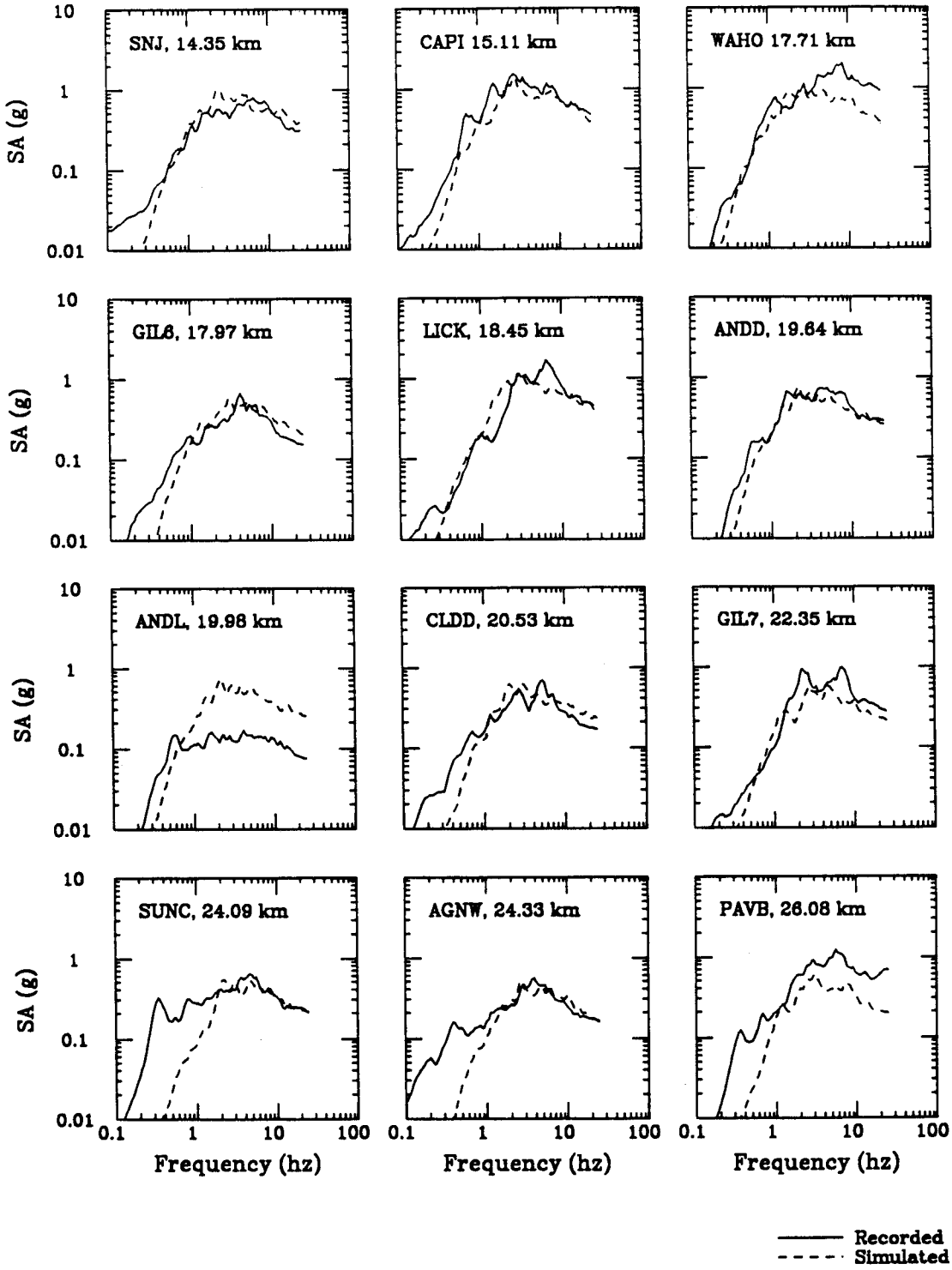

Figure 3-9 (Continued). Comparison of observed and modeled 5% damped acceleration response spectra for the 1989 Loma Prieta earthquake. Model results are from the semi-empirical ground motion model.

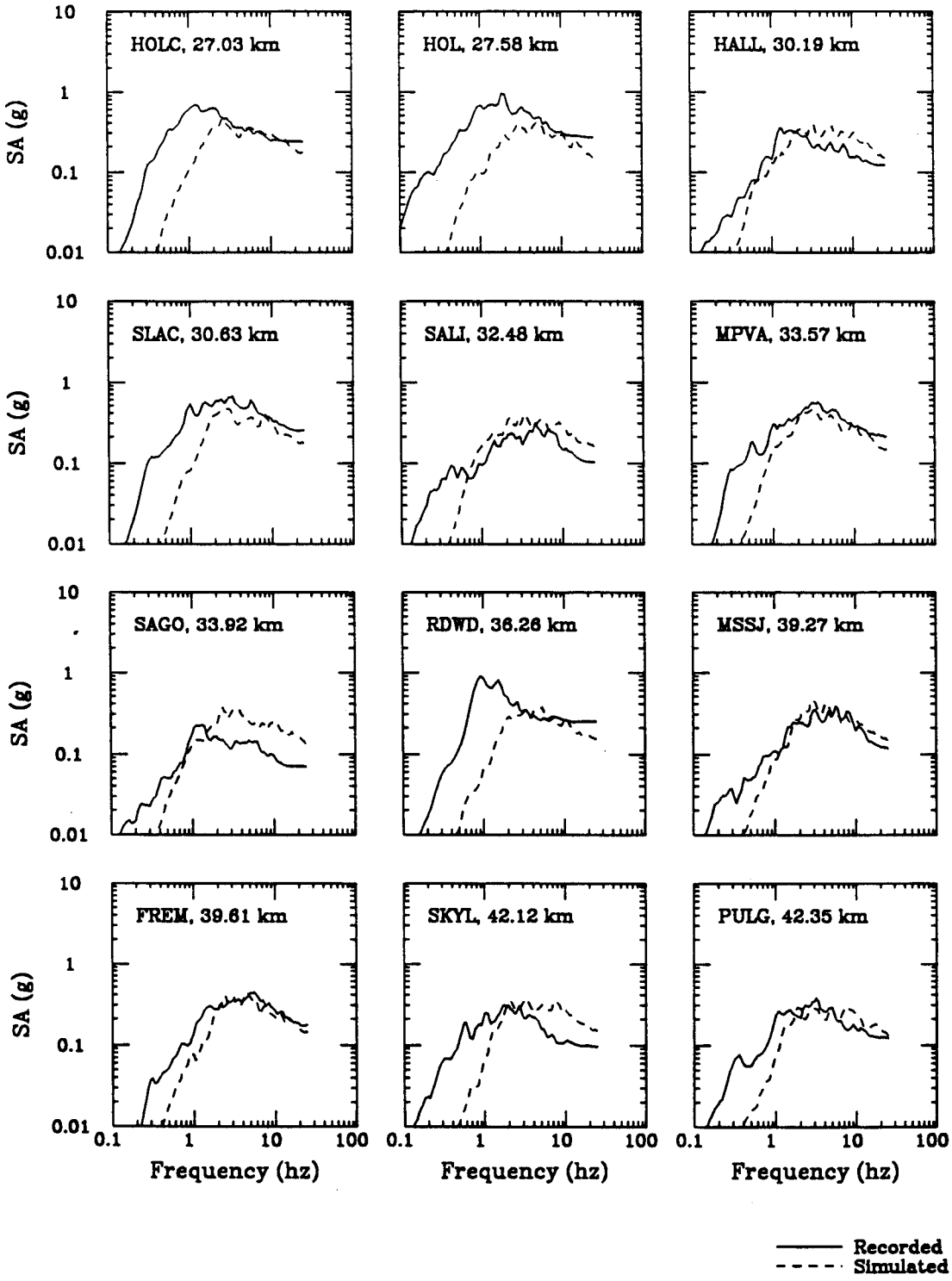

Figure 3-9 (Continued). Comparison of observed and modeled 5% damped acceleration response spectra for the 1989 Loma Prieta earthquake. Model results are from the semi-empirical ground motion model.

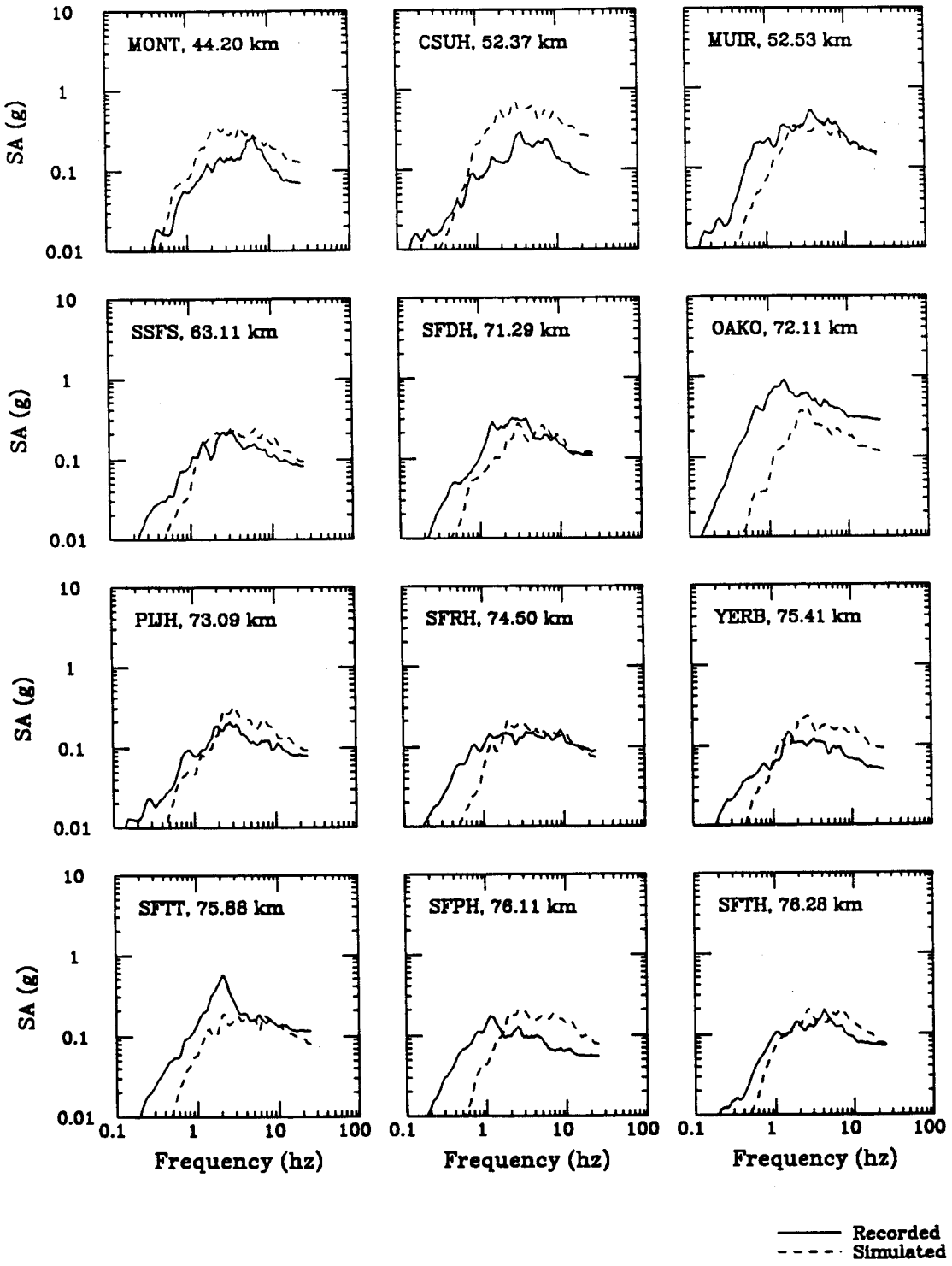

Figure 3-9 (Continued). Comparison of observed and modeled 5% damped acceleration response spectra for the 1989 Loma Prieta earthquake. Model results are from the semi-empirical ground motion model.

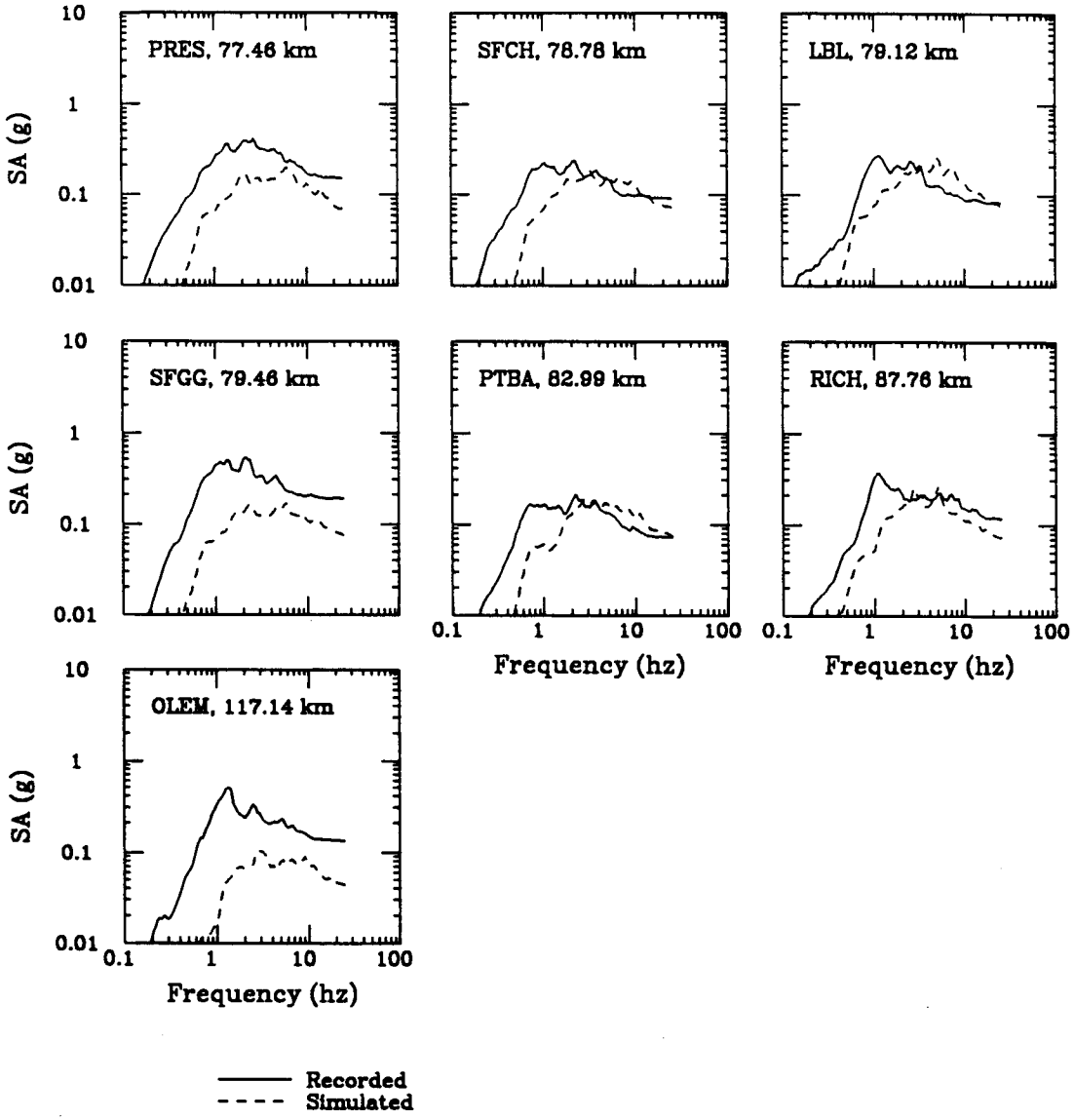

Figure 3-9 (Continued). Comparison of observed and modeled 5% damped acceleration response spectra for the 1989 Loma Prieta earthquake. Model results are from the semi-empirical ground motion model.

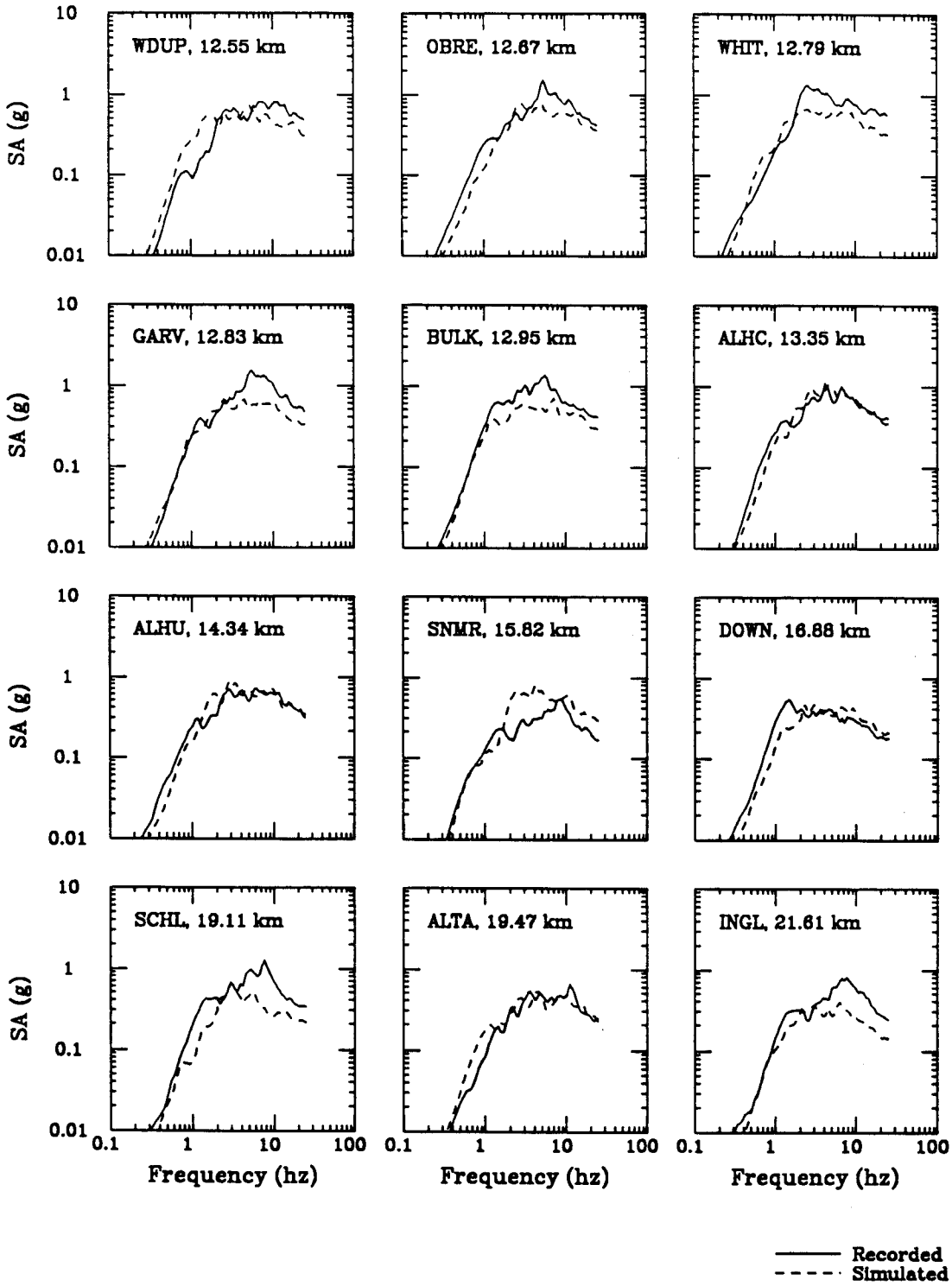

Figure 3-10. Comparison of observed and modeled 5% damped acceleration response spectra for the 1987 Whittier Narrows earthquake. Model results are from the semi-empirical ground motion model.

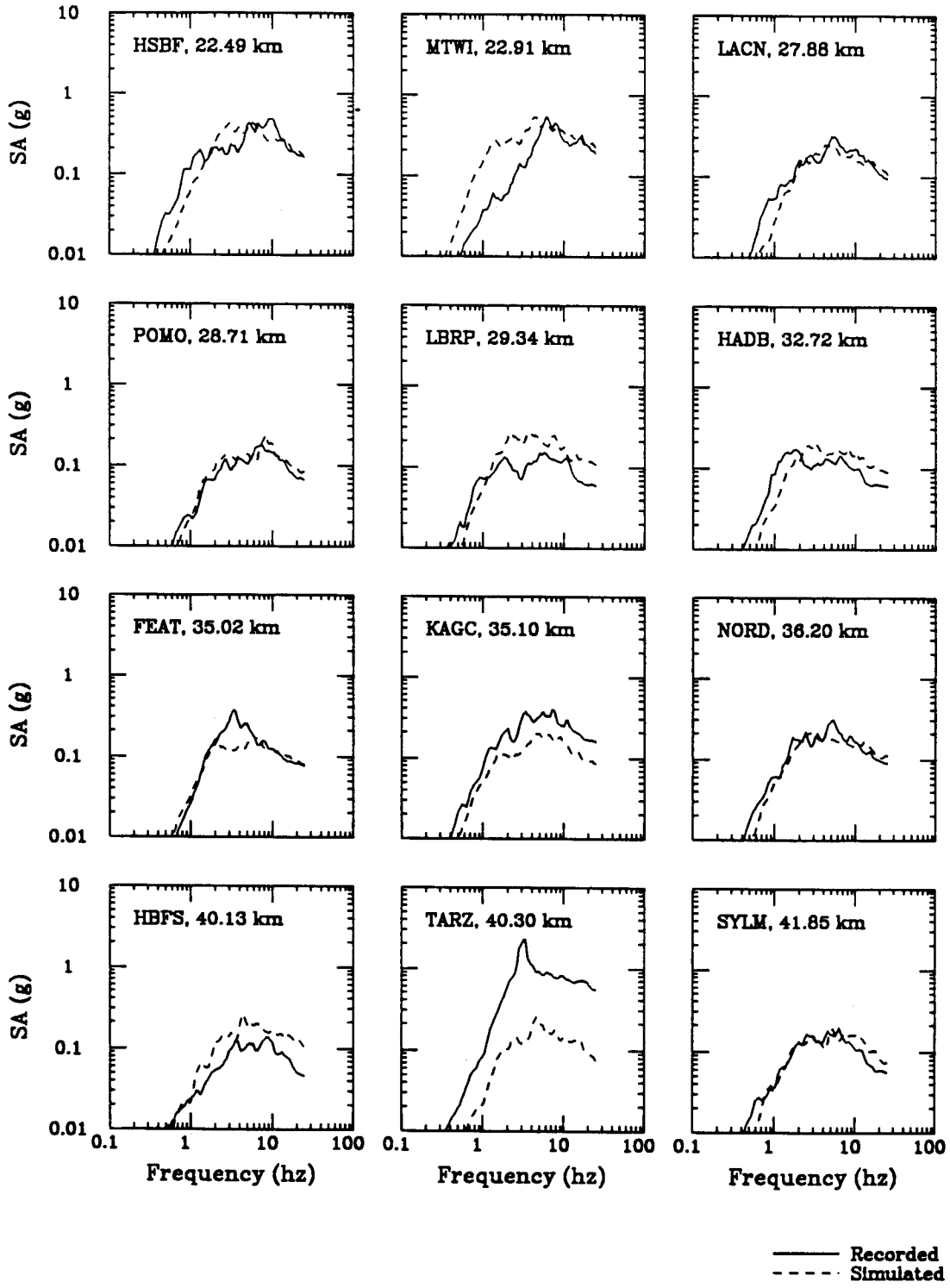

Figure 3-10 (Continued). Comparison of observed and modeled 5% damped acceleration response spectra for the 1987 Whittier Narrows earthquake. Model results are from the semi-empirical ground motion model.

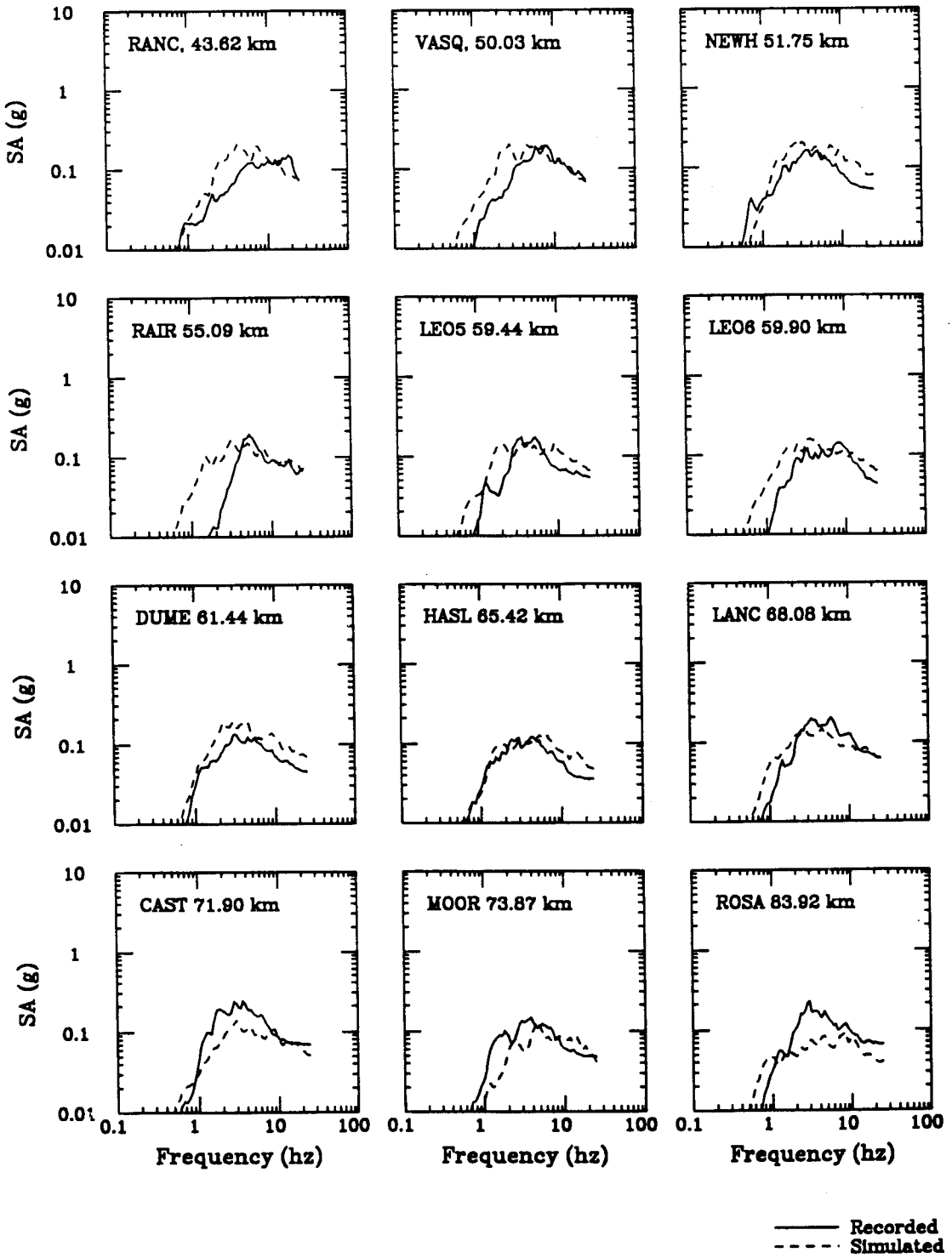

Figure 3-10 (Continued). Comparison of observed and modeled 5% damped acceleration response spectra for the 1987 Whittier Narrows earthquake. Model results are from the semi-empirical ground motion model.

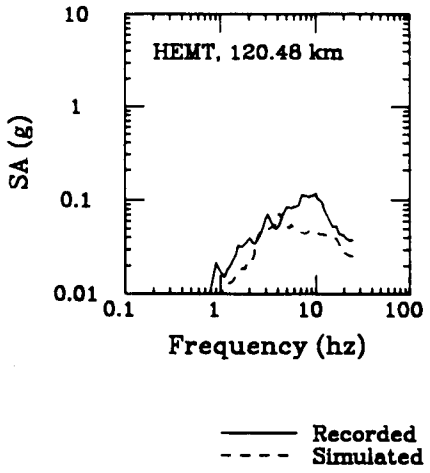

Figure 3-10 (Continued). Comparison of observed and modeled 5% damped acceleration response spectra for the 1987 Whittier Narrows earthquake. Model results are from the semi-empirical ground motion model.

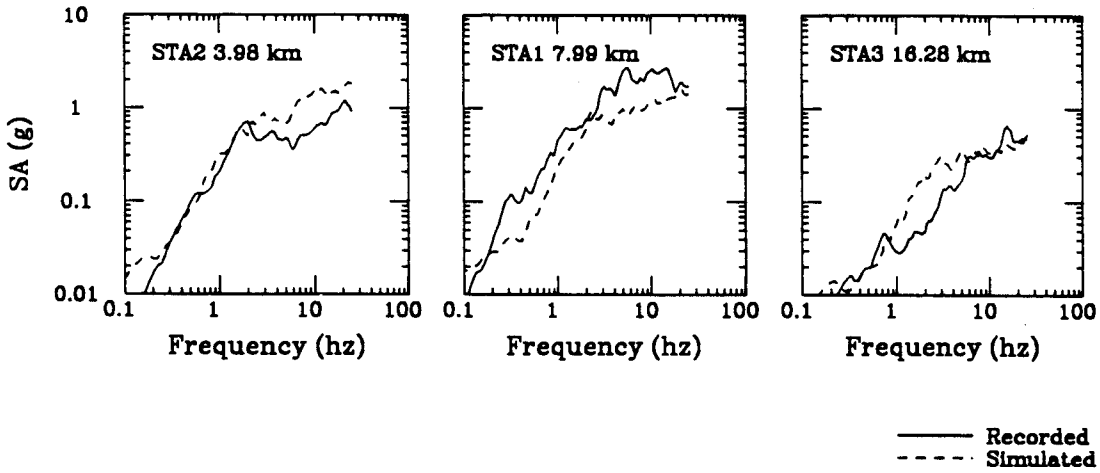

Figure 3-11. Comparison of observed and modeled 5% damped acceleration response spectra for the 1985 Nahanni earthquake. Model results are from the semi-empirical ground motion model.

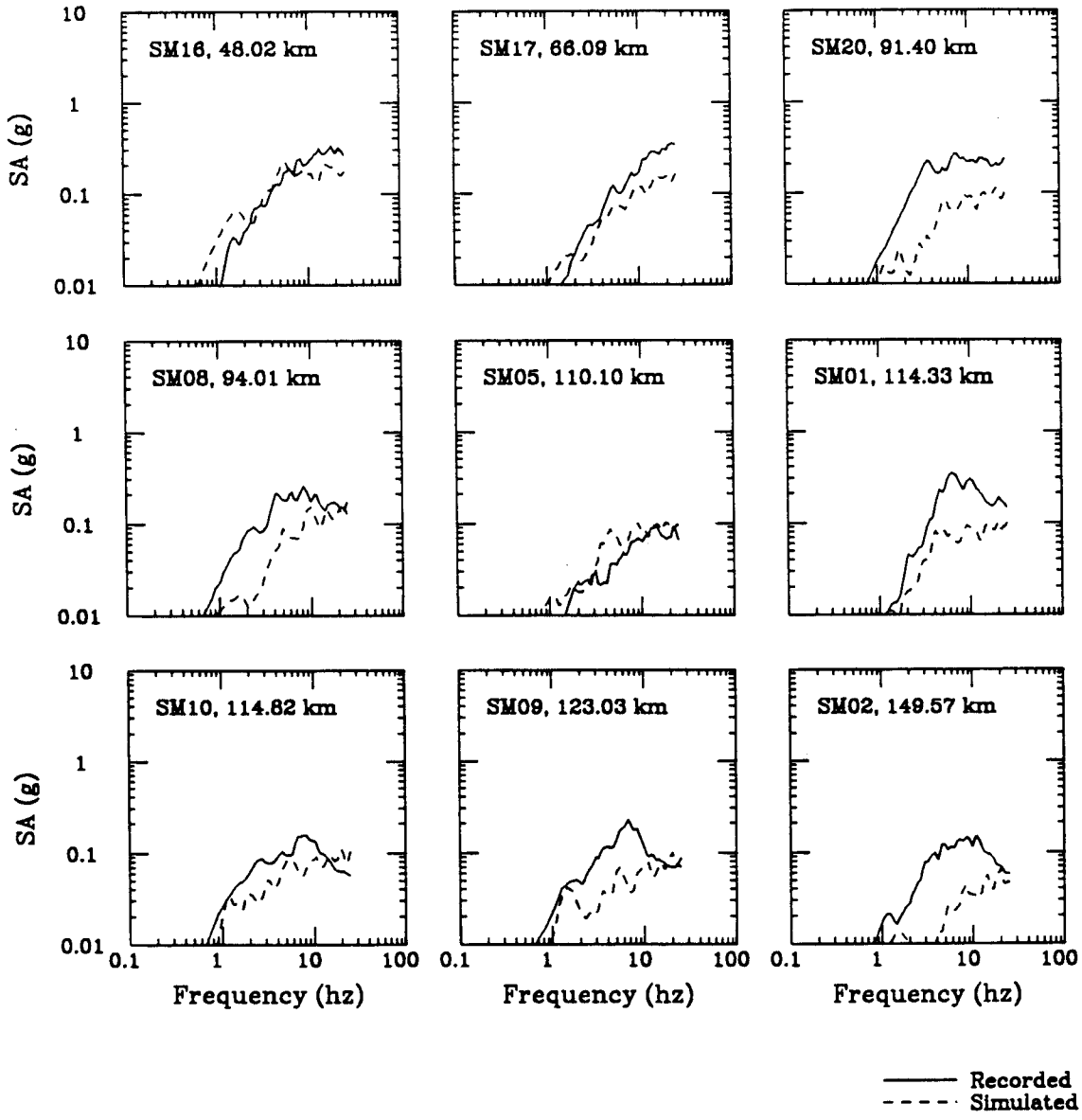

Figure 3-12. Comparison of observed and modeled 5% damped acceleration response spectra for the 1988 Saguenay earthquake. Model results are from the semi-empirical ground motion model.

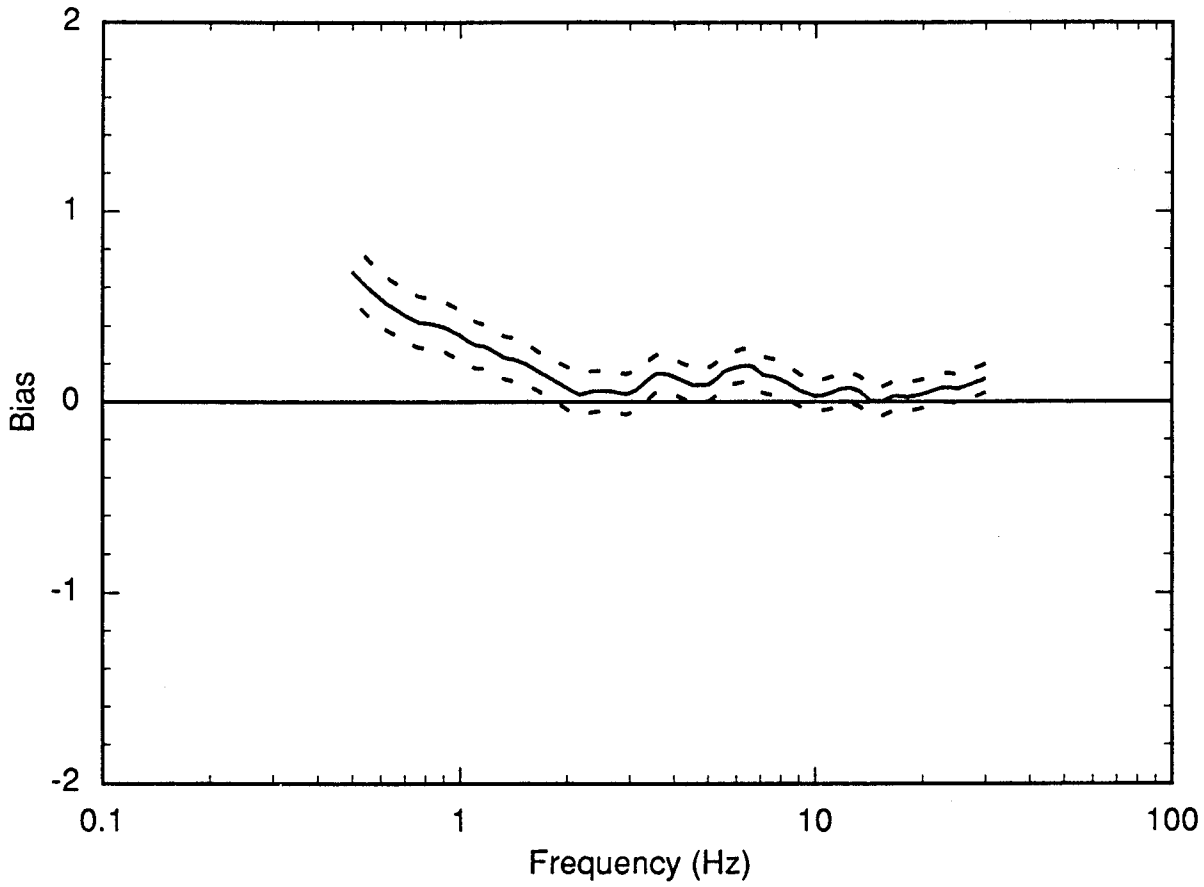

Figure 3-13a. Modeling bias computed from recordings at 104 stations for the Loma Prieta, Whittier Narrows, Nahanni, and Saguenay earthquakes using the semi-empirical ground motion model. Dashed lines represent 90% confidence limits.

standard error, averaged over all stations for all events, are shown in Figure 3-13. Averaged over the four events, there is no significant bias (Figure 3-13a) for frequencies above 2 Hz. The standard error is about 0.5 for peak acceleration and for frequencies above about 10 Hz, and grows to about 0.6 at 3 Hz. Since the bias is low for frequencies above 2 Hz, the standard error (Figure 3-13b) does not change very much when corrected for model bias.

In this application of the semi-empirical ground motion model, the simulations were done for a reference site condition appropriate for average surface conditions in the region in which each earthquake occurred. However, the data against which these simulations is compared used all available digital recordings regardless of site conditions. Consequently, the standard error of the modeling method contains a significant contribution from these unmodeled site effects. The incorporation of site effects in the semi-empirical procedure, as intended in these guidelines and implemented in the stochastic approach, would appreciably reduce the standard error.

3.4 Comparison of Models

As is evident from Sections 3.2 and 3.3, both the stochastic and semi-empirical ground motion models accurately predict ground motions for earthquakes of moderate magnitudes (**M** 5.8 to 7.0) over a broad range of frequencies, particularly above 1 Hz. It is worthwhile to reexamine the variability and biases of the two modeling approaches using only common event-station pairs. Altogether there

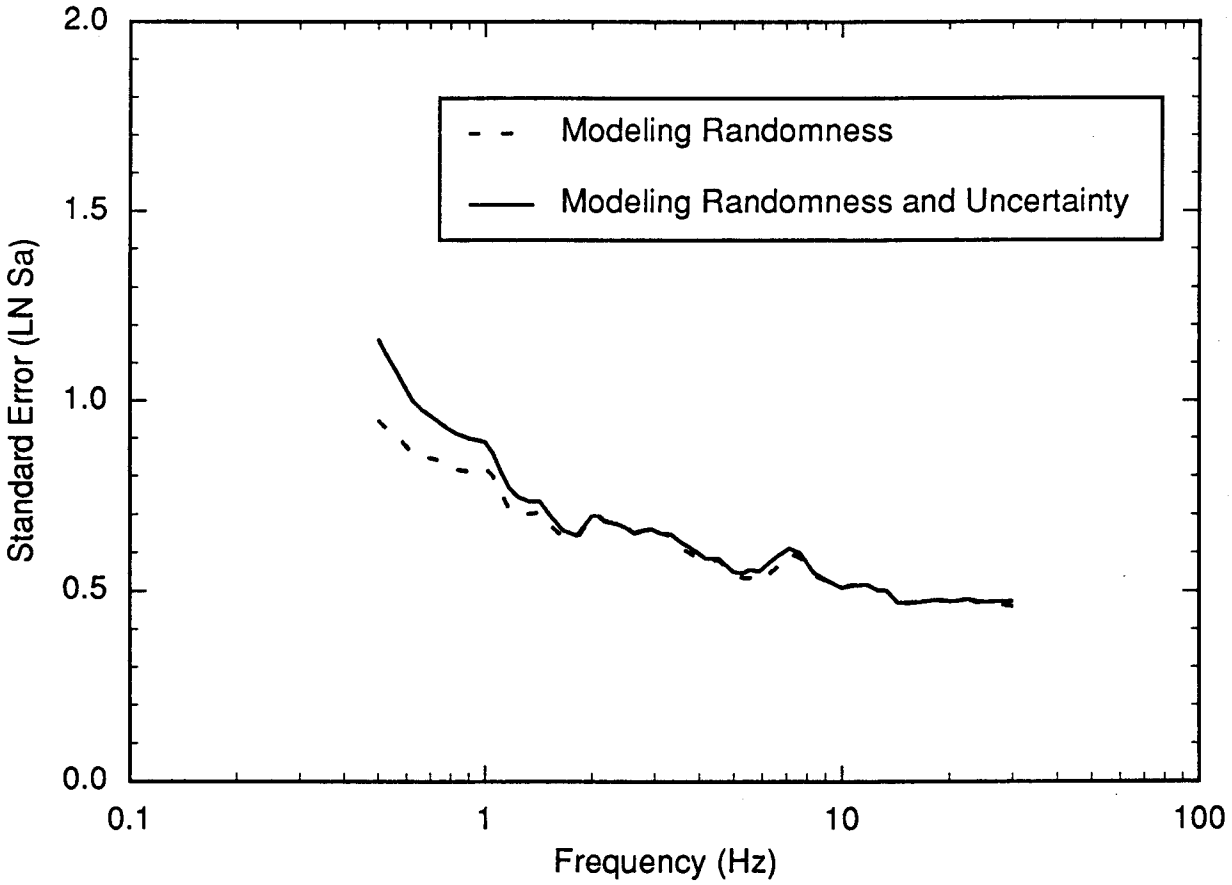

Figure 3-13b. Standard error of modeling or modeling variability (natural log) computed from recordings at 104 stations for the Loma Prieta, Whittier Narrows, Nahanni, and Saguenay earthquakes using the semi-empirical ground motion model. Dashed line, total variability (modeling uncertainty plus randomness); solid line, corrected for model bias.

are 39 sites for which recordings of horizontal acceleration spectra were modeled using both ground motion models. These stations are noted in Tables 3-2 to 3-5. The selection of additional sites chosen for each model comparison is discussed in Sections 3.2 and 3.3. The sites in common represent nearly all rock sites within 200 km of their respective sources. In particular, for the Whittier Narrows earthquake, a number of soil sites included in the semi-empirical validation were excluded from the stochastic model validation. Also, for the Saguenay earthquake, the stochastic model validation included a number of rock sites at distances beyond 200 km not considered for the semi-empirical model validation.

For the 39-station subset of sites, the standard errors of the residuals (modeling variability) and the modeling biases are presented for the two models in Figures 3-14 and 3-15. For the stochastic model, the differences in modeling bias between the predictions using the original 61-station set (Figure 3-6a) and the 39-station subset (Figure 3-14a) are not statistically significant. For the modeling variability, the total randomness and uncertainty for the 39-station set (Figure 3-14b) is actually lower than for the 61-station set (Figure 3-14b). This is largely due to a large contribution to the variability in the 61-station set from the Saguenay event; and many of these stations are not in the 39-station set.

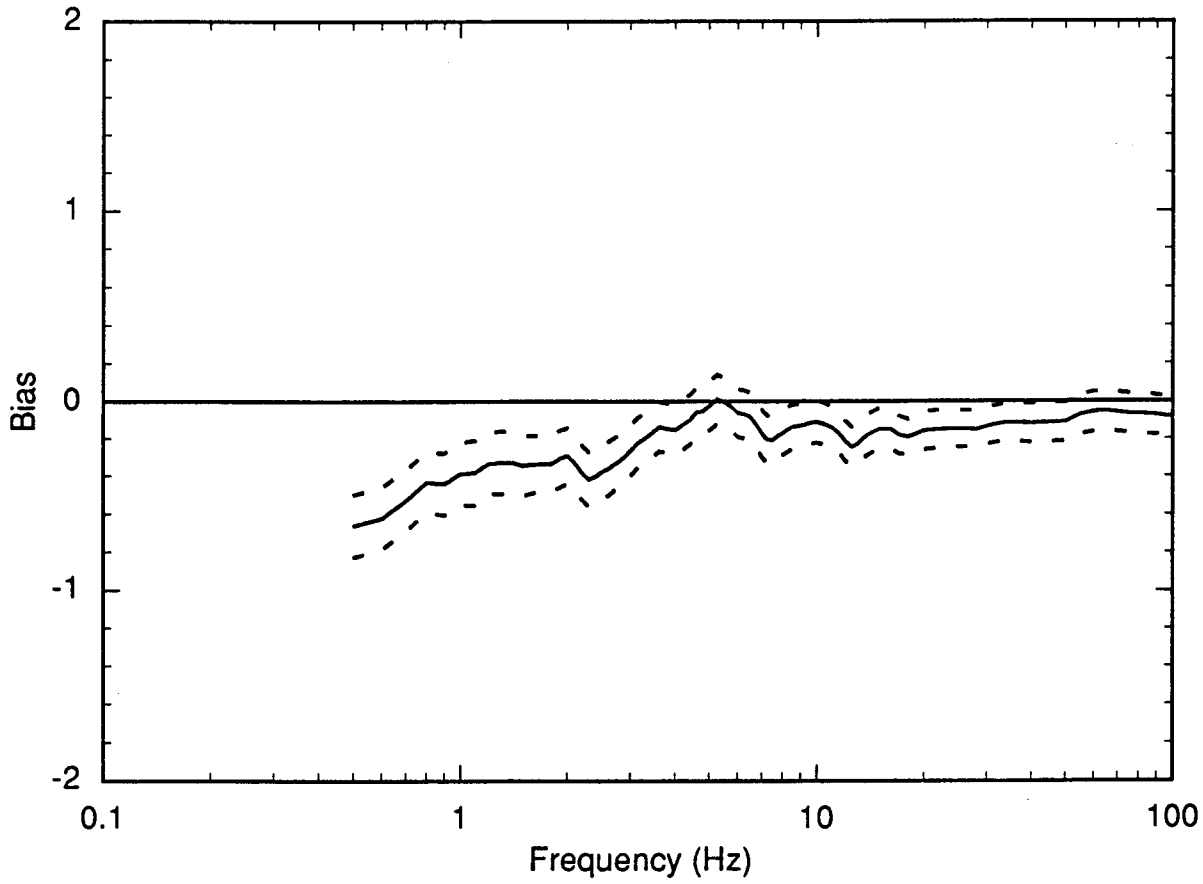

Figure 3-14a. Modeling bias computed from recordings at the subset of 39 stations for the Loma Prieta, Whittier Narrows, Nahanni, and Saguenay earthquakes using the stochastic ground motion model. Dashed lines represent 90% confidence limits.

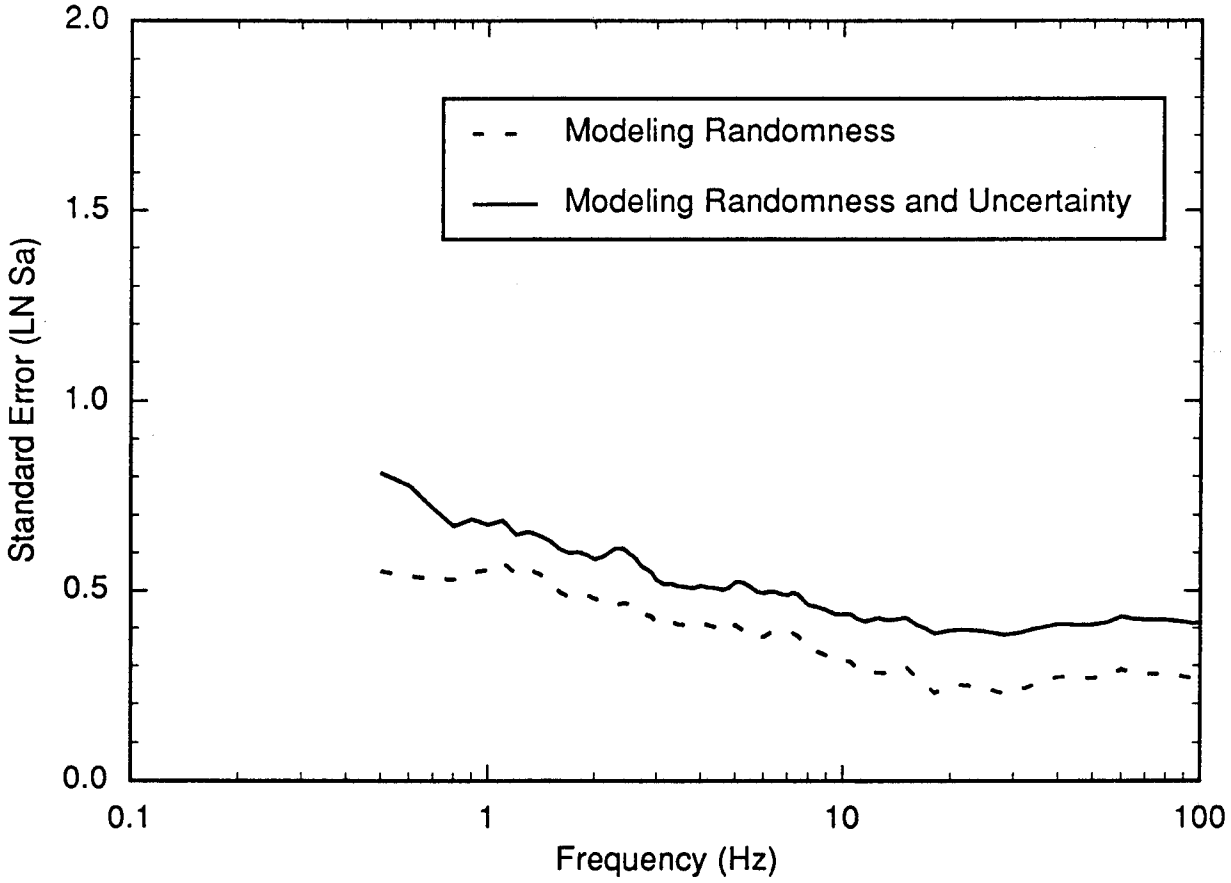

Figure 3-14b. Modeling variability (natural log) computed from recordings at the subset of 39 stations for the Loma Prieta, Whittier Narrows, Nahanni, and Saguenay earthquakes using the stochastic ground motion model. Dashed line, total variability (modeling uncertainty plus randomness); solid line, corrected for model bias and site term D.

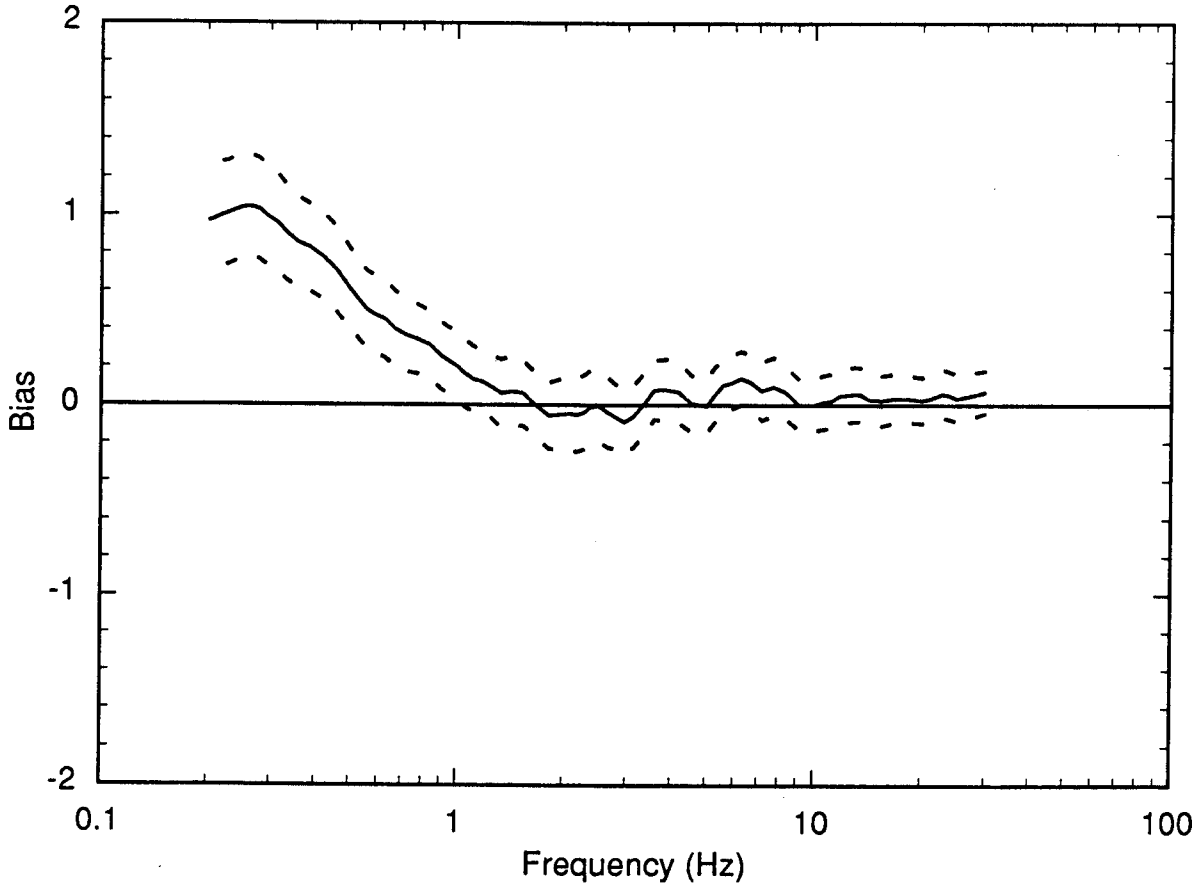

Figure 3-15a. Modeling bias computed from recordings at the subset of 39 stations for the Loma Prieta, Whittier Narrows, Nahanni, and Saguenay earthquakes using the semi-empirical ground motion model. Dashed lines represent 90% confidence limits.

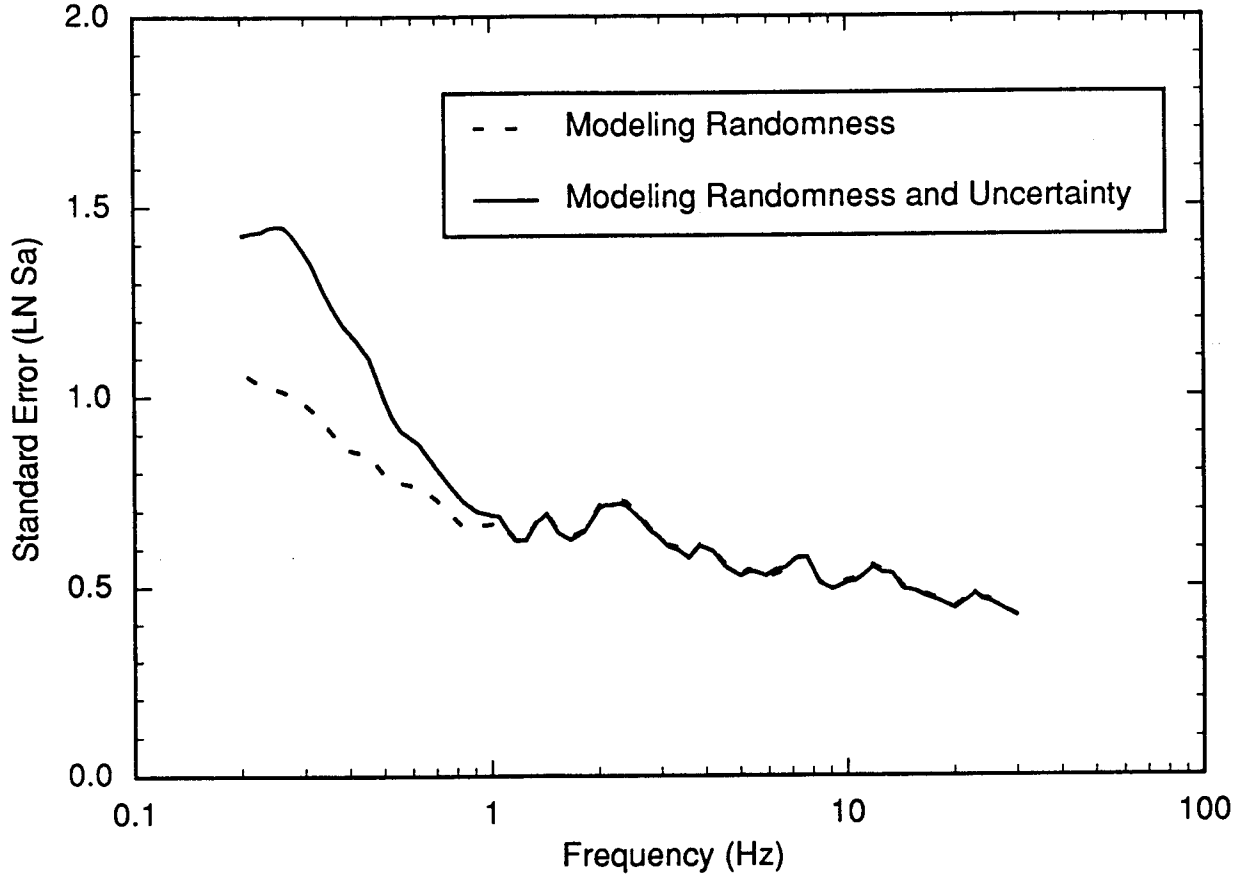

Figure 3-15b. Modeling variability (natural log) computed from recordings at the subset of 39 stations for the Loma Prieta, Whittier Narrows, Nahanni, and Saguenay earthquakes using the semi-empirical ground motion model. Dashed line, total variability (modeling uncertainty plus randomness); solid line, corrected for model bias.

For the semi-empirical model, the differences in modeling bias between the 104-station and 39-station predictions are not statistically significant. For the modeling variability, neither the differences in the random (corrected for model bias) nor the random and uncertain (not corrected for bias) portions of variability are much different for the two sets of stations. It is clear from this comparison that differences in station selection between the two validation procedures did not bias the results.

Although the ground motion models differ in certain fundamental ways regarding assumptions for source, path and site effects, both models yield accurate predictions of recorded strong motions. The stochastic model used does not incorporate finite source effects, and therefore is expected to predict motions less well at very close source distances. Generally speaking, however, this model has been shown to predict high frequencies with considerable accuracy, while overpredicting low frequencies at close distances. This effect is indicated in the response spectra in Figure 3-2 for distances < 50 km, and is shown by negative model bias in Figures 3-6a and 3-14a. In fact, these figures show that the stochastic model is conservative at all frequencies, significantly so below 3 Hz and marginally so at higher frequencies. At high frequency, particularly above 5 Hz, the incorporation of the site-specific kappa parameter provides a significant reduction (about 20%) in modeling variability.

The semi-empirical model uses a hybrid empirical-theoretical approach to incorporate finite source effects. This approach can provide a reduction in uncertainty for ground motion predictions for large earthquakes at very close distances. The lack of a site term tends to make this model have slightly higher uncertainty at higher frequencies, where site factors often dominate. Although the generalized ray method of modeling wave propagation effects used in this model (see Appendix 3.B) is expected to be slightly more accurate, especially at low frequencies (for a specific structure) than that used in the stochastic model (see Appendix 3.A), these differences do not appear to be significant in modeling the variability for the four events. These results indicate that both models produce comparably accurate predictions of strong ground motions over the frequency range of interest, 1 to 35 Hz.

The stochastic and semi-empirical ground motion models are each used in future sections, but for different purposes. For ground motion prediction of a future event, the variability of source, path and site parameters causes extensive averaging of ground motion effects. These effects tend to smooth over the deterministic aspects of any given earthquake, and make the stochastic model particularly well suited to the task. The more computationally intensive and rigorous semi-empirical model, using generalized rays (Appendix 3.B), was used to develop the crustal structure regionalization in Section 5.

For the prediction of ground motion at rock sites in eastern North America, the results of Sections 3.2 and 3.3 indicate that both the semi-empirical and stochastic ground motion models are well validated. Due largely to its simplicity and computational efficiency, the stochastic model was selected to make the many thousands of simulations necessary to develop the engineering ground motion model described in Section 9. The results presented in this section indicate that both models would indeed have yielded quite similar results, both in the median and the variability. Thus, there is greater confidence that the results are not biased by implementing but one modeling method in the final analysis.

References

Abrahamson, N.A., P.G. Somerville, and C.A. Cornell (1990). Uncertainty in numerical strong motion predictions. Proc. *Fourth U.S. Nat. Conf. Earth. Engin., Palm Springs*, CA., 1, 407–416.

Anderson, J.G. (1986). Implications of attenuation for studies of the earthquake source. *Earthquake Source Mechanics*. Edited by S. Das, J. Boatwright, C. Scholz, Am. Geophys. Union Monograph, 37, 311–318.

Anderson, J.G., and S.E. Hough (1984). A model for the shape of the Fourier amplitude spectrum of acceleration at high frequencies. *Bull. Seism. Soc. Am.*, 74, 1969–1993.

Atkinson, G.M. (1984). Attenuation of strong ground motion in Canada from a random vibrations approach. *Bull. Seism. Soc. Am.*, 74(5), 2629–2653.

Boore, D.M. (1983). Stochastic simulation of high-frequency ground motions based on seismological models of the radiated spectra. *Bull. Seism. Soc. Am.*, 73, 1865–1894.

Boore, D.M. (1986). Short-period P- and S-wave radiation from large earthquakes: implications for spectral scaling relations. *Bull. Seism. Soc. Am.*, 76(1) 43–64.

Boore, D.M., and G.M. Atkinson (1987). Stochastic prediction of ground motion and spectral response parameters at hard-rock sites in eastern North America. *Bull. Seism. Soc. Am.*, 77(2), 440–467.

Boore, D.M. and G.M. Atkinson (1992). Source spectra for the 1988 Saguenay, Quebec, earthquakes. *Bull. Seism. Soc. Am.*, 82(2), 683–719.

Boore, D.M. and W.B. Joyner (1984). A note on the use of random vibration theory to predict peak amplitudes of transient signals. *Bull. Seism. Soc. Am.*, 74, 2035–2039.

Brune, J.N. (1970). Tectonic stress and the spectra of seismic shear waves from earthquakes. *J. Geophys. Res.* 75, 4997–5009.

Brune, J.N. (1971). Correction. *J. Geophys. Res.* 76, 5002.

Fehler, M. and W.S. Phillips (1991). Simultaneous inversions for Q and source parameters of microearthquakes accompanying hydraulic fracturing in granitic rocks, *Bull. Seism. Soc. Am.*, 81, 553–575.

Hanks, T.C. (1982). f_{max}. *Bull. Seism. Soc. Am.*, 72, 1867–1879.

Hanks, T.C., and H. Kanamori (1979). A moment magnitude scale. *J. Geophys. Res.*, 84, 2348–2350.

Hanks, T.C., and R.K. McGuire (1981). The character of high-frequency strong ground motion. *Bull. Seism. Soc. Am.*, 71, 2071–2095.

Hartzell, S.H., and T.H. Heaton (1988). Failure of self-similarity for large (Mw > 8-1/4) earthquakes, *Bull. Seism. Soc. Am.*, 78, 478–488.

Hartzell, S.H. and M. Iida (1990). Source complexity of the 1987 Whittier Narrows, California, earthquake from the inversion of strong motion records. *J. Geophys. Res.* 95(B8), 12475–12485.

Heaton, T.H. (1990). Evidence for and implications of self-healing pulses of slip in earthquake rupture, Phys. Earth Planet. Interiors 64, 1–20.

Helmberger, D.V. and D.G. Harkrider (1978). Modeling earthquakes with generalized ray theory, *Proc. IUATM Symposium: Modern Problems in Elastic Wave Propagation*, Wiley, New York, 499–518.

Hough, S.E., J.G. Anderson, J. Brune, F. Vernon III, J. Berger, J. Fletcher, L. Haar, T. Hanks, and L. Baker (1988). Attenuation near Anza, California. *Bull. Seism. Soc. Am.*, 78(2), 672–691.

Mendoza, C. and S.H. Hartzell (1988). Aftershock patterns and mainshock faulting, *Bull. Seism. Soc. Am. 78*, 1438–1449.

Ou, G.B., and R.B. Herrmann (1990). A statistical model for ground motion produced by earthquakes at local and regional distances. *Bull. Seism. Soc. Am.*, 80, 1397–1417.

Saikia, C.K. (1992). Ground motions in greater Los Angeles due to a magnitude 7.0 earthquake on the Elysian Thrust Fault, *Bull. Seism. Soc. Am.*, 80, submitted.

Schnabel, P.B., J. Lysmer, and H.B. Seed (1972). *SHAKE: a Computer Program for Earthquake Response Analysis of Horizontally Layered Sites*. Earthq. Engin. Res. Center, Univ. of Calif. at Berkeley, EERC 72-12.

Silva, W.J. (1976). Body Waves in a Layered Anelastic Soil. *Bull. Seis. Soc. Am.*, vol. 66, 5, 1539–1554.

Silva, W.J. (1991). Global characteristics and site geometry. *Proceedings: NSF/EPRI Workshop on Dynamic Soil Properties and Site Characterization.* Electric Power Res. Inst., EPRI NP-7337.

Silva, W.J., and R.B. Darragh (1993). *Engineering Characterization of earthquake Strong Ground Motion Recorded at Rock Sites.* Electric Power Res. Inst., EPRI TR-102262.

Silva, W.J., and R.K. Green (1989). Magnitude and distance scaling of response spectral shapes for rock sites with applications to North American tectonic environment. Earthquake Spectra, 5(3), 591–624

Silva, W.J., and K. Lee (1987). *WES RASCAL code for synthesizing earthquake ground motions.* State-of-the-Art for Assessing Earthquake Hazards in the United States, Report 24, U.S. Army Engineers Waterways Experiment Station, Misc. Paper S-73-1.

Silva, W.J., and R.B. Darragh, C. Stark, I. Wong, J.C. Stepp, J. Schneider, and S.J. Chiou (1990). A methodology to estimate design response spectra in the near-source region of large earthquakes using the Band-Limited-White-Noise Ground Motion Model. *Fourth U.S. Nat'l Confer. Earthq. Engin.*, Palm Springs, California. EERI: 1.

Somerville, P. G., J. P. McLaren, C. K. Saikia, and D. V. Helmberger (1990). The 25 November 1988 Saguenay, Quebec Earthquake: Source Parameters and the Attenuation of Strong Ground Motion, *Bull. Seism. Soc. Am.*, 80, 1118–1143.

Somerville, P.G., M.K. Sen and B.P. Cohee (1991). Simulation of strong ground motions recorded during the 1985 Michoacan, Mexico and Valparaiso, Chile earthquakes, *Bull. Seism. Soc. Am.*, 81, 1–27.

Somerville, P.G., N.F. Smith and R.W. Graves (1992a). The effect of critical Moho reflections on the attenuation of strong motion from the 1989 Loma Prieta earthquake, in The October 17, 1989 Loma Prieta Earthquake, U.S.G.S. Professional Paper, in press.

Somerville, P.G., D.J. Wald and N.F. Smith (1992b). Prediction of the near-source ground accelerations of the Loma Prieta earthquake using a heterogeneous slip model, submitted for publication.

Toro, G.R., and R.K. McGuire (1987). An investigation into earthquake ground motion characteristics in eastern North America. *Bull. Seism. Soc. Am.*, 77, 468–489.

Wald, D.J., L.J. Burdick, and P.G. Somerville (1988a). Simulation of acceleration time histories close to large earthquakes. *Earthquake Engineering and Soil Dynamics II—Recent Advances in Ground-Motion Evaluation*, Proc. Am. Soc. Civil Engin., Specialty Conf., Park City, Utah, 20, 430–444.

Wald, D.J., P.G. Somerville, and L.J. Burdick (1988b). The Whittier Narrows, California earthquake of October 1, 1987-simulation of recorded accelerations. *Earthquake Spectra*, 4(1), 139–156.

Wald, D.J., D.V. Helmberger, and T.H. Heaton (1991). Rupture model of the 1989 Loma Prieta earthquake from the inversion of strong-motion and broadband teleseismic data. *Bull. Seism. Soc. Am.*, 81(5), 1540–1572.

Wald, D. J., P.G. Somerville, and N.F. Smith (1992). A test of the predictability of the near-source ground accelerations of the 1989 Loma Prieta earthquake, submitted for publication.

4

QUANTIFICATION OF SEISMIC SOURCE EFFECTS

There are three main parameters of the seismic source for the stochastic ground motion simulation procedure described in Section 3.2. These are magnitude, stress drop (corner frequency), and the relation between source distance and equivalent point-source distance (accounts for effect of extended sources). The development of the source parameters are briefly described in this section. A complete description of the development of the source parameters is given in Volume 5 of this report (EPRI, 1993).

4.1 Magnitude

Both m_{Lg} and moment magnitude, **M**, are used to characterize earthquake size for the development of the engineering model in Section 9. The use of m_{Lg} provides a link to ENA earthquake catalogs and to current and past practice. The use of **M** provides a more direct and physically based estimate of ground motion. A relation between m_{Lg} and **M** including the effect of stress drop is developed in Volume 5 using a hybrid approach. The stochastic ground motion model in Section 3.2 is used to develop an average M_0–m_{Lg} relationship. Empirical data are then used to validate this relationship and to quantify the variability in m_{Lg} given M_0 and the dependence of m_{Lg} on stress drop.

4.2 Stress Drop

For a fixed magnitude or moment, the stress drop in the stochastic source model (Eq. 3.1) directly scales ground motions for frequencies above the corner frequency (Silva, 1991). In the frequency range of interest, 1–35 Hz, the stress drop is therefore one of the controlling parameters for the point-source model (Section 9).

In Volume 5 two representations of stress drop are considered: the Brune stress drop and the high frequency stress parameter. While the differences in measured stress drops using the two definitions are not significantly different, the high frequency stress parameter provides slightly more conservatism in estimated ground motion. Part of this conservatism may be due to the existence of a double corner in the source spectrum (Atkinson, 1993). The distribution of stress drop values is therefore constrained by values of the high-frequency stress parameter in developing the engineering model in Section 9. Stress drops ranging from 20 to 600 bars have been considered, and this variability is partitioned between randomness and uncertainty. The median stress drop for ENA is determined to be 120 bars.

4.3 Source Depth

The source depth distributions for ENA events developed in Section 5.2 are based on the locations of earthquake hypocenters (i.e., the point of initiation of source rupture). However, the stochastic ground motion model described in Section 3.2 yields simulations of ground motions relative to an asperity (i.e., a zone of greatest slip and greatest high-frequency radiation). Moreover, because the stochastic model used here considers source radiation from a point, geometrical effects of an extended fault that are significant at close distances are not explicitly considered in the simulations. Therefore, a conversion from hypocentral depth to asperity depth that accounts approximately for the extended source effect is derived. In addition, geometrical constraints on the spatial extent of the source are developed in terms of the probability that a large magnitude event will occur at shallow focal depths.

References

Atkinson, G. M. (1993). Earthquake source spectra in Eastern North America, submitted to *Bull. Seism. Soc. Am.*

EPRI (1993). Guidelines for determining design basis ground motions, Electric Power Research Institute, Palo Alto, Calif., Report TR-102293, Vol. 5.

Silva, W. J. (1991). Global characteristics and site geometry, Proceedings: NSF/EPRI Workshop on Dynamic Soil Properties and Site Characterization, Electric Power Research Institute, Report NP-7337.

5

QUANTIFICATION OF CRUSTAL PATH EFFECTS

Ground motion attenuation is the decay of ground motion amplitudes with increasing distance from the seismic source. Ground motion attenuation can vary across the U. S. due to differences in the properties of the rocks and Earth's crust. For example, as discussed in Section 1.5, the ground motions in the EUS attenuate less rapidly than ground motions in the WUS. These differences in the rate of attenuation of ground motion are called crustal path effects.

There are several factors that account for crustal path effects. These include large scale crustal velocity structure, anelastic absorption, and scattering. In the ground motion simulation procedures described in Section 3, path effects are included through 1-D velocity models and Q. The 1-D velocity model accounts for the large scale features of the crust such as the thickness of the crust (depth of the Moho boundary). The simplest models of crustal structure assume that the crust is a homogeneous whole-space or a half-space. For a whole-space, the exponent of the distance term in Eq. 3.1, called the geometrical spreading coefficient, is unity (R^{-1} attenuation). The Q model accounts for anelastic absorption, scattering, and any other features that attenuate the ground motion differently from the geometrical spreading assumed in the model. For a given seismic source and focal depth, the geometrical spreading coefficient and Q account for the character of the ground motion attenuation.

Region-specific crustal path effects can modify the rate of attenuation of ground motion such that the geometric spreading coefficient becomes distance dependent (see Appendix 3A). If the variations in crustal velocity structure and Q are large enough, the distance dependence of the geometrical spreading coefficient can be significantly different from region to region.

In this section, the objective is to determine if there are significant variations in the ground motion attenuation in the EUS that would warrant sub-dividing the EUS into multiple distinct ground motion attenuation regions. The approach used in this section is to first divide the EUS into multiple regions based upon seismological and geological factors. Numerical simulation procedures (Section 3.3) are then used to compute ground motions for each region. The simulated ground motions for each region are then compared to one another to determine if the seismological and/or geological differences result in significantly different ground motion attenuation. Regions that produce similar ground motion attenuation are combined into groups of ground motion attenuation regions. In Section 9, separate attenuation relations are derived for each distinct ground motion attenuation group.

5.1 Importance of Consideration of Both Velocity Structure and Q

Differences in observed ground motion attenuation rates are often attributed to differences in Q; however, the velocity structure can also have an important effect on ground motion attenuation. The importance of considering effects of both Q and velocity structure variations is discussed below.

The influence of Q on the attenuation of ground motion grows with the length of the path, and is frequency dependent (see Eq. 3.1). Within one hundred km of the source, its influence in the eastern United States is relatively small except in the Gulf Coast region. However, for the frequencies of interest here (above 1 Hz), it is expected to become increasingly important beyond 100 km, and beyond a few hundred km the rate of decay of ground motion attenuation is expected to be dominated by Q effects.

In contrast, velocity structure effects are most important for source distances less than two hundred km. At short distances, the attenuation is affected by the velocity gradient between the seismic source and the receiver. At moderate distances, reflected waves can influence the rate of attenuation. This effect is illustrated schematically in Figure 5-1, in which the effect of both the direct wave (labelled S) and waves that are reflected from discontinuities in seismic velocity and density such as the Conrad and Moho discontinuities (labelled S_cS and S_mS) are included. The effect of crustal structure can become significant when the reflected waves reach the critical angle, i_{crit}, and are completely reflected back to the surface at the critical distance, R_{crit}. In the critical distance range, the velocity structure can lead to distance dependent variations in the rate of attenuation (increase or decrease of geometrical spreading coefficient). Beyond two hundred km, the large number of multiply reflected phases contributing to the ground motions, and the larger distance over which scattering effects can occur, subdues effects of velocity structure on the rate of attenuation.

Since the effects of velocity structure and Q both contribute to the shape of the attenuation curve, there are tradeoffs involved in the estimation of each from a set of empirical data. Since the effect of Q is relatively small inside 100 km, this tradeoff should not result in a great deal of uncertainty in the major effects of velocity structure at these distances, such as the effect of critical reflections from the lower crust. However, at distances beyond 100 km, the effects of velocity structure and Q become more difficult to separate given that Q represents all factors that affect the attenuation that are not included in the geometrical spreading model. In this situation, it is usually necessary to make certain assumptions about the form of the Q function or the geometrical

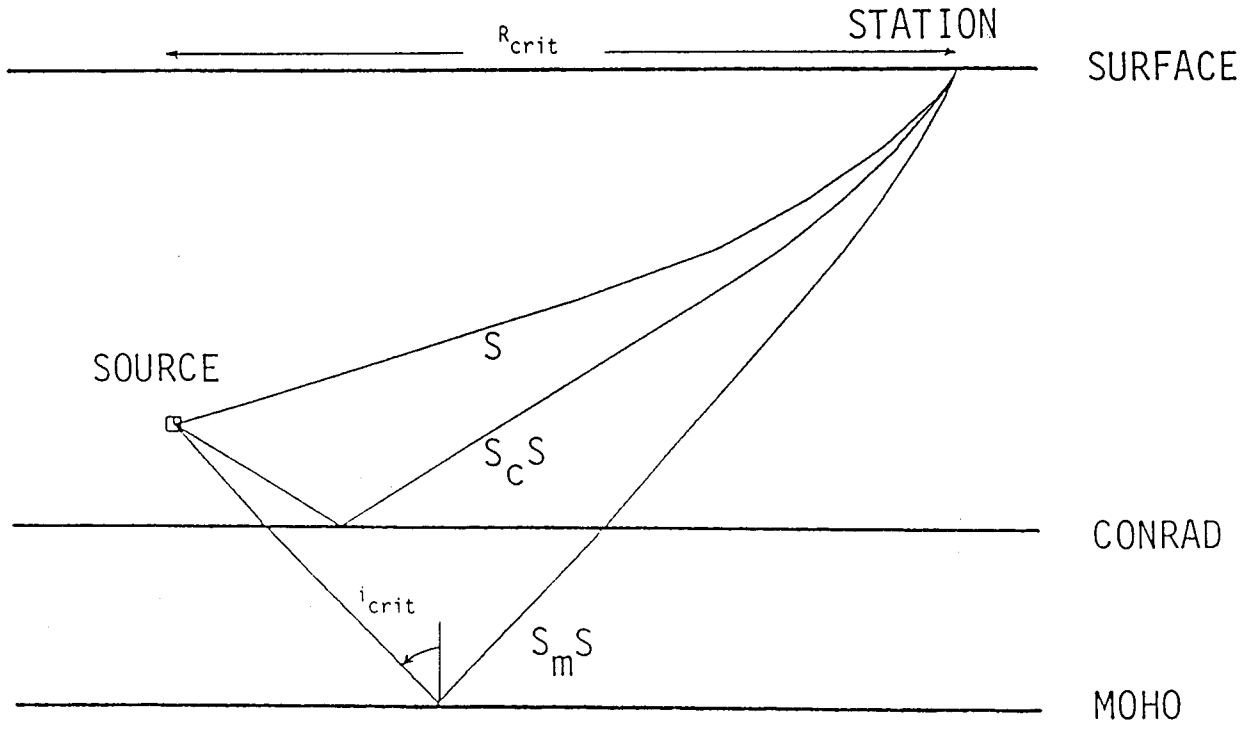

Figure 5-1. Schematic diagram of the wave propagation model, with direct waves (S) and waves ScS and SmS reflected from the Conrad and Moho layers. At the critical angle (i_{crit}), the incident wave is totally reflected back to the surface at distances starting at the critical distance R_{crit}.

spreading coefficient at large distances in order to develop a set of consistent parameters describing these two effects (Atkinson and Mereu, 1992).

5.1.1 Demonstration with Empirical Attenuation Data

Atkinson and Mereu (1992) derived an empirical ground motion attenuation function from a set of ECTN recordings of one hundred small and moderate magnitude earthquakes in southeastern Canada. As an example, a subset of the data at 2 Hz are shown in Figure 5-2a. In this plot, station corrections and event corrections (determined by regression analysis) have been applied to the data. The median curve from a regression using a trilinear form of the attenuation is shown by the solid line. Averaged over about one hundred events, the geometrical spreading term was found to be $R^{-1.1}$ within 70 km and $R^{0.0}$ between 70 and 130 km; beyond 130 km the data are compatible with geometric spreading coefficients in the range of 0.5 to 1.0, with differing associated Q models. The attenuation for 1/R and for the Mid-continent structure computed using the stochastic model from Section 3.2 are also shown in Figure 5-2a. The curves for the stochastic model have been averaged over focal depths of 5, 10, and 15 km using focal depth weights that are consistent with the Atkinson data set (See Appendix 5b). In the distance range of 50 to 120 km, the Mid-continent structure model produces flattening of the attenuation in comparison to 1/R attenuation that is similar to the flattening for the empirical curve. For this data set, the use of the Mid-continent structure produces a better fit to the empirical attenuation than the use of 1/R attenuation over the distance range of 50 to 100 km. The median regression values for other frequencies are also shown in Figure 5-2b. They also shown the flattening of the attenuation in the range of 70 to 130 km. This flattening of the attenuation function in the distance range of 70 to 130 km is consistent with crustal structure effects resulting from critical reflections from layers in the lower crust (Burger et al., 1987). In a separate study, the flat shape in the attenuation of strong ground motion from the 1988 Saguenay earthquake in the distance range of 60 to 120 km was attributed by Somerville et al. (1990) to the effect of critical reflections from the lower crust. The distance dependence of the geometric spreading coefficient shows that the effect of crustal velocity structure on ground motion attenuation can be important.

5.1.2 Demonstration by Modeling of Attenuation from Small Events

The effect of crustal velocity structure on ground motion attenuation can also be seen by modeling the attenuation from small magnitude events. The amplitudes of recorded ground motions of ENA earthquakes are compared to those calculated using synthetic seismograms that include the effects of wave propagation in a layered crust.

The simulation procedure used to generate synthetic seismograms is similar to that described in Section 3.3. The principal difference is that a single source function, constructed to match a specified source spectrum, is used in place of empirical source functions. Due to the small set of rays used in the calculations, the simulations are not appropriate for distances greater than 200 km.

The Fourier amplitude of the source function is taken as a Brune source with a stress drop of 100 bars. (Since we will be comparing the relative rates of attenuation between regions and not the absolute amplitudes, the value of the stress drop is not important.) The phase spectrum for each source has been derived from a segment of the SM16 recording of the 1988 Saguenay earthquake having a duration of the inverse of the lower corner frequency of the Saguenay event.

5.1.2.1 Analysis of Ten Grenville Events

Initially, we modeled the attenuation of ten earthquakes that were well recorded by the ECTN in the Northern Grenville-Superior Region of southeastern Canada. We generated source spectra by estimating the seismic moment from the Lg magnitude and using a Brune source spectrum with a stress drop of 100 bars. Since the seismic moment estimates derived in this way are subject to considerable uncertainty, we normalized the synthetic seismograms to fit the recorded response spectral velocity at 5% damping at 2 Hz, averaged over stations within 200 km. Although we were not able to check absolute amplitude information with this procedure, we were able to compare the shapes of the observed and synthetic attenuation. Frequency-dependent station corrections derived by Atkinson and Mereu (1992) were applied to the recorded data.

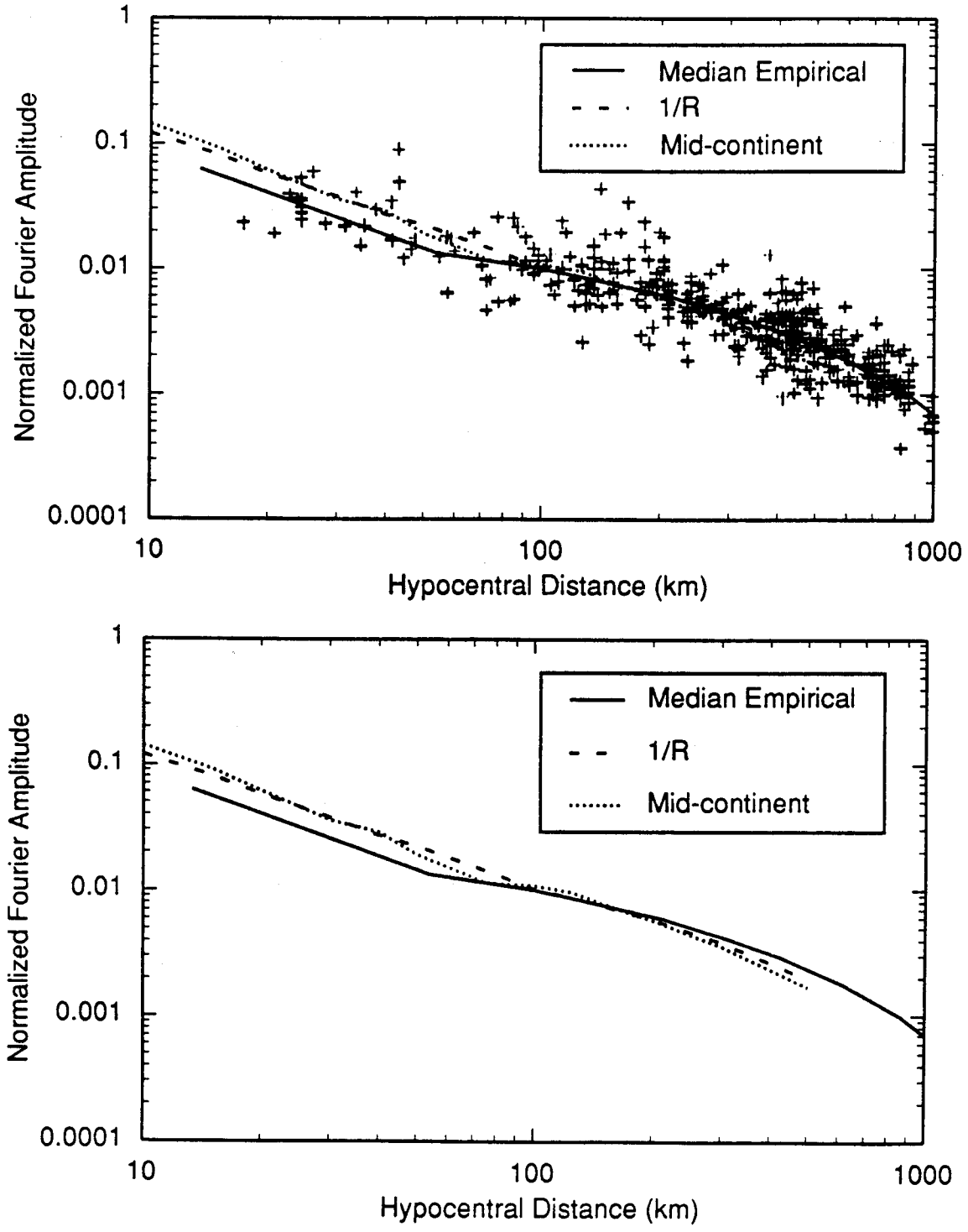

Figure 5-2a. Top frame: Empirical attenuation in southeastern Canada for Fourier amplitude at 2 Hz from Atkinson and Mereu (1992). Station corrections and source corrections have been applied. The solid curve is the regression fit to these data. The dashed and dotted lines are based on the stochastic model described in Section 3.2. Bottom frame: Without data.

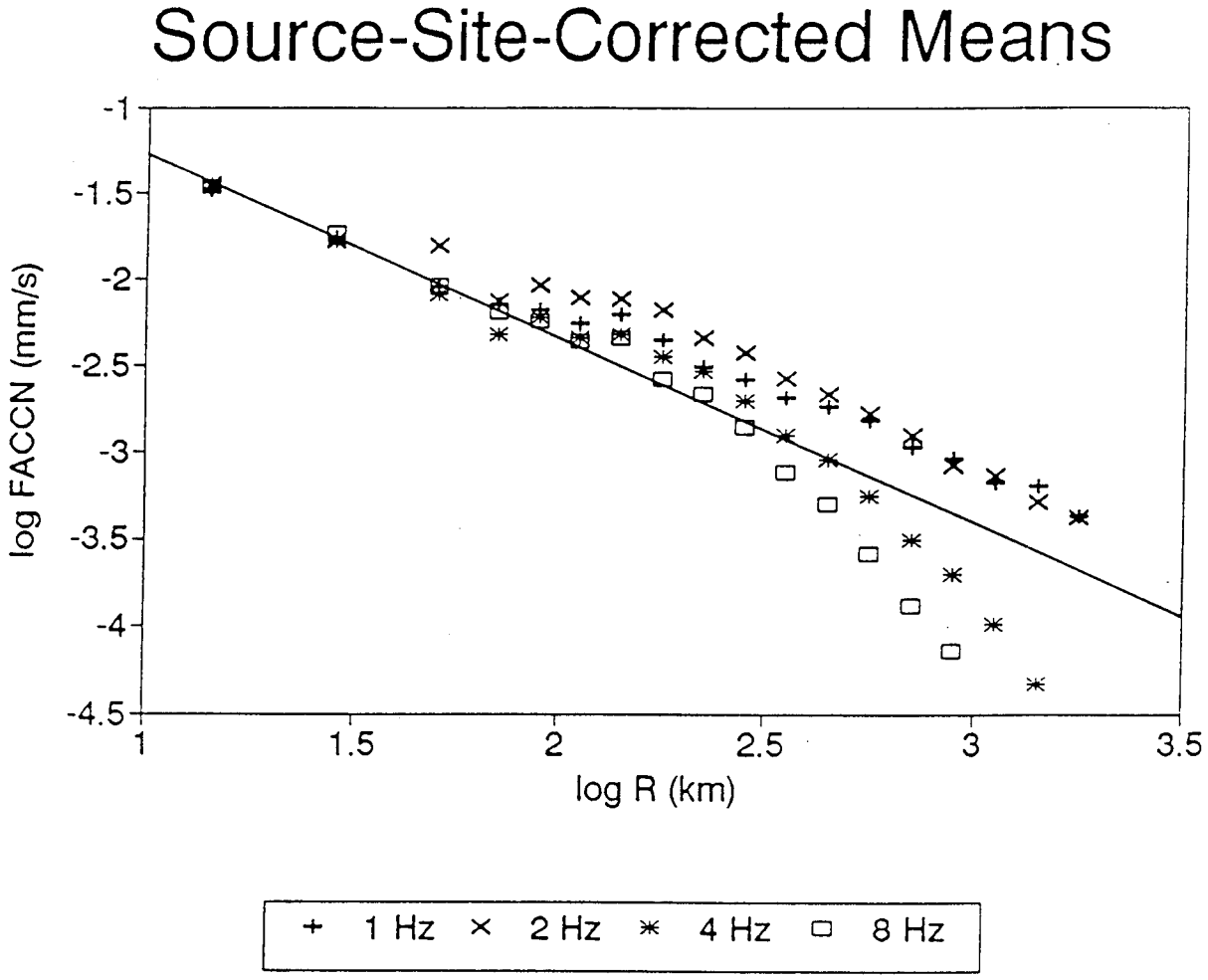

Figure 5-2b. Mean empirical attenuation in southeastern Canada for Fourier amplitudes. Source: Atkinson and Mereu, 1992.

The locations of the ten events, and of the recording stations, are shown in Figure 5-3, and the events are listed in Table 5-1. Five of the events occurred in the West Quebec seismic zone. For these events, we used a crustal structure model derived from the 1982 COCRUST experiment (Mereu et al., 1986), shown on the left side of Figure 5-4. The other five events occurred in or near the Charlevoix seismic zone. For these events, we used a crustal structure model derived by Woodward-Clyde Consultants (1991) from modeling the Saguenay earthquake sequence, shown on the right side of Figure 5-4.

The ten Grenville events include both shallow and deep earthquakes in both the West Quebec and Charlevoix regions. From an analysis of the empirical data and from modeling, we find that the largest variation in the attenuation among these events is due to differences in focal depth, and that the differences in crustal structure are of secondary importance. To illustrate this effect, we selected the events of 03/10/88 and 11/11/87, at depths of 12 and 21 km, respectively, in the West Quebec region, and the events of 90/04/21 and 88/11/25 (the Saguenay earthquake), at depths of 10 and 26 km, respectively, in

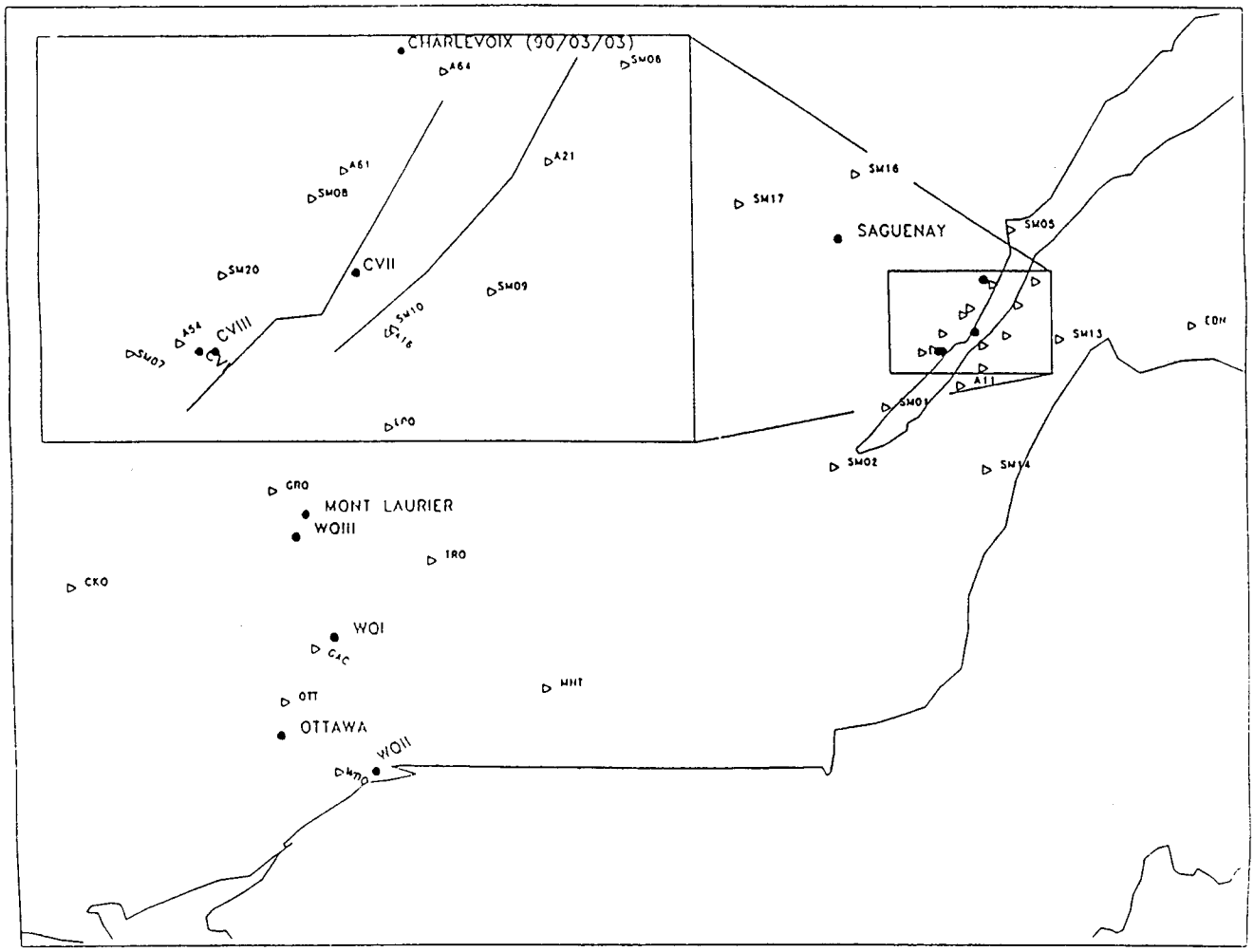

Figure 5-3. Map showing the locations of the ten earthquakes in the Northern Grenville-Superior region and the recording stations used in the analysis.

the Charlevoix region. Profiles of recorded and synthetic vertical velocity seismograms are compared in Figures 5-5 through 5-8 for each of the four events. The records are aligned in absolute time, and the expected times of the direct and reflected waves are shown. Velocity waveforms are displayed to facilitate the correlation of seismic phases.

For the shallow West Quebec event of 03/10/88, the largest arrivals in the recorded seismograms occur near the travel time of the direct wave at distances within 70 km. However, at stations beyond 70 km, the largest arrivals in the data occur following the times of the Conrad and Moho reflections. In the synthetic seismograms, the largest arrivals occur with the direct wave at distances less than 100 km, and with the Moho reflection at distances larger than 100 km.

Table 5-1

List of Earthquakes Used in Ground Motion Attenuation Modeling

						# Stations		
Location	**Date**	**Lat**	**Long**	**Depth**	**Mag**	**< 80 km**	**<120**	**Crustal Model**
West Quebec Ottawa	83 10 11	45.20	–75.750	15.0	4.1	3	3	Grenville Ontario
West Quebec*	87 11 11	45.776	–75.336	21.1	3.2	3	5	Grenville Ontario
West Quebec*	88 03 10	46.34	–75.67	12.0	3.7	2	4	Grenville Ontario
Charlevoix	88 03 13	47.445	–70.376	6.8	3.1	7	7	Grenville Saguenay
West Quebec	88 08 09	45.007	–74.993	9.5	3.4	2	4	Grenville Ontario
Charlevoix Saguenay	88 11 25	48.117	–71.183	26.0	6.5	2	8	Grenville Saguenay
Charlevoix	89 11 22	47.445	–70.345	8.1	3.4	7	7	Grenville Saguenay
Charlevoix*	90 03 03	47.856	–69.977	20.0	3.6	7	7	Grenville Saguenay
Charlevoix*	90 04 21	47.553	–70.070	9.6	3.1	7	7	Grenville Saguenay
West Quebec Mont Laurier	90 10 19	46.474	–75.591	13.0	5.1	1	2	Grenville Ontario
Central Virginia	87 04 11	37.664	77.903	8.7	1.7	6	6	Atlantic Coastal Plain
Central Virginia	87 04 14	37.862	77.543	11.7	0.6	4	7	Atlantic Coastal Plain
Giles County	86 08 09	36.787	–80.726	10.5	2.2	5	7	Southern Appalachians
Giles County	87 11 21	36.755	–80.713	5.0		4	6	Southern Appalachians
East Tennessee	88 01 08	35.290	–84.203	15.0	2.3	4	7	Southern Appalachians
East Tennessee	88 02 11	35.468	–84.311	20.3	2.3	6	7	Southern Appalachians
New Madrid	91 05 04	35.555	–89.802	7.1	4.6	3	5	New Madrid-McCamy

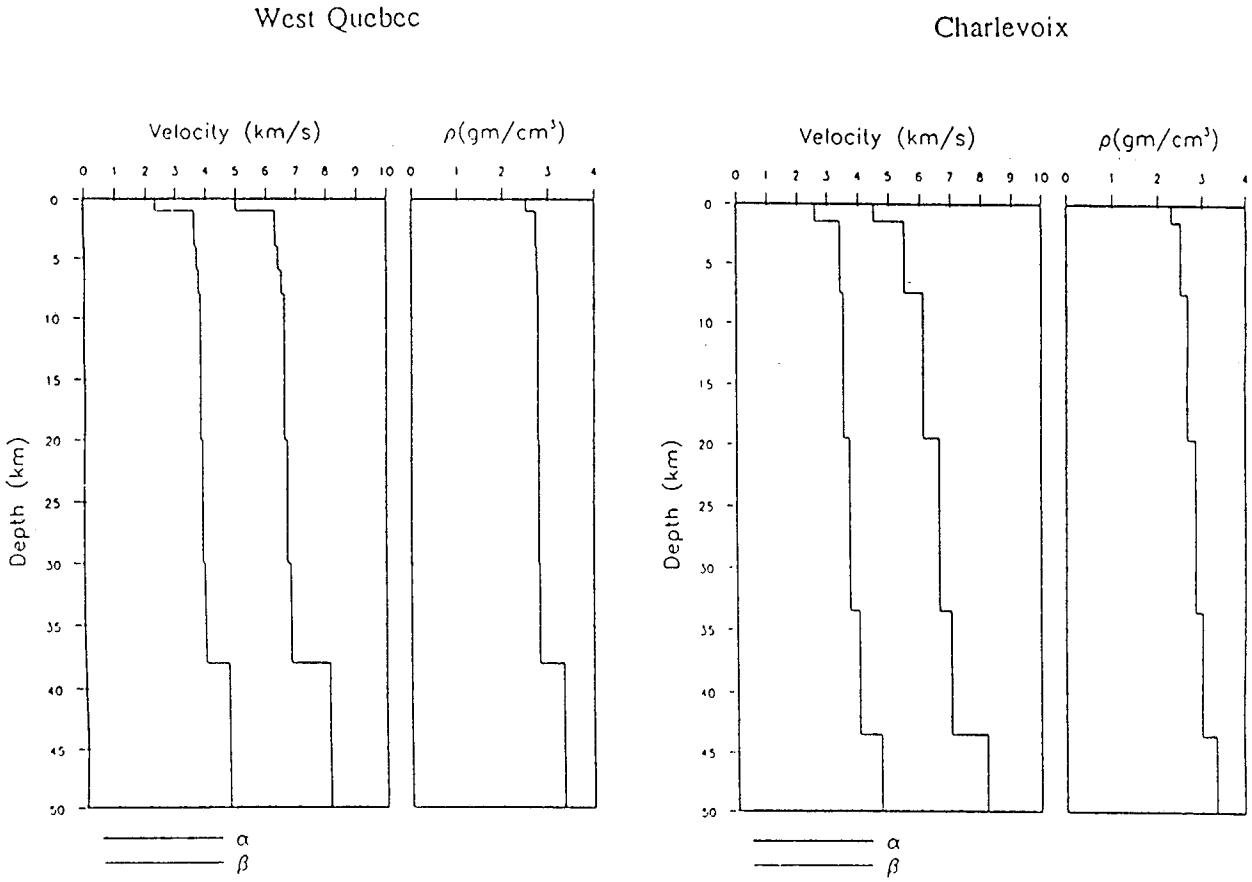

Figure 5-4. Left: Crustal structure model for the Ottawa and Mont Laurier earthquakes, modified from Mereu et al. (1986). Right: Crustal structure model for the Saguenay and Charlevoix earthquakes, from Somerville et al. (1990)

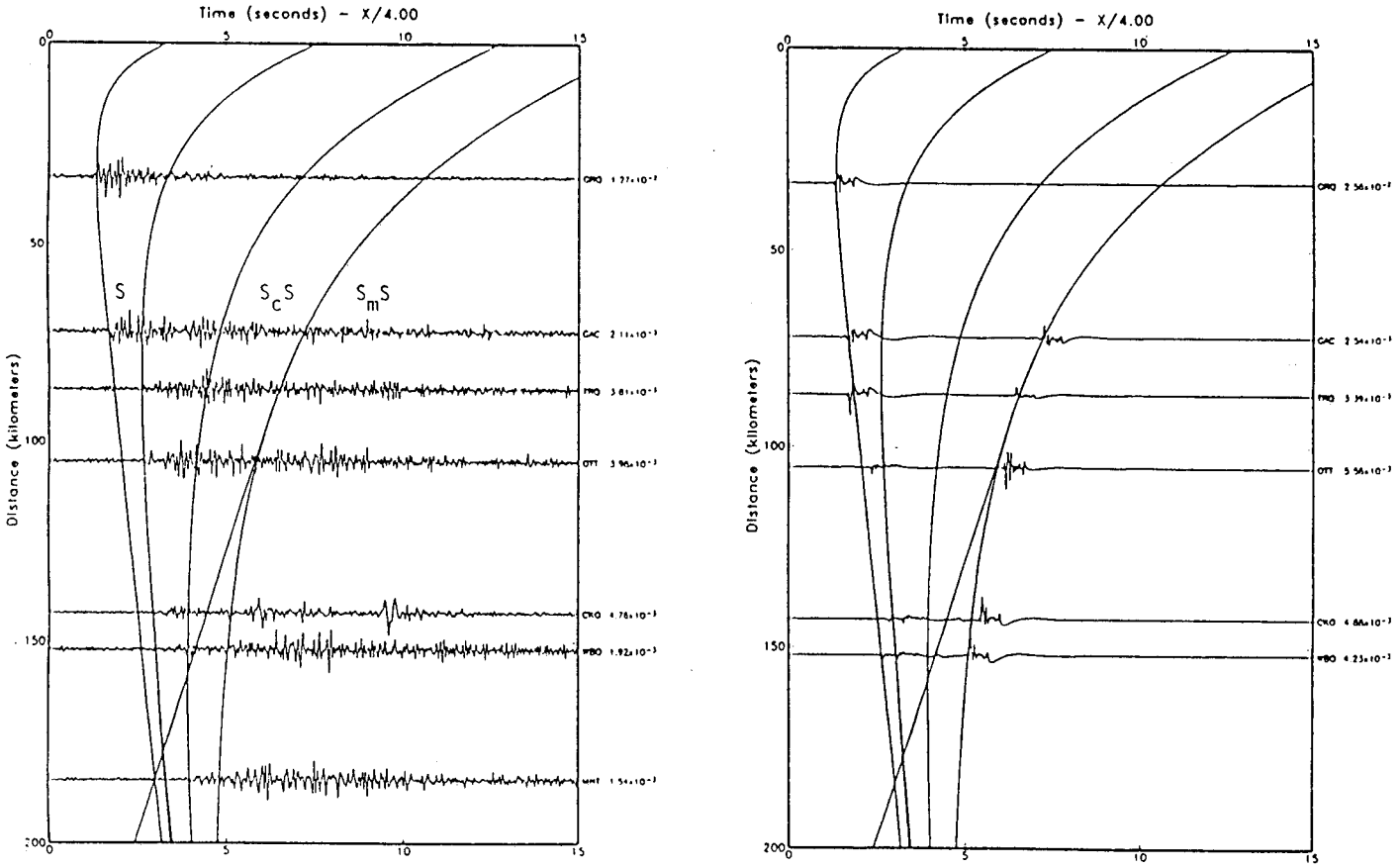

Figure 5-5. Comparison of recorded (left) and synthetic (right) vertical velocity seismograms for the 03/11/88 West Quebec event, shown with predicted travel times for direct and reflected waves. To display S wave arrivals, the time scale is the travel time reduced by 4 km/sec.

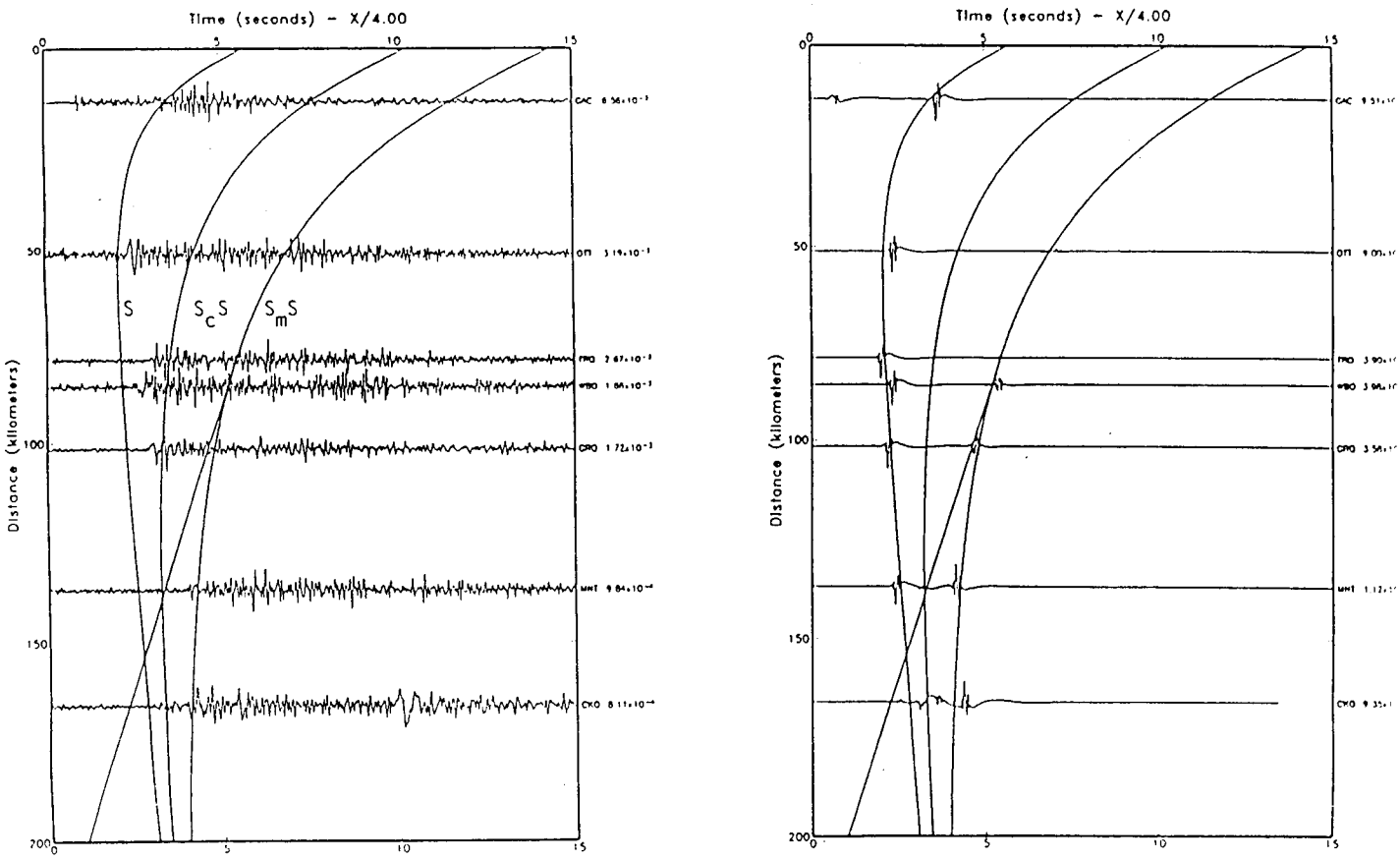

Figure 5-6. Comparison of recorded (left) and synthetic (right) vertical velocity seismograms for the 11/11/87 West Quebec event, shown with predicted travel times for direct and reflected waves. To display S wave arrivals, the time scale is the travel time reduced by 4 km/sec.

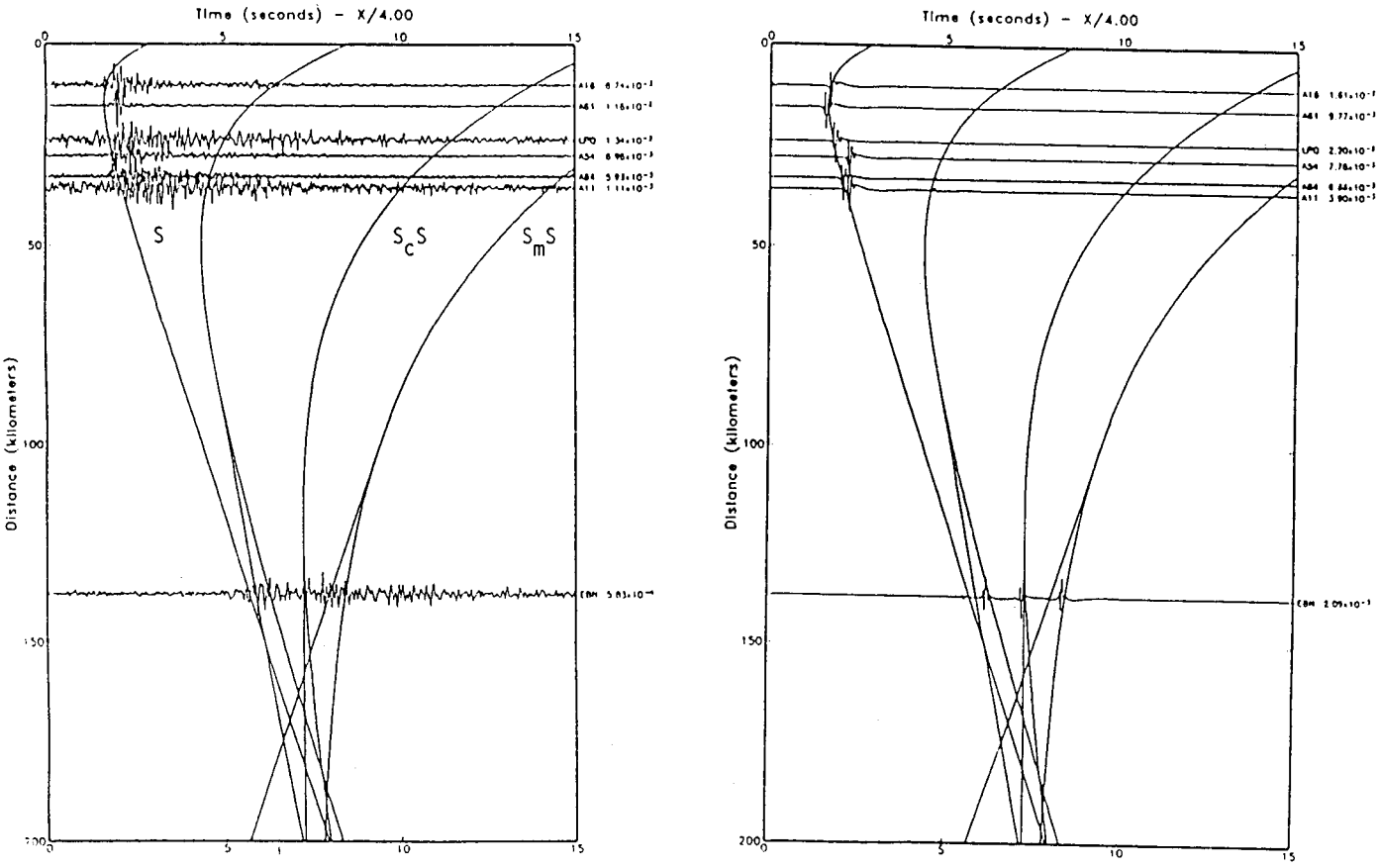

Figure 5-7. Comparison of recorded (left) and synthetic (right) vertical velocity seismograms for the 04/21/90 Charlevoix event, shown with predicted travel times for direct and reflected waves. To display S wave arrivals, the time scale is the travel time reduced by 4 km/sec.

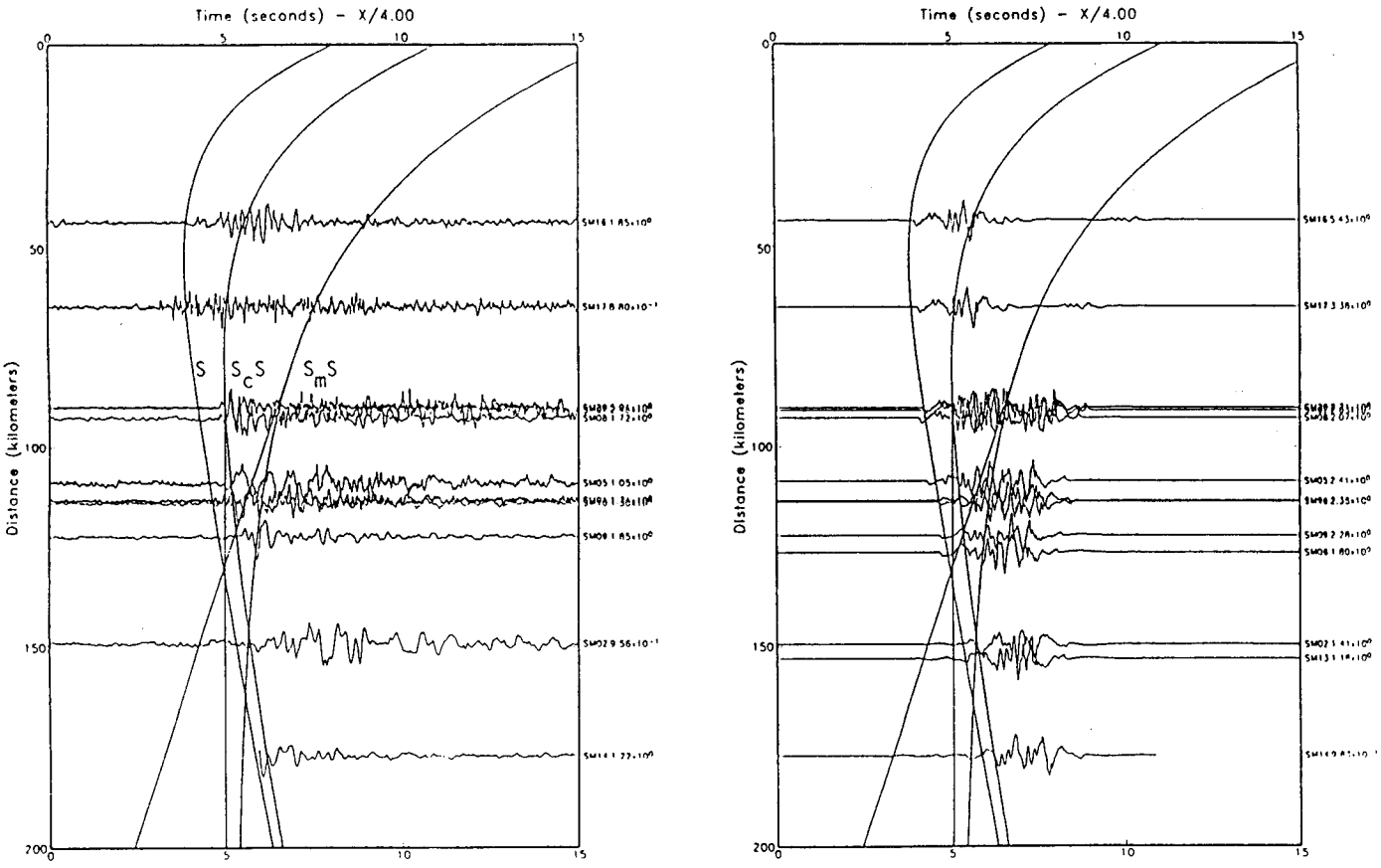

Figure 5-8. Comparison of recorded (left) and synthetic (right) vertical velocity seismograms for the 11/25/88 Saguenay event, shown with predicted travel times for direct and reflected waves. To display S wave arrivals, the time scale is the travel time reduced by 4 km/sec.

For the deep West Quebec event of 11/11/87, as shown on Fig. 5-6, the phases contributing the peak velocity on the recorded seismograms appear to show a progression from the direct wave at the stations within 50 km, to include reflected phases at distances beyond 70 km. This is also seen in the synthetic seismograms.

For the shallow Charlevoix event of 04/21/90, the largest velocities are associated with the direct wave at stations within 40 km, while at 140 km there are contributions from several different arrivals; the same is true for the synthetic seismograms.

For the deep Saguenay event of 11/25/88, the phases contributing the peak velocity on the recorded seismograms are interpreted as a progression from the direct wave at the two closest stations to the Conrad reflection for stations between 80 and 115 km to the Moho reflection at stations beyond 120 km. In the synthetic seismograms, the Moho reflection becomes strong at distances beyond 80 km.

The attenuation of recorded and synthetic response spectral velocity at 2 Hz for 5% damping for shallow and deep events are compared in Figure 5-9. The top panels include the three deep events (deeper than 20 km) and the bottom panels include the seven shallow events. For each set of events, the data in the distance range of 0 to 200 km are shown on the left and the synthetic values are shown on the right. The ground motion values for each event were normalized by fitting a least squares straight line and selecting a specific distance (40 km) at which the

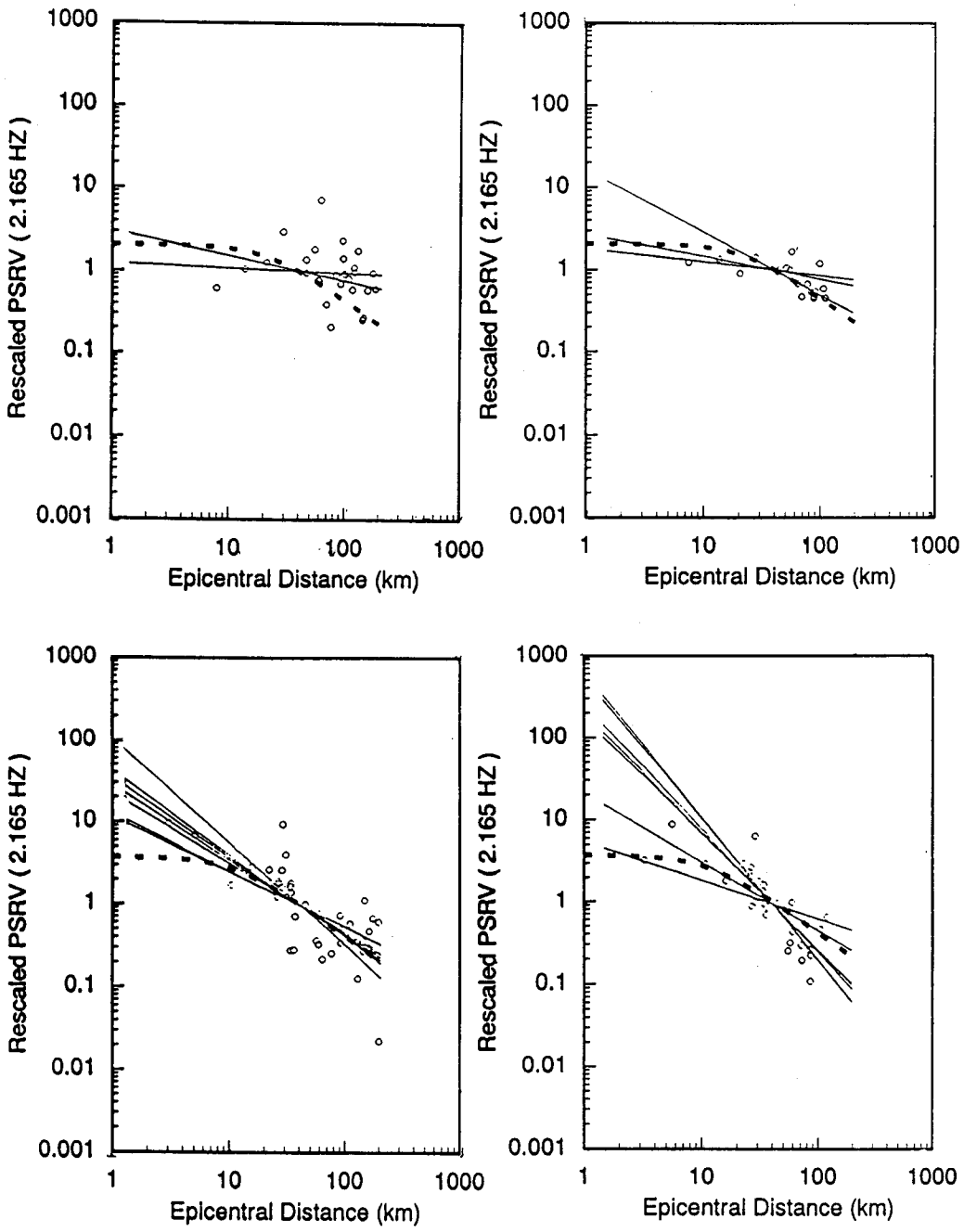

Figure 5-9. Comparison of recorded and synthetic peak acceleration as a function of distance for ten Grenville region earthquakes. Recorded PSRV at 5% damping at 2 Hz is shown on the left, and synthetic values are shown on the right. The top plots are for the three deep events, and the bottom plots are for the seven shallow events. Least-squares fits to each event, normalized at 40 km, are shown by the straight lines. The 1/R attenuation is shown by the dashed line.

amplitudes were normalized. These lines are shown together with the ground motion values. The dashed lines show the 1/R attenuation for the average focal depth of each subset. For deep sources (top panels of Figure 5-9), the wave propagation model predicts a slower rate of attenuation than does the 1/R model. The data (top left panel) also show attenuation that is slower than 1/R. For shallow sources (bottom panels), both the wave propagation and the data are consistent with 1/R attenuation except at short distances. The two data points at distances less than 10 km show larger ground motions than predicted by 1/R attenuation. The wave propagation model predicts a similar high motion for one of the two data points, but the model predicts the same as 1/R for the other data point.

There is a systematic difference in the slopes of the lines for the shallow and deep events; this difference is more pronounced in the data than in the synthetics. In both the West Quebec and Charlevoix regions, deep events attenuate more gradually than shallow events in the distance range of 0 to 200 km. The attenuation of the shallow events is similar to the average attenuation function derived empirically from about one hundred events, described by Atkinson and Mereu (1992; Figure 5-2), reflecting the fact that most of these events had shallow focal depths. In summary, in both the West Quebec and Saguenay-Charlevoix regions we find that the shape of the attenuation in both the recorded and synthetic data is dependent on the focal depth of the earthquake.

The residuals for all ten events are plotted as a function of distance in Figure 5-10 for response spectral velocity at 1, 2, 5 and 10 Hz. Residuals for shallow events (shallower than 20 km) are shown as open boxes, while residuals for deep events are shown as crosses. Generally, for each of these depth categories, there are no significant trends with distance, indicating that the shape of the attenuation of the data is adequately matched by the wave propagation method. The overall lack of distance trends in the residuals indicates that the flattening of the attenuation curve due to critical reflections is consistent between the data and the wave propagation model. The residuals, averaged over distance, for frequencies of 1, 2, 5 and 10 Hz, are tabulated in Table 5-2. The response spectral standard errors are about 0.235 $\log_{10}$ units (a factor of 1.7) on average.

We tested whether using the actual focal depth of the earthquake produced a better fit to the recorded data than assuming a focal depth of 11 km for all events. The residuals increased by about 10% when a focal depth of 11 km was used in place of the actual focal depth. This is a further indication that the focal depth influences the recorded data in the sense predicted by the wave propagation method.

5.1.2.2 Analysis of Ten Eastern North American Events

To evaluate how well ground motion attenuation inside 120 km in some other regions of eastern North America is modeled by our simulation procedure, we selected an additional six events that occurred in three other regions. These events occurred in the Atlantic Coastal Plain, Southern Appalachian, and New Madrid Regions, and are listed together with the selected Grenville events (identified by asterisks) in Table 5-1. The locations of the events are shown in Figure 5-11. We used the same procedure as for the Grenville events, except that station corrections were not available for the New Madrid event.

The attenuation for these events is described qualitively as follows. The attenuation for the Giles County earthquake in the Southern Appalachian Region is gradual in the distance range of 30 to 100 km, due to critical reflections from the Conrad, is matched well by the model. Two earthquakes in Central Virginia in the Atlantic Coastal Plain Region have recordings close enough (20 km) to show the rapid attenuation at short distances before the critical reflection from the Conrad layer causes more gradual attenuation beginning at 50 km. Two earthquakes in eastern Tennessee in the Southern Appalachian Region occurred beneath the Conrad and have rapid attenuation out to 100 km. An earthquake in the New Madrid Region has fairly rapid attenuation out to 100 km, where critical Moho reflections begin to arrive and make the attenuation more gradual.

The residuals for all ten events are plotted as a function of distance in Figure 5-12 for response spectral velocity at 1, 2, 5 and 10 Hz and for peak acceleration (within the 12 Hz bandwidth of the instrument) and peak velocity. Residuals for shallow events (shallower than 20 km) are shown as open boxes, while residuals for deep events

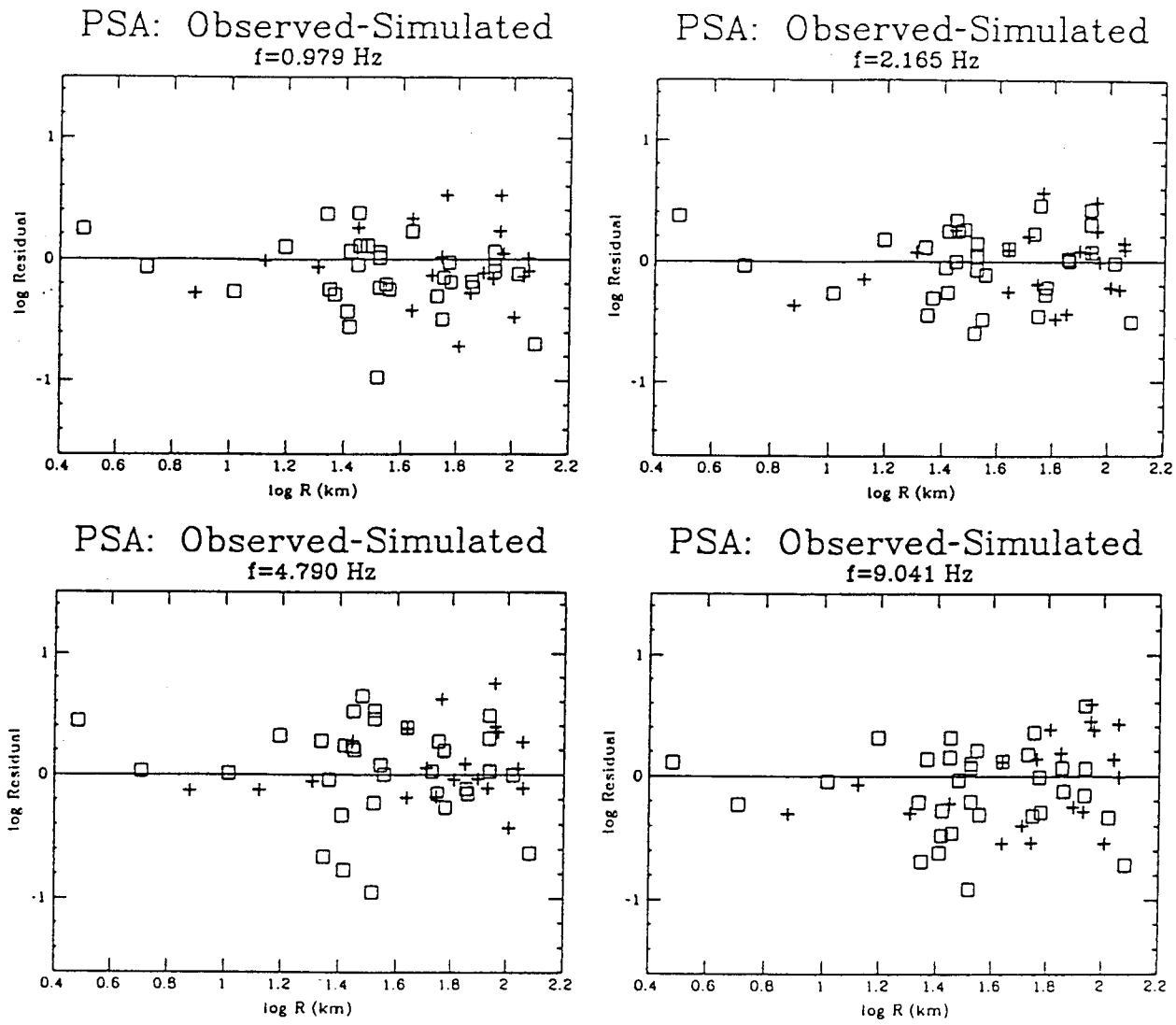

Figure 5-10. Residuals between recorded and synthetic response spectral velocity at 5% damping at 0.98, 2.2, 4.8, and 9.0 Hz, and peak acceleration and velocity, as a function of distance for ten Grenville region earthquakes. The open boxes are for shallow events (less than 20 km deep), while the crosses are for deep events.

Table 5-2

Comparison of Recorded and Synthetic PSRV Standard Errors of Log_{10} Residuals for Brune Source Spectrum

Event	1.0 Hz	2.2 Hz	4.8 Hz	9.0 Hz
83/10/11	0.224	0.140	0.289	0.183
87/11/11	0.102	0.153	0.178	0.162
88/03/10	0.066	0.060	0.107	0.147
88/03/13	0.278	0.271	0.262	0.214
88/08/09	0.171	0.339	0.379	0.317
88/11/25	0.367	0.298	0.246	0.204
89/11/22	0.338	0.316	0.451	0.403
90/03/03	0.309	0.280	0.261	0.291
90/04/21	0.157	0.121	0.198	0.194
90/10/19	0.126	0.311	0.267	0.222
87/04/11	0.185	0.208	0.261	0.347
87/04/14	0.254	0.256	0.263	0.322
87/11/21	0.282	0.213	0.399	0.451
88/01/08	0.234	0.168	0.196	0.278
88/02/11	0.127	0.173	0.103	0.165
91/05/04	0.064	0.125	0.125	0.261

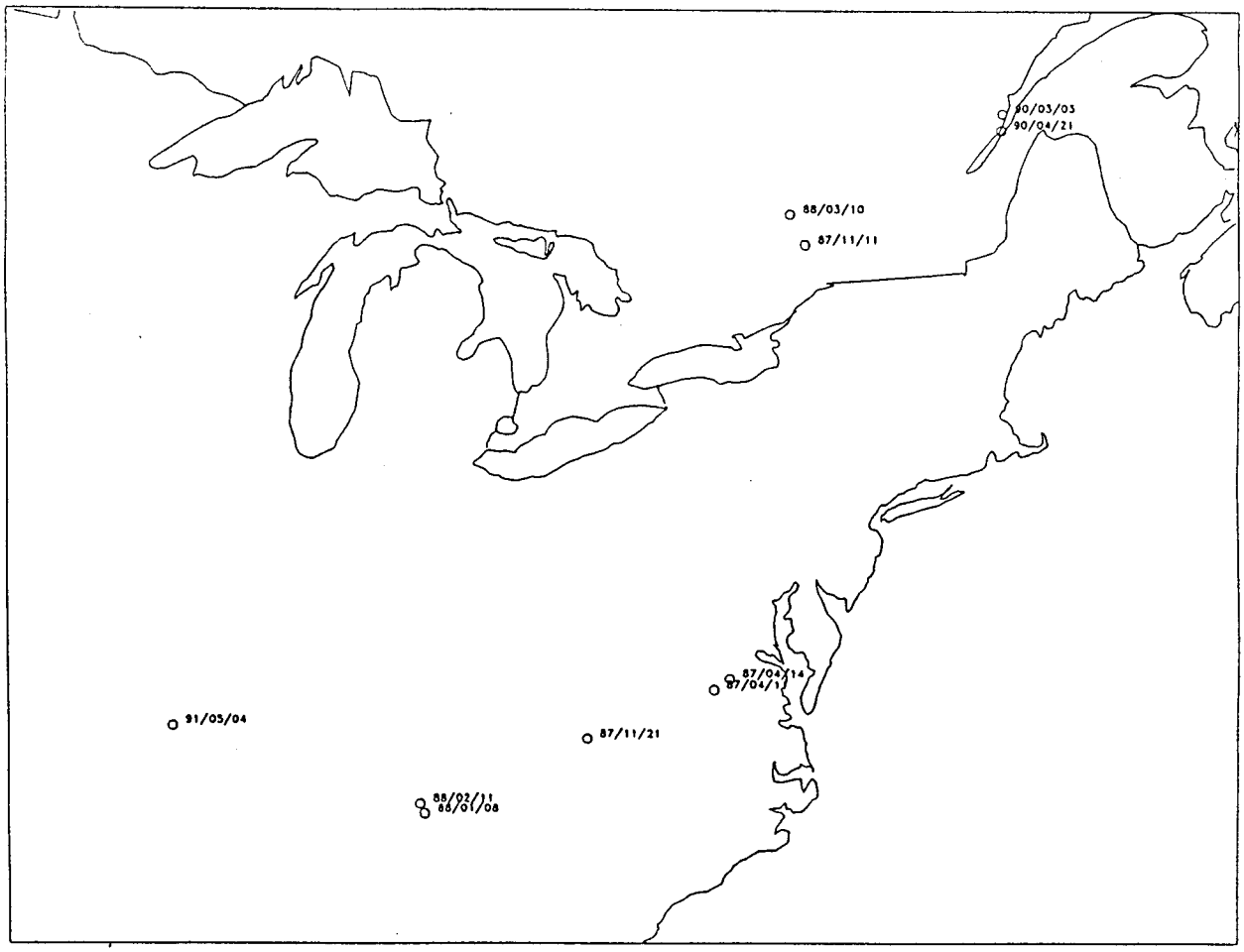

Figure 5-11. Map showing the locations of the ten earthquakes in eastern North America used in the analysis.

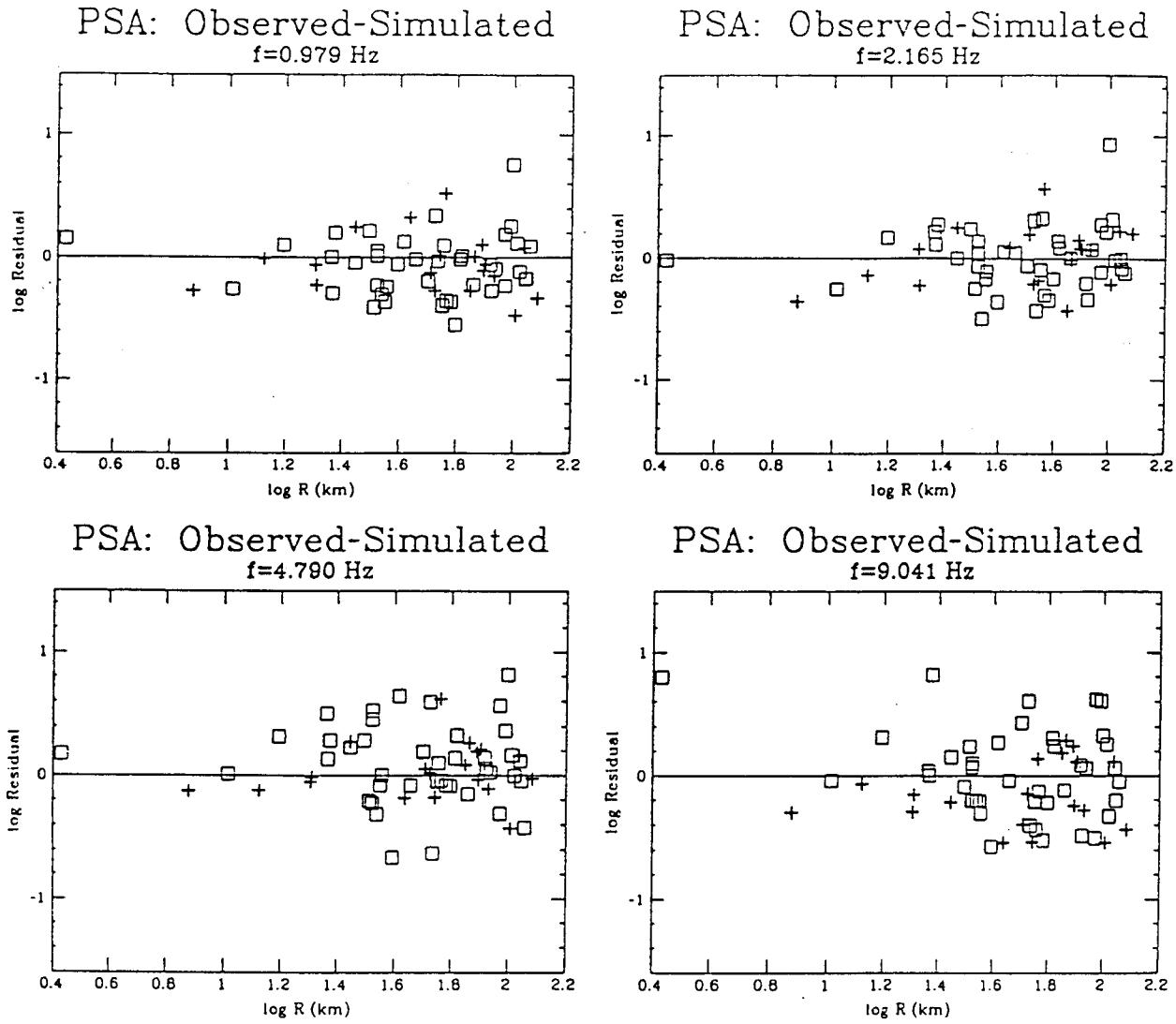

Figure 5-12. Residuals between recorded and synthetic response spectral velocity at 5% damping at 0.98, 2.2, 4.8, and 9.0 Hz, and peak acceleration and velocity, as a function of distance for ten eastern North American earthquakes. The open boxes are for shallow events (less than 20 km deep), while the crosses are for deep events.

are shown as crosses. As for the ten Grenville events shown in Figure 5-10, there are generally no significant trends with distance for each depth category, indicating that the shape of the attenuation of the data is consistent with the wave propagation method. The residuals, averaged over distance, for frequencies of 1, 2, 5 and 10 Hz are tabulated in Table 5-2. The response spectral standard errors are about 0.206 $\log_{10}$ units (a factor of 1.6) on average.

5.1.3 Conclusions

The simple wave propagation model that we have used generates arrivals due to the direct wave and to waves reflected from boundaries in a flat layered crustal model. For the sixteen eastern North America events that we have analyzed, we generally see that the timing of the largest arrivals in the empirical data, for distances greater than 50 km, is consistent with the timing of the arrival of reflected waves. The simulations which include crustal structure effects produce a better match to the data than simple 1/R attenuation. The overall lack of distance trends in the residuals indicates that the flattening of the attenuation curve due to critical reflections is similar in the data and in the wave propagation model. We conclude that crustal structure can have an important effect on ground motion attenuation for distances within 200 km.

5.2 Regionalization of Crustal Velocity Structure, Q, and Focal Depth

As shown in Section 5.1, the velocity structure and focal depth can significantly impact the propagation of seismic waves. In addition, Q also has a significant impact on ground motion attenuation. Variations of crustal velocity structure, Q, and focal depth distribution form the basis for regionalization of crustal path effects.

5.2.1 Crustal Velocity Structure Regionalization

A large body information on the crustal structure of the eastern United States has recently been summarized by Pakiser and Mooney (1989) in a volume entitled "Geophysical Framework of the Continental United States." From the information presented in this volume, it is evident that the velocity structure of the earth's crust in the central and eastern United States varies considerably from region to region. Differences exist in the thickness of the crust, the velocities of the upper and lower crust, and the presence or absence of surficial sedimentary deposits. Variations result primarily from differences in composition and tectonic history. By considering crustal structure in a broad sense, it is possible to identify large regions in which the average structure is similar. These regions can then form the basis for regional models of attenuation founded on calculations of wave propagation in these different crustal structures.

Although the velocity structure of the crust in the central and eastern United States is complex and three-dimensional, it is possible to describe separate regions based on average crustal velocity structure. In a previous study for EPRI (Woodward-Clyde Consultants, 1991), information on crustal structure was reviewed to identify 16 regions in which the structure is uniform to a first approximation. Crustal P-wave velocities for these regions were modeled as horizontal layers of uniform thickness. Some region boundaries are uncertain primarily from insufficient data coverage. Detailed seismic investigations of crustal velocity structure are usually carried out in areas of geologic interest or where anomalies are known to be present. These are not necessarily the best areas to resolve the placement of region boundaries or to characterize the average crustal structure between these boundaries.

In defining regions of similar crustal structure, three criteria played a major role: crustal thickness, the presence or absence of a high-velocity (P-wave velocity > 7 km/sec) lower crust, and the velocity structure of the upper crust. These factors were applied in sequence to arrive at the final regionalization. The two cross sections across the central United States at latitudes 37° and 49°, developed by Braile (1989) and reproduced in Figure 5-13, were especially helpful in developing the regionalization and the velocity models of the regions. In addition, correlations with geologic or tectonic structures were used to guide the delineation of region boundaries. The interpretations of gross geologic structure for the northern and southern Appalachians (summarized in Taylor, 1989), and the crustal age terranes identified by Bickford and others (1986) were especially useful.

5.2.1.1 Crustal Thickness

Over much of the central and eastern United States, crustal thickness is fairly uniform and lies between about 35 and 45 km (e.g., Braile, 1989; Taylor, 1989; Mooney and Braile, 1989). Three regions exhibit a somewhat thicker crust of about 45 to 50 km: the south-central Appalachians from eastern Tennessee to northern Virginia, the Superior basin beneath Lake Superior, and the western-most Great Plains. Along the Atlantic and Gulf coasts, the crust thins to 30 km or less.

5.2.1.2 Presence of High Velocity Lower Crust

The presence of a high-velocity lower crust provides another basis for differentiating crustal regions in the central and eastern United States. This layer, if present, is characterized by a (P-wave) velocity of about 7.2 to 7.4 km/sec, and a thickness of 10 to 15 km. High-velocity lower crust appears to exist along much of the southern

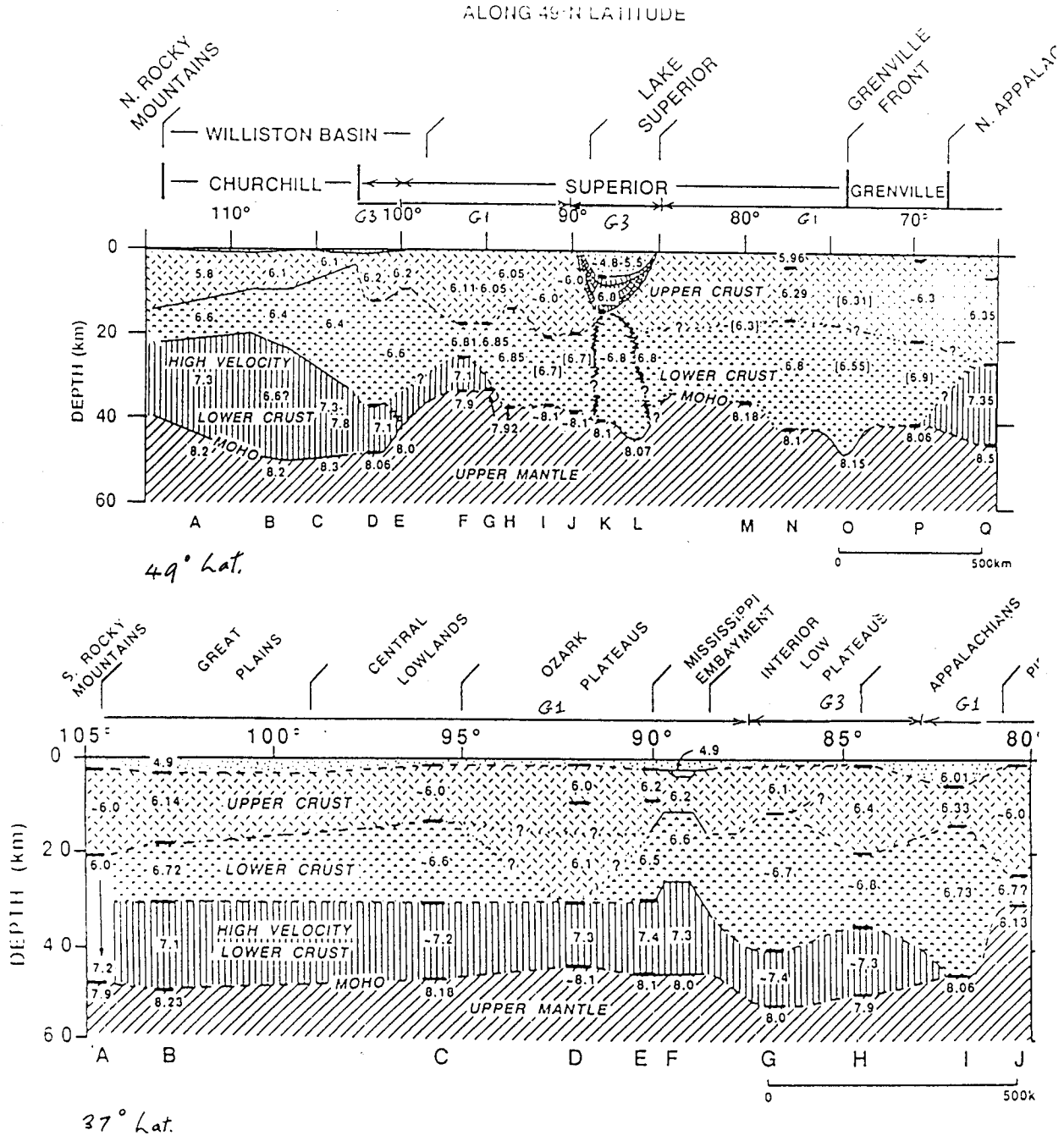

Figure 5-13. Profiles of crustal structure across the eastern United States at latitudes 49° and 37° (Braille at al., 1989).

and western edge of the craton in the central United States (Braile, 1989). Braile (1989) interprets the existence of such a layer along latitude 37 N from the southern Rocky Mountains to the Appalachians. To the north, his summary of crustal structure shows a similar layer associated with the Williston basin (Braile, 1989). A profile in eastern Colorado, however, does not show this layer (Braile, 1989). A high-velocity lower crust also exists beneath central New England (Taylor, 1989). This layer probably represents mafic material associated with an island arc that was accreted to the North American craton during Ordovician time. Various geologic evidence suggests that the island arc was founded on oceanic material (Taylor, 1989). In contrast, accreted island arc material in the southern Appalachians is not associated with a high-velocity lower crust. In this region the island arc appears to have developed on transitional (rifted) continental crust (Taylor, 1989).

5.2.1.3 Upper Crustal Structure

The third factor considered in defining regions of similar crustal velocity is the structure of the upper crustal layers. In general, this structure is described by a layer of about velocity 6.0 km/sec overlying a layer of about velocity 6.6 km/sec. In some areas such as the coastal margin of the Gulf Coast from the Mississippi Delta to East Texas, a lower velocity layer is observed near the surface associated with sedimentary deposits, as described in Section 5.5.5. In a region centered on central Tennessee, the velocity of the surface layer is anomalously high (6.4 km/sec). Off the coast of New England, the lower velocity upper crustal layer appears to be missing.

5.2.1.4 Crustal Structure Regions

The crustal velocity structure regions are listed in Table 5-3 and shown in Figure 5-14. Crustal velocity models for each region are given in Appendix 5A, together with a summary of the considerations that led to the selection of each crustal model. A summary plot of the P-wave velocity structures is shown in Figure 5-15. Generally, there is no parallel information on shear wave velocity structure, and we have assumed Poisson's ratio in the crust to be 0.25. This is compatible with the average value of 0.258, with a standard deviation of 0.034, derived from 64 estimates of crustal Poisson's ratio in continental North America by Braile et al. (1989). To estimate densities (ρ), we used the relation: $\rho = 0.162\,\alpha + 1.723$, for P-wave velocity a larger than 3.0, based on the data of C. Drake shown in Figure 7-7 by Grant and West (1965).

Parallel to the development of this regionalization of crustal structure, a regionalization of eastern North America based on genetic origin was developed independently (EPRI, 1991). This genetic regionalization is shown in Figure 5-16. As would be expected, there is some correspondence between the structural and genetic regions, although the boundaries are generally not identical and there is a larger number of genetic regions than structural regions. The approximate correspondence between the two regionalizations is indicated in Table 5-3. The genetic (tectonic) domains are used to regionalize focal depth in Section 5.2.3.

5.2.2 Q Regionalization

As mentioned in Section 5.1, the Q model depends on the selected geometrical spreading model. However, for the tests of regional differences in ground motion attenuation, we are concerned only with relative differences in the ground motion and not the absolute levels. Therefore, we only need to use Q models that are consistent with one another and not necessarily consistent with the geometrical spreading model.

In a previous study for EPRI, Gupta et al. (1989) developed a consistent regionalization of Q models for North America. Their data set consists of short-period, three-component recordings from the LRSM (Long Range Seismic Measurements) and RSTN (Regional Seismic Test Network) stations. A total of over 1300 recordings from 107 earthquakes at distances up to 2000 km were studied. The Lg phase was narrow-bandpass filtered to obtain spectral amplitudes over the frequency range of 0.5 to 8 Hz. Observed spectral amplitudes were decomposed into station, source, and distance terms by regression. They found that there is a substantial increase in Q with frequency of about a factor of 3 from 1 to 8 Hz.

The Q values were separated into 8 geophysically distinct regions based on Bouguer gravity contours that delineated major divisions of the ENA crust (EPRI, 1986). The 8 regions are shown in Figure 5-17. Although there is often a correlation between crustal velocity structure and Q, the Q region boundaries do not correspond to the velocity structure region boundaries shown in Figure 5-14. The Q regions were correlated to the velocity structure regions based on the extent of the overlap of the regions with additional consideration for the location of the majority of the seismicity in the velocity structure region. That is, more weight was given to

Table 5-3

Crustal Velocity Structure Regions and Correlation with Tectonic Domains

Crustal Velocity Structure Regionalization		Tectonic Domains (Genetic Regionalization)	
No.	**Name**	**No.**	**Name**
1.	Offshore New England	218	Margin
2.	Northern Appalachians	221	Magdalen
3.	Atlantic Coastal Plain	218	Margin
4.	Gulf Coast Plain	216	Gulf Coast
		225	Ouachita
5.	Southern Appalachians	223	Piedmont
		224	Valley & Ridge
6.	Central Tennessee	223	Piedmont
		224	Valley & Ridge
		226	Grenville
7.	Western Tennessee	230	Granite-Rhyolite—East
8.	New Madrid Rift	228	Reelfoot Rift
		229	Cottage Grove—Rough Ck.
9.	Ozarks	230	Granite-Rhyolite—East
10.	Northern Grenville - Superior	236	Superior
		226	Grenville
		227	St. Lawrence—Ottawa
		222	Acadia
11.	Lake Superior Basin	235	Keweenawan
12.	Mid-continent	230	Granite-Rhyolite—East
		233	Panokean
13.	Northern Great Plains	237	Trans Hudson
14.	Central Plains	255	Central Plains
15.	Southern Great Plains	231	Granite-Rhyolite—West
		232	Oklahoma Aulacogen
16.	Williston Basin	238	Wyoming

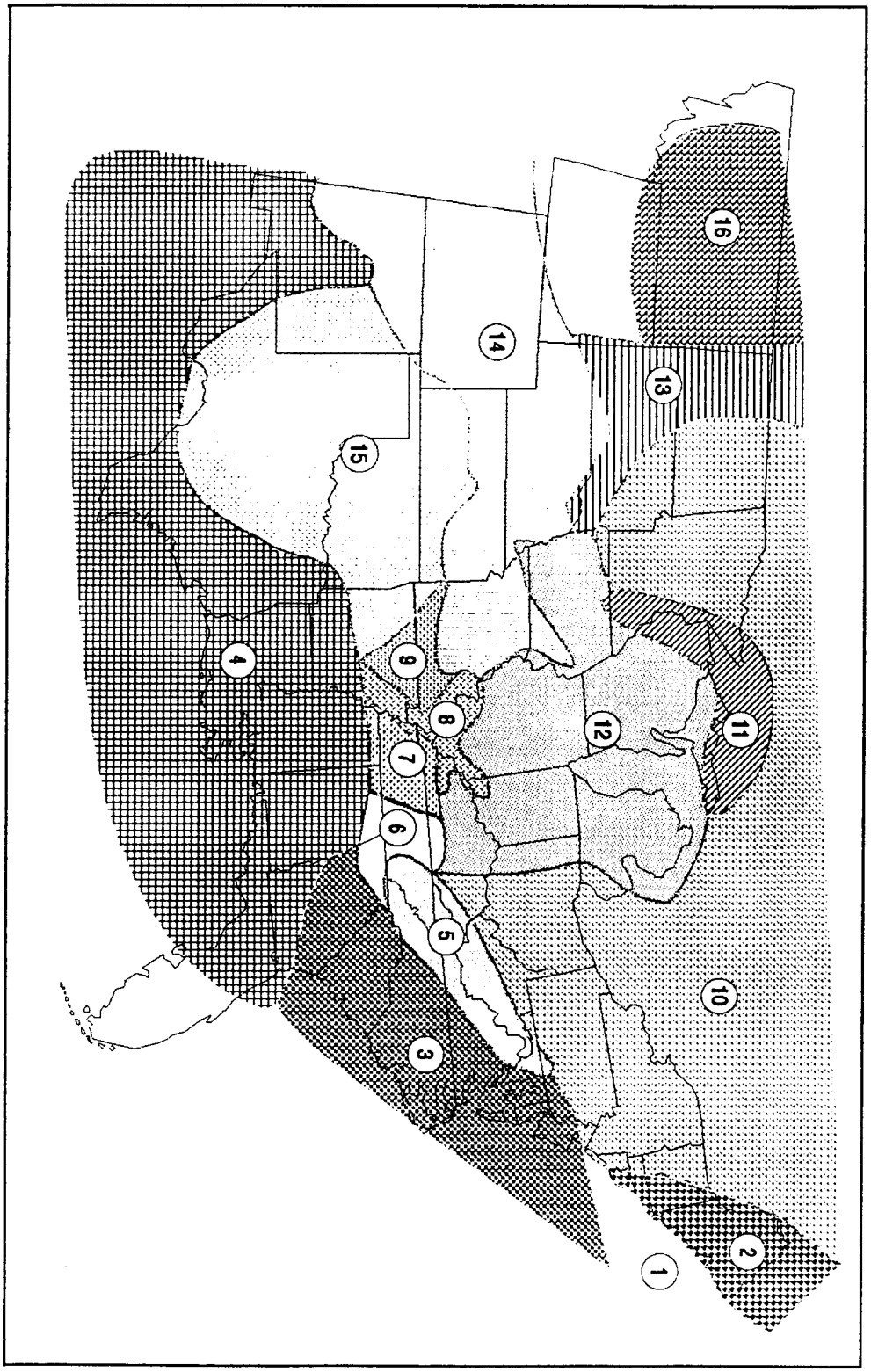

Figure 5-14. Crustal structure regionalizations for the EUS (Woodward-Clyde, 1991).

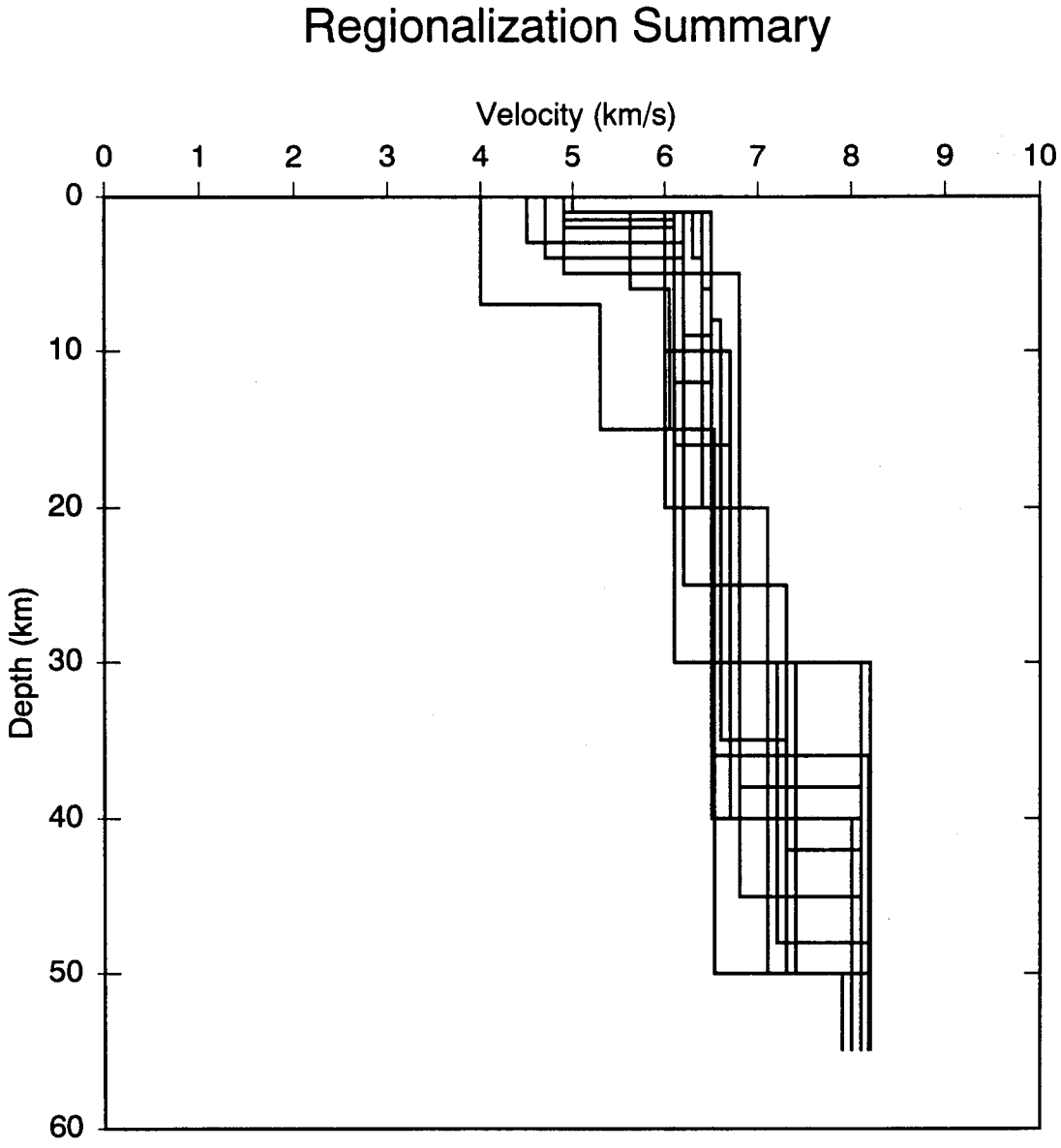

Figure 5-15. Summary of velocity models for the 16 regions shown in Figure 5-12.

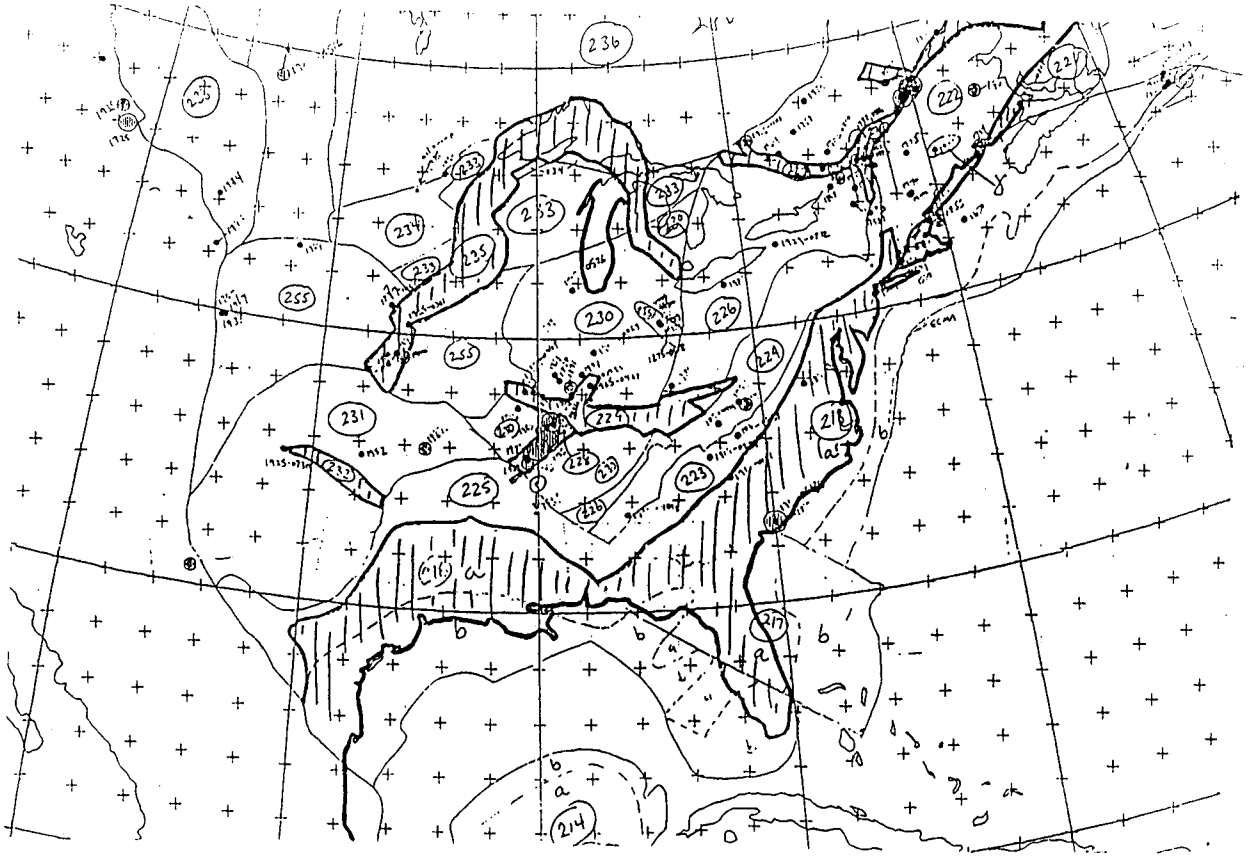

Figure 5-16. Crustal structure regionalization for eastern North America based on genetic origin.

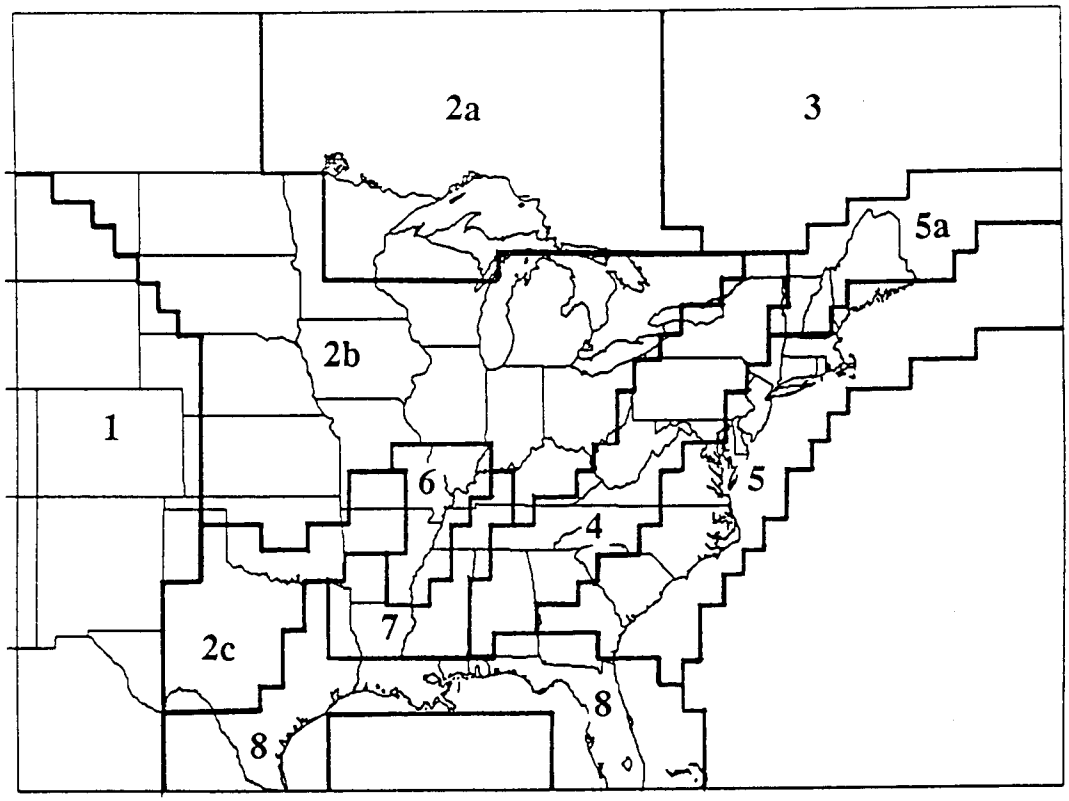

Figure 5-17. Regionalization of Q models from the Gupta et al. (1989) study.

areas of overlap that contained the majority of the seismicity in a velocity structure region. The correlation of the velocity structure and Q regions is listed in Table 5-4. Only 5 of the 8 Q regions are used as Q models for the 16 velocity structure regions. The Q values computed by Gupta et al. for the 5 regions are listed in Table 5-5.

The Q values from Gupta et al. were fit to the form

$$Q = Q_0 f^{\eta} \qquad \text{(Eq. 5-1)}$$

using a weighted least-squares regression with the weights inversely proportional to the variance of the observation. As shown in Figures 5-18a–e, the 1.25 Hz Q value deviates significantly from the trend of the frequency dependence at the higher frequencies implying a change in the functional form of the Q model at low frequencies. Since this study is primarily concerned with frequencies greater than 1 Hz and Q does not significantly affect ground motions calculations in the distance range of interest at frequencies below a few Hz, the 1.25 Hz values were not used in the regression analysis. Excluding the 1.25 Hz values leads to an underestimation of Q, and hence a slight over-estimation of ground motion, at low frequencies. The resulting Q models are listed in Table 5-6 and are plotted against the data in Figures 5-18a–e. The five Q models are compared in Figure 5-19. Four of the five Q models are similar. The exception is Q8 (Gulf Coast region) which has much lower Q than the other four models.

5.2.3 Focal Depth Distribution Regionalization

In addition to the crustal properties, the focal depth of earthquakes can also have a significant effect on ground motion attenuation. Systematic variations in focal depth between regions based on tectonic type is also used as a basis for regionalizing ground motion attenuation in the EUS.

Table 5-4

Correlation of Q Regions to Velocity Structure Regions

Velocity Structure Region	Q Region
1	1
2	1
3	1
4	8
5	4
6	4
7	4
8	6
9	2
10	4
11	2
12	2
13	2
14	1
15	2
16	1

Table 5-5

Q Values from Gupta et al. (1989)

	Region 1		Region 2		Region 4		Region 6		Region 8	
Freq Band	**Q**	σ	**Q**	σ	**Q**	σ	**Q**	σ	**Q**	σ
0.75–1.75	1046	165	1226	66	1961	217	1264	227	223	43
1.5–2.5	832	70	984	29	1281	62	948	86	315	56
2.0–4.0	1045	79	1229	32	1426	57	1020	73	503	109
3.0–5.0	1231	100	1487	42	1521	61	1304	103	605	166
4.0–6.0	1381	123	1684	54	1773	77	1385	120	605	166
5.0–7.0	1581	197	1999	80	2200	114	1671	205	660	253
6.0–8.0	1299	186	2416	119	2339	137	2706	604	2065	5091

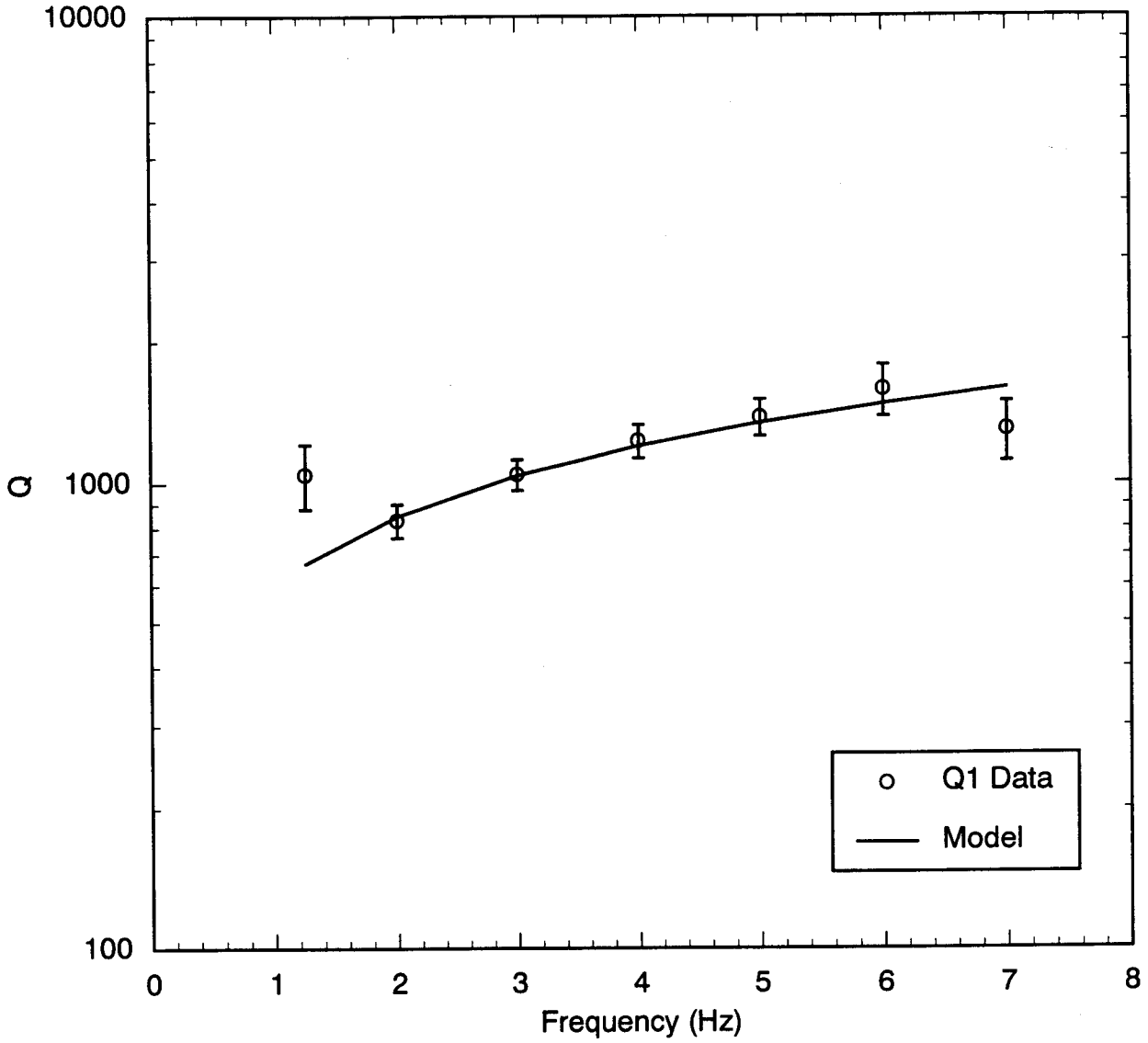

Figure 5-18a. Comparison of Q data from the Gupta et al. (1989) study with the parametric model for region Q1. The 1 Hz value was not used in the regression because it did not fit the trend of the other frequencies and is at the lower bound of the frequency band of interest.

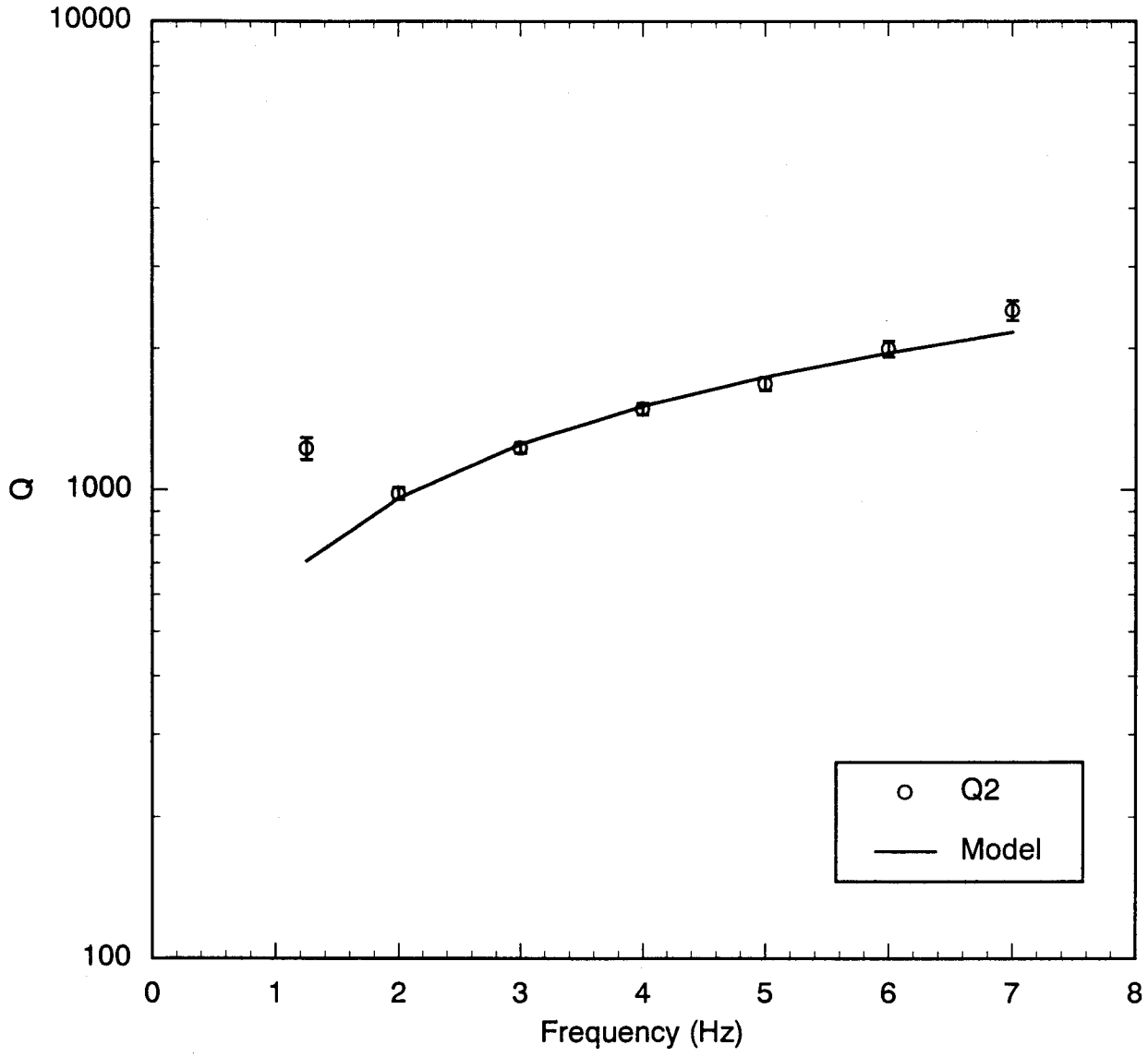

Figure 5-18b. Comparison of Q data from the Gupta et al. (1989) study with the parametric model for region Q2. The 1 Hz value was not used in the regression because it did not fit the trend of the other frequencies and is at the lower bound of the frequency band of interest.

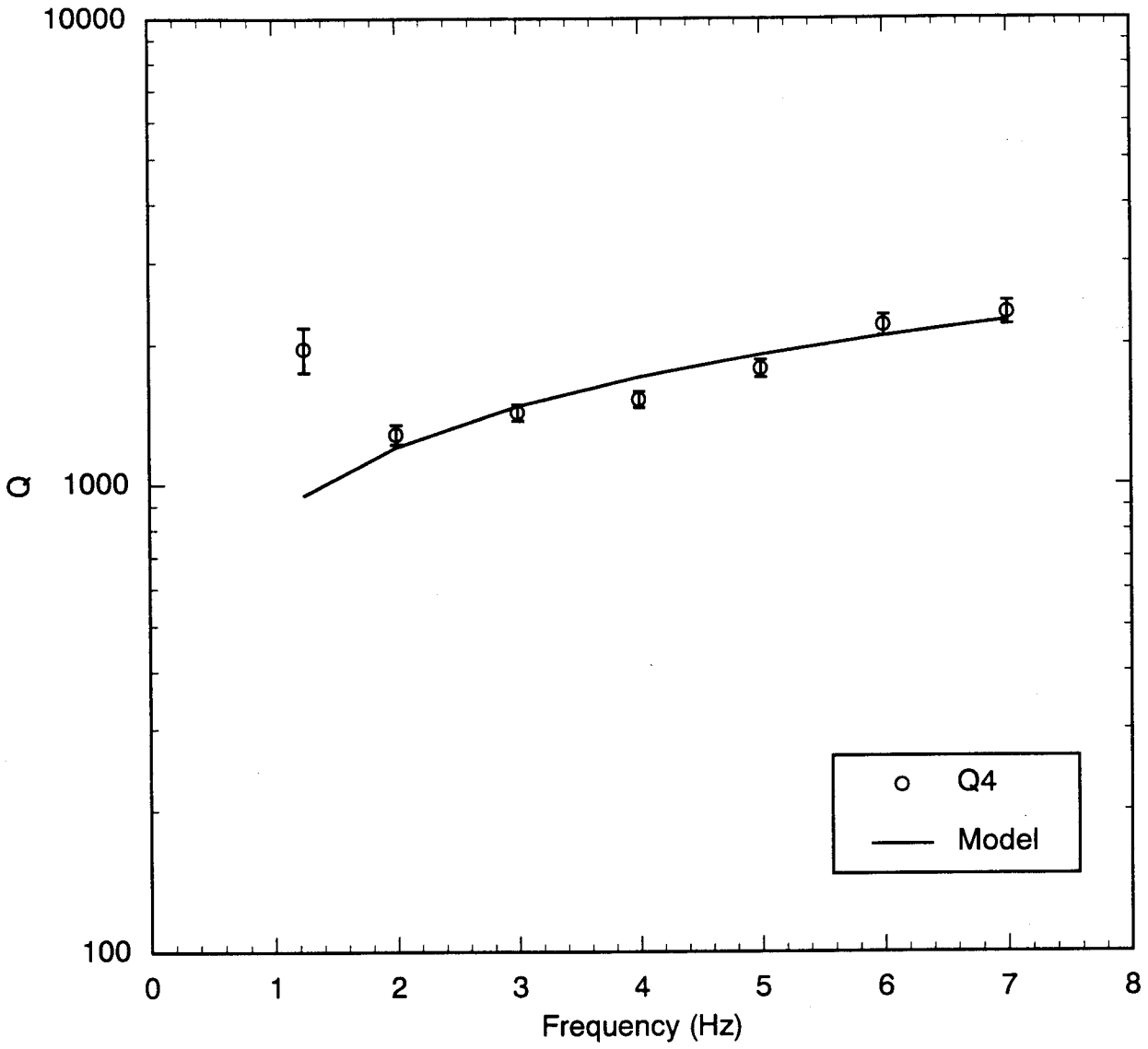

Figure 5-18c. Comparison of Q data from the Gupta et al. (1989) study with the parametric model for region Q4. The 1 Hz value was not used in the regression because it did not fit the trend of the other frequencies and is at the lower bound of the frequency band of interest.

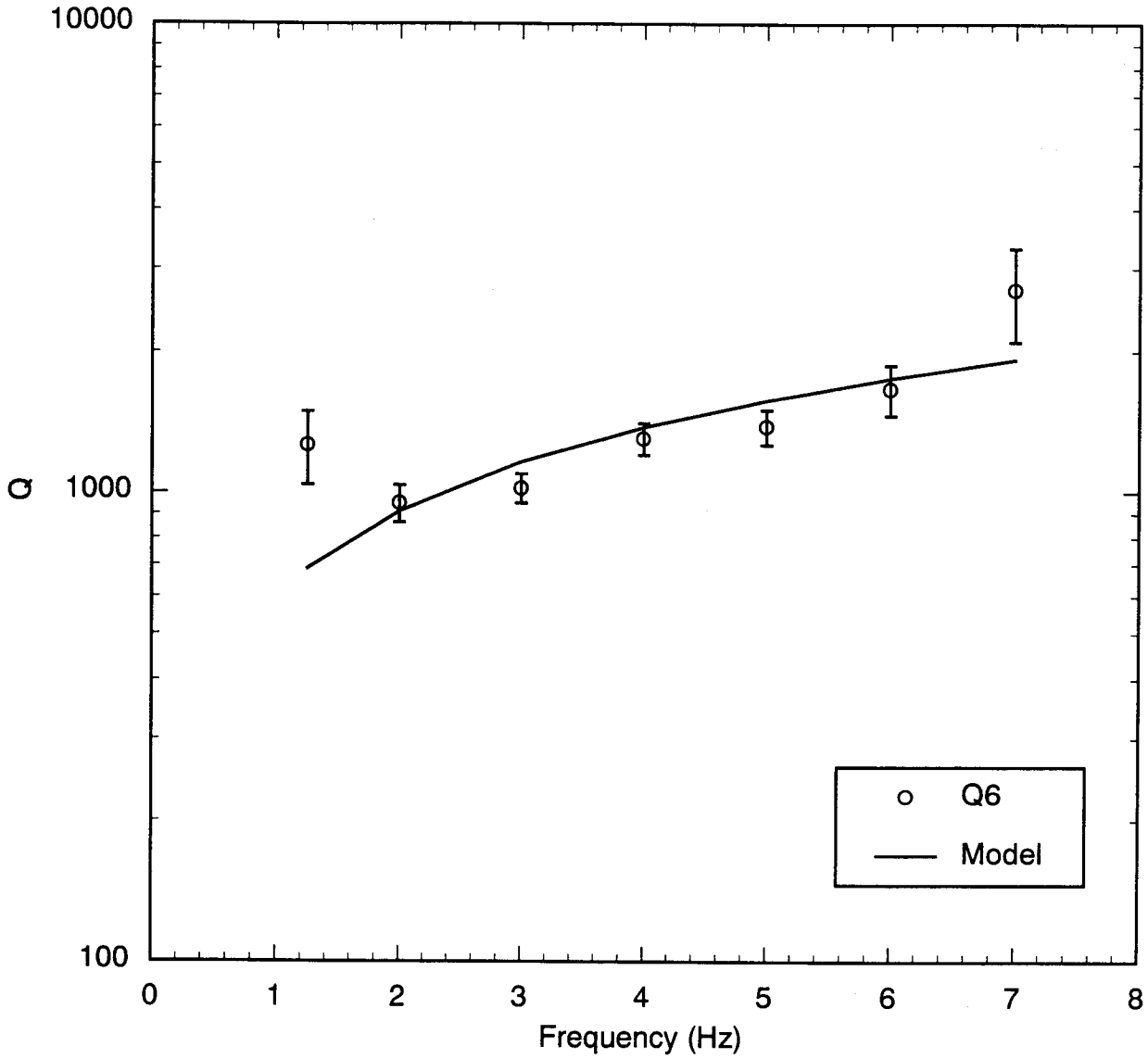

Figure 5-18d. Comparison of Q data from the Gupta et al. (1989) study with the parametric model for region Q6. The 1 Hz value was not used in the regression because it did not fit the trend of the other frequencies and is at the lower bound of the frequency band of interest.

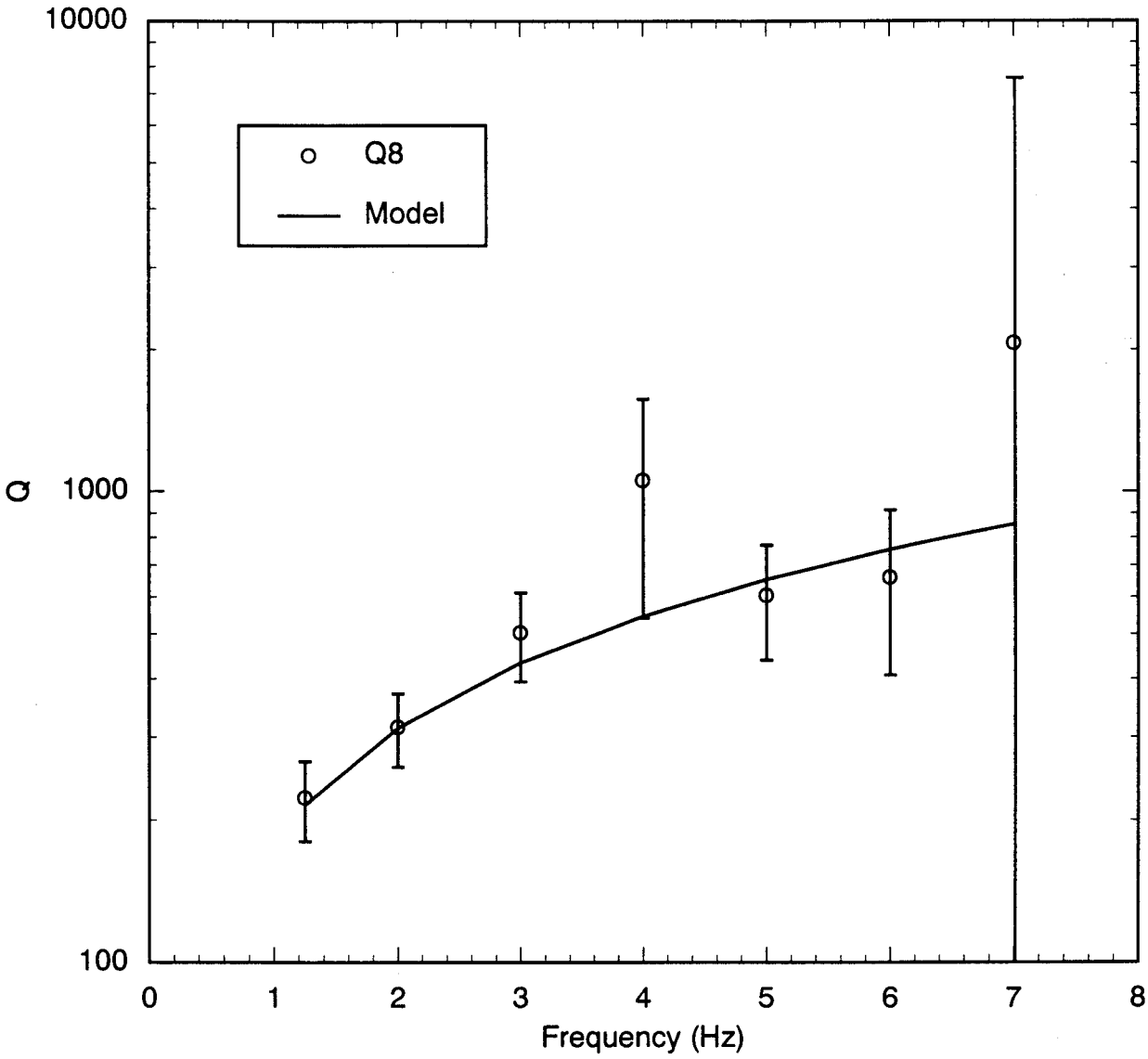

Figure 5-18e. Comparison of Q data from the Gupta et al. (1989) study with the parametric model for region Q8. The 1 Hz value was not used in the regression because it did not fit the trend of the other frequencies and is at the lower bound of the frequency band of interest.

Table 5-6

Q Models

Q Region	Model
1	$600\ f^{0.50}$
2	$610\ f^{0.65}$
4	$850\ f^{0.50}$
6	$600\ f^{0.60}$
8	$180\ f^{0.80}$

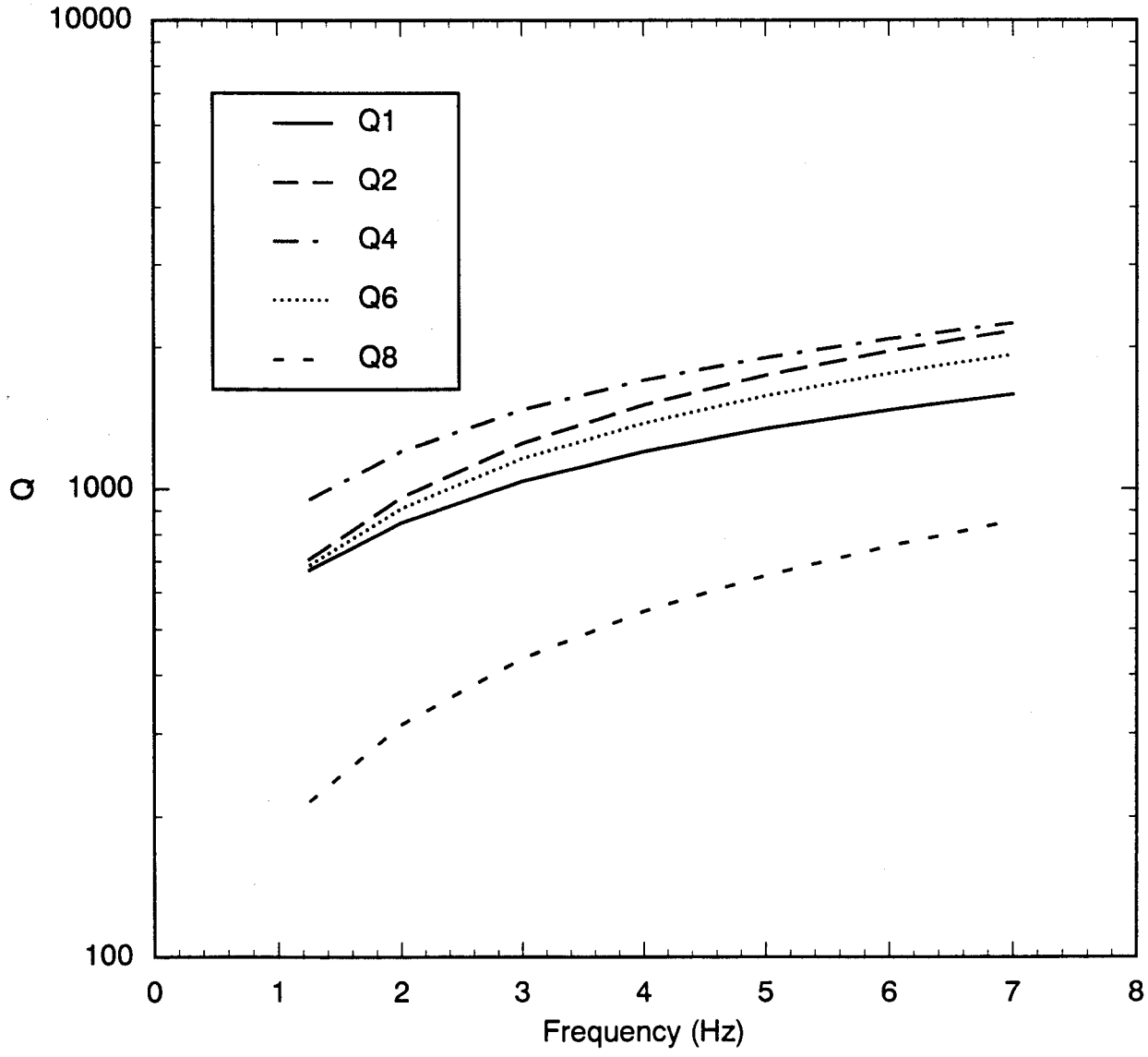

Figure 5-19. Comparison of the five Q models used to represent the Q for the 16 velocity regions.

The rate of seismicity in ENA is low and the catalog of moderate to large magnitude earthquakes in ENA with known focal depth is sparse. Therefore, we consider earthquakes in other analogous tectonic regions to provide a larger data set with greater statistical significance. ENA is a classified as a Stable Continental Region (SCR). Other SCR regions include parts of Africa, Asia/Russia, Australia, Europe, India, and South America.

The focal depth distributions are developed using the EPRI SCR Earthquake Catalog (Johnston, 1993). All events in the EPRI data base of magnitude 5 or larger having an assigned tectonic type are considered. For events with multiple depth assignments, the preferred depth is used. Of the six SCR regions, only Africa and Australia had earthquake depth distributions similar to that of ENA. The depth distributions of these three continents and their combined depth distribution are shown in Figure 5-20. The combined distribution of Eastern North America, Africa, and Australia will be referred to as EAA.

The characteristics of earthquake focal depths in eastern North America have been summarized by Wheeler and Johnston (1993) as follows. The depths of these earthquakes range from 3 to 32 km. There may be systematic variations of focal depth with geological terrain. The deeper events may indicate the presence of mafic or granulite rocks, whereas unusually shallow large earthquakes have only been observed in the central craton. In the central craton, earthquake depths are concentrated at about 5 km, with a range of 3 to 18 km. In the New Madrid region, focal depths are concentrated at about 7 km with a range of 5 to 12 km. Appalachian earthquakes tend to be shallower (in the depth range of 5 to 8 km) than those of comparable size in the late Proterozoic continental margin that underlies the borders of the northwest Appalachian orogen (in the depth range of 8 to 14 km). Deep earthquakes (> 25 km) have only been observed beneath the late Proterozoic margin.

Based on the apparent correlation between focal depth and geologic terrain, the depth distributions for the ENA and EAA are subdivided according to tectonic type: margin, rift, or other. Margins include all crust between the landward limit of normal faulting or significant tectonic thinning and the continental/oceanic transition zone. Rifts are zones of large-scale normal faulting embedded within continental crust and include all crust that lies within the outermost rift-related normal faults. Regions of stable continental crust that are neither margins nor rifts are classified as "other" regions. A map showing the rift, margin and "other" regions in ENA is shown in Figure 5-16. The depth distributions for EAA are shown in Figure 5-21. The depth distributions for both ENA and EAA are tabulated in Table 5-7.

The statistical properties of the depth distribution for margins, rifts, and other regions are compared in Appendix 5B for both the ENA and EAA data sets. These comparisons are summarized below. The depth distributions for rifts and "other" regions are not significantly different from each other so these two categories are combined into non-margins. The depth distribution for margins is significantly different from that of non-margins at the 95% confidence level. This comparison only deals with the focal depths and not with the resulting ground motions. The effect of the different focal depths on ground motion is addressed in Section 9.

In comparing the ENA and EAA distributions we found that the larger EAA data set is applicable to the ENA at all focal depths for margins and at focal depth less than 30 km for non-margins. Therefore, the EAA depth distribution for non-margins is truncated at 30 km for application to the ENA. The resulting depth distributions smoothed over 5 km distance bins are shown in Figure 5-22. The corresponding normalized depth weights for the two tectonic categories are listed in Table 5-8. A generic model that does not distinguish between margins and non-margins is listed in Table 5-9.

5.3 Effects of Crustal Velocity Structure on Ground Motions

The effects of crustal structure are studied using numerical simulations. For this analysis, the semi-empirical simulation procedure using generalized rays described in Section 3.3 is used to generate ground motions for each crustal structure. In this section, we consider the effects of crustal structure variations between regions (inter-region variations) as well as crustal structure variation within a region (intra-region variations).

5.3.1 Intra-Regional Variation (for Fixed Q)

The intra-regional variations of ground motion attenuation are estimated for a fixed Q model. That is, only the effects of changing the velocity structure of the crust are

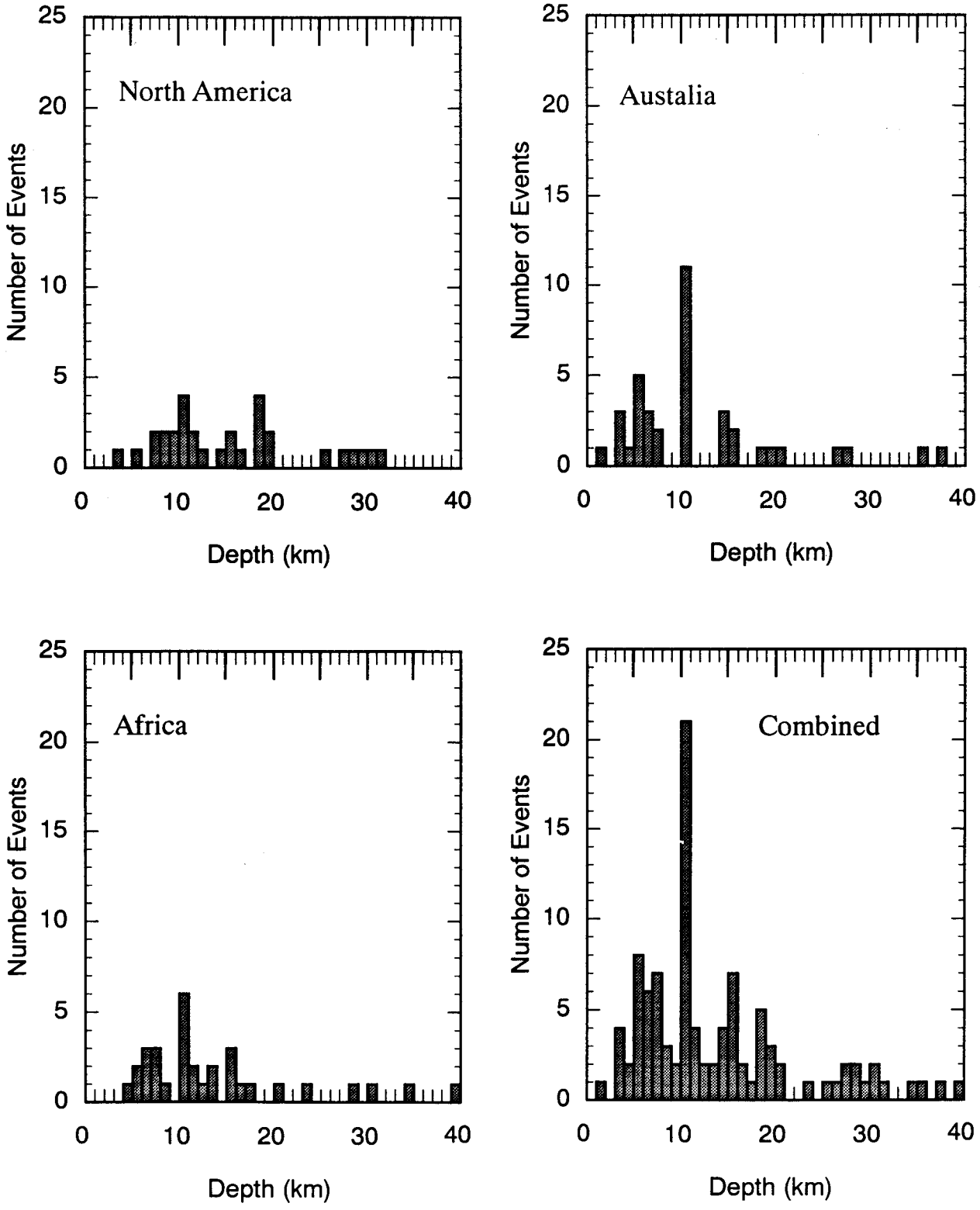

Figure 5-20. Focal depth distributions for eastern North America, Australia, and Africa from the EPRI Stable Continental Regions Catalog.

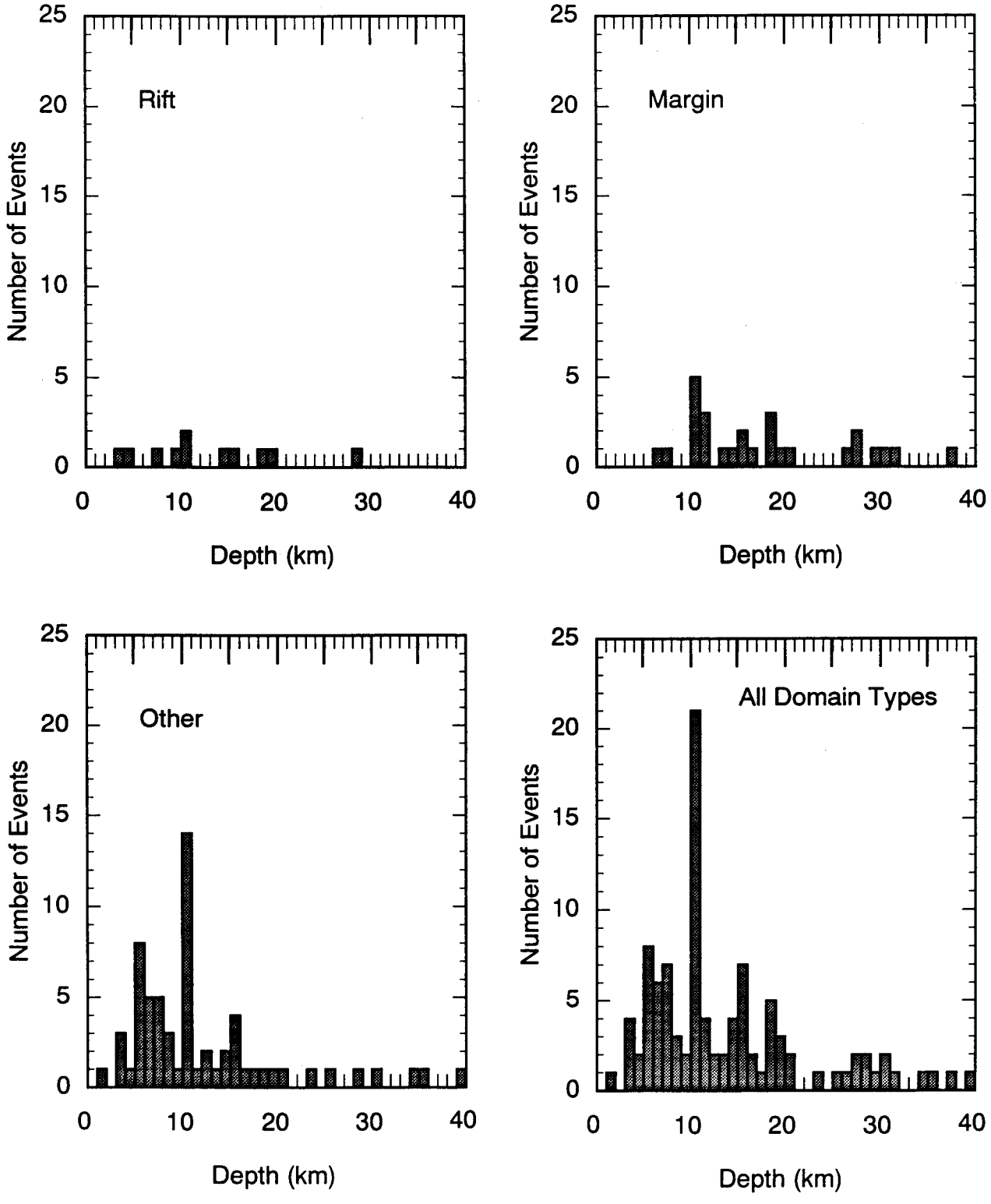

Figure 5-21. Separation of focal depths in the combined eastern North America, Africa, Australia data set according to tectonic type: rift, margin, and other. The distribution for margins has a deeper median depth than for rifts or other regions.

Table 5-7

Depth Distributions of Earthquakes in Eastern North America (ENA) and Eastern North America, Australia, and Africa (EAA)

Region:	ENA	EAA	ENA	ENA	ENA	EAA	EAA	EAA
Type:	All	All	Rift	Margin	Other	Rift	Margin	Other
DEPTH	No.	No.	No.	No.	No.	No.	No.	No.
1	0	1						1
2	0	0						
3	1	4	1			1		3
4	0	2				1		1
5	1	8			1			8
6	0	6					1	5
7	2	7		1	1	1	1	5
8	2	3			2	0		3
9	2	2	1		1	1		1
10	4	21			4	2	5	14
11	2	4		2			3	1
12	1	2			1			2
13	0	2					1	1
14	1	4			1	1	1	2
15	2	7	1		1	1	2	4
16	1	2		1			1	1
17	0	1						1
18	4	5		3	1	1	3	1
19	2	3	1	1		1	1	1
20	0	2					1	1
21	0	0						
22	0	0						
23	0	1						1
24	0	0						
25	1	2			1		1	1
26	0	2					2	
27	1		0		1			
28	1	3			1	1	1	1

Table 5-7 (Continued)

Depth Distributions of Earthquakes in Eastern North America (ENA) and Eastern North America, Australia, and Africa (EAA)

Region:	ENA	EAA	ENA	ENA	ENA	EAA	EAA	EAA
Type:	All	All	Rift	Margin	Other	Rift	Margin	Other
DEPTH	No.	No.	No.	No.	No.	No.	No.	No.
29	1	1		1			1	
30	1	2		1			1	1
31	1	0		1				
32	0	0						
33		0						
34		1						1
35		1						1
36		0						
37		1					1	
38		0						
39		0						
40		0						
41		1						1
42		0						
43		1						1

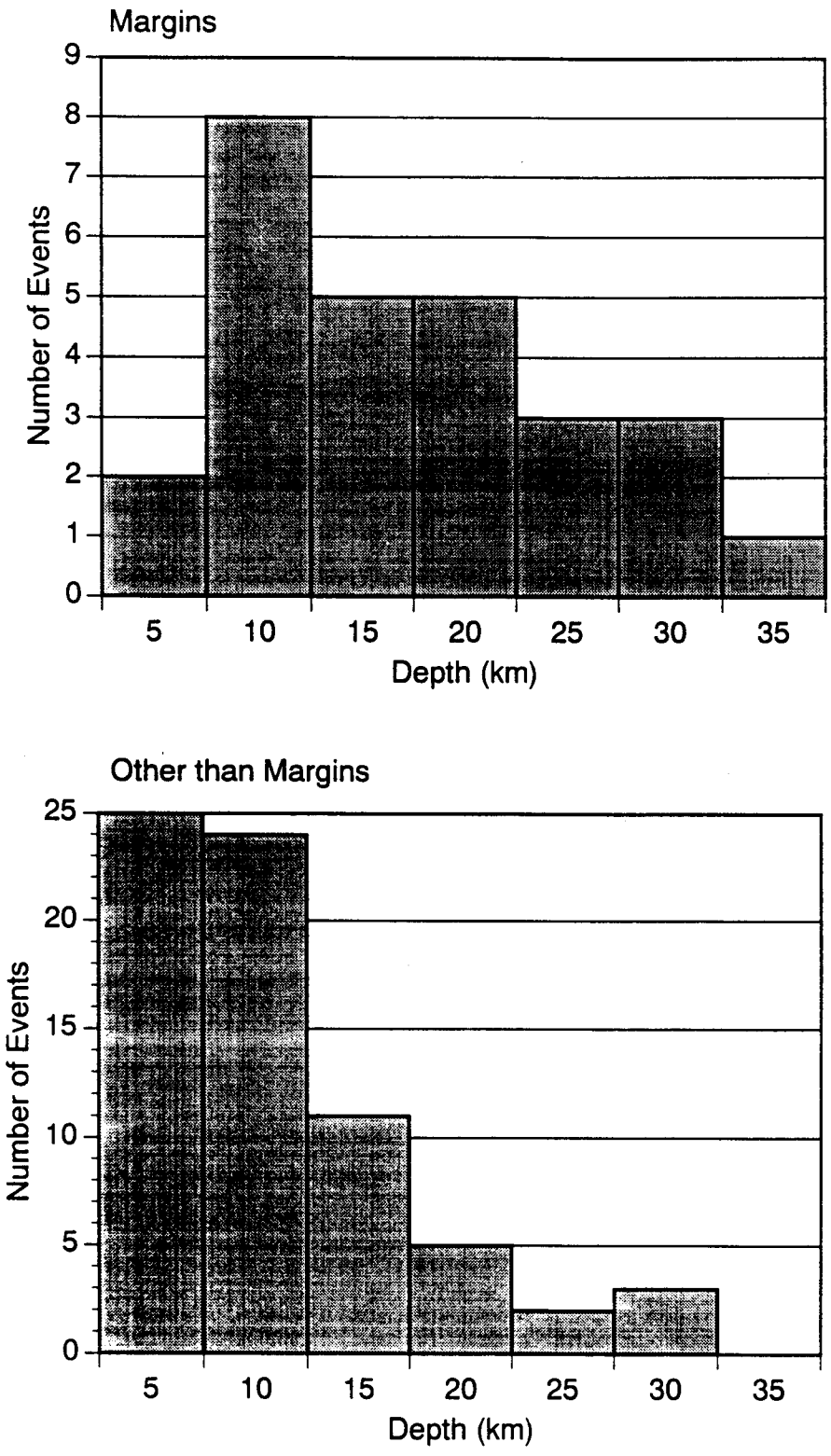

Figure 5-22. Depth distribution model for margins and non-margins based on the combined eastern North America, Africa, Australia data set. This depth distribution model is considered in the regression analysis in Section 9.

Table 5-8

Weights for Depth Distribution Model (EAA)

Depth	Margins	Non-Margins
5	0.077	0.352
10	0.308	0.338
15	0.192	0.155
20	0.192	0.070
25	0.115	0.042
30	0.115	0.042

Table 5-9

Weights for Generic Depth Distribution Model (EAA)

Depth	Weight
5	0.216
10	0.320
15	0.171
20	0.070
25	0.077
30	0.019

considered. The resulting variability represents our uncertainty in determining the crustal velocity structure for a given region. Three different effects are considered: variations of the velocities and layer thicknesses of the flat layered model, variations of Poisson's ratio, and variations from a flat-layered model (laterally varying structure).

5.3.1.1 Effect of Uncertainty in Crustal Structure within a Region

Within a given region, there are several sources of uncertainty in the idealized crustal structure model used to model ground motion attenuation. First, there is uncertainty in the crustal structure at a given location within a region due to the limitations of experimental measurements. This may be reflected in different models of crustal structure derived from the same experimental data, or from different sets of experimental data recorded over the same profile. Second, there may be variation in the actual crustal structure within the region. This may be reflected by differences in crustal structure obtained in different locations within the region.

We used four different crustal models from the Northern Grenville—Superior region, and four different crustal models from the New Madrid Rift region to evaluate the effect of these uncertainties in crustal structure on the variability of ground motions. The same Q model was used in each structure to isolate the effects of the velocity structure. Synthetic seismograms were computed for source depths of 4.5, 9.5, 14.5, 19.5, 24.5, and 29.5 km. (The source depths are at fractional integer depths to avoid locating the source at a layer boundary.)

The four crustal models for the Northern Grenville—Superior region are listed in Table 5-10 and shown in Figure 5-23. The West Quebec, Charlevoix and Berry models represent models at different locations in the region, whereas the West Quebec and Gradient models represent different models at the same location.

Table 5-10

Intra-Region Crustal Models for the Northern Grenville—Superior Region

Vp (km/sec)	Vs (km/sec)	Density (gm/cc)	Thickness (km)	Depth to Top
		Grenville—West Quebec		
5.0	2.34	2.53	1.0	0
6.3	3.64	2.74	3.0	1.0
6.4	3.70	2.76	2.0	4.0
6.5	3.76	2.78	2.0	6.0
6.6	3.82	2.79	12.0	8.0
6.7	3.87	2.81	10.0	20.0
6.8	3.93	2.83	8.0	30.0
8.1	4.68	3.35	—	38.0
		Grenville—Gradient		
5.0	2.34	2.53	1.0	0
6.3	3.64	2.74	3.0	1.0
6.4	3.70	2.76	2.0	4.0
6.5	3.76	2.78	2.0	6.0
6.6	3.82	2.79	12.0	8.0
6.7	3.87	2.81	10.0	20.0
6.8	3.93	2.83	3.0	30.0
7.0	4.05	2.86	3.0	33.0
7.2	4.16	2.89	2.0	36.0
7.4	4.28	2.92	2.0	38.0
7.6	4.39	2.95	2.0	40.0
7.8	4.51	2.99	1.0	42.0
8.0	4.62	3.35	—	43.0

Table 5-10 (Continued)

Intra-Region Crustal Models for the Northern Grenville—Superior Region

Vp (km/sec)	Vs (km/sec)	Density (gm/cc)	Thickness (km)	Depth to Top
		Grenville—Charlevoix		
4.5	2.6	2.30	1.44	0
5.5	3.4	2.50	6.0	1.44
6.1	3.5	2.67	12.0	7.44
6.6	3.7	2.85	14.0	19.44
7.0	4.0	3.02	10.0	33.44
8.2	4.7	3.35	—	43.44
		Grenville—Berry		
5.0	2.34	2.53	2	0
6.3	3.65	2.74	17	2
6.8	3.93	2.83	22	19
8.2	4.74	3.35	—	41

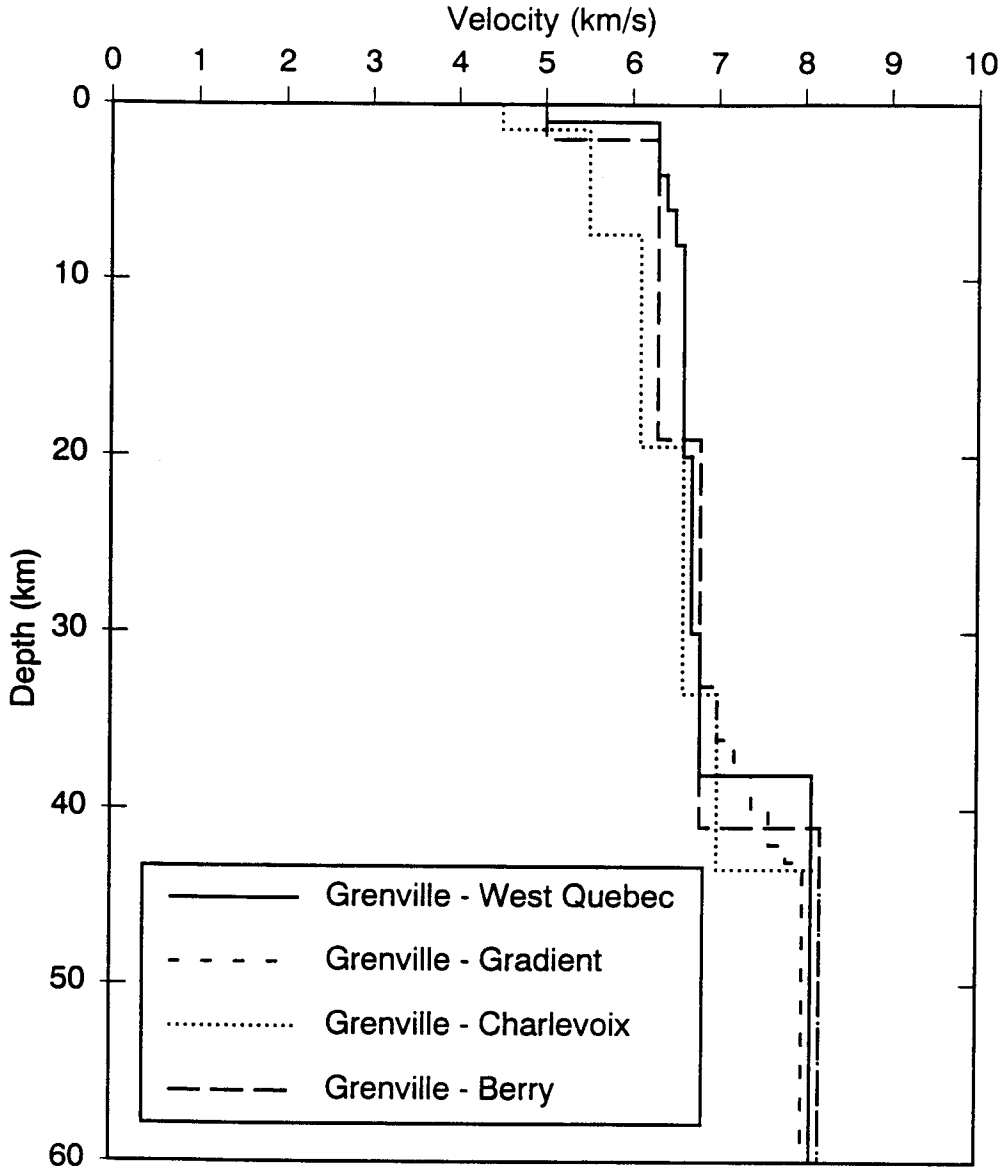

Figure 5-23. Four velocity models used for the Grenville region to represent variability of the velocity model within a region.

The West Quebec model for the Central Metasedimentary Belt near Mont Laurier, Quebec was derived from the profile for Point C in Line CD in Mereu et al. (1986). The Gradient model for the Central Metasedimentary Belt was derived from Point C (the same point as in the West Quebec model) in the intersecting Line CB in the same study. The Gradient model is identical to the West Quebec model above 30 km, but below 30 km has a velocity gradient to a deeper Moho in place of a step change in velocity at the Moho. The Charlevoix model for the north shore of the St. Lawrence River in Quebec was derived by Somerville et al. (1990) using data from the Saguenay earthquake sequence of 1988. The Berry model for northeast Quebec was derived by Berry and Fuchs (1973).

The four crustal models for the New Madrid Rift region are listed in Table 5-11 and shown in Figure 5-24. The

Table 5-11

Intra-Region Crustal Models for the New Madrid Rift Region

Vp (km/sec)	Vs (km/sec)	Density (gm/cc)	Thickness (km)	Depth to Top
		New Madrid—McCamy		
4.7	2.72	2.48	4	0
6.2	3.58	2.73	5	4
6.5	3.76	2.78	21	9
7.4	4.28	2.92	15	30
8.1	4.68	3.35	—	45
		New Madrid—Flank		
4.9	2.83	2.52	3.0	0.0
6.2	3.58	2.73	11.0	4.0
6.6	3.82	2.79	18.0	14.0
7.3	4.22	2.91	9.0	32.0
8.0	4.62	3.35	—	41.0
		New Madrid—Ginzburg		
4.9	2.83	2.52	5	0
6.2	3.58	2.73	9	5
6.6	3.82	2.79	12	14
7.3	4.22	2.91	20	26
8.0	4.62	3.35	—	46
		New Madrid—Saikia		
3.60	2.10	2.20	0.50	0
5.60	3.28	2.50	1.00	0.5
6.15	3.60	2.70	8.00	1.5
6.40	3.70	2.90	10.00	9.5
7.45	4.20	3.00	20.00	19.5
8.18	4.78	3.34	—	39.5

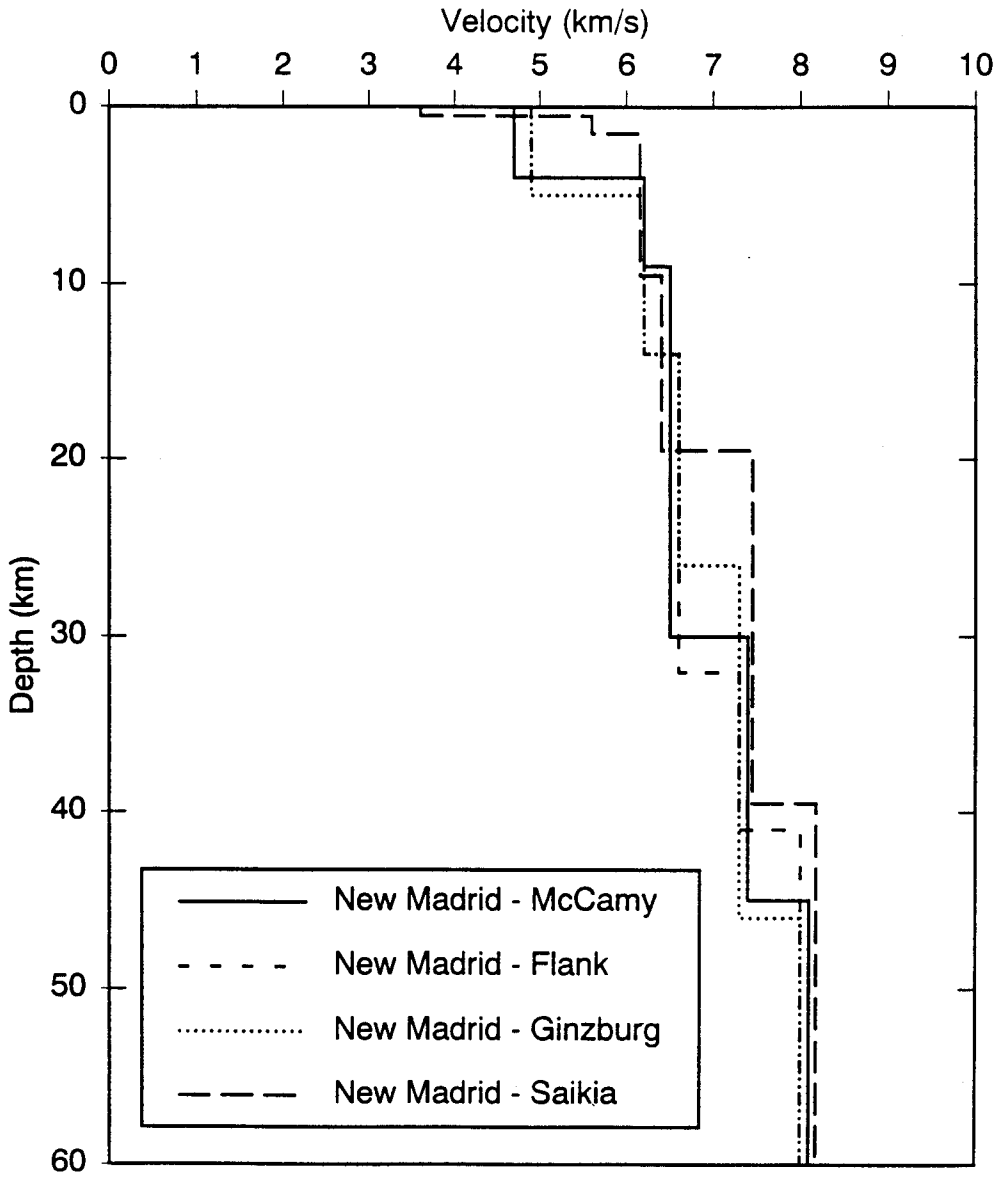

Figure 5-24. Four velocity models used for the New Madrid region to represent variability of the velocity model within a region.

McCamy, Ginzburg, and Saikia models represent models at different locations in the region, while the McCamy and Flank models represent different models at the same location.

The McCamy model was derived by McCamy and Meyer (1966) from a line from Cape Girardeau, Mo. to Little Rock, Ark. that lies along the northwest flank of the rift. The Flank model was derived by Ginzburg et al. (1983) from a profile that overlies that of the McCamy model. The Ginzburg model, derived in the same study, is for a profile along the axis and through the center of the New Madrid rift. The Saikia model was derived from modeling of earthquake and explosion body waves and surface waves near Dyersburg, Tennessee on the southeast flank of the rift by Saikia et al. (1992).

The standard error of spectral acceleration is shown as a function of distance for the New Madrid region for 1, 5 and 15 Hz in Figures 5-25a,b,c. In these figures, the standard error is shown separately for source depths of 4.5, 9.5, and 19.5 km. The ground motions from shallow focal depths are more sensitive to the velocity structure than the ground motions from the deep focal depths. The standard error in ground motion amplitude has a maximum at distances of 30 to 80 km associated with the variation in the Moho depth. The standard error of spectral acceleration for the Grenville region for 1, 5 and 15 Hz is shown in Figures 5-26a,b,c. For this region,

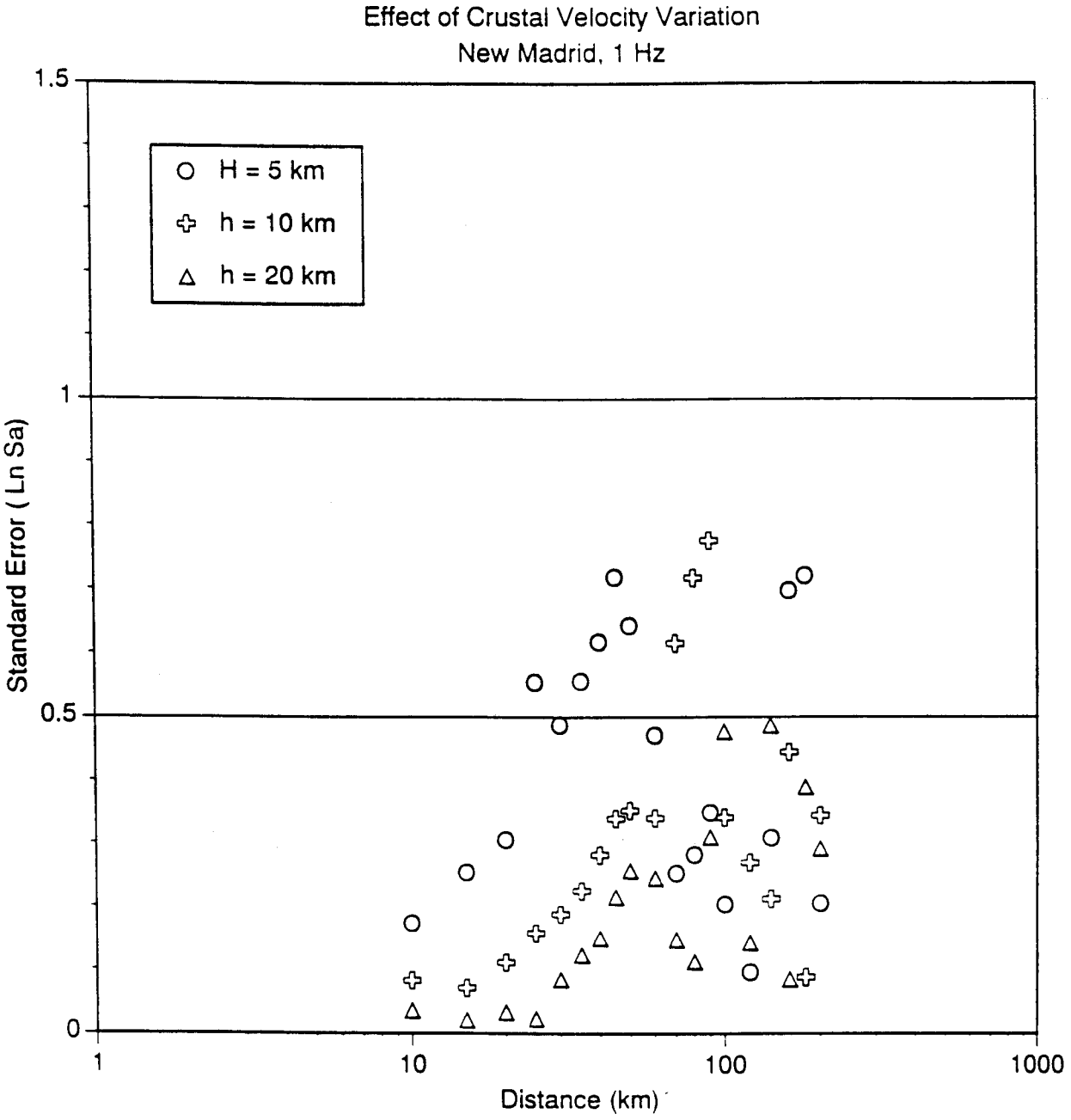

Figure 5-25a. Variability of spectral acceleration at 1 Hz due to crustal velocity uncertainty within the New Madrid region. The variability is computed separately for each focal depth.

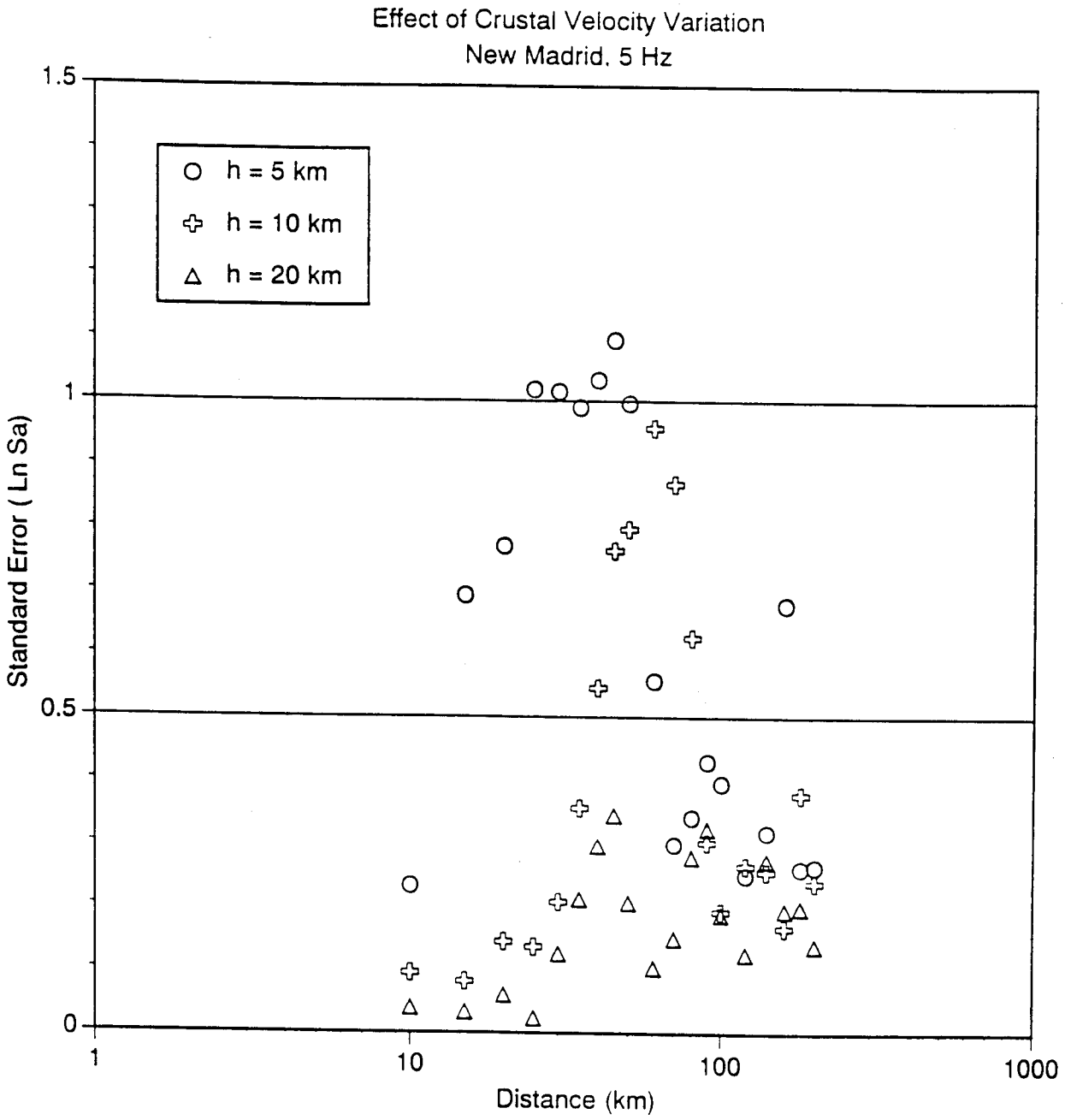

Figure 5-25b. Variability of spectral acceleration at 5 Hz due to crustal velocity uncertainty within the New Madrid region. The variability is computed separately for each focal depth.

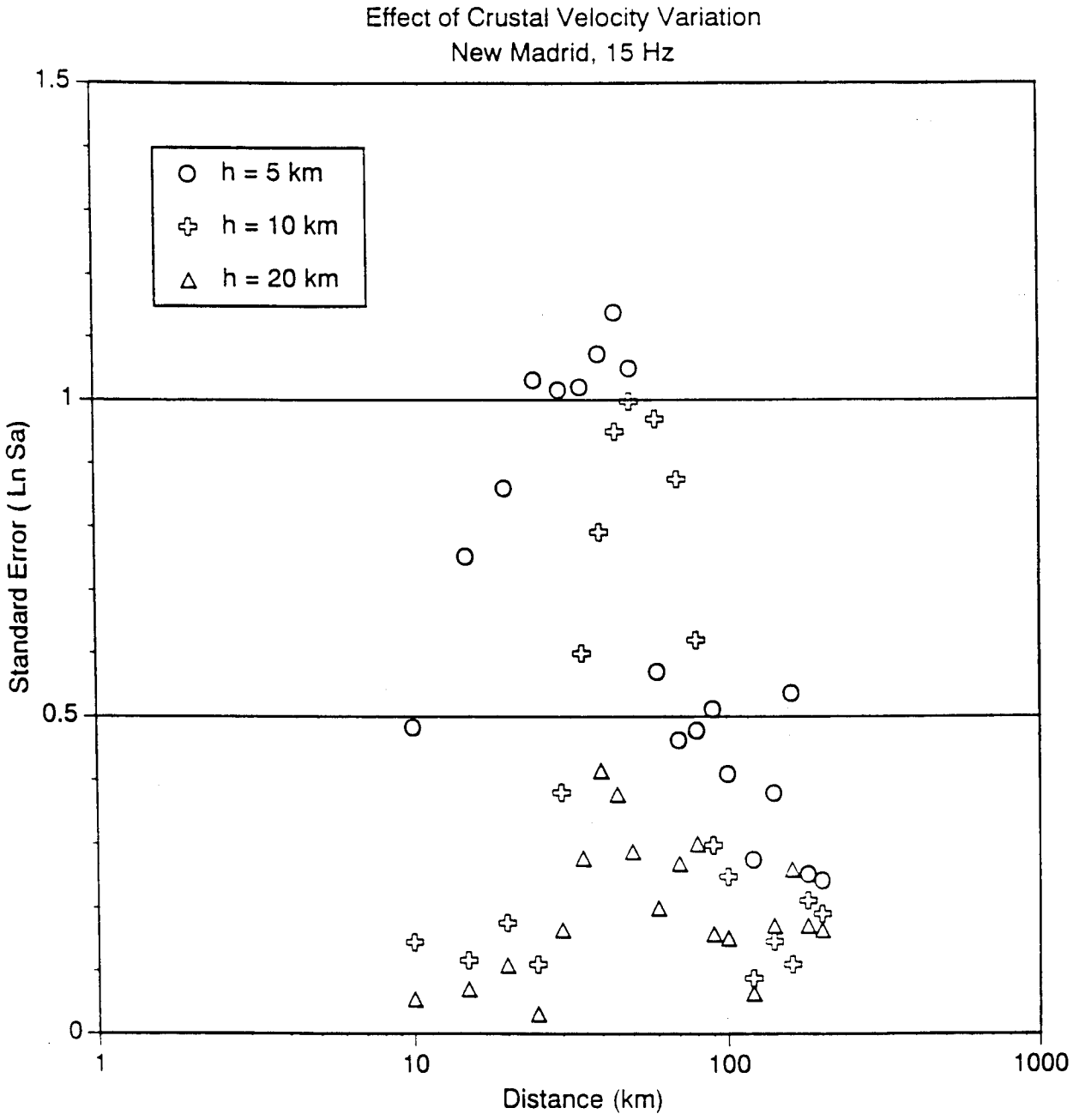

Figure 5-25c. Variability of spectral acceleration at 15 Hz due to crustal velocity uncertainty within the New Madrid region. The variability is computed separately for each focal depth.

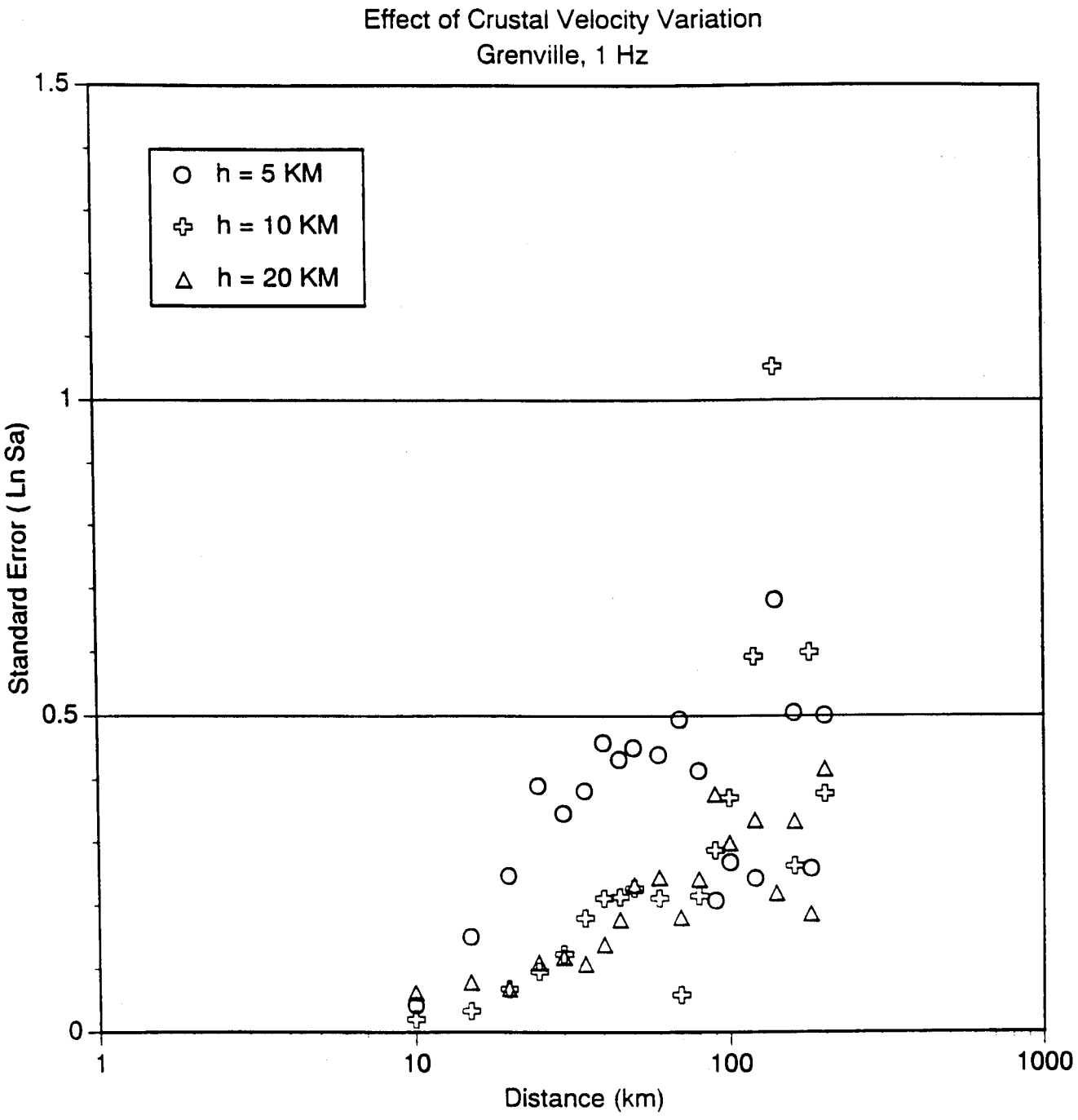

Figure 5-26a. Variability of spectral acceleration at 1 Hz due to crustal velocity uncertainty within the Grenville region. The variability is computed separately for each focal depth.

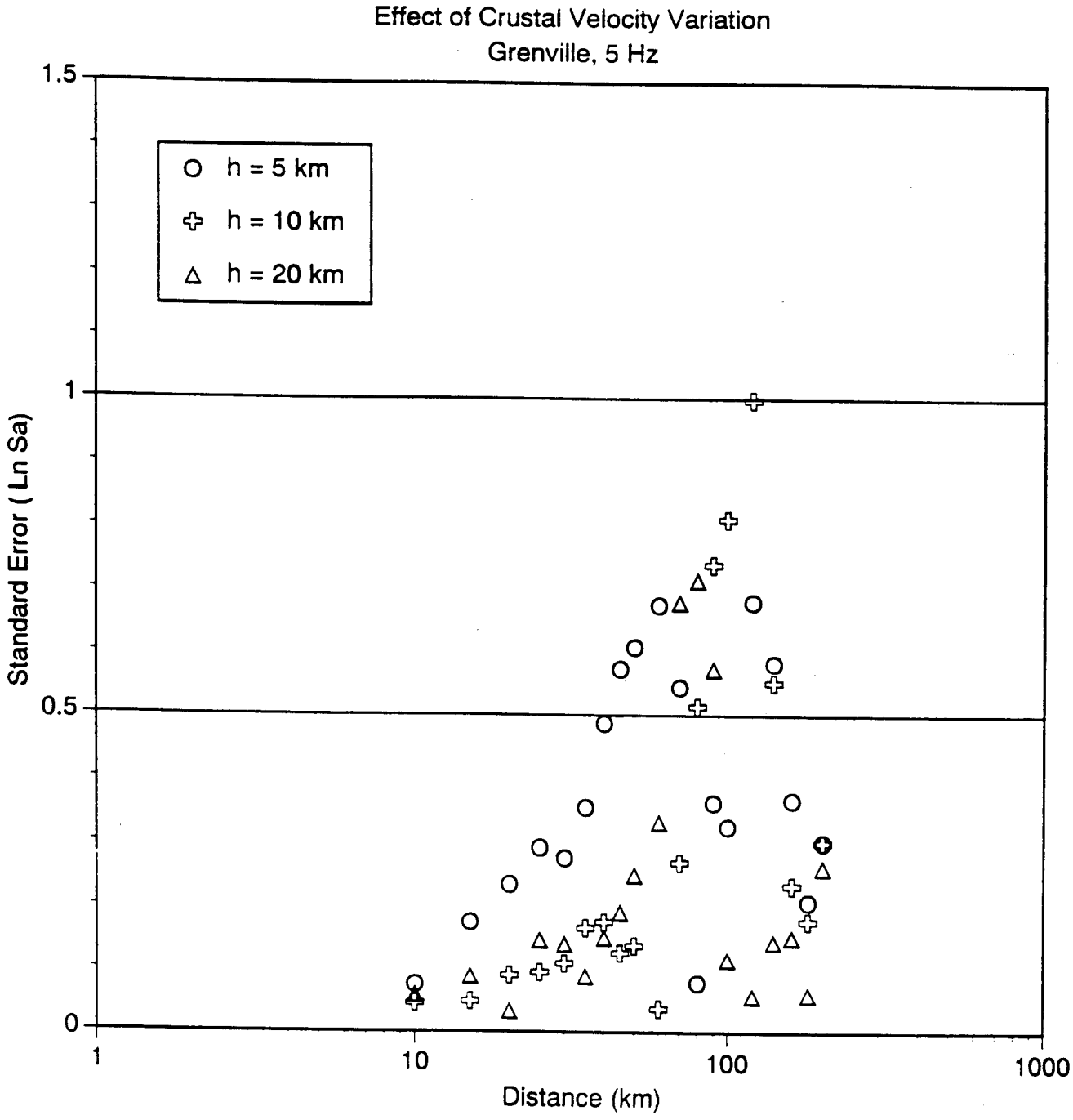

Figure 5-26b. Variability of spectral acceleration at 5 Hz due to crustal velocity uncertainty within the Grenville region. The variability is computed separately for each focal depth.

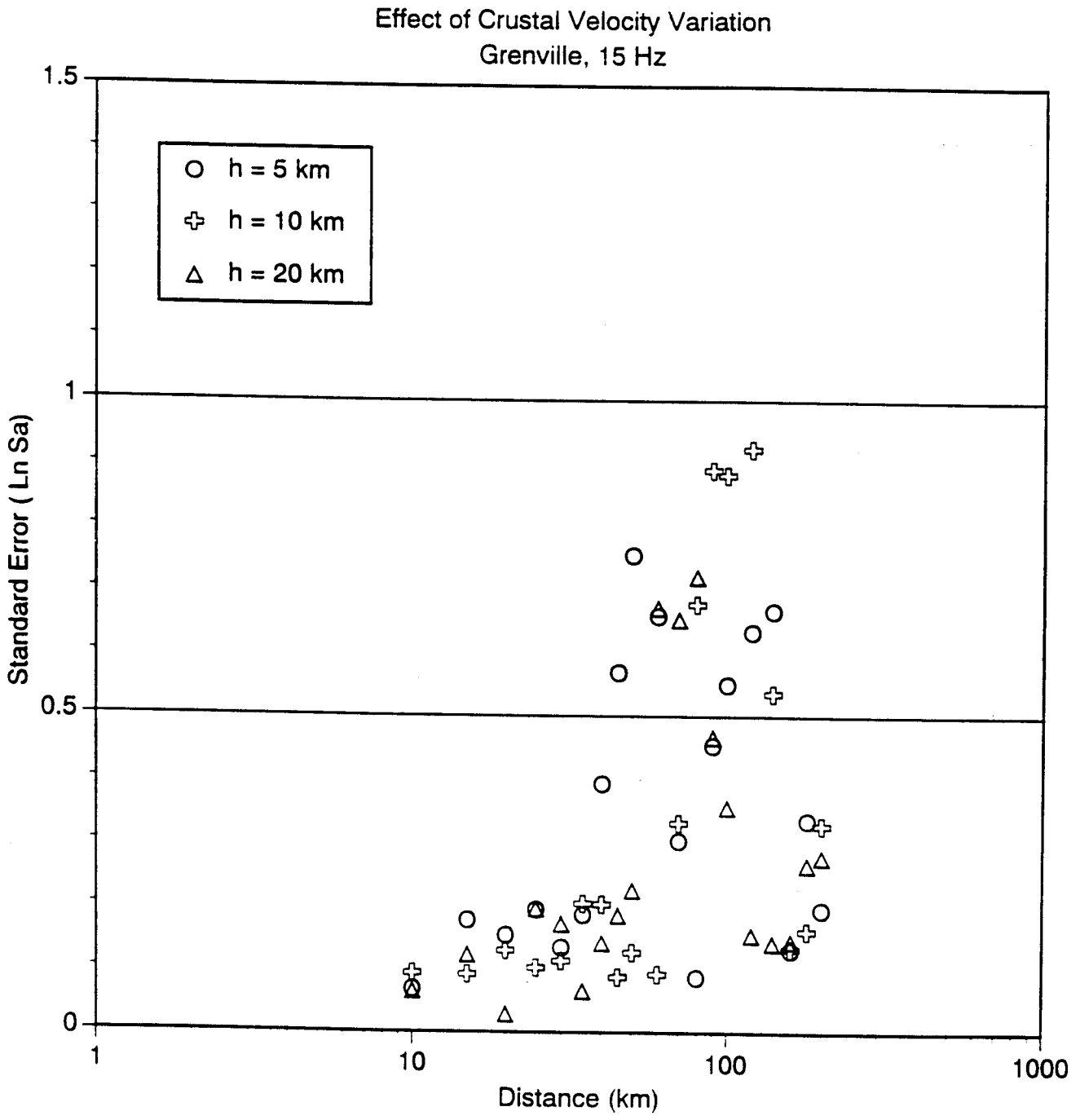

Figure 5-26c. Variability of spectral acceleration at 15 Hz due to crustal velocity uncertainty within the Grenville region. The variability is computed separately for each focal depth.

the maximum standard error is shifted to distances of 80 to 120 km again associated with the variation in Moho depth. The depth of the Moho affects the distance range at which the maximum standard error occurs. In general, the deeper the Moho, the larger the distance at which the maximum occurs.

In Figures 5-25 and 5-26 the variation of ground motion for a given crustal structure is shown for three depths. To account for the variability in focal depth, the ground motion variability is computed using a weighted average over focal depths where the weights are given by the EAA generic depth distribution (Table 5-9). The standard errors of the mean spectral acceleration are shown in Figures 5-27a,b,c for 1, 5, and 15 Hz.

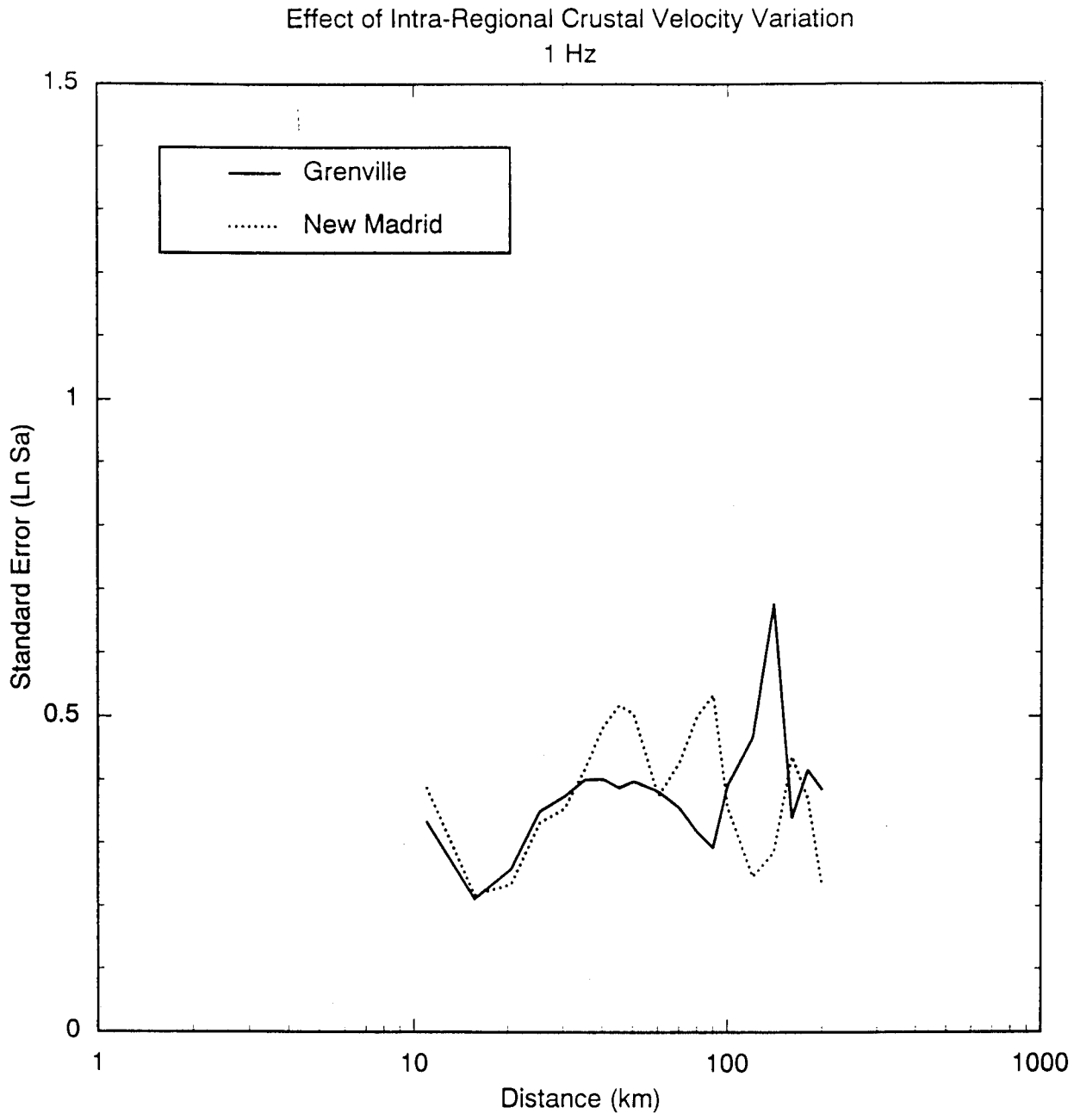

Figure 5-27a. Variability of spectral acceleration at 1 Hz due to crustal velocity uncertainty within the Grenville and New Madrid region. The variability includes variability in focal depth.

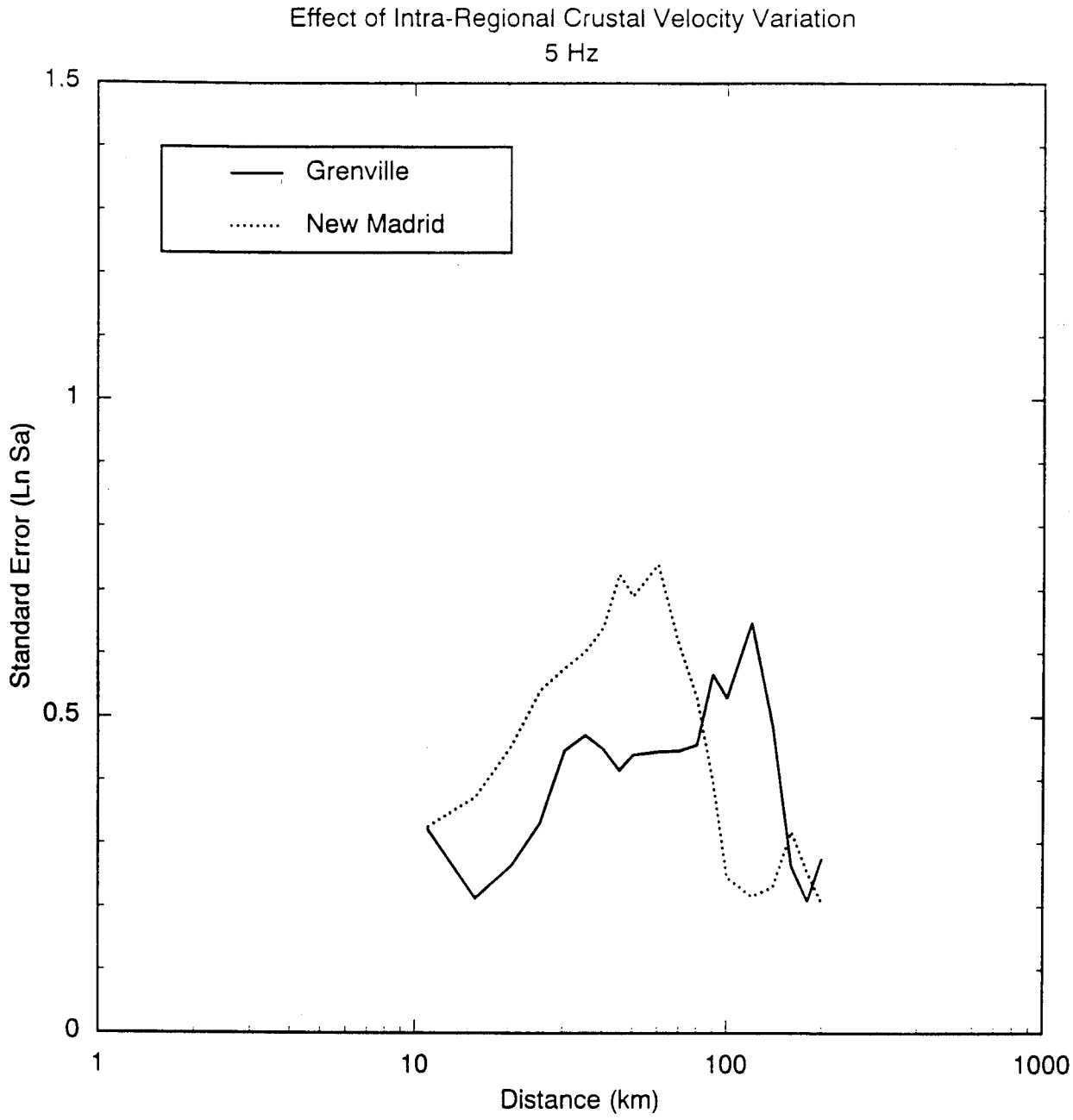

Figure 5-27b. Variability of spectral acceleration at 5 Hz due to crustal velocity uncertainty within the Grenville and New Madrid region. The variability includes variability in focal depth.

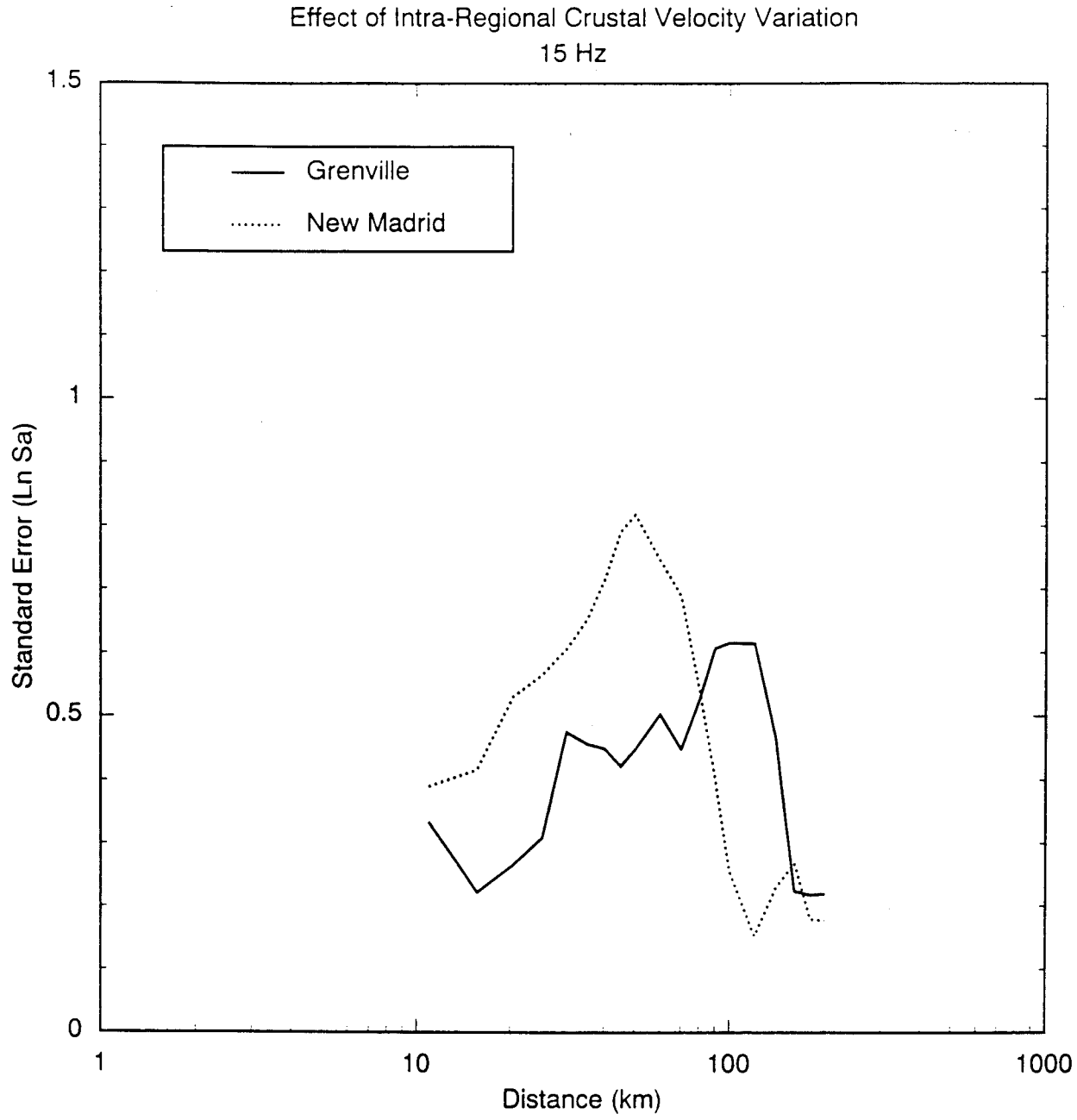

Figure 5-27c. Variability of spectral acceleration at 15 Hz due to crustal velocity uncertainty within the Grenville and New Madrid region. The variability includes variability in focal depth.

5.3.1.2 Uncertainty in Poisson's Ratio

The regionalization of crustal structure described in Section 5.1 is based of necessity on P-wave velocity structure, because S-wave velocity structure is typically not determined in crustal refraction studies. To estimate S-wave velocity models, which are more important than P-wave velocity models for strong ground motion modeling, we assumed a Poisson's ratio of 0.25 with a standard deviation of 0.034, derived from 64 estimates of crustal Poisson's ratio in continental North America by Braile et al. (1989). This uncertainty in the value of Poisson's ratio that is used to convert the P-wave velocities to S-wave velocities constitutes an additional source of uncertainty in crustal velocity structure. The uncertainty in ground motion attenuation due to this uncertainty in Poisson's ratio was estimated by perturbing the S-wave velocities of the Mid-continent region velocity model (see Section 5.2) by an amount corresponding to plus or minus one standard deviation in Poisson's ratio. The resulting crustal models are listed in Table 5-12.

Ground motions were computed for the Mid-continent crustal structure using the three Poisson's ratios. The variability of ground motion including the effect of uncertainty in Poisson's ratio is not significantly larger than the variability due to crustal structure uncertainty alone. Therefore, uncertainty is Poisson's ratio is not considered further.

5.3.1.3 Laterally Varying Structure

The regionalization of crustal structure described in Section 5.1 implies the existence of lateral variations in crustal structure at the boundaries of the regions. Although the nature of these boundaries has not been explored in most regions, there are several locations in the EUS in which they have. One of these locations is the New Madrid Rift area, in which the New Madrid region is surrounded by transitions in crustal structure to the south (Gulf Coast Plain); east (West Tennessee); north (Mid-continent); and west (Ozarks). Another is in Virginia, where there is a very large thickening of the

Table 5-12

Crustal Models Representing Variability in Poisson's Ratio

Vp (km/sec)	Vs (km/sec)	Density (gm/cc)	Thickness (km)	Depth to Top
Mid-continent—Base Case				
4.9	2.83	2.52	1	0
6.1	3.52	2.71	11	1
6.5	3.75	2.78	28	12
8.0	4.62	3.35	—	40
Mid-continent—Slow S Wave Velocity				
4.9	2.69	2.52	1	0
6.1	3.35	2.71	11	1
6.5	3.57	2.78	28	12
8.0	4.40	3.35	—	40
Mid-continent—Fast S Wave Velocity				
4.9	2.95	2.52	1	0
6.1	3.69	2.71	11	1
6.5	3.91	2.78	28	12
8.0	4.82	3.35	—	40

crust between central Virginia in the Atlantic Coastal Plain region and Giles County in the Southern Appalachian region.

In the following, we assess whether the variability in attenuation calculated from these variations in crustal structure within a region provides a realistic estimate of the variability in attenuation in data recorded within that region.

In a previous study, Saikia et al. (1992) analyzed the attenuation of vertical component S-waves from four small earthquakes in the New Madrid Rift area. Three of the four earthquakes occurred near the boundary of the New Madrid Rift, while one occurred within the Rift, and all recordings were made within the New Madrid Rift region, as shown in Figure 5-28. The three events were the 8 April 1981 Greenville, Illinois event at a depth of 5 km near the boundary with the Mid-continent region; the 7 August 1981 Dyersburg, Tennessee event at 23 km near the boundary with the West Tennessee region; and the 19 January 1983 Barney, Arkansas event at 4 km near the boundary with the Ozarks region. The event within the New Madrid region occurred near Equality, Illinois on 29 June 1984 at a depth of 7 km.

Although the paths of these recordings mostly lie within the New Madrid region, the thickness of the crust varies from about 40 to 47 km within the region. The attenuation of the recorded peak acceleration and velocity are compared with that of synthetic seismograms calculated using generalized ray theory for each event in Figures 5-29 and 5-30. Separate crustal structure models, shown in Figure 5-31, were used in calculating the attenuation for each earthquake.

The large variations in the shape of the calculated attenuation from event to event are due to variations in crustal structure and source depth. Similar variations exist in the empirical attenuation from event to event, which has an additional variability due to site effects (which are not modeled and are thus absent in the synthetics). To quantify the event-to event variability in attenuation we have measured the standard deviation of the peak acceleration and velocity from a 1/R attenuation for each event in the distance range of 0 to 300 km for both the recorded and synthetic values. The results are summarized in Table 5-13. The standard deviations vary from 0.19 to 0.28 for the recorded peak velocities, and from 0.19 to 0.34 for the recorded peak accelerations. These variations are comparable to those of the simulations, which are from 0.11 to 0.34 for peak velocities and from 0.10 to 0.34 for peak accelerations. We conclude that in the New Madrid rift region, the variability in ground motion attenuation due to variations in crustal structure may be reasonably estimated from synthetic attenuation relations derived from representative variations in crustal structure.

A much larger change in crustal structure occurs across the boundary between the Atlantic Coastal Plain and Southern Appalachian Regions in Virginia. An interpretation of the crustal structure of the area by Pratt et al. (1988) along a west-northwest profile is shown in Figure 5-32. A contour map of crustal thickness, derived using the time term method by James et al. (1968), is shown in Figure 5-33. The thickness of the Moho increases from about 30 km in the vicinity of Chesapeake Bay to 55 km in Giles County, over a distance of about 300 km. A profile across this crustal thickness gradient was chosen to coincide with the locations of small earthquakes recorded on the VPI Network shown in Figure 5-34. The crustal structure across this cross section was approximated using a horizontally layered upper crust and a planar Moho dipping at about 5 degrees to the west (Figure 5-35). As an alternative to a flat Conrad layer at a depth of 15 km, a Conrad layer that dips to the east at about 5 degrees is also shown.

A systematic difference is observed in the attenuation of ground motion amplitudes in either direction along this profile. For events in Central Virginia, the attenuation is rapid in the thickening direction toward Giles County, but for events in Giles County, the attenuation in the thinning direction toward Central Virginia is gradual. These trends persist after station terms have been removed, as described by Saikia et al. (1992). Using generalized ray synthetic seismograms, we have examined the influence of crustal models having flat and dipping Moho interfaces on the attenuation of ground motion in either direction along this profile. The results are summarized in Figures 5-36 and 5-37. Using flat layered models of the crust at the source location at either end of the profile does not produce a difference in attenuation. Introducing a dipping Moho flattens the attenuation toward Central Virgina at distances of 150 to 300 km, but not enough to match the flattening in the recorded data. The dipping Moho has relatively little effect on the attenuation toward Giles County. Introducing a Conrad

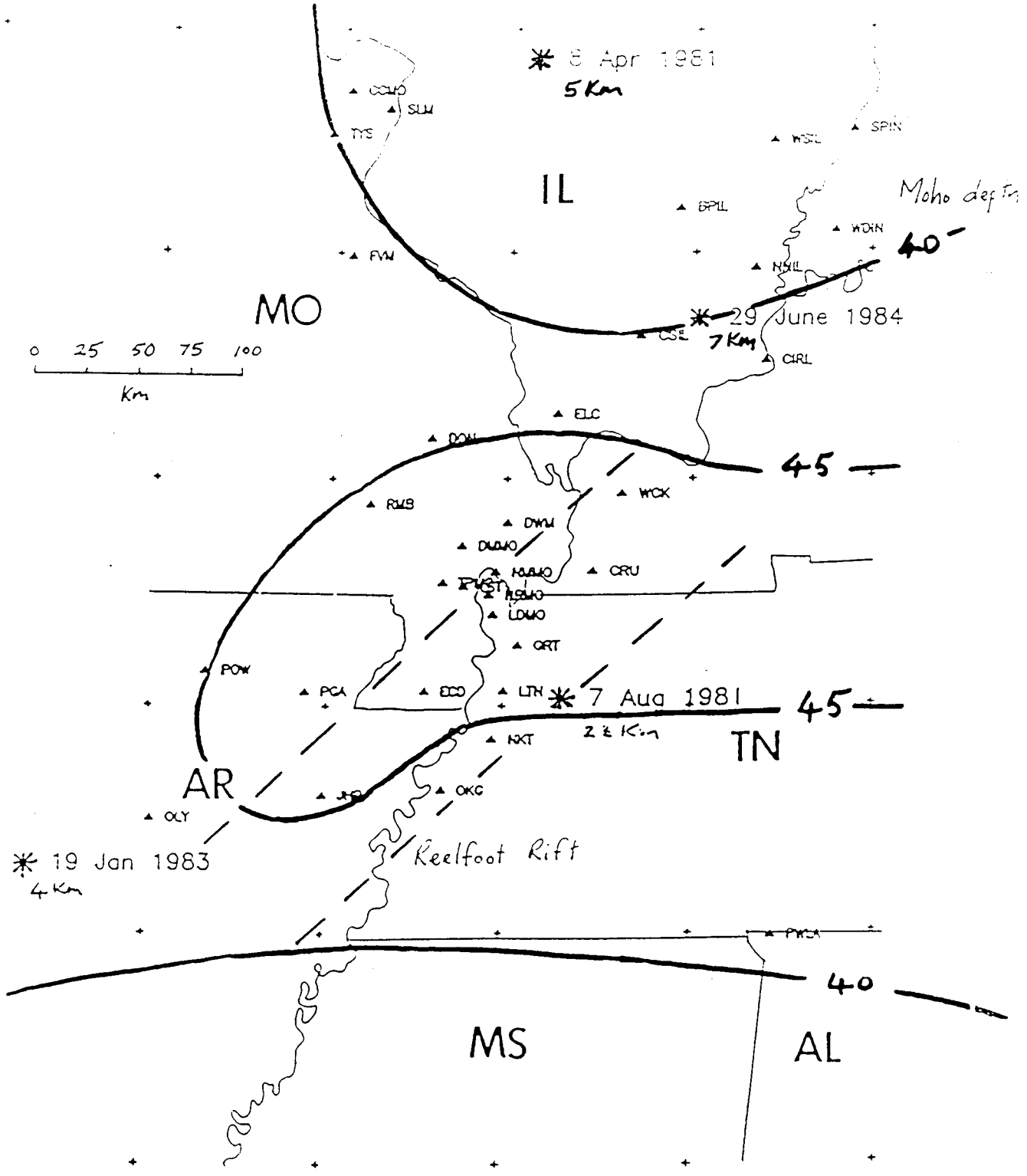

Figure 5-28. Location of the four events in the New Madrid region. The contours indicate the depth of the Moho. For these events, the Moho depth varies from 40 to 47 km.

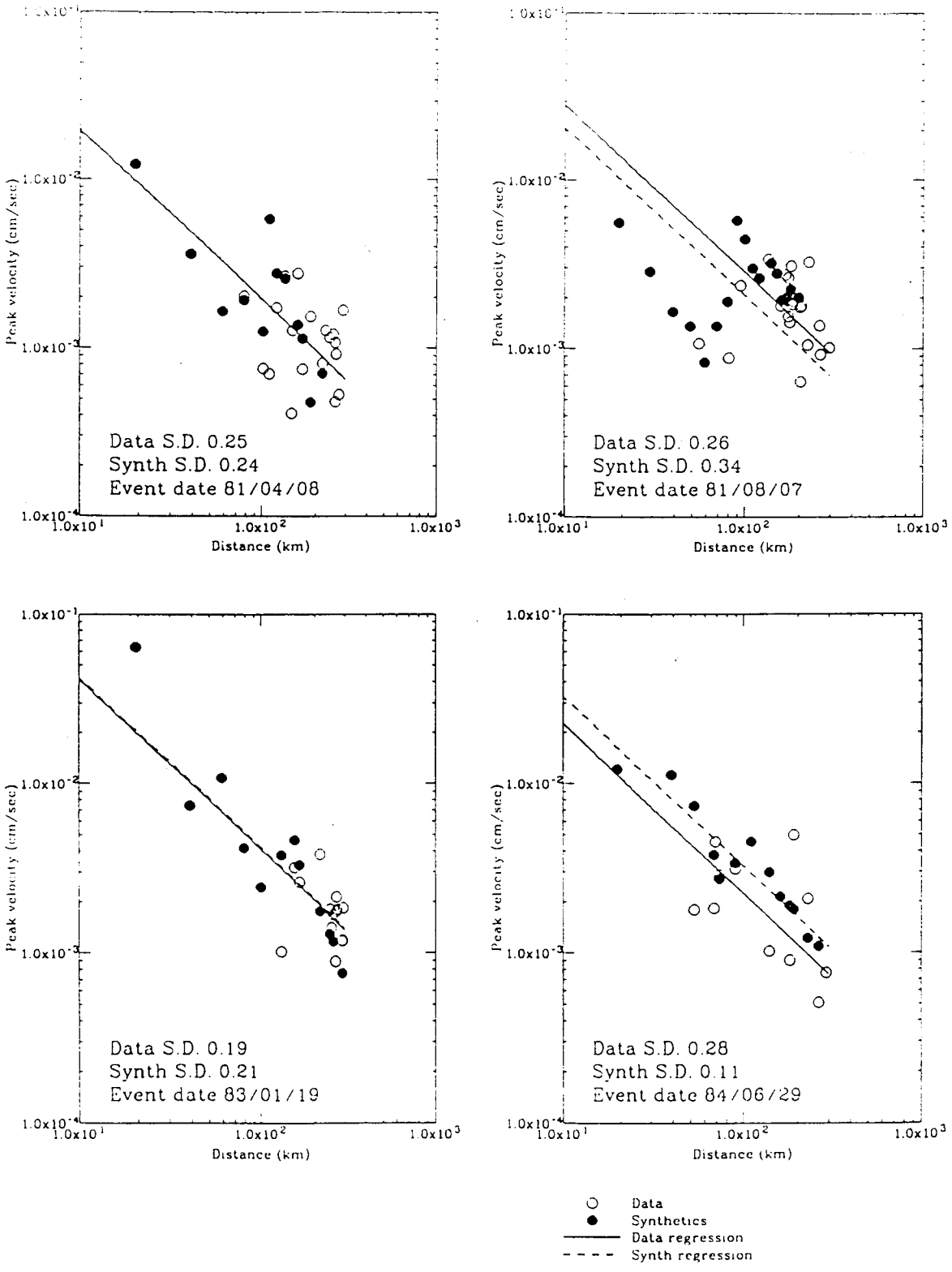

Figure 5-29. Observed and synthetic attenuation of peak acceleration for the four events in the New Madrid region. Straight lines are fits to the observed and synthetic values using a 1/R relation.

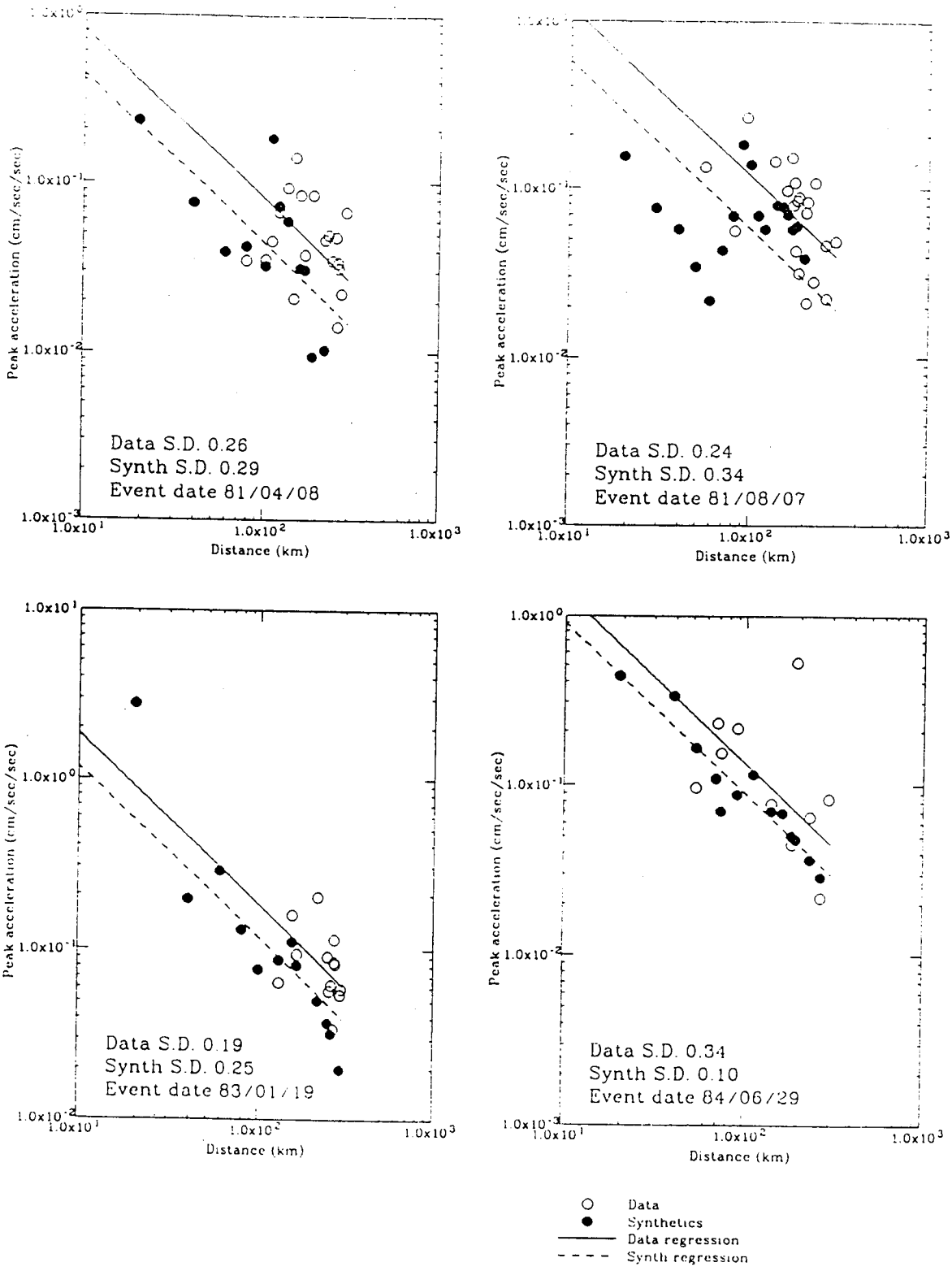

Figure 5-30. Observed and synthetic attenuation of peak acceleration for the four events in the New Madrid region. Straight lines are fits to the observed and synthetic values using a 1/R relation.

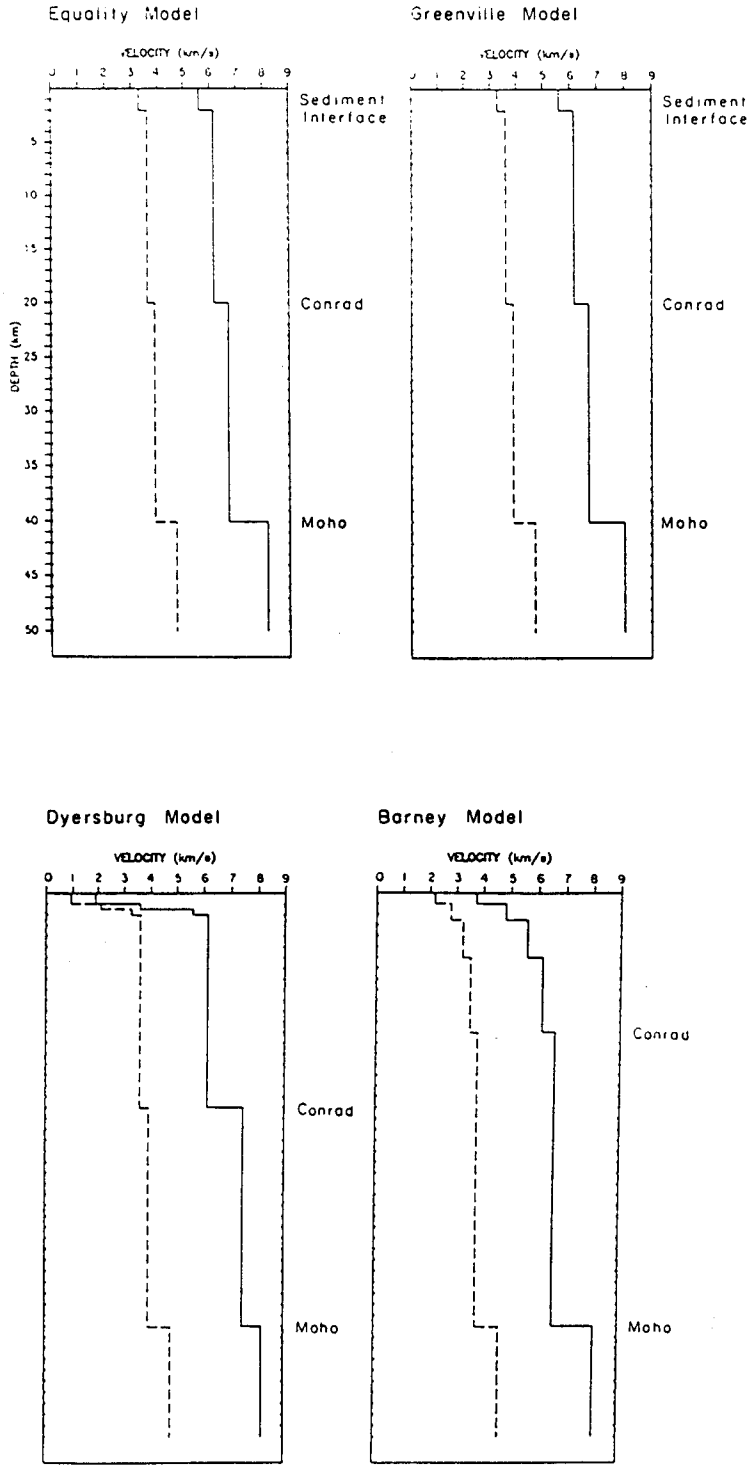

Figure 5-31. Velocity models for the four events in the Grenville region.

Table 5-13

Variability* in Ground Motion Attenuation within the New Madrid Region

Event Date and Location	Peak Velocity Recorded	Peak Velocity Synthetic	Peak Acceleration Recorded	Peak Acceleration Synthetic
81.04.08 Greenville, IL	0.25	0.24	0.26	0.29
81.08.07 Dyersburg, TN	0.28	0.11	0.34	0.10
83.01.19 Barney, AK	0.19	0.21	0.19	0.25
84.06.29 Equality, IL	0.26	0.34	0.24	0.34

* Expressed as a natural logarithm of standard error of values about a 1/R line

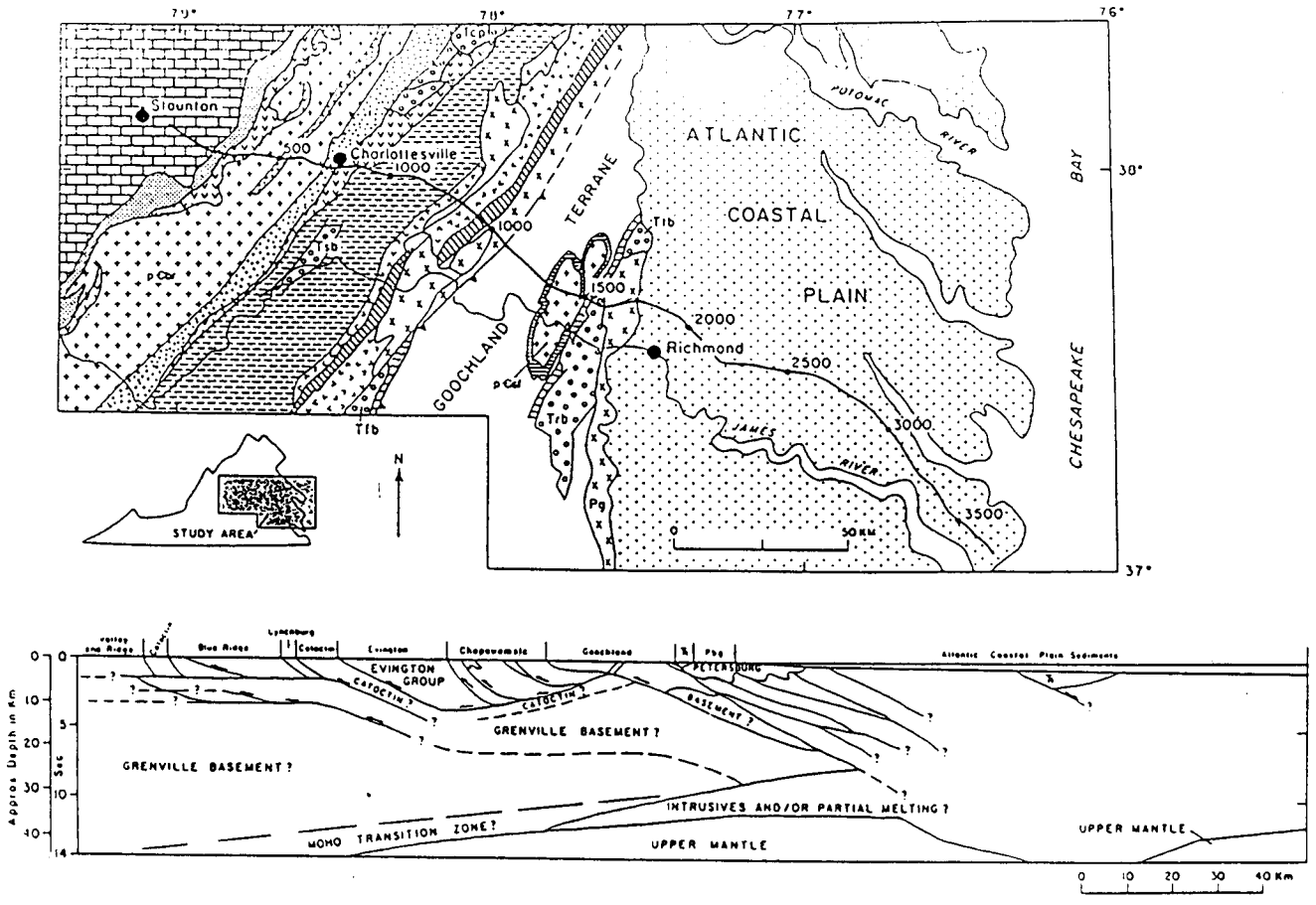

Figure 5-32. Crustal structure cross section across the boundary between the Atlantic Costal Plain and Southern Appalachian Regions in Virginia.

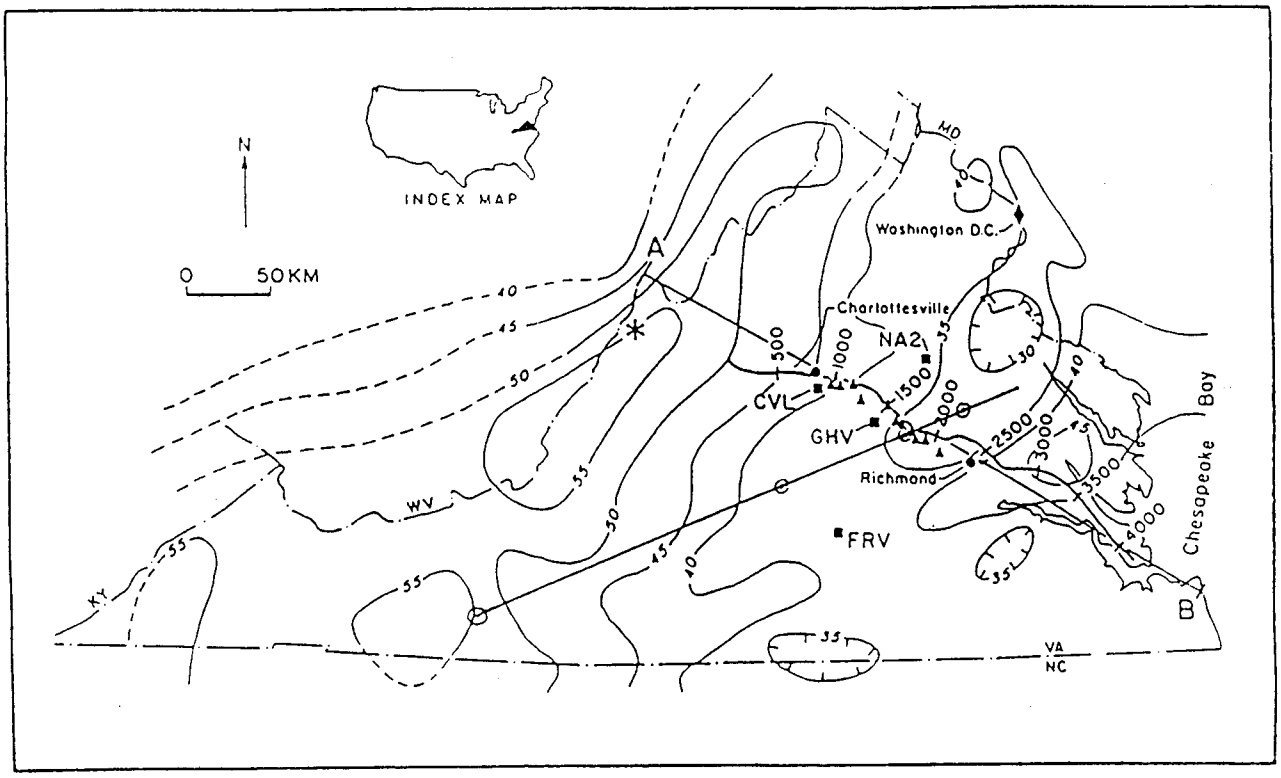

Figure 5-33. Contour of crustal thickness in Virginia.

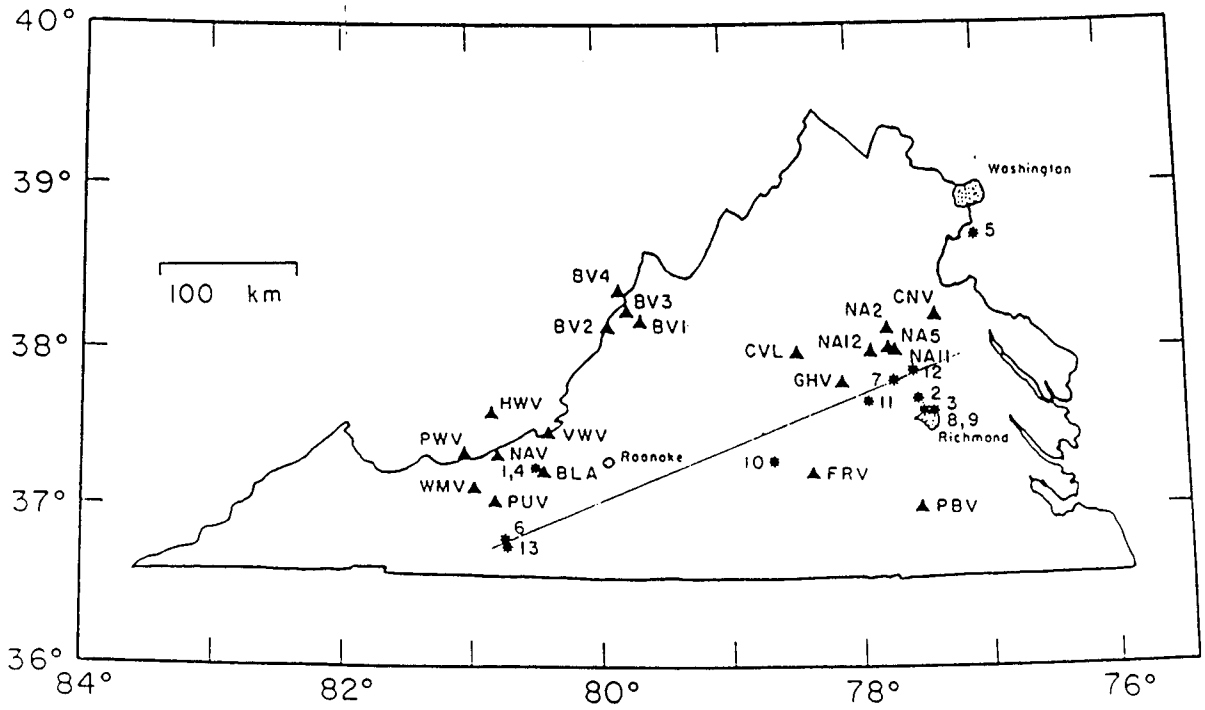

Figure 5-34. Earthquake locations and VPI network.

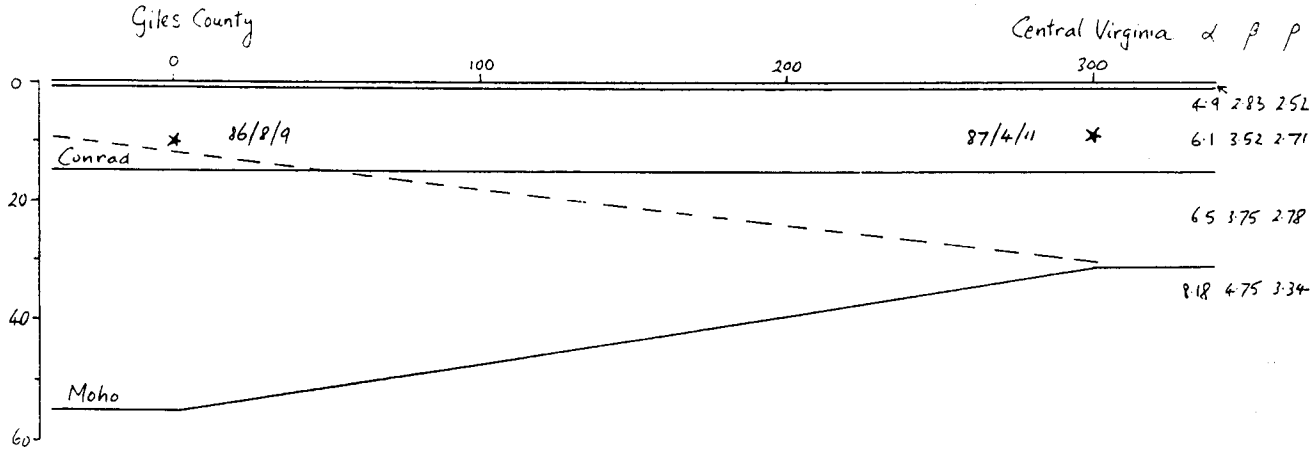

Figure 5-35. Two-dimensional crustal model from Giles County to Central Virginia. An alternative model with a dipping Conrad in addition to the dipping Moho is shown by the dashed line.

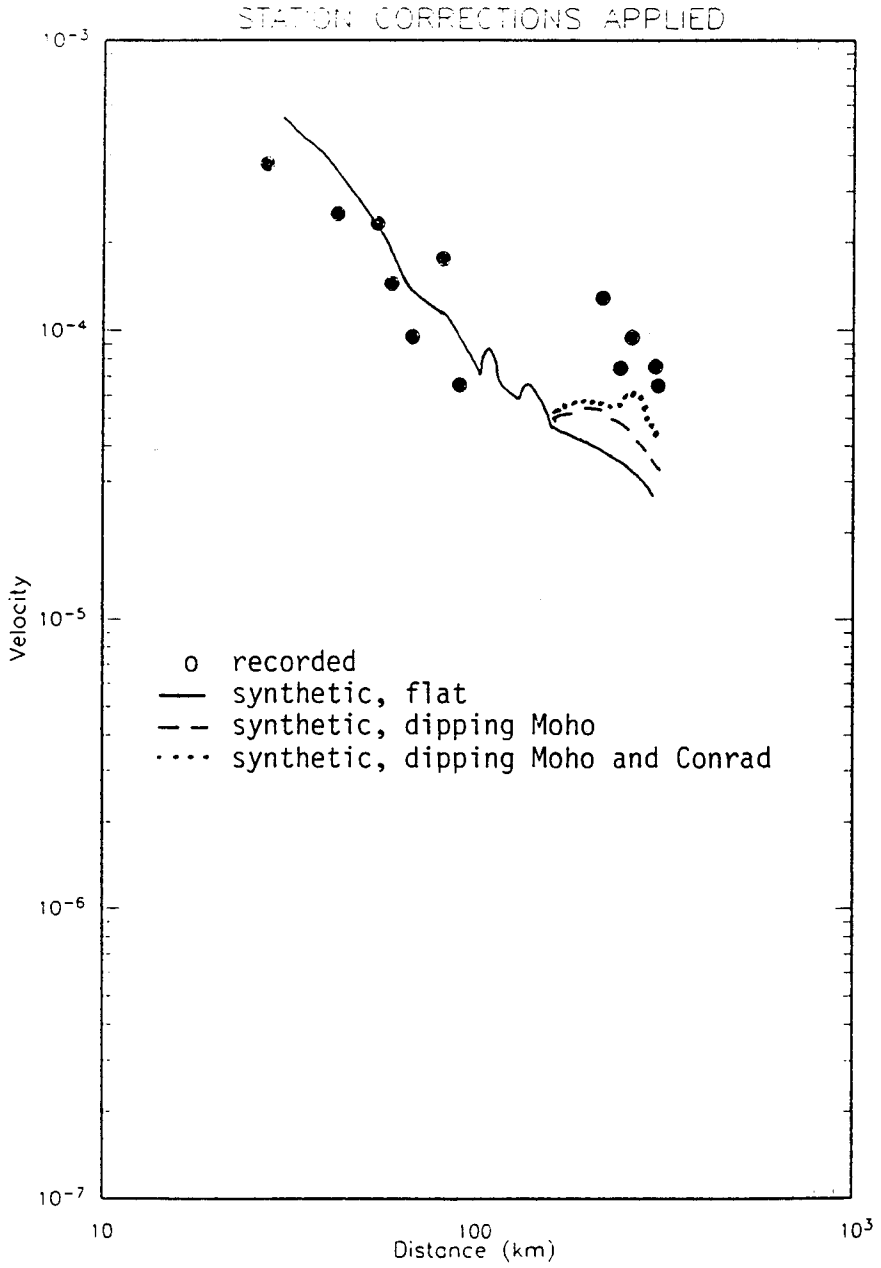

Figure 5-36. Attenuation of peak velocity from Giles County toward Central Virginia. The attenuation predicted by the synthetic motions is shown by the curves.

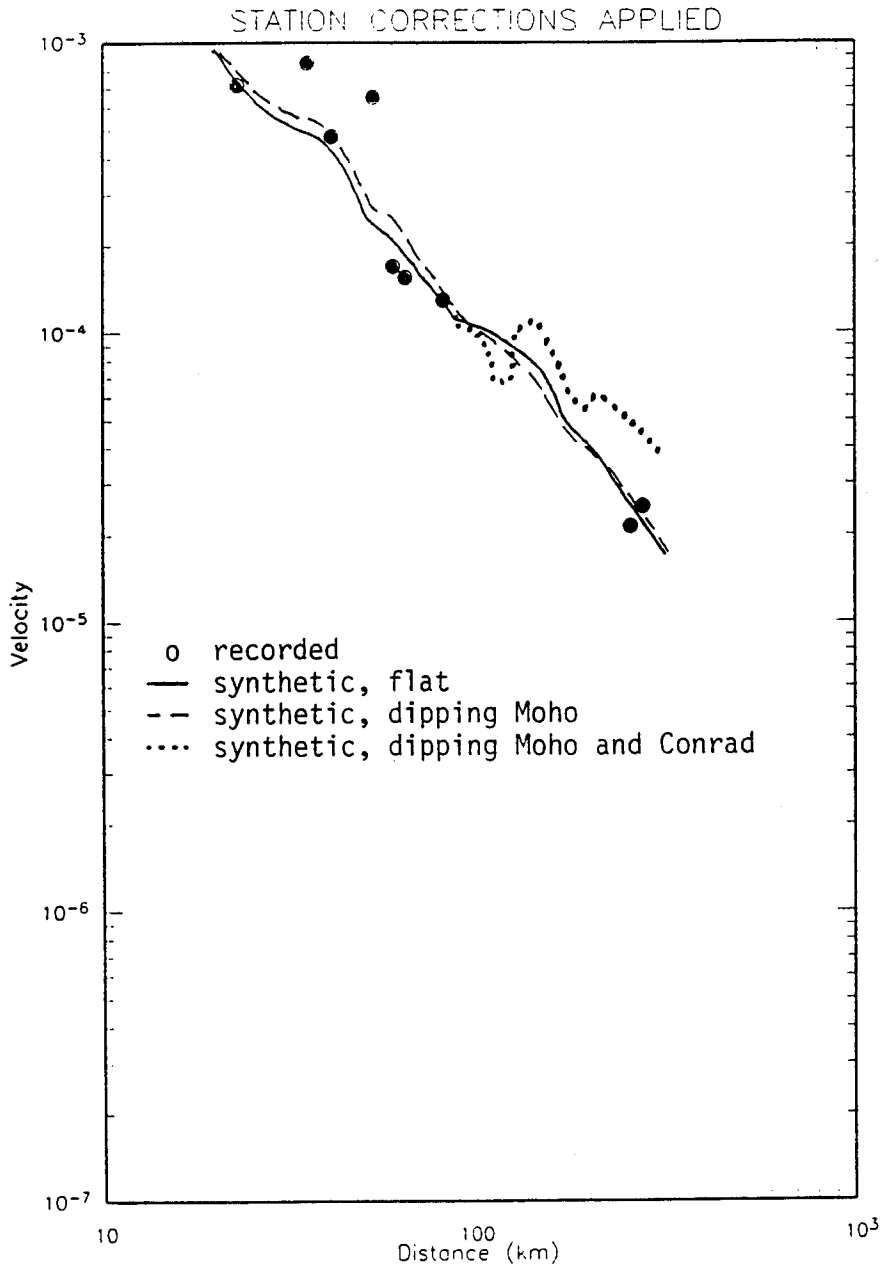

Figure 5-37. Attenuation of peak velocity from Central Virginia toward Giles County. The data show more rapid attenuation than from Giles County toward Central Virginia. The attenuation predicted by the synthetic motions is shown by the curves.

layer that dips in the opposite direction to the Moho, as suggested by the interpreted profile shown in Figure 5-32 and shown as a dashed line in Figure 5-35, produces additional flattening of the attenuation toward Central Virginia, but still not enough to match the recorded data. The dipping Conrad also causes more gradual attenuation toward Giles County, which is not observed in the recorded data. The addition of crustal multiples has little effect on the attenuation.

In summary, we observe gradual attenuation toward Central Virginia and rapid attenuation toward Giles County. Using flat layered models of the crust at the source location at either end of the profile, we qualitatively reproduce the observed trend, but quantitatively the observed difference is greater than that simulated. Including a dipping Moho enhances the agreement with the data. We conclude that the variability in ground motion attenuation due to lateral variation in crustal structure in Virginia is larger than would be estimated from the variability in attenuation derived from flat layered crustal models that span the range of structure model variation. This is contrary to the conclusion that we reached for the New Madrid data, and may reflect the much larger degree of variation and complexity in crustal structure in Virginia than in New Madrid. The difference in crustal structure between Central Virginia and Giles County may be large enough to warrant using a separate ground motion attenuation region in the southern Appalachians in which Giles County is located, as described in Section 5.5.

5.3.2 Inter-Regional Variation (for Fixed Q)

A subset of the 16 regions shown in Figure 5-12 is used to examine the inter-regional velocity structure variation on ground motion attenuation. The subset consists of four regions that represent the extremes of the full 16 regions. These four are New Madrid, Gulf Coast, Grenville, and Western Tennessee. The ground motion attenuation for the 4 regions are computed using numerical simulations for a fixed Q model to isolate the effects of the velocity structure on the ground motion. The variability of the ground motion due to variation in focal depth for each velocity structure is shown in Figures 5-38a and b for 5 and 15 Hz. In these figures, the thin line shows the average standard error of ground motion using region-specific mean attenuation for each region. The heavy line shows the standard error of the ground motion using a single region independent mean attenuation for all four regions. The difference between these two curves indicates the potential reduction in the standard error that can be realized by regionalizing the attenuation. The main difference is in the distance range 80 to 150 km due to variations in the Moho depth for the four regions.

5.4 Effects of Crustal Q and Kappa Structure

The effect of variation in Q and kappa on ground motion is examined using the generalized ray simulation procedure described in Section 3.3. The effect of variation in Q is analyzed for both intra-region variations and inter-region variations.

5.4.1 Effect of Variations in Q on Ground Motion

The effect of intra-region variation of Q on ground motion attenuation is estimated using three Q models developed for the New Madrid velocity structure (see Appendix 5A). The ground motions were computed for each Q model. The resulting variability of the ground motion is shown in Figure 5-39 for distances of 50, 100, and 200 km. The effect of uncertainty in Q becomes significant at distances greater than 100 km.

The effect of inter-region variation of Q on ground motion attenuation depends on the regions compared. For fifteen of the sixteen regions, the Q models are similar and the effect of inter-region variation of Q is small. This is not the case for the Gulf Coast region. Using the Mid-continent region as a representative crustal structure, the ground motions for the Mid-continent region for Q models 4 and 8 are shown in Figure 5-40a, b, c. The lower Q values for Q8 result in about a factor of 2 decrease in ground motion at frequencies of 5–15 Hz at distances greater than 100 km.

5.4.2 Effects of Variation in Kappa on Ground Motions

Although kappa is a site parameter, the kappa value for rock is effectively part of the path. Strong ground motion observed at hard rock sites in eastern North America appears to have different spectral properties than those typical of western North American rock motions. The differences in spectral content can perhaps be most easily seen in 5% damped spectral amplification (Sa/a) computed from recordings typical of WNA and ENA tectonic environments. Figure 5-41 shows average spectral

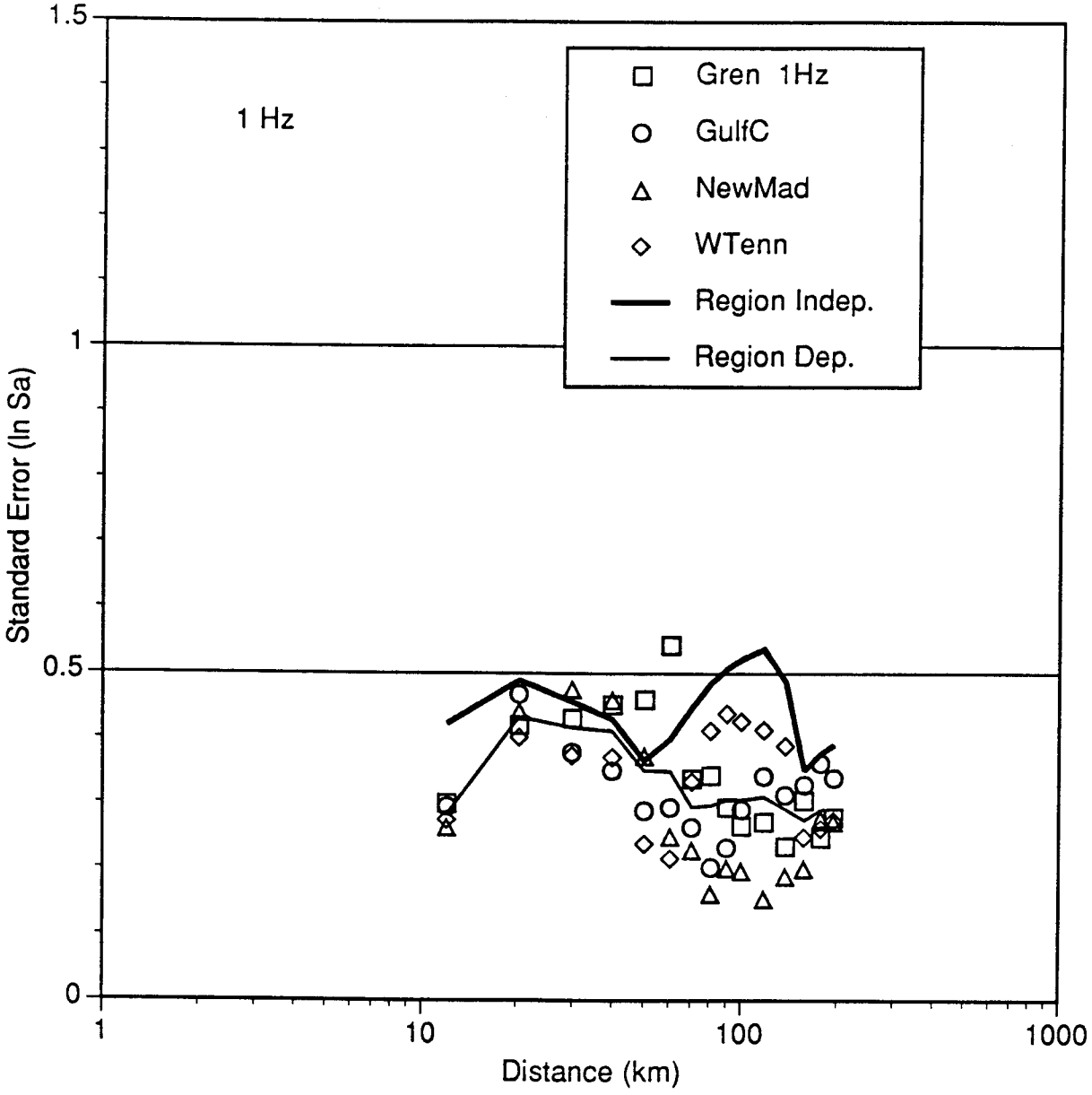

Figure 5-38a. Effect of inter-region crustal velocity variations on the variability of spectral acceleration at 1 Hz.

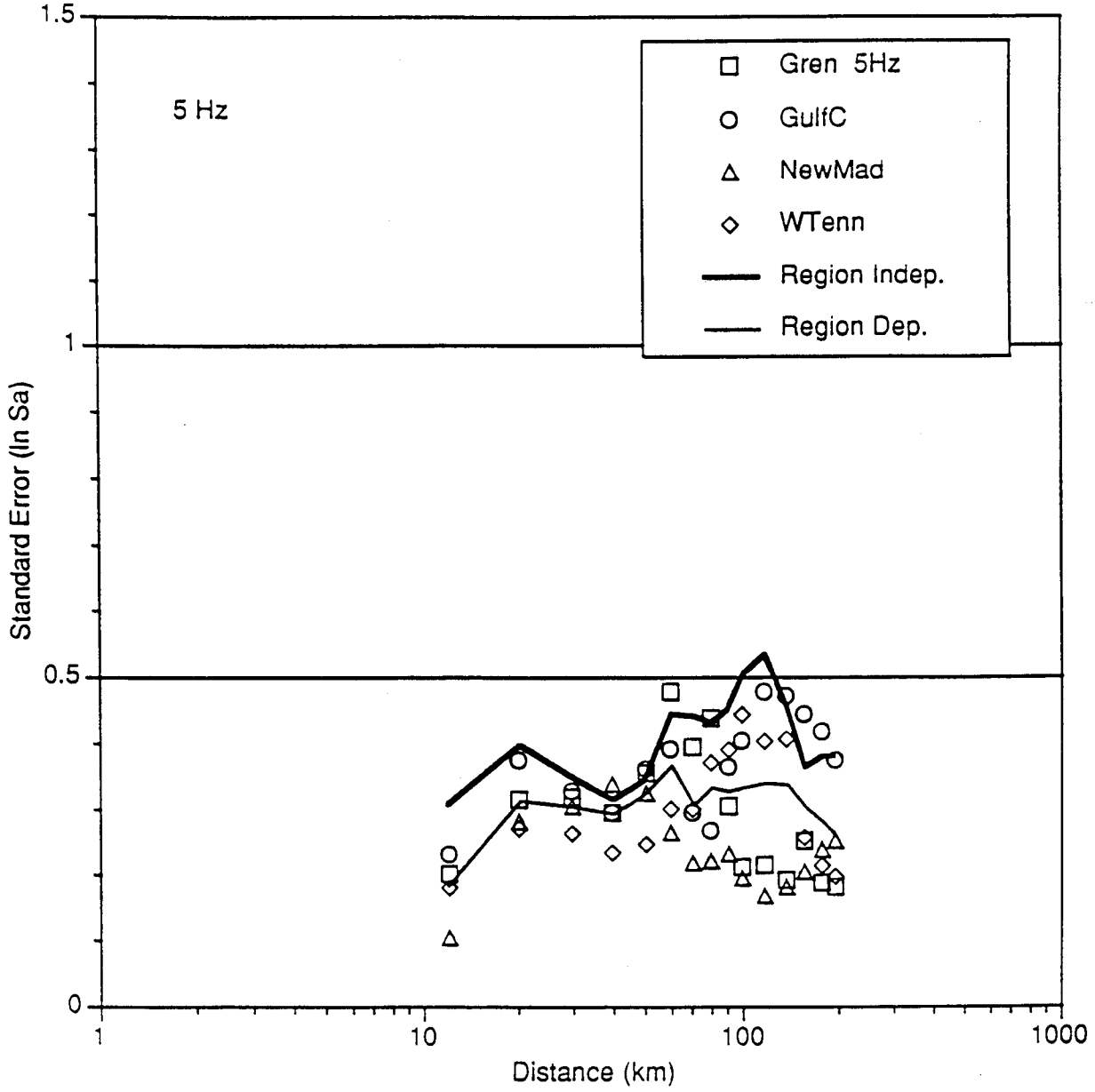

Figure 5-38b. Effect of inter-region crustal velocity variations on the variability of spectral acceleration at 5 Hz.

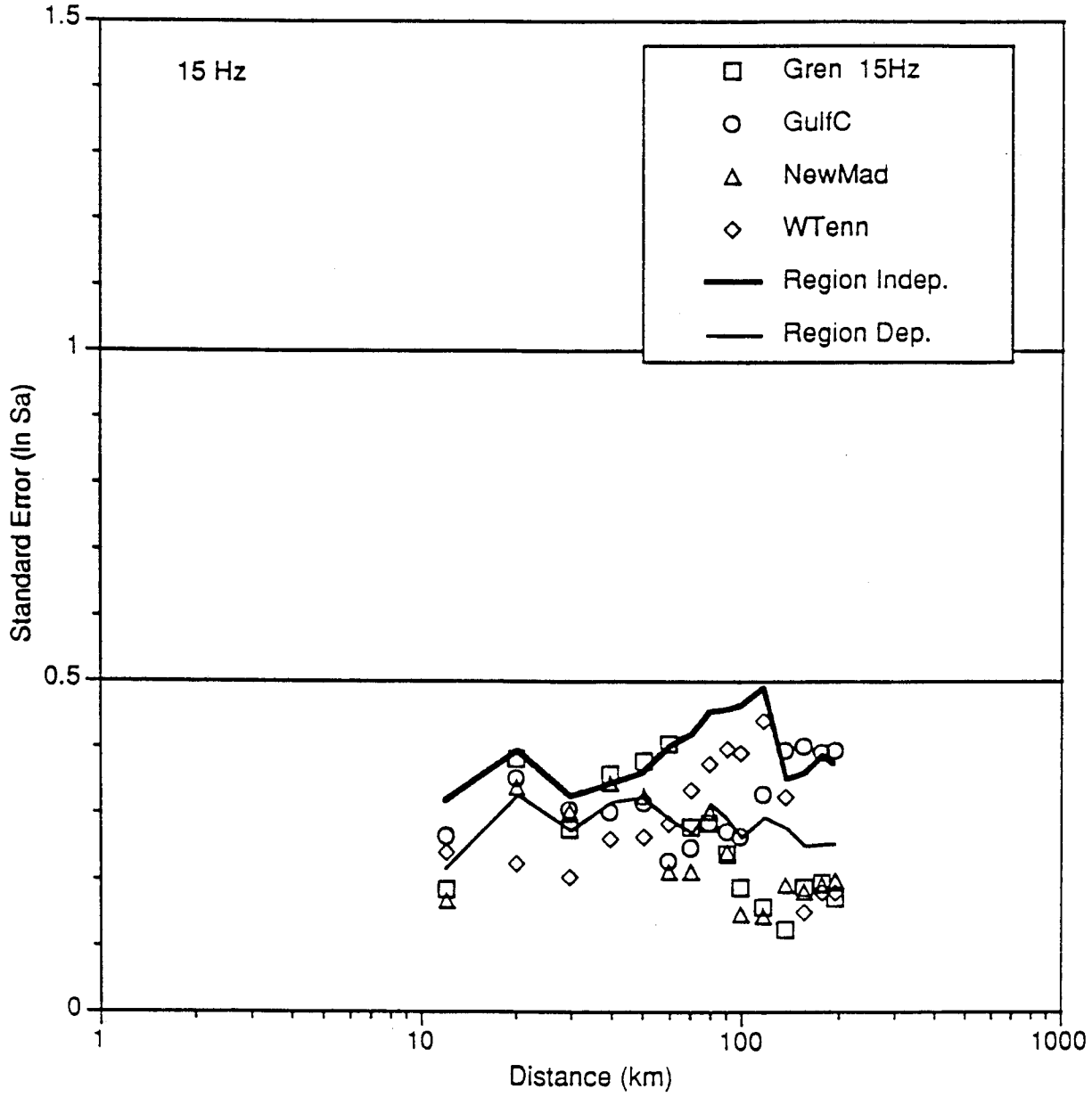

Figure 5-38c. Effect of inter-region crustal velocity variations on the variability of spectral acceleration at 15 Hz.

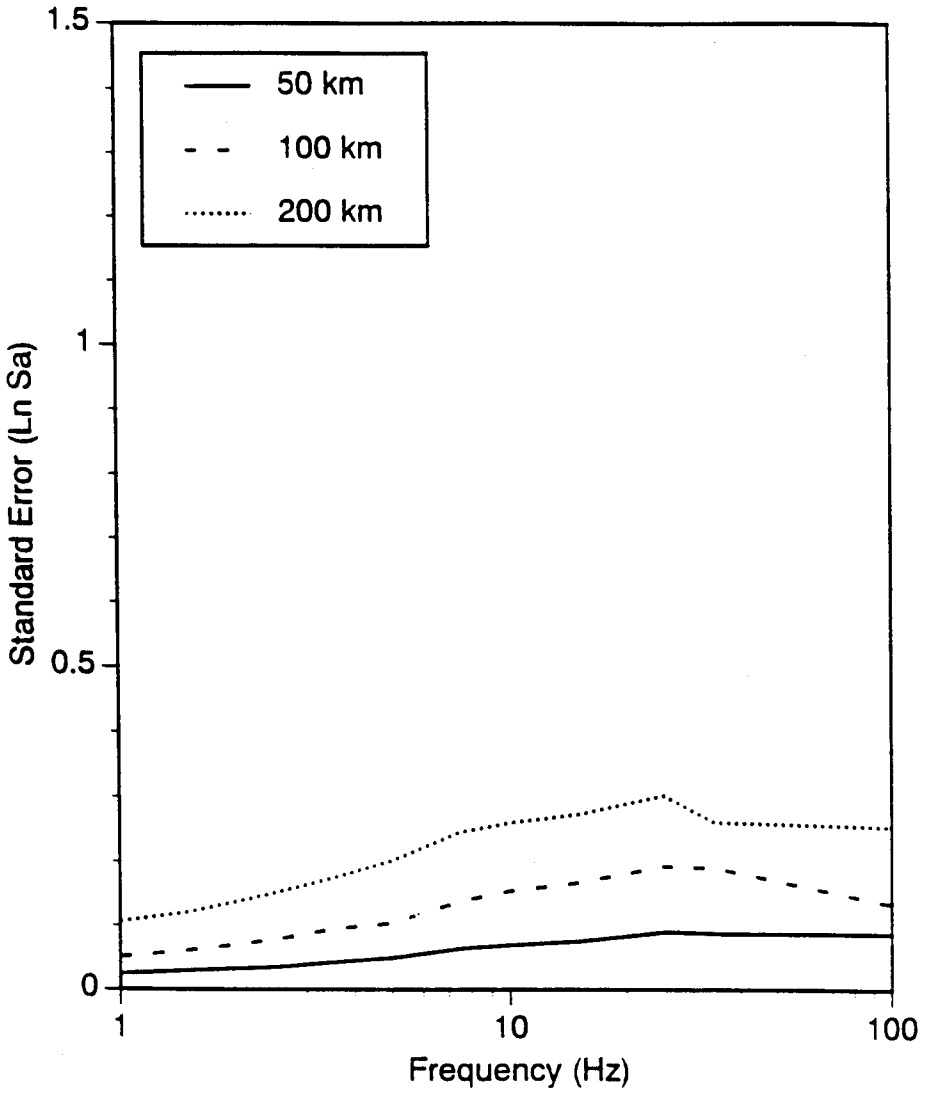

Figure 5-39. Effect of variability of Q within a region on the variability of spectral acceleration.

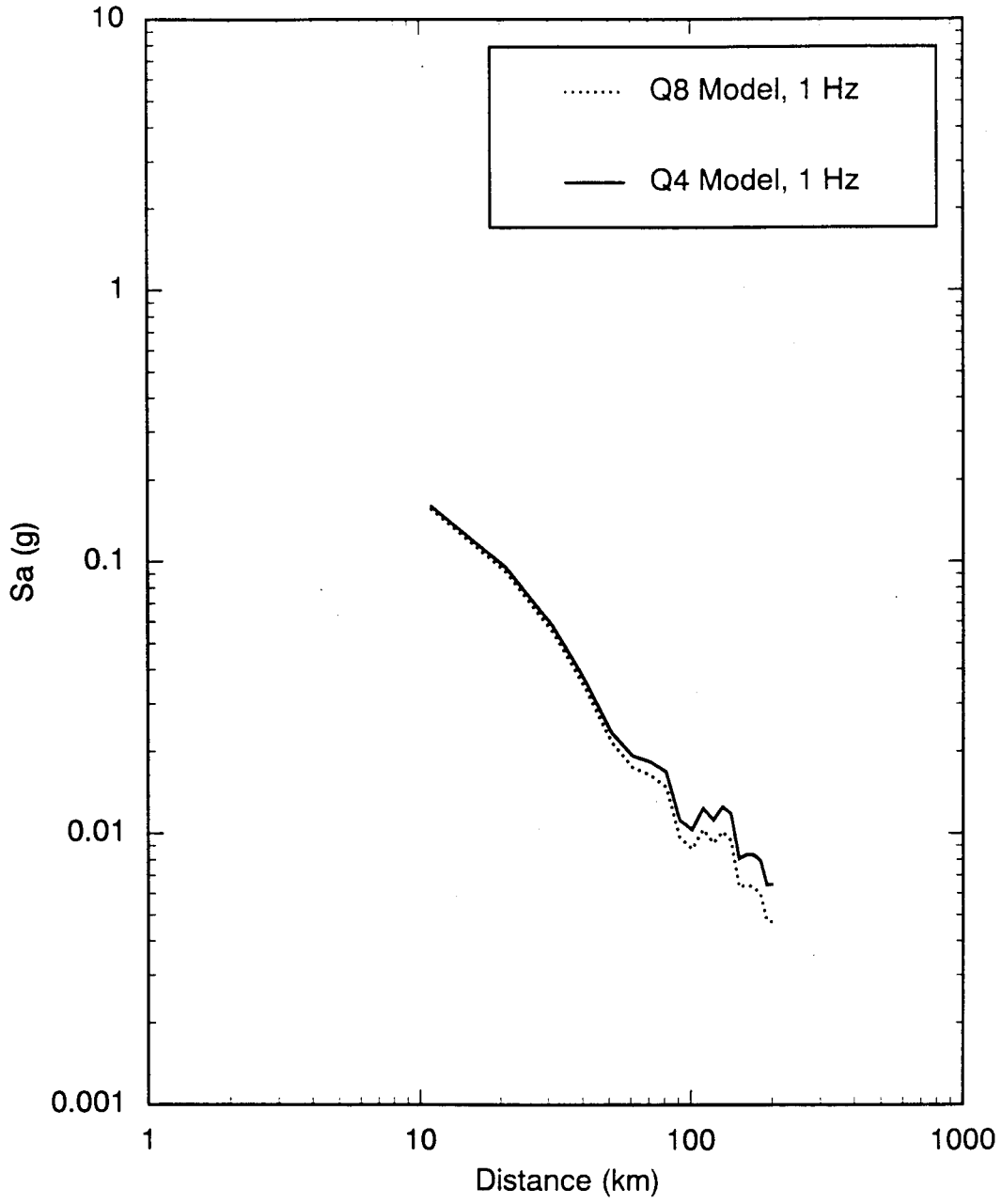

Figure 5-40a. Effect of variability of Q between regions on the rate of attenuation of spectral acceleration at 1 Hz.

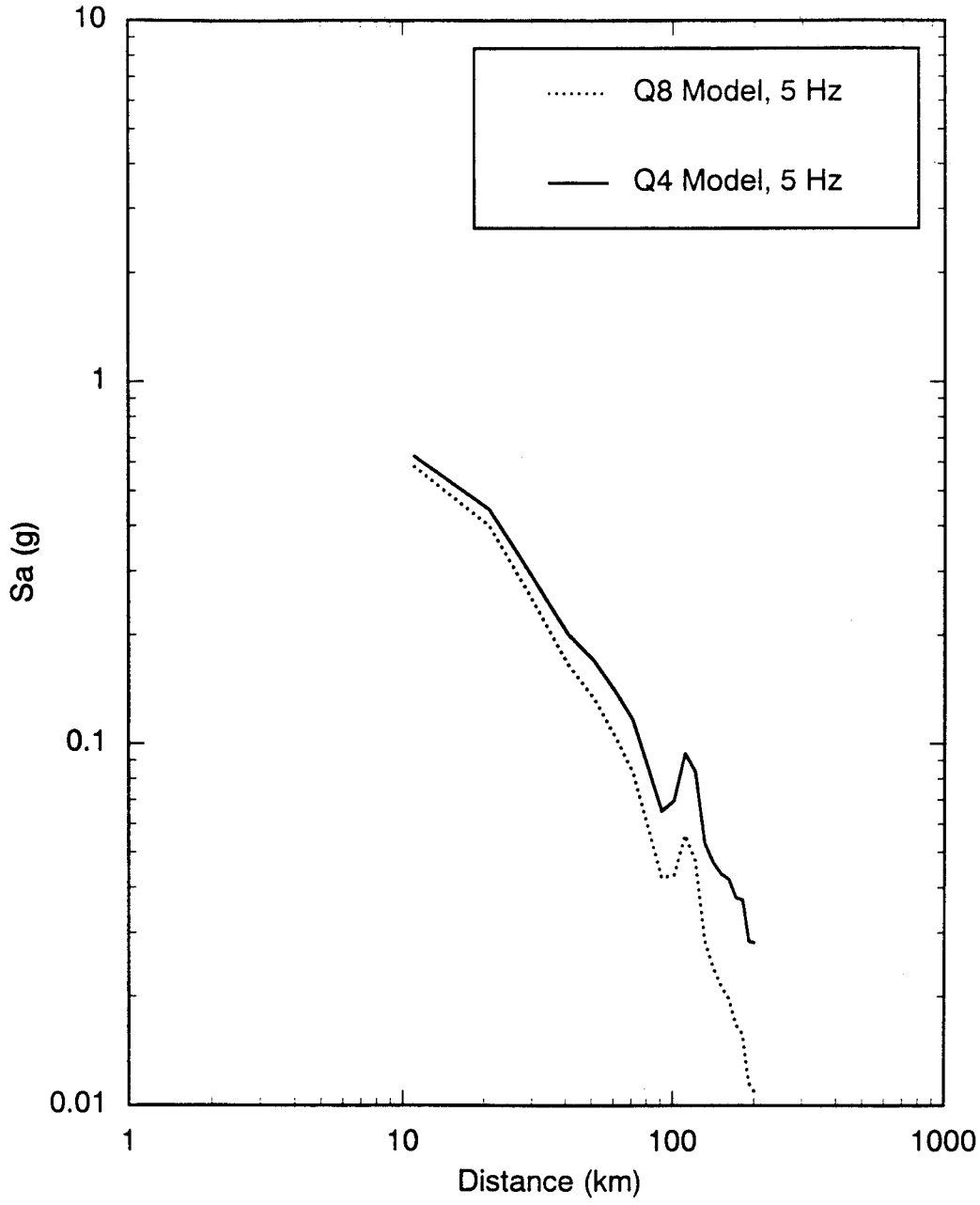

Figure 5-40b. Effect of variability of Q between regions on the rate of attenuation of spectral acceleration at 5 Hz.

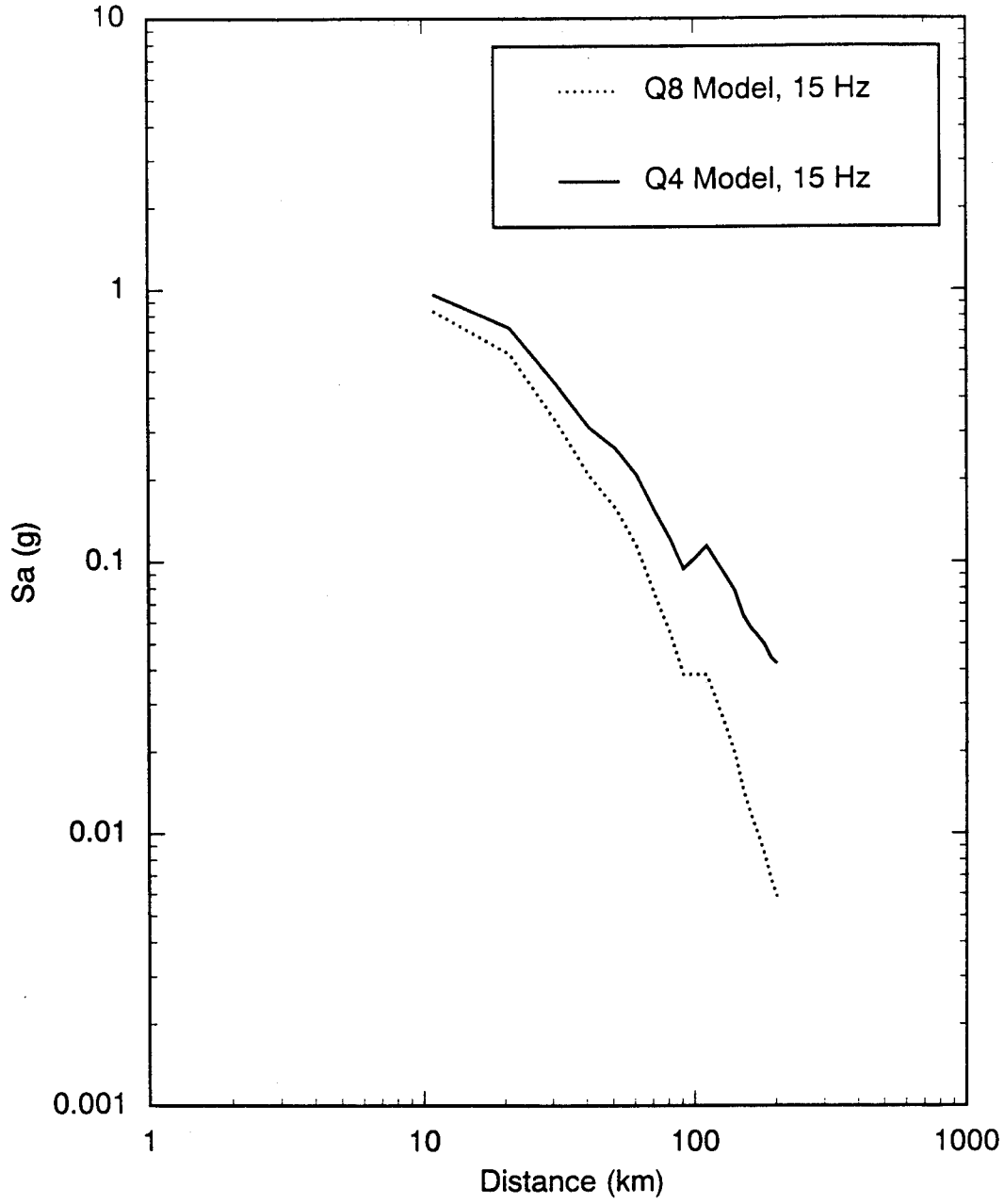

Figure 5-40c. Effect of variability of Q between regions on the rate of attenuation of spectral acceleration at 15 Hz.

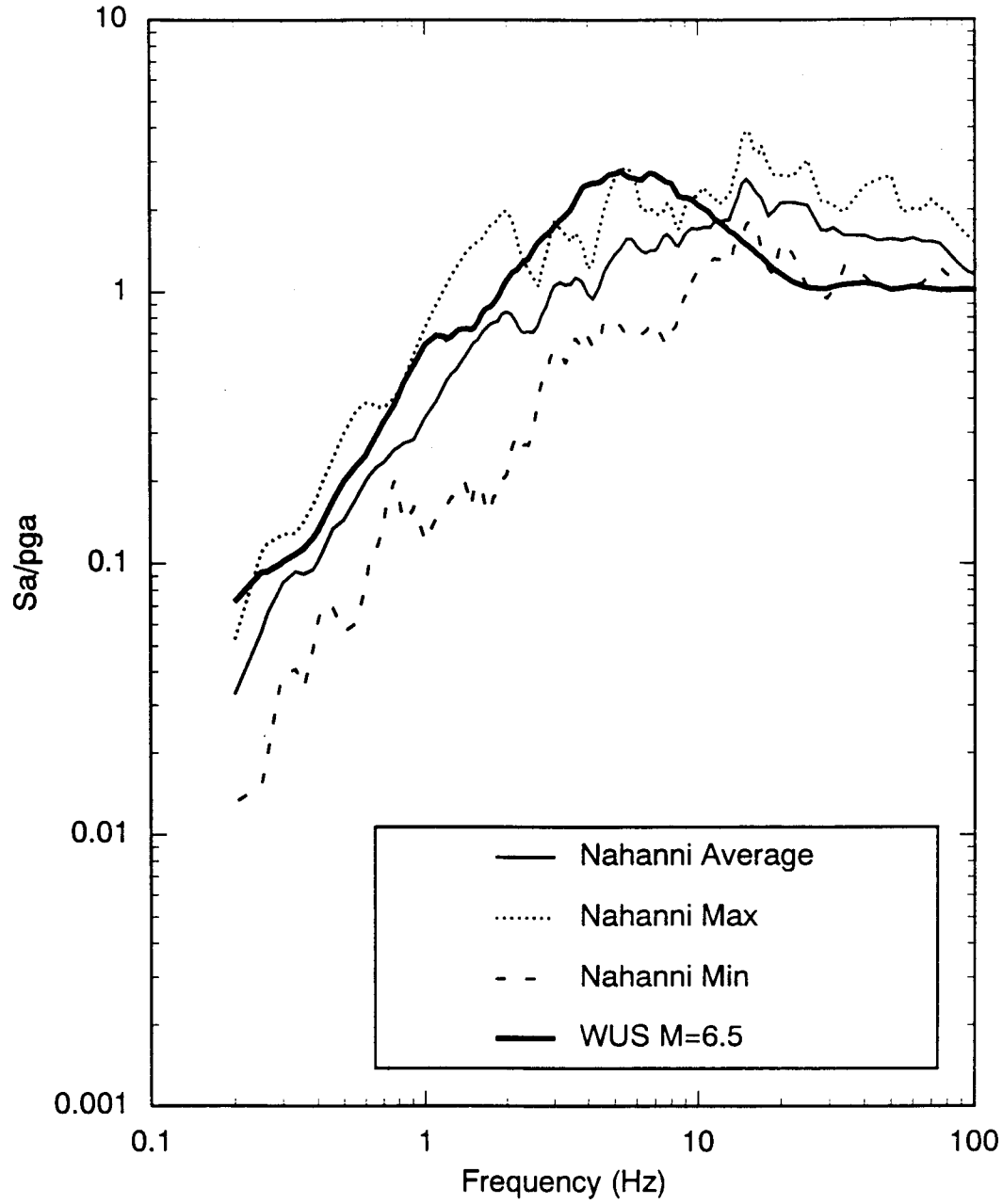

Figure 5-41. Comparison of an average spectral shape for a hard rock site (Nahanni) with an average spectral shape for WUS rock sites. This illustrates the difference between spectral shapes for typical hard rock sites in the EUS and rock sites in the WUS.

shapes computed from recordings made on rock of a Nahanni earthquake (**M** 6.8) compared to an average spectral shape computed from **M** 6.5 western US rock motions (1971 San Fernando, **M** 6.6 and the 1979 Imperial Valley, **M** 6.4 earthquakes). The differences in spectral content are significant and indicate that, for the same level of peak acceleration, ENA spectral content is higher than that in western North America for frequencies greater that 10 Hz.

Other sources of data also indicate that ENA ground motion recorded at hard rock or very shallow soil sites is richer in high frequency energy relative to analogous western US recordings. These include aftershocks of the 1982 Miramichi, New Brunswick event (Cranswick et al., 1985), the 1982 Enola, Arkansas swarm (Harr et al., 1984), and the 1986 Northeastern Ohio event and its aftershocks (Wesson and Nicholson, 1986).

The trends shown in these data are consistent with the rock or shallow stiff soil recordings of strong ground motion. They indicate a significant and reasonably consistent difference in high frequency spectral content between representative rock motion in western and eastern North America crust.

In the stochastic model used here, (Section 3.2) the differences in spectral content between WNA and ENA at distances less than about 50 km is attributed to near surface crustal damping (Anderson and Hough, 1984; Silva and Darragh, 1993). The near surface damping parameter, kappa, is used to model the effects of rate independent damping in the crustal rocks in the upper 1–2 km of the crust. Typical values for this parameter in western North America are about 0.03–0.04 sec (Silva and Darragh, 1993) and about 0.006 sec for hard rock ENA sites (Silva and Darragh, 1993).

To illustrate the differences in spectral content predicted by the stochastic model for western and eastern North American rock motions, the **M** 6.5 empirical spectral shapes shown in Figure 5-41 are modeled using Q and kappa values appropriate for either ENA or WNA holding other source parameters constant. For WNA the stress drop is taken as 100 bars, the Q(f) model is $150\ f^{0.6}$, and kappa is 0.040 sec (Silva and Darragh, 1993). To model the **M** 6.5 ENA spectral shape, the stress drop is also taken as 100 bars, but with the Q(f) model of $670\ f^{0.33}$ (Atkinson, 1993), and the kappa value of 0.006 sec. Figure 5-42a shows the predicted spectral shape with ENA, Q, and kappa and the average Nahanni spectral shape. Figure 5-42b shows the predicted spectral shape with WNA, Q, and kappa and the average San Fernando and Imperial Valley spectral shape. As can be seen from these figures, the stochastic model captures the spectral shapes for both regions throughout most of the frequency range. The overprediction of the spectral shape computed from recordings of the Nahanni **M** 6.8 earthquake at periods shorter than about 0.05 sec may be an artifact of the recording instrument. The strong motion accelerographs (SMA-1) have corner frequencies near 0.04 sec. While instrument corrections were performed, they are notoriously difficult to correct with confidence through an instrument corner unless very accurate phase and amplitude calibrations are available.

Figures 5-43 and 5-44 show response spectral shapes representative of ENA motions recorded at hard rock sites and stochastic model predictions for magnitude ranges of **M** 5.4–5.7 and **M** 4.0–4.8 respectively. The magnitude 5.4–5.7 range includes 4 recordings from 2 events and the magnitude 4.0–4.8 range includes 22 recordings from 3 events. The model predictions with a kappa value of 0.006 sec captures the overall spectral composition of the observed motions with reasonable accuracy.

The standard deviation is assumed to be 0.4 natural logarithm units based on the range of kappa values estimated by regression for 20 rock site recordings of the 1989 Loma Prieta Earthquake (Schneider et al. 1993). This variability in the kappa values from the WUS is assumed to be applicable to the kappa values from the EUS.

The variability of ground motion due to variability in kappa values is shown in Figure 5-45 for a site at a distance of 50 km. (Since kappa is a site term, the results are not sensitive to the distance.) For soft-rock sites, the variability of kappa has a significant effect on the high frequency ground motion variability; however, for hard-rock sites, the variability in kappa does not have a significant effect on the ground motion because the median kappa value is small.

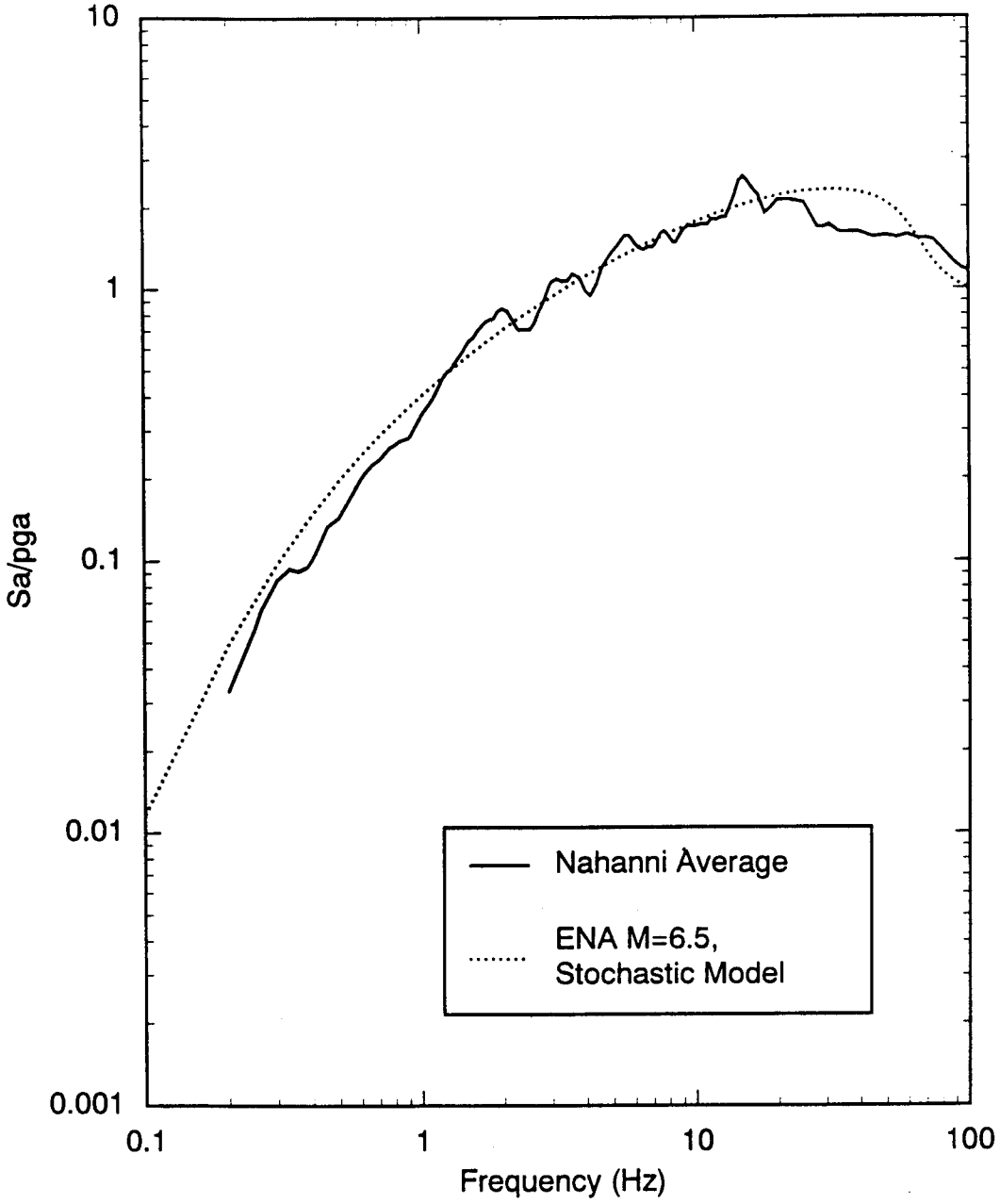

Figure 5-42a. Comparison of average spectral shapes for hard rock sites from the Nahanni event (Figure 5-41) with the predicted ENA shape based on the stochastic ground motion model. The stochastic model captures the spectral shape for hard rock sites.

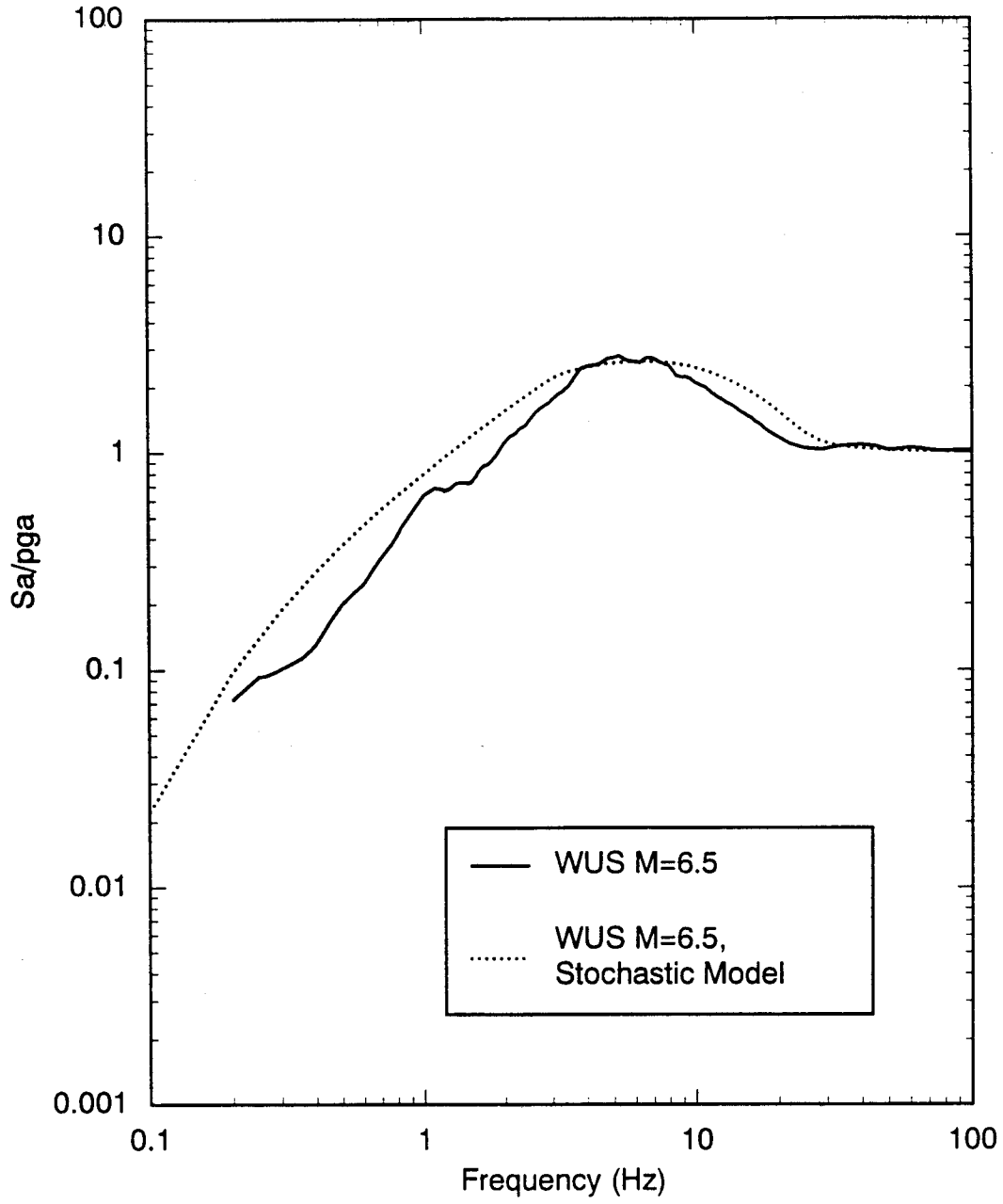

Figure 5-42b. Comparison of average spectral shapes for hard rock sites from WUS events (Figure 5-41) with the predicted WUS shape based on the stochastic ground motion model.

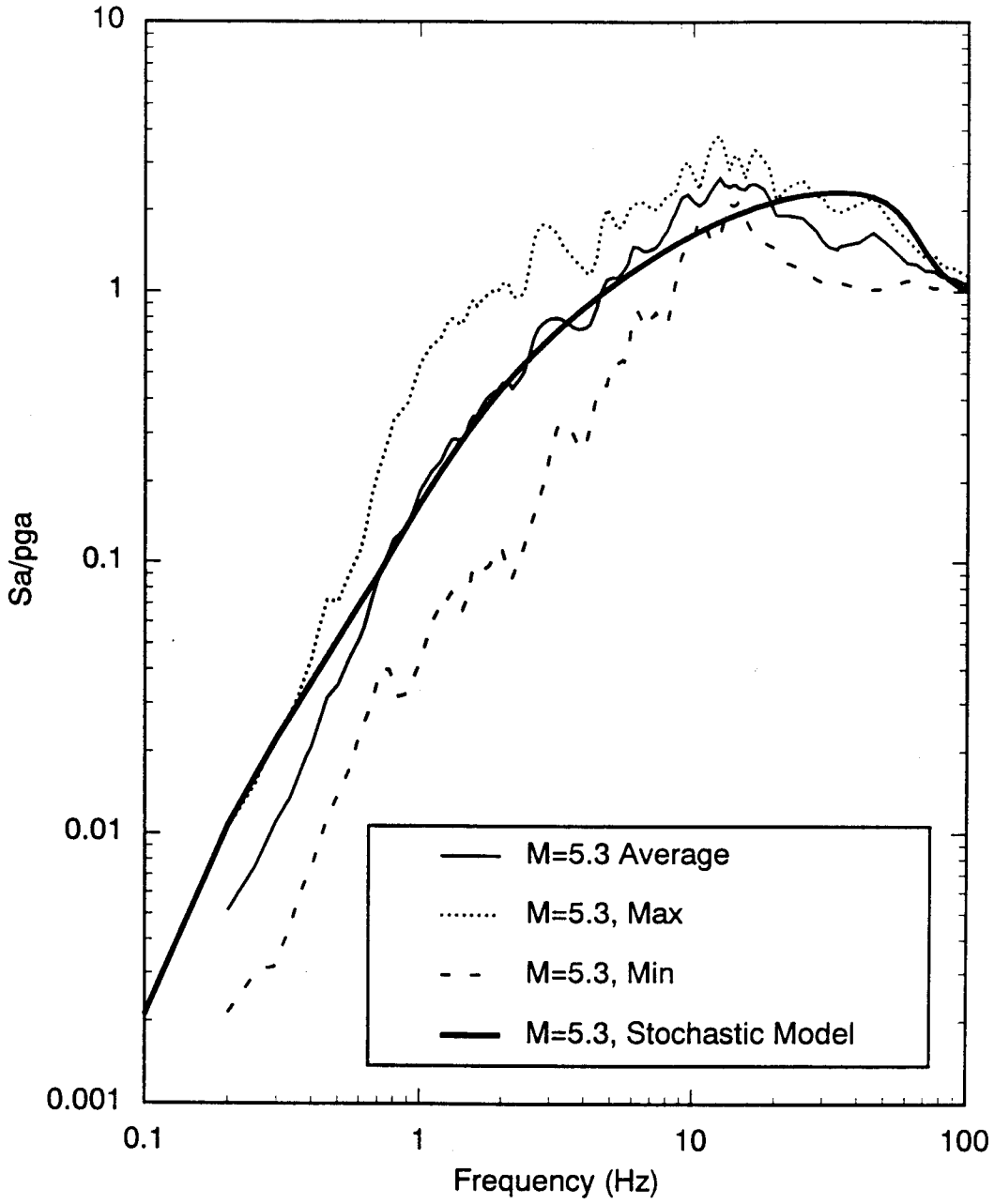

Figure 5-43. Comparison of recorded and predicted spectral shapes for ENA hard rock sites for M 5.4–5.7.

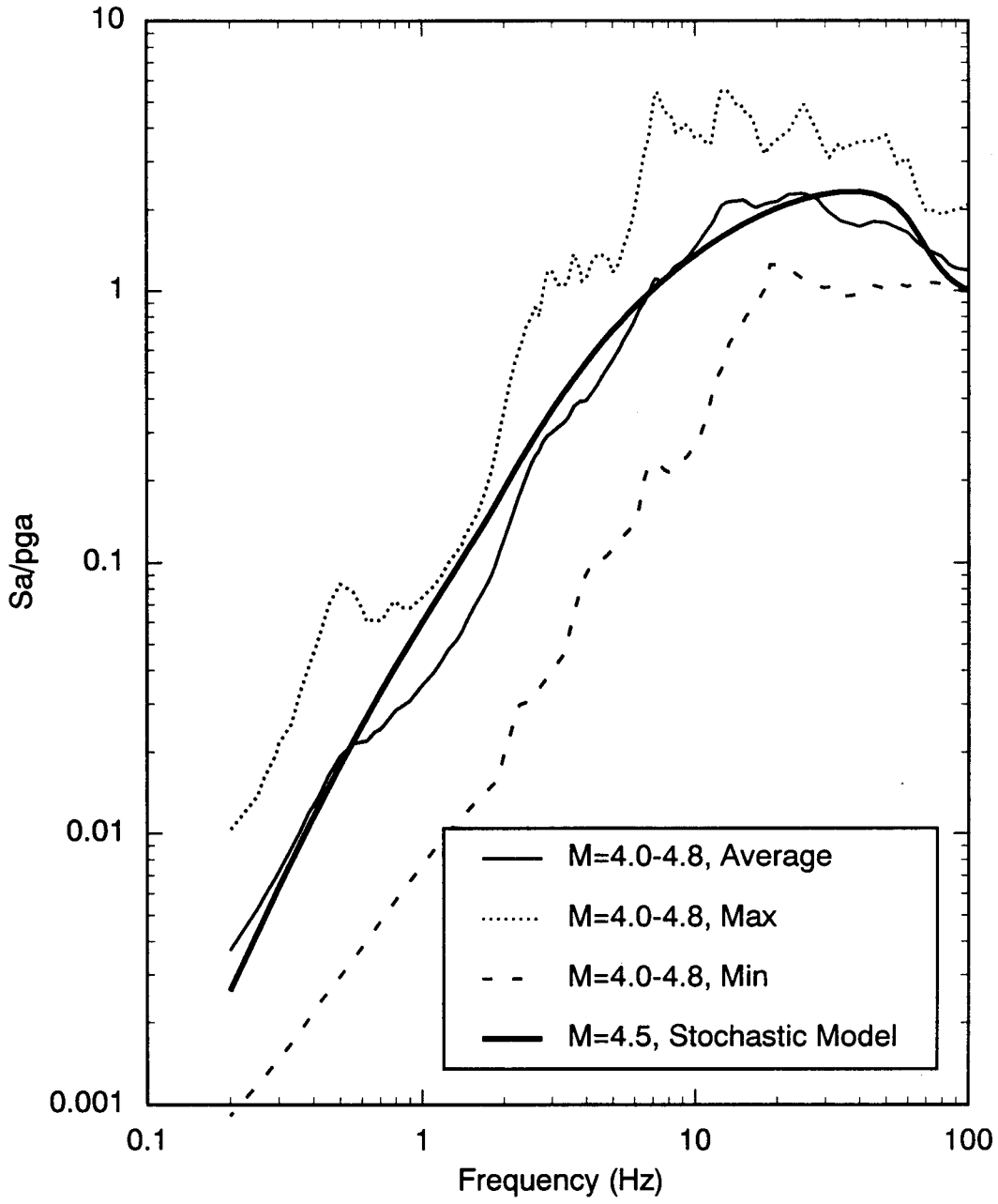

Figure 5-44. Comparison of recorded and predicted spectral shapes for ENA hard rock sites for M 4.0–4.8.

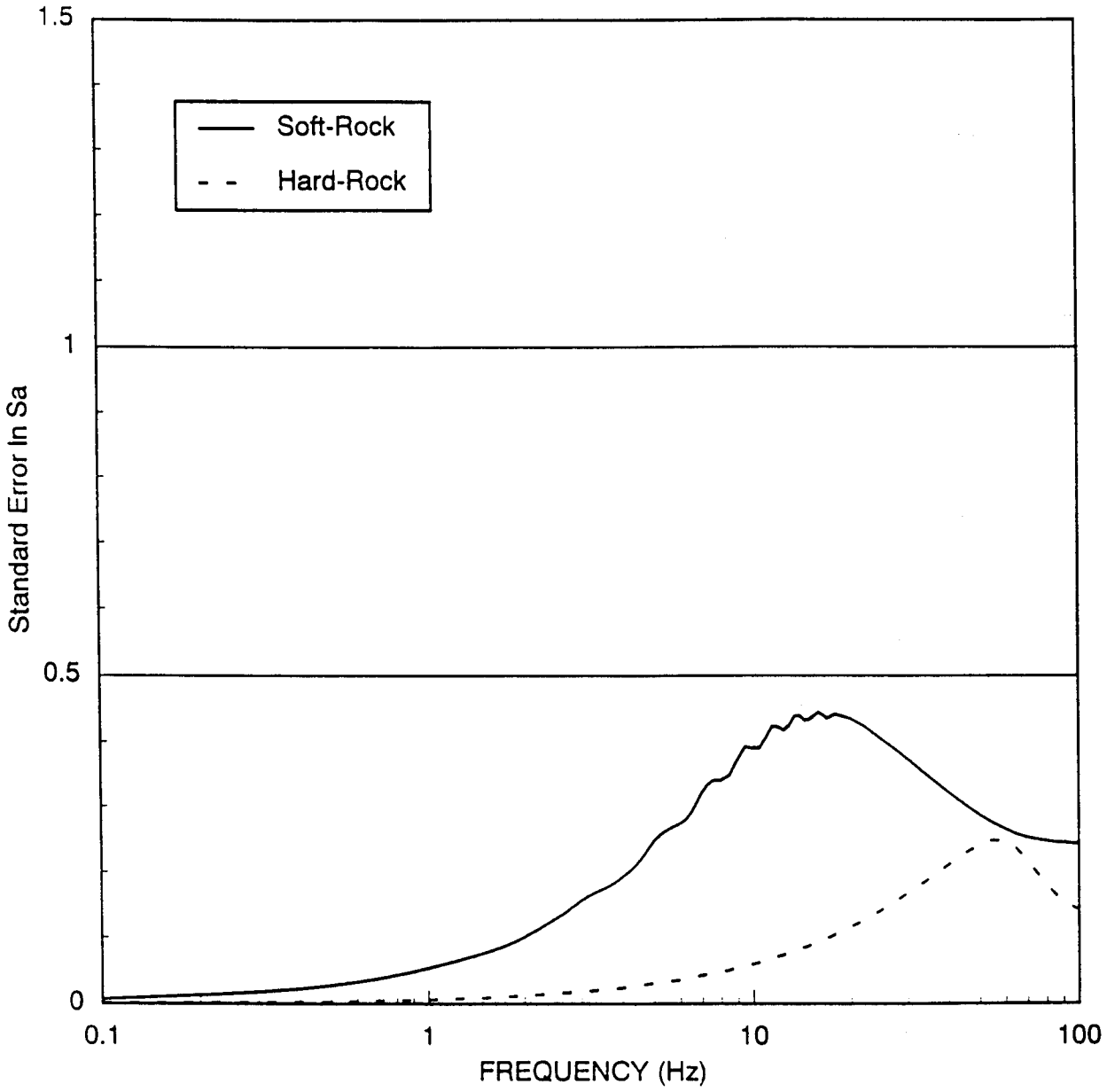

Figure 5-45. Effect of variability of kappa on the variability of spectral acceleration.

5.5 Ground Motion Regionalization

The objective of this section is to determine how the regional variation of velocity structure, Q, and focal depth, discussed previously can best be implemented into a general attenuation relation for modeling ground motion attenuation in the EUS.

5.5.1 Approach

The philosophy used in determining the number of regions with distinct ground motion attenuation considered 4 factors: the ground motion differences should have both statistical and practical significance; the differences should be systematic; and the modeled differences should be robust.

For the ground motion differences to be of statistical significance, variations in the mean ground motion must be resolvable given the randomness of the focal depth and the uncertainty of the Q model for each region. For the differences to be of practical significance, variations in the mean ground motion must be large enough to warrant modeling them given the size of the uncertainty of ground motion within a region. For the differences to be systematic, they should be consistent over a range of distances and periods.

For each of the 16 regions shown in Figure 5-12, numerically simulated ground motions were generated using the generalized ray method described in Section 3.3. These simulations were examined to determine the number of regions with distinct ground motion attenuation.

A non-parametric attenuation relation was estimated for the response spectral values for each frequency and region. Each frequency was fit independently and the variability in focal depth and intra-regional variation in Q were included. This gave a mean attenuation relation and the variance of the mean for the log spectral values. This variance represents the intra-regional variation. The non-parametric relations were computed at 10 km distance intervals and at the following frequencies: 1.0, 1.5, 2.5, 3.45, 5.0, 7.5, 10, 15, 25, and 34 Hz. These non-parametric relations were compared to each other to determine the number of distinct regions. The criteria for determining distinct regions is given below.

5.5.2 Description of Criteria

The initial criteria used to define significant differences in ground motion are as follows:

1. The differences in the medians must be significant at the 95% confidence level.
2. The difference in the medians must be greater than 20 percent.
3. Criteria 1 and 2 must be met for 3 consecutive distances and frequencies and the polarity of the difference in the medians must also be consistent over this distance and frequency range. (For this analysis, the distance criterion corresponds to a 30 km range.)

The robustness of the modeled differences is checked by varying these criteria and by using different focal depth distributions.

5.5.3 Results

Examples of the median spectral acceleration at 5 Hz for each of the 16 regions is shown in Figure 5-46 for the EAA depth distribution for combined margins and non-margins (denoted h2). These ground motions include effects of both velocity structure and Q. This figure shows that some of the regions exhibit different attenuation from the average. For example, region 4 (Gulf Coast) has very different attenuation. The attenuation relations for all of the 16 regions are compared quantitatively below.

For the initial comparison, the attenuation for each region is compared to the attenuation for every other region. The results of this initial comparison of the attenuation for the 16 regions is summarized in a correlation matrix shown in Table 5-14. In this table, a 1 indicates that the attenuation for the pair of regions is not significantly different according the defined criteria (correlated), whereas a 0 indicates that attenuation is significantly different (uncorrelated).

Using the correlation matrix, the regions are combined into larger groups with similar (not distinct) attenuation. This grouping is done with the goal of finding a base group that contains as many regions as possible. The remaining regions are then grouped by minimizing the total number of groups needed to include all the regions. This initial grouping led to 3 attenuation groups listed below.

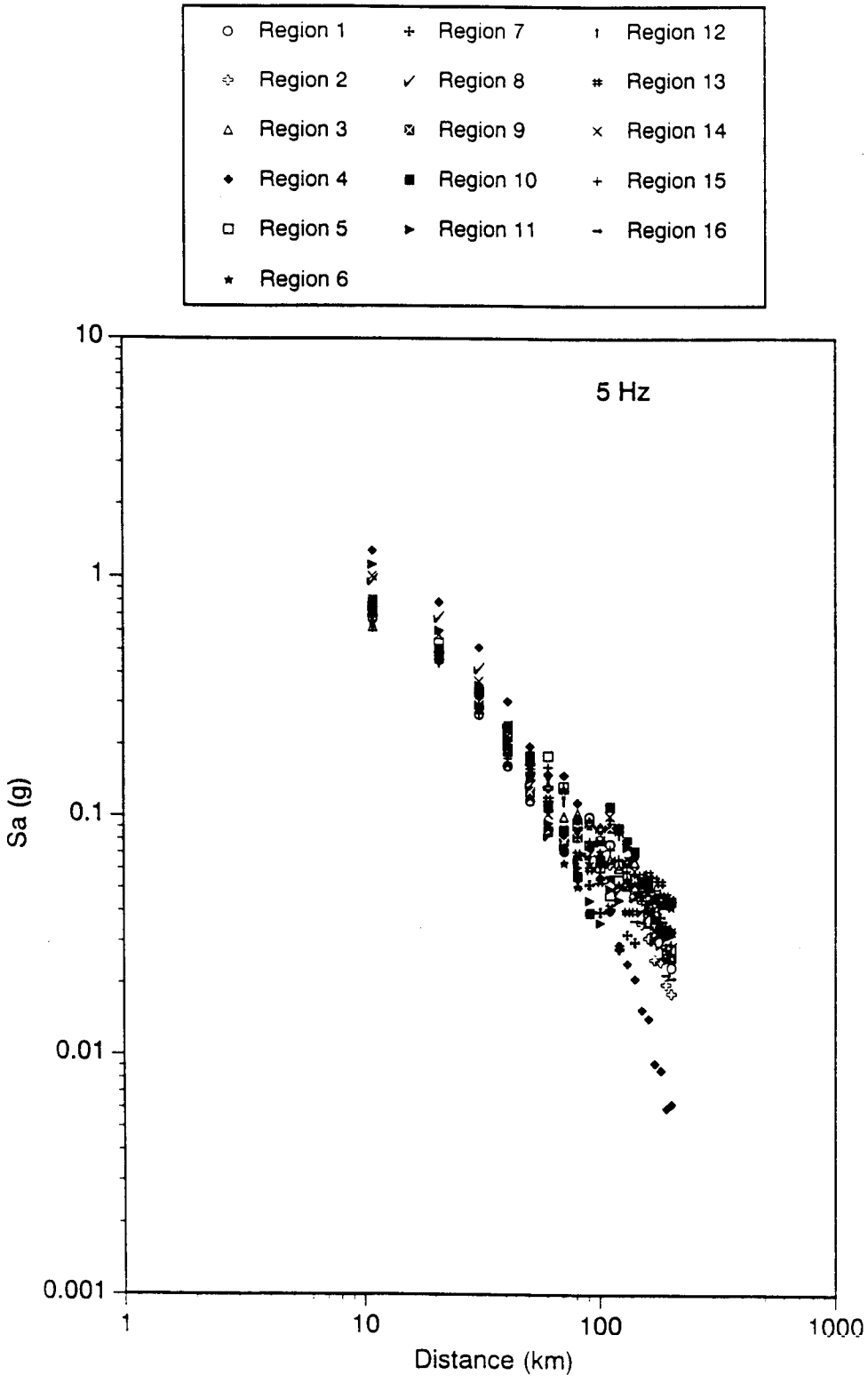

Figure 5-46. Comparison of median ground motion attenuation of spectral acceleration at 5 Hz for the 16 regions.

Table 5-14

Correlation Matrix for Ground Motion Attenuation Between Regions

	Regions															
Region	**1**	**2**	**3**	**4**	**5**	**6**	**7**	**8**	**9**	**10**	**11**	**12**	**13**	**14**	**15**	**16**
1	1	1	1	0	0	1	0	0	1	1	0	1	0	0	0	0
2	1	1	1	0	1	0	0	0	1	0	0	1	0	1	0	1
3	1	1	1	0	1	0	0	0	1	0	0	1	0	0	1	1
4	0	0	0	1	0	0	0	0	0	0	0	0	0	0	0	0
5	0	1	1	0	1	0	0	0	0	0	0	1	0	0	1	1
6	1	0	0	0	0	1	0	0	0	0	0	1	1	0	0	0
7	0	0	0	0	0	0	1	0	0	0	0	0	1	0	0	0
8	0	0	0	0	0	0	0	1	0	0	1	1	0	1	0	1
9	1	1	1	0	0	0	0	0	1	1	0	1	0	1	1	0
10	1	0	0	0	0	0	0	0	1	1	0	1	0	1	0	0
11	0	0	0	0	0	0	0	1	0	0	1	1	1	0	0	0
12	1	1	1	0	1	1	0	1	1	1	1	1	0	1	1	0
13	0	0	0	0	0	1	1	0	0	0	1	0	1	0	0	0
14	0	1	0	0	0	0	0	1	1	1	0	1	0	1	0	0
15	0	0	1	0	1	0	0	0	1	0	0	1	0	0	1	0
16	0	1	1	0	1	0	0	1	0	0	0	0	0	0	0	1

A 1 indicates the attenuation for the pair of regions is similar. A 0 indicates that the attenuation for the pair of regions is different.

Attenuation Group	Regions
1	1, 2, 3, 5, 8, 9, 10, 12, 14, 15, 16 (6,11)
2	4
3	7, 13 (6,11)

Regions 6 and 11 are on the border between groups 1 and 3.

For each group, the median ground motion is computed. Regions 6 and 11 are excluded from the group average for both group 1 and group 3 since they are borderline regions. The attenuation for the individual regions is then compared to average attenuation for each group and a new correlation matrix is produced showing the correlation between the attenuation for each region and the average attenuation for each group. To test the robustness of the correlations, this process was repeated for alternative depth distributions and different significance criteria. The alternative depth models are described in Appendix 5B.

The preferred depth distribution developed in Section 5.2.3 which distinguishes between margins and "other than margins" is depth distribution model h3 in Table 5-15. These two depth distributions (margins and "other than margins") form a single depth distribution model. Regions 1, 3, and 4 are considered margins and the remaining regions are "other than margins". The generic depth distribution developed in Section 5.2.3 which does not distinguish between margins and "other than margins" is depth distribution model h1 in Table 5-15. In considering multiple depth models, we do not compare

Table 5-15

Correlation Matrices for Ground Motion Attenuation Between Individual Regions and Group Averages

	h1			h2			h3		
Region	**G1**	**G2**	**G3**	**G1**	**G2**	**G3**	**G1**	**G2**	**G3**
1	0	0	0	0	0	0	1	0	0
2	1	0	0	1	0	0	1	0	0
3	1	0	0	1	0	0	0	0	0
4	0	1	0	0	1	0	0	1	0
5	1	0	0	1	0	0	1	0	0
6	0	0	0	1	0	1	0	0	0
7	0	0	1	0	0	1	0	0	1
8	1	0	0	0	0	1	1	0	0
9	1	0	0	1	0	0	1	0	0
10	0	0	0	0	0	0	0	0	0
11	1	0	1	0	0	1	1	0	0
12	1	0	0	1	0	0	1	0	0
13	0	0	1	0	0	1	0	0	1
14	1	0	0	0	0	0	0	0	0
15	1	0	0	1	0	0	1	0	0
16	0	0	0	0	0	0	0	0	0

Focal Depth Distributions (see Appendix 5B):
- h1 EAA (Generic)
- h2 ENA (Generic)
- h3 EAA (margins and other than margins) Margin Regions: 1,3,4
- h4 Atkinson (rifted and non-rifted) Rifted Regions: 8,11,2,10,12,14,15
- h5 Atkinson (rifted and non-rifted) Rifted Regions: 8, 11
- h6 Wheeler

Distinct Criteria:
1. Significant difference in mean at 95% confidence level.
2. Difference in median ground motion ≥ 20%.
3. Criteria 1 and 2 hold for 3 consecutive distances and frequencies with consistent polarity of difference.

Table 5-15 (Continued)

Correlation Matrices for Ground Motion Attenuation Between Individual Regions and Group Averages

	h4			h5			h6		
Region	**G1**	**G2**	**G3**	**G1**	**G2**	**G3**	**G1**	**G2**	**G3**
1	0	0	0	0	0	0	0	0	0
2	1	0	0	0	0	0	1	0	0
3	0	0	0	0	0	0	1	0	0
4	0	1	0	0	1	0	0	1	0
5	1	0	0	1	0	0	1	0	0
6	0	0	0	0	0	0	0	0	0
7	0	0	1	0	0	1	0	0	1
8	0	0	0	0	0	0	0	0	0
9	0	0	0	0	0	0	1	0	0
10	1	0	0	0	0	0	0	0	0
11	0	0	0	0	0	0	0	0	1
12	1	0	0	1	0	0	1	0	0
13	0	0	1	0	0	1	0	0	1
14	1	0	0	0	0	0	0	0	0
15	1	0	0	0	0	0	1	0	0
16	0	0	0	0	0	0	0	0	0

Focal Depth Distributions (see Appendix 5B):

- h1 EAA (Generic)
- h2 ENA (Generic)
- h3 EAA (margins and other than margins) Margin Regions: 1,3,4
- h4 Atkinson (rifted and non-rifted) Rifted Regions: 8,11,2,10,12,14,15
- h5 Atkinson (rifted and non-rifted) Rifted Regions: 8, 11
- h6 Wheeler

Distinct Criteria:

1. Significant difference in mean at 95% confidence level.
2. Difference in median ground motion ≥ 20%.
3. Criteria 1 and 2 hold for 3 consecutive distances and frequencies with consistent polarity of difference.

the ground motions computed for alternative depth distribution models, but rather consider the differences in attenuation between regions for a given depth distribution model.

The results using the initial criteria are summarized in Table 5-15. This table shows that regions 4, 7, 13, and 16 are distinct from the base group (G1) for all of the depth distributions considered. Region 4 defines its own group (G2) which is distinct from all other regions. Group 3, defined by regions 7 and 13 is indistinct from a few regions in the base group for some depth distributions. Region 16 is distinct from all three groups for all depth distributions; however, as will be shown below this result is not robust.

The attenuation of spectral acceleration at 5 Hz for the three groups is plotted in Figure 5-47. The difference between G1 and G2 is quite strong with G2 yielding less attenuation at short distances and more attenuation at large distances. The difference between G3 and G1 is primarily at the distance range of 80 to 150 km and is likely related to the depth of the Moho for regions 7 and 13.

To test the robustness of the regionalization, the criteria for determining distinct regions was varied. For small changes in the criteria, region 16 became indistinct from G1. For these same variations in criteria, regions 7 and 13 remain distinct for most of the depth distributions and region 4 remains distinct from G1 for all depth distributions.

The distinction between the attenuation for G1 and G3 is not as strong as the distinction between attenuation for G1 and G2. The difference between G1 and G3 is restricted to a limited distance range (80–150 km) and the ground motions for G3 are lower than the ground motions for G1 over this distance range. The G1 model yields a conservative estimate of the ground motion for G3. Therefore, for this project G3 is lumped with G1. As a result, two distinct ground motion attenuation regions are defined: the Gulf Coast (G2) and everything else (G1).

5.5.3.1 Selection of Representative Velocity Models

A velocity model representative of group 1 attenuation was found by comparing the attenuation of each of the regions within group 1 with the average attenuation for group 1. The variance of the difference between the ground motion for each region and the ground motion for the group average was computed. Regions 3 and 12 gave the smallest variances for multiple depth distributions. An example of the attenuation for these two regions is shown in Figure 5-48 for peak acceleration. Region 12 was selected as the representative velocity model for group 1. Group 2 is simply defined by region 4.

The attenuation of ground motion for the two distinct regions is compared in Figures 5-49a, b, c. The Gulf Coast region (G2) has larger motions at short distances and lower motions at large distances compared with the Mid-continent region (G1). The Gulf Coast attenuation does not exhibit a flattening of the attenuation relation at 80 to 130 km that is seen for the Mid-continent region.

5.5.4 Possible Benefits of Finer Regionalization

Although group G3 was not used in this study, for sites in these regions there are possible benefits to using a finer regionalization that includes a distinct attenuation region, G3. In particular, the attenuation for G3 produces lower ground motion for the distance range of 80 to 150 km. If this distance range is of importance to a particular site then it would be beneficial to use a region specific ground motion model.

For G3, the ground motion difference at distances of 80 to 150 km is up to a factor of 1.5 smaller than for the base model. The effect on the hazard depends on the location of the seismic sources; therefore, the decision to develop a G3 attenuation relation would be a site-specific consideration.

5.5.5 Treatment of Regions With Low Near-Surface Velocities

The coastal margin of the Gulf Coast from the Mississippi Delta to East Texas has lower seismic velocities and a higher velocity gradient in the upper crust than those of the general crustal model that was used to represent the Gulf Coast Region as a whole. Therefore, the Gulf Coast ground motion attenuation relation developed in Section 9 may not be applicable to the coastal margin of the Gulf Coast. A crustal model that represents the coastal margin was developed by replacing the 7 km thick top layer of the initial model with two layers. The revised model is listed together with the general model in Table 5-16. Sites in the coastal margin of the Gulf Coast should consider the effects of this coastal margin velocity structure model on the predicted ground motions.

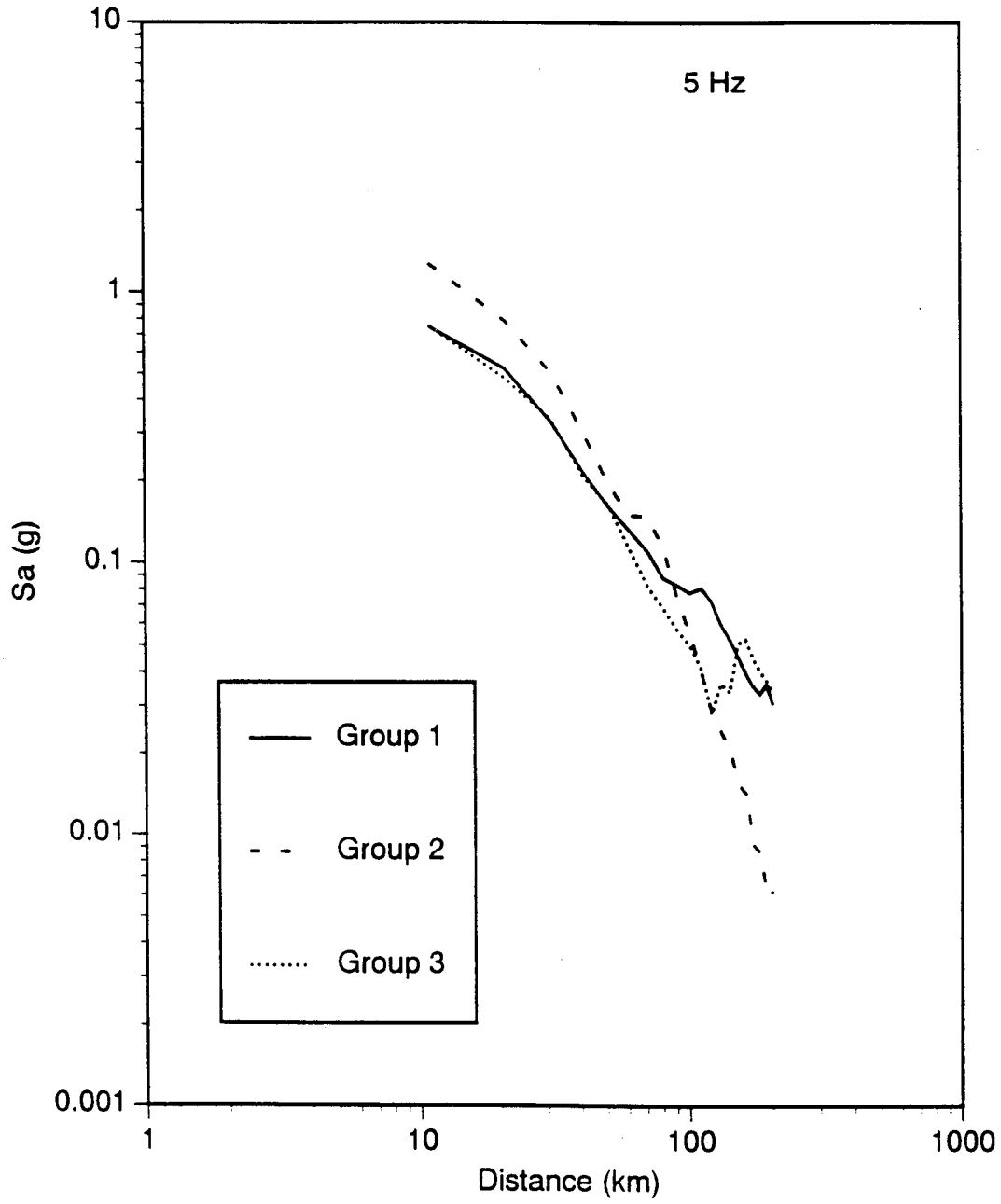

Figure 5-47. Comparison of median ground motion attenuation of spectral acceleration at 5 Hz for the three attenuation groups.

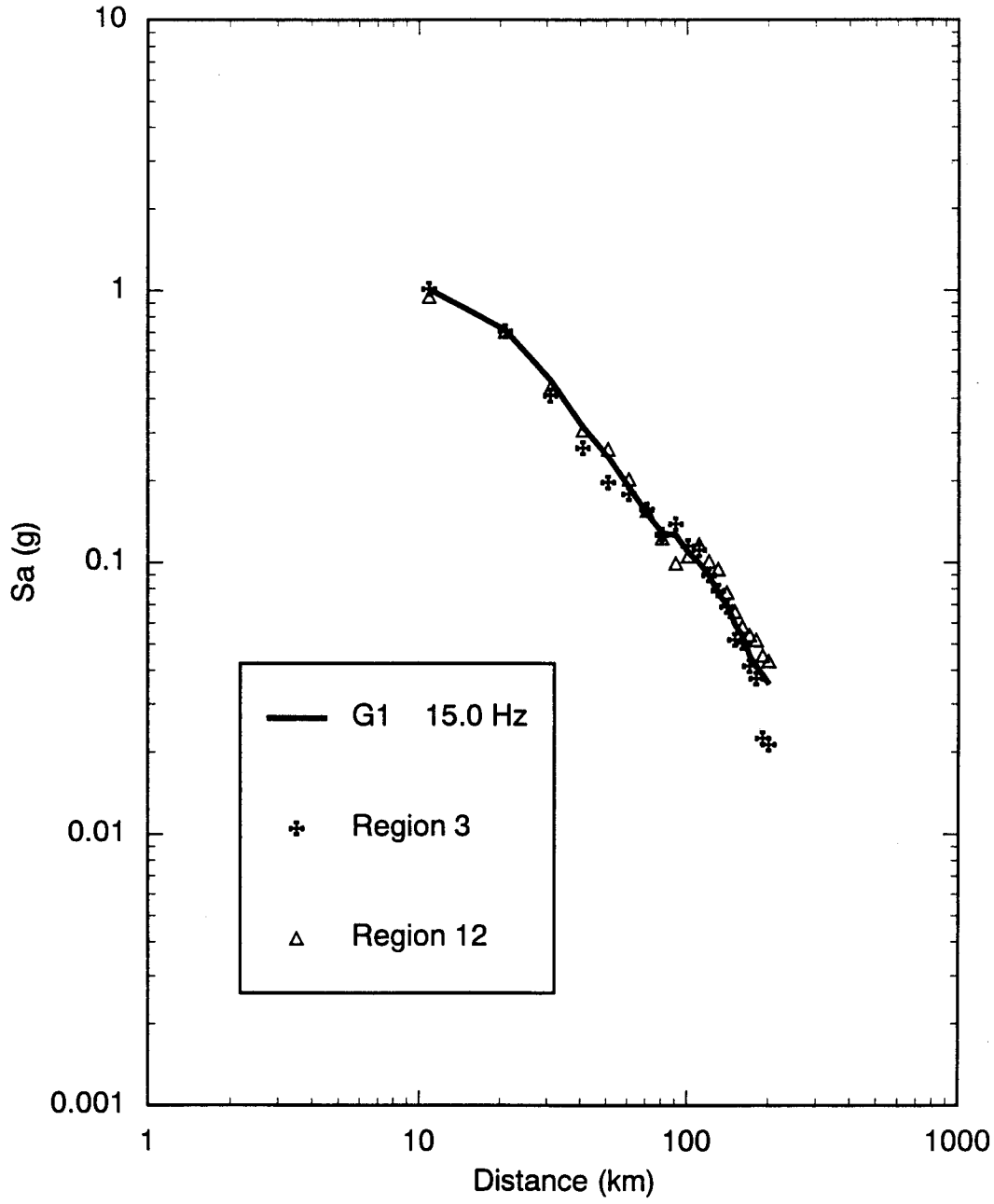

Figure 5-48. Comparison of G1 attenuation of spectral acceleration at 5 Hz with the attenuation for regions 3 and 12. Over all frequencies, the velocity structure for region 12 best approximates the attenuation for G1.

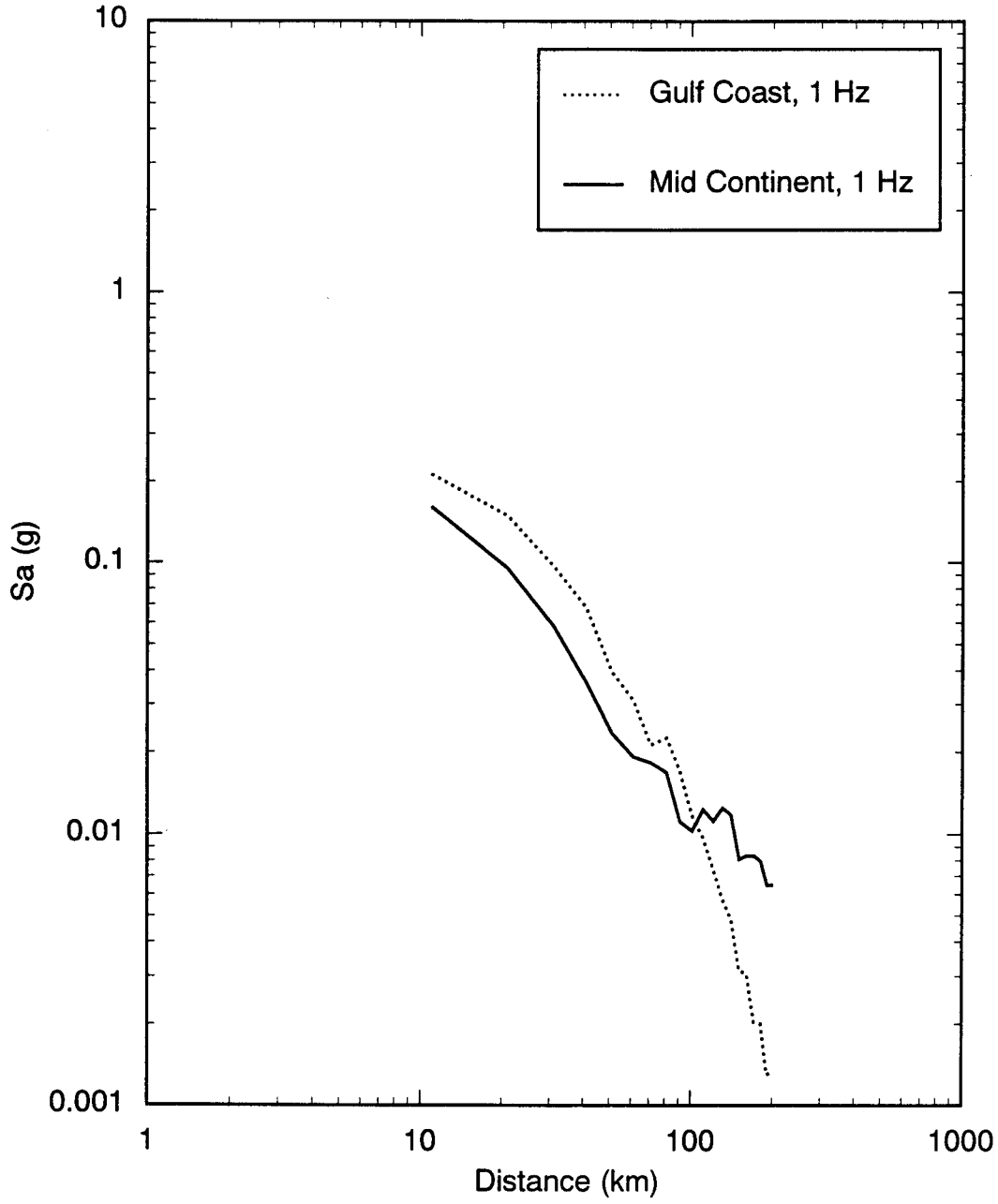

Figure 5-49a. Comparison of G1 and G2 attenuation of spectral acceleration at 1 Hz.

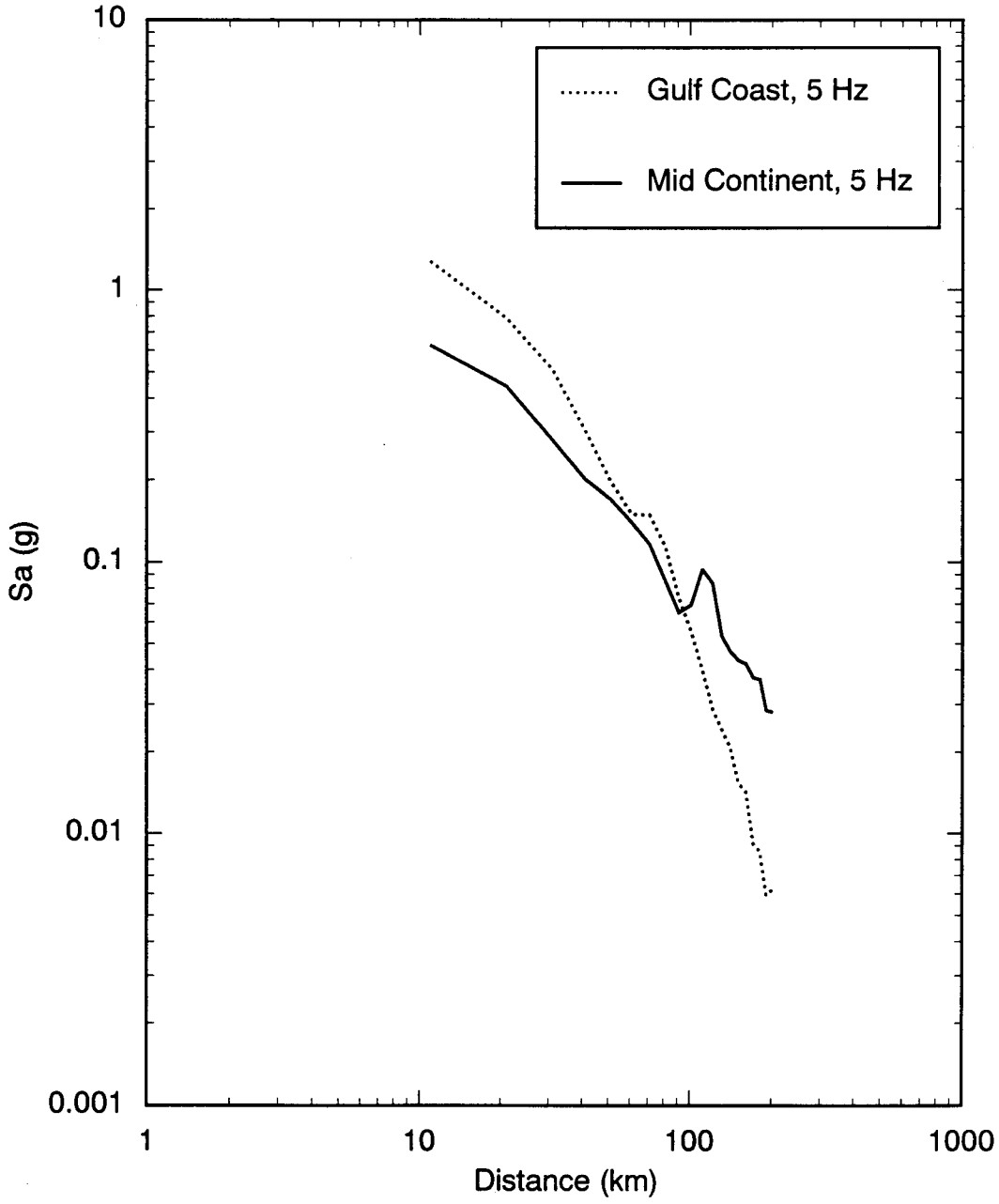

Figure 5-49b. Comparison of G1 and G2 attenuation of spectral acceleration at 5 Hz.

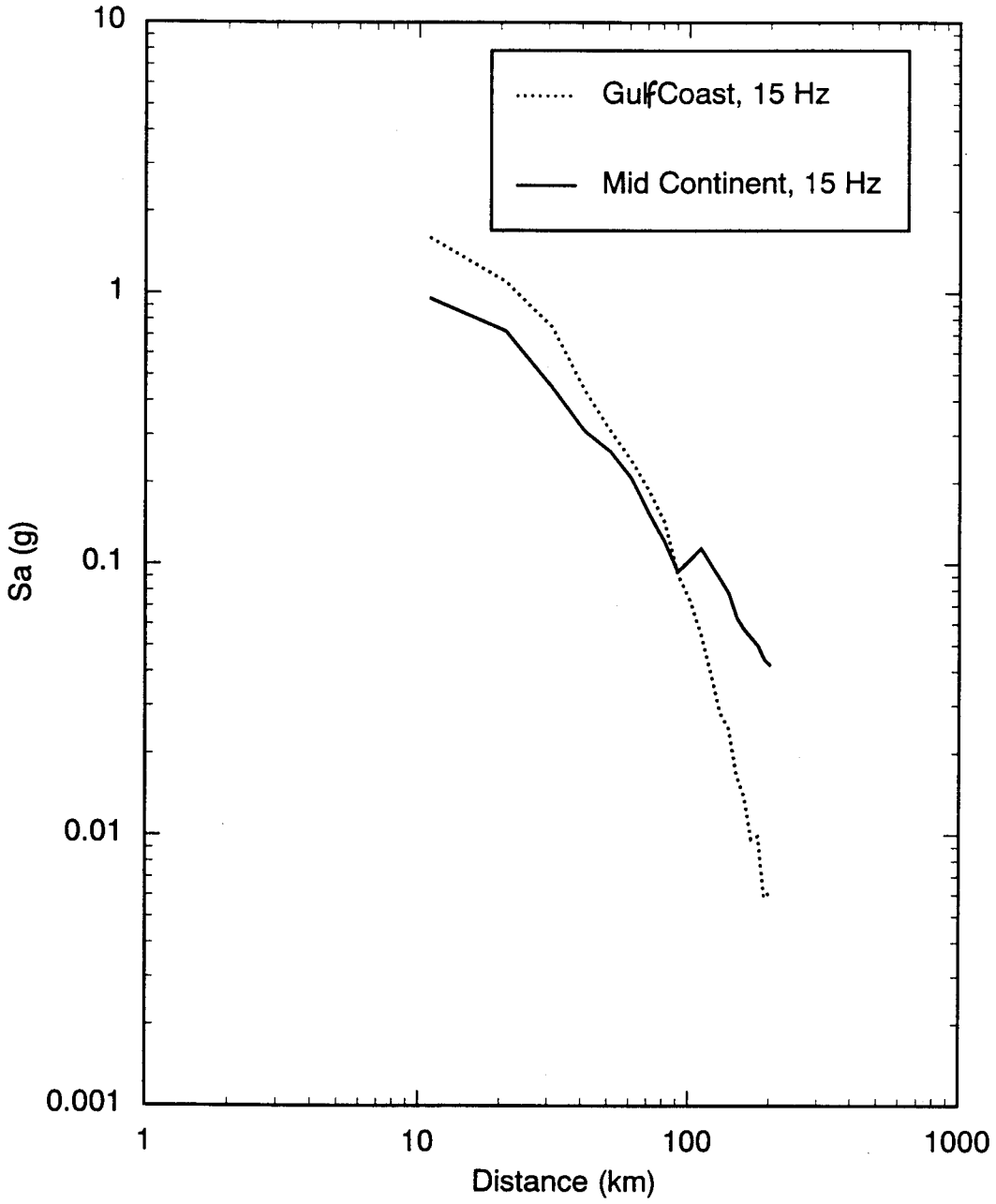

Figure 5-49c. Comparison of G1 and G2 attenuation of spectral acceleration at 15 Hz.

Table 5-16

Gulf Coastal Plain

Vp (km/sec)	Vs (km/sec)	Density (gm/cc)	Thickness (km)	Depth to Top
		General Model		
4.0	2.31	2.37	7	0
5.3	3.05	2.58	8	7
6.5	3.76	2.7	15	15
8.2	4.74	3.40	—	30
		Coastal Margin Model		
2.2	0.82	2.00	3	0
3.4	1.82	2.27	4	3
5.3	3.05	2.58	8	7
6.5	3.76	2.78	15	15
8.2	4.74	3.40	—	30

The coastal margin may have some amplifications above the G2 model ground motions due to low velocities near the surface. One alternative approach is to use the G1 rock attenuation with the deep soil site amplifications from Section 6.

5.6 Q Models for the Two Attenuation Regions

The analysis of regional differences in ground motion attenuation in Section 5.5 used a regionalization of the Q that was self-consistent but not necessarily consistent with the semi-empirical simulation procedure. This was acceptable in that analysis because we were interested in the relative differences in the ground motion attenuation and not in the absolute values. However, this is not the case when the simulated motions are used to derive an attenuation relation (Section 9). Therefore, Q models that are consistent with the geometrical spreading term used with the stochastic simulation procedure are developed for the two attenuation groups (G1 and G2) determined in Section 5.5.

The background region, G1, is represented by the Mid-continent velocity structure. Q models for the EUS from various studies that used geometrical spreading terms similar to that computed for the Mid-continent velocity structure at large distances are shown in Figure 5-50. Based on these studies, median, high, and low Q models were developed. They are shown by the dashed lines in Figure 5-50. The selected Q models used in the simulations are listed in Table 5-17.

Region G2 is represented by the Gulf Coast velocity structure. Fewer Q models from other studies are available for this region. Two Q models from other studies using geometrical spreading terms similar to the stochastic model are also shown in Figure 5-51. For comparison, the Q model estimated for the Loma Prieta earthquake by inversion of the Fourier amplitude spectra (Section 3) is also shown. The Q for the Gulf Coast is closer to a WUS Q than it is to typical EUS Q. Based on these models, median, high, and low Q models were developed. Median, high, and low Q models are shown by the dotted lines in Figure 5-51. The selected Q models used in the simulations are listed in Table 5-17.

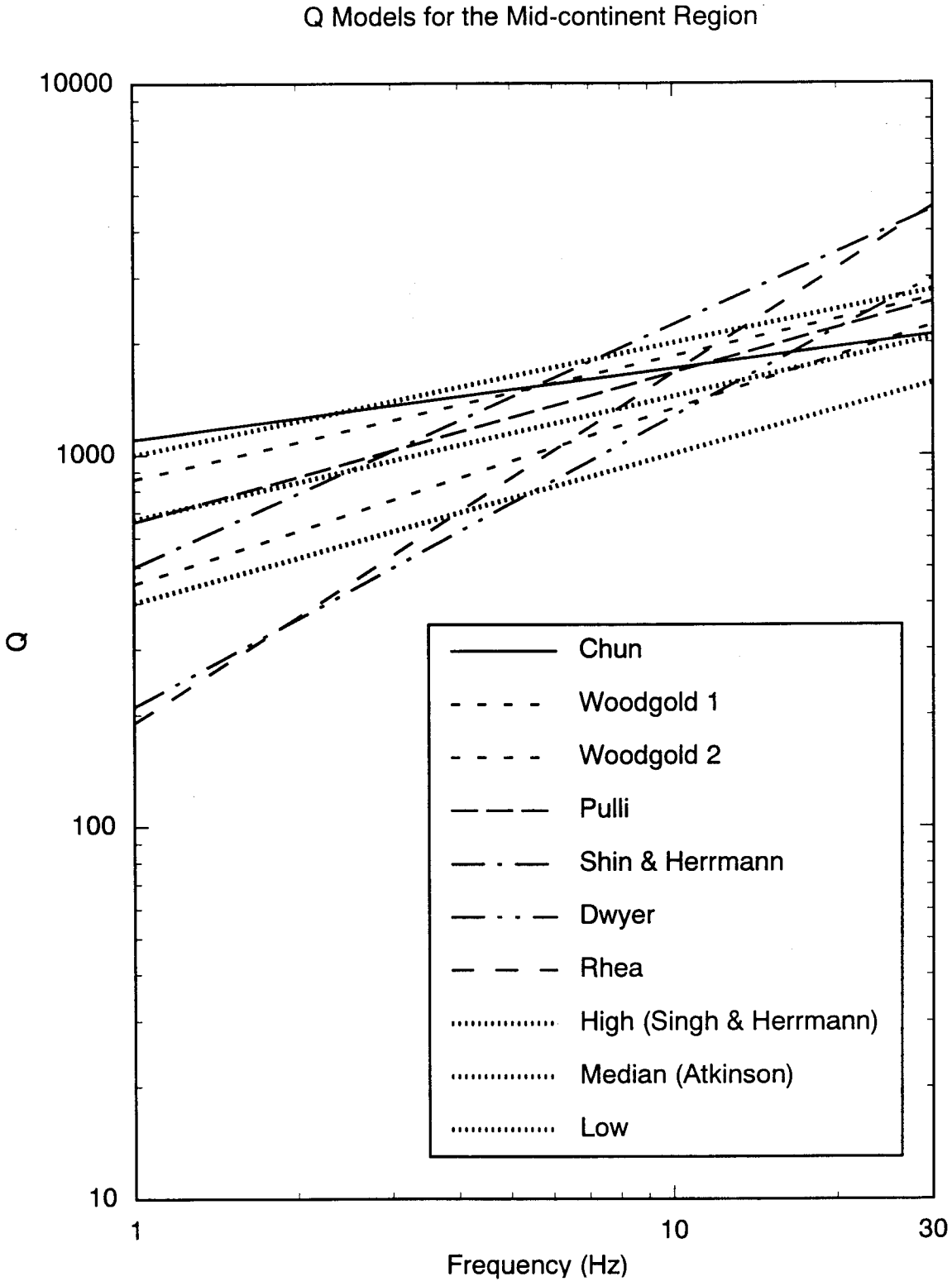

Figure 5-50. Q models for the Mid-continent region. The dashed lines are the median, high, and low Q models used to generate the ground motions analyzed in Section 9.

Table 5-17

Q Models Used with the Stochastic Simulation Procedure

	Mid-continent		Gulf Coast	
	Q_0	η	Q_0	η
high	1000	0.3	500	0.3
median	670	0.33	300	0.3
low	400	0.4	200	0.3

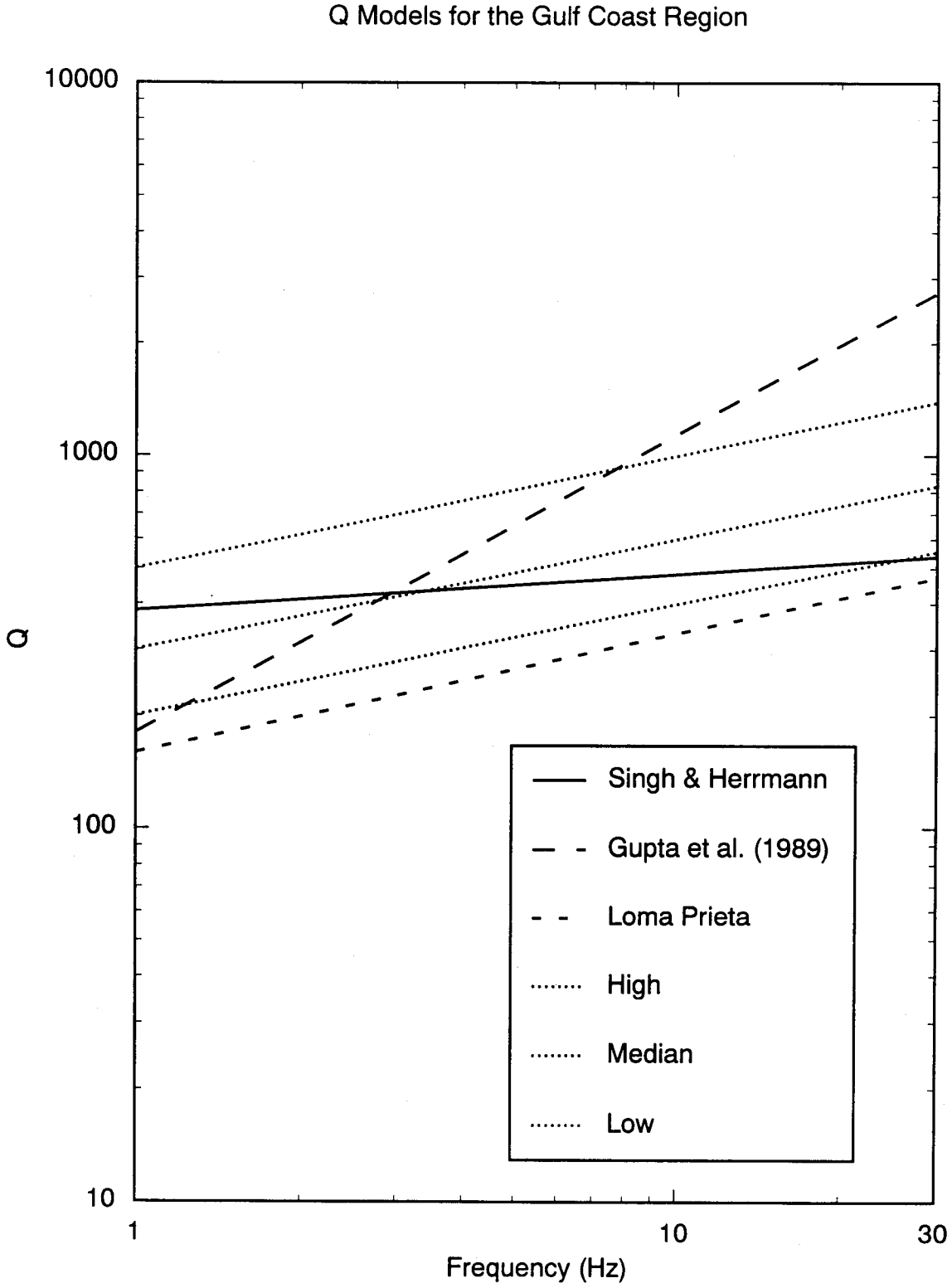

Figure 5-51. Q models for the Gulf Coast region. The dashed lines are the median, high, and low Q models used to generate the ground motions analyzed in Section 9.

References

Abrahamson, N.A., P.G. Somerville, and C. Allin Cornell (1990). Uncertainty in numerical strong motion predictions, *Proc. 4th National U.S. Conference on Earthquake Engineering*, Palm Springs, I, 407–416.

Anderson, J.G. and S. E. Hough (1984). A model for the shape of the Fourier amplitude spectrum of acceleration at high frequencies, *Bull. Seism. Soc. Am.* 74, 1961–1993.

Atkinson, G.M. and R.F. Mereu (1992). The shape of ground motion attenuation in southeastern Canada, *Bull. Seism. Soc. Am.* 82, 2104–2031.

Atkinson, G.M. (1993). Earthquake source spectra in Eastern North America, submitted to Bull. Seism. Soc. Am.

Berry, M.J. and K. Fuchs (1973). Crustal structure of the Superior and Grenville provinces of the northeastern Canadian Shield, *Bull. Seism. Soc. Am.* 63, 1393–1432.

Bickford, M.E., W.R. Van Schmus, and I. Zietz (1986). Proterozoic history of the midcontinent region of North America, *Geology*, Vol. 14, pp. 492–496.

Boore, D. M. and G. M. Atkinson (1987). Stochastic prediction of ground motion and spectra response parameters at hard-rock sites in eastern North America, *Bull. Seism. Soc. Am.* 77, 440–467.

Braile, L.W. (1989). Crustal structure of the continental interior, in Pakiser, L.C., and W.D. Mooney, eds., *Geophysical framework of the continental United States, Geologic Society of America memoir 172*, Boulder, Colorado, pp. 285–315.

Braile, L.W., W. J. Hinze, R. R. B. von Freze, and G. R. Keller (1989). Seismic properties of the crust and uppermost mantle of the conterminous United States and adjacent Canada, in Pakiser, L.C., and W.D. Mooney, eds., *Geophysical framework of the continental United States, Geologic Society of America memoir 172*, Boulder, Colorado, pp. 655–680.

Burger, R.W., P.G. Somerville, J.S. Barker, R.B. Herrmann, and D.V. Helmberger (1987). The Effect of Crustal Structure on Strong Ground Motion Attenuation Relations in Eastern North America, *Bull. Seism. Soc. Am.*, 77, 420–439.

Chun, Y. K., G. F. West. R. J. Kokoski, and C. Samson (1987). A novel technique for measuring Lg attenuation: results from eastern Canada between 1 to 10 Hz, *Bull. Seism. Soc. Am.*, 77, 398–419.

Cram, I.H. (1961). A crustal structure refraction survey in South Texas, *Geophysics 26*, 560–573.

Cranswick, E., R. Wetmiller, and J. Boatwright (1985). High-frequency observations and source parameters of microearthquakes recorded at hard-rock sites, *Bull. Seism. Soc. Am.*, 75, 1535–1567.

Dobrin, M.B. (1976). *Introduction to Geophysical Prospecting*, McGraw-Hill Inc., third edition.

Dorman, J., J. Lamar Worzel, R. Leyden, T.N. Crook, and M. Hatziemanuel (1972). Crustal section from seismic refraction measurements near Victoria, Texas, *Geophysics 37*, 325–336.

Dwyer, J. J., R. B. Herrmann, and O. W. Nuttli (1984). Use of a digital seismic network to study regional Lg attenuation and coda Q in the central Mississippi Valley, *Earthquake Notes*, 55, 7–8.

Ebeniro, J.O., Y. Nakamura, D.S. Sawyer and W.P. O'Brien (1988). Sedimentary and crustal structure of the northwestern Gulf of Mexico, *J. Geophys. Res. 93*, 9075–9092.

EPRI (1986). Bouguer Gravity Anomalies Map, Plate 11, EPRI Seismic Hazard Research Program, Data Management Project, RP2556.

Ginzburg, A., W. D. Mooney, A. W. Walter, W. J. Lutter, and J. H. Healy (1983). Deep structure of the northern Mississippi Embayment, *American Association of Petroleum Geologists Bulletin 67*, 2031–2046.

Grant, F. S. and G. F. West (1965). *Interpretation Theory in Applied Geophysics*, New York, McGraw-Hill.

Gupta, I. N, K. L. McLaughlin, R. A. Wager, R. S. Jih, and T. W. McElfresh (1989). *Seismic wave attenuation in eastern North America*, EPRI Report NP-6304.

Harr, L. C., J. B. Fletcher, and C. S. Mueller (1984). The 1982 Enola, Arkansas, swarm and scaling of ground motion in the eastern United States, *Bull. Seism. Soc. Am.*, 74, 2463–2482.

Helmberger, D.V. and D.G. Harkrider (1978). Modeling earthquakes with generalized ray theory, Proc. IUATM Symposium: *Modern Problems in Elastic Wave Propagation*, Wiley, New York, 499–518.

James, D.E., T.J. Smith, and J.S. Steinhart (1968). Crustal structure of the middle Atlantic states, *J. Geophys. Res. 73*, 1983–2008.

Johnston, A. C. (1993). *The stable continental interior data base, in The Earthquakes of Stable Continental Regions: an Assessment of Large Earthquake Potential*, EPRI Report TR 102261.

Lash, C.C. (1980). Shear waves, multiple reflections, and converted waves found by a deep vertical wave test (vertical seismic profiling), *Geophysics*, 45, 1373–1411.

McCamy, K. and R.P. Meyer (1966). Crustal results of fixed multiple shots in the Mississippi Embayment, in Steinhart, J.S. and Smith, T.J., Eds., *AGU Geophysical Monograph 10*, 166–180.

Mereu, R. et al. (1986). The 1982 COCRUST seismic experiment across the Ottawa-Bonnechere graben and Grenville Front in Ottawa and Quebec, *G.J.R. Astron. Soc. 84*, 491–514.

Mooney, W.D. and L.W. Braile (1989). The seismic structure of the continental crust and upper mantle of North America, in Bally, A.W. and A.R. Palmer, eds., *The Geology of North America—An Overview, The Geology of North America*, Vol. A, Geological Society of America, Boulder, Colorado, pp. 39–52.

Pakiser and Mooney (1989). Tectonic framework of the Coterminous United States, *Bull. Geol. Soc. Am.*

Pratt, T.L., C Coruh, J.K. Costain and L. Glover (1988). A geophysical study of the earth's crust in central Virginia: implications for Appalachian structure, *J. Geophys. Res. 93*, 6649–6667.

Pulli, J. J. (1984). Attenuation of coda waves in New England, *Bull. Seism. Soc. Am.*, 74, 1149–1166.

Rhea, S. (1984). Q determined from local earthquakes in the South Carolina coastal plain, *Bull. Seism. Soc. Am.*, 74, 2257–2268.

Saikia, C.K., P.G. Somerville, D.V. Helmberger, M.K. Sen, J.P. McLaren, L.J. Burdick, and N.F. Smith (1992). *Ground motion attenuation and earthquake source scaling in eastern North America*, Electric Power Research Institute, TR-100409, Tier 2, Research Project 2556-6, Final Report, Palo Alto, California.

Saikia, C.K. (1992). Ground motions in greater Los Angeles due to a magnitude 7.0 earthquake on the Elysian Thrust Fault, *Bull. Seism. Soc. Am.*, 80, submitted.

Shin, T. C. and Herrmann (1987). Lg attenuation and source studies using 1982 Miramichi data, *Bull. Seism. Soc. Am.*, 77, 384–397.

Silva, W. J. and R. Darragh (1993). *Engineering characterization of earthquake strong ground motion recorded at rock sites*, Electric Power Research Institute, Report TR-102261.

Singh, S. and R. B. Herrmann (1983). Regionalization of crustal coda Q in the continental United States, *J. Geophys. Res.*, 88, 527–538.

Somerville, P. G., J. P. McLaren, C. K. Saikia, and D. V. Helmberger (1990). The 25 November 1988 Saguenay, Quebec Earthquake: Source Parameters and the Attenuation of Strong Ground Motion, *Bull. Seism. Soc. Am.*, 80, 1118–1143.

Taylor, S.R. (1989). Geophysical framework of the Appalachians and adjacent Grenville Province, in Pakiser, L.C., and W.D. Mooney, eds., *Geophysical framework of the continental United States, Geological Society of America Memoir 172*, Boulder, Colorado, pp. 317–348.

Trehu, A.M., K.D. Klitgord, D.S. Daywer, and R.T. Buffler (1989). Atlantic and Gulf of Mexico continental margins, in Pakiser, L.C. and Mooney, W.D. (eds), *Geophysical Framework of the Continental United States, Geological Society of America Memoir 172*, 349–382.

Wald, D. J., P.G. Somerville, and N.F. Smith (1992). A test of the predictability of the near-source ground accelerations of the 1989 Loma Prieta earthquake, submitted for publication.

Wald, D. J., L.J. Burdick and P.G. Somerville (1988a). Simulation of acceleration time histories close to large earthquakes, in Von Thun, J.L. (ed)., Proceedings of the Earthquake Engineering and Soil Dynamics II Conference, *American Society of Civil Engineers, Geotechnical Special Publication No. 20*, 430–444.

Wald, D. J., P.G. Somerville and L.J. Burdick (1988b). The Whittier Narrows, California earthquake of October 1, 1987 —simulation of recorded accelerations, *Earthquake Spectra 4*, 139–156.

Wesson, R. L. and C. Nicholson (1986). Studies of the January 31, 1986 northeastern Ohio earthquake, U.S. Geol. Surv. Open-File Report 86–331.

Wheeler, R. L. and A. C. Johnston (1993). Geological implications of earthquake source parameters in central and eastern North America, *Seism. Res. Let.*, 63, 491–514.

Woodgold (1990). Estimation of Q in eastern Canada using coda waves, *Bull. Seism. Soc. Am.*, 80, 411–429.

Woodward-Clyde Consultant (1991). Regionalization of crustal structure in Eastern North America, Draft Report to EPRI.

6

QUANTIFICATION OF SITE EFFECTS

6.1 Introduction

The objective of this section is to develop and present soil amplification factors for 5% damped response spectra, peak acceleration, and peak particle velocity which may be applied to the ground motion model of Section 9 to accommodate the effects of soils on a generic basis. A set of five generic soil categories ranging in depth from 20 ft to 500 ft are presented as well as depth dependent modulus reduction and damping curves. One-dimensional equivalent-linear site response analyses are used to develop median and 1 sigma estimates of the soil response. The amplification factors are computed for control motions with Eastern North America characteristics and vary in level from 0.05g to 1.25g. In addition, preliminary results are presented for the vertical-to-horizontal (V/H) ratio at both rock and soil sites. Based on these results, guidelines are presented for computing vertical motions for the Midcontinent and Gulf Coast crustal structures as well as the five soil site categories.

A set of generic modulus reduction and damping curves reflecting the effects of confining pressure are used in the site response analyses. The curves are developed in Appendix 7.A based on laboratory testing results presented in Section 8.

The major issues in predicting the effects of site response to strong ground motion have been evaluated in Appendix 6-B. These issues include the adequacy of the vertically propagating shear-wave model, the in situ strain dependencies of dynamic material properties, and how the effects of material nonlinearities are treated computationally (i.e., nonlinear analyses versus equivalent-linear analyses). To evaluate these factors, nonlinear analyses using computer codes DESRA-2C, SUMDES, and TESS were compared to equivalent-linear analyses and to recorded strong ground motions at three reference sites; Gilroy 2, Treasure Island, and the Lotung, Taiwan LSST site. The analyses used geotechnical site models based on laboratory testing of undisturbed samples and geophysical surveys. In addition, the analysis procedures were compared to each other using synthetic control motions ranging from 0.50 to 1.25g with the 120 ft Category 3 shear-wave velocity profile (Section 6.3.3).

The results of the analyses comparison and validation with recorded motions indicate that conventional one-dimensional site response analyses incorporating nonlinear soil behavior based upon careful laboratory testing and with reasonably accurate soil profiles can accurately predict the effects of soils. Additionally, for the profiles and motions studied, little difference was seen between fully nonlinear and equivalent-linear analyses. Based upon these results, the equivalent-linear approach is used in the following analyses.

6.2 Overview

Observations of the effects of the ground on shaking during earthquakes have a long history. Del Barrio, in the 1855 Proceedings of the University of Chile states[1] "...a movement...must be modified while passing through media of different constitutions. Therefore, the earthquake effects will arrive to the surface with higher or lesser violence according to the state of aggregation of the terrain which conducted the movement. This seems to be, in fact, what we have observed in the Colchagua Province (of Chile) as well as in many other cases" (Del Barrio, 1855). In 1862, Mallet (1862) noted the effect of

1. Translated from the old Spanish by Professor Ricardo Dobry.

geology upon earthquake damage. Milne (1908) observed that in soft "damp" ground it was easy to produce vibrations of large amplitudes and long duration, while in rock it was difficult to produce vibrations of sufficient amplitude to be recorded.

Wood (1908) and Reid (1910), using apparent intensity of shaking and distribution of damage in the San Francisco Bay area during the 1906 earthquake, gave evidence that the severity of shaking can be substantially affected by the local geology and soil conditions. Gutenberg (1927, 1957) developed amplification factors representing different site geology by examining recordings of microseisms and earthquakes from instruments located on various types of ground.

Figure 6-1 shows average spectral shapes (response spectral acceleration divided by peak acceleration) computed from recordings made on rock and soil sites at close distances to earthquakes in the magnitude range of about **M** 6 to 7. The differences in spectral shapes are significant and depend strongly upon the general site classifications. These variations in spectral content represent average site dependent ground motion characteristics and result from vertical variations in soil material properties (Hayashi et al., 1971; Mohraz, 1976; Seed et al., 1976). Due primarily to the limited number of records from earthquakes of different magnitudes, spectral content in terms of response spectral shapes was for some time interpreted not to depend upon magnitude nor distance, but primarily on the stiffness and depth of the local soil profile. However, with an increase in the strong motion database, it has become apparent that spectral shapes depend strongly upon magnitude as well as site conditions (Joyner and Boore, 1982, Idriss, 1985; Silva and Green, 1989), and distance (Silva and Green, 1989), and that site effects extend to rock sites as well (Boatwright and Astrue, 1983; Campbell 1981, 1985, 1988; Cranswick et al., 1985; Silva and Darragh, 1993).

Examples of differences in spectral content largely attributable to one-dimensional site effects at rock sites can be seen in comparisons of response spectral shapes computed from motions recorded in both active and stable tectonic regions (Silva and Darragh, 1993). Figure 6-2 shows average spectral shapes (Sa/amax) computed from recordings made on rock at close distances to large and small earthquakes (Table 6-1). For both magnitudes (moment magnitude **M** 6.4 and 4.0), the motions recorded in Eastern North America (ENA), a stable tectonic region, show a dramatic shift in the maximum spectral shape toward higher frequencies compared to the Western North American (WNA) motions. These differences in spectral content are significant and are interpreted as primarily resulting from differences in the shear-wave velocity and damping in the rocks directly beneath the site (Boore and Atkinson, 1987; Toro and McGuire, 1987; Silva and Green, 1989; Silva and Darragh, 1993). Also evident in Figure 6-2 is the strong magnitude dependency of the response spectral shapes. The smaller earthquakes show a much narrower bandwidth. This is a consequence of higher corner frequencies for smaller magnitude earthquakes (Boore, 1983; Silva and Green, 1989; Silva and Darragh, 1993).

The difference in spectral content due to soil site effects, as shown in Figure 6-1, and due to rock site effects, as shown in Figure 6-2, are dramatic and illustrate the degree to which one-dimensional site conditions (vertical variations in dynamic material properties) control strong ground motions.

Since the 1930's, a number of Japanese seismologists have made contributions to the theory of site response (e.g., Sezawa and Kanai, 1932; Kanai, 1950; Kanai et al., 1959; Tanaka et al., 1973). These contributions generally included observations of site amplification effects from small earthquakes and theoretical developments for solutions of the wave equation for sites with up to three layers. Input motion was assumed to be vertically propagating shear waves. A rate-dependent material damping was included through viscosity terms. These investigators generally found reasonable agreement between theory and observation in amplitude and predominant period of site resonances. Observations included simultaneous recordings at depth in mines and at the surface. In addition, microtremor observations were made at different locations and at different times. One of the main observations by these workers was that ground motion on soil deposits is generally higher than that occurring on adjacent rock outcrops. Their theoretical developments indicate that this observed phenomenon was likely caused by the lower wave velocities in soil deposits and resonances due to reverberations in the soil column. Some of these studies were incorporated into early engineering practice in Japan.

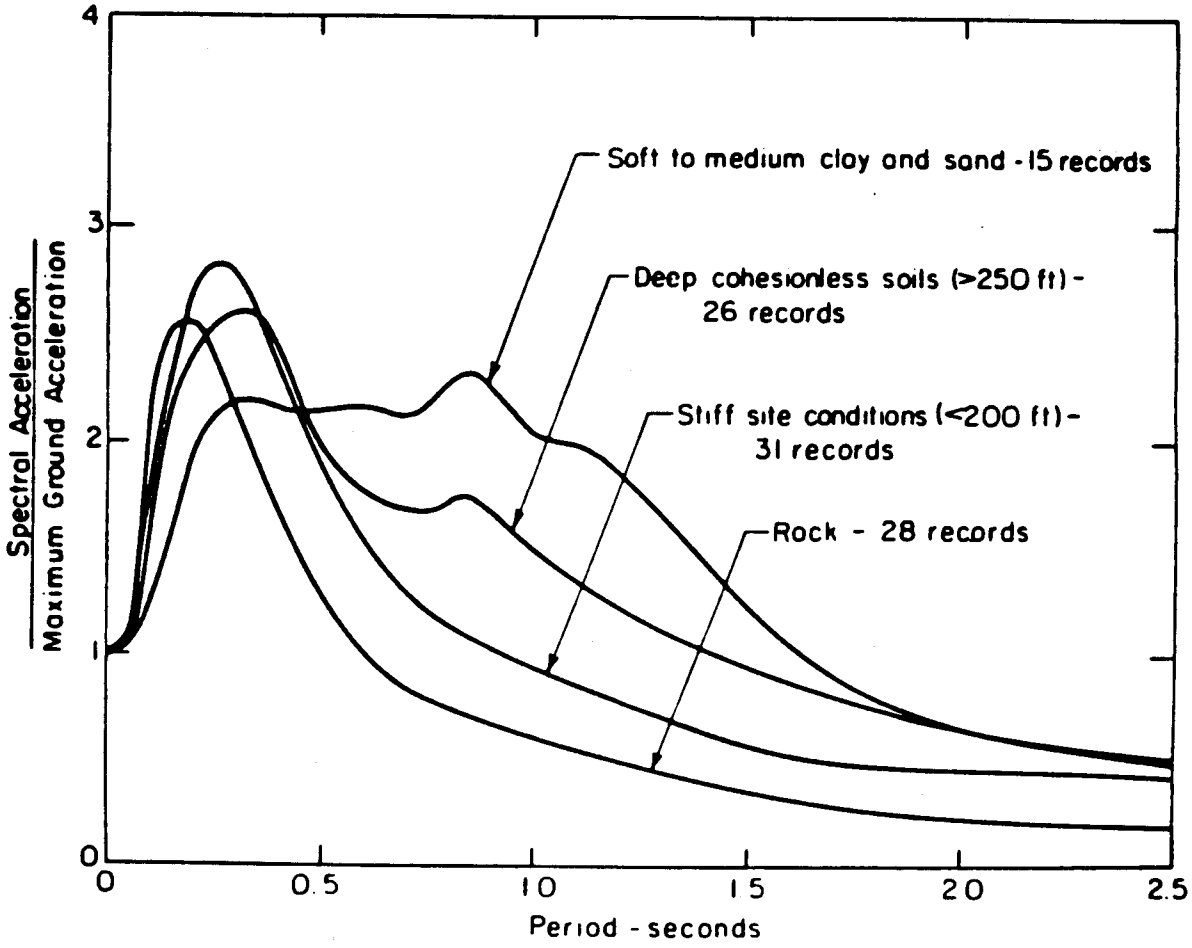

Figure 6-1. Average 5% damping response spectral shapes (Sa/amax) computed from motions recorded on different soil conditions (after Seed, et al., 1976).

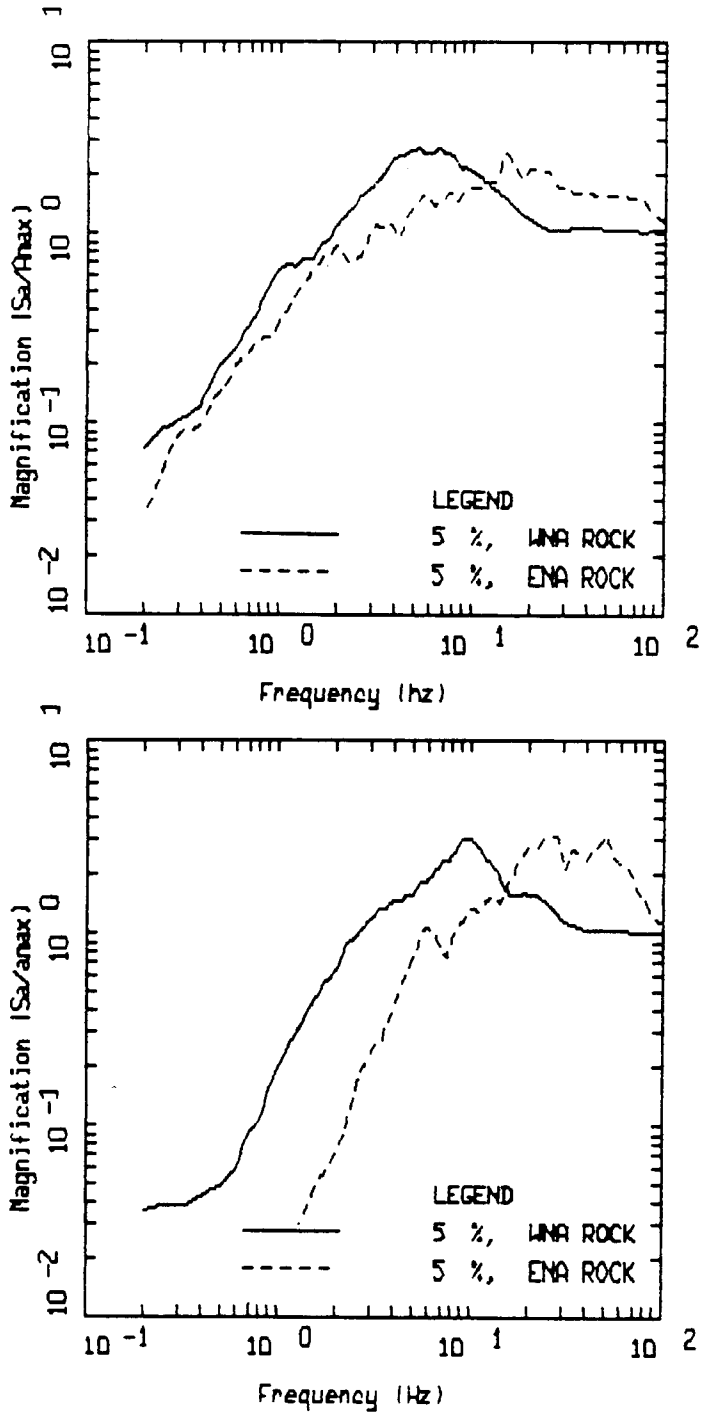

Figure 6-2. Average 5% damping response spectral shapes (Sa/amax) computed from motions recorded on rock sites at close distances to M = 6.4 earthquakes (top figure) and M = 4.0 earthquakes (bottom figure). In each figure the solid line corresponds to motions recorded in WNA, dashed line to motions recorded in ENA. (See Table 6-1 for a list of earthquakes, sites, distances, and average peak accelerations).

Table 6-1

Earthquakes and Stations Used for Comparison of ENA and WNA 5% Damped Response Spectral Shapes

Earthquake	Date	Magnitude (M_L)	(M)	Source Depth (km)	Epicentral Distance (km)	Station	USGS No.	Reprocessed Average Horizontal Peak Acceleration (g)
San Fernando	710209	6.4	6.6	8.4	23.0	Lake Hughes 12	128	0.316
					26.3	Lake Hughes 9	127	0.147
					27.3	Lake Hughes 4	126	0.184
					33.8	Griffith Park	141	0.185
					36.1	Seis. Lab.	266	0.151
					43.2	Santa Anita	104	0.194
Nahanni	851223	6.4 (m_b)	6.8[2]	18.0	8.0	Site #1		1.176
					9.0	Site #2		0.450
					20.0	Site #3		0.202
Coalinga Aftershocks								
A	83050322	3.8		7.64	8.54	LLN		0.0053
D	83050700	3.9		8.92	8.39	LLN		0.0189
K	83051013	3.9		4.79	12.46	LLN		0.0036
K3	83051405	3.9		11.18	5.56	VEW		0.0269
M	83051414	3.9		9.15	4.94	LLN		0.0084
New Brunswick	820331	4.01[1]		5[3]	4	Mitchell Road		0.2000

1. After Choy and Boatwright (1988).
2. After Boore and Atkinson (1987).
3. After Toro and McGuire (1987).

6.2.1 Recent Observations and Development

Haskell (1960) extended the early work of Thompson (1950), and introduced the elegant matrix operator formalism which allowed the treatment of compressional and vertically polarized shear (SV), as well as horizontally polarized shear (SH), wavefields with arbitrary angles of incidence and more general material damping. This frequency domain wave-propagation approach (Thompson-Haskell method) also increased computational efficiency, allowing many layers with constant material properties to be incorporated into the analyses. This development coincided with the emergence of digital computers, and the combination permitted more accurate modeling of soil variability. This approach was subsequentially generalized by Gilbert (Gilbert and Backus, 1966) to allow continuous changes in material properties with depth (Yamamoto, 1983). These procedures marked the early beginnings of computational seismology. At the time, however, they were not widely employed in the engineering community.

Paralleling these wave propagation developments, site response analyses were being performed for engineering purposes using a lumped-mass approach (Idriss and Seed, 1968). This formulation provided a useful representation for vertically propagating shear or compression waves. Early lumped-mass approaches suffered from the constraint of a rigid base (Moriwaki and Doyle, 1978). The rigid base trapped wave energy within the soil column, and hence reflected waves were not permitted to radiate into the half-space. This artificial limitation, in some cases, resulted in unrealistic site response analyses. The later development of the Lysmer-Kuhlemeyer dashpot (Lysmer and Kuhlemeyer, 1975) for finite element applications largely resolved this difficulty by allowing the rigid half-space to act like a linear elastic half-space.

In the early sixties, Duke and his co-workers at UCLA (Duke and Leeds, 1962) extended Kanai's formulation (Kanai, 1950) to an arbitrary number of layers which included viscosity terms. By the late sixties and the early seventies, seismologists were routinely utilizing the Thompson-Haskell formulation in crustal response analyses (e.g., Phinney, 1964; Randall, 1967; Knopoff, 1964, Kurita, 1973; Leblanc, 1967; Ishii and Ellis, 1970) and to infer crustal compression and shear-wave velocities. Borcherdt (1971) and Silva (1976) extended the matrix formulation to enable the exact treatment of damping so that soils with high shear- wave damping could be modeled (Joyner, et al., 1976; Johnson and Silva, 1981).

These developments allowed more detailed and varied analyses of linear site response observations and provided a focus for further observations. For example, Borcherdt and Gibbs (1976), Seed et al. (1969), Wiggins (1964), Idriss and Seed (1968), Berrill (1977), and Duke and Mal (1978) have shown that during small and large earthquakes the surface soil motion can differ in significant and predictable ways from that on adjacent rock outcrops. In addition, other investigations have utilized explosion data either independently or in conjunction with earthquake data to examine site response characteristics (Murphy et al., 1971; Rogers et al., 1983; and Hays et al., 1979). Recent work using horizontal as well as vertical arrays of instruments have demonstrated the general consistency of the site response for seismic events of different sizes, distances, and azimuths (Tucker et al., 1984; Benites, et al., 1985; Silva et al., 1988, Silva et al., 1991; Su et al., 1992; Silva and Stark, 1992).

Results of these and other studies have generally concurred that the motion at the surface of soft sites is greater than that at stiff sites for the same level of relatively low excitation. Additionally, these studies have demonstrated, in a general sense, the adequacy of assuming plane-wave propagation in modeling linear one-dimensional site response for engineering purposes. (It should be noted that one-dimensional modeling may not be appropriate where significant lateral heterogeneity exists; e.g., King and Tucker, 1984; Barel and Gariel, 1986).

The physical mechanism responsible for the observed soil amplification is an increase in wave amplitude as propagation velocity decreases toward the surface. If material damping is neglected, the decrease in shear-wave velocity toward the surface results in an increase in motions. This arises because flow of energy per unit time and per unit area (energy flux) $\rho V_S u^2$ (ρ = density, V_S = propagation velocity, u = particle velocity; Aki and Richards, 1980) is conserved. Therefore if V_S decreases, u must increase in an elastic system. In any soil or rock column, however, some material damping is always present and the net amplification (or deamplification) involves an interplay between counteracting effects. This may result in some cases in an amplification of peak particle velocity and a deamplification of peak acceleration due to the different frequency content of the two measures of ground motion.

The other phenomenon which is observed, and is predicted by simple shear-beam theory, is the presence of resonances. These are due simply to the constructive interference of upgoing and downgoing waves in the soil column. Since there is a stiffness contrast at the soil/rock boundary, a fraction of the seismic energy that enters the soil column can become trapped as upgoing and downgoing wave-fields reflected successively from the free surface and the bedrock. Resonances occur at the surface due to constructive interference at frequencies given by multiples of one-quarter wavelength of the shear or compression waves in the soil column. The spectral amplitudes of the resonances are determined by the stiffness and density contrast at the rock/soil interface as well as details of the variation of shear modulus and soil density with depth.

The resonance phenomena and the general increase in amplitude with decreasing velocity of propagation are greatly affected by material damping. This causes the multiply-reflected energy to gradually damp out and can be observed as a successive decrease in spectral amplitudes at the higher modes (Silva et al., 1988).

It is important to point out that the near-surface amplification of ground motion may occur at rock sites as well. Physically, all that is required is a significant change in propagation velocity over a depth range of at least one-quarter wavelength (Joyner and Fumal, 1984). This effect may be responsible for a tendency of soft rock (sedimentary) to show some amplification relative to hard rock (granitic) (Campbell, 1985) if near surface velocity gradients are present.

In summary, the effects of surficial materials are dependent upon the dynamic material properties of the soil as well as the underlying rock, the soil depth, and wave frequency.

6.2.2 Variability in Site Response

Other factors which influence site effects and their variability arise from the contributions due to lateral changes in material properties as well as topographic effects. Non-vertical spatial variation in propagation path parameters can have significant effects upon both the amplitude of site response and its frequency dependence. Examples of these nonhomogeneous conditions include dipping structures such as an inclined soil/rock interface, lensing of soil layers, and basin or valley features. These propagation-path perturbations can scatter energy as well as change the modes of propagation both locally and over considerable distances. Wave scattering is the primary cause of incoherence of strong ground motion over rather short distances (King and Tucker, 1982; Abrahamson, 1985). Acceleration at soft sites (shear-wave velocity less than about 1000 ft/sec) generally becomes incoherent for frequencies above about 5 Hz over distances of 300–600 feet and greater (Abrahamson, 1985).

Some or all of these nonhomogeneous factors are present at *all* sites to some degree in both soil and rock. Naturally the degree of perturbation varies with each site and with frequency. Neglecting structure effects, the variability encountered in observations of site response may largely be due to these lateral changes in dynamic material properties as well as topography. For example, the presence of a dipping soil/rock interface or topographic surface may make site response strongly dependent upon source azimuth and, to some extent, source depth. Examples of the presence of a dipping interface and topographic relief are the Gilroy 1 and 2 rock/soil pair in California (Appendix 6.B) and the Rocco and Forgaria-Carnino pair at Friuli respectively (Silva et al., 1988).

While the presence of these two-dimensional features is likely to some extent at most sites, in many cases the effects on ground motion predicted by the simple plane layered models and vertical propagating shear waves predominate over the frequency range of engineering interest (Seed and Idriss, 1969; Joyner et al., 1976, 1981; Silva et al., 1988; Idriss, 1990, 1991; Appendix 6.B). The simple plane-wave propagation model for the one-dimensional case consequently represents a useful analytical tool to approximate site effects.

6.2.3 Material Nonlinearities

It is well known from laboratory testing that soils exhibit pronounced nonlinear behavior under shear loading conditions (see Sections 7 and 8). Shear modulus decreases with increasing strain with an accompanying increase in material damping (Drnevich et al., 1966; Seed and Idriss, 1970; Hardin and Drnevich, 1972; Seed et al., 1984). If this observation is applicable to in-situ soil properties subject to earthquake loading, then site response calculations must accommodate these strain dependencies as material nonlinearities.

The strain dependence of soil modulus and material damping has been well documented in numerous laboratory studies for sands and clays (Drnevich et al., 1966; 1967; Seed and Idriss, 1970; Hardin and Drnevich, 1972; Silver and Seed, 1971; Seed et al., 1984) (see Section 8). Various parametric relationships have been proposed to determine values of maximum shear modulus (at small strain levels) and variations of shear modulus and material damping with strain (Hardin and Drnevich, 1971; Martin, 1975). Nonlinear soil models which have been primarily developed from laboratory test results and utilized in dynamic analyses, include the Ramberg-Osgood model (Streeter et al., 1974; Faccioli et al., 1973), an elasto-plastic model (Richart, 1975), Iwan-type model (Joyner and Chen, 1975; Dames & Moore and Science Applications, Inc., 1978; and Taylor and Larkin, 1978), the hyperbolic model (Hardin and Drnevich, 1972; Finn et al., 1975), the endochronoic model (Day, 1979), and the Davidenkov model (Martin, 1975; Pyke, 1979).

Each of the nonlinear models mentioned has certain limitations and advantages in describing the response of soils to the type of loading produced by seismic disturbances. An effort has been made in some models to predict permanent deformations, while others have included pore water pressure build-up and dissipation. Strain dependency of material properties from laboratory data is universally observed. It is reproducible and becomes significant for high levels of earthquake loading, i.e., shearing strains $>10^{-2}$%.

6.2.4 Implications for Site Response Calculations

Clearly if in situ soil is behaving as laboratory-derived models suggest, nonlinear effects must be incorporated into site response analyses. In general, strain dependence of modulus and damping would result in a nonlinear wave equation with the full finite strain terms (Biot, 1965; Murnaghan, 1937). In this case, superposition is invalid, the wave equation does not separate into P, SV, and SH fields, and Fourier analysis cannot be applied. The approach generally adopted is to assume infinitesimal displacements, utilize a linear wave equation, and confine the nonlinearity to the constitutive relation.

If a nonlinear constitutive relation is utilized, then velocities and damping become strain dependent. This can result in a wavefield and site response that depart significantly from linear one-dimensional theory. For high levels of motion strain dependent wave velocities would generally result in a lower characteristic site period. Strain-dependent damping would generally reduce overall response at high strain levels. Depending upon site structure and input motion, these effects could be very large and must be incorporated into site response analyses (Appendix 6.B). Either nonlinear or equivalent-linear approaches may be used to accommodate nonlinear soil response and, as indicated in the introduction, Appendix 6.B shows a comparison of the two approaches to each other and to recorded motions.

6.2.5 Field Evidence of Soil Nonlinearity

It has long been recognized that there may be problems associated with laboratory testing of soil samples (Woods, 1968; Seed and Idriss, 1970). Accurate determination of shear moduli is complicated by the effects of sample disturbance. Additionally, resonant column and cyclic triaxial tests do not exactly simulate the dynamic stress paths caused by the passage of shear waves in the frequency range of several seconds to over 20 Hz. In situ measurements with stress waves representative of earthquake loading would eliminate these problems, but it is very difficult to induce large strains with controlled amplitudes in natural deposits.

To investigate this problem, two approaches have been utilized: (1) controlled sources employing large-strain-inducing generators; and (2) site response analysis utilizing earthquake or explosion data recorded by horizontal and vertical arrays. The controlled source approach, utilizing soil boring pressureometers, torsional borehole devices, and even controlled explosions, has demonstrated soil nonlinearities (Dobry, 1991). The soil nonlinearity that was observed was either in strain dependent shear-wave velocity or load-deformation relations. Laboratory and field derived curves were in reasonable agreement. Japanese investigators (Tokimatsu and Midorikawa, 1981) have utilized the change in predominant period of site resonances (as observed in response spectra) for different levels of seismic excitation to infer strain dependent velocity changes. The modulus reduction curves obtained in this manner agree in substance with laboratory derived curves for the same sites. A recent analysis of transfer functions and amplification factors computed from strong motion data found evidence of nonlinear soil response (Silva et al., 1988; Silva et al., 1989; Chang et al., 1990; Silva et al.,1991; Su et al., 1992; Silva and Stark, 1992).

Other investigators, using simple qualitative comparisons of ground response patterns for areas comprised of stiff and soft sites between small magnitude sources and intensity data from large local earthquakes (Borcherdt and Gibbs, 1976; Benites et al., 1985) have not observed departures from linear conditions. Shear-wave data from vertical arrays have been adequately modeled by linear theory up to 20%g (Shima, 1962; Seed and Idriss, 1970; Joyner et al., 1976; Johnson and Silva, 1981, Chang et al., 1986). The consistency of the transfer function between a soil site and a rock site has been examined for various levels of shaking (Murphy and Lahoud, 1969; Rogers et al., 1974; Hays et al., 1979; Joyner et al., 1981; Rogers et al., 1984; Tucker and King, 1984; Jarpe et al., 1988). In all of these analyses, the authors do not indicate significant evidence of nonlinear soil response. However, it should be emphasized that in a majority of the cases analyzed, average shear strains throughout the soil column were probably less than 10^{-2}%. At this strain level, the modulus reduction curve, such as shown in Figure 6-9, predicts a shear-wave velocity decrease of only about 8%, well within the variability of these analyses.

6.3 Site Response Model

Certainly the most satisfying approach to account for the effects of surficial materials on strong ground motion is empirical. Ideally amplification factors could be developed based entirely upon observation of strong ground motion. Past studies using data recorded on rock and on different classes of soil profiles, such as stiff soils and deep cohesionless soils, have demonstrated large differences in spectral amplification (Sa/amax) and in spectral velocity due to the presence of the soils (Seed et al., 1976; Mohraz, 1976; Joyner and Fumal, 1984). While these studies are extremely useful in a general sense, the limited number and size of earthquakes and different types of profiles preclude relying directly upon empirical results. In particular, few data are available for very high levels of shaking and for a variety of site conditions. Also, few recording sites have detailed soil profiles for which reliable soil properties are available. Because of these limitations, some form of computational analysis is desirable and direct observations of soil response can then be used as calibrations and to provide a basis for assessing the reasonableness of the results of analytical computations.

The conventional computational approach in developing spectral amplification factors appropriate for specific soil profiles would involve selection of suitable time histories to serve as control motions and a suitable computational formulation to transmit the motion through the profile.

6.3.1 Equivalent-Linear Computational Scheme

The computational scheme which has been most widely employed to evaluate one-dimensional site response assumes vertically-propagating plane shear waves. Departures of soil response from a linear constitutive relation are treated in an approximate manner through the use of the equivalent-linear approach.

The equivalent-linear approach, in its present form, was introduced by Seed and Idriss (1970). This scheme is a particular application of the general equivalent linear theory introduced by Iwan (1967). Basically, the approach is to approximate a second order nonlinear equation, over a limited range of its variables, by a linear equation. Formally this is done in such a way that an average of the difference between the two systems is minimized. This was done in an ad-hoc manner for ground response modeling by defining an effective strain which is assumed to exist for the duration of the excitation. This value is usually taken as 65% of the peak time-domain strain calculated at the midpoint of each layer, using a linear analysis. Modulus and damping curves are then used to define new parameters for each layer based on the effective strain computations. The linear response calculation is repeated, new effective strains evaluated, and iterations performed until the changes in parameters are below some tolerance level. Generally a few iterations are sufficient to achieve a strain-compatible linear solution.

This stepwise analysis procedure was formalized into a one-dimensional, vertically propagating shear-wave code called SHAKE (Schnabel et al., 1972). Subsequently, this code has become easily the most widely used analysis package for one-dimensional site response calculations.

The advantages of the equivalent-linear approach are that parameterization of complex nonlinear soil models is avoided and the mathematical simplicity of linear

analysis is preserved. A truly nonlinear approach requires the specification of the shapes of hysteresis curves and their cyclic dependencies. In the equivalent-linear methodology the soil data are utilized directly and, because at each iteration the problem is linear and the material properties are frequency independent, the damping is rate independent and hysteresis loops close.

The most significant advantage of the equivalent-linear formulation is the preservation of the superposition principle. For linear systems, this principle permits spectral decomposition and frequency-domain solutions. One can then make use of the propagator matrix solution scheme (Haskell, 1960; Schnabel et al., 1972; Silva, 1976) for very efficient frequency domain solutions of the wave equation. The superposition principle then permits a spectral recomposition of the wavefields (sum over frequencies) through an inverse Fourier or Laplace transform. A non-subtle result of this is that the deconvolution process, that of propagating the control motion down rather than up, results in a unique solution. That is, for a given motion at the surface, within an equivalent-linear framework there is only one base motion (solution). In reality of course, if the soils are behaving in a nonlinear fashion and have degraded, many different input motions at the base of the soil could have resulted in a similar surface response.

While the assumptions of vertically propagating shear waves and equivalent-linear soil response certainly represent approximations to actual conditions, their combination has achieved demonstrated success in modeling observations of site effects (Schnabel et al., 1972; Silva et al., 1988).

6.3.2 Computational Scheme

The computational scheme employed to compute the site response uses the stochastic model (Section 3) to generate the power spectral density and spectral acceleration of the rock or control motion. This motion or power spectrum is then propagated through the one-dimensional soil profile using the plane-wave propagators of Silva (1976). In this formulation only SH waves are considered. Arbitrary angles of incidence may be specified but normal incidence is used throughout the present analyses.

In order to treat possible material nonlinearities, the equivalent-linear formulation is employed. Random process theory is used to predict peak time domain values of shear strain based upon the shear strain power spectrum. In this sense the procedure is analogous to the program SHAKE except that peak shear strains in SHAKE are measured in the time domain. The purely frequency domain approach obviates a time domain control motion and, perhaps just as significant, eliminates the need for a suite of analyses based on different input motions. This arises because each time domain analysis may be viewed as one realization of a random process. In this case, several realizations of the random process must be sampled to have a statistically stable estimate of site response. The realizations are usually performed by employing different control motions with approximately the same level of peak acceleration.

In the case of the frequency domain approach the estimates of peak shear strain as well as oscillator response are, as a result of the random process theory, fundamentally probabilistic in nature. Stable estimates of site response can then be computed by forming the ratio of spectral acceleration predicted at the surface of a soil profile to the spectral acceleration predicted for the control motion.

The procedure of generating the stochastic power spectrum (Section 3), computing the equivalent-linear layered-soil response, and estimating peak time domain values has been incorporated into a code termed RASCALS.

6.3.3 Generic Soil Profile

The generic median soil profile adopted for the site response analyses in this study is shown in Figure 6-3. This standard profile was chosen to be consistent with the generally stiff soils present under nuclear power plants located in the eastern and central United States and is intended to capture the behavior of soils ranging from gravels and sands to low plasticity sandy clays. The profile is based upon the sand-like profiles used by Bernreuter et al. (1985) from their review of FSARs and PSARs for nuclear plant sites and is similar to their generic profiles. It was decided not to include a separate suite of categories of constant shear-wave velocity with depth for sites with largely uniform profiles as their response is very similar to that of the generic gradient model (Section 6.4.2.3). Other profiles with very soft near surface soils are not considered as such sites would probably not be of interest for a NPP.

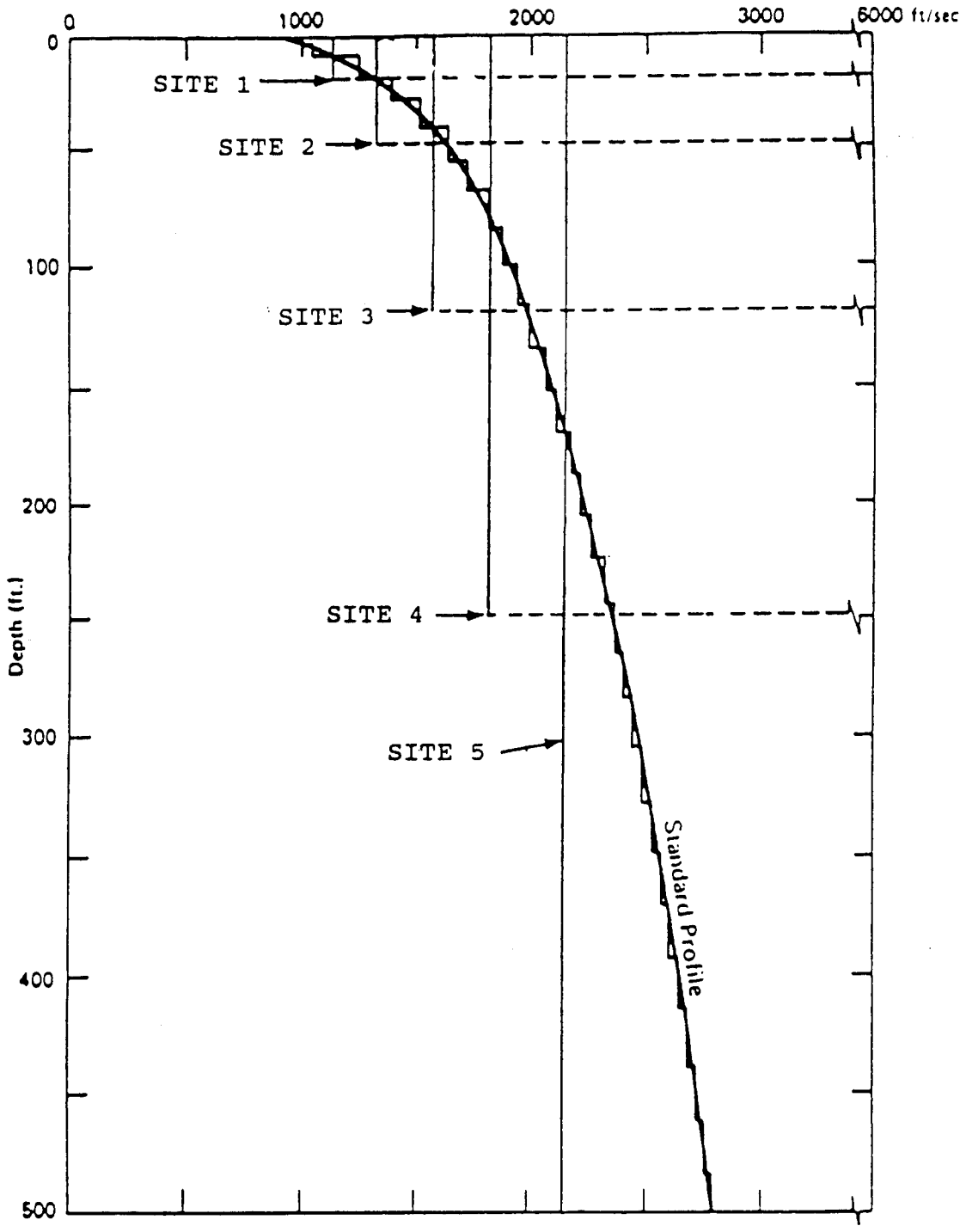

Figure 6-3. Standard soil profile appropriate for the Central and Eastern United States sites (gradient). Site categories 1–5 are indicated by their respective soil column depths. Constant shear-wave velocity profiles represent averages (over travel time) of the gradient profiles for each site category.

Table 6-2

Site Categories and Depth Ranges

Category	Median Depth (ft)	Range[1](ft)
1	20	10–30
2	50	31–80
3	120	81–180
4	250	181–400
5	500	401+

1. Range of profile depth over which category applies as well as range of depth randomization for each category (Category 5 was randomized over the range of 401–1000 ft).

The number of site categories adopted for analysis is five and they are shown in Figure 6-3. The depths and depth ranges of the five categories are shown in Table 6-2. The constant velocity profiles indicated in Figure 6-3 show the average (weighted harmonic mean) velocity of the standard gradient model for each category. As previously mentioned, response analyses performed with the gradient model and with the constant shear-wave velocity model produce very similar response results. As a result, only the gradient models are used in the development of the site amplification factors.

In order to accommodate variation in shear-wave velocity profiles for the range of central and eastern North American sites, the median profile velocities and profile depth (depth-to-rock) are randomized using the model presented in Appendix 6.A. The uncertainty model for velocity and depth randomization is based on a probabilistic analysis of over 350 profiles taken from sites predominately in the conterminous United States. The statistics then represent both western and eastern sites as too few profiles were available for eastern sites alone to provide meaningful statistics. In the analyses, 50 random profiles for each category are used to develop the median and one-sigma response characteristics of the categories.

The 50 randomized profiles are presented in Figure 6-4 through 6-8 for Categories 1–5. The median profile is shown as the dashed line on each figure (note the velocity scale changes with each category). The bedrock median velocity is 6000 ft/sec and represents an average (assuming log normal distribution) of bedrock velocities beneath soil profiles for sites east of latitude 105°W (37 sites). The corresponding value for sites west of latitude 105°W is about 3000 ft/sec. These values (particularly the eastern at 6000 ft/sec) may be biased somewhat low as the drilling, particularly at deep stiff profiles, may not have penetrated far enough into unweathered basement to obtain shear-wave velocities representative of good quality rock. For the generic profile considered here, the effects of a higher median velocity are small (Section 6.4.2.2) and a lower median bedrock velocity results in lower amplification factors so the issue is not considered significant in applications to generic amplification factors. The uncertainty of the bedrock velocity (σ_{ln}) in taken as 0.30. This represents the expected variability in good competent basement rock in the central, eastern and southeastern United States.

While the median bedrock velocity beneath the eastern sites is about 6000 ft/sec, this value does not correspond to the surface shear-wave velocities of the Midcontinent and Gulf Coast crustal structures (Section 5.2). The shear-wave velocity of the top 1 km thick layer of the Midcontinent structure is about 9300 ft/sec while the top 7 km of the Gulf Coast structure has a velocity of about 7600 ft/sec. Both of these values are above the median 6000 ft/sec suggesting that the assumption of a uniform Poisson's ratio of 0.25 (used in deriving the crustal shear-wave velocities from measured compression-wave profiles) may not be appropriate in the very shallow

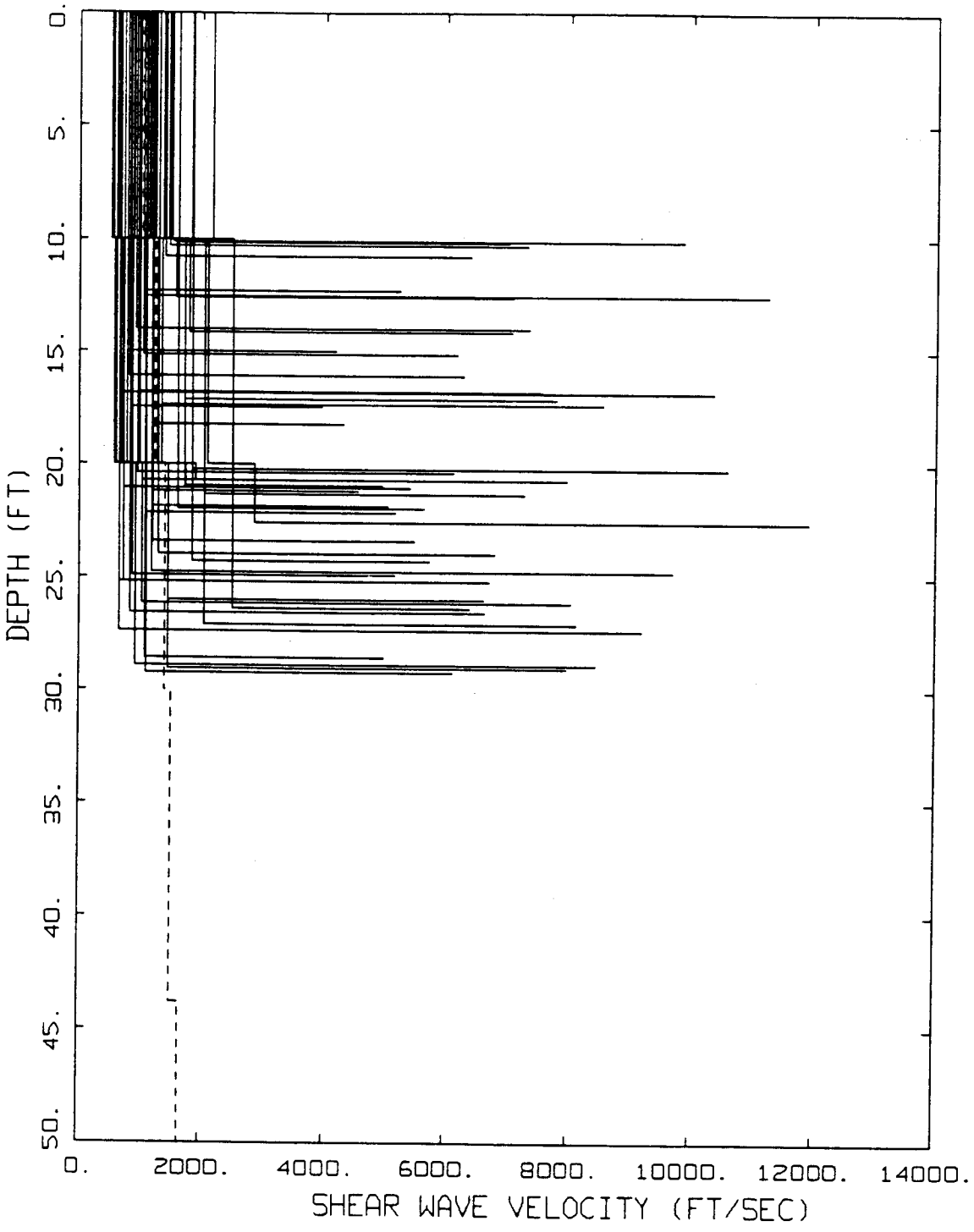

Figure 6-4. Randomized shear-wave velocity profiles (velocity and depth randomized) for Category 1 with a median depth of 20 ft and a depth range of 10–30 ft. Median soil profile is dashed and median bedrock velocity is 6000 ft/sec.

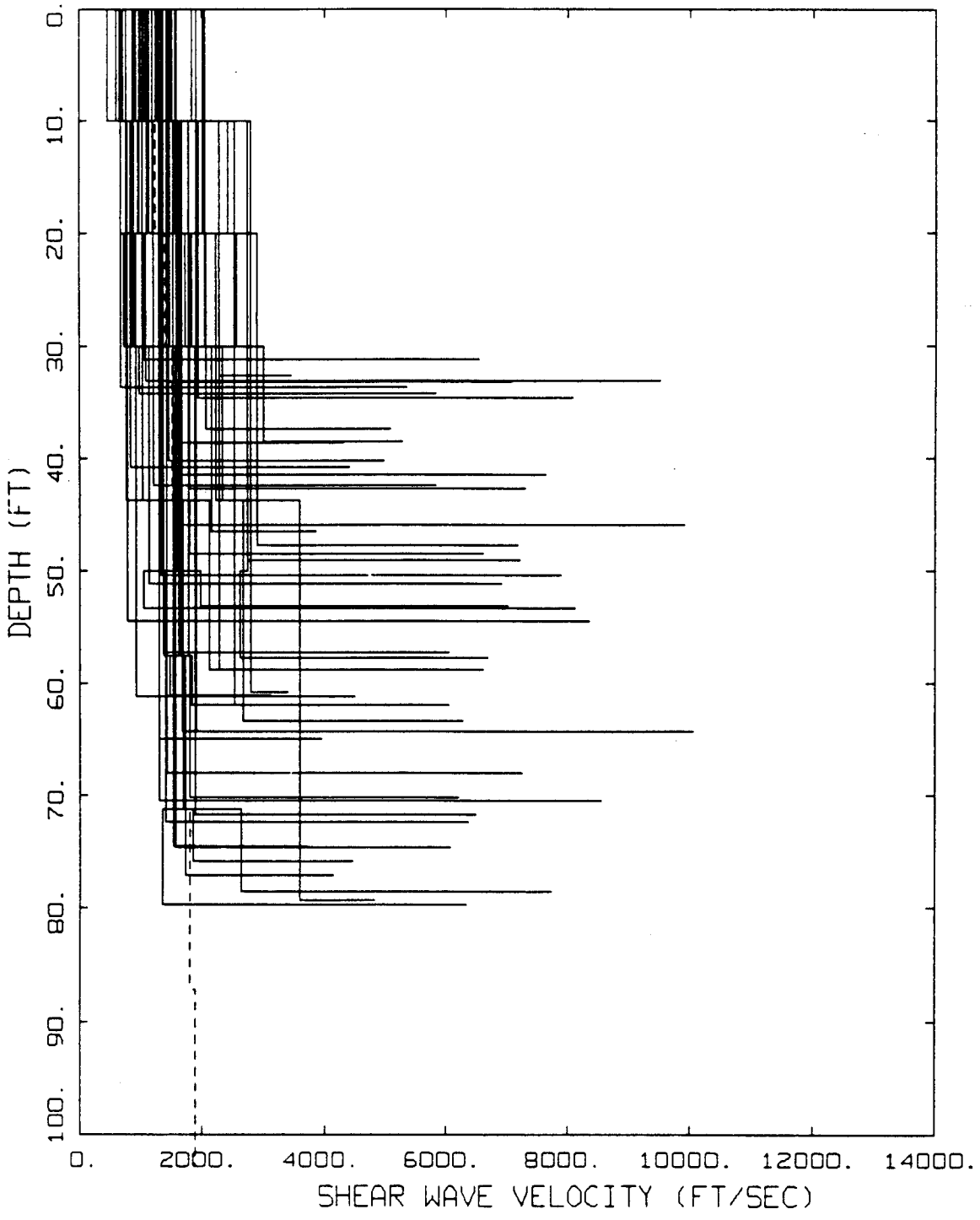

Figure 6-5. Randomized shear-wave velocity profiles (velocity and depth randomized) for Category 2 with a median depth of 50 ft and a depth range of 31–80 ft. Median soil profile is dashed and median bedrock velocity is 6000 ft/sec.

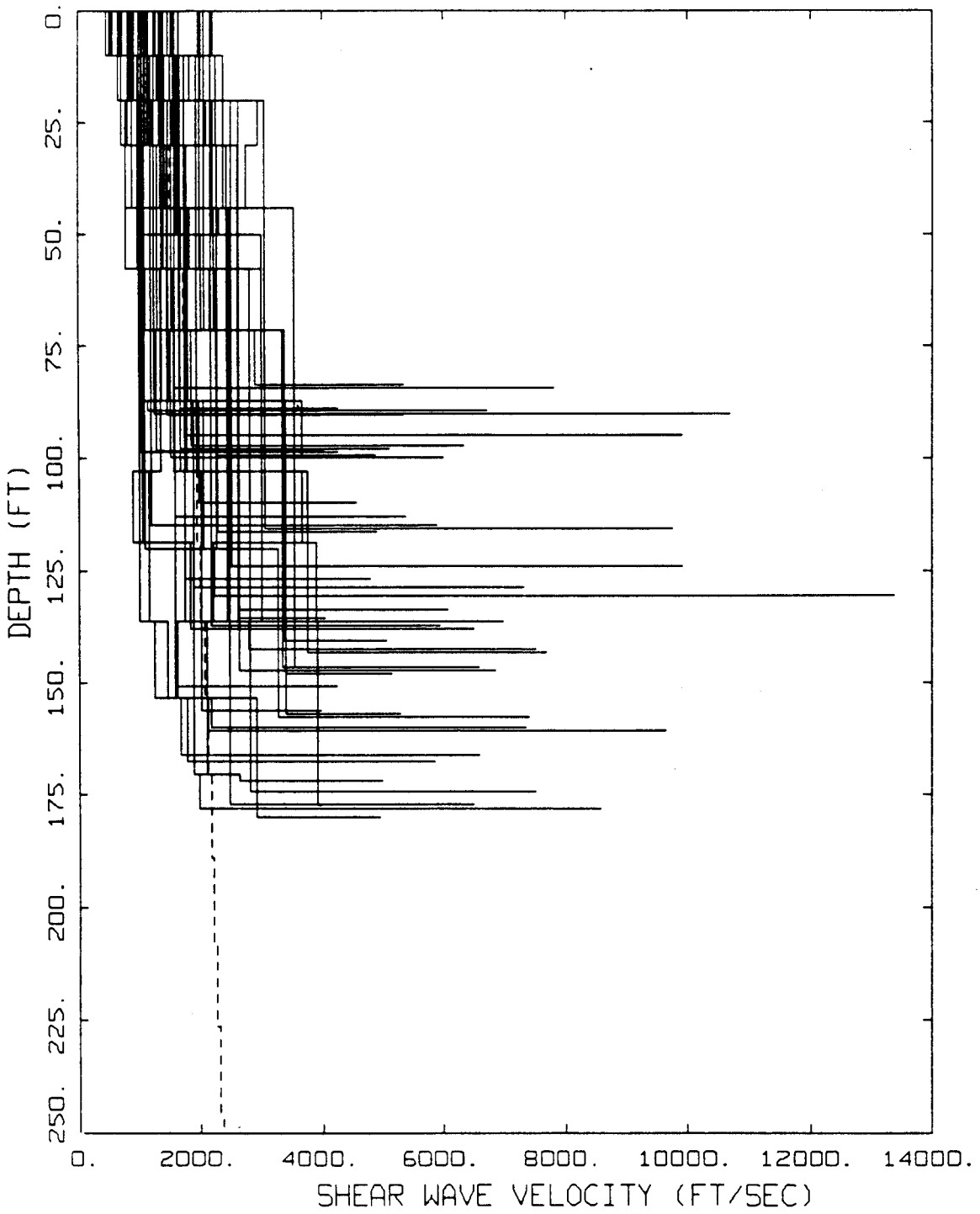

Figure 6-6. Randomized shear-wave velocity profiles (velocity and depth randomized) for Category 3 with a median depth of 120 ft and a depth range of 81–180 ft. Median soil profile is dashed and median bedrock velocity is 6000 ft/sec.

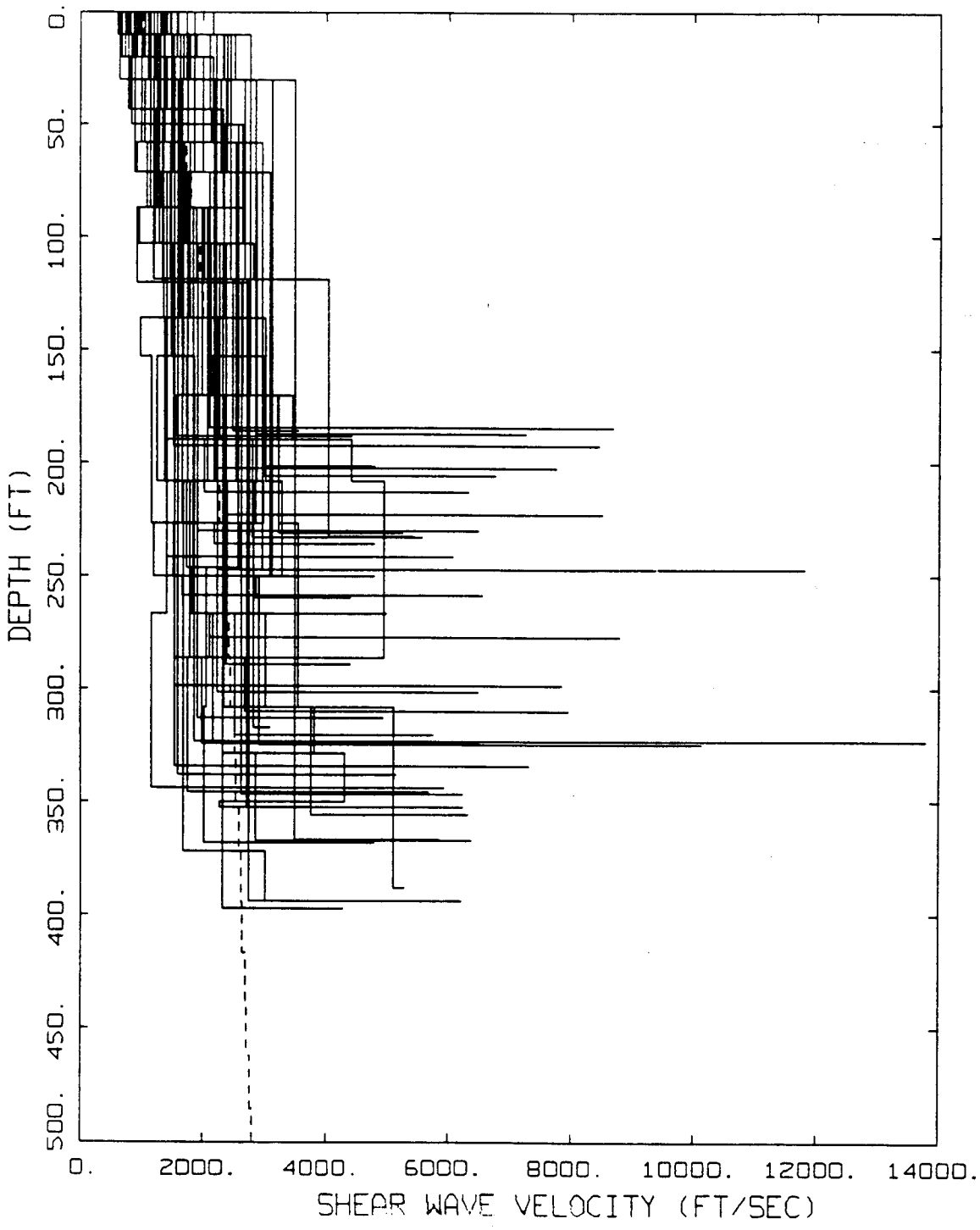

Figure 6-7. Randomized shear-wave velocity profiles (velocity and depth randomized) for Category 4 with a median depth of 250 ft and a depth range of 181–400 ft. Median soil profile is dashed and median bedrock velocity is 6000 ft/sec.

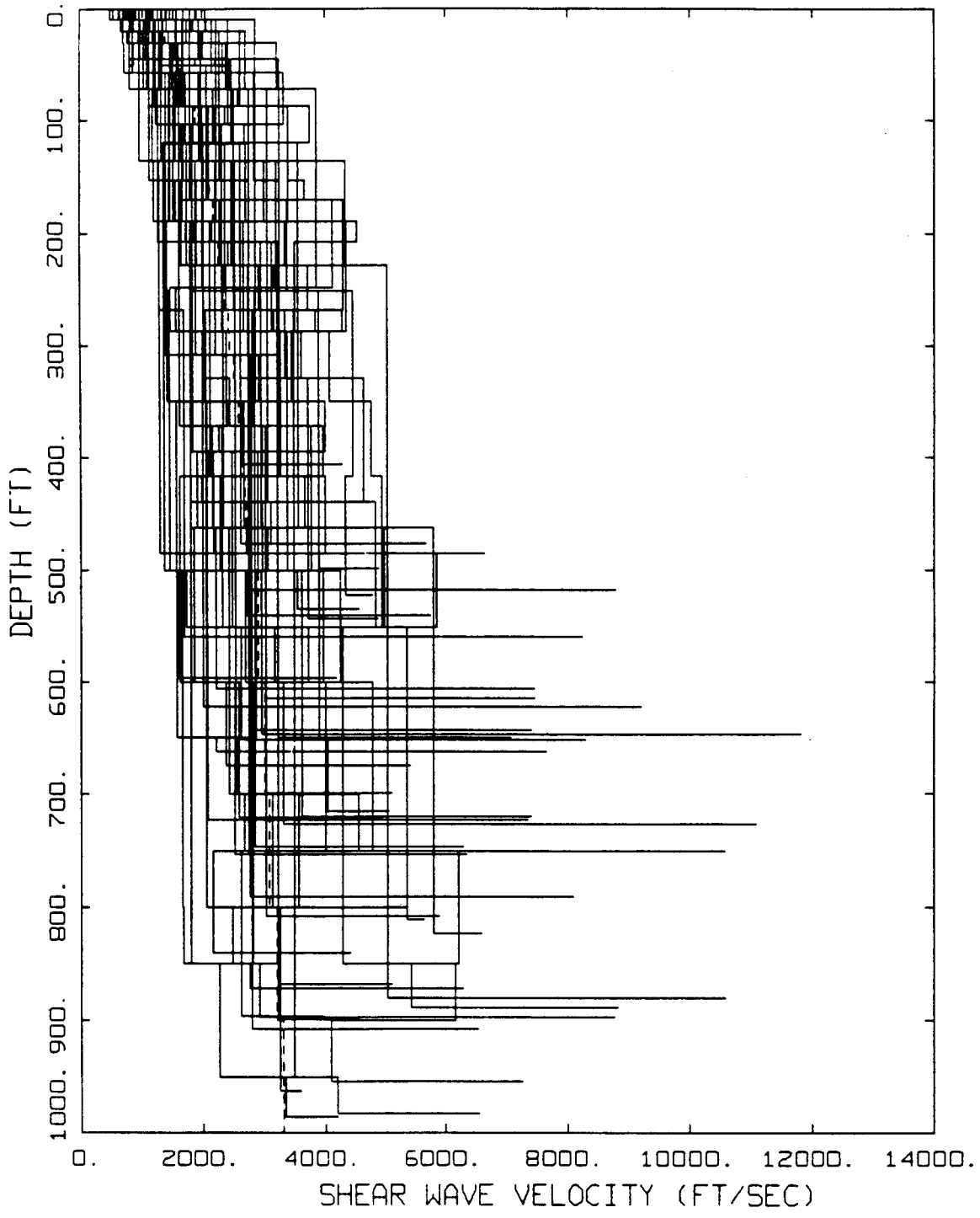

Figure 6-8. Randomized shear-wave velocity profiles (velocity and depth randomized) for Category 5 with a median depth of 500 ft and a depth range of 401+ ft (lower limit on depth randomization is 1000 ft). Median profile is dashed and median bedrock velocity is 6000 ft/sec.

crust. To assess the effects of including a crustal velocity gradient to go from 6000 ft/sec at the surface to 11,550 ft/sec at 1 km in the Midcontinent structure (the velocity at 1 km) and to 7600 ft/sec at the same depth in the Gulf Coast crustal structure, amplification factors were computed for Categories 2 and 5 using control motions with and without a gradient. The results are nearly identical since the control motions are always adjusted by varying the distance to the same fixed acceleration level. The very nature then of the way the amplification factors are defined, relative to outcrop peak acceleration values makes them reasonably insensitive to crustal velocity gradients. Care should be exercised, however, in applying factors taken from observations in the western United States or computed with a median bedrock velocity of 3000 ft/sec to significantly higher velocity eastern crustal conditions. In this case the implied crustal velocity gradient might be great enough to significantly affect the soil amplification.

The depth variation in each category was constrained to the ranges in depth to which each category applies. For example, Category 1 has a median depth of 20 ft and is intended to be applicable to profiles with depths ranging from 10–30 ft (0–9 ft is considered rock). The randomized depths were therefore constrained between 10–30 ft. For random profiles that exceeded 20 ft, the median Category 1 depth, properties from Category 2 were used. For Category 5, appropriate for profiles ranging in depth from 401 ft to bottomless soil sites, the depth randomization was initially limited to 750 ft. An additional Category 6, with a median depth of 1000 ft, was taken to apply for profiles of depths from 751 ft and beyond (randomized depths of 751 to 1250 ft). Very little difference was observed in the computed amplification factors for Categories 5 and 6 (median depths of 500 and 1000 ft) for frequencies around 1 Hz and above, so Category 6 was eliminated. To adequately sample the wider range in profile depth which Category 5 now represents, the random sampling was extended to between 401 and 1000 ft.

6.3.4 Modulus Reduction and Damping Curves

Figure 6-9 shows the modulus reduction and damping curves appropriate for the generic soil profile. The effects of confining pressure are reflected in the depth ranges shown, with less damping and higher G/G_{max} for a given strain level as the depth increases. The development of the generic curves is presented in Appendix 7-A.

In order to accommodate variability in the modulus reduction and damping curves on a generic basis, the curves were independently randomized about the values shown in Figure 6-9. A log normal distribution was assumed with a σ_{ln} of 0.35 at a cyclic shear strain of 3×10^{-2}% with upper and lower bounds of 2σ. The truncation was necessary to prevent modulus reduction or damping models that are not physically possible. The random curves are generated by sampling the transformed normal distribution with a σ_{ln} of 0.35, computing the change in normalized modulus reduction or percent damping at 3×10^{-2}% shear strain, and applying this factor at all strains. The random perturbation factor is reduced or tapered near the ends of the strain range to preserve the general shape of the median curves. Figures 6-10 through 6-15 show 20 of the 50 realizations for each of the six sets of curves. As the figures indicate, the suites of curves are smooth and are constrained to preserve the general shape of the median curves.

6.3.5 Specification of Control Motion

As previously discussed (Section 6.1), strong ground motion observed at rock sites in Eastern North America has different spectral properties than that typical of Western North America rock motions (Figure 6-2). The difference in spectral content shown in Figure 6-2 is significant and indicate that, for the same level of peak acceleration, ENA spectral content is higher than that in the WNA for frequencies greater than approximately 10 Hz.

Other sources of data also indicate that ENA ground motion recorded at rock or very shallow soil sites is richer in high frequency energy relative to analogous WNA recordings. These include aftershocks of the 1982 Miramichi, New Brunswick event (Cranswick et al., 1985), the 1982 Enola, Arkansas swarm (Harr et al., 1984), and the 1986 Northeastern Ohio event (Wesson and Nicholson, 1986) and its aftershocks (USGS, 1986).

The trends shown in these data are consistent with the rock or stiff soil recordings of strong ground motion. They indicate a significant and reasonably consistent difference in high frequency spectral content between the representative rock motion in the WNA and ENA crust. This observation suggests that it is necessary to use ground motion representative of the ENA region to serve as control or input motion for computing site response effects in ENA.

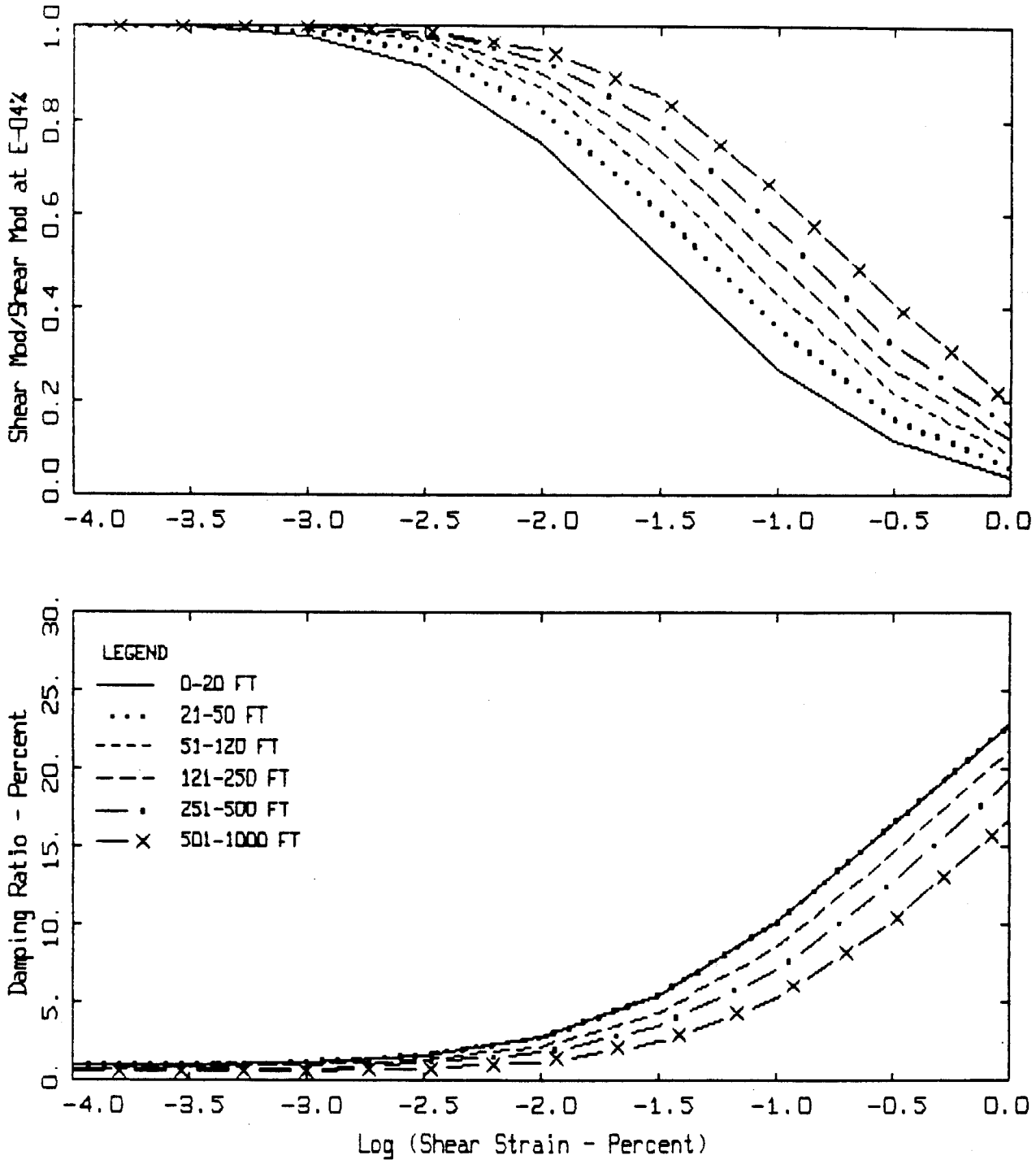

Figure 6-9. Modulus reduction and damping curves (median) used in the site response analyses. Damping curves are the same for depths ranging from 0 to 120 ft.

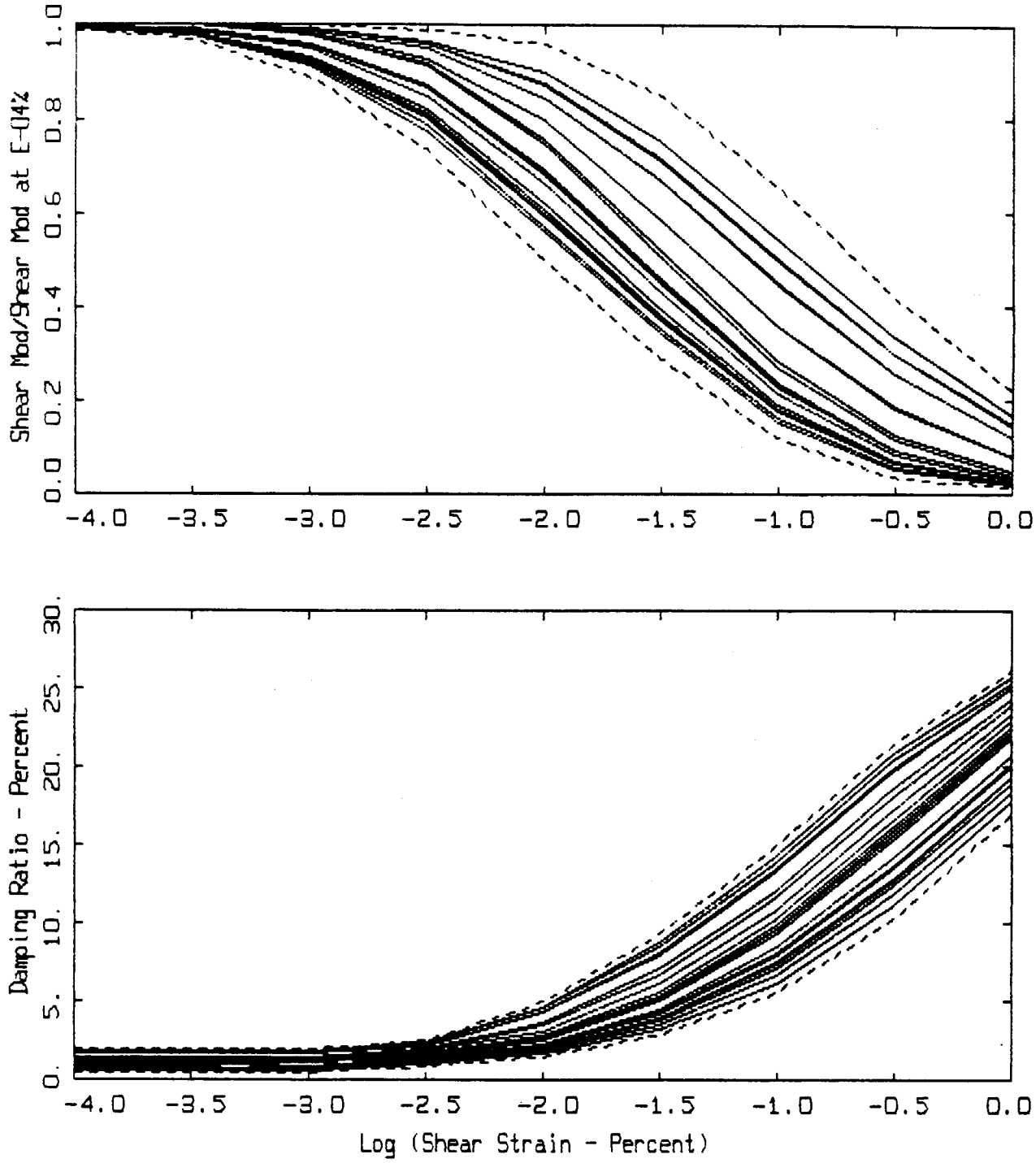

Figure 6-10. Example of randomized modulus reduction and damping curves (20) taken from the suite of 50 used in the analyses. Dashed lines are upper- and lower-bounds. Depth range is 0–20 ft.

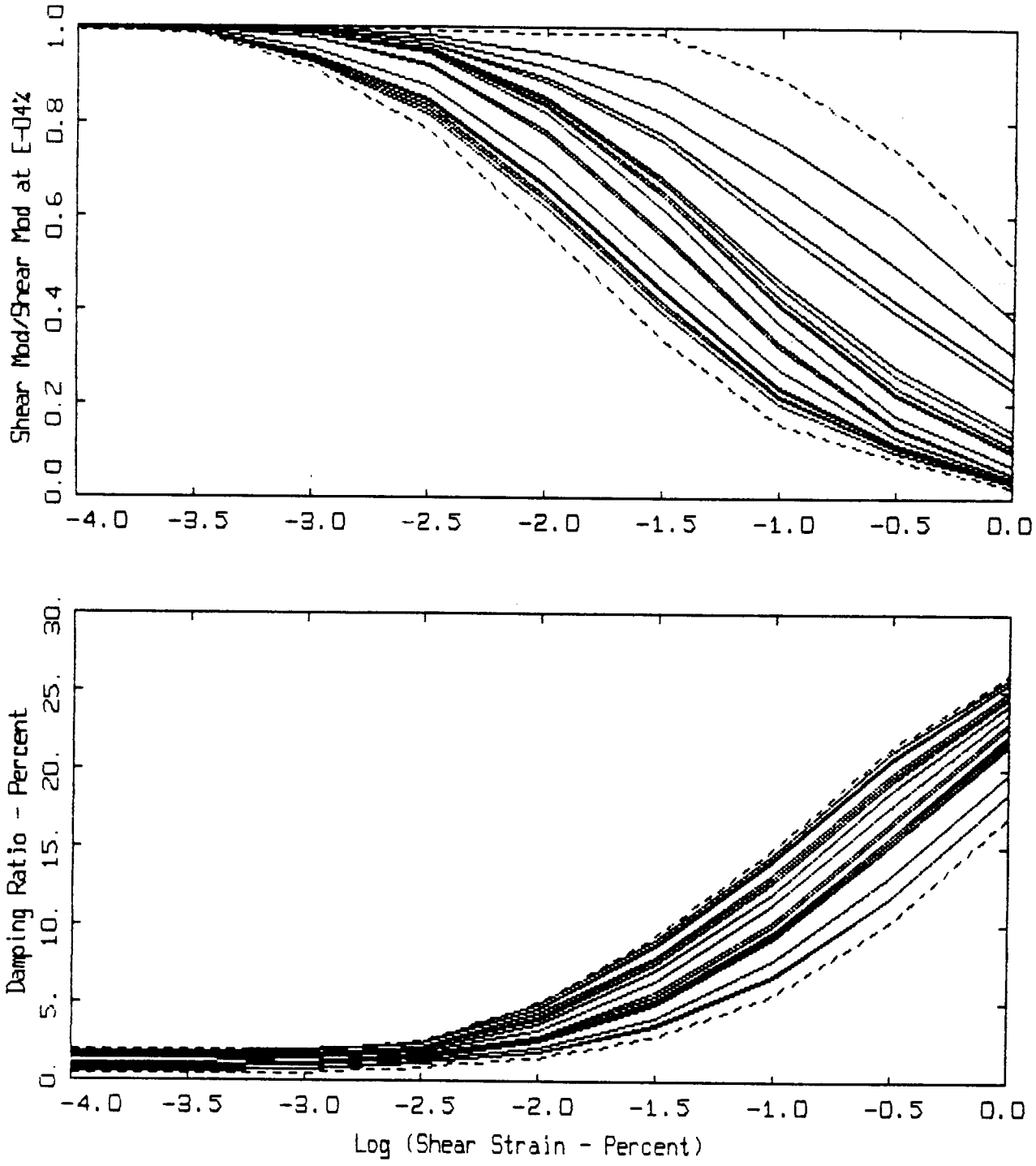

Figure 6-11. Example of randomized modulus reduction and damping curves (20) taken from the suite of 50 used in the analyses. Dashed lines are upper- and lower-bounds. Depth range is 21–50 ft.

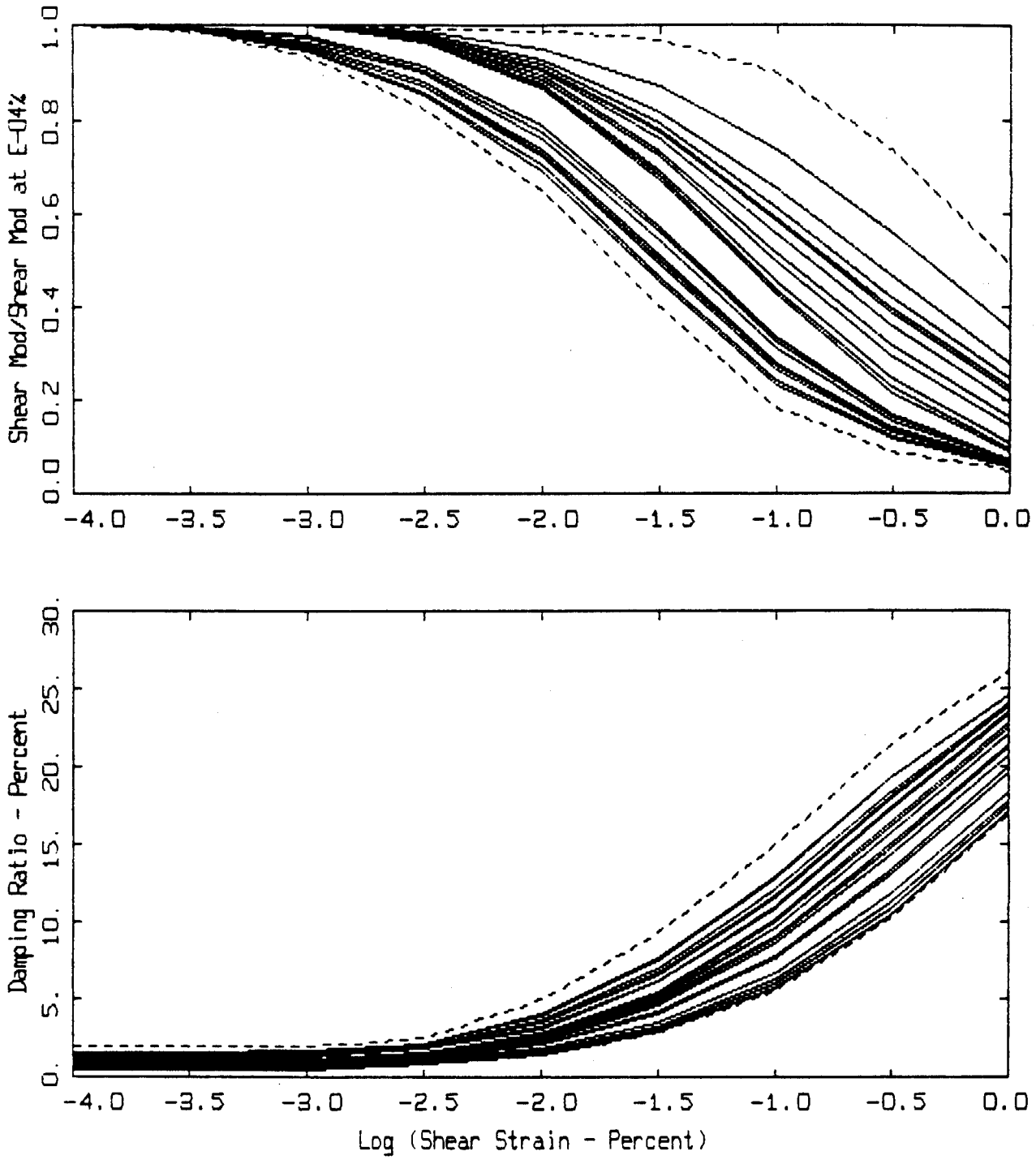

Figure 6-12. Example of randomized modulus reduction and damping curves (20) taken from the suite of 50 used in the analyses. Dashed lines are upper- and lower-bounds. Depth range is 51–120 ft.

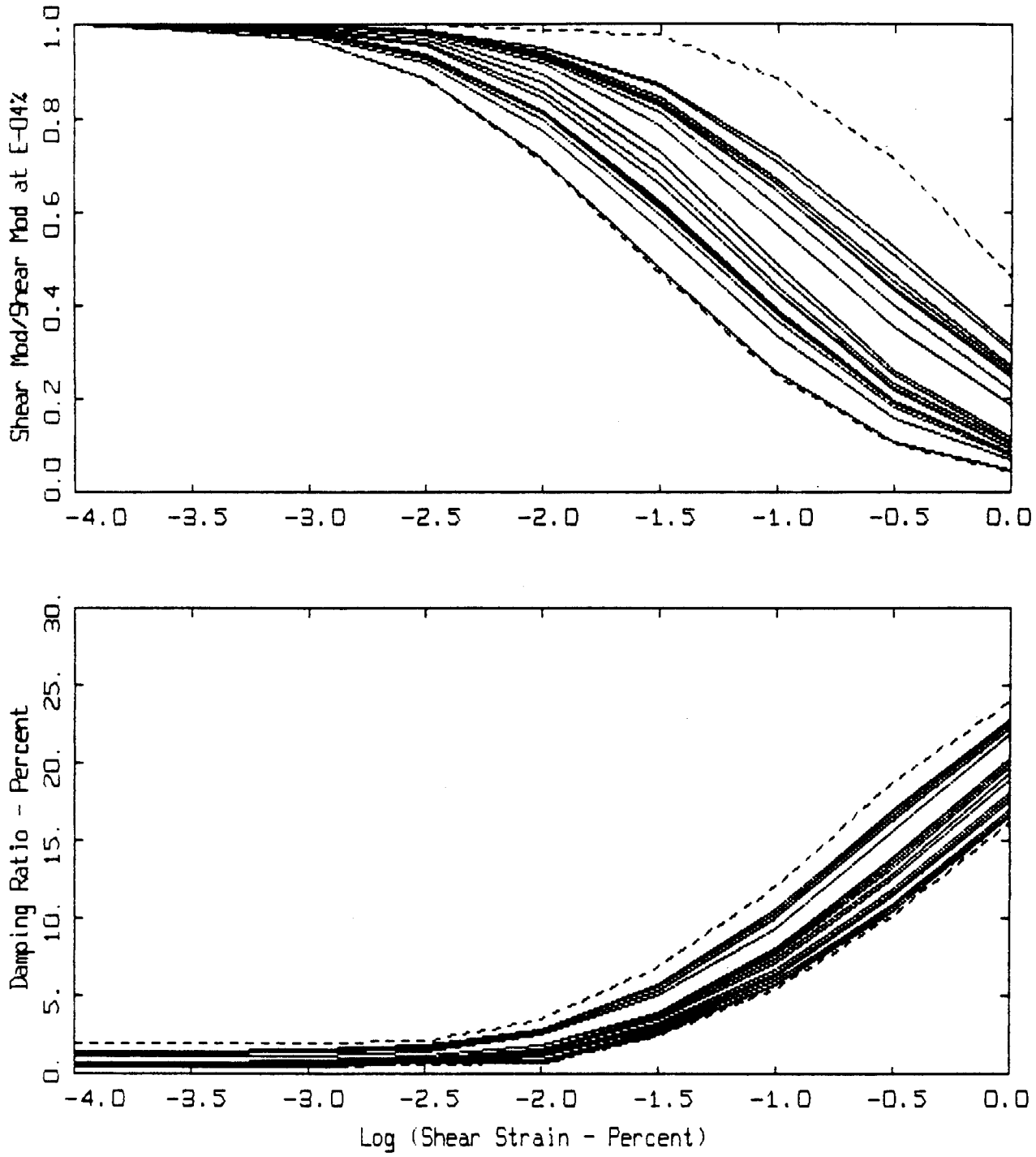

Figure 6-13. Example of randomized modulus reduction and damping curves (20) taken from the suite of 50 used in the analyses. Dashed lines are upper- and lower-bounds. Depth range is 121–250 ft.

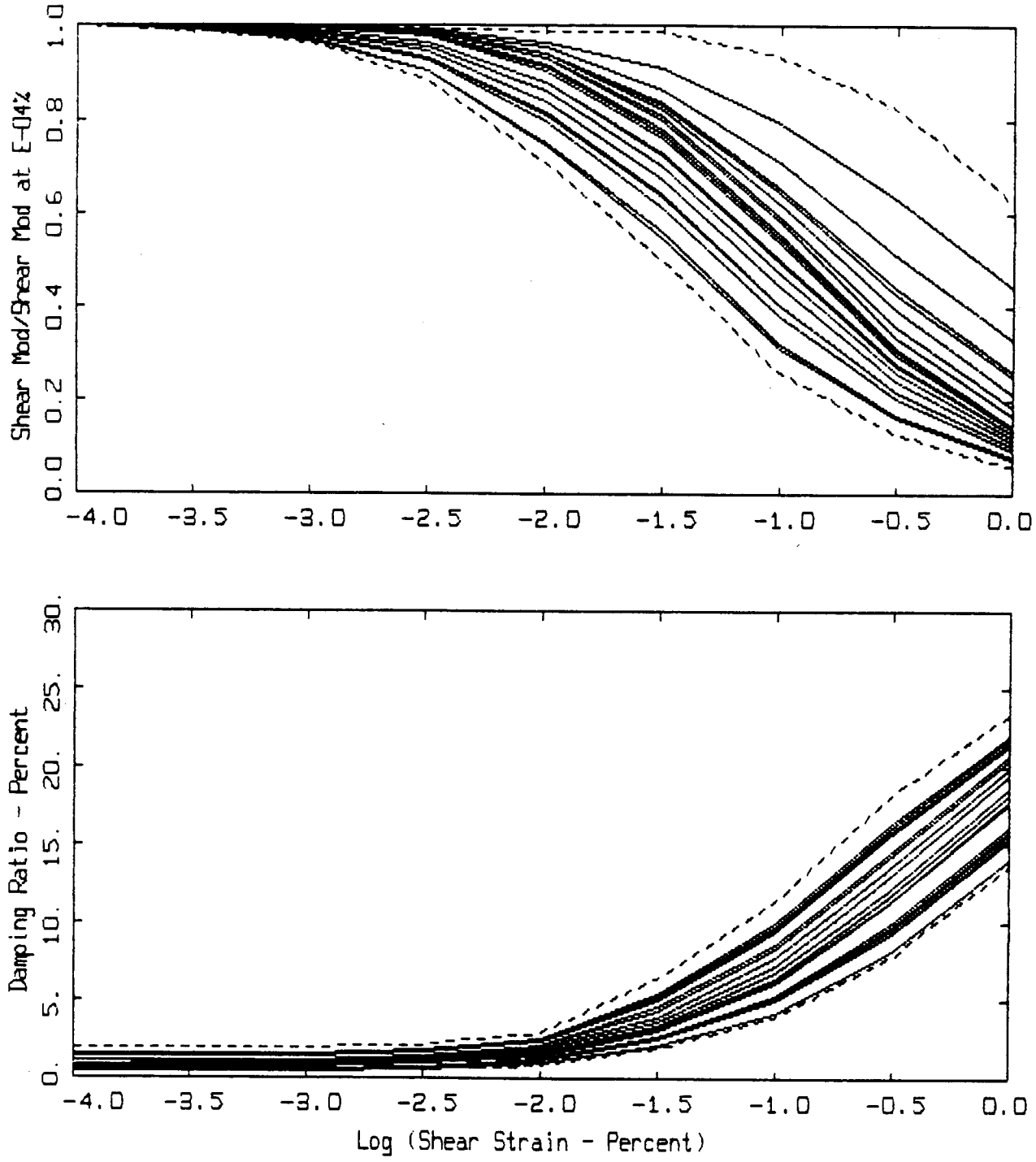

Figure 6-14. Example of randomized modulus reduction and damping curves (20) taken from the suite of 50 used in the analyses. Dashed lines are upper- and lower-bounds. Depth range is 251–500 ft.

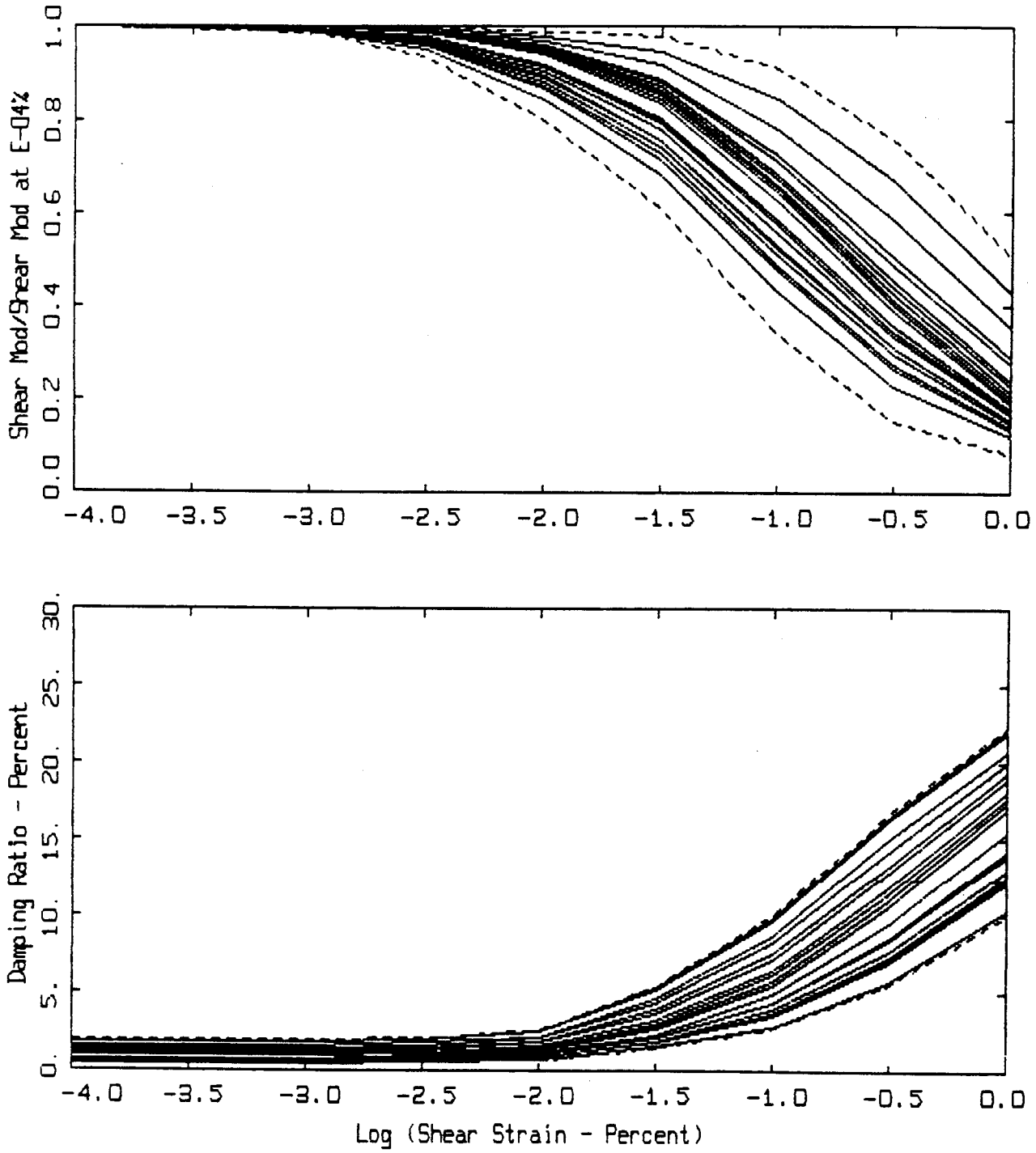

Figure 6-15. Example of randomized modulus reduction and damping curves (20) taken from the suite of 50 used in the analyses. Dashed lines are upper- and lower-bounds. Depth range is 501–1000 ft.

Since the computational scheme used to compute the motions at the surface of the profiles does not require time histories for control motions (Section 6.3.1), the point-source stochastic ground motion model presented in Section 3 may be used to define the outcrop power spectral density. In order that the outcrop motions used to excite the soil profile are in general accord with the final engineering model presented in Section 9 for rock motions, the base case or mean source and propagation path parameters listed in Table 3-1 were used. The point source was assumed to have a depth of 10 km in the Midcontinent crustal structure. Since the control motions are computed for fixed peak acceleration levels and moment magnitudes (Table 6-3), the crustal structure was taken as a half-space. Figure 6-16 shows the suite of response spectra computed for the seven of the eight levels of control motions shown on Table 6-3 (0.05g is not shown in Figures). A low-pass filter (5-pole Butterworth) has been applied at 62.5 Hz to emulate the effects of processing and to bring the spectral levels to saturation at peak acceleration for frequencies near 100 Hz.

6.4 Development of Site Amplification Factors

Site amplification factors are computed as the ratio of 5% damping response spectral acceleration (Sa) computed at the surface of each site for each randomized profile to 5% damping response spectral acceleration (Sa) computed for the bedrock (outcrop) motion. In addition, both peak acceleration and peak particle velocity were computed for the site and outcrop as well. Levels of input motion (rock outcrop) of 0.05, 0.1, 0.2, 0.3, 0.5, 0.75, 1.0, and 1.25g were used to accommodate effects of material nonlinearity upon site response. Table 6-3 shows the magnitudes (**M**), distances (R), peak accelerations, and peak particle velocities of the outcrop motions. Also shown are the predominant frequencies, estimated from the random process theory, associated with the peak accelerations and peak particle velocities. Of interest is the much higher predominant frequency associated with peak acceleration than is generally exhibited for WNA motions. Interestingly, the predominant frequencies associated with peak particle velocities are generally close to those appropriate for WNA. The outcrop V/A (cm/sec/g) ratios display expected magnitude dependency and weak dependence upon distance.

6.4.1 Amplification Factors

The amplification factors, 5% damped Sa (soil)/Sa (rock), were computed at approximately 90 frequencies from approximately 0.25 Hz to 50 Hz. The frequency range of interest is from 1 Hz to 34 Hz and more specifically at discrete frequencies of 1.0, 1.5, 2.5, 3.45, 5.0, 7.5, 10.0, 15.0, 25.0, and 34.0 Hz.

Table 6-3

Magnitudes (M) and Distances Used in Outcrop Motions

Ap(g)	f_p (Hz)[1]	V_p (cm/sec)[2]	f_p (Hz)[1]	V/A(cm/sec/g)	M	R(km)
0.05	17.47	2.63	2.32	52.57	6.0	58.75
0.10	20.58	4.62	2.66	46.14	6.0	35.32
0.20	22.87	8.40	2.94	41.97	6.0	20.15
0.30	23.82	12.10	3.07	40.34	6.0	14.20
0.50	23.93	26.14	2.35	52.27	6.5	12.25
0.75	23.93	49.31	1.86	65.72	7.0	11.52
1.00	23.79	77.74	1.59	77.73	7.5	11.99
1.25	24.16	95.61	1.62	76.46	7.5	9.78

1. Predominant frequencies associated with peak acceleration and peak particle velocity estimated by random process theory.
2. V_p = Peak particle velocity.

Outcrop motions are computed assuming a halfspace with a source region shear-wave velocity and density of 3.5 km/sec and 2.7 cgs, a stress drop of 120 bars, a kappa value of 0.006 sec, and a $Q(f) = 670\ f^{0.33}$.

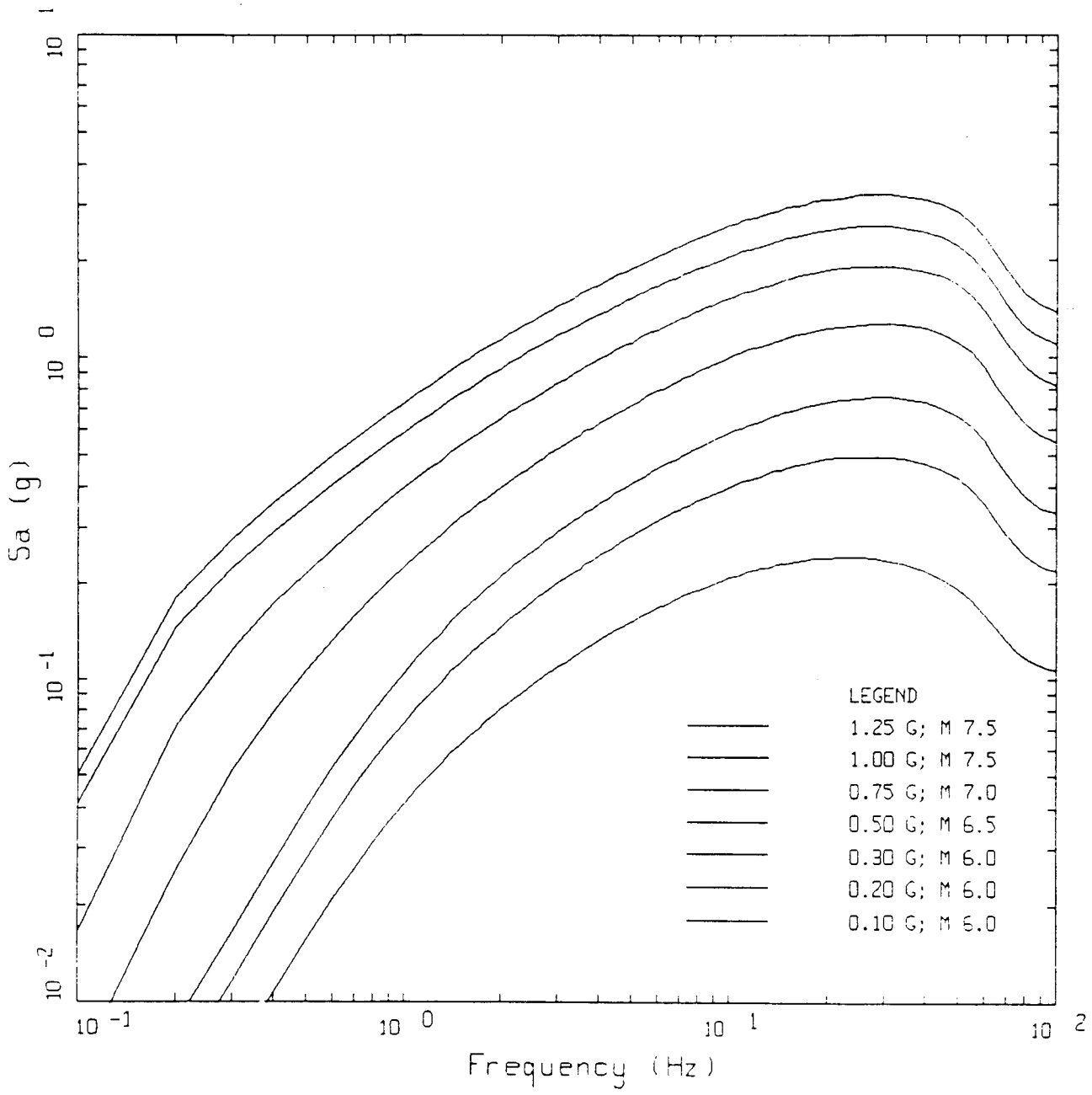

Figure 6-16. Pseudo-absolute acceleration response spectra (5% damping) computed for the outcrop or control motions (Table 6-3).

The entire set of factors is shown in Appendix 6.C, Figure Sets 6.C.1–6.C.5 for the five soil categories. As an example, Figures 6-17 to 6-19 show the factors and sigma values computed for Category 3 (120 ft) with control motions of 0.10, 0.50, and 1.00g. Due to the randomizing over depth, only a minor contribution to the fundamental resonance is present. This is a desirable feature for generic amplification factors and closely resembles recently derived empirical Western North America amplification factors (Section 6.5).

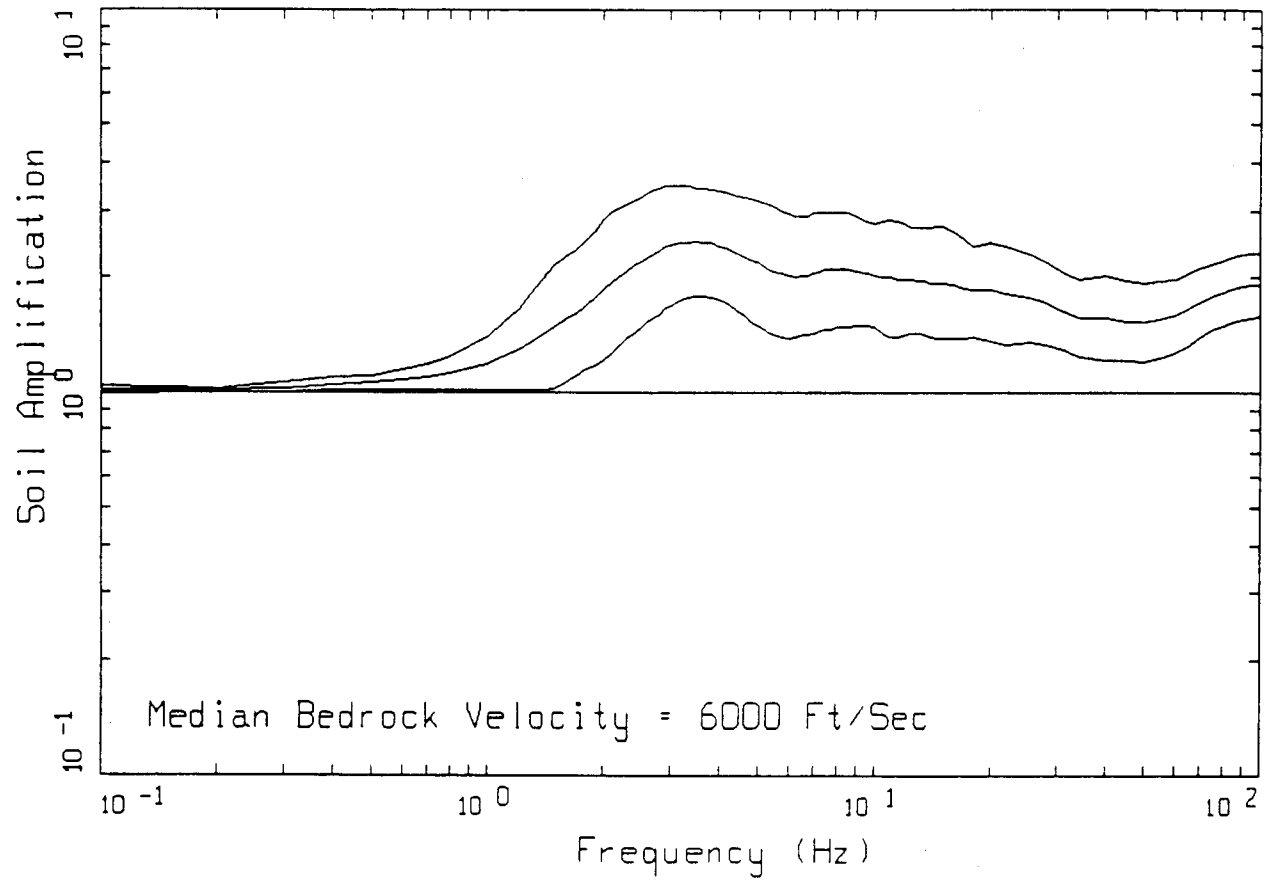

CATEGORY 3 (120 FT)

LEGEND

CONTROL MOTION 0.10 G; + 1 SIGMA OF 50 RANDOMIZED PROFILES
DEPTH RANDOMIZED BETWEEN 81 & 180 FT.

CONTROL MOTION 0.10 G; MEDIAN OF 50 RANDOMIZED PROFILES
DEPTH RANDOMIZED BETWEEN 81 & 180 FT.

CONTROL MOTION 0.10 G; - 1 SIGMA OF 50 RANDOMIZED PROFILES
DEPTH RANDOMIZED BETWEEN 81 & 180 FT.

Figure 6-17. Category 3 (81–180 ft) median and 1 sigma amplification factors for 5% damped response spectra. Control motion is 0.10 g.

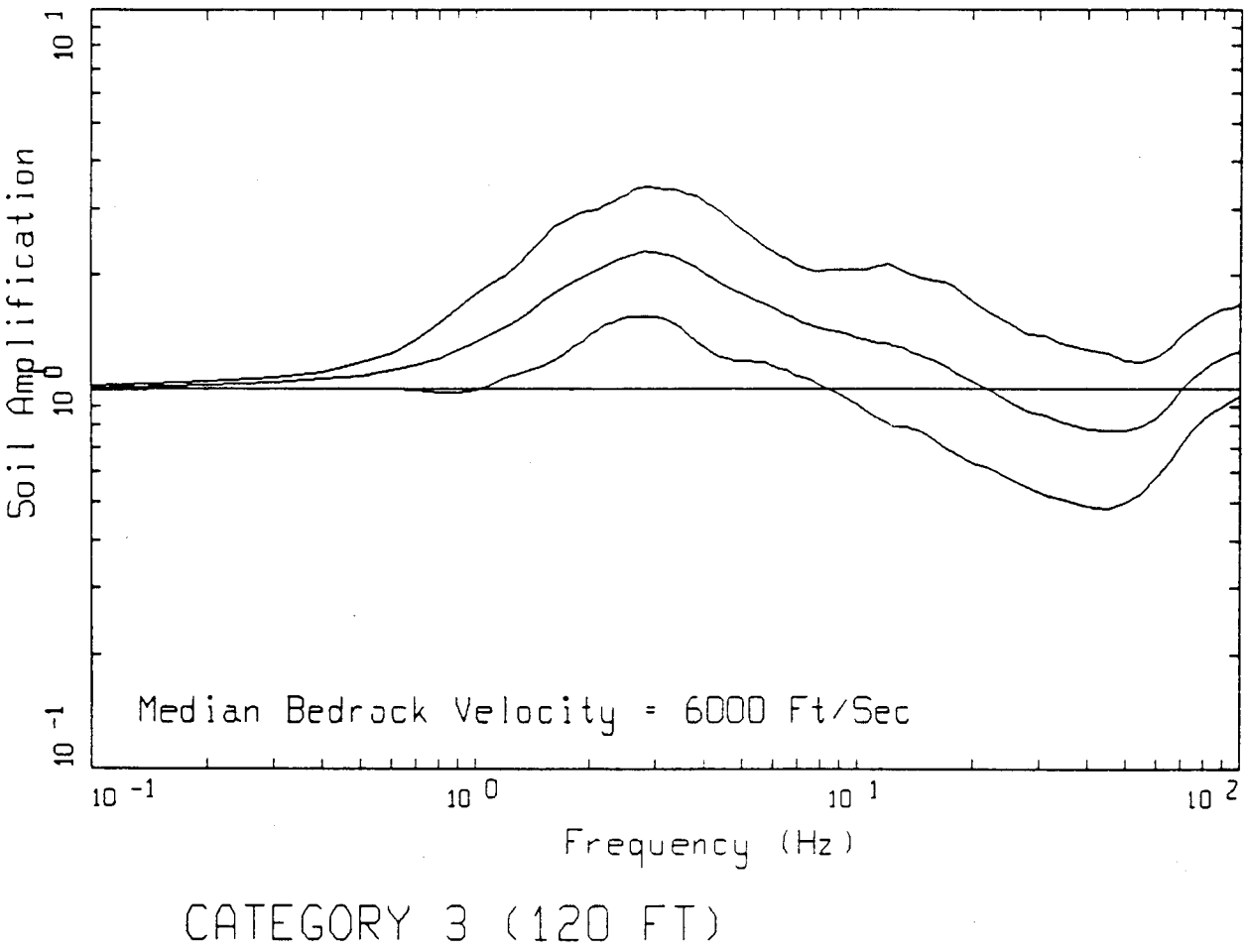

Figure 6-18. Category 3 (81–180 ft) median and 1 sigma amplification factors for 5% damped response spectra. Control motion is 0.50 g.

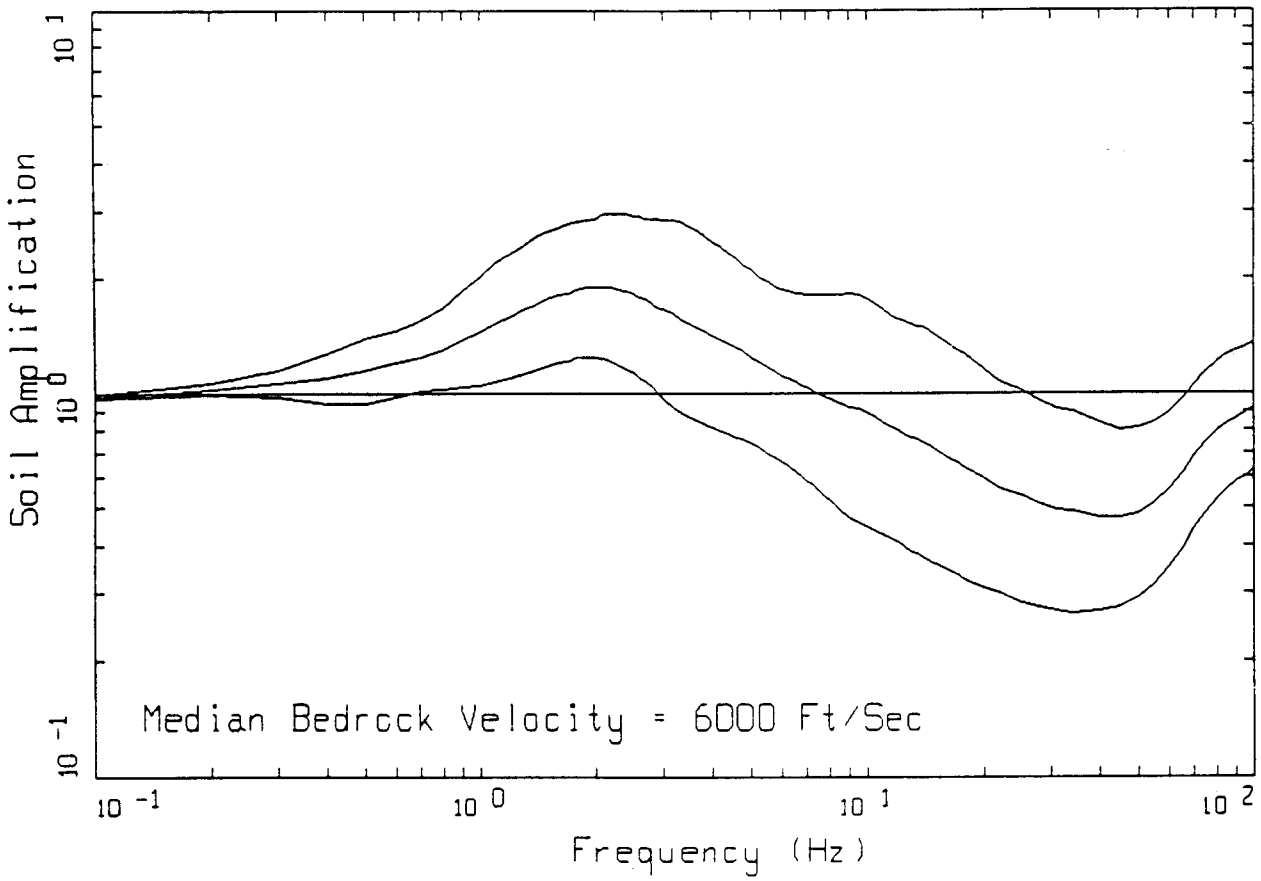

LEGEND

——— CONTROL MOTION 1.00 G; + 1 SIGMA OF 50 RANDOMIZED PROFILES
DEPTH RANDOMIZED BETWEEN 81 & 180 FT.

——— CONTROL MOTION 1.00 G; MEDIAN OF 50 RANDOMIZED PROFILES
DEPTH RANDOMIZED BETWEEN 81 & 180 FT.

——— CONTROL MOTION 1.00 G; - 1 SIGMA OF 50 RANDOMIZED PROFILES
DEPTH RANDOMIZED BETWEEN 81 & 180 FT.

Figure 6-19. Category 3 (81–180 ft) median and 1 sigma amplification factors for 5% damped response spectra. Control motion is 1.00 g.

Table 6-4 summarizes the amplification factors for the five categories and eight input acceleration levels. The largest uncertainty (σ_{ln}) is about 0.4 (Table 6-4) and occurs near the fundamental resonance of the median profile where the soil column is, on average, having its greatest amplification effects (Toro et al., 1992). The effects of damping are seen in the decrease in amplitude with increasing frequency. The reversal in this trend near 50 Hz occurs where the rock outcrop acceleration response spectra (Figure 6-16) begin to saturate to peak acceleration. At 100 Hz the amplification factors are then essentially peak acceleration ratios.

Subtle effects of nonlinear response are seen in Figure 6-18 in the flatter slope and more pronounced resonance shown in the 16^{th} percentile factor compared to the 84^{th} percentile. For the higher motions, the overall damping is greater possibly due to higher bedrock velocities and softer profiles than median values. For the higher levels of control motions, 0.50g in Figure 6-18 and 1.00g in Figure 6-19, the nonlinear effects are dramatic. There is a decrease in the maximum spectral amplification and an increasing fall-off with frequency. Also, the largest uncertainties, for the 1.00g control motions (Figure 6-19), are not at the median resonance but at very high frequencies (30-40 Hz). For very high levels of motion, the predominant effect of the soil column is attenuation through damping rather than amplification through the velocity gradient. An important inference from these results is that for high levels of motion, accurate prediction of site response depends more strongly on an accurate model of the dependency of material damping and shear modulus on shear strain than on the shear-wave velocity profile. This result is substantiated in the comparisons of site response analyses to recorded motions in Appendix 6-B.

For the 1.0g control motions, the computed amplification factors show a sharp decrease with increasing frequency and are less than one above about 8 Hz. The minimum value is about 0.5, close to the empirical minimum of 0.6 (Section 6.5). For the largest control motions, 1.25g, the maximum cyclic shear strains average around 0.5%.

A convenient visual presentation of the amplification factors is shown in Figures 6-20 to 6-27. Each figure shows the factors plotted versus median profile depth for five levels of control motion: 0.10, 0.30, 0.50, 0.75, and 1.00g. Figures 6-20 to 6-25 are for oscillator frequencies 1.0, 2.5, 5.0, 10.0, 25.0, and 34.0 Hz. Figures 6-26 and 6-27 show predicted amplifications for peak accelerations and peak particle velocities respectively.

The spectral amplification figures, in a general sense, show a frequency-dependent resonance versus depth. The amplification factors generally increase with depth at 1.0 Hz and show a peak at 2.5 Hz at a depth near 120 feet. The peak shifts as expected, and is located near a soil depth of 50 feet for a frequency of 5.0 Hz. At 10.0 Hz, the trend shown by the 1 Hz calculations has reversed and the peak is occurring between the surface and 20 feet. The peak acceleration amplification factors (Figure 6-26) follow the trend of the 10.0 and 25.0 Hz response spectral amplification factors (Figures 6-22 and 6-24). Peak acceleration factors for Western North America, due to lower frequency content, might be expected to follow more closely the trend shown by the 2.5 and 5.0 Hz response spectral amplification factors. Peak particle velocity (Figure 6-27) is in general agreement with the trends shown by a combination of the 1.0 and 2.5 Hz response spectral amplification factors. This is in accord with the lower predominant frequencies associated with the input (rock outcrop) particle velocities (Table 6-3) compared to the corresponding accelerations. The predominant frequencies at the surface of the profiles for accelerations and particle velocities is approximately 10–20 Hz and 1–3 Hz respectively, and is naturally site dependent.

The effects of nonlinear soil response are easily seen in the range in amplification for different input motions. The effect appears to be both frequency and soil-depth dependent. For low frequencies (1.0 and 2.5 Hz) and shallow profiles (< 120 ft) the results do not depend strongly upon input acceleration level. As the profile deepens and as frequency increases, the dependence upon input acceleration level increases substantially. However, it should be kept in mind that the results span an *order of magnitude* in input acceleration levels (0.1–1.0g) which would correspond to a change of slightly more than three magnitude units at a fixed distance (assuming log (Ap) = 0.3 **M**; Boore, 1983). Even with this range in motions, the maximum average variation of the amplification factors is approximately 50%.

The general trend of decreasing amplification with increasing levels of input motion is shown consistently with peak acceleration, peak particle velocity, and response

Table 6-4

Median Amplification Factors and Standard Deviations Computed for 5% Damped Response Spectra, Peak Acceleration, and Peak Particle Velocity

	Category 1		Category 2		Category 3		Category 4		Category 5		Input[1]
Frequencies (Hz)	20' (10–30')		50' (31–80')		120' (81–180')		250' (181–400')		500' (401– + ')		(rock outcrop) (g)
	Median	Sigma[2]	Median	Sigma	Median	Sigma	Median	Sigma	Median	Sigma	
1.00	1.02	0.02	1.05	0.03	1.18	0.14	1.67	0.36	2.10	0.36	0.05
	1.02	0.02	1.05	0.04	1.19	0.16	1.71	0.37	2.10	0.37	0.10
	1.02	0.02	1.06	0.05	1.23	0.21	1.77	0.38	2.08	0.38	0.20
	1.03	0.03	1.07	0.06	1.26	0.24	1.82	0.38	2.07	0.39	0.30
	1.03	0.05	1.09	0.09	1.33	0.29	1.91	0.39	2.00	0.42	0.50
	1.05	0.09	1.13	0.14	1.39	0.27	2.01	0.39	1.81	0.50	0.75
	1.09	0.16	1.19	0.21	1.45	0.33	2.01	0.37	1.81	0.46	1.00
	1.10	0.18	1.23	0.23	1.52	0.35	2.05	0.38	1.72	0.46	1.25
1.50	1.03	0.03	1.10	0.07	1.44	0.35	2.25	0.36	1.82	0.40	0.05
	1.04	0.04	1.11	0.08	1.48	0.37	2.27	0.36	1.83	0.40	0.10
	1.04	0.05	1.13	0.11	1.53	0.35	2.30	0.36	1.80	0.39	0.20
	1.05	0.06	1.16	0.14	1.58	0.35	2.32	0.35	1.78	0.38	0.30
	1.08	0.10	1.22	0.21	1.70	0.38	2.29	0.36	1.72	0.36	0.50
	1.12	0.19	1.31	0.30	1.79	0.39	2.15	0.36	1.62	0.46	0.75
	1.16	0.20	1.35	0.29	1.76	0.41	1.95	0.38	1.56	0.39	1.00
	1.17	0.19	1.39	0.32	1.77	0.41	1.86	0.39	1.45	0.43	1.25
2.50	1.08	0.08	1.30	0.21	2.15	0.39	2.12	0.32	1.98	0.30	0.05
	1.09	0.10	1.34	0.26	2.19	0.39	2.10	0.31	1.96	0.30	0.10
	1.12	0.13	1.42	0.33	2.21	0.37	2.05	0.30	1.91	0.30	0.20
	1.15	0.19	1.48	0.36	2.23	0.35	1.99	0.32	1.85	0.29	0.30
	1.22	0.29	1.58	0.37	2.25	0.38	1.83	0.36	1.73	0.35	0.50
	1.24	0.24	1.62	0.40	2.11	0.40	1.66	0.43	1.52	0.48	0.75
	1.25	0.33	1.58	0.44	1.81	0.47	1.51	0.48	1.37	0.47	1.00
	1.28	0.36	1.51	0.44	1.65	0.49	1.47	0.46	1.23	0.51	1.25

1. For levels of control motion between those shown, linear interpolation may be used to determine the appropriate amplification factors.
2. Sigma (ln).

Table 6-4 (Continued)

Median Amplification Factors and Standard Deviations Computed for 5% Damped Response Spectra, Peak Acceleration, and Peak Particle Velocity

	Category 1		Category 2		Category 3		Category 4		Category 5		Input[1]
Frequencies (Hz)	20' (10–30')		50' (31–80')		120' (81–180')		250' (181–400')		500' (401– + ')		(rock outcrop) (g)
	Median	Sigma[2]	Median	Sigma	Median	Sigma	Median	Sigma	Median	Sigma	
3.45	1.16	0.17	1.66	0.40	2.50	0.34	1.94	0.34	2.03	0.32	0.05
	1.19	0.21	1.73	0.41	2.47	0.33	1.92	0.35	2.01	0.31	0.10
	1.25	0.28	1.81	0.42	2.43	0.35	1.85	0.36	1.97	0.33	0.20
	1.31	0.35	1.87	0.44	2.38	0.36	1.78	0.35	1.91	0.34	0.30
	1.34	0.30	1.91	0.47	2.19	0.41	1.62	0.34	1.66	0.40	0.50
	1.38	0.39	1.78	0.46	1.83	0.48	1.50	0.39	1.33	0.54	0.75
	1.32	0.42	1.61	0.47	1.54	0.57	1.34	0.43	1.10	0.47	1.00
	1.31	0.39	1.51	0.48	1.43	0.57	1.27	0.44	0.94	0.51	1.25
5.00	1.41	0.43	2.34	0.49	2.22	0.35	1.95	0.31	1.91	0.30	0.05
	1.46	0.43	2.33	0.46	2.18	0.38	1.91	0.31	1.84	0.30	0.10
	1.51	0.41	2.28	0.44	2.09	0.41	1.82	0.31	1.73	0.32	0.20
	1.54	0.41	2.23	0.47	1.99	0.40	1.73	0.30	1.65	0.34	0.30
	1.58	0.45	1.98	0.42	1.77	0.40	1.56	0.37	1.38	0.40	0.50
	1.51	0.45	1.73	0.41	1.48	0.45	1.33	0.45	1.03	0.48	0.75
	1.37	0.50	1.53	0.47	1.25	0.52	1.14	0.51	0.84	0.46	1.00
	1.35	0.51	1.41	0.53	1.11	0.54	1.04	0.49	0.71	0.50	1.25
7.50	1.87	0.51	2.35	0.41	2.09	0.34	2.03	0.35	1.86	0.28	0.05
	1.89	0.50	2.26	0.39	2.08	0.35	1.98	0.35	1.79	0.29	0.10
	1.93	0.50	2.12	0.35	1.96	0.34	1.85	0.33	1.63	0.30	0.20
	1.90	0.51	2.03	0.35	1.82	0.31	1.74	0.32	1.47	0.31	0.30
	1.79	0.49	1.83	0.41	1.47	0.33	1.43	0.38	1.10	0.37	0.50
	1.61	0.55	1.58	0.53	1.22	0.44	1.12	0.45	0.78	0.55	0.75
	1.44	0.69	1.42	0.64	1.00	0.58	0.90	0.52	0.62	0.52	1.00
	1.38	0.69	1.29	0.69	0.89	0.65	0.80	0.53	0.51*	0.54	1.25

1. For levels of control motion between those shown, linear interpolation may be used to determine the appropriate amplification factors.
2. Sigma (ln).

Table 6-4 (Continued)

Median Amplification Factors and Standard Deviations Computed for 5% Damped Response Spectra, Peak Acceleration, and Peak Particle Velocity

	Category 1		Category 2		Category 3		Category 4		Category 5		Input[1]
Frequencies (Hz)	20' (10–30')		50' (31–80')		120' (81–180')		250' (181–400')		500' (401– + ')		(rock outcrop) (g)
	Median	Sigma[2]	Median	Sigma	Median	Sigma	Median	Sigma	Median	Sigma	
10.00	2.28	0.54	2.15	0.38	2.15	0.33	2.01	0.26	1.85	0.26	0.05
	2.26	0.54	2.10	0.36	2.01	0.31	1.91	0.27	1.72	0.27	0.10
	2.16	0.50	2.04	0.37	1.81	0.33	1.75	0.30	1.49	0.30	0.20
	2.05	0.49	1.91	0.39	1.66	0.34	1.60	0.33	1.31	0.34	0.30
	1.85	0.50	1.66	0.45	1.37	0.41	1.25	0.40	0.95	0.44	0.50
	1.60	0.61	1.48	0.53	1.10	0.56	0.97	0.48	0.65	0.58	0.75
	1.36	0.70	1.21	0.64	0.89	0.69	0.75	0.54	0.50*	0.51	1.00
	1.27	0.70	1.06	0.71	0.77	0.68	0.66	0.54	0.41*	0.52	1.25
15.00	2.40	0.41	2.04	0.29	2.07	0.33	1.91	0.24	1.66	0.27	0.05
	2.34	0.42	1.90	0.29	1.93	0.34	1.76	0.24	1.50	0.29	0.10
	2.20	0.44	1.75	0.32	1.70	0.37	1.51	0.28	1.25	0.34	0.20
	2.03	0.46	1.67	0.34	1.53	0.37	1.32	0.34	1.07	0.39	0.30
	1.79	0.52	1.42	0.41	1.22	0.47	1.02	0.46	0.72	0.48	0.50
	1.51	0.62	1.18	0.53	0.92	0.60	0.76	0.55	0.47*	0.55	0.75
	1.28	0.78	1.01	0.64	0.72	0.70	0.58*	0.59	0.37*	0.46	1.00
	1.16	0.82	0.88	0.71	0.61	0.69	0.50*	0.59	0.30*	0.45	1.25
25.00	2.31	0.36	2.05	0.27	1.90	0.24	1.74	0.25	1.39	0.26	0.05
	2.21	0.38	1.93	0.30	1.76	0.27	1.55	0.29	1.20	0.29	0.10
	1.97	0.36	1.78	0.32	1.48	0.30	1.27	0.38	0.94	0.37	0.20
	1.81	0.38	1.63	0.36	1.26	0.36	1.07	0.43	0.76	0.40	0.30
	1.56	0.43	1.32	0.46	0.93	0.47	0.76	0.49	0.50*	0.43	0.50
	1.29	0.57	1.03	0.58	0.68	0.56	0.56*	0.53	0.35*	0.46	0.75
	1.07	0.71	0.84	0.67	0.53*	0.64	0.44*	0.54	0.29*	0.38	1.00
	0.97	0.76	0.72	0.72	0.46*	0.64	0.38*	0.52	0.24*	0.37	1.25

1. For levels of control motion between those shown, linear interpolation may be used to determine the appropriate amplification factors.
2. Sigma (ln).
* A lower limit of 0.6 should be substituted for these values.

Table 6-4 (Continued)

Median Amplification Factors and Standard Deviations Computed for 5% Damped Response Spectra, Peak Acceleration, and Peak Particle Velocity

	Category 1		Category 2		Category 3		Category 4		Category 5		Input[1]
Frequencies (Hz)	20' (10–30')		50' (31–80')		120' (81–180')		250' (181–400')		500' (401– + ')		(rock outcrop) (g)
	Median	Sigma[2]	Median	Sigma	Median	Sigma	Median	Sigma	Median	Sigma	
34.00	2.12	0.27	1.96	0.21	1.78	0.19	1.58	0.18	1.29	0.23	0.05
	2.00	0.28	1.81	0.23	1.57	0.23	1.38	0.23	1.07	0.27	0.10
	1.84	0.30	1.60	0.28	1.31	0.32	1.09	0.33	0.79	0.33	0.20
	1.70	0.33	1.45	0.33	1.12	0.38	0.90	0.37	0.64	0.35	0.30
	1.45	0.44	1.17	0.45	0.82	0.48	0.65	0.44	0.44*	0.36	0.50
	1.21	0.60	0.93	0.58	0.61	0.55	0.49*	0.46	0.32*	0.41	0.75
	1.00	0.75	0.76	0.67	0.49*	0.61	0.39*	0.46	0.27*	0.34	1.00
	0.89	0.79	0.65	0.71	0.41*	0.59	0.34*	0.45	0.24*	0.35	1.25
Ap (site)/Ap (rock)	2.29	0.17	2.15	0.17	2.12	0.19	1.95	0.17	1.82	0.20	0.05
	2.28	0.15	2.08	0.16	1.98	0.19	1.79	0.17	1.63	0.20	0.10
	2.18	0.15	1.93	0.17	1.76	0.21	1.56	0.19	1.38	0.21	0.20
	2.05	0.18	1.80	0.19	1.59	0.23	1.40	0.21	1.21	0.23	0.30
	1.83	0.25	1.58	0.25	1.34	0.28	1.17	0.26	0.99	0.25	0.50
	1.60	0.35	1.37	0.33	1.13	0.34	0.99	0.30	0.82	0.26	0.75
	1.41	0.45	1.21	0.39	0.97	0.40	0.86	0.33	0.73	0.26	1.00
	1.32	0.47	1.10	0.43	0.88	0.40	0.78	0.33	0.62	0.47	1.25
PGV(site)/ PGV(rock)	1.23	0.10	1.33	0.12	1.53	0.17	1.71	0.18	1.88	0.19	0.05
	1.25	0.10	1.35	0.12	1.55	0.16	1.71	0.17	1.87	0.19	0.10
	1.27	0.10	1.36	0.12	1.55	0.15	1.70	0.16	1.83	0.18	0.20
	1.27	0.09	1.36	0.11	1.54	0.14	1.68	0.15	1.80	0.17	0.30
	1.18	0.05	1.24	0.08	1.37	0.11	1.48	0.14	1.62	0.16	0.50
	1.13	0.03	1.16	0.05	1.24	0.08	1.34	0.12	1.46	0.14	0.75
	1.09	0.03	1.12	0.04	1.18	0.07	1.27	0.12	1.38	0.13	1.00
	1.09	0.03	1.11	0.04	1.17	0.07	1.25	0.09	1.37	0.24	1.25

1. For levels of control motion between those shown, linear interpolation may be used to determine the appropriate amplification factors.
2. Sigma (ln).
* A lower limit of 0.6 should be substituted for these values.

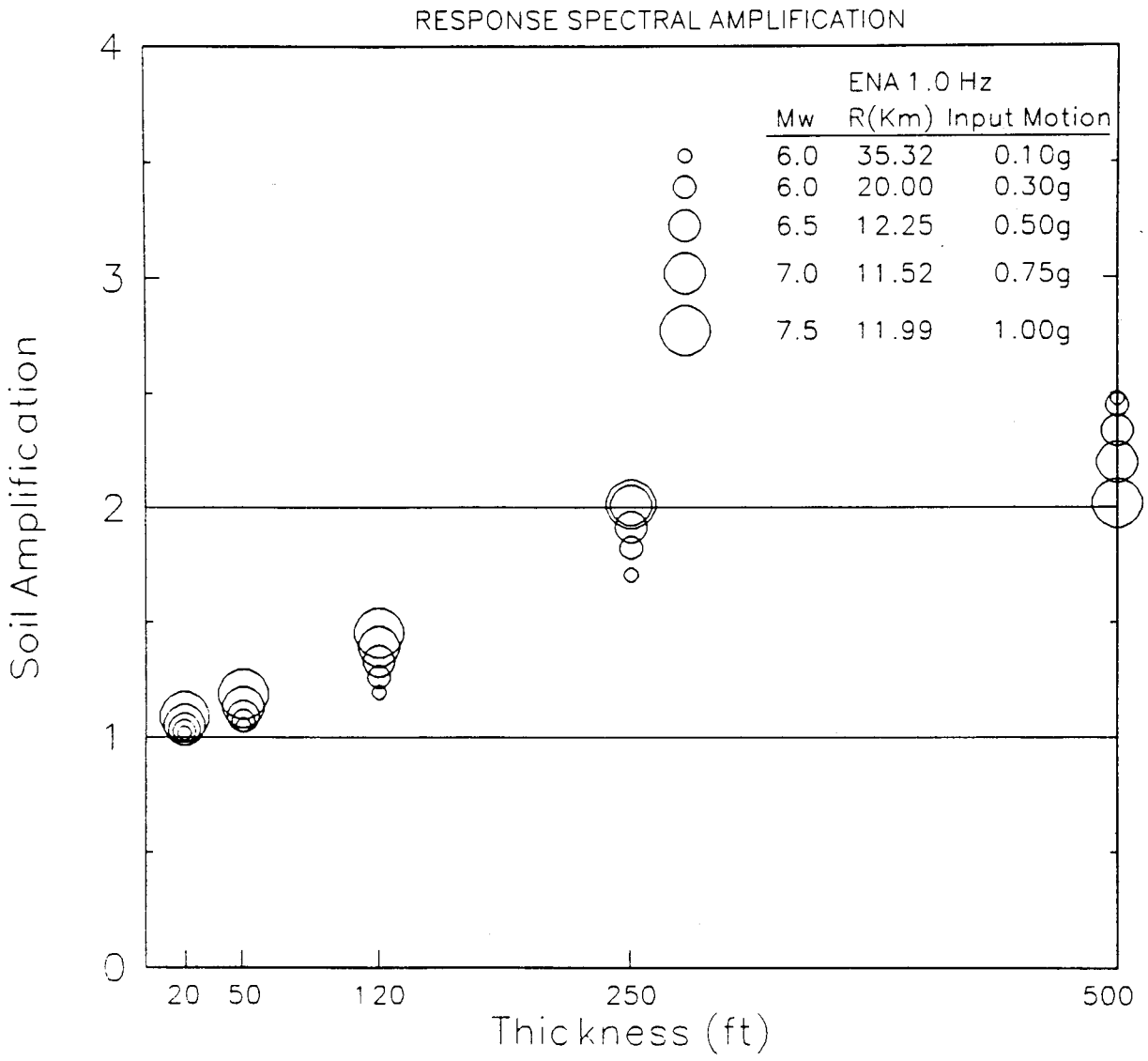

Figure 6-20. Plot of median 5% damped response spectral amplification factors computed for the five site categories (Table 6-2) at a frequency of 1 Hz. Size of symbol indicates level of input (rock outcrop) acceleration (0.1, 0.3, 0.5, 0.75, 1 g).

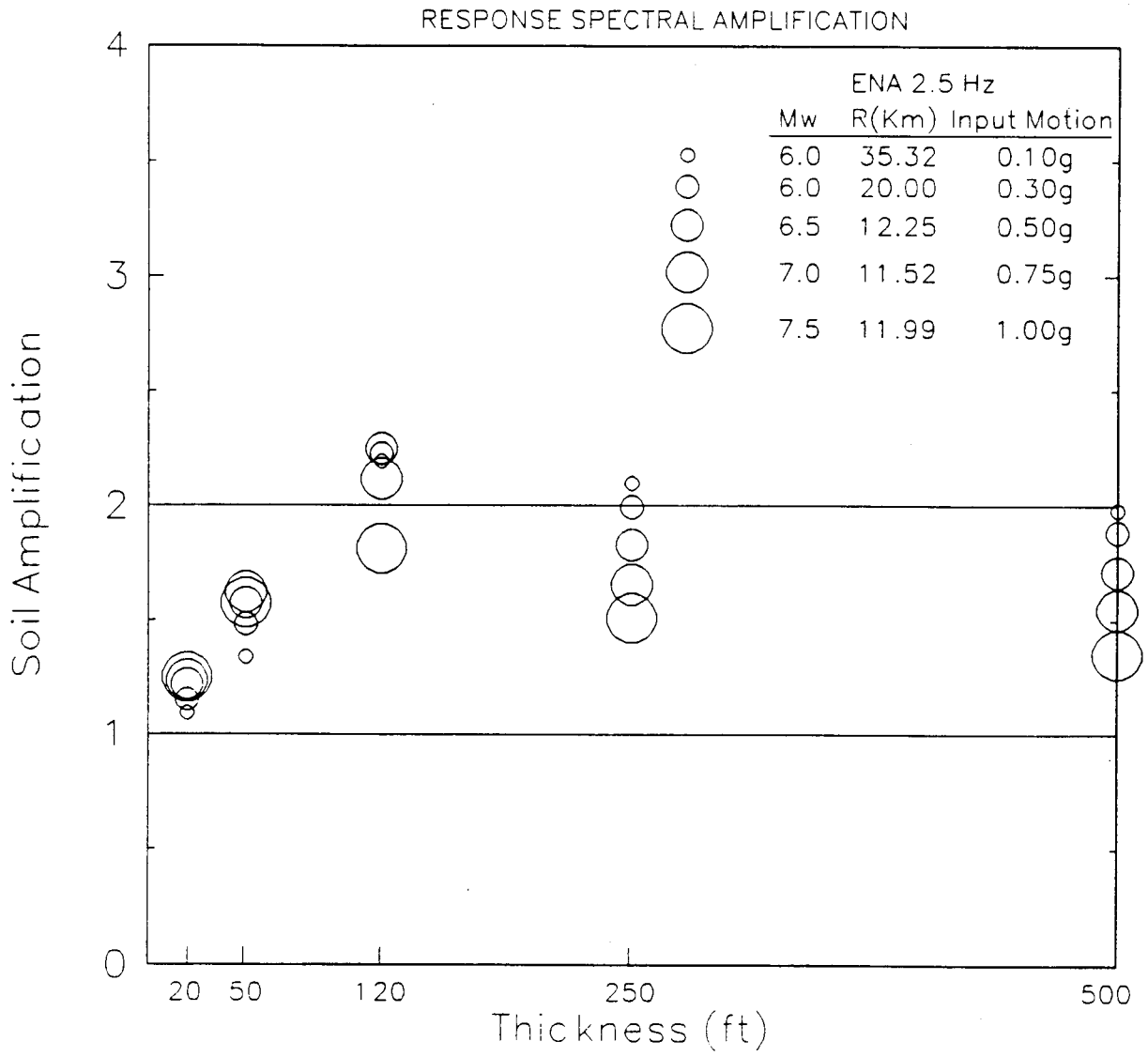

Figure 6-21. Plot of median 5% damped response spectral amplification factors computed for the five site categories (Table 6-2) at a frequency of 2.5 Hz. Size of symbol indicates level of input (rock outcrop) acceleration (0.1, 0.3, 0.5, 0.75, 1 g).

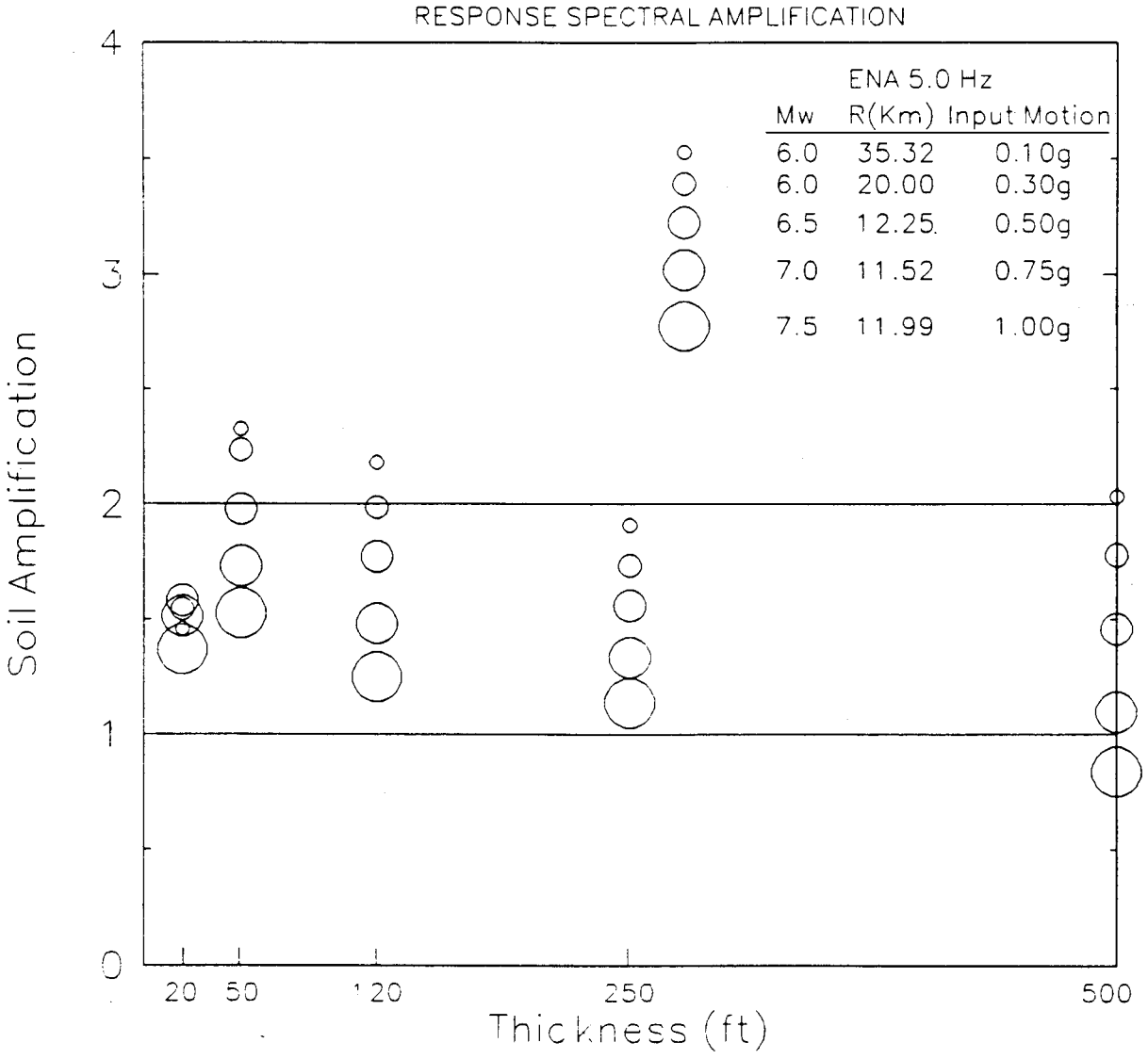

Figure 6-22. Plot of median 5% damped response spectral amplification factors computed for the five site categories (Table 6-2) at a frequency of 5.0 Hz. Size of symbol indicates level of input (rock outcrop) acceleration (0.1, 0.3, 0.5, 0.75, 1 g).

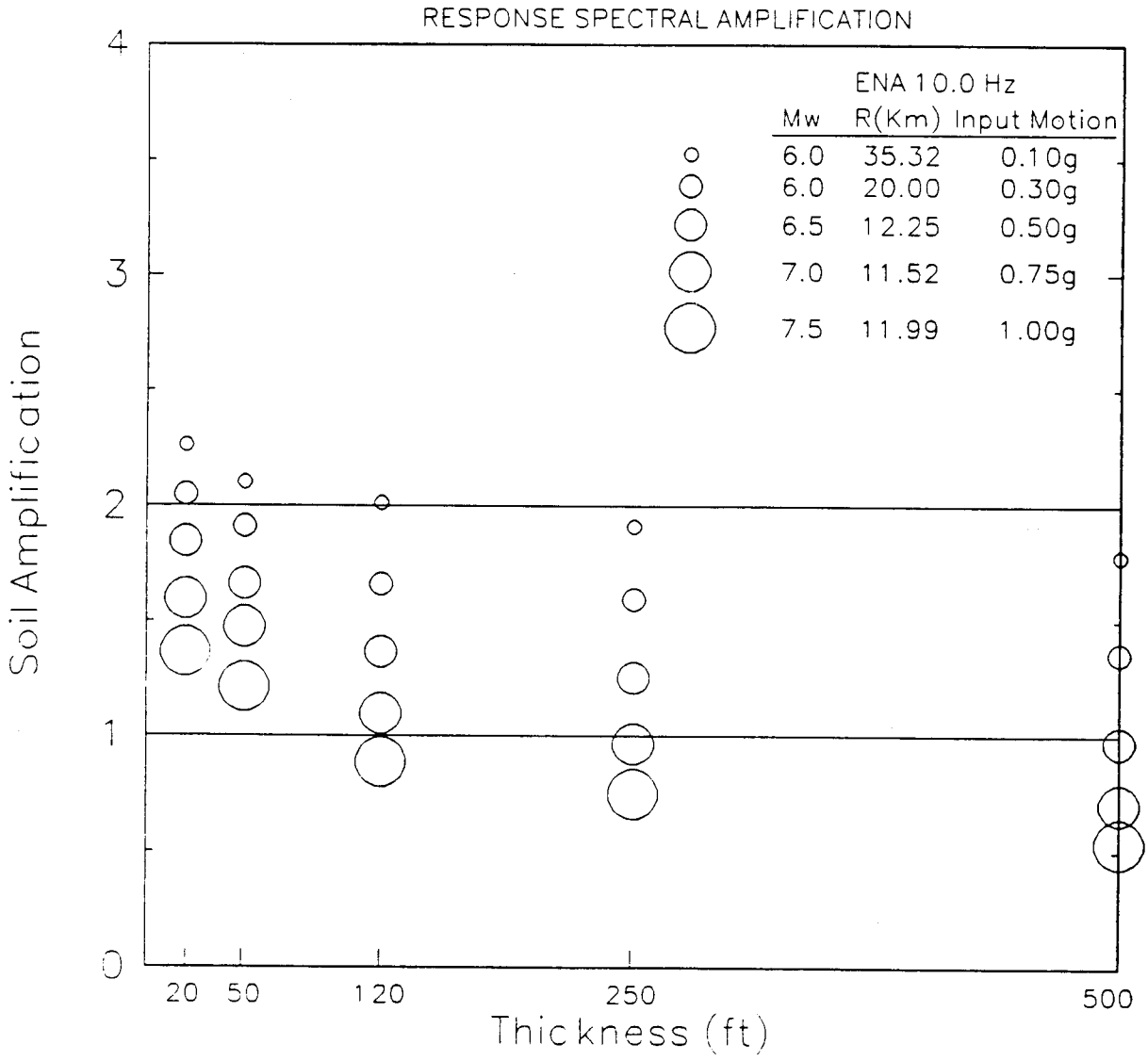

Figure 6-23. Plot of median 5% damped response spectral amplification factors computed for the five site categories (Table 6-2) at a frequency of 10.0 Hz. Size of symbol indicates level of input (rock outcrop) acceleration (0.1, 0.3, 0.5, 0.75, 1 g).

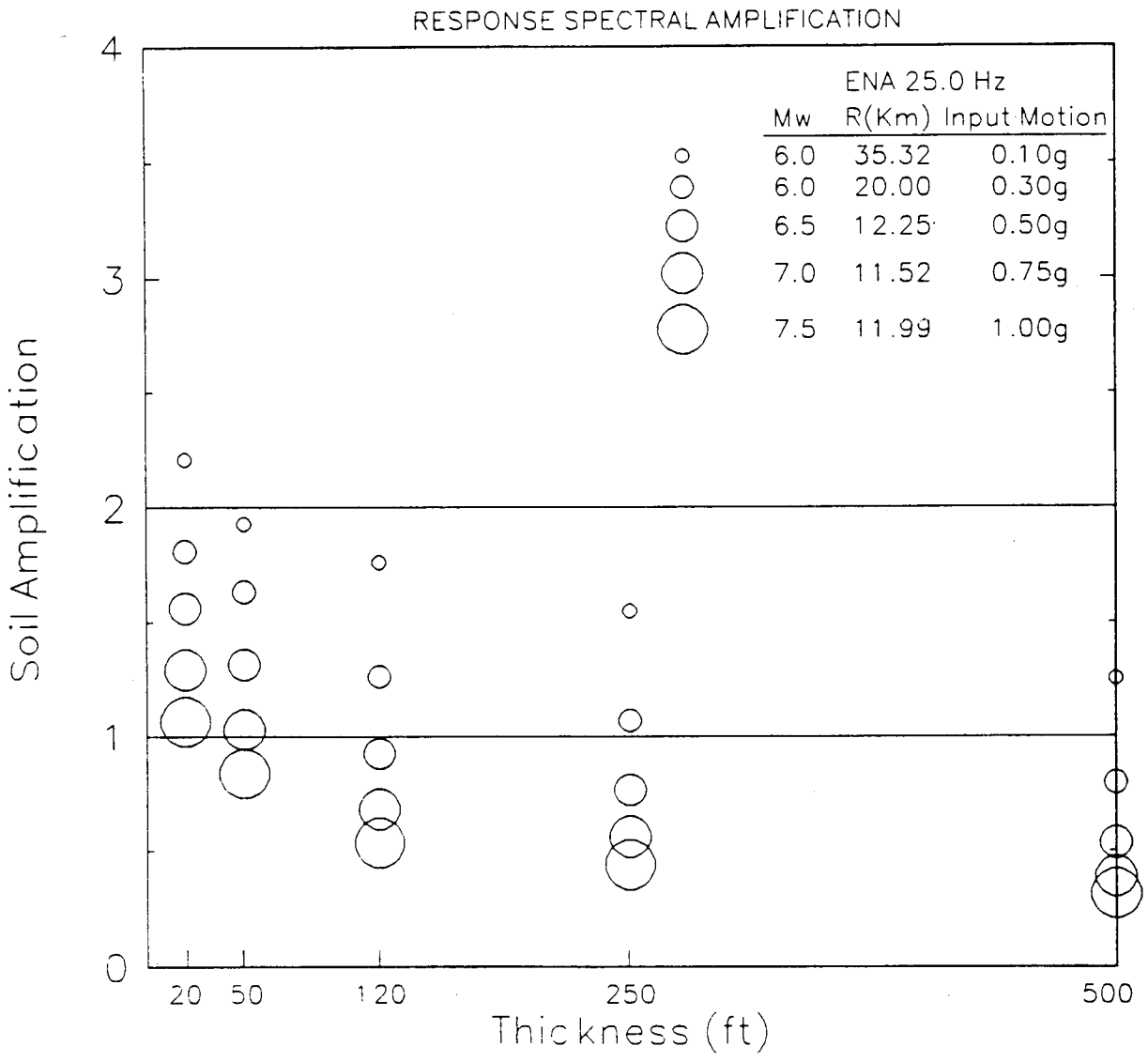

Figure 6-24. Plot of median 5% damped response spectral amplification factors computed for the five site categories (Table 6-2) at a frequency of 25.0 Hz. Size of symbol indicates level of input (rock outcrop) acceleration (0.1, 0.3, 0.5, 0.75, 1 g).

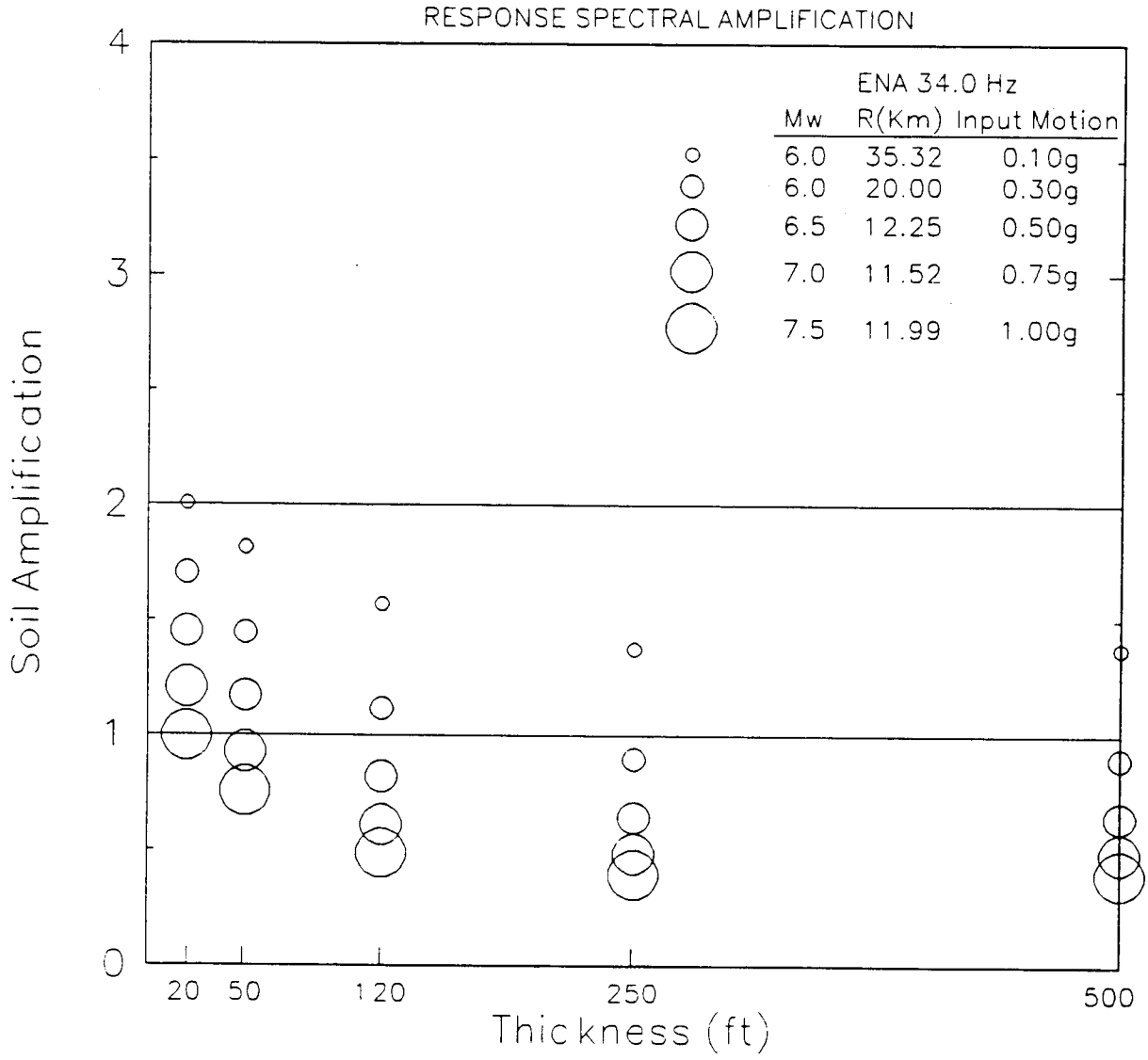

Figure 6-25. Plot of median 5% damped response spectral amplification factors computed for the five site categories (Table 6-2) at a frequency of 34.0 Hz. Size of symbol indicates level of input (rock outcrop) acceleration (0.1, 0.3, 0.5, 0.75, 1 g).

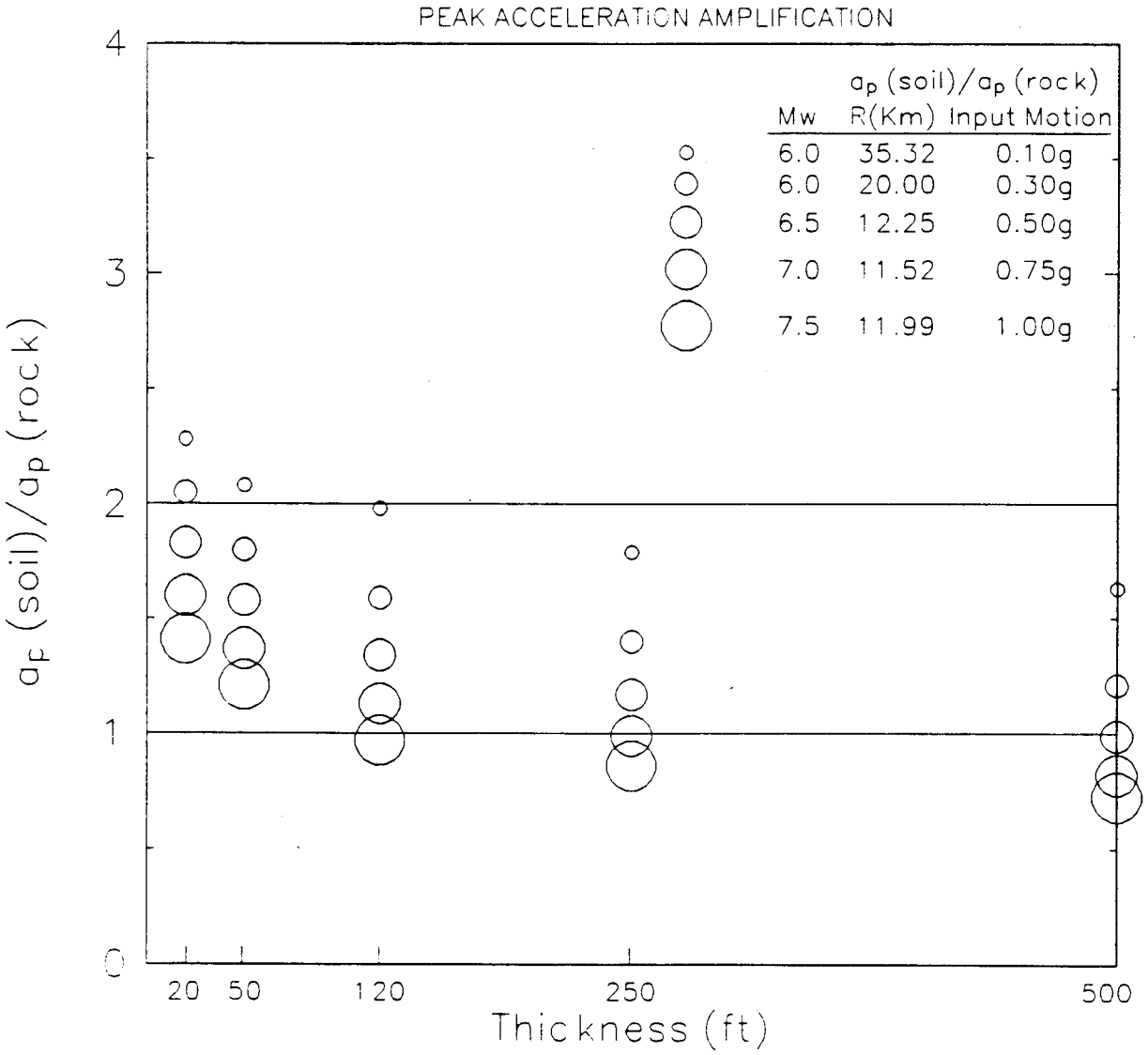

Figure 6-26. Plot of computed median amplification of peak acceleration for the five site categories (Table 6-2). Size of symbol indicates level of input (rock outcrop) acceleration (0.1, 0.3, 0.5, 0.75, 1 g).

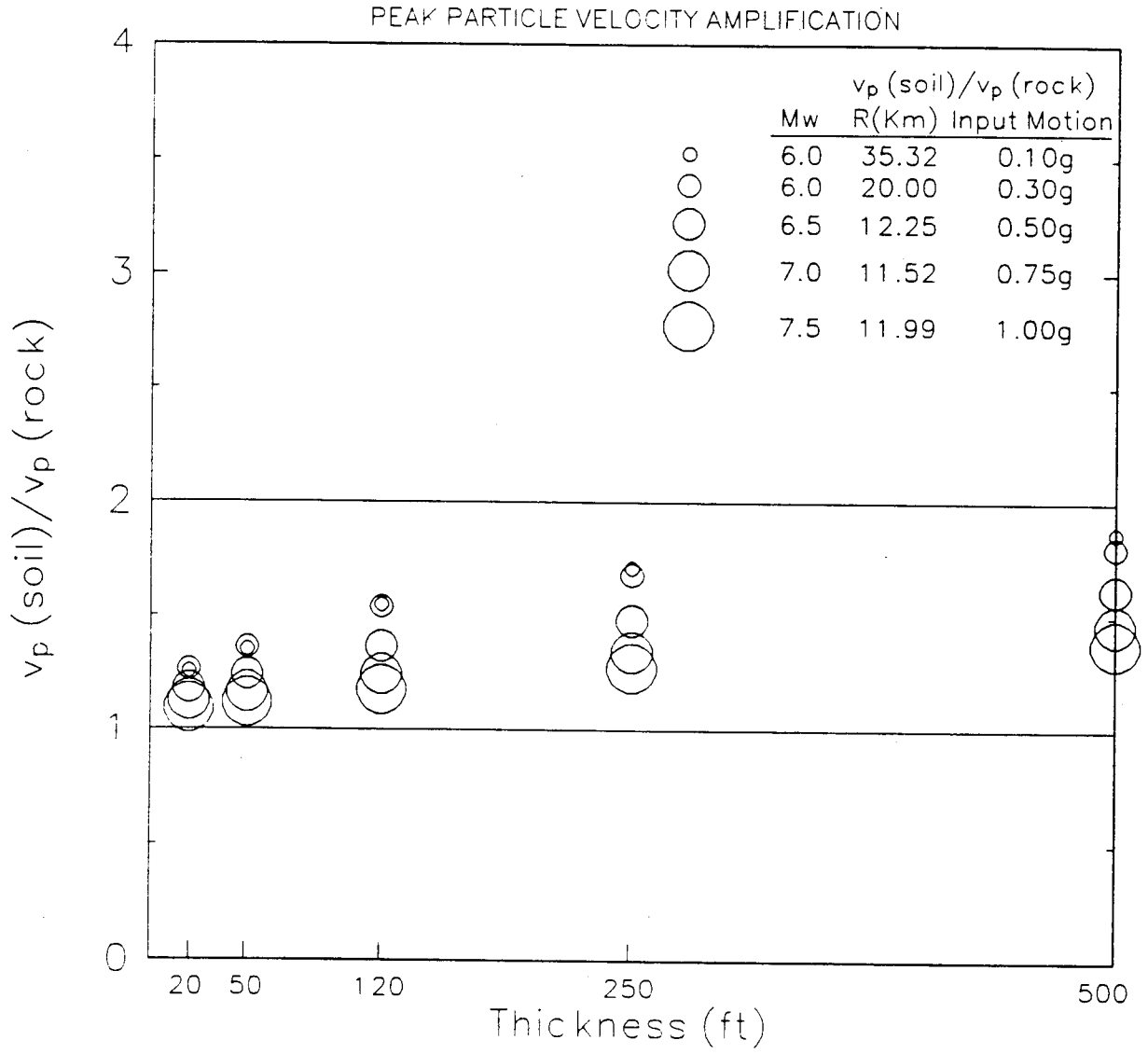

Figure 6-27. Plot of computed median amplification of peak particle velocity for the five site categories (Table 6-2). Size of symbol indicates level of input (rock outcrop) acceleration (0.1, 0.3, 0.5, 0.75, 1 g).

spectral amplification at high frequency (10.0, 25.0, 34.0 Hz) and may be a consequence of increased damping at higher overall shear-strain levels. At lower frequencies, however, there are some reversals to this trend. This may be associated with a shifting and an accompanying increase in amplitude of resonances along with an increase in shear-wave amplification due to a greater velocity gradient for higher levels of input motion. In some cases these effects may predominate over increased damping at lower frequencies. As described earlier, the net amplification is a trade-off of counteracting effects between soil damping, resonance effects, and an increase in shear-wave amplitude due to velocity gradients.

The amplification factors for the deepest profiles at high frequencies are predicted to be significantly less than one for higher levels of input motion. This can be attributed to the effects of damping and may be exaggerated. In order to adjust the predicted amplifications for these possible effects in a conservative manner, a lower bound of 0.6 is adopted for the set of computed amplification factors. This value is in agreement with the lower bound in the empirical factors for Western North America (Section 6.5, Figure 6-38).

The 5% damped response spectral amplification factors together with those predicted for peak acceleration and peak particle velocity are summarized in Table 6-4 for each level of input (rock outcrop) acceleration. The entries with asterisks are those which are lower than the adopted minimum of 0.6. In these cases the value of 0.6 should be substituted for use. To accommodate levels of input motion between entries on the table, simple linear interpolation is recommended.

It should be reiterated that these amplification factors approximately account for the effects of surficial geology by generic soil category. Although detailed site specific results could be different from those predicted for these generalized categories, we believe that the results presented in Table 6-4 are appropriate and represent a state-of-the-art assessment for use in seismic hazard estimation for the Central and Eastern United States.

6.4.2 Consideration of Special Cases

In the development of the amplification factors there are issues of importance regarding the effects of a number of parameters. In particular, the effects of control motion magnitude, bedrock velocity, and nature of the profile gradient should be addressed. In the following sections, the effects of these issues on the computed amplification factors will be quantified by making comparisons to the amplification factors computed using base case parameters with results using different magnitudes, median bedrock velocities, and uniform profiles rather than profiles with a velocity gradient.

6.4.2.1 Effects of Control Motion Magnitude

For the same peak acceleration value, the magnitude of the control motions can be changed with a change in distance, all other parameters remaining constant. The change in magnitude results in a change in corner frequency which primarily affects the low frequencies and, consequently, peak particle velocity. Since shear strain levels have a dependence on particle velocity, a change in magnitude, while keeping the peak acceleration constant by changing the distance, could result in a change in the computed amplification factors.

To evaluate the size of these effects, amplification factors for Category 2 (50 ft) with control motions of 0.30 and 0.50g were computed using **M** 7.5 instead of **M** 6.0 (0.30g) and **M** 6.5 (0.50g) (Table 6-3) for the control motions. The results are shown in Figures 6-28 and 6-29 for the two levels of control motions. The solid lines represent the amplification factors computed with the base case magnitudes (**M** 6.0 and **M** 6.5) while the dotted lines are for the **M** 7.5 control motions. The effects of the greater low-frequency energy (larger outcrop peak particle velocities) associated with the larger magnitude is to build up slightly higher strain levels resulting in a small decrease in the amplification factors. The effect is small but it does illustrate the effect of frequency content on nonlinear soil response and suggests caution in simply scaling recorded motions for site response analyses.

6.4.2.2 Effects of Bedrock Velocity

The impedance contrast across the soil-rock interface is a controlling factor of how much energy is transmitted to the profile as well as how much is reflected back into the profile. To examine the sensitivity of the amplification factors to the median bedrock velocity, amplification factors for Categories 2 and 5 were computed using median bedrock velocities of 3000 ft/sec and 9000 ft/sec. The results show a slight increase in the factors using the median bedrock velocity of 9000 ft/sec and a substantial decrease with the 3000 ft/sec median bedrock velocity.

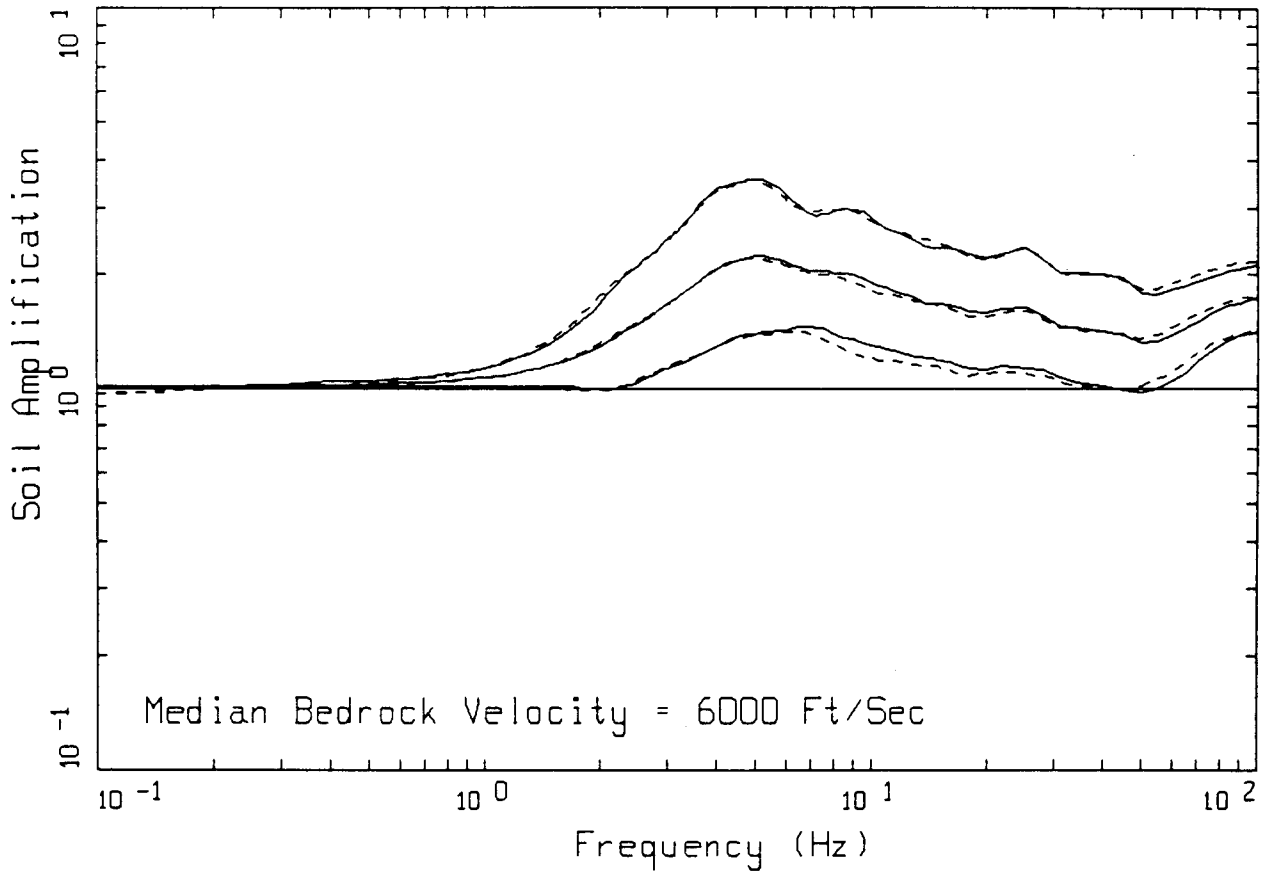

CATEGORY 2 (50 FT)

LEGEND

——— CONTROL MOTION 0.30 G; + 1 SIGMA OF 50 RANDOMIZED PROFILES
DEPTH RANDOMIZED BETWEEN 31 & 80 FT, M 6.0

——— CONTROL MOTION 0.30 G; MEDIAN OF 50 RANDOMIZED PROFILES
DEPTH RANDOMIZED BETWEEN 31 & 80 FT, M 6.0

——— CONTROL MOTION 0.30 G; - 1 SIGMA OF 50 RANDOMIZED PROFILES
DEPTH RANDOMIZED BETWEEN 31 & 80 FT, M 6.0

- - - - - CONTROL MOTION 0.30 G; + 1 SIGMA OF 50 RANDOMIZED PROFILES
DEPTH RANDOMIZED BETWEEN 31 & 80 FT, M 7.5

- - - - - CONTROL MOTION 0.30 G; MEDIAN OF 50 RANDOMIZED PROFILES
DEPTH RANDOMIZED BETWEEN 31 & 80 FT, M 7.5

- - - - - CONTROL MOTION 0.30 G; - 1 SIGMA OF 50 RANDOMIZED PROFILES
DEPTH RANDOMIZED BETWEEN 31 & 80 FT, M 7.5

Figure 6-28. Effects of control motion magnitude on amplification factors. Category 2 (31–80 ft) median amplification factors computed for control motion of 0.30 g. Solid lines are for M 6.0 and dashed lines are for M 7.5.

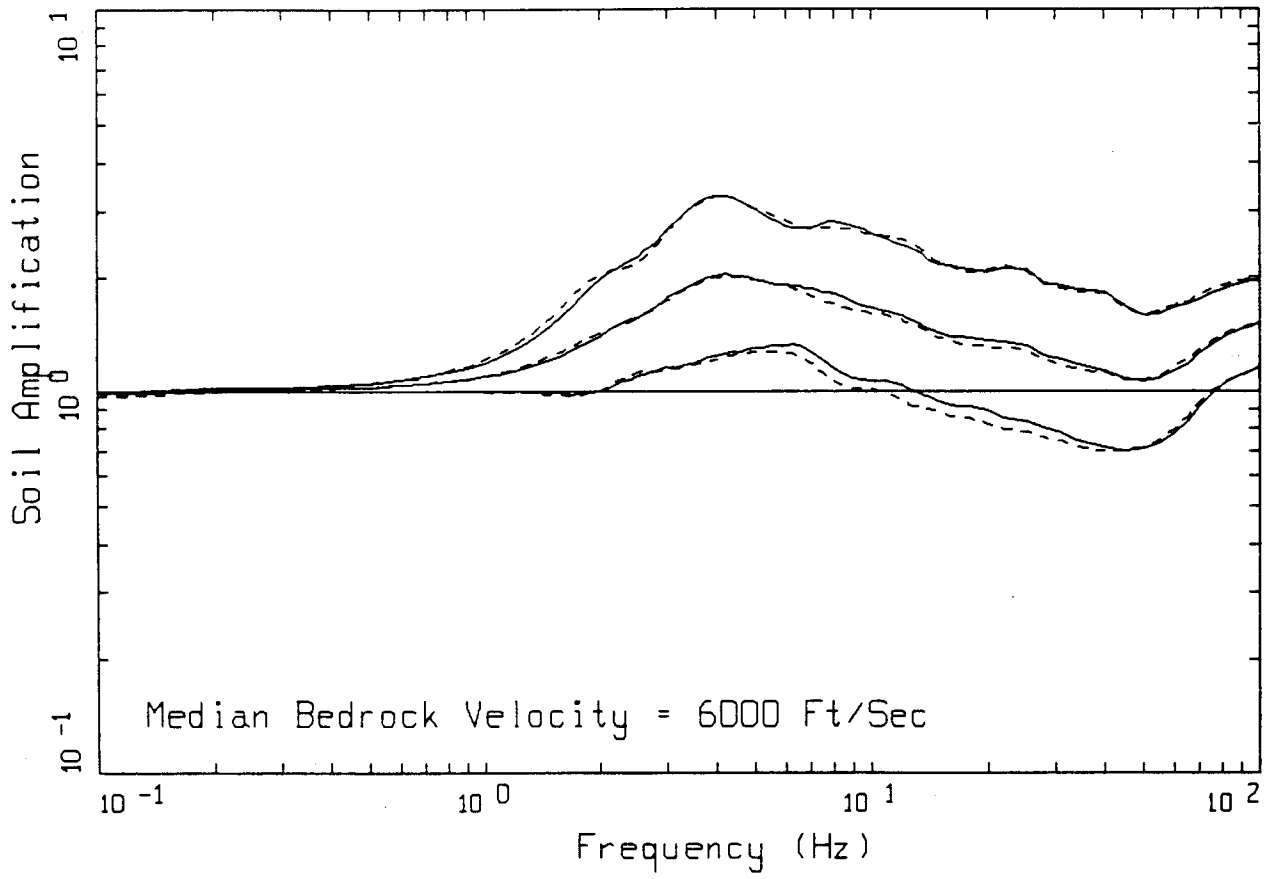

LEGEND

———— CONTROL MOTION 0.50 G; + 1 SIGMA OF 50 RANDOMIZED PROFILES
DEPTH RANDOMIZED BETWEEN 31 & 80 FT, M 6.5

———— CONTROL MOTION 0.50 G; MEDIAN OF 50 RANDOMIZED PROFILES
DEPTH RANDOMIZED BETWEEN 31 & 80 FT, M 6.5

———— CONTROL MOTION 0.50 G; - 1 SIGMA OF 50 RANDOMIZED PROFILES
DEPTH RANDOMIZED BETWEEN 31 & 80 FT, M 6.5

- - - - - CONTROL MOTION 0.50 G; + 1 SIGMA OF 50 RANDOMIZED PROFILES
DEPTH RANDOMIZED BETWEEN 31 & 80 FT, M 7.5

- - - - - CONTROL MOTION 0.50 G; MEDIAN OF 50 RANDOMIZED PROFILES
DEPTH RANDOMIZED BETWEEN 31 & 80 FT, M 7.5

- - - - - CONTROL MOTION 0.50 G; - 1 SIGMA OF 50 RANDOMIZED PROFILES
DEPTH RANDOMIZED BETWEEN 31 & 80 FT, M 7.5

Figure 6-29. Effects of control motion magnitude on amplification factors. Category 2 (31–80 ft) median amplification factors computed for control motion of 0.50 g. Solid lines are for M 6.5 and dashed lines are for M 7.5.

Figures 6-30 and 6-31 for Category 5 using a control motion of 0.50g illustrate the general results. Figure 6-30 shows the amplification factors using both the base case median bedrock velocity of 6000 ft/sec (solid line), and the velocity of 9000 ft/sec (dotted lines). The factors computed using the higher bedrock velocity are slightly larger at low frequencies and about the same at high frequencies. Similar degrees of differences are present in the other categories with the maximum departure being about 10% for Category 1.

Using a median bedrock velocity of 3000 ft/sec, compared to 6000 ft/sec results in a significant difference in amplification factors. This represents a factor of two reduction in the impedance contrast and reduces the motions a maximum of about 30% near the profile resonance and, due to the nonlinear soil response, progressively less at higher frequencies. This trend is illustrated in Figure 6-31 which shows median amplification factors computed for Category 5, with a control motion of 0.50g using both 6000 ft/sec and 3000 ft/sec median bedrock velocities. The lower velocity results show a slightly lower frequency resonance with lower amplitude. As frequency increases, the difference in the two factors decreases.

The effects of median basement shear-wave velocity are not large for a 50% increase but do result in slightly greater (maximum about 10%) factors near the profile resonance. On the other hand, a 100% reduction in the median bedrock velocity, from 6000 ft/sec to 3000 ft/sec, results in an overall reduction in the amplification factors by about 30% near the profile resonance and progressively less for higher frequencies.

6.4.2.3 Effects of Uniform Velocity Profiles

While most shear-wave velocity profiles show a general increase in velocity with depth, generally most rapid near the surface, there are profiles which increase only slightly in velocity with increasing depth. Generally larger amplification is expected from profiles with strong velocity gradients as opposed to more uniform profiles, with all other factors remaining the same. As a result, it is believed that the amplification factors computed using the generic profile, which contains a strong velocity gradient, particularly in the upper 100 ft (Figure 6-3), are not unconservative in applications to generally uniform profiles.

To quantify this, amplification factors were computed for Categories 3 (120 ft) and 4 (250 ft) profiles using a constant shear-wave velocity of 1500 ft/sec, near the average velocity of Category 4 (about 1800 ft/sec, Figure 6-3). The results are compared to the gradient model in Figures 6-32 and 6-33 for a control motion of 0.50g. The amplification factors computed using the gradient model (base case) exceed those of the uniform profile except near 1 Hz for Category 3 profiles. The uniform profile factors are slightly larger near 1 Hz because its median resonance occurs at a lower frequency than that of the gradient model. In general, the gradient model results in higher factors than the uniform profile, particularly if the median resonances are at about the same frequency, as is the case with Category 4.

6.5 Comparison of Computed Amplification Factors to Empirical and other Analytical Results

Direct comparison of the results presented here with other results for 5% damped response spectral amplification factors, as well as for peak acceleration and peak particle velocity, is complicated by several factors. Comparisons with empirical observations at well-defined soil sites appropriate for Eastern North America motions are not possible. Few, if any, recordings exist made at soil/rock pairs with soil sites representative of our classifications and at close distances to large (m_b>5) events. Also not enough data exist, particularly at close distances, at both rock and soil sites to sufficiently constrain empirical attenuation relationships (Section 2). Recordings of aftershocks of Eastern North America events (Boatwright and Astrue, 1983; Mueller and Cranswick, 1985; Cranswick et al., 1985) show rather large amplifications at high frequencies for very shallow soil sites or fractured rock sites relative to hard-rock sites.

Comparisons with Western North America observations are complicated by differences in underlying rock shear-wave velocities (Section 6.4.2.2) as well as differences in high frequency spectral content of the control motions (Section 6.4.2.1).

An additional complicating factor arises in comparisons between response spectral ratios and Fourier spectral ratios (Silva et al., 1988). Caution must be exercised in making inferences about amplification factors appropriate for 5% damped response spectra based upon

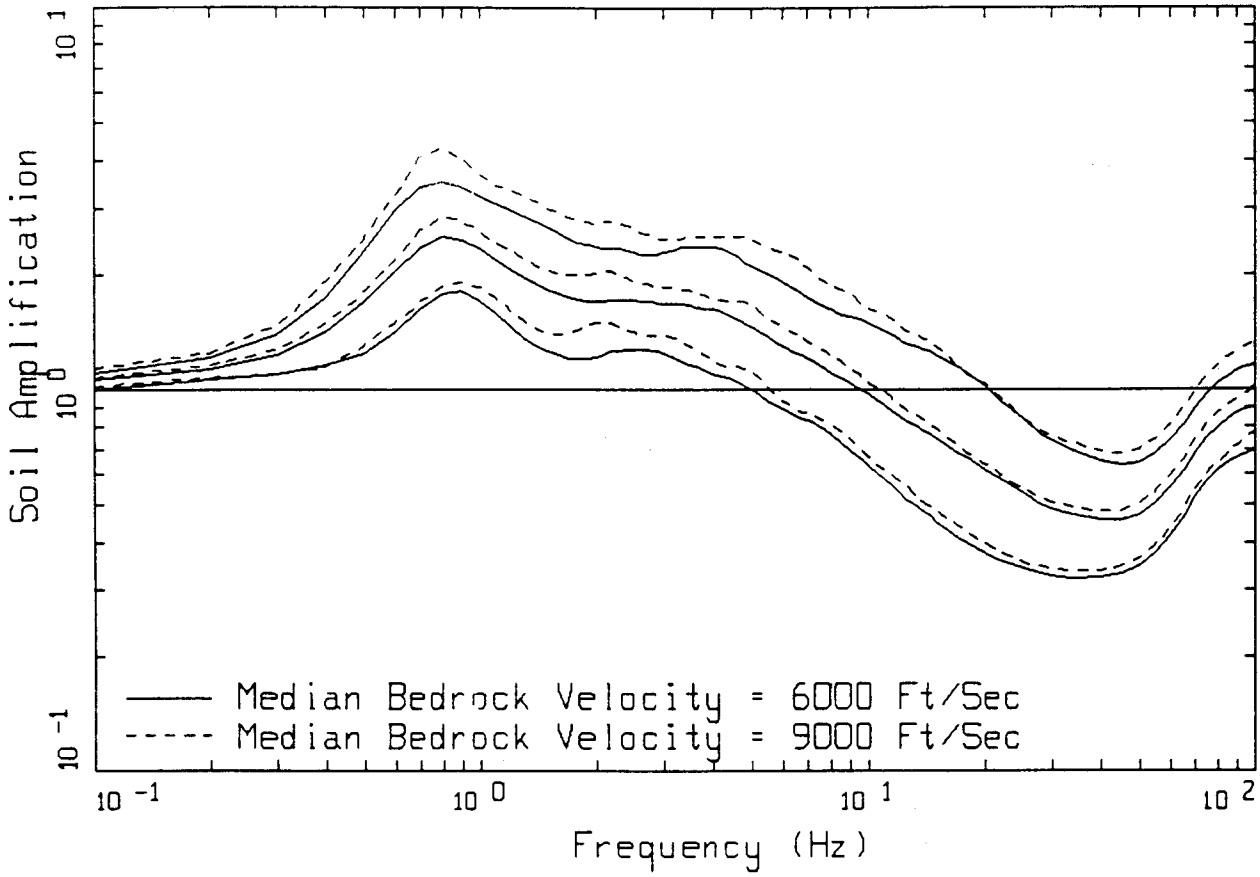

LEGEND

——— CONTROL MOTION 0.50 G; + 1 SIGMA OF 50 RANDOMIZED PROFILES
DEPTH RANDOMIZED BETWEEN 401 & 1000 FT

——— CONTROL MOTION 0.50 G; MEDIAN OF 50 RANDOMIZED PROFILES
DEPTH RANDOMIZED BETWEEN 401 & 1000 FT

——— CONTROL MOTION 0.50 G; - 1 SIGMA OF 50 RANDOMIZED PROFILES
DEPTH RANDOMIZED BETWEEN 401 & 1000 FT

- - - - - CONTROL MOTION 0.50 G; + 1 SIGMA OF 50 RANDOMIZED PROFILES
DEPTH RANDOMIZED BETWEEN 401 & 1000 FT

- - - - - CONTROL MOTION 0.50 G; MEDIAN OF 50 RANDOMIZED PROFILES
DEPTH RANDOMIZED BETWEEN 401 & 1000 FT

- - - - - CONTROL MOTION 0.50 G; - 1 SIGMA OF 50 RANDOMIZED PROFILES
DEPTH RANDOMIZED BETWEEN 401 & 1000 FT

Figure 6-30. Effects of bedrock velocity on amplification factors. Category 5 (401+ft) median amplification factors computed for control motion of 0.50 g. Solid lines are with median bedrock shear-wave velocity of 6000 ft/sec and dashed lines are with 9000 ft/sec.

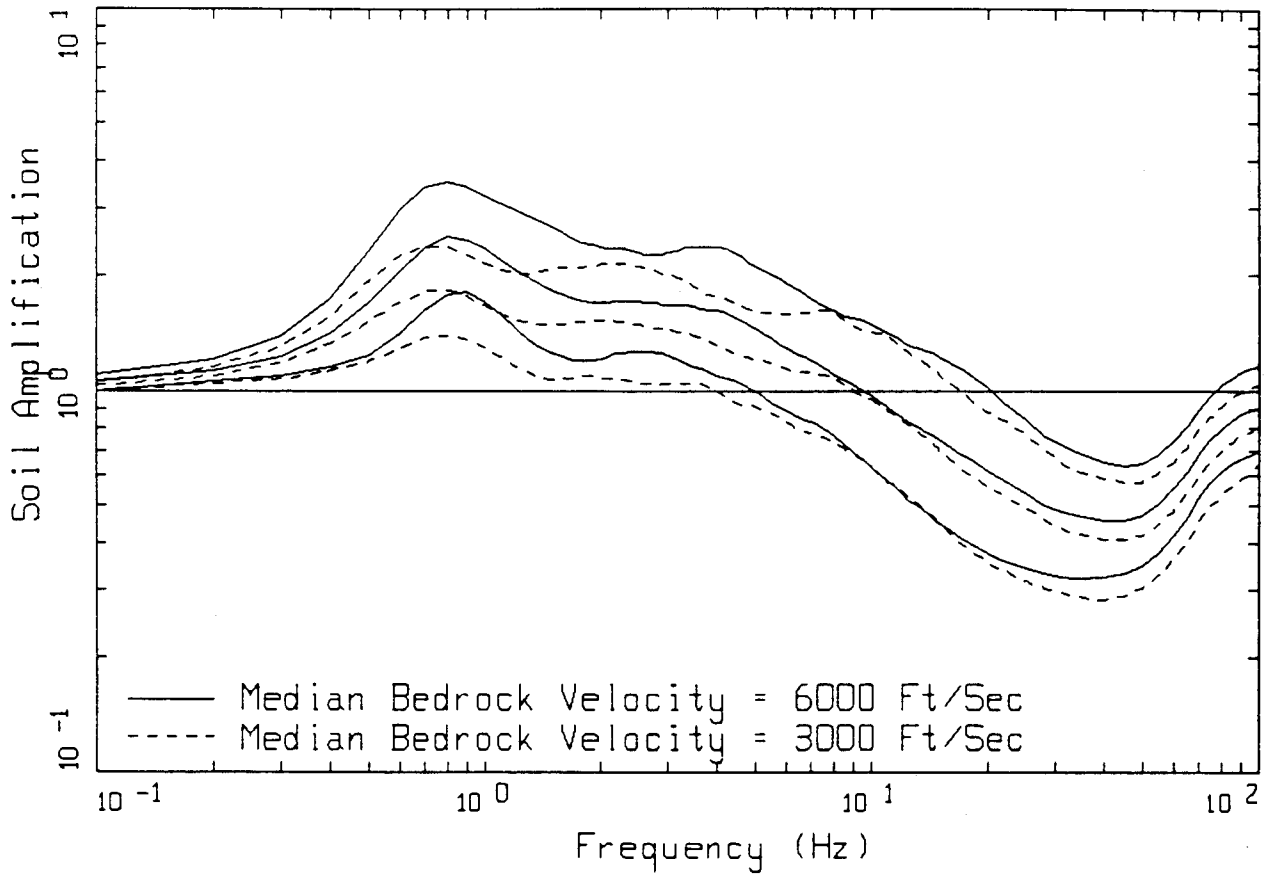

LEGEND

——— CONTROL MOTION 0.50 G; + 1 SIGMA OF 50 RANDOMIZED PROFILES
DEPTH RANDOMIZED BETWEEN 401 & 1000 FT

——— CONTROL MOTION 0.50 G; MEDIAN OF 50 RANDOMIZED PROFILES
DEPTH RANDOMIZED BETWEEN 401 & 1000 FT

——— CONTROL MOTION 0.50 G; - 1 SIGMA OF 50 RANDOMIZED PROFILES
DEPTH RANDOMIZED BETWEEN 401 & 1000 FT

- - - - - CONTROL MOTION 0.50 G; + 1 SIGMA OF 50 RANDOMIZED PROFILES
DEPTH RANDOMIZED BETWEEN 401 & 1000 FT

- - - - - CONTROL MOTION 0.50 G; MEDIAN OF 50 RANDOMIZED PROFILES
DEPTH RANDOMIZED BETWEEN 401 & 1000 FT

- - - - - CONTROL MOTION 0.50 G; - 1 SIGMA OF 50 RANDOMIZED PROFILES
DEPTH RANDOMIZED BETWEEN 401 & 1000 FT

Figure 6-31. Effects of bedrock velocity on amplification factors. Category 5 (401+ft) median amplification factors computed for control motion of 0.50 g. Solid lines are with median bedrock shear-wave velocity of 6000 ft/sec and dashed lines are with 3000 ft/sec.

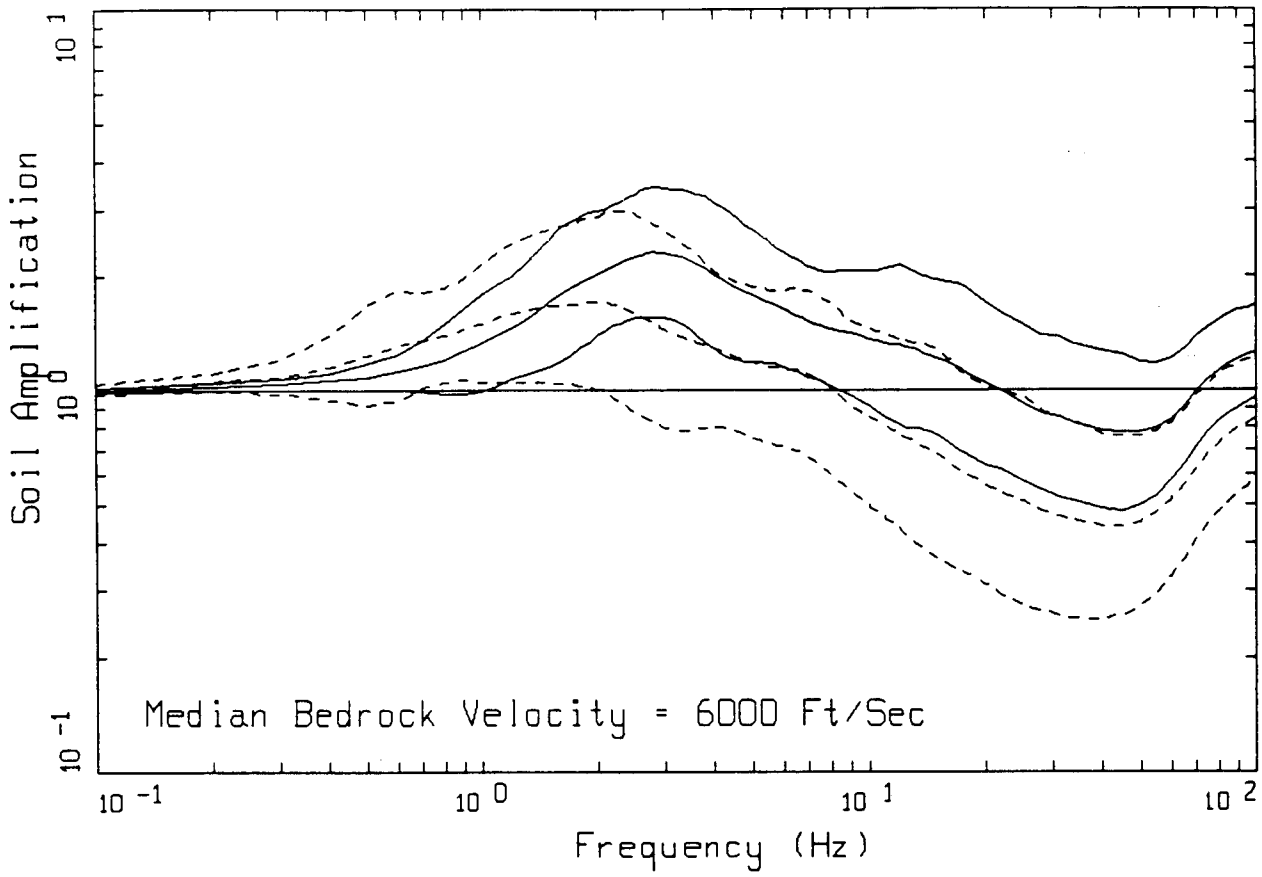

CATEGORY 3 (120 FT)

LEGEND

——— CONTROL MOTION 0.50 G; + 1 SIGMA OF 50 RANDOMIZED PROFILES
DEPTH RANDOMIZED BETWEEN 81 & 180 FT

——— CONTROL MOTION 0.50 G; MEDIAN OF 50 RANDOMIZED PROFILES
DEPTH RANDOMIZED BETWEEN 81 & 180 FT

——— CONTROL MOTION 0.50 G; - 1 SIGMA OF 50 RANDOMIZED PROFILES
DEPTH RANDOMIZED BETWEEN 81 & 180 FT

- - - - - CONTROL MOTION 0.50 G; + 1 SIGMA OF 50 RANDOMIZED UNIFORM PROFILES
DEPTH RANDOMIZED BETWEEN 81 & 180 FT

- - - - - CONTROL MOTION 0.50 G; MEDIAN OF 50 RANDOMIZED UNIFORM PROFILES
DEPTH RANDOMIZED BETWEEN 81 & 180 FT

- - - - - CONTROL MOTION 0.50 G; - 1 SIGMA OF 50 RANDOMIZED UNIFORM PROFILES
DEPTH RANDOMIZED BETWEEN 81 & 180 FT

Figure 6-32. Effects of uniform profiles on amplification factors. Category 3 (81–180 ft) median amplification factors computed for a control motion of 0.50 g. Solid lines are using gradient profile, dashed lines are using uniform profile.

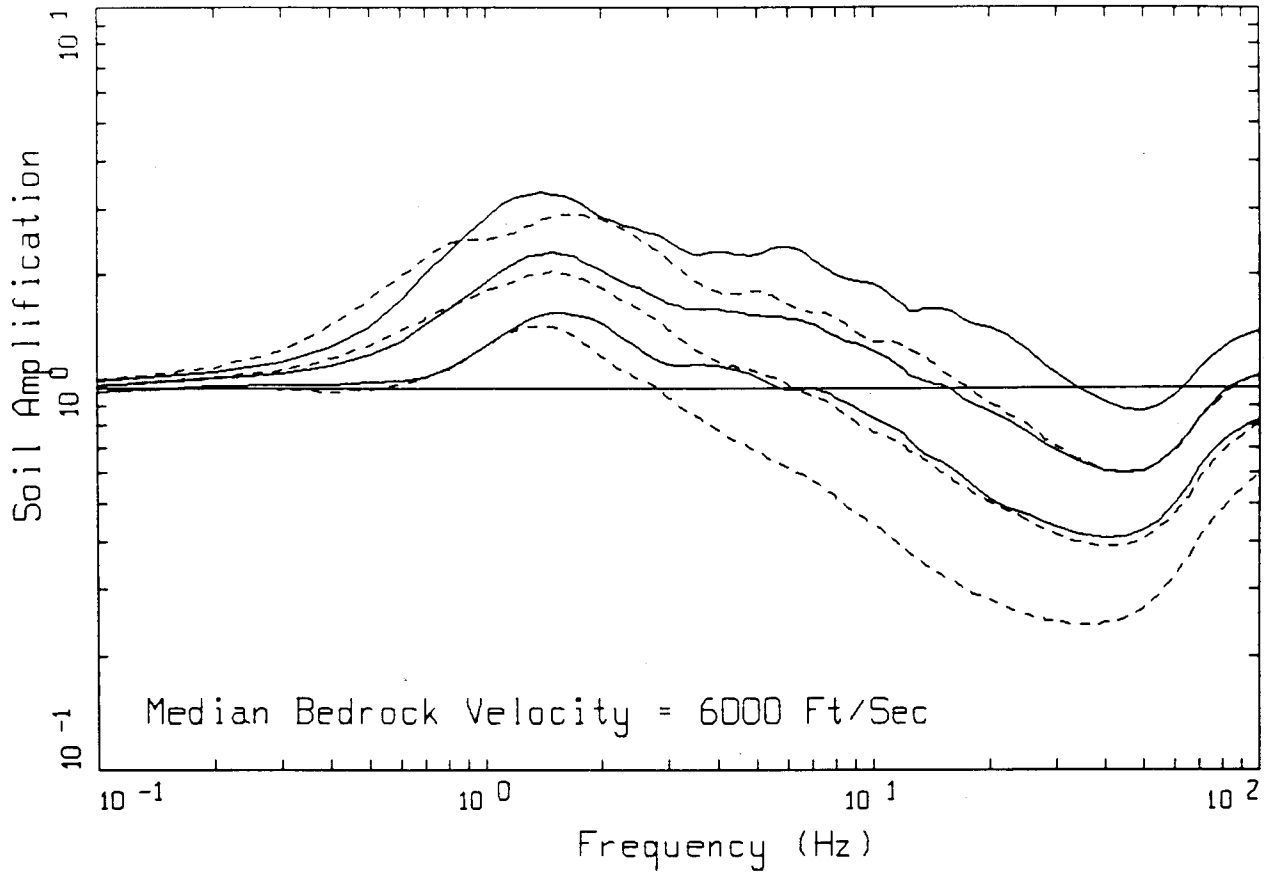

CATEGORY 4 (250 FT)

LEGEND

——— CONTROL MOTION 0.50 G; + 1 SIGMA OF 50 RANDOMIZED PROFILES
DEPTH RANDOMIZED BETWEEN 181 & 400 FT

——— CONTROL MOTION 0.50 G; MEDIAN OF 50 RANDOMIZED PROFILES
DEPTH RANDOMIZED BETWEEN 181 & 400 FT

——— CONTROL MOTION 0.50 G; - 1 SIGMA OF 50 RANDOMIZED PROFILES
DEPTH RANDOMIZED BETWEEN 181 & 400 FT

- - - - - CONTROL MOTION 0.50 G; + 1 SIGMA OF 50 RANDOMIZED UNIFORM PROFILES
DEPTH RANDOMIZED BETWEEN 181 & 400 FT

- - - - - CONTROL MOTION 0.50 G; MEDIAN OF 50 RANDOMIZED UNIFORM PROFILES
DEPTH RANDOMIZED BETWEEN 181 & 400 FT

- - - - - CONTROL MOTION 0.50 G; - 1 SIGMA OF 50 RANDOMIZED UNIFORM PROFILES
DEPTH RANDOMIZED BETWEEN 181 & 400 FT

Figure 6-33. Effects of uniform profiles on amplification factors. Category 4 (181–400 ft) median amplification factors computed for a control motion of 0.50 g. Solid lines are using gradient profile, dashed lines are using uniform profile.

analyses performed with Fourier amplitude spectral densities. Silva et al.(1988) show that the difference between response spectra and Fourier amplitude spectra in computing the effects of site response is frequency and site dependent, and can vary with magnitude as well, even for linear site response.

In addition to the differences between response and Fourier spectral amplifications resulting from analytical procedures, observationally this difference will likely be greater. This arises because the Fourier spectrum for a transient event must be smoothed over neighboring frequencies to produce statistically stable estimates. This procedure degrades resolution but must necessarily be performed to reduce the variance of the estimates prior to taking ratios. If the proper smoothing is not performed, statistical fluctuations in the Fourier spectra may seriously bias the ratios. As a consequence of the necessity to smooth, the estimates of site response based upon Fourier amplitude spectra computed from observations may be directly related to the degree and nature of the smoothing process. Because of this, comparisons between soil site effects based upon Fourier amplitude spectra computed from observations to computations using response spectra are unclear and will not be pursued.

6.5.1 Comparisons to Empirical Results

Although direct comparisons of the amplification factors presented in Table 6-4 for ENA with other results is not strictly appropriate due to differences in bedrock velocities and control motion spectral content, similarities should exist both in sizes of factors and in trends. Comparisons with empirical results can then provide a basis from which to judge the reasonableness of the computed values.

In order to provide a basis for comparison to empirical amplification factors, regression analyses for peak acceleration and 5% damped response spectra were performed on a set of reprocessed strong motion data (Appendix 2.C). The data set represents available unprocessed strong motion records from earthquakes in active tectonic regions with **M** above about 5.8. The data were reprocessed on an individual record basis to extend both the high and low frequency limits (Silva and Abrahamson, 1992). The reprocessed data set then represents an extensive set of uniformly processed records with an optimal usable bandwidth for each record.

In the regression analyses a functional form was selected which directly evaluates the soil-to-rock amplification factors. The functional form of the ratio was taken to allow for a nonlinear relationship between the motion on soil and that on rock (Equation 2C-1 in Appendix 2.C). The results for both deep and shallow soil show a clear dependence of the amplification factors on magnitude and distance, or equivalently on rock peak acceleration level. For a given magnitude, the amplification factors increase with increasing distance. The soil motions increase with increasing distance at a greater rate than the corresponding rock motions. The trend is identical to that shown in the computed amplification factors and is due to the effects of nonlinear soil response.

In order to provide a direct comparison between the computed amplification factors for Eastern North America and the empirical Western North America factors at different rock acceleration levels, empirical motions were calculated at rupture distances of 1, 5, 10, 25, and 50 km for rock, deep soil, and shallow soil for **M** 6.5 (majority of the data) (Appendix 2.C). The corresponding rock or "control" motion peak acceleration values are 0.06, 0.12, 0.26, 0.42, and 0.75g. The closest outcrop control motion values used in computing the amplification factors are 0.05, 0.10, 0.30, 0.50, and 0.75g (Table 6.3). Figures 6-34 to 6-38 show the comparisons of the computed amplification factors and the corresponding empirical factors for the five outcrop peak acceleration values. Only deep soil is used in the comparison because these sites represent the bulk of the data and therefore provide better constrained regression results. To provide soil/rock conditions closer to Western North America, the computed amplification factors are shown with median bedrock velocities of both 3000 ft/sec and 6000 ft/sec.

For the smallest control motions, about 0.05g, Figure 6-34 shows similar levels of amplification for the empirical and theoretical factors, particularly for the results using the median bedrock velocity of 3000 ft/sec. Interestingly, both the analytical and empirical results peak near 1 Hz with the empirical showing a broader peak possibly due to a wider sampling in depth range. For these low levels of motion the empirical and analytical factors are greater than one for all frequencies.

The next higher level of control or rock motions, about 0.10g, are shown in Figure 6-35. Both the empirical and analytical amplification factors are reduced at higher

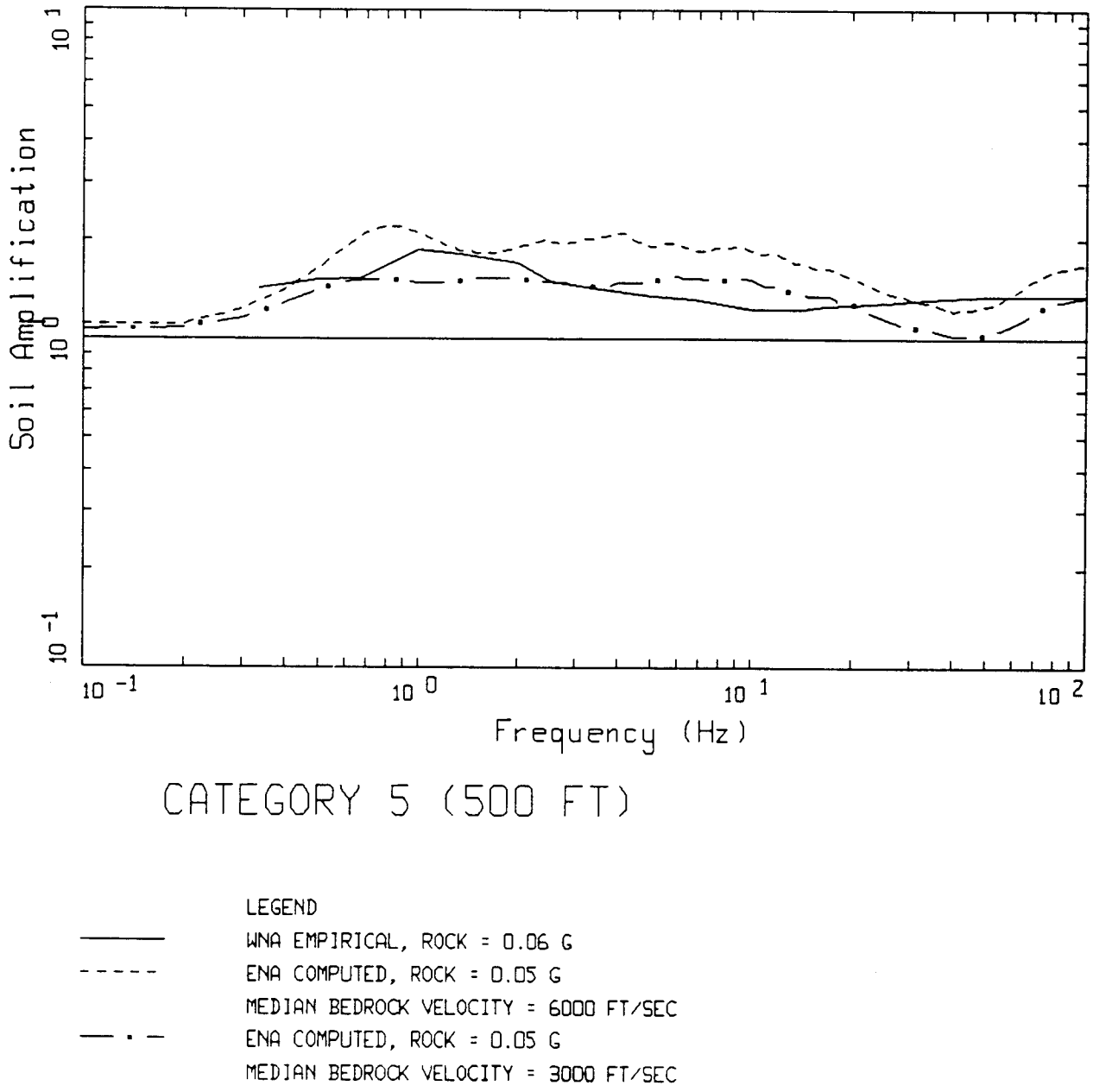

Figure 6-34. Comparison of empirical western North America amplification factors for deep stiff soil (solid line) to computed factors for eastern North America for Category 5 (401+ft). Dashed line is with median bedrock velocity of 6000 ft/sec, dash-dotted line is with median bedrock velocity of 3000 ft/sec. Control or corresponding rock outcrop motion is 0.06 g for the empirical factors and 0.05 g for the analytical factors.

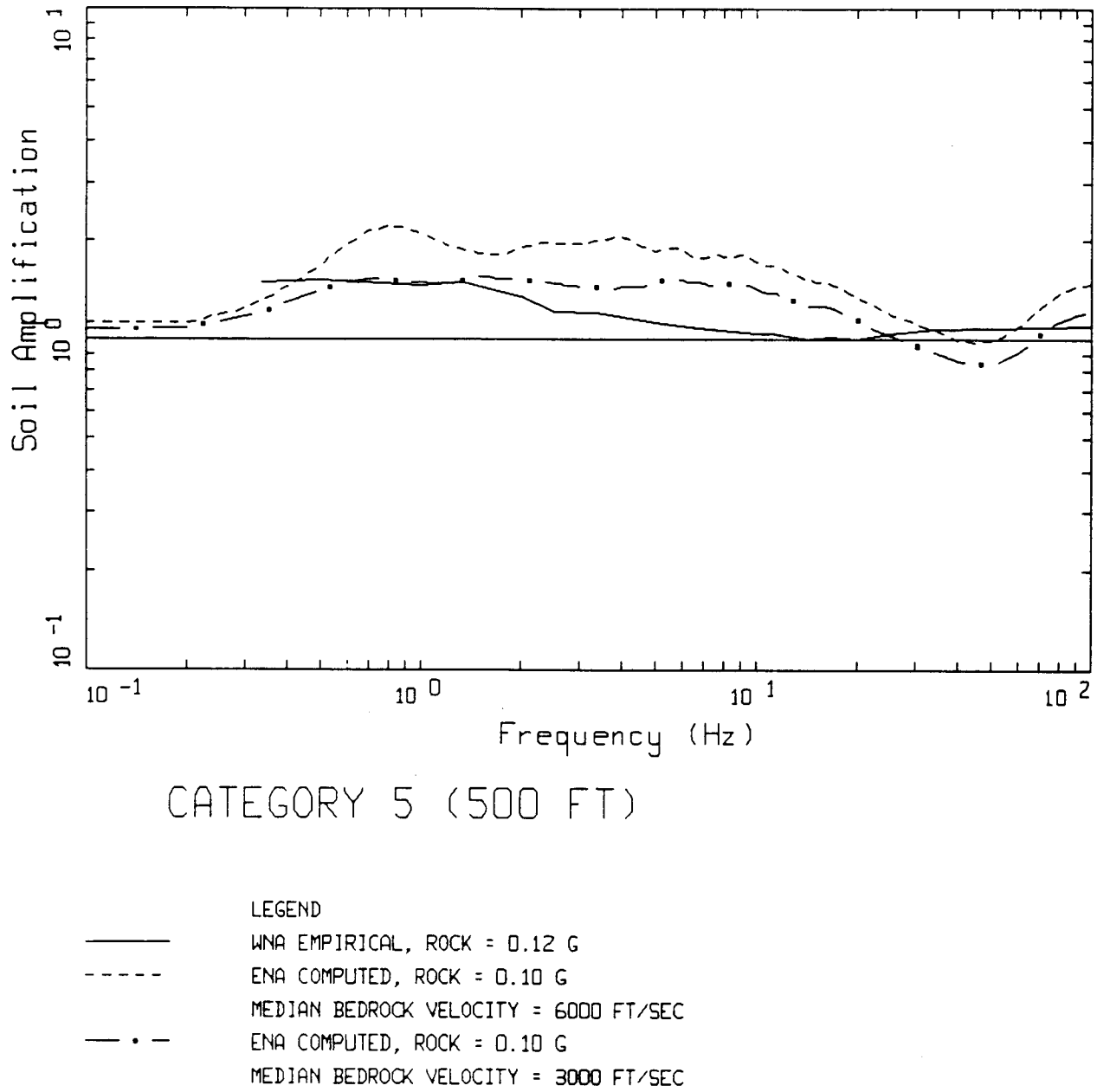

Figure 6-35. Comparison of empirical western North America amplification factors for deep stiff soil (solid line) to computed factors for eastern North America for Category 5 (401+ft). Dashed line is with median bedrock velocity of 6000 ft/sec, dash-dotted line is with median bedrock velocity of 3000 ft/sec. Control or corresponding rock outcrop motion is 0.12 g for the empirical factors and 0.10 g for the analytical factors.

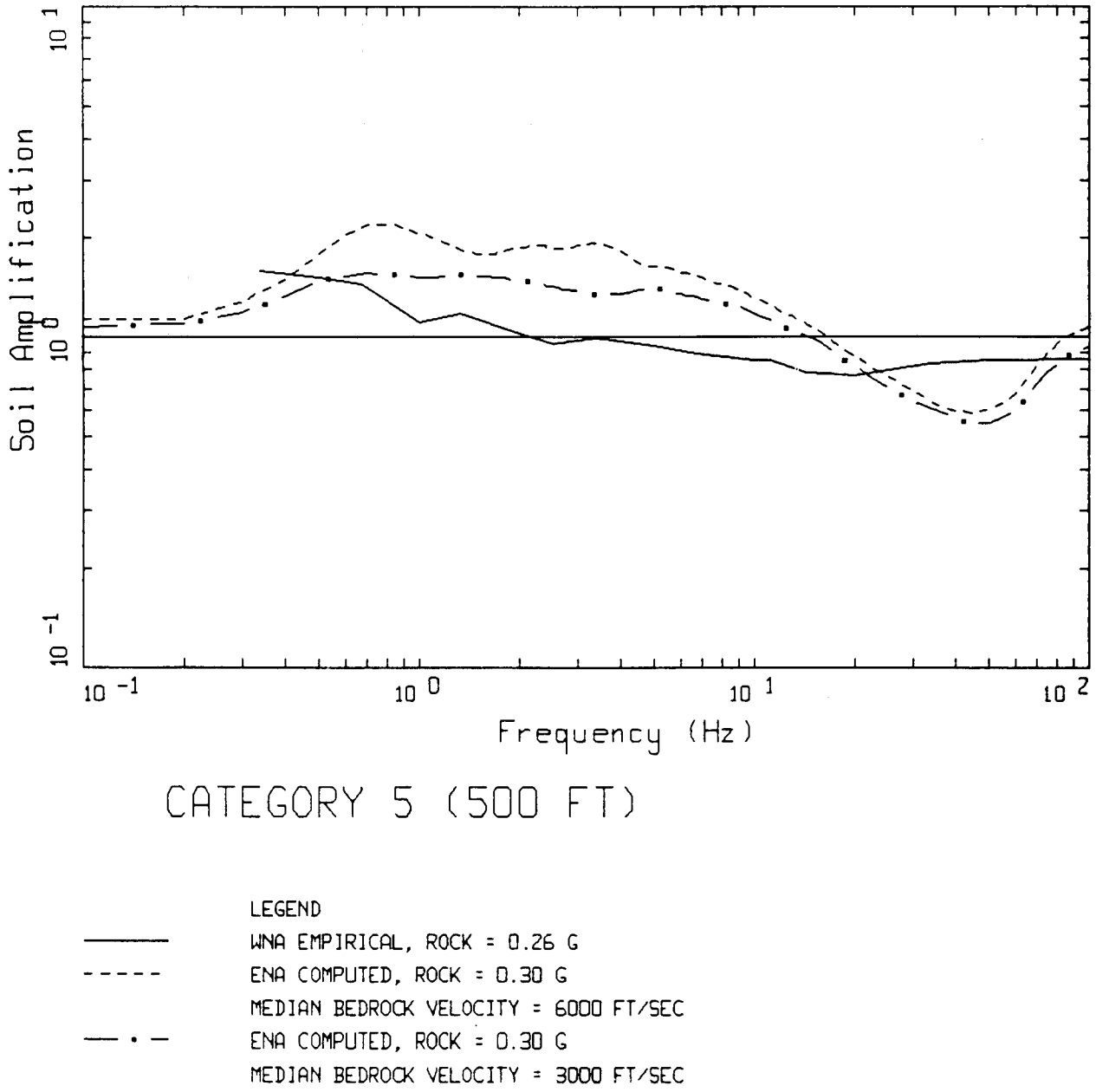

Figure 6-36. Comparison of empirical western North America amplification factors for deep stiff soil (solid line) to computed factors for eastern North America for Category 5 (401+ft). Dashed line is with median bedrock velocity of 6000 ft/sec, dash-dotted line is with median bedrock velocity of 3000 ft/sec. Control or corresponding rock outcrop motion is 0.26 g for the empirical factors and 0.30 g for the analytical factors.

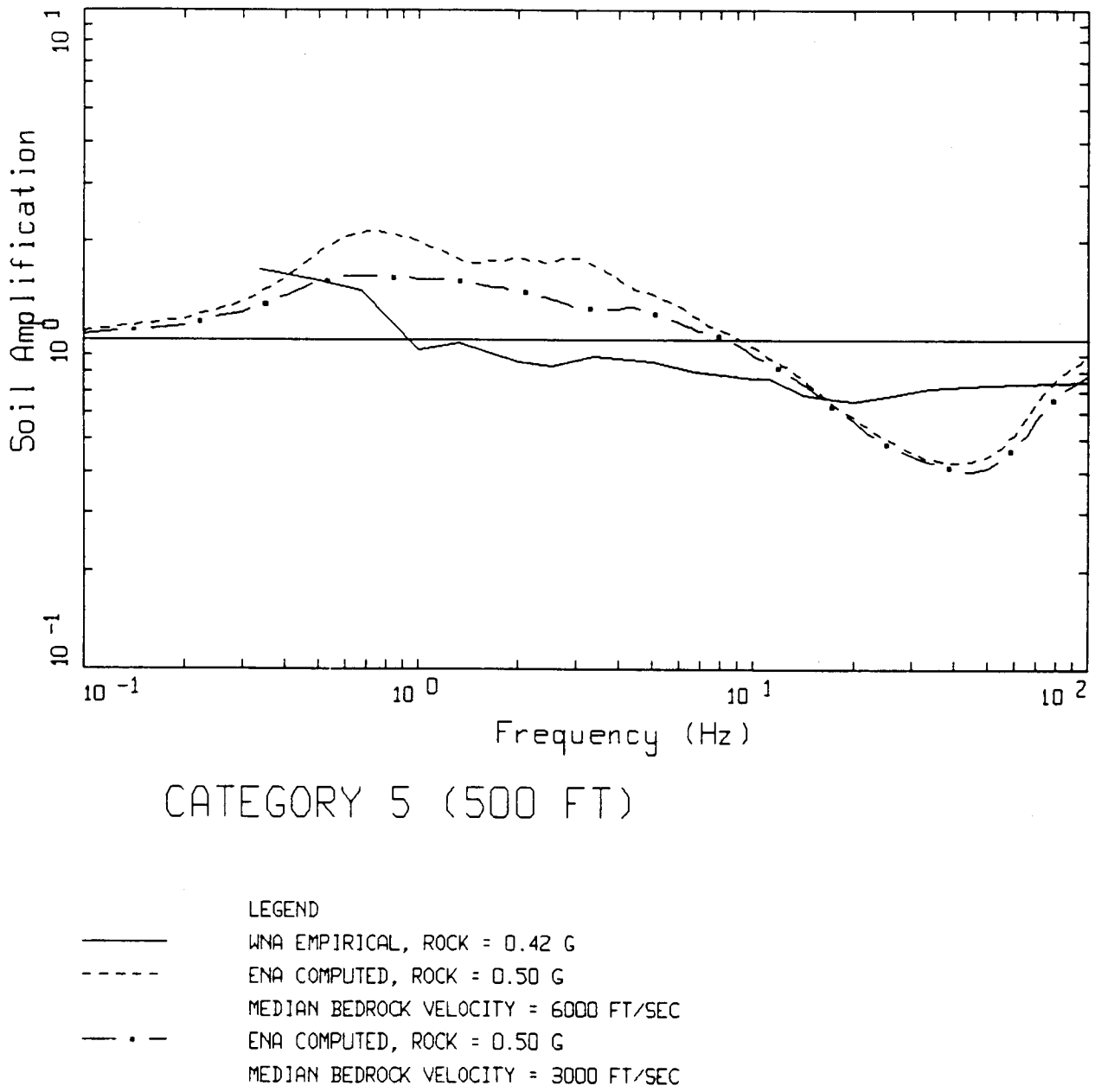

Figure 6-37. Comparison of empirical western North America amplification factors for deep stiff soil (solid line) to computed factors for eastern North America for Category 5 (401+ft). Dashed line is with median bedrock velocity of 6000 ft/sec, dash-dotted line is with median bedrock velocity of 3000 ft/sec. Control or corresponding rock outcrop motion is 0.42 g for the empirical factors and 0.50 g for the analytical factors.

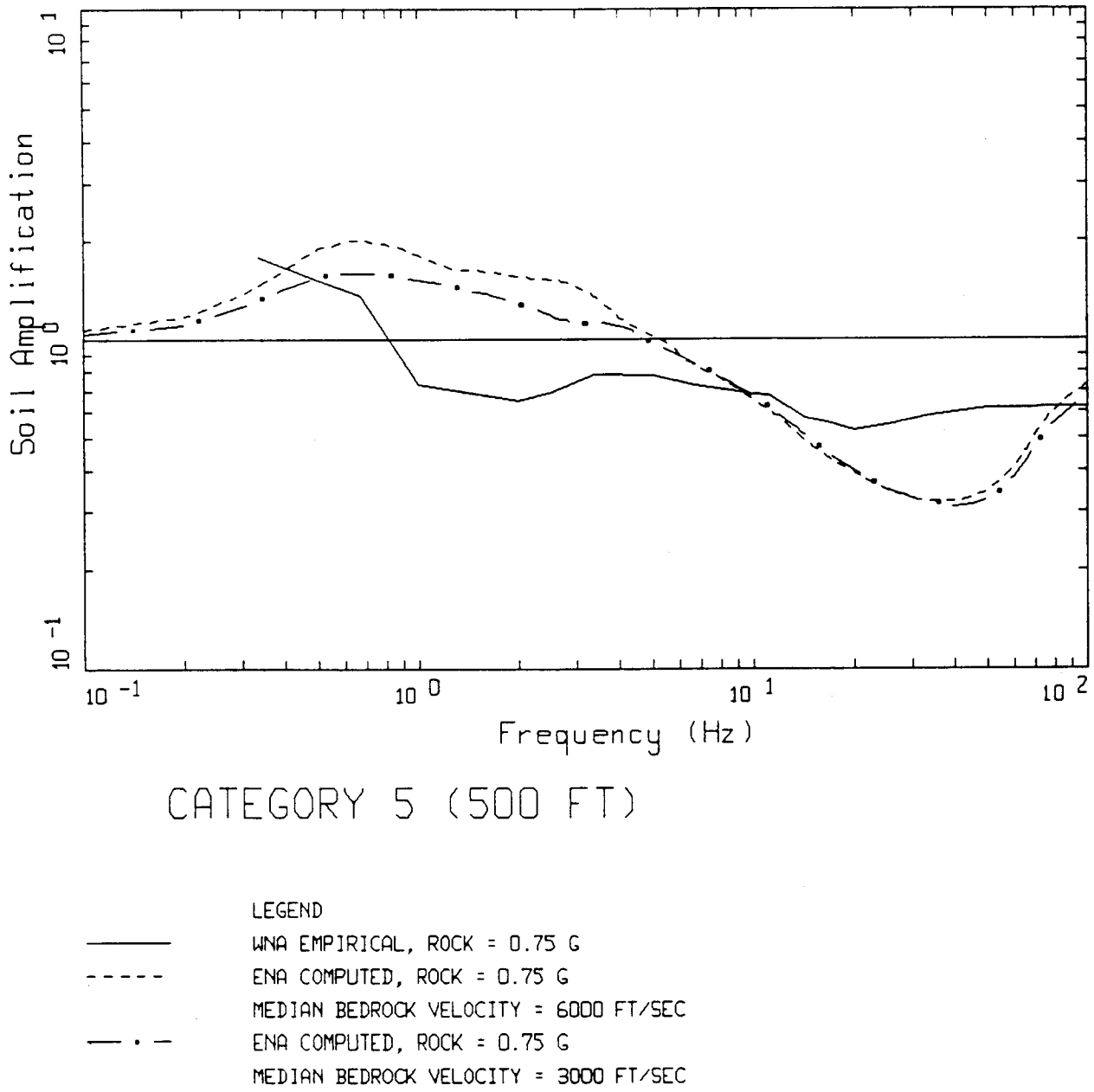

Figure 6-38. Comparison of empirical western North America amplification factors for deep stiff soil (solid line) to computed factors for eastern North America for Category 5 (401+ft). Dashed line is with median bedrock velocity of 6000 ft/sec, dash-dotted line is with median bedrock velocity of 3000 ft/sec. Control or corresponding rock outcrop motion is 0.75 g for the empirical factors and 0.75 g for the analytical factors.

frequencies with the empirical showing the greatest decrease. This result, expected at higher levels of motion, is surprising and suggests that the effects of nonlinear soil response can extend down to low levels of control motions, even into the range of 5–10%g. The analytical results do not show nearly as great a decrease, possibly because the median profile is comparatively stiff. Figure 6-36 shows the factors for about 0.30g rock motions and both the empirical and analytical factors show a further decrease. The analytical factors are less than the empirical above about 20 Hz which may reflect higher soil damping due to the larger high frequency energy content in the Eastern North America control motions (Section 6.2). The minimum in the empirical factors occurs near 20 Hz, unlike in the analytical factors where it occurs near 50 Hz and is much sharper as well. As previously indicated, this feature in the analytical factors is due to the effects of kappa (0.006 sec) and the low-pass filter at 62.5 Hz. The soil spectra are nearly flat in this range due to the damping (the minima are more pronounced at higher levels of motion) while the rock spectra are falling off to peak acceleration levels with increasing frequency (Figure 6-16). This trend is shifted to lower frequencies for Western North America motions due to the higher average kappa values (0.04 sec, Silva and Darragh, 1993). The effect is also less pronounced for the western motions because the effects of the high kappa values gradually reduces the high frequency energy to low levels before the antialias filters are applied.

The two highest levels of motions, about 0.50 and 0.75g, are shown in Figures 6-37 and 6-38. While some data exist for the 0.50g results, the 0.75g amplification factors are largely extrapolations. As with the lower levels of motions, the trend in the empirical is for decreasing amplification with increasing levels of motion. The analytical factors exceed the empirical at low frequencies and are smaller above 20 Hz for 0.50g and about 10 Hz for 0.75g control motions.

The results of these comparisons are very encouraging. The analytical amplification factors show very similar shapes and trends to the empirical. Both are generally smooth and for the lowest motions, show peaks near 1 Hz, and are greater than one for all frequencies. At higher levels of motion, both the empirical and analytical factors are reduced in amplitude with the empirical showing a larger dependence at the lower levels of motions (0.05 to 0.10g). The analytical factors are generally greater than the empirical at low frequency, even for the bedrock velocity of 3000 ft/sec. This is possibly due to the relatively stiff median shear-wave velocity profile. At higher frequencies and higher levels of motion, the analytical factors are less than the empirical which may be a result of a greater amount of high frequency energy in the eastern control motions.

These comparisons are very favorable and suggest that the combination of (1) the vertically propagating shear-wave model, (2) generic modulus reduction and damping curves based on recent high quality laboratory testing and reflecting the effects of confining pressure, and (3) the equivalent-linear methodology represents an accurate analytical tool in estimating the effects of soils on strong ground motions.

6.5.2 Comparisons to Analytical Results

Comparisons with results based upon computations using similar methodologies can also be useful to assess the reasonableness of the computational procedures. Both types of comparisons are shown in Table 6-5.

The Lawrence Livermore National Laboratory entries (Bernreuter et al., 1985) are average results of response spectral ratios computed from SHAKE analyses using predominately Western North America outcrop motions with Central and Eastern North American generic soil profiles. In the Lawrence Livermore Laboratory analyses, the median damping has been fixed at 7% and is noted in the table. Alongside the Lawrence Livermore Laboratory entries are the results of the present study (Table 6-4) for an input acceleration level of 0.75g, which corresponds to an average shear-wave damping of approximately 7%. While the site categories and ranges of the two studies are not identical, considerable overlap does exist. A comparison of the results from the analytical studies shows very similar results for low frequencies with the difference increasing with increasing frequency. This would be expected considering the different high frequency spectral content of the outcrop motions used in the two studies. However, even at the higher frequencies the trends with profile depth are similar. At higher frequencies, the factors computed using outcrop motions with Eastern North America spectral content decrease more rapidly with soil depth than those computed using control motions with correspondingly less energy. These trends are similar to the Western North America empirical results and are likely due to

Table 6-5

Reported Analytical Amplification Factors

	Analytical Results							
Frequency (Hz)	**2 31'–80'**	**L* 25'–80'**	**3 81'–180'**	**L* 81'–180'**	**4 180'–400'**	**L* 181'–300'**	**5 400'+**	**L* 650'**
1.0	1.13	1.10	1.39	1.30	2.01	1.50	1.81	1.70
2.5	1.62	1.20	2.11	1.70	1.66	1.90	1.55	1.50
5.0	1.73	1.65	1.48	1.85	1.33	1.50	1.03	1.10
10.0	1.48	1.90	1.10	1.70	0.97	1.30	0.65	0.80
25.0	1.03	1.70	0.68	1.70	0.60	1.40	0.60	0.90
A_p site/ A_p rock	1.37	1.70	1.13	1.70	0.99	1.40	0.82	1.00
V_p site/ V_p rock	1.16	—	1.24	—	1.34	—	1.46	—

2, 3, 4, 5: values taken from Table 6-4 for input motion of 1.25 g (corresponds to average damping of approximately 7%).
L*: Lawrence Livermore National Laboratory with 7% median damping (Bernreuter et al., 1985).

the lower frequency western outcrop motions. Typical rock motions for tectonically active regions generally have substantially reduced energy, relative to corresponding eastern motions for frequencies above about 10 Hz for the same level of peak acceleration (Figure 6-2). As a result, damping may be depleting the higher frequencies to a relatively greater degree using eastern input motions.

Boore and Joyner (1991) have recently developed Fourier amplitude amplification factors for deep stiff (200 ft and beyond, UBC Category S2) Central and Eastern North America sites. The factors result from a linear analysis using a profile similar to Category 5 and extended to depth of about 2000 ft. The average damping in the profile is approximately 2%. While it is difficult to directly compare Fourier amplification factors to 5% damped response spectral amplification general agreement should exist for the common ranges in profiles. Figures 6-39 and 6-40 show the Boore and Joyner Fourier amplification factors compared to the response spectral factors for all five categories at two levels of control motion, 0.10 and 0.50g. For a rock outcrop motion of 0.10g, the average damping for Category 5 (randomized depth 401–1000 ft) is about 1–2% and 3–4% for 0.50g control motions. From the figures, it is apparent that the results are in close agreement recognizing that the Fourier amplification factors are applicable to sites ranging from about 200 ft to bottomless profiles. At 0.10g, Figure 6-39, the amplification factors for each category form a family of curves beginning at low frequency with Category 5. The approximately constant levels are generally consistent with those of Boore and Joyner out to about 5 Hz where the Fourier amplification curve begins to fall off more rapidly. Beyond that the response spectrum factors exceed the Fourier factors.

At 0.50g input motion, Figure 6-40, the response spectra factors show a reduced amplitude particularly in the higher frequencies, reflecting the effects of nonlinear soil response, a trend similar to that shown in the empirical amplification factors for Western North America (Figure 6-37). Due to the assumptions of linearity, the Fourier amplification factors are independent of control motion amplitude. At these high levels of motion, an average of Categories 3, 4, and 5 (120 ft to 500 ft) amplification factors would be quite similar to the linear factors from about 1 Hz to about 5 Hz and lower beyond. Adding in the 0.10g factors would likely result in a similar set of factors over the range of 1–20 Hz. Considering that the

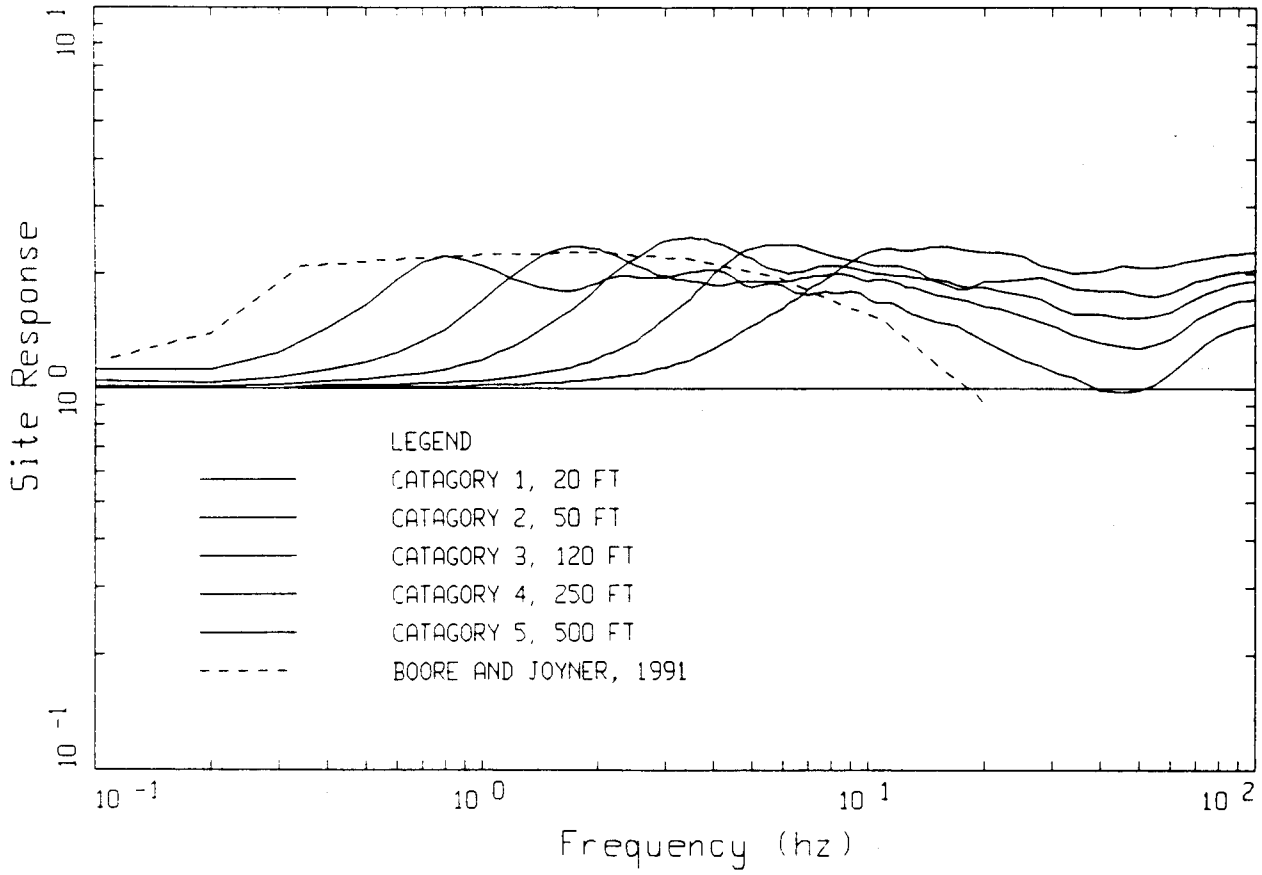

Figure 6-39. Comparison of Boore and Joyner (1992) linear amplification factors of Fourier amplitude spectra for eastern North America S2 (stiff soil > 200 ft depth) sites (dashed line) to median response spectra factors for Categories 1–5 (solid lines). The median factors for the Categories form a family of curves beginning at low frequency for Category 5. Control motion is 0.10 g for the Categories. The Fourier amplitude factors are linear and independent of control motion amplitude.

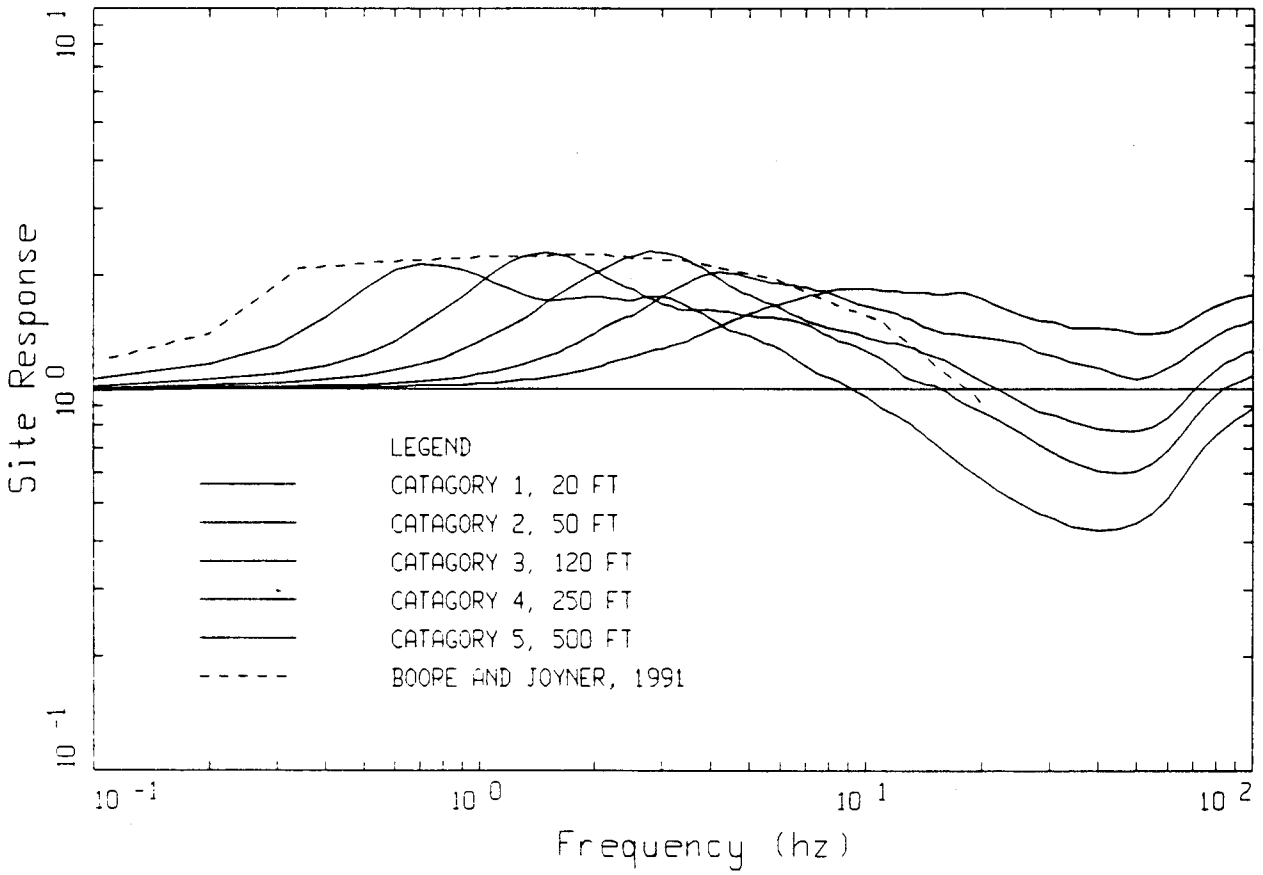

Figure 6-40. Comparison of Boore and Joyner (1992) linear amplification factors of Fourier amplitude spectra for eastern North America S2 (stiff soil > 200 ft depth) sites (dashed line) to median response spectra factors for Categories 1–5 (solid lines). The median factors for the Categories form a family of curves beginning at low frequency for Category 5. Control motion is 0.50 g for the Categories. The Fourier amplitude factors are linear and independent of control motion amplitude.

linear Fourier amplification factors were computed using a similar velocity profile but extended to about 2000 ft and considering completely different assumptions concerning material damping (constrained to observations for the Mississippi Embayment, Boore and Joyner, 1991) the agreement between the two is quite good and suggest that a large uncertainty does not exist in estimating the effects of site condition on strong ground motions.

6.6 Assessment of Vertical Motions

This section treats the specification of the vertical component of strong ground motions. First a summary is presented of the current approach to specifying the vertical component of strong ground motions followed by development of a preliminary computational model based on the stochastic ground motion model (Section 3). Model predictions are then compared to empirical Western

North America vertical-to-horizontal (V/H) ratios. Finally, guidelines are suggested for specifying vertical component motions for Midcontinent and Gulf Coast rock sites as well as the five soil site categories.

6.6.1 Current Approach

The current procedures for the selection of the vertical component of earthquake ground motions include those that are used for buildings and industrial facilities (other than nuclear plants) and those that are specified for nuclear plants in documents such as Reg Guide 1.60.

6.6.1.1 Buildings and Industrial Facilities

Typically, the vertical component is seldom used for these structures. When it is used in the analysis, the spectral ordinates of the vertical component are considered to be 2/3 those of the spectral ordinates of the horizontal component. For some critical structures, and when the structure is within a short distance of the source, the spectrum of the vertical component is selected to be equal to or slightly larger than the horizontal spectrum for frequencies greater than about 2 Hz. In many instances, a set of motions (two horizontal and one vertical component), that had been recorded at close distances to the source, is used in this case. Because of the scarcity of such recorded data, however, it is not possible to utilize this procedure at many sites.

Nuclear Plants: The most widely used procedure to specify the vertical component for nuclear plants has been the procedure included in Reg Guide 1.60. The spectral ordinates for the vertical component are set equal to those of the horizontal component at high frequencies (greater than about 10 Hz) and in the "acceleration" region (typically ranging from about 2 to about 10 Hz) of the spectrum. In the velocity and displacement regions (ie. for frequencies less than about 2 or 3 Hz), the spectral ordinates of the vertical component are set equal to 2/3 those of the horizontal component.

For some recent analyses for nuclear plants, the spectral ordinates at a nearby rock outcrop were selected to be 2/3 those of the horizontal spectral values for the entire frequency range. This vertical rock outcrop motion was then used as input rock outcrop motion to a soil column to calculate the vertical motion at the soil site.

In the Standard Review Plan (NUREG-0800) or Reg Guide 1.60, neither specific recommendations are made nor are guidelines presented regarding applications to eastern sites. As a result, even with the reservation that the computational model presented in the next section is preliminary, it is felt beneficial to present recommendations for vertical-to-horizontal ratios which specifically consider the differences in typically western and eastern strong ground motions.

6.6.2 Computational Model

To model vertical motions, incident inclined compression waves from the stochastic ground motion model (Equation 3-1) are assumed incident at the top of the source layer and the P-SV propagators of Silva (1976) are used to model the crust and soil response to inclined P-SV wavefields. The angle of incidence at the top of the source layer is computed by two-point ray tracing through the crust and soil column (if present) assuming incident compression waves.

To model soil response, a soil column is placed on top of the crustal structure and the incident inclined P-SV wavefield is propagated to the surface where the vertical (or radial) motions are computed.

At close distances, for typical crustal structures without strong near-surface compression-wave velocity gradients, the predominant motion on the vertical component is principally due to the SV wavefield. In a soil column (particularly deep profiles) however, because there is usually a large compression-wave velocity gradient, larger for compression waves than for shear waves as Poisson's ratio generally decreases with depth, the vertical component is usually controlled by the compression wavefield. The separation of rock and soil sites in terms of predominant wavefields in the vertical component depends on specific velocity profiles (soil as well as crustal), source depth and mechanism through their effect on incidence angles, as well as the depth of the water table.

The water table may be a significant factor at soil and perhaps soft rock sites because a significant increase in the compression-wave velocity to values near the fluid phase (about 5000 ft/sec) is generally encountered. Typically at soil and soft rock sites, beginning at the surface, a velocity gradient exists for both compression and shear waves with a Poisson's ratio in the range of about 0.3 to 0.4. Poisson's ratio may decrease with depth slightly until the water table is reached where it jumps to values approaching 0.5. At this point, the fluid phase controls the compression-wave velocity until a depth is reached where the compression- wave velocity of the

skeleton material exceeds the fluid phase velocity. From this point on, Poisson's ratio generally shows an overall slow decrease with depth.

This trend is clearly seen in the profile of Poisson's ratio shown in Figure 6-41. The Poisson's ratio is based on velocities measured with a suspension log tool in a deep hole at the Savannah River site. The water table is located at a depth approximately where the log begins (near 40 ft) and shows a general decrease with increasing depth to about 500 ft. Below 500 ft, the profile becomes more erratic as a different formation is encountered. However, even with these fluctuations, the overall trend is for Poisson's ratio to decrease as the skeleton compression-wave velocity increases. Naturally, site specific factors influence the picture but this overall trend is a generally common feature of soil and soft rock sites.

On a generic basis, the most straightforward approach to model the vertical motions is to assume that the water table is at the surface. The effects of placing the water table at some depth below the surface will depend on the exact depth, the compression-wave damping above the water table, and, to some degree, on source distance and depth, and may result in increased motions at high frequencies. Since these sensitivities are not yet resolved, the current analyses will assume the water table is at the surface and concentrate on general trends in the computed vertical-to-horizontal response spectral ratios. Conservative recommendations will then be given as a guide in assessing vertical motions. Site specific analyses should be conducted with ranges of compression- and shear-wave velocities and water table depths based on measured values.

6.6.2.1 Treatment of Soil Response for Vertical Motions

Commonly equivalent-linear site response analyses for vertical motions have used strain iterated shear moduli from a horizontal motion analysis to adjust the compression-wave velocities assuming either a strain independent Poisson's ratio or bulk modulus. Some fraction (generally 100% to 30%) of the strain iterated shear-wave damping is used to model the compression-wave damping and a linear analyses is performed for vertically propagating compression waves using the horizontal control motions scaled by 2/3 (I.M. Idriss, 1993, personal communication).

The equivalent-linear approach implicitly assumes some coupling between horizontal and vertical motions. This is necessitated by the lack of well determined degradation and damping curves for the constrained modulus. Ideally, the strain dependency of the constrained modulus should be determined independently of the shear modulus. Also, the approach assumes vertically-propagating compression waves and not inclined P-SV waves. Additionally, the use of some fraction of the horizontal control motion is an approximation and does not reflect the generally greater high-frequency content of vertical component motions at rock sites due to lower kappa values (Section 6.6.2.2, Anderson, 1991).

Alternatively, fully nonlinear analyses can be made using two- or three-component control motions (Costantino, 1967; 1969; Li et al., 1992). These nonlinear analyses require two- or three-dimensional soil models which describe plastic flow and yielding and the accompanying volume changes as well as coupling between vertical and horizontal motions through Poisson's effect. While these analyses are important to examine expected dependencies of computed motions on material properties and may have applications in studies of soil compaction, deformation, slope stability, and component coupling, the models are very sophisticated and require specification of many parameters, at least some of which are poorly understood.

In the current implementation of the equivalent-linear approach to estimate vertical to horizontal response spectral ratios, the horizontal component analyses are performed for vertically propagating shear waves using the RVT methodology (Section 6.2.1). To compute the vertical motions, a linear analysis is performed for incident inclined P-SV waves using low-strain, compression- and shear-wave velocities derived from the generic shear-wave velocity profiles and an assumed Poisson's ratio (Section 6.6.3). The water table is taken at the surface and compression-wave damping is assumed to be equal to the low strain shear-wave damping (Johnson and Silva, 1981). The horizontal component and vertical component analyses are assumed to be independent.

These approximations, linear analysis for the vertical component and uncoupled vertical and horizontal components, have been checked by comparing results of fully nonlinear analyses at reference sites Gilroy 2 and

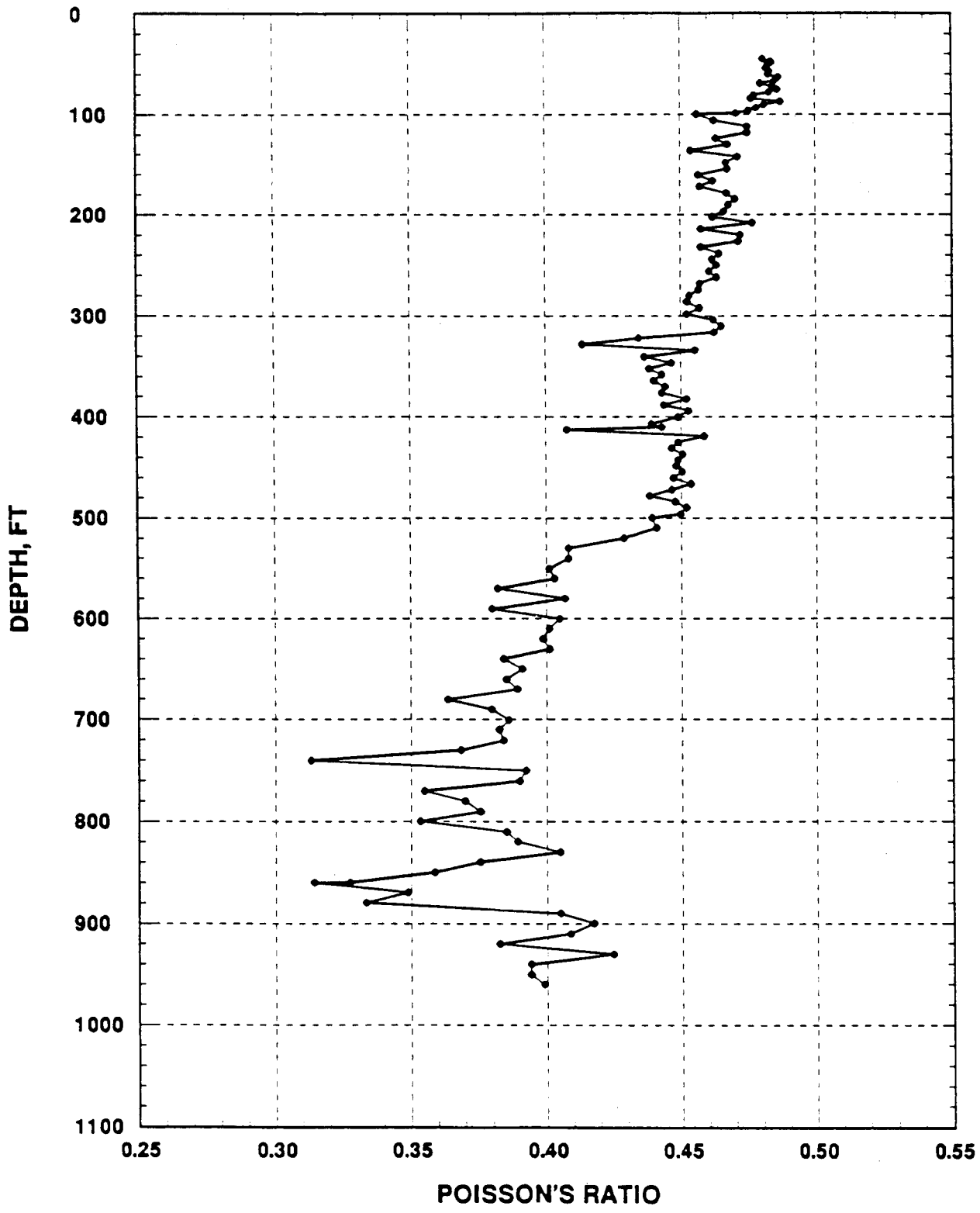

Figure 6-41. Plot of Poisson's ratio verses depth based on suspension log compressional- and shear-wave velocities at the Savannah River Site.

Treasure Island to recorded vertical and horizontal motions from the 1989 Loma Prieta earthquake (Appendix 6-D). The nonlinear analyses indicate that little coupling exists between the vertical and horizontal motions for the ranges in control motions analyzed (maximum 0.473g at Gilroy 1, Appendix 6.B). Since the median generic profiles, Categories 1–5, are much stiffer than the Gilroy 2 profile (Appendix 6.B), resulting in significantly lower strains for the same control motions, the conclusions of Appendix 6.D are assumed to apply to the higher levels of control motions used in computing the amplification factors (Table 6-3). These assumptions are expected to result in conservative estimates of vertical motions since a higher degree of coupling implies degradation of constrained modulus and an accompanying increase in compression-wave damping.

6.6.2.2 Model Validation

The computational model is validated by modeling vertical component response spectra from the 1989 **M** 6.9 Loma Prieta earthquake at 22 rock and 2 soil sites (Gilroy 2 and Treasure Island). The fault distance range (surface projection of the top of the rupture surface) is from 1 to 80 km. Site specific kappa values for the vertical components at the rock sites are based on template fits of response spectral shapes computed assuming a Q(f) of 150 $f^{0.6}$ and a moment magnitude of **M** 6.9. The kappa values average about half that obtained using a similar procedure applied to the horizontal components (Silva and Stark, 1992; Silva and Darragh, 1993). These results are consistent with Anderson (1991) who found vertical component kappa values about half that of the horizontal components at rock sites. A summary of the sites, distances (hypocentral), and kappa values is given in Table 6-6. The compression and shear-wave soil velocity profiles are shown in Appendix 6.B.

In the simulations, the point source is located at a depth of 12 km (Silva and Stark, 1992) and the crustal model of Wald et al. (1991) is used. A stress drop of 200 bars is assumed which results in a source duration of about 6–7 sec, appropriate for the bi-lateral rupture of this earthquake (Wald et al., 1991; Silva and Stark, 1992).

Results of the modeling are shown in Figure 6-42 where the empirical and computed vertical component 5% damped response spectra are shown for each site. The model appears to capture the level and overall shape of the response spectra at most sites reasonably well. For the sites with distances of about 20 km, the incidence angle at the layer above the source is around 60°; for more distant sites, a greater angle of incidence results in a general underprediction of motions which becomes progressively worse as distance increases. As a result, an upper-bound incidence angle is set at 60°. Apparently too little upward propagating energy from the point source is entering the structure. One could partition the energy into upward and downward propagating fields from the source (Harkrider, 1981) based on focal mechanism and treat the wave propagation in a more computationally rigorous manner. However, these results indicate that such a computationally demanding approach may not be warranted and suggest that the vertical motions possess a large stochastic component which is captured reasonably well by a physically simple model. Additionally, since the primary interest in the vertical component motions is at close distances (< 20 km) where it can equal or exceed the horizontals at some frequencies (Section 6.6.4), the 60° upper bound is not of major practical concern.

A quantification of the goodness-of-fit to the vertical motions is shown in the uncertainty, Figure 6-43, and in the computed bias, Figure 6-44. The uncertainty plot indicates low levels of misfit particularly for frequencies exceeding about 6–7 Hz. Overall, the simple model appears to produce levels of uncertainty comparable to the horizontal component (Section 3.0). However, it should be kept in mind that this validation exercise is for one earthquake only and should be applied to a number of earthquakes and many more sites before the model can be considered carefully validated.

The model bias, Figure 6-44, indicates generally unbiased estimates except for frequencies around 4 Hz. This negative bias represents an overprediction and results from a resonance in the Wald et al. crustal model that is clearly seen in the plots of response spectra (Figure 6-42). If the velocity structure had been randomized in a manner similar to that done with the soil profiles and a median response spectrum computed for each site, it is likely that the bias would be near zero throughout most of the frequency range.

6.6.3 Velocity Models

6.6.3.1 Crustal Models

To compute outcrop vertical-to-horizontal response spectral ratios, the two standard crustal models are used: Midcontinent and Gulf Coast (Section 5). The shear- and compression-wave velocities for these two regions are shown in Figure 6-45. The compression-wave

Table 6-6

Loma Prieta Modeling Summary For Vertical Motions

Name	Label	κ (sec)^2	R (km)
Corralitos	COR	0.028	12.0
Los Gatos	LGPC	0.012	12.4
Branciforte Dr.	BRAN	0.020	15.6
Gilroy 1	GL1	0.012	19.2
Gilroy 2	GL2[1]	0.029	20.0
Santa Cruz	UCS	0.020	20.0
UCSC—Seismic Lab	UCSC	0.020	23.3
Gilroy 6	GL6	0.025	26.8
SLAC	SLA	0.030	30.5
Redwood City—Cañada	RDC	0.060	39.9
SAGO South	SAS	0.050	40.8
APEEL 7	A07	0.050	45.6
APEEL 10	A10	0.050	45.6
Monterrey City Hall	MON	0.030	45.6
Belmont—2 story	BEL	0.040	47.5
APEEL 2E, CUSH	A2E	0.020	54.3
Sierra Point	SSP	0.020	66.1
SF Diamond Heights	SFD	0.020	74.0
Piedmont J.H.	PHS	0.025	75.0
SF Rincon	SFR	0.020	76.9
Yerba Buena Island	YBI	0.040	77.9
SF Pacific Heights	SFH	0.040	78.9
SF Telegraph Hill	SFT	0.020	78.9
Treasure Island	TRI[1]	0.029	79.9
SF Cliff House	SFC	0.040	80.9

1. Soil sites.
2. Kappa values are relative to the fixed Q(f) of 150 $f^{0.6}$. For soil sites the average kappa value of 0.029 sec is used for the shallow crust beneath the profiles.

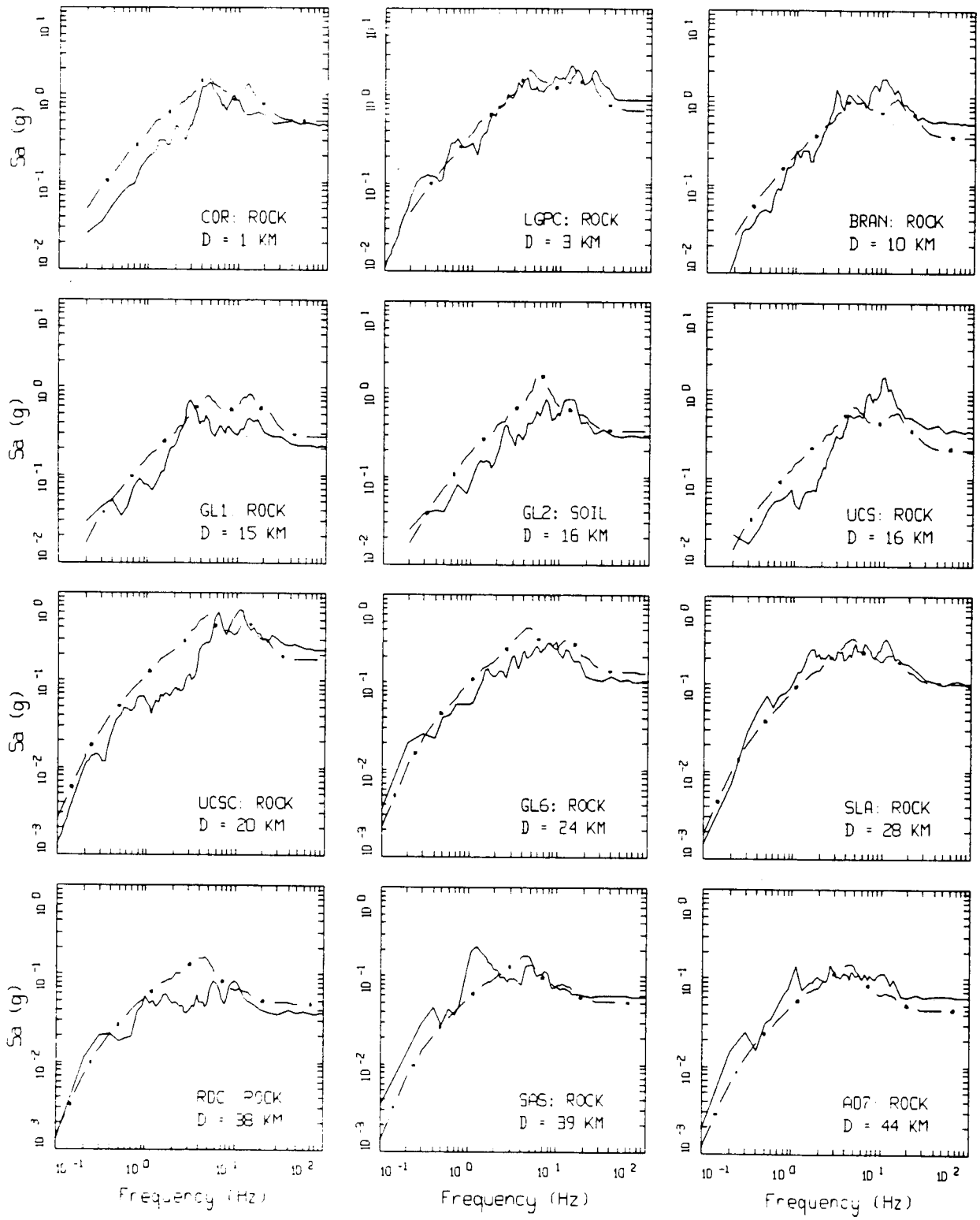

Figure 6-42. Comparison of 5% damped vertical component response spectra for the 1989 Loma Prieta earthquake. Solid lines are from recordings and dash-dot lines are model predictions, page 1 of 2.

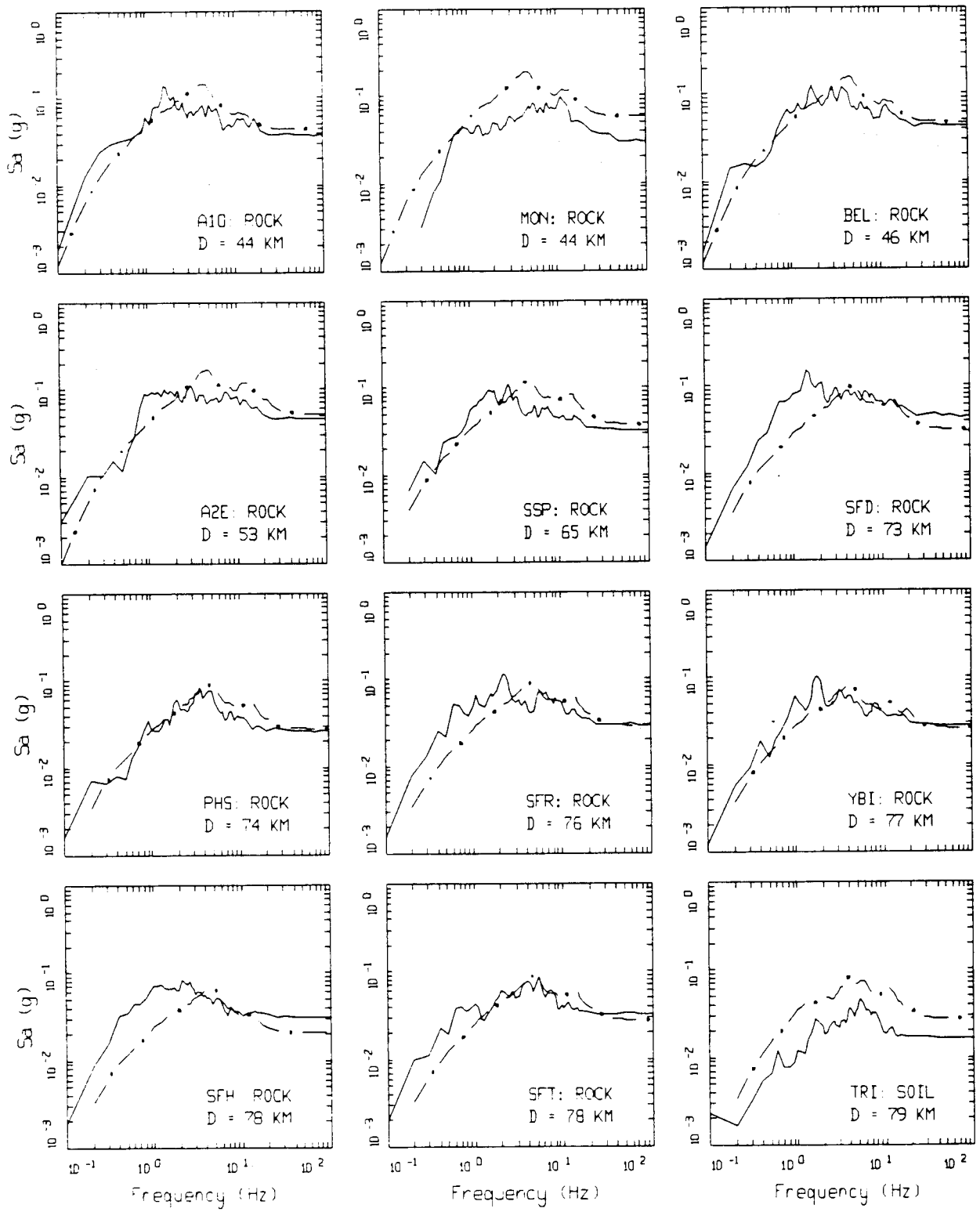

Figure 6-42. Continued, page 2 of 2.

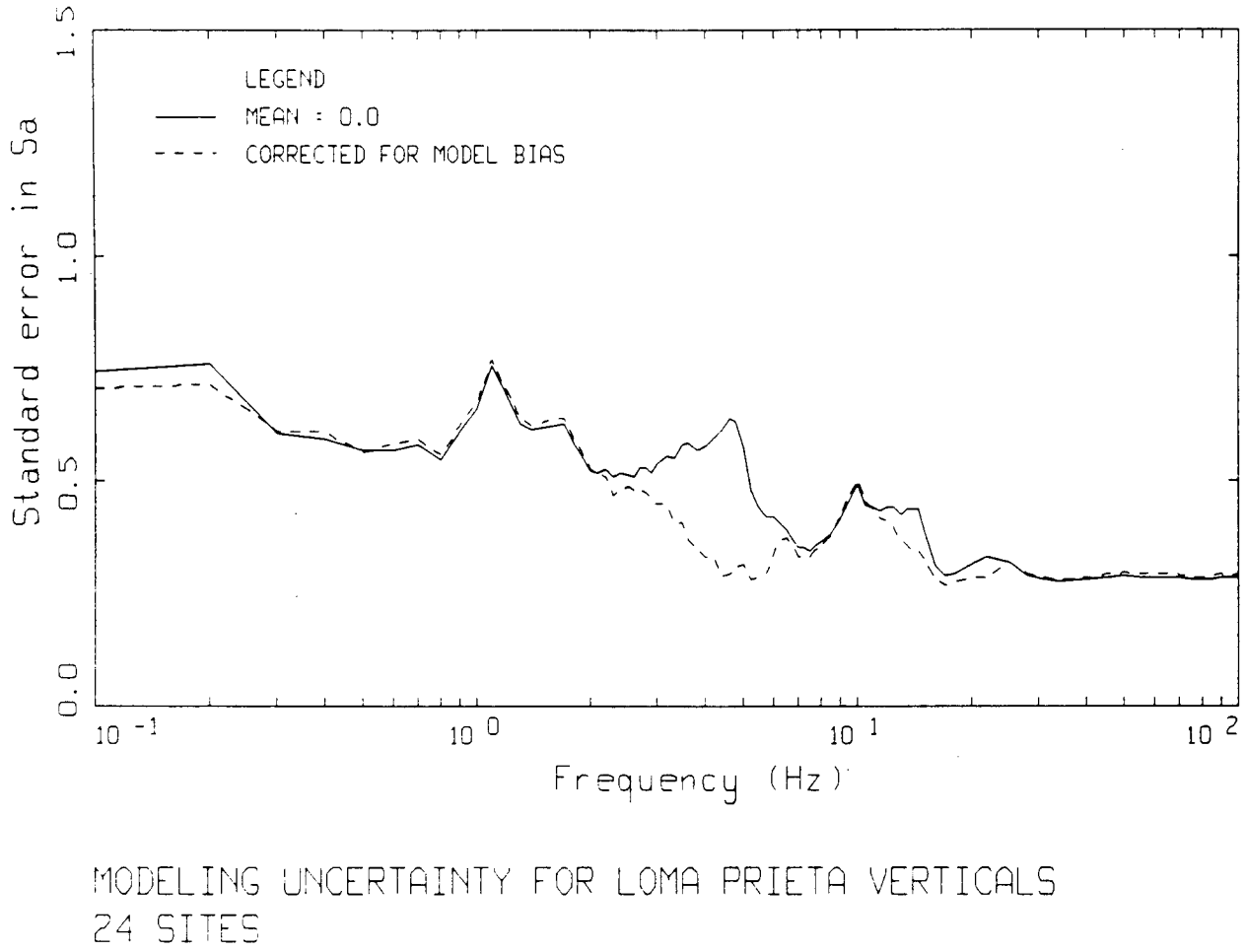

Figure 6-43. Standard error (natural log) of modeling uncertainty computed for the Loma Prieta earthquake using vertical motions. Solid line, total uncertainty; dashed line, corrected for model bias.

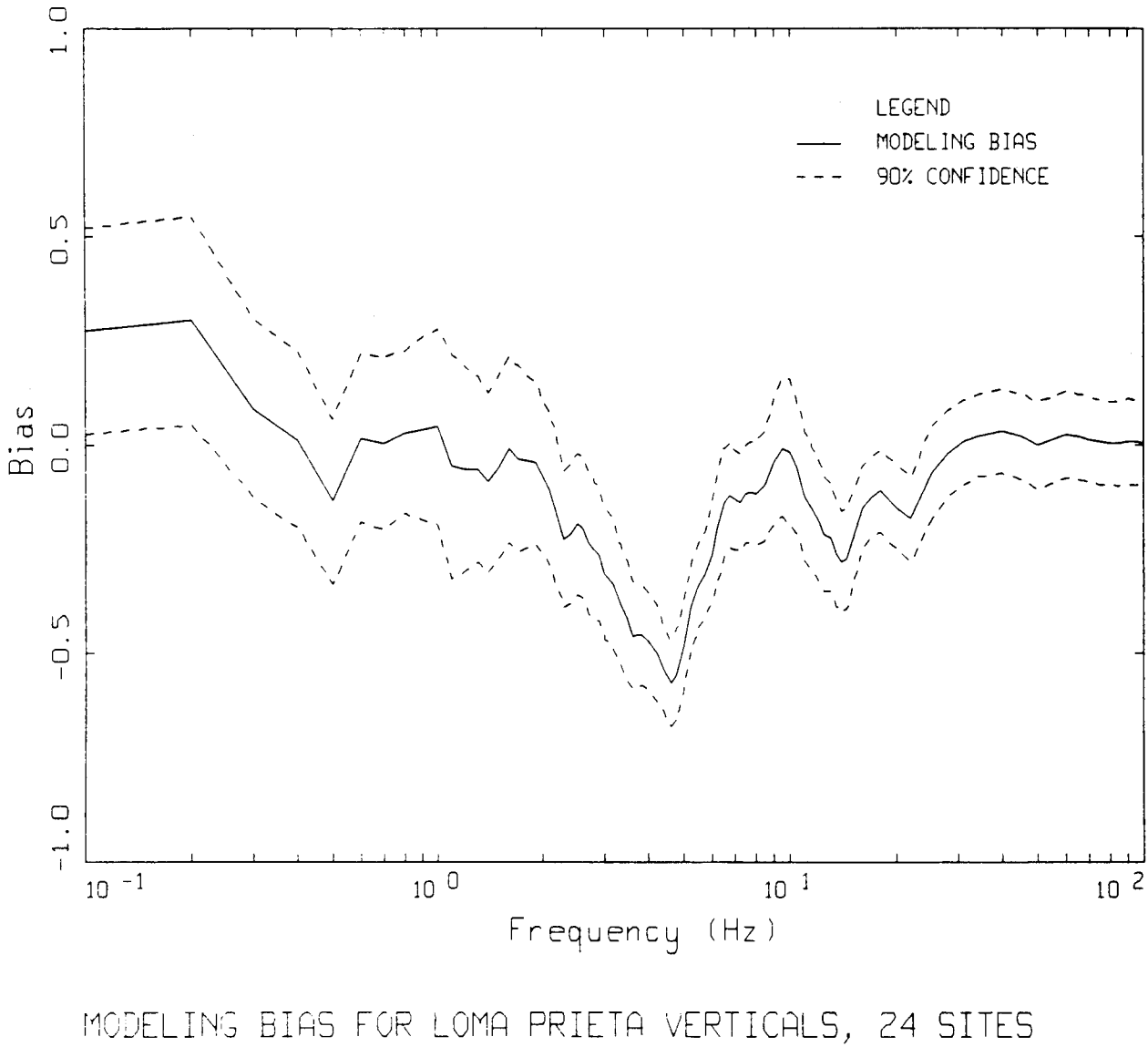

Figure 6-44. Modeling bias computed for the Loma Prieta earthquake using vertical motions. Dashed lines represent 90% confidence limits.

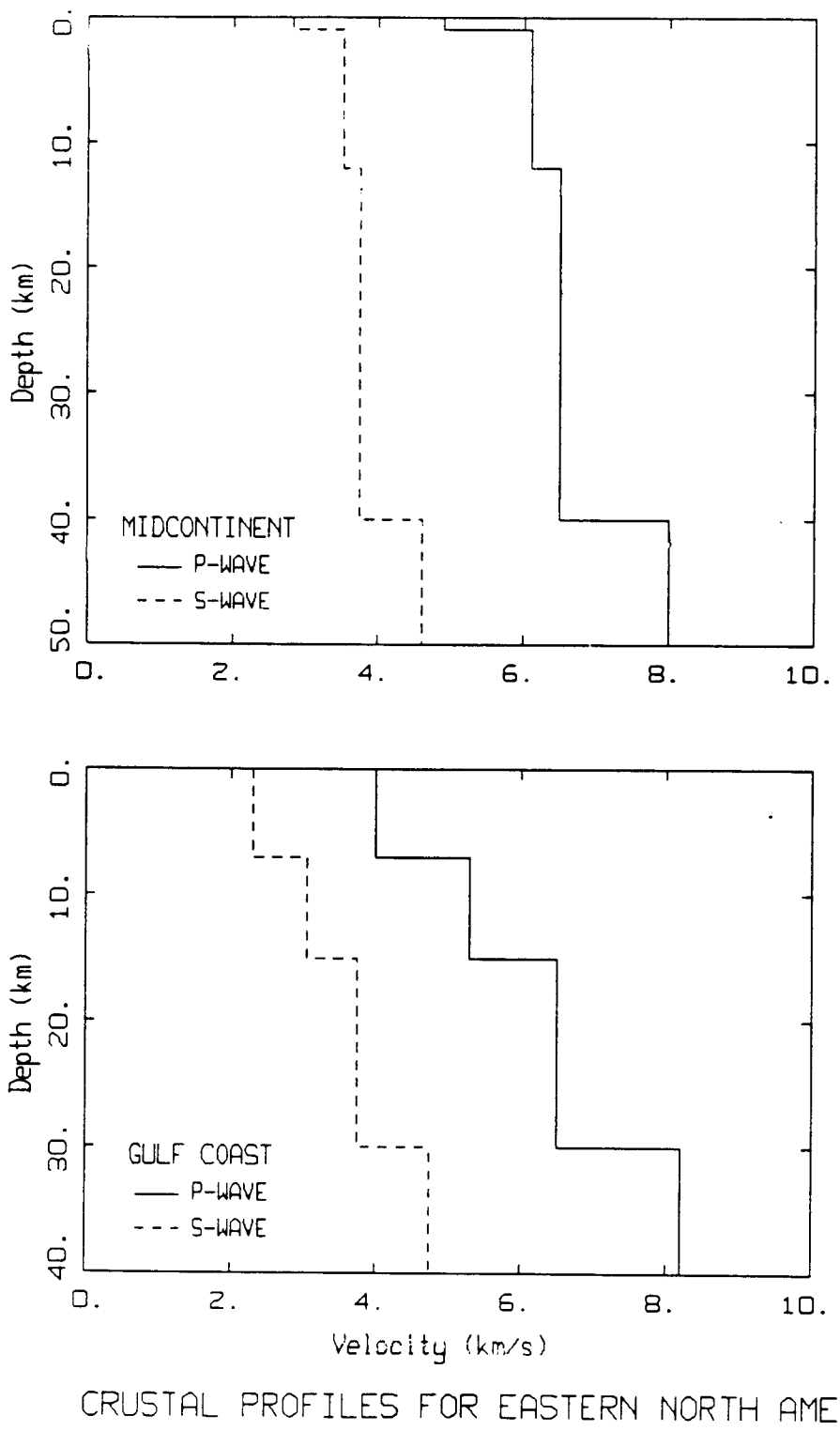

Figure 6-45. Compressional- and shear-wave velocities for the Midcontinent and Gulf-Coast crustal models.

velocities represent measured values based on a number of long range refraction studies while the shear-wave models are derived from the compression-wave velocities assuming a constant Poisson's ratio of 0.25.

6.6.3.2 Soil Models

The shear-wave velocity model is based on the median profiles of the five site categories shown in Figure 6-3. The corresponding compression-wave velocities are computed by assuming a Poisson's ratio that decreases linearly with depth. The intercept and slope are based on the Savannah River suspension log results (Figure 6-41). The Savannah River data represents the best constrained compression- and shear-wave velocity measurements for deep profiles in the profile database. The equation for Poisson's ratio is given by

$$\sigma(z) = 0.48 - 2.6 \times 10^{-4} z \qquad \text{(Eq. 6-1)}$$

where $\sigma(z)$ is Poisson's ratio and z is depth in meters. This equation assumes the water table extends to the surface. The bedrock compression-wave velocity is computed by assuming a Poisson's ratio of 0.25.

In the site response analyses for the vertical component, the small-strain shear-wave damping is used for the compression-wave damping. These values are around 1% and decrease slightly with depth. The values are listed in Table 6-7. As indicated previously, linear analyses are performed for the vertical components.

6.6.4 Development of Vertical-to-Horizontal Ratios

In computing the horizontal and vertical ground motion, a stress drop of 120 bars is used along with a source depth of 10 km. A kappa value of 0.003 sec is used for the vertical motions, one-half the median hard rock shear-wave value of 0.006 sec (Table 3-1). Appropriate velocities and densities are taken from each crustal model at a depth of 10 km. The Q(f) models used are appropriate to each crustal model (Table 3-1) and assume shear-wave propagation. This is not an important issue since motions are computed out to 50 km only (the main focus is within 20 km) and the crustal Q(f) models have very little effect at these distances in the frequency range of interest, 1–34 Hz.

6.6.4.1 Outcrop V/H Ratios

Since the V/H response spectral ratios for outcrop motions are independent of strain level, they are computed for a single magnitude, **M** 6.5, at a suite of epicentral distances. As with the soil profiles, the crustal velocities should be randomized and median and one sigma estimates of the ratios computed. However, probabilistic analyses have not been performed on the crustal velocities in a manner similar to that on the profiles (Appendix 6.A). As a result, only deterministic results are available for the standard crustal models and generic median profiles.

Figures 6-46 and 6-47 show the V/H ratios for the Mid-continent and Gulf Coast crustal models for distances 1, 5, 10, 15, 20, 30, 40, and 50 km. As expected, the ratios are largest at the closest distances. The ratios for 1 km and 5 km are close to one another for both crustal models and exceed 1 for frequencies above about 20 Hz. The ratios at greater distances decrease rapidly as the incidence angle increases and reach a nearly constant value around 0.6–0.8 for frequencies below 20–30 Hz. This range is in good agreement with that of Boore and Atkinson (1992) who found an average V/H value of about 0.65 over the frequency range of 1–15 Hz for a suite of ECTN recordings of Lg waves at distances exceeding about 200 km.

Table 6-7

Shear- and Linear Compressional-Wave Damping Verses Depth Used in Vertical Site Response Analyses

Depth Range (ft)	Shear-Wave Damping Ratio (%),Q	Compressional-Wave Damping Ratio (%),Q
0–120	1.0, 50.0	1.0, 50.0
121–250	0.8, 62.5	0.8, 62.5
251–500	0.7, 71.4	0.7, 71.4

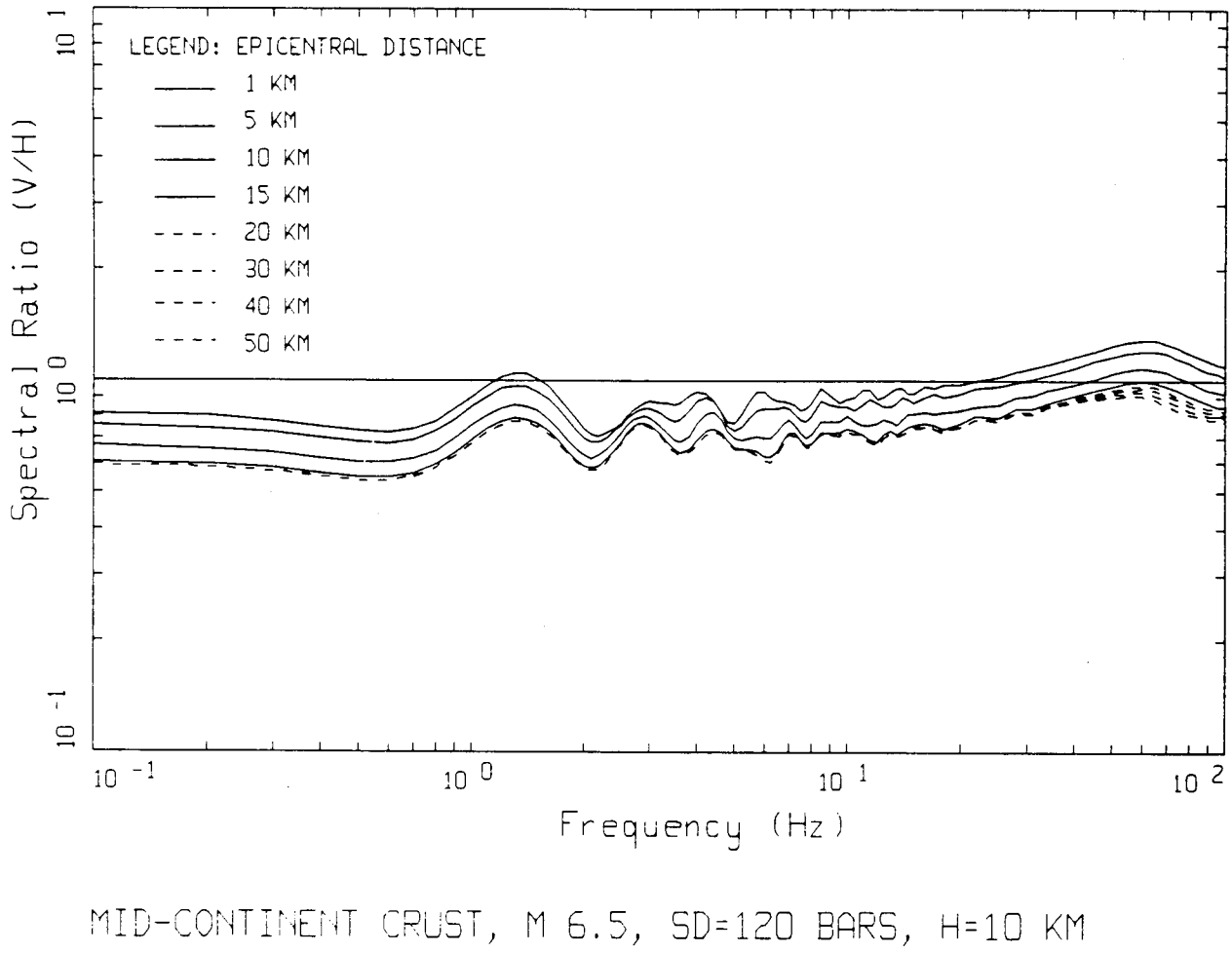

Figure 6-46. Vertical-to-horizontal (V/H) 5% damped response spectral ratios computed for the Midcontinent crustal model.

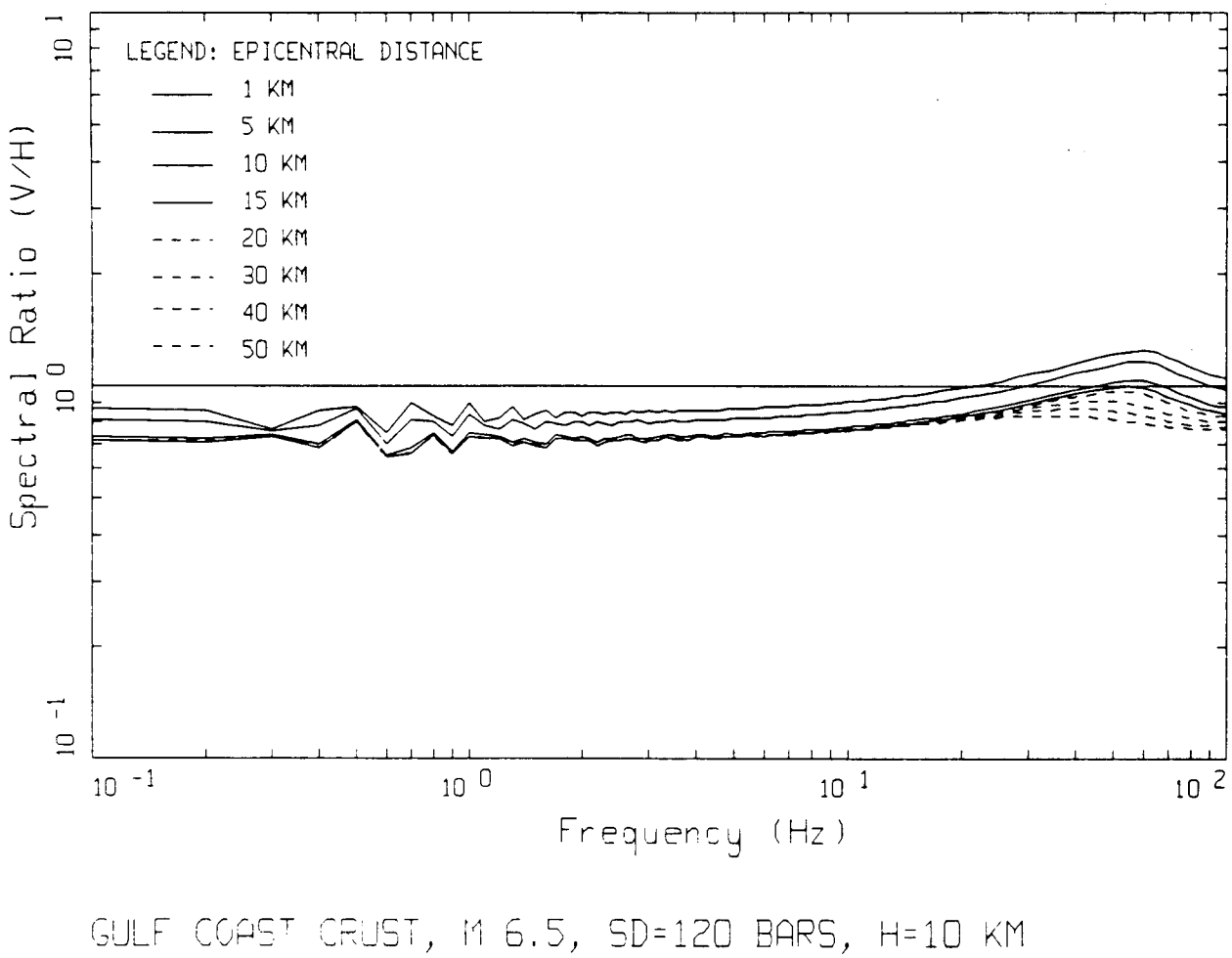

Figure 6-47. Vertical-to-horizontal (V/H) 5% damped response spectral ratios computed for the Gulf-Coast crustal model.

The rock V/H ratios depend strongly on the velocity gradient and are lower for crustal models with steep velocity gradients in the shallow crust. This has the effect of steepening the raypaths through refraction, thereby enriching the horizontal components relative to the vertical. This is demonstrated in the V/H ratios computed for the Wald et al. (1991) crustal model which is appropriate for California using the same magnitude, source depth, and set of distances. Figure 6-48 shows the ratios computed for the Wald et al. (1991) crust and, except for the large resonances, which should be averaged out by randomizing the velocities, the ratios are, on average, substantially less than the corresponding eastern ratios.

These results of linear analyses suggest that at hard rock sites, such as the Midcontinent and Gulf Coast crustal models, V/H ratios are expected to be larger than corresponding ratios at soft rock sites, providing the soft rock remains linear at high levels of input motion. There is empirical evidence, however, that soft rock sites display characteristics of nonlinear response in V/H ratios showing large V/H ratios at close distances for large magnitude earthquakes (Section 6.6.5). These large ratios are not expected at hard rock sites and illustrate the inappropriateness of applying empirical results from one tectonic regime to another.

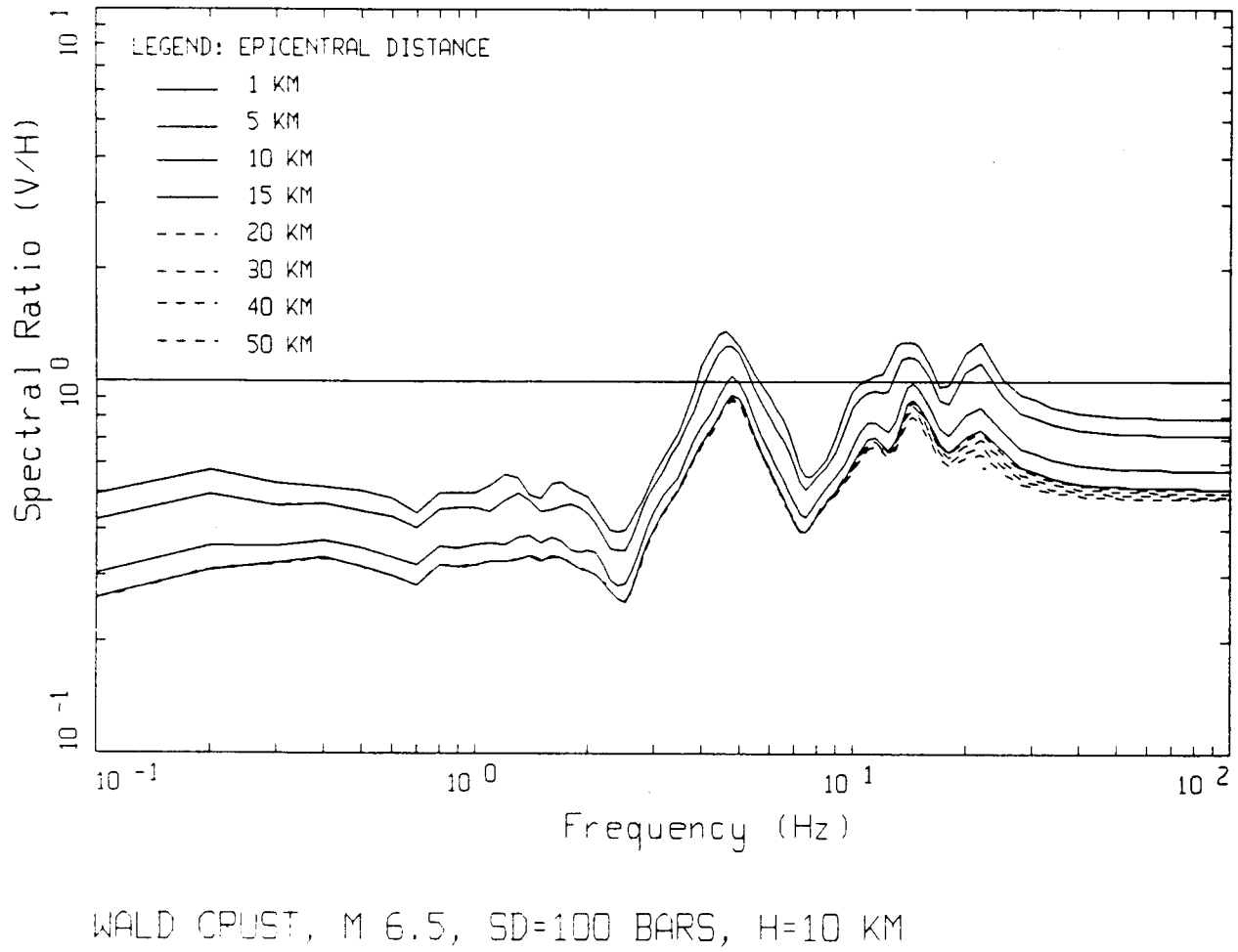

Figure 6-48. Vertical-to-horizontal (V/H) 5% damped response spectral ratios computed for the Wald et al. (1991) crustal model.

The peak acceleration ratios are shown in Table 6-8 for both crustal structures. At the closest distance, 1 km, the ratio is about 1 and decreases rapidly out to about 20 km where it stabilizes to about 0.75–0.80.

6.6.4.2 Soil V/H Ratios

To illustrate the effects of nonlinear soil response on the computed V/H ratios for each profile category, four peak acceleration levels of horizontal outcrop motions are used: 0.10, 0.30, 0.50, and 1.00g. The magnitudes (M) and epicentral distances are listed in Table 6-3. Table 6-8 shows the peak acceleration ratios and Figures 6-49 through 6-53 show the V/H ratios for the five site categories (1–5).

For all of the categories, at the lowest level of control motion, the V/H ratios remain about 0.8 or less for frequencies less than about 30 Hz. At higher levels of motion, and for progressively deeper profiles, the ratios can be significantly greater than one at high frequencies. The large V/H ratios at high frequency for Categories 2–5 at high levels of control motion are a consequence of high levels of strain iterated damping in the horizontal motions coupled with a linear analyses using low damping (about 1%, Table 6-7) in the vertical analyses. Also, not randomizing the profiles and developing median ratios exaggerates the resonance effects of the soil column. This is shown in the sharp peaks and troughs seen in the ratios.

Table 6-8

Vertical-to-Horizontal Peak Acceleration Ratios

Site	Distance (km)	Vpga/Hpga
Midcontinent	1	1.03
	5	0.96
	10	0.86
	15	0.80
	20	0.78
	30	0.77
	40	0.76
	50	0.75
Gulf-Coast	1	0.99
	5	0.94
	10	0.84
	15	0.82
	20	0.81
	30	0.79
	40	0.77
	50	0.76

Table 6-8 (Continued)

Vertical-to-Horizontal Peak Acceleration Ratios

Soil Site	Rock Outcrop (g)	Vpga/Hpga
1	0.10	0.48
	0.30	0.53
	0.50	0.57
	1.00	0.65
2	0.10	0.54
	0.30	0.85
	0.50	0.67
	1.00	0.83
3	0.10	0.58
	0.30	0.46
	0.50	0.77
	1.00	1.01
4	0.10	0.62
	0.30	0.76
	0.50	0.87
	1.00	1.17
5	0.10	0.66
	0.30	0.64
	0.50	0.96
	1.00	1.33

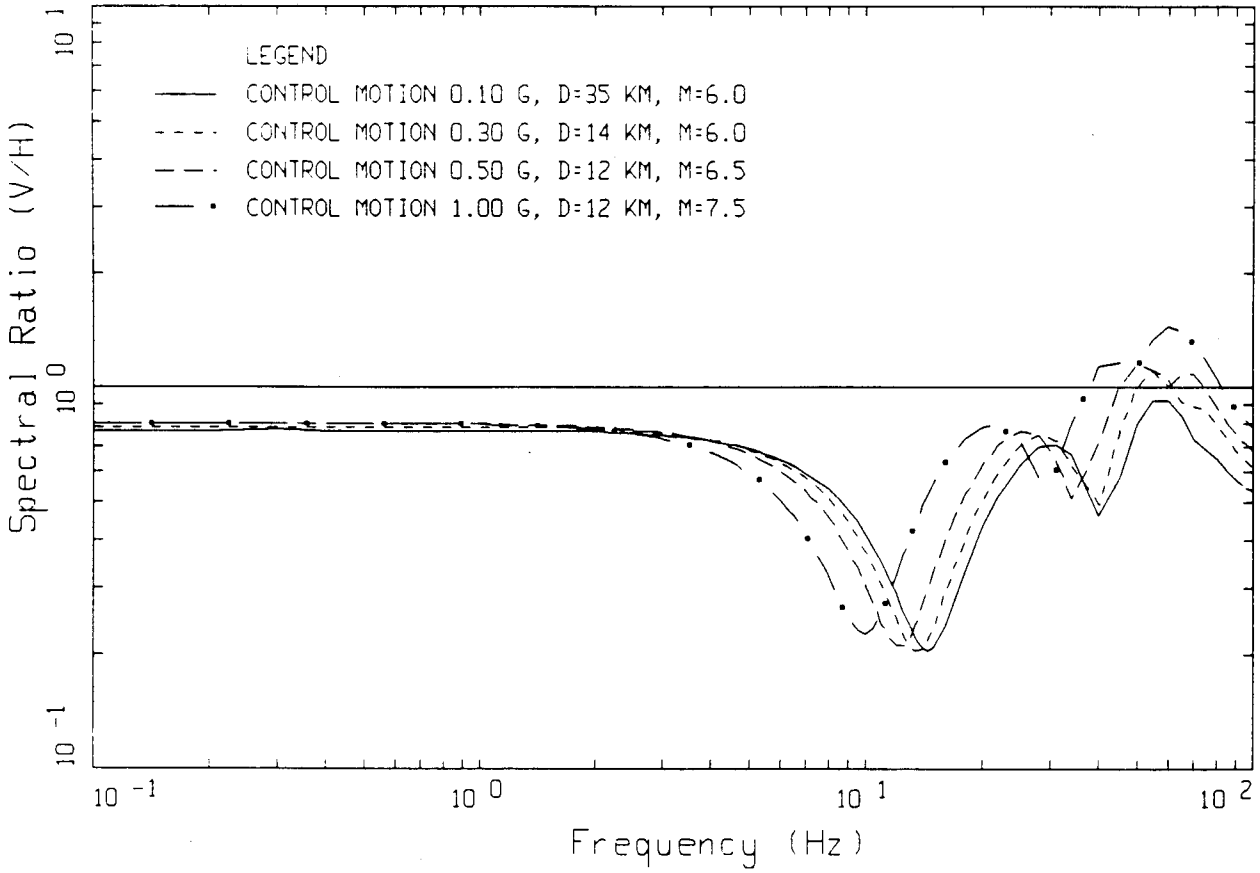

Figure 6-49. Vertical-to-horizontal (V/H) 5% damped response spectral ratios computed for the Category 1 (20 ft) soil profile.

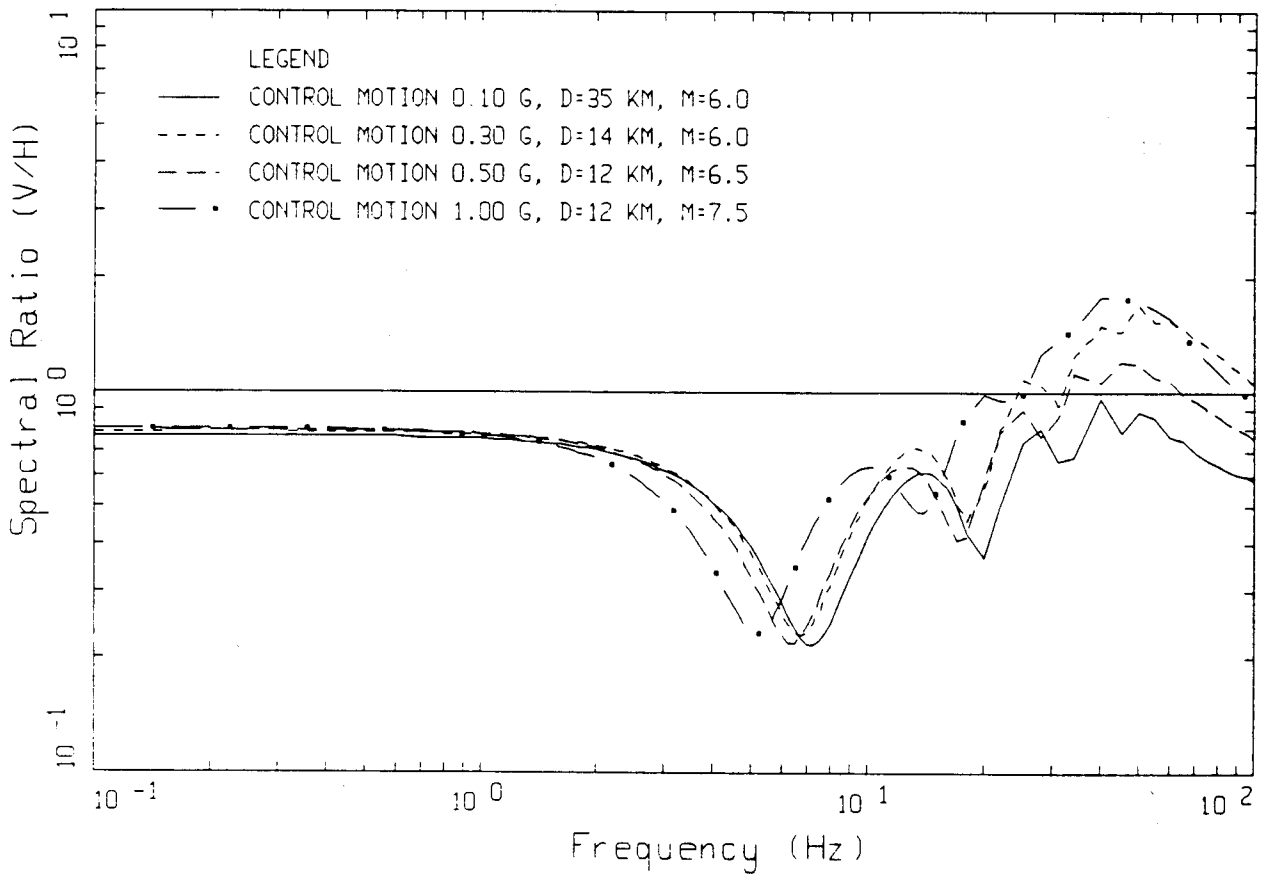

Figure 6-50. Vertical-to-horizontal (V/H) 5% damped response spectral ratios computed for the Category 2 (50 ft) soil profile.

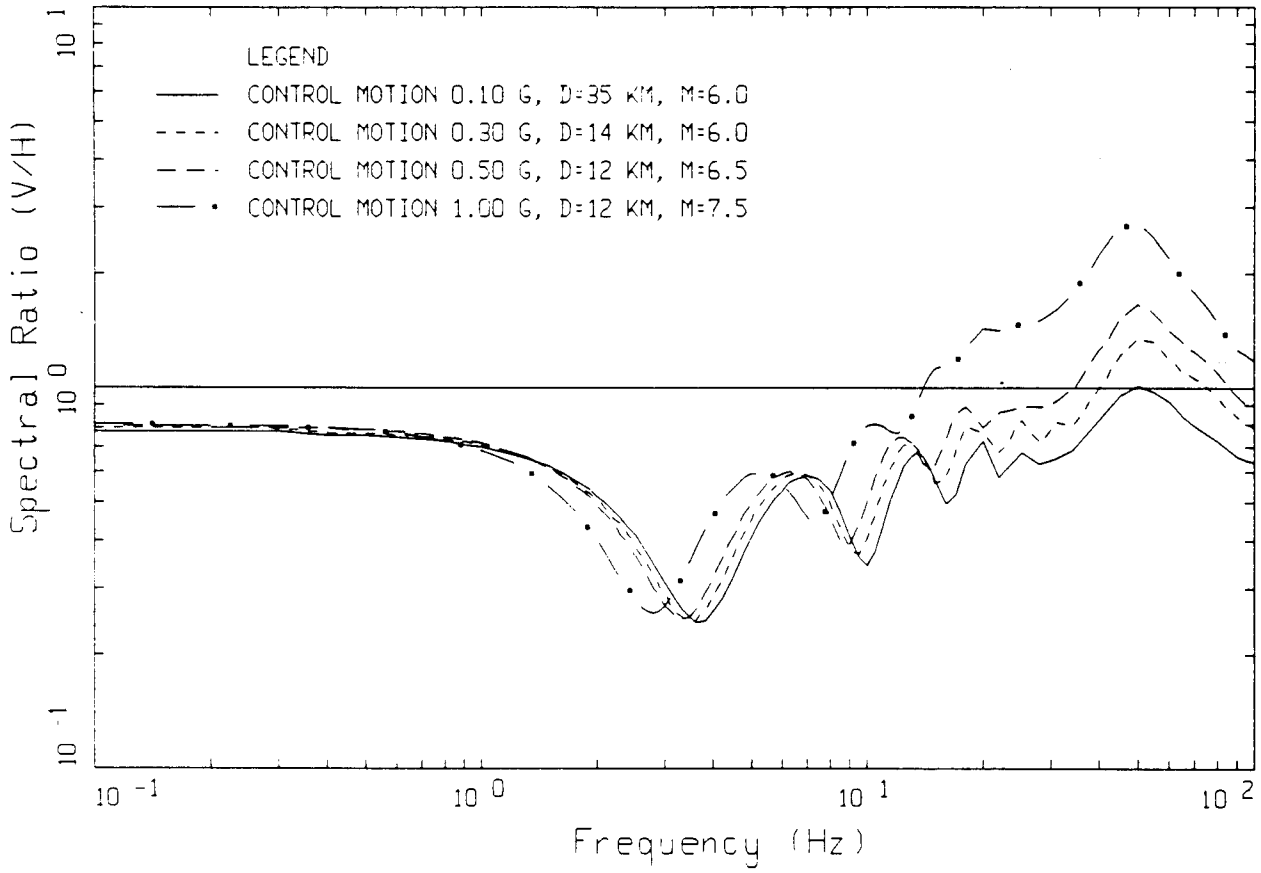

Figure 6-51. Vertical-to-horizontal (V/H) 5% damped response spectral ratios computed for the Category 3 (120 ft) soil profile.

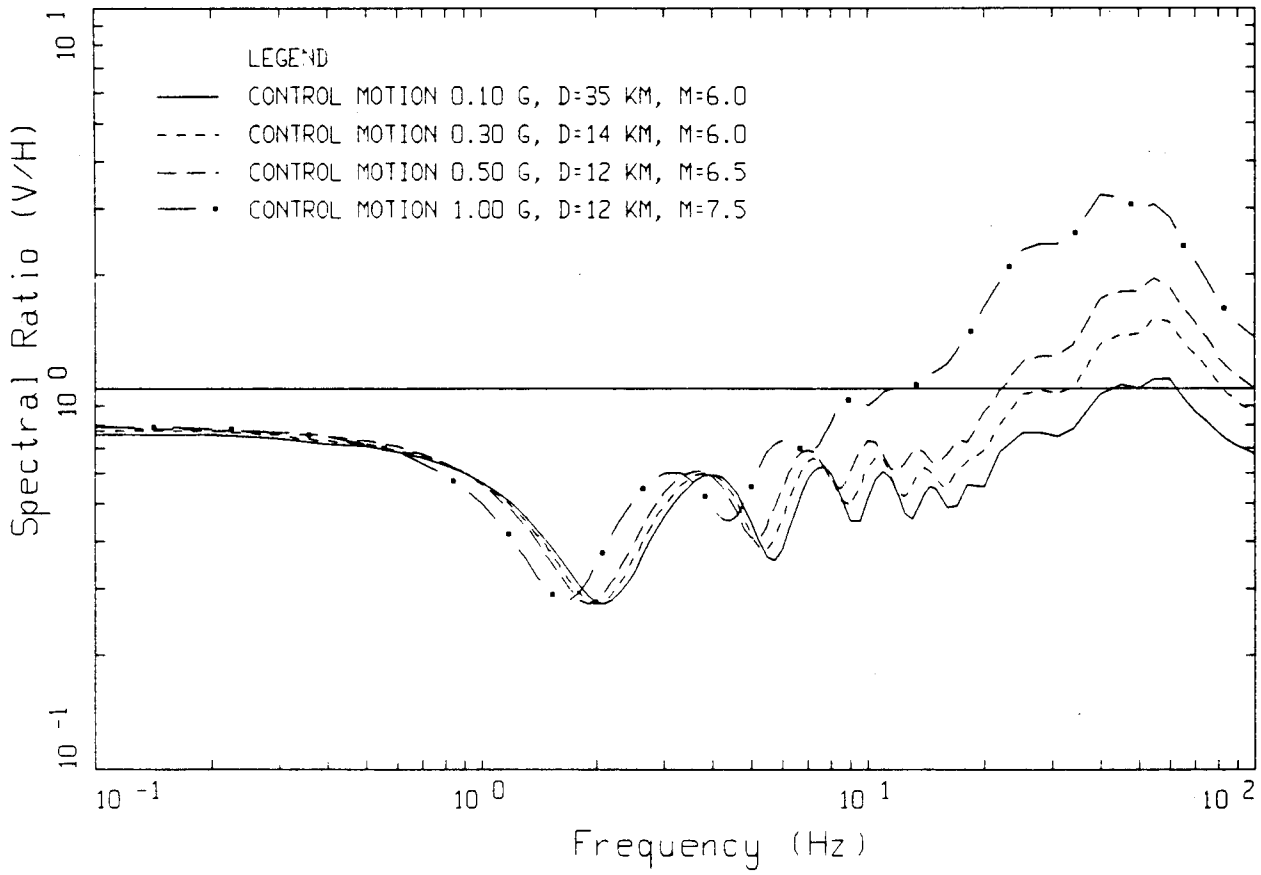

Figure 6-52. Vertical-to-horizontal (V/H) 5% damped response spectral ratios computed for the Category 4 (250 ft) soil profile.

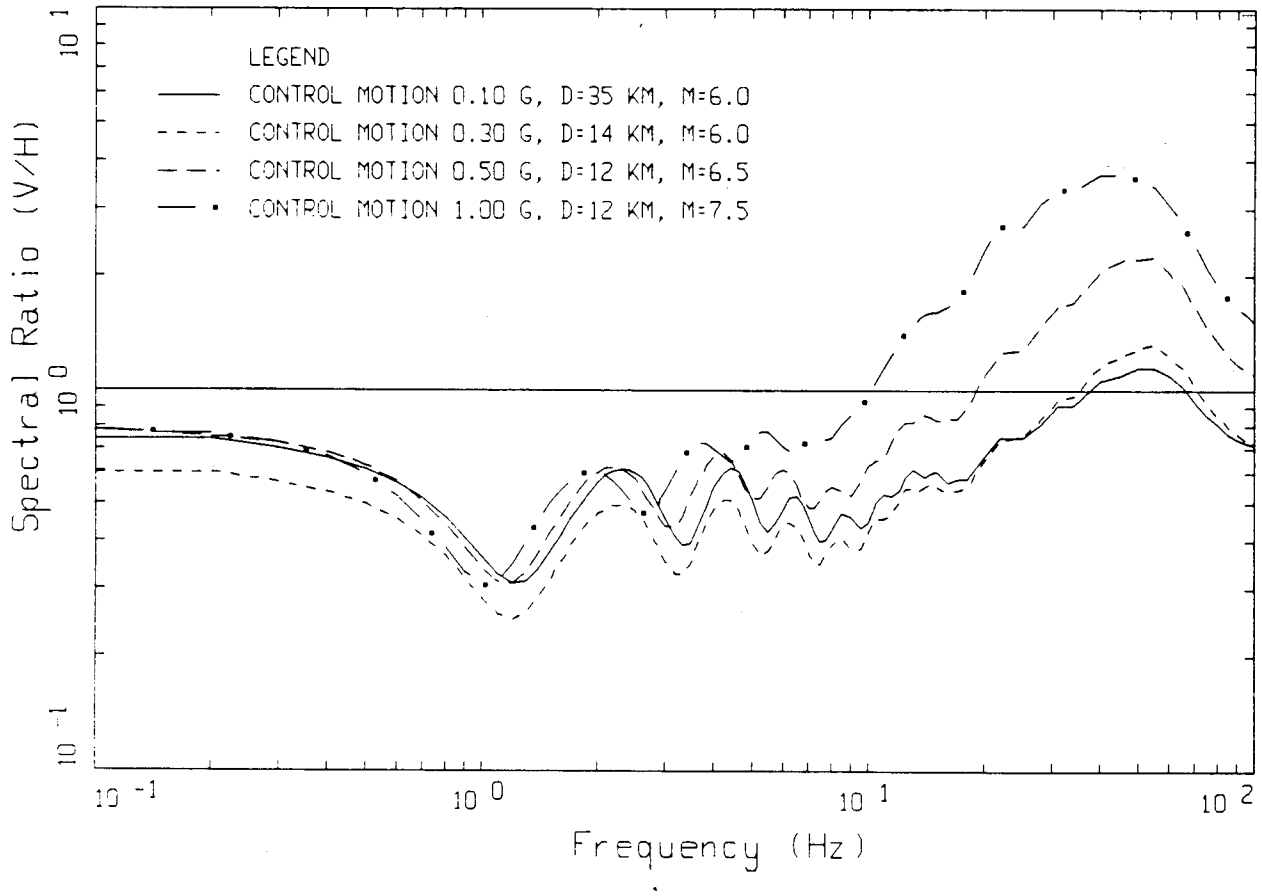

Figure 6-53. Vertical-to-horizontal (V/H) 5% damped response spectral ratios computed for the Category 5 (500 ft) soil profile.

The high peak acceleration ratios for Categories 4 and 5 (Table 6-8) at the 1.0g control motion also reflect these effects. As a result of these factors, the large values shown in the ratios are extreme effects and do not represent expected median values. Because of this and due to the preliminary nature of the model, the concentration is on the general trends shown in the V/H ratios and recommendations will be based on these features.

6.6.5 Comparison of Computed Vertical-to-Horizontal Ratios To Empirical Ratios

Due to the lack of a sufficient number of recordings (Section 2), meaningful comparisons to empirical V/H ratios for Eastern North America sites is limited to distant sites and Lg waves. As suggested in Section 6.6.4.1 on outcrop V/H ratios, the ratios computed for both the Midcontinent and Gulf Coast crustal models at distances beyond about 20 km show general accord with the empirical ratios of Boore and Atkinson (1992) out to the limit of their data, 15 Hz. For comparisons at closer distances and for soil sites, the only source of data are Western North America recordings (Appendix 2.C).

As with the comparisons of computed amplification factors to empirical Western North America amplification factors (Section 6.5.1), complications arise due to differences in bedrock velocities, crustal velocity gradients, and spectral content of the control motions (Section 6.3.5). However, the same general trends should exist except that the Western North America V/H ratios are expected to be generally lower than the eastern ratios due to higher velocity gradients typical in the shallow western crust.

6.6.5.1 Outcrop V/H Ratios

Figure 6-54 shows the empirical V/H ratios for the magnitude range of **M** 7.0–7.3 at four median distances ranging from 3.5 km to 74.7 km (Appendix 2.C). At the largest distance, and lowest level of motion, the ratio is in the range of 0.4 to about 0.7 at low frequencies, similar to that computed for the Wald et al. crust. This range reflects the expected lower V/H ratios for typical Western North America crustal structure. An unexpected feature however, is the strong distance and frequency dependence shown in the empirical rock outcrop V/H ratios. These ratios more closely resemble a smoothed version of those computed for the soil sites. Of particular interest is the increase in the ratio going from a median distance of 74.7 km to 37.8 km. This large change may be associated with a change in predominant wave type or to nonlinear rock response.

Some support does exist for nonlinear effects at rock sites. Gibbs et al. (1992) measure a significant increase in kappa values (suggesting lower velocity and higher damping) for earthquakes recorded at the rock site Gilroy 1 as the level of motion increases. Laboratory dynamic testing of soft rocks shows modulus reduction and damping strain dependencies very similar to that of soils (Ken Stokoe, personal communication). Additionally, recent drilling and logging at a number of rock sites which recorded the 1989 Loma Prieta earthquake (CUREE) show shallow velocities not unlike soil sites.

The empirical results for Western North America show a lower V/H ratio at large distance than the eastern ratios, possibly reflecting the differences in shallow crustal velocity gradients. For the softer western rock sites, a strong dependence on distance, or alternatively level of motion, is shown in the V/H ratios and results in values greater than one at very close distances (large motions) for frequencies above about 6 Hz. This strong dependence may be due to the nonlinear response of the soft rock and is not expected at hard rock eastern sites.

6.6.5.2 Soil V/H Ratios

The Western North America empirical ratios for deep firm soils are shown in Figure 6-55 for the same magnitude and distance ranges. The deep soils show very similar trends to the rock V/H ratios with somewhat more of a distance or level of motion dependence. At low frequencies, the ratio is in the range of about 0.3–0.5, slightly lower than the rock ratios for the same frequency range. At closer distances, the ratios increase more rapidly with frequency than the rock ratios but reach about the same levels. The trend is similar to that shown in the eastern ratios, particularly for the deep Category 5 (500 ft) profile (Figure 6-53). Both the empirical and analytic all-derived ratios (Category 5) show a dip near 1 Hz, increase with increasing frequency, and then turn over. The high-frequency peak or plateau (in the empirical) occurs near 10 Hz in the empirical and near 50 Hz in the analytical. A similar feature was noted in the comparisons of empirical western and analytical eastern amplification factors (Section 6.5.1) and is related to the differences in the eastern and western kappa values for the vertical motions.

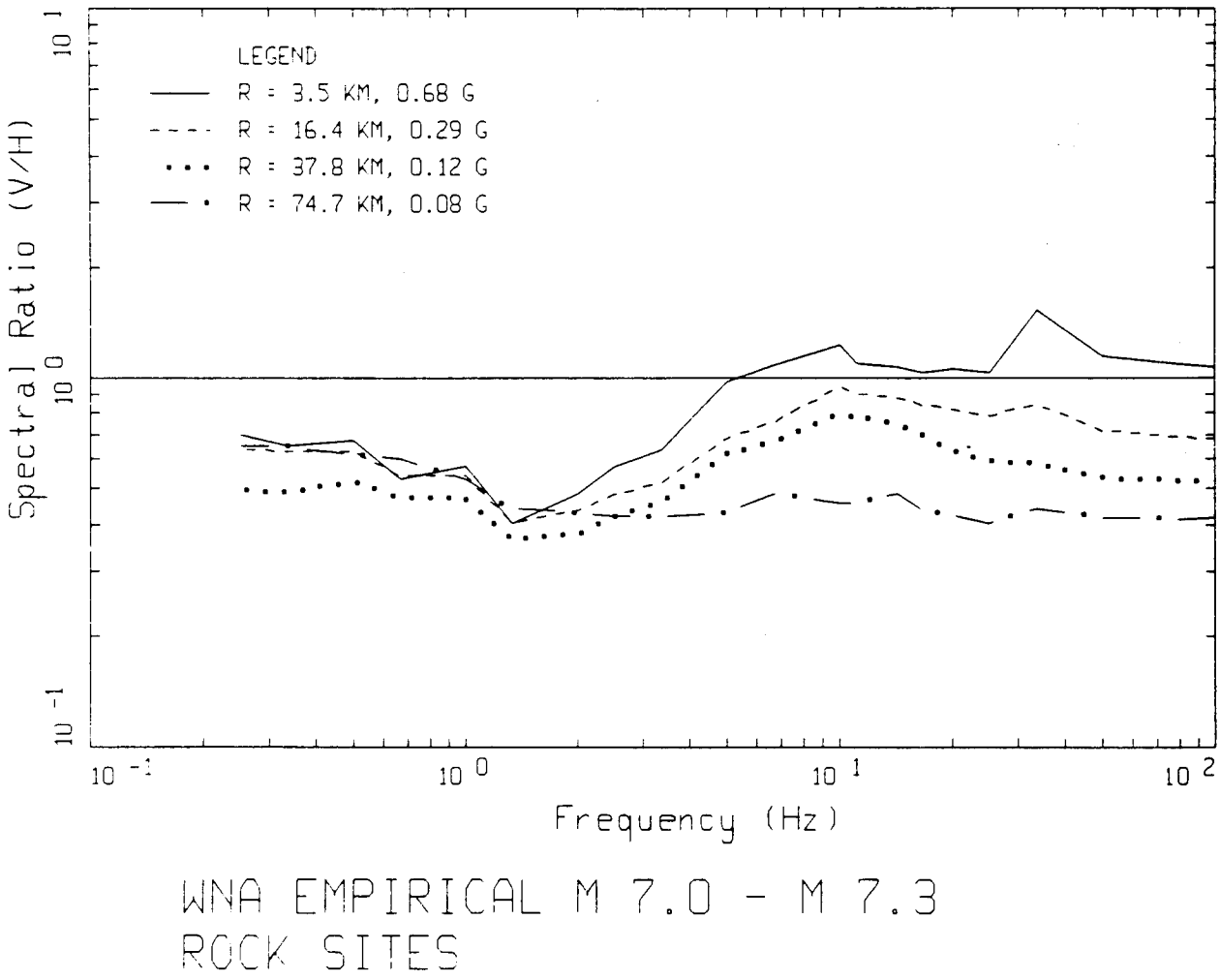

Figure 6-54. Empirical V/H ratios at rock sites for western North America earthquakes of magnitudes M 7.0–7.3. Peak acceleration values are for rock outcrop horizontal motions.

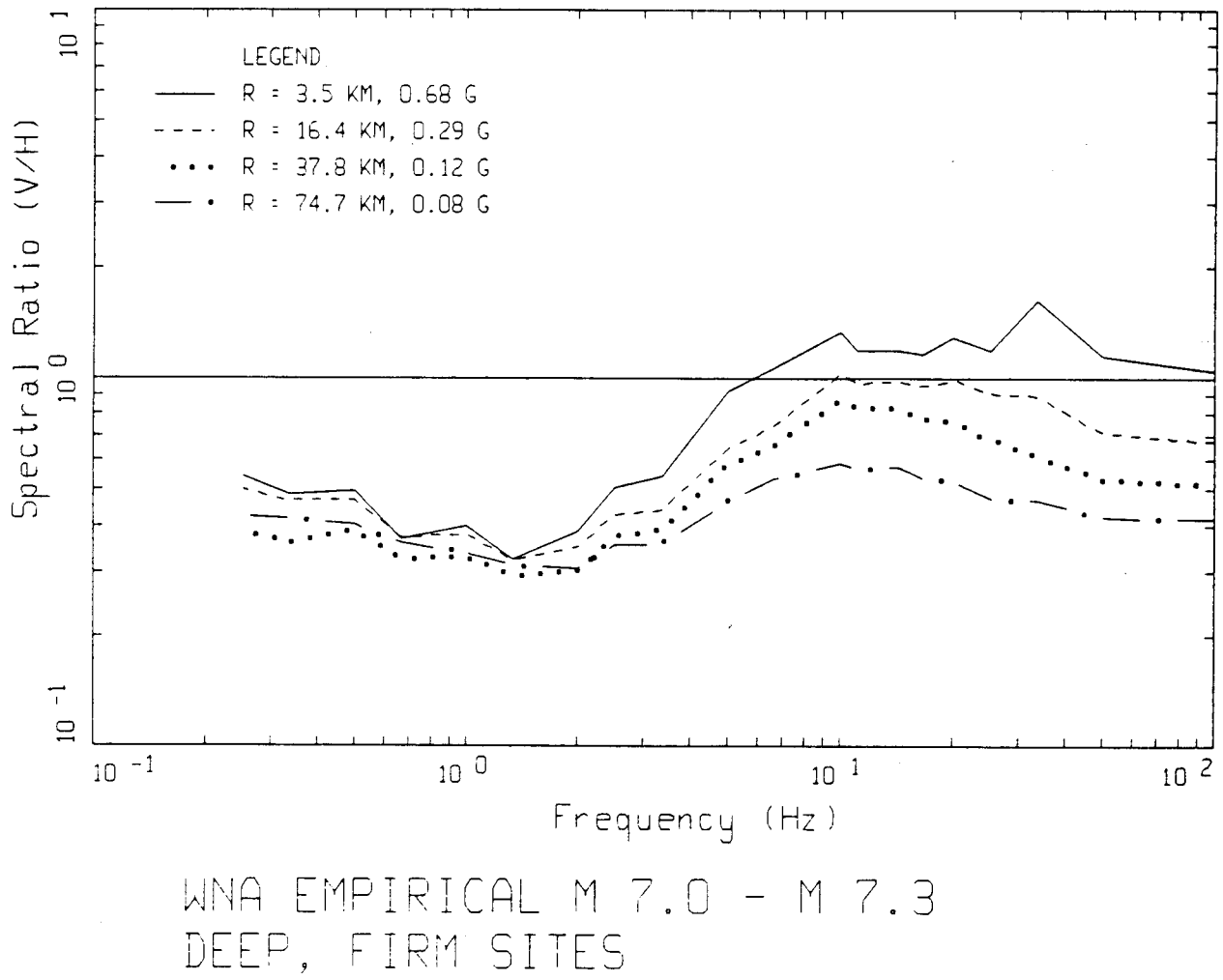

Figure 6-55. Empirical V/H ratios at deep soil sites for western North America earthquakes of magnitudes M 7.0–7.3. Peak acceleration values are for rock outcrop horizontal motions.

The deep soil empirical and analytical V/H ratios show very similar trends with frequency and with distance. The analytic ratios show exaggerated features because no averaging process has be done over profile compression and shear-wave velocities and damping, profile depth, depth of water table, Poisson's ratio, and modulus reduction and damping curves. Contributing to the difference at high frequency is the difference in energy content of the control motions. In view of these factors, the very simple model generally provides an accurate reflection of the trends seen in the empirical V/H ratios and may be used to suggest guidelines in estimating vertical component strong ground motions in applications to eastern rock and soil conditions.

6.6.6 Recommendations

Results of the modeling, although of a preliminary nature, indicate that V/H ratios for eastern sites are likely to be somewhat higher than V/H ratios for western United States under comparable site conditions, source sizes, and distances. The exception is at rock sites and at higher levels of motions where western empirical

V/H ratios show possible effects of nonlinear response resulting in large ratios at high frequency. Because of the hard rock conditions implied in the Midcontinent and Gulf Coast crustal models, similar trends are not expected to occur at these sites with the V/H ratios remaining less than one at large distance and near to slightly above one at close distances and at high frequencies.

The modeling at soil sites shows exaggerated features in the V/H ratios which are due primarily to purely deterministic analyses using only a single set of parameters as well as maintaining low (≈ 1%) compression-wave damping, even at very high levels of motion. The results do, however, suggest that large vertical component motions are possible at close distances for large magnitude sources, particularly for deeper profiles. As a result, it is not recommended that conventional approaches to specifying vertical component motions which are based largely on western empirical as well as analytical analyses be used. It is recommended rather that the following general guidelines be implemented recognizing that they are based on trends shown in the modeling results and do not represent the confidence inherent in empirical well calibrated and mature analytical results.

For rock sites in Eastern North America, the following recommendations are made:

1. For distances beyond 20 km, the V/H ratio should be 0.7,
2. For distances between 20 km and 10 km, the V/H ratio should be 0.7 up to 20 Hz and increase to 1.0 from 20 Hz to 30 Hz,
3. For distances within 10 km, the V/H ratio should be 1 up to 20 Hz and increase to 1.2 from 20 Hz to 30 Hz.

The recommended V/H ratios are shown diagrammatically in Figure 6-56[2] and are meant to apply from 1–34 Hz. For peak acceleration V/H ratios, a value of 0.8 is recommended for distances exceeding 10 km and 1.0 for closer distances. These values are based on the computed peak acceleration ratios listed in Table 6-8.

For applications to soil sites, the V/H ratios for each level of control motion were averaged over the five categories. The combination is justified on the basis of the preliminary nature of the model and simplifies the recommendations into two main categories: rock and soil. Figure 6-57 shows the V/H ratios for the combined categories at each control motion (horizontal component rock outcrop) level: 0.10, 0.30, 0.50, and 1.00g. Based on these soil V/H ratios, the following recommendations are made for the soil site V/H ratios in Eastern North America:

1. For control motions less than 0.10g, the V/H ratio should be 0.7,
2. For control motions between 0.10g, and less than 0.30g, the V/H ratio should be 0.7 up to 20 Hz and increase to 1.0 from 20 Hz to 30 Hz,
3. For control motions between 0.30g, and less than 0.50g, the V/H ratio should be 0.7 to 20 Hz and increase to 1.2 from 20 Hz to 30 Hz,
4. For control motions of 0.50g and greater, the V/H ratio should be 0.7 up to 10 Hz and increase to 1.5 from 10 Hz to 20 Hz.

The recommended V/H ratios for soil sites are shown in Figure 6-58[2]. As with the rock sites ratios, the frequency range of applicability is from 1 to 34 Hz.

For peak acceleration, based on Table 6-8, the following guidelines are offered. For control motions up to 0.30g, a value of 0.7 is recommended, above 0.30g and up to 0.50g the ratio should be increased to 0.8. At control motions of 0.5g and above a value of 1.2 is recommended.

It should be emphasized that these recommendations for V/H ratios are based on a single preliminary model which has not matured with applications by other individuals to a wide variety of cases. Also results of other models have not been incorporated into the recommendations. The guidelines are intended to reflect these uncertainties and still provide a reasonable basis for the specification of vertical component strong ground motions at both rock and soil sites on a generic basis in the central, eastern, and southeastern United States.

2. The figures show a logarithmic transition of levels for convenient comparison to other V/H plots. In practice either a logarithmic, semi-logarithmic, or linear transition may be implemented.

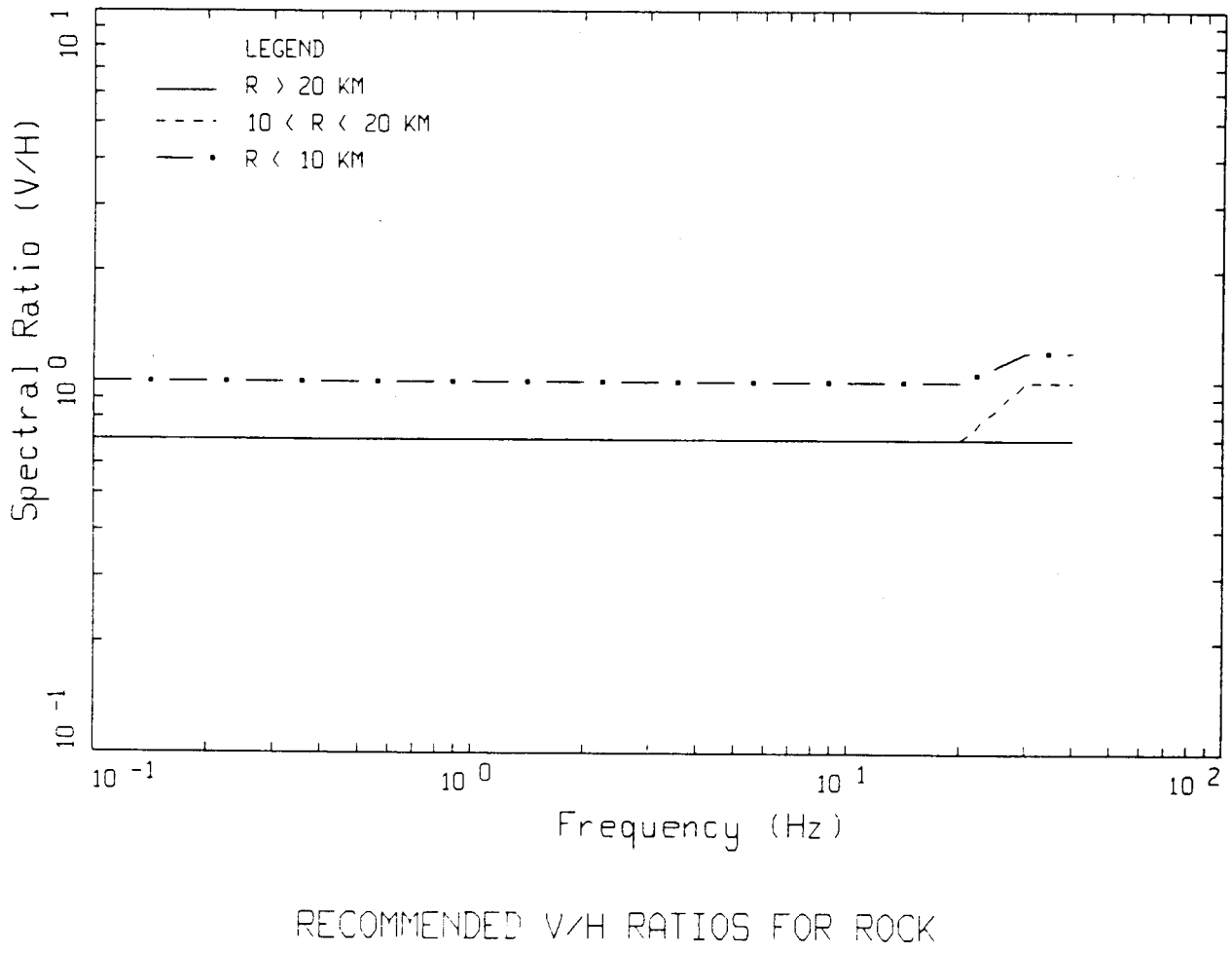

Figure 6-56. Recommended 5% damped V/H ratios for rock sites. Frequency range of application is from 1 Hz to 34 Hz.

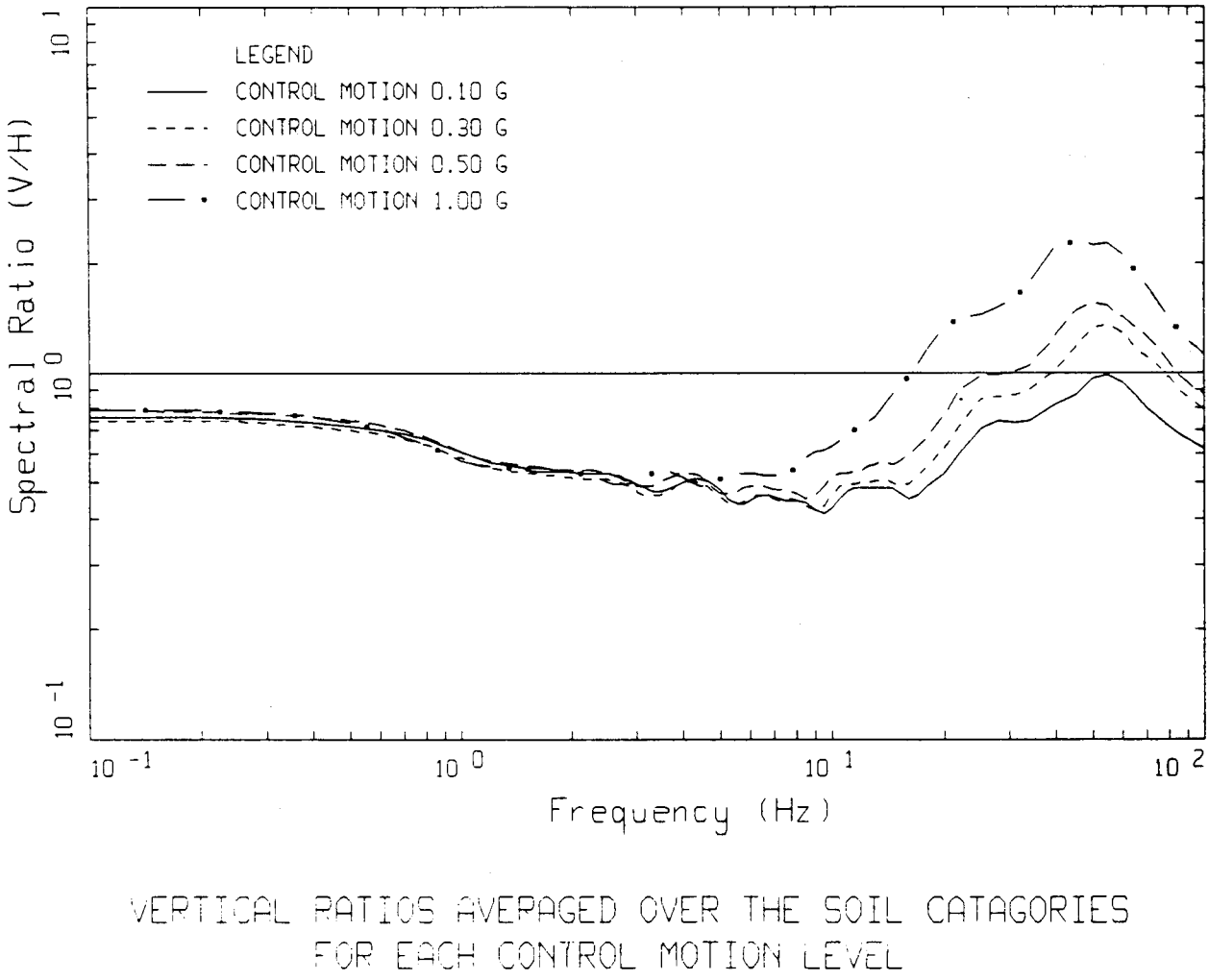

Figure 6-57. Log average V/H ratios for all five soil Categories (20 ft–500 ft).

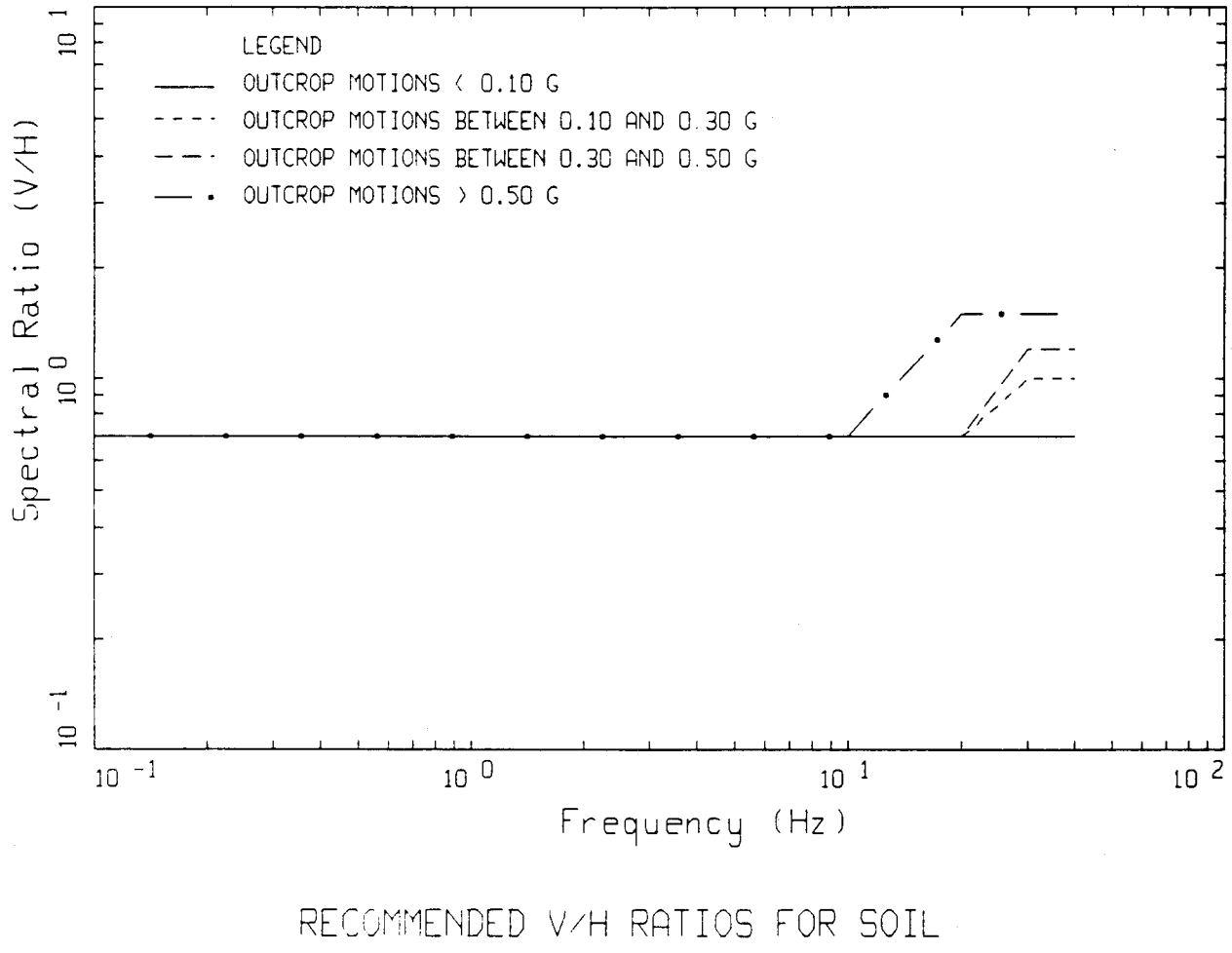

Figure 6-58. Recommended 5% damped V/H ratios for soil sites. Frequency range of application is from 1 Hz to 34 Hz.

References

Abrahamson, N.A. (1985). *Estimation of seismic wave coherency and rupture velocity using the Smart 1 strong-motion array recordings.* Earthquake Engin. Res. Center, Univ. of Calif. at Berkeley, UCB/EERC-85/02.

Aki, K. and P.G. Richards (1980). *Quantitative seismology theory and methods.* W.H. Freeman and Company, San Francisco. 1.

Anderson, J.G. (1991). A preliminary descriptive model for the distance dependence of the spectral decay parameter in southern California. *Bull. Seism. Soc. Am.*, 81(6):2186–2193.

Benites, R., W.J. Silva and B. Tucker (1985). Measurements of ground response to weak motion in La Molina Valley, Lima, Peru. Correlation with strong ground motion. Earthquake Notes, Eastern Section, *Bull. Seism. Soc. of Am.*, 55(1).

Bernreuter, D.L., J.B. Savy, R.W. Mensing, J.C. Chen and B.C. Davis (1985). *Seismic hazard characterization of the eastern United States.* Lawrence Livermore National Laboratory, UCID-20421, 1&2.

Berrill, J.B. (1977). Site effects during the San Fernando, California, earthquake. *Proceedings of the Sixth World Conf. on Earthquake Engin.*, India, 432–438.

Biot, M.A. (1965). *Mechanics of incremental deformations.* New York: John Wiley and Sons.

Boatwright, J. and M. Astrue (1983). Analysis of the aftershocks of the New Brunswick earthquake. Workshop on Site-Specific Effects of Soil and Rock on Ground Motion and the Implications for Earthquake-Resistant Design. USGS Open-File Rept. 83–245.

Boore, D.M. (1983). Stochastic simulation of high-frequency ground motions based on seismological models of the radiated spectra. *Bull. Seism. Soc. Am.*, 73:1865–1894.

Boore, D.M. and G.M. Atkinson (1987). Stochastic prediction of ground motion and spectral response parameters at hard-rock sites in Eastern North America. *Bull. Seism. Soc. Am.*, 77(2):440–467.

Boore, D.M. and G.M. Atkinson (1992). Source spectra for the 1988 Saguenay, Quebec, earthquakes. *Bull. Seism. Soc. Am.*, 82(2):683–719.

Boore, D.M. and W.B. Joyner (1991). Estimation of ground motion at deep-soil sites in Eastern North America. *Bull. Seism. Soc. Am.*, 81(6):2167–2185.

Borcherdt, R.D. (1971). *Inhomogeneous body and surface plane waves in a generalized viscoelastic half-space.* Ph.D. Dissertation, Univ. of Calif. at Berkeley.

Borcherdt, R.D. and J.F. Gibbs (1976). Effects of local geologic conditions in the San Francisco Bay region on ground motions and the intensities of the 1906 earthquake. *Bull. Seism. Soc. Am.*, 66:467–500.

Campbell, K.W. (1981). Near-source attenuation of peak horizontal acceleration. *Bull. Seism. Soc. Am.*, 71(6): 2039–2070.

Campbell, K.W. (1985). *Strong motion attenuation relations: a ten-year perspective.* Earthquake Spectra, 1:759–804.

Campbell, K.W. (1988). *Predicting strong ground motion in Utah.* Evaluation of Regional and Urban Earthquake Hazards and Risk in Utah, edited by W.W. Hays and P.L. Gori, USGS Prof. Paper.

Chang, N.Y., M.J. Huang, B.H. Lien and F.K. Chang (1986). EQGEN: a user-friendly artificial earthquake simulation program. *Proceedings of the Third U.S. Natl. Conf. on Earthquake Engin.*, Charleston, South Carolina, 1:439–450.

Chang, T.S., P.S. Tang, C.S. Lee and H. Hwang (1990). Evaluation of liquefaction potential in Memphis and Shelby County. Nat'l Center for Earthquake Engin. Res., NCEER-90-0018.

Costantino, C.J. (1967). Finite element approach to wave propagation problems. *J. Engin. Mechanics Div.*, 93.

Costantino, C.J. (1969). Two dimensional wave propagation through nonlinear media. *J. Computational Physics*, 4.

Cranswick, E., R. Wetmiller and J. Boatwright (1985). High-frequency observations and source parameters of microearthquakes recorded at hard-rock sites. *Bull. Seism. Soc. Am.*, 75(6):1535–1567.

Day, S.M. (1979). Three-dimensional finite difference simulation of fault dynamics. Systems, Science and Software final report sponsored by the National Aeronautics and Space Administration. SSS-R-80-4295.

Dobry, R. (1991). Low and high-strain cyclic material properties. Chapter 3 in Proceedings: NSF/EPRI Workshop on Dynamic Soil Properties and Site Characterization. Palo Alto, Calif.: Electric Power Research Institute, NP-7337.

Drnevich, V.P., J.R. Hall Jr. and F.E. Richart Jr. (1966). *Large amplitude vibration effects on the shear modulus of sand.* University of Michigan Report to Waterways Experiment Station, Corps of Engineers, U.S. Armay, Contract DA-22-079-eng-340.

Drnevich, V.P., J.R. Hall Jr. and F.E. Richart Jr. (1967). Effects of amplitude of vibration on the shear modulus of sand. *Proceedings of the Intl. Symp. on Wave Prop. and Dyn. Properties of Earth Matls.*, Univ. of New Mexico, Albuquerque, New Mexico.

Duke, C.M. and Leeds (1962). Site characteristics of southern California strong motion earthquake stations, Part I. Univ. of Calif. Los Angeles, Dept. of Eng., Rept. 62–55.

Duke, C.M. and A.K. Mal (1978). Site and source effects on earthquake ground motion. Univ. of Calif. Los Angeles, Dept. of Engin. Rept. 7890.

Faccioli, E.E., V. Santayo and J.L. Leone (1973). Microzonation criteria and seismic response studies for the city of Managua. *Proceedings of the Earthquake Engin. Res. Dist. Conf. Managua*, Nicaragua, Earthquake of December 23, 1972, 1:271–291.

Finn, W.D.L., K.W. Lee and G.R. Martin (1975). Stress-strain relations for sand in simple shear. ASCE Nat'l Convention, Denver, Colorado, Meeting Preprint 2517. Also in Soil Mechanics Series No. 26, Dept. of Civil Engineering, University of British Columbia, Vancouver, B.C.

Gibbs, J.F., D.M. Boore, W.B. Joyner and T.E. Fumal (1992). The attenuation of seismic shear waves in quaternary alluvium in Santa Clara Valley, California. Submitted to Bull. Seism. Soc. Am.

Gilbert, F. and G.E. Backus (1966). Propagator matrices in elastic wave and vibration problems. *Geophysics.*, 31:326–332.

Gutenberg, B. (1927). *Grundlagen der erdlebenkunde.* Berlin.

Gutenberg, B. (1957). Effects of ground on earthquake motion. *Bull. Seism. Soc. Am.*, 47: 221–250.

Hardin, B.O. and V.P. Drnevich (1972). Shear modulus and damping in soils: design equations and curves. *J. of the Soil Mech. and Found. Div.*, ASCE, 98(GT7):667–692.

Harkrider, D.G. (1981). *Coupling near source phenomena into surface wave generation.* Identification of Seismic Sources—Earthquake or Underground Explosion, E.S. Huseby and S. Mykkeltveir, eds., D. Reidel Publ. Co., Boston, 277–326.

Harr, L.C., J.B. Fletcher and C.S. Mueller (1984). The 1982 Enola, Arkansas, swarm and scaling of ground motion in the eastern United States. *Bull. Seism. Soc. Am.*, 74:2463–2482.

Haskell, N.A. (1960). Crustal reflection of plane SH waves. *J. Geophys. Res.*, 65:4147–4150.

Hayashi, S., H. Tsuchida and E. Kurata (1971). Average response spectra for various subsoil conditions. *Third Joint Meeting, US-Japan Panel on Wind and Seismic Effects*, UJNR, Tokyo.

Hays, W.W., A.M. Rogers and K.W. King (1979). Empirical data about local ground response. *Proceedings of the Second U.S. Nat. Conf. on Earthquake Engin.*, Earthquake Engin. Res. Inst., 223–232.

Idriss, I.M. (1985). Evaluating seismic risk in engineering practice. *Proceedings of the Eleventh Int. Conf. on Soil Mech. and Foundation Engin.*, San Francisco, A.A. Balkema, Rotterdam, ed., 1:255–320.

Idriss, I.M. (1990). Response of soft soil sites during earthquakes. Presented at a Memorial Symposium to Honor Prof. Harry Seed, Univ. of Calif. at Berkeley.

Idriss, I.M. (1991). Earthquake ground motions at soft soil sites. *Proceedings: 2nd Int'l Conf. on Recent Adv. in Geotech. Earthquake Engin. and Soil Dyn.*, St. Louis, Missouri, Invited Paper LP01, 2265–2272.

Idriss, I.M. and H.B. Seed (1968). *Seismic response of horizontal soil layers*, J. Soil Mech. Foundations Div., ASCE, 94(SM4):1003–1031.

Ishii, H. and R.M. Ellis (1970). Multiple reflection of plane P and SV waves by a dipping layer. *Geophys. J.*, 20:11–30.

Iwan, W.D. (1967). On a class of models for the yielding behavior of continuous and composite systems. *J. Appl. Mech.*, 34:612–617.

Jarpe, S.P., Cramer, C.H., Tucker, B.E. and Shakal, A.F. (1988). A comparison of observations of ground response to weak and strong ground motion at Coalinga, California. *Bull. Seism. Soc. Am.*, 78(2):421–435.

Johnson, L.R. and W. Silva (1981). The effects of unconsolidated sediments upon the ground motion during local earthquakes. *Bull. Seism. Soc. Am.*, 71:127–142.

Joyner, W.B. and D.M. Boore (1982). Prediction of earthquake response spectra. *Proceedings of the 51st Annual Conv., Structural Engin. Assoc. of Calif.*, also USGS Open-File Rept. 82–977.

Joyner, W.B. and A.T.F. Chen (1975). Calculation of nonlinear ground response in earthquakes. *Bull. Seism. Soc. Am.*, 65:1315–1336.

Joyner, W.B. and T.E. Fumal (1984). Use of measured shear-wave velocity for predicting geologic site effects on strong ground motion. *Proceedings of the Eighth World Conf. on Earthquake Engin.*, San Francisco, 2:777–783.

Joyner, W.B., R.E. Warrick and T.E. Fumal (1981). The effect of quaternary alluvium of strong ground motion in the Coyote Lake, California Earthquake of 1979. *Bull. Seism. Soc. Am.*, 71(4):1333–1349.

Joyner, W.B., R.E. Warrick and A.A. Oliver III (1976). Analysis of seismograms from a downhole array in sediments near San Francisco Bay. *Bull. Seism. Soc. Am.*, 66: 937–958.

Kanai (1950). Effect of solid viscosity of surface layer on earthquake motions and the nature of surface layer. *Bull. Earth. Res. Inst.*, 20.

Kanai, Suzuki and Yoshizawa. (1959). Comparative studies of earthquake motions on the ground and underground (multiple reflection problem). *Bull. Earth. Res. Inst.*, 34: 53–88.

King, J.L. and B.E. Tucker (1982). Analysis of differential array data from El Centro, U.S.A and Garm, U.S.S.R. *3rd Int'l Confer. on Microzonation*, Seattle, Washington.

Knopoff, L. (1964). A matrix method for elastic wave problems. *Bull. Seism. Soc. Am.*, 54:431–438.

Kurita, T. (1973). A procedure for elucidating fine structure of the crust and upper mantle from seismological data. *Bull. Seism. Soc. Am.*, 63:189–209.

Leblanc, G.S.J. (1967). Truncated crustal transfer functions and fine crustal determination. *Bull. Seism. Soc. Am.*, 57:719–733.

Li, S.X., Z.L. Wang, C.K. Shen (1992). *SUMDES: A nonlinear procedure for response analysis of horizontally-layered sites subjected to multi-directional earthquake loading*. Dept. of Civil Engin. Univ. of Calif. Davis.

Lysmer, J. and R.L. Kuhlemeyer (1975). Finite dynamic model for infinite media. *J. Engin. Mech. Div.*, ASCE, 95(EM4):859–877.

Mallet, R. (1862). *Great Neopolitan earthquake of 1857*, London. 1 and 2.

Martin, P.P. (1975). *Non-linear methods for dynamic analysis of ground response*. Ph.D. Thesis, Univ. of Calif. at Berkeley.

Milne, J. (1908). *Seismology*. London, 2nd edition.

Mohraz, B. (1976). A study of earthquake response spectra for different geological conditions. *Bull. Seism. Soc. Am.*, 66(3):915-935.

Moriwaki, Y. and E.H. Doyle (1978). Site effects on microzonation in offshore areas. *Proceedings of the 2nd Int'l Conf. on Microzonation*, San Francisco, 3:1433–1441.

Murnaghan, F.D. (1937). Finite deformations of an elastic solid. *Am. J. Mathematics*, 59.

Murphy, J.R., A.H. Davis and N.L. Weaver (1971). Amplification of seismic body waves by low-velocity surface layers. *Bull. Seism. Soc. Am.*, 61:109–145.

Murphy, J.R. and J.A. Laboud (1969). Analysis of seismic peak amplitudes from underground nuclear detonations. *Bull. Seism. Soc. Am.*, 59:2325–2342.

Phinney, R.A. (1964). Structure of the earth's crust from spectral behavior of long period waves. *J. Geophys. Res.*, 69:2997–3017.

Pyke, R.M. (1979). Nonlinear models for irregular cyclic loadings. *J. Geotech. Engin. Div.*, ASCE, 105(GT6), 715–726. Discussion and Closure, 106(GT11):1277–1281.

Randall, M.J. (1967). Fast programs for layered half-space problems. *Bull. Seism. Soc. Am.*, 57:1299–1315.

Reid, H.F. (1910). The California earthquake of April 18, 1906. *The Mechanics of the Earthquake*, Carnegie Inst. of Washington, Publ. 87, 21.

Richart, F.E. (1975). Some effects of dynamic soil properties on soil-structure interaction. *J. of the Geotech. Engin. Div.*, ASCE, 101(GT12):1197–1240.

Rogers, A.M., R.D. Borcherdt, P.A. Covington and D.M. Perkins (1984). A comparative ground response study near Los Angeles using recordings of Nevada nuclear tests and the 1971 San Fernando earthquake. *Bull. Seism. Soc. Am.*, 74:1925–1949.

Rogers, A.M., J.C. Tinsley and W.W. Hays. (1983). The issues surrounding the effects of geologic conditions on the intensity of ground shaking. USGS Open File Report 83–845.

Rogers, A.M, J.C. Tinsley, W.W. Hays and K.W. King (1974). Evaluations of the relation between near-surface geological units and ground response in the vicinity of Long Beach, California. *Bull. Seism. Soc. Am.*, 69:1603–1622.

Schnabel, P.B., J. Lysmer and H.B. Seed (1972). *SHAKE: A computer program for earthquake response analysis of horizontally layered sites.* Earthquake Engin. Res. Center, Univ. of Calif. at Berkeley, UBC/EERC 72-12.

Seed, H.B. and I.M. Idriss (1969). The influence of soil conditions on ground motions during earthquakes. *J. Soil Mech. Found. Engin. Div.*, ASCE, 94:93–137.

Seed, H.B. and I.M. Idriss (1970). *Soil moduli and damping factors for dynamic response analyses.* Earthquake Engin. Res. Center, Univ. of Calif. at Berkeley, UBC/EERC 70-10.

Seed, H.B., C. Ugas and J. Lysmer (1976). Site-dependent spectra for earthquake-resistant design. *Bull. Seism. Soc. Am.*, 66:221–243.

Seed, H.B., R.T. Wong, I.M. Idriss and K. Tokimatsu (1984). *Moduli and dynamic factors for dynamic analyses of cohesionless soils.* Earthquake Engin. Res. Center, Univ. of Calif. at Berkeley, UBC/EERC-84/14.

Sezawa and Kanai. (1932). Possibility of free oscillations of strata excited by seismic waves. *Bull. Earthq. Res. Inst.*, 10:273.

Shima, E. (1962). Modifications of seismic waves in superficial soil layers as verified by comparative observations on and beneath the surface. *Bull. Earth. Res. Inst.*, Tokyo University, 40:187–259.

Silva, W.J. (1976). Body waves in a layered anelastic solid. *Bull. Seis. Soc. Am.*, 66(5):1539–1554.

Silva, W.J. (1991). Site geometry and global characteristics. Chapter 6 in *Proceedings: NSF/EPRI Workshop on Dynamic Soil Properties and Site Characterization.* Palo Alto, Calif: Electric Power Research Institute, NP 7337.

Silva, W.J. and N.A. Abrahamson (1992). Quantification of long period strong ground motion attenuation for engineering design. CDMG draft report.

Silva, W.J. and R. Darragh (1993). *Engineering characterization of earthquake strong ground motion recorded at rock sites.* Palo Alto, Calif: Electric Power Research Institute, TR-102262.

Silva, W.J., R.B. Darragh, R.K. Green and F.T. Turcotte (1989). Estimated ground motions for a new Madrid event. U.S. Army Engineer Waterways Experiment Station, Wash., DC, Misc. Paper GL-89-17.

Silva, W.J. and R.K. Green (1989). Magnitude and distance scaling of response spectral shapes for rock sites with applications to North American tectonic environment. *Earthquake Spectra,* 5(3):591–624.

Silva, W.J. and K. Lee (1987). WES RASCAL code for synthesizing earthquake ground motions. State-of-the-Art for Assessing Earthquake Hazards in the United States, Report 24, U.S. Army Engineers Waterways Experiment Station, Miscellaneous Paper S-73-1, 120 p.

Silva, W.J. and C.L. Stark (1992). Source, path, and site ground motion model for the 1989 M 6.9 Loma Prieta earthquake. CDMG draft final report.

Silva, W.J., T. Turcotte and Y. Moriwaki (1988). *Soil response to earthquake ground motion.* Palo Alto, Calif: Electric Power Research Institute, RP-2556-07.

Silver, M.L. and H.B. Seed (1971). Deformation characteristics of sands under cyclic loading. *J. Soil Mech. Foundations Div.,* ASCE, 97(SM8):1081–1098.

Streeter, V.L., E.B. Wylie and F.E. Richart Jr. (1974). Soil motion computations by characteristics methods. *J. Geotech. Engi. Div.,* ASCE, 100(GT3):247–263.

Su, F., K. Aki, T. Teng, Y. Zeng, S. Koyanagi and K. Mayeda (1992). The relation between site amplification factor and surficial geology in central California. *Bull. Seism. Soc. Am.,* 82(2):580–602.

Tanaka, T., S. Yoshizawa, T. Morishita, K. Osaka and Y. Osawa (1973). Observation and analysis of underground earthquake motions. *Proceedings of the 5th World Conf. on Earthquake Engin.,* Rome, Italy, 1:658–667.

Taylor, P.W. and T.J. Larkin (1978). Seismic site response of nonlinear soil media. *J. Geotech. Engin. Div.,* ASCE, 104(GT3).

Thomson, W.T. (1950). Transmission of elastic waves through a stratified solid medium. *J. Applied Physics.,* 21.

Tokimatsu, K. and S. Midorikawa (1981). Nonlinear soil properties estimated from strong motion accelerograms. Int'l Conf. on Recent Adv. in Geotech. Earthquake Engin. and Soil Dyn., Rolla, Missouri.

Toro, G.R. and R.K. McGuire (1987). An investigation into earthquake ground motion characteristics in Eastern North America. *Bull. Seism. Soc. Am.,* 77:468–489.

Toro, G.R., W.J. Silva, R.K. McGuire and R.B. Herrmann (1992). Probabilistic seismic hazard mapping of the Mississippi Embayment. *Seism. Res. Letters,* 63(3):449–475.

Tucker, B.E. and J.L. King (1984). Dependence of sediment-filled valley response on the input amplitude and the valley properties. *Bull. Seism. Soc. Am.,* (74):153–165.

Tucker, B.E. and J.L. King, D. Hatzfeld and I.L. Nersesov (1984). Observations of hard-rock site effects. *Bull. Seism. Soc. Am.,* 74:121–136.

United States Geological Survey (1986). *Preliminary report on aftershock sequence for earthquake of January 31, 1986 near Painesville, Ohio.* Sponsored by Electric Power Research Institute, R.D. Borcherdt, ed., USGS Open-File Report 86-181.

Valera, J.E., E. Berger, H.-S. Kim, J.E. Reaugh, R.D. Golden and R. Hofmann (1978). *Study of nonlinear effects on one-dimensional earthquake response.* Palo Alto, Calif.: Electric Power Research Institute, NP-865.

Wald, D.J., D.V. Helmberger and T.R. Heaton (1991). Rupture model of the 1989 Loma Prieta earthquake from the inversion of strong motion and broadband teleseismic data. *Bull. Seism. Soc. Am.*, 81(5):1540–1572.

Wesson, R.L. and C. Nicholson (1986). Studies of the January 31, 1986 northeastern Ohio earthquake. USGS Open-File Rept. 86 331.

Wiggins, J.H. (1964). Effects of site conditions on earthquake intensity. *J. Structural Div.*, ASCE 90(2), Part I.

Wood, H.O. (1908). Distribution of apparent intensity in San Francisco, in the California earthquake of April 18, 1906. *Report of the State Earthquake Investigation Commission*, Wash., D.C.: Carnegie Institute, 1:220–245.

Woods, R.D. (1968). Screening of surface waves in soils. *J. Soil Mech. and Found., Div. ASCE*, 94(SM4):951–979.

Yamamoto, T. (1983). Propagation matrix for continously layered porous seabeds. *Bull. Seism. Soc. Am.*, 73:1599–1620.

7

GUIDELINES FOR THE CONDUCT OF SITE INVESTIGATIONS AND SITE RESPONSE ANALYSES

7.1 Introduction

This section contains guidelines for the conduct of site investigations, including in situ and laboratory measurement of dynamic properties, and the conduct of site response analyses. These guidelines are only intended to cover those aspects of site investigations and in situ and laboratory measurement of dynamic properties that are necessary for conducting site response analyses for determining free-field design ground motions. They do not cover properties that may be needed for the evaluation of site stability, including the potential for liquefaction, or the design of foundations and structures including the effects of soil-structure interaction where appropriate. However, much of the discussion will have more general application, particularly with regard to the determination of the dynamic properties of soils for use in soil-structure interaction analyses.

The requirements for site investigations for various levels of screening or site selection studies and final site specific studies clearly vary. These guidelines are directed to final site specific studies but it is recommended that a phased approach be followed and it may well be that the first of the two phases recommended for a site-specific study is also appropriate for use in site selection studies or for checking that the response of a specific site falls within the standard plant design parameters.

These guidelines are deliberately general in nature and lack specific detail on many points because: (1) these details will vary depending on the actual site conditions; (2) the level of detail required may vary with the type of analyses that are to be conducted and the results that are obtained; and (3) practice on some key issues is still evolving.

Because of this, there are human factors which must be considered in the conduct of these and similar studies which may turn out to be more important than the adherence to specific technical guidelines. In particular it is essential to have personnel involved on a daily basis who have relevant previous experience and a demonstrated ability to learn from that experience. It is also necessary to have personnel involved who are able to identify and evaluate current research activity in order to evaluate the practicality of using techniques which are still under research and development in a project environment. These questions cannot be covered simply by having well qualified personnel on a review panel. If reliance is to be placed on the expertise of personnel outside the project team, such personnel must be involved as "working consultants" rather than "review consultants".

Much relevant guidance on site investigations and laboratory measurement of soil properties is given in the following U.S. Nuclear Regulatory Commission guides:

Regulatory Guide 1.132 Site Investigations for Nuclear Power Plants (September 1977);

Regulatory Guide 1.138 Laboratory Investigations of Soils for Engineering Analysis and Design of Nuclear Power Plants (April 1978).

However, these guides are now a little dated and do not adequately cover the interrelationship of field and laboratory measurement of properties and their use in analyses including appropriate treatment of uncertainties.

An explanation of terminology, a summary of present (1992) knowledge and an extensive reference list on

dynamic soil properties are provided in Appendix 7.A; descriptions of field and laboratory measurement techniques used in this study and some significant advances that have been made, especially with respect to measurements of damping, are given in Section 8, Appendix 8.A and Appendix 8.B; and descriptions and examples of current methods of site response analyses are given in Appendix 6.B. These guidelines should be read in conjunction with these and any subsequent reviews.

7.2 Required Data, Measurement Techniques, and Uncertainties

Equivalent linear analyses of site response require estimates of the shear modulus at small strains, G_{max}, or the shear wave velocity, V_s, and modulus reduction and damping curves for each layer used in the analysis. This is also the minimum information needed to construct a nonlinear model. Additional information may be required for nonlinear models which follow rate of loading and cyclic loading effects in greater detail. For screening and preliminary site specific studies it may be adequate to estimate G_{max} or V_s profiles and to use standard modulus reduction and damping curves of the kind that are presented in Section 7.A.6. Several empirical expressions are available for G_{max} as discussed in Section 7.A.5 and empirical correlations between V_s and various other soil properties are also available but such correlations should be used with great caution since V_s can be affected very significantly by factors such as age and stress history which are not reflected in simple measures or indexes of soil properties.

For final site-specific studies it is imperative that both G_{max} and the modulus reduction and damping curves be measured for the actual soils at the site if uncertainties in these quantities are to be minimized. Three general approaches are available:

7.2.1 In Situ Measurements

While there are obvious advantages to making all measurements of properties in situ, the only parameters that can reliably be measured in the field at present (1992) are the shear wave velocity, V_s, and the compression wave velocity, V_p. While very significant advances have been made in measuring low strain damping in situ in recent years, and in this project as reported in Appendix 8.A, standardized measurement and data reduction techniques have not yet emerged. Techniques to measure shear modulus and damping at larger strains in the field have been suggested from time to time but no viable techniques are yet available. Presently available techniques for measuring velocities in situ include:

7.2.1.1 SASW

Spectral analysis of surface waves—an approach used at shallow depths, particularly in soils in which it is difficult to drill and sample.

7.2.1.2 Crosshole

Requires at least two, preferably three or four, closely spaced borings—likely provides the most accurate and repeatable measurements and allows measurement of shear wave anisotropy which may aid in interpretation of lateral stresses—requires accurate measurement of borehole diameter and drift and in practice usually limited to depths of several hundred feet—covered in part by ASTM Standard D4428.

7.2.1.3 Downhole

Can be conducted in a single boring although measurement of borehole diameter and drift is still desirable—can provide very accurate measurements but more susceptible to measurement and interpretation errors than the crosshole technique—problems resulting from deviation of ray path from the direct source-to-receiver path could be minimized by using two or more downhole receivers—effective depth limited by use of surface sources but use of downhole sources could make technique viable to greater depths.

7.2.1.4 Seismic Cone

Similar in principle to downhole—very fast but usually limited to depths of about 100 feet by capacity of thrusting system and rods.

7.2.1.5 Suspension Logger

Desirably run in uncased borehole which limits demonstration of repeatability but results compare favorably with good crosshole and downhole measurements—samples small volumes of soil at high frequencies and shows more local variability than other techniques—can be used at depths up to 1000 feet.

The field investigations of reference sites reported in Section 8 and Appendices 8.A have indicated that generally similar results can be obtained using each of these techniques but that they all have some limitations. Thus it is desirable to use a minimum of two different

measurement techniques on critical sites so that they can serve as a cross check on each other and on the occurrence of gross errors. Most of the above techniques also allow the possibility of measuring low-strain damping in situ and the results obtained in this study and other recent work in this field should be evaluated in order to maximize the possibility of obtaining usable data on damping in conjunction with the measurement of velocities. It should be noted, however, that differing estimates of damping may be obtained from downhole and crosshole tests because of scattering, reflection and transmission effects, and that the effect of the frequency of excitation may need to be taken into account in comparing different field methods as well as in comparing field and laboratory measurements.

7.2.2 Laboratory Measurements

A variety of laboratory tests are available for measuring both G_{max} and the modulus reduction and damping curves at larger strains. In earlier work the strain ranges over which most test equipment could operate reliably was limited and different tests would be used to measure G_{max} and to obtain modulus reduction and damping curves. This has led on some occasions to obvious inconsistencies, but better quality work usually shows relatively good agreement between the results of different types of laboratory tests and newer equipment, which is generally capable of operating over wider strain ranges, minimizes this problem.

The most common laboratory tests are:

7.2.2.1 Resonant Column

Usually applied in torsion on solid cylinders but can be used for longitudinal excitation also—usually limited to small strains but can develop intermediate strain levels using softer or smaller diameter test specimens—typically resonance is obtained at frequencies in the order of 100 Hz and the possible effects of frequency and the many repetitions of loading to which the sample is subjected should be taken into account in interpreting the results obtained—measured values of damping may be erroneously high unless correction is made for back-emf effects—covered in part by ASTM Standard D4015.

7.2.2.2 Cyclic Triaxial

Involves axial loading of solid cylinders—shear modulus and damping are not measured directly but are interpreted from Youngs modulus and damping—traditionally used at larger strains but can be extended to smaller strains with special equipment and instrumentation—errors commonly result from poor seating of test specimens but these errors can be minimized by use of seating compounds and/or on-sample measurement of strains—covered in part by ASTM Standard D3999.

7.2.2.3 Cyclic Simple Shear

Loading conditions more closely approximate those in the field but it is more difficult to set up undisturbed samples—again used more at larger strains but can be extended to smaller strains with special equipment and instrumentation.

7.2.2.4 Cyclic Torsional Shear

Can be conducted using solid or hollow cylinders—hollow cylinders give greatest control over the stress state but make testing of undisturbed samples very difficult—perhaps the easiest configuration for testing over a very wide strain range.

Again, no single test is free of limitations and it is desirable to test the same soil in two or more kinds of apparatus as a cross-check. While it is traditional to present the results of these tests just as values of G_{max} and modulus reduction and damping curves, the stress-strain curves should also be recorded and presented even when the intent is to conduct only equivalent linear analyses since the stress-strain loops can provide important clues regarding the validity of the data. When nonlinear analyses are to be run it is even more critical to record and present the stress-strain loops and to track the development of any excess pore pressures.

7.2.3 Backcalculation from Observations of Ground Motion

An important third source of data on dynamic properties is provided by backcalculation from observations of ground motions at vertical arrays or close by soil/rock station pairs. This technique will not usually be practical as part of a specific site investigation unless the site is located in a highly seismic area, however, estimates of both the G_{max} profile and the modulus reduction and damping curves that can be obtained by backcalculation can provide important insight into the uncertainty associated with various field and laboratory measurement techniques if detailed investigations are performed at the same site. In non-seismic areas it is not possible to obtain data on the strain dependence of

dynamic properties but observation of microtremors in vertical arrays may provide a cross-check on other measurements of the G_{max} or V_s profile.

7.2.4 Sources of Uncertainty

While it is very easy to make both random and systematic gross errors in both field and laboratory measurements, these can be minimized by: (1) Using properly trained and experienced personnel; (2) Following appropriate quality assurance procedures; and (3) Always using two or more different procedures to obtain key measurements. However, there are additional sources of uncertainty which from a practical point of view often cannot be eliminated. It is of the greatest importance that the engineers involved in both the measurement of properties and their use in analyses understand the sources of these uncertainties so that they can work towards minimizing them and, where they cannot be reduced to the level at which they are no longer significant, accounting for them in conducting and interpreting the results of the analyses. These sources of uncertainty include:

7.2.4.1 Inherent Variability of Soil Deposits

When soil profiles are divided by geologists or engineers into layers that might be assigned short descriptions such as silty clay or gravelly sand, the soils within these layers are rarely homogeneous. This can be readily seen if the grain size curves or the Atterberg limits for a number of samples from one layer are plotted together.

Also changes of soil type can often be seen within the length of a sample that has been taken from within a broadly defined layer that might otherwise be assumed to be homogeneous. This is especially true if borings have been logged principally from cuttings. Ideally, small diameter continuous borings and/or cone soundings should be made prior to drilling larger diameter borings to obtain samples for more sophisticated laboratory tests, both to quantify the variability of the deposit and to optimize locations for sampling.

As a general rule, finer grained soils that have been deposited in a low-energy environment will be more uniform than coarser grained soils deposited in high-energy environments. Residual soils and other soils with variable cementation may also show high variability even though cuttings and samples appear to be uniform. Thus an understanding of the regional and site geology and depositional history is important to planning and executing studies of soil properties.

7.2.4.2 Inherent Anisotropy

Even soils which are apparently homogeneous usually exhibit at least some degree of inherent anisotropy as a result of the impact of their method of deposition and subsequent stress history on the soil fabric. Commonly, but not always, this leads to the strength and stiffness being lower for shearing on horizontal planes as opposed to vertical planes. Inherent anisotropy is one of the contributors to shear wave velocity varying with direction and to differences in behavior in different types of laboratory tests.

7.2.4.3 Anisotropic In Situ Stresses

Additional anisotropy of in situ soil properties can result from an anisotropic state of stress being superimposed on inherent anisotropy. Virtually all soils are subjected to an anisotropic state of stress in the field, with the lateral effective stress being about half the vertical effective stress for normally consolidated soils, but increasing with the degree of overconsolidation. Because the shear wave velocity is a function of the effective stresses only in the direction of wave propagation and the direction of particle motion, that is, the plane of polarization, but not in the third direction measured shear wave velocities may vary with the direction and polarity of the waves that are generated.

7.2.4.4 Drilling and Sampling Disturbance

While it is obvious that samples may suffer from disturbance as a result of poor drilling, sampling and sample handling practices, it is not so widely recognized that some disturbance is inevitable as a result of release of the in situ stresses. This problem becomes more severe with increasing depth, and even if it is possible to establish the in situ state of stress and replicate this state of stress in the laboratory, it may not be possible to eliminate the effects of unloading and reloading the sample. It is well established that the shear modulus tends to increase and the damping decrease with the time that samples are consolidated under sustained pressure in the laboratory and it has sometimes been suggested that extrapolation of laboratory results to the geologic age of the soil provides the best estimate of the in situ behavior, but this procedure does not necessarily compensate correctly for

the differences in the stress states in the field and in the laboratory and for the stress path followed in the sampling and reconsolidation process.

7.2.4.5 Limitations of Laboratory Equipment

No laboratory equipment is capable of fully representing the in situ stress state and deformation conditions including the three-dimensional nature of earthquake ground motion. Thus, all laboratory testing devices represent a compromise of one kind or another and it should not be surprising that there are some differences between results of cyclic loading tests performed in different kinds of apparatus.

7.2.5 Interpretation of Measured Values

It should be apparent from the foregoing discussion that no data, be it acquired in the field or the laboratory, should automatically be used in analyses without some thought being given to the necessity for integrating it with data from other sources and making judgements as to the most appropriate values for use in analyses. Nonetheless, substantial progress has been made in the care with which both field and laboratory tests are conducted so that it is now generally possible to obtain reasonable agreement between the values of V_s or G_{max} measured in the laboratory and the field. Indeed, this is a basic check that should always be made to confirm that the samples as reconsolidated and tested in the laboratory are representative of field conditions. While measurement of low strain damping in situ remains a difficult task, encouraging progress has been made on that subject in the course of this study, and it is generally desirable that field and laboratory measurements of low strain damping also be compared.

7.3 Sequencing of Work

While it has been customary to: (1) conduct a field investigation; (2) conduct laboratory tests; and (3) conduct analyses, these elements must not be treated as independent work items but must be integrated with each other.

A generally appropriate program is:

7.3.1 Review Regional and Site Geology

This should include a detailed review of available literature, a review of aerial photographs and other remote-sensing imagery and may include trenching and mapping. Particular emphasis should be placed on establishing the depositional history of the site.

7.3.2 Conduct Geophysical Surveys

These should include refraction and/or reflection surveys to establish the depth to bedrock and deeper stratigraphy for up to several miles around the site and more detailed site surveys which might include both reflection and ground penetrating radar to investigate the uniformity of near surface soils and the presence of buried channels or any other unusual features.

7.3.3 Conduct Preliminary Subsurface Investigations

This should include both cone penetration tests and borings with more or less continuous sampling and extensive classification and consolidation tests in order to develop a detailed geotechnical site characterization. Interaction between the project geologists, geophysicists and geotechnical engineers is essential at this stage. Samples should be examined for datable material and the depositional history of the site should be refined.

Wherever practical, at least three borings should be extended 50 feet into bedrock, or a stiffer layer which shows a strong impedance contrast relative to the surficial soils, and shear and compression wave velocities should be measured using at least two different techniques. If there is found to be a significant gradient in the seismic velocities within the bedrock, subsequent borings should be extended as necessary to determine the extent of the weathered or lower velocity material. The preceding guidelines also apply to rock sites. At soil sites, if bedrock, or a well-defined impedance contrast is not found within 500 feet of the surface, trial site response analyses should be conducted using assumed soil properties in order to determine an appropriate depth of exploration. A limited number of high-quality undisturbed samples should be taken, possibly utilizing several types of samplers, in order to optimize sampling and sample handling procedures for the types of soil encountered. Special sampling techniques such as grouting or freezing and overcoring shall be developed for hard to sample soils. All borings should be surveyed for diameter and drift prior to the installation of casing. Piezometers should be installed at appropriate depths should there be any suggestion of perched water tables or artesian conditions.

At least three samples for each major soil type and each 100 feet of depth should be tested in the laboratory in order to determine both G_{max} and modulus reduction and

damping curves using at least two different techniques for each class of measurement. The equipment used to conduct these tests should be the equipment intended for use in the final test program. Procedures for checking the uniformity of samples, such as x-raying, and for assessing and minimizing the degree of disturbance involved in extracting and reconsolidating samples should be established. Although there is some evidence for nonlinear behavior at soft rock sites, linear behavior may be assumed in lieu of conducting site-specific tests to determine modulus reduction and damping curves for rock.

7.3.4 Conduct Preliminary Site Response Analyses

Preliminary analyses should be conducted using each of the three velocity profiles determined in the preliminary subsurface investigation and a range of modulus reduction and damping curves based on the preliminary laboratory test program. The sensitivity of the computed results to variations in the method of analysis and variations in the velocity profiles and properties should be investigated with a view to defining those elements of the analysis that make the greatest contribution to the uncertainty associated with the computed motions. Appropriate efforts should then be extended to limit these uncertainties in the final subsurface investigations and analyses.

7.3.5 Conduct Final Subsurface Investigations

In the final subsurface investigation a minimum of three additional deep borings should be drilled and shear and compression wave velocities should again be measured using at least two different techniques. Additional deep borings may be necessary to establish site-specific estimates of the variability of material properties for use in site response analyses. High-quality undisturbed samples should be taken as necessary to ensure the availability for testing for G_{max} and modulus reduction and damping curves of at least six samples for each major soil type and 100 feet of depth by two different methods. Arrangements must be made in advance to ensure that all tests are completed within three months of sampling.

7.3.6 Conduct Final Site Response Analyses

Final site response analyses should be conducted using at least two different methods of analysis. Normally the primary method of analysis will use equivalent linear soil properties but the results obtained for higher amplitude input motions should be checked by comparing them with at least one method that uses a nonlinear soil model. For sites that include saturated loose or medium-dense cohesionless soils, at least one effective stress nonlinear analysis method should be used.

Uncertainties in both the shear wave velocity profile and the shear modulus reduction and damping curves should be taken into account in analyses of horizontal motions. At low levels of motion it may be expected that the computed results will be relatively sensitive to variations in the shear wave velocity profiles and the impedance contrast at the base of the model and relatively insensitive to the modulus reduction and damping curves. At higher levels of motion the computed results should be less sensitive to the shear wave velocity profile and the impedance contrast at the base of the model and more sensitive to the modulus reduction and damping curves. In lieu of conducting sufficient tests to determine statistically significant site-specific measures of the uncertainties in these quantities, or otherwise establishing typical site-specific measures of these uncertainties, the distributions developed and used in this study may be adopted. These are a log normal variation of shear wave velocity with a standard deviation σ_{ln} of 0.39 and a log normal variation of the modulus reduction factor and damping ratio with a standard deviation σ_{ln} of 0.35 at a cyclic shear strain of 3×10^{-2} percent with truncation at the 2σ level. Because they have been developed with the intent of covering a range of site conditions, these measures of uncertainty are somewhat larger than might be expected to result from site-specific studies. A suggested methodology for including such uncertainties in site response analyses is described in Appendix 6.A.

Analyses of vertical motions may be conducted independently of analyses of horizontal motions. In lieu of conducting site-specific field and laboratory studies of the variation of constrained modulus and damping with strain, it should be assumed that material behavior in constrained compression is linear, with the constrained moduli derived from the measured compression wave velocities applying at all strains, and the damping ratios being equal to or less than the low strain shear damping ratios at all strains.

7.3.7 Specification of Input Motions

The control motion for site response analyses should be specified as an "outcropping" motion and have the special characteristics appropriate for Eastern North America hard rock conditions (see Sections 6 and 9). This motion should then be applied at the base of the analytical model where the base is located at the soil-bedrock interface or at a depth where there is otherwise a strong impedance contrast, or at a depth of 500 feet if no strong impedance contrast exists above 500 feet and it can be shown that the computed surface motions are not sensitive to the depth of the model.

In general, a suite of at least four time histories should be used to provide control motions for site response analyses although a single time history may be used provided its power spectral density satisfies the Standard Review Plan guideline (NUREG-800, Section 3.7.1).

The preferred approach to generating time histories for site response analysis involves application of spectral matching techniques to generate spectrum compatible time histories. Various approaches can be used to accomplish this but the resulting acceleration histories should be checked to ensure that they have realistic integrations to velocity and displacement. Alternately, a suite of suitably scaled observed records can be used provided their average envelopes the design spectra and individual records are scaled by no more than about thirty percent of their original amplitudes.

8

FIELD AND LABORATORY INVESTIGATIONS

8.1 Introduction

This section summarizes the field and laboratory investigations that have been performed for the ground motion project. These investigations provide the framework for the development of: 1) a site effects model (Section 6), and 2) guidelines for conduct of geotechnical studies and site response analyses (Section 7).

The field and laboratory investigations focus on characterizing the soil at three reference sites. Two of the reference sites, Treasure Island and Gilroy 2, are located in the San Francisco Bay area (Figure 8-1). The third site is at Lotung, Taiwan (Figure 8-2). Each of these sites was chosen based on the prior existence and availability of weak- and strong-motion seismic recordings and on the geologic conditions at the site.

Each site was characterized in terms of its dynamic soil properties. The characterization studies included field explorations involving soil and rock drilling and sampling. At two of the three sites seismic and other geophysical testing was also performed. The characterization studies also included a series of laboratory tests to determine shear modulus and material damping properties of intact soil samples from the sites, and the variations of these material properties with loading and boundary conditions.

8.1.1 Motivation

The primary motivation for these field and laboratory investigations was to provide data that could be used to support the overall project objective: to improve the confidence in predicting ground motion during seismic events. Given that ground motion is strongly influenced by the dynamic properties of near-surface soil, it is important to measure dynamic soil properties and to understand or quantify the variability resulting from these measurements. If these properties cannot be determined with confidence, then the resulting ground motion prediction must invoke a correspondingly large degree of uncertainty.

The primary motivation for the field and laboratory investigations is satisfied in this project by developing a database of reliable dynamic properties at the three reference sites. The most critical dynamic properties for ground motion estimation are shear modulus and material damping ratio for each significant soil layer. The main boundary and loading conditions that influence shear modulus and material damping ratio include the level of shearing strain, state of effective confinement, frequency of cyclic loading, duration of loading under sustained confinement, and number of repetitions of loading. As these boundary and loading conditions can change the shear modulus and material damping ratio by a factor of 10 or more, the database includes an evaluation of the effects of boundary and loading conditions on the magnitude and variation in shear modulus and material damping ratio. This information serves as a basis for determining material models used in the analytical predictions discussed in Section 6.

A second motivation for this work is to quantify the confidence to which dynamic soil properties can be determined. To accomplish this, various state-of-the-art field and laboratory testing methods were used at each reference site. For the geophysical methods employed, different travel paths, sampling intervals, and loading frequencies were used to define a range of reasonable velocity variations. Similarly, laboratory tests were conducted under different boundary and loading conditions

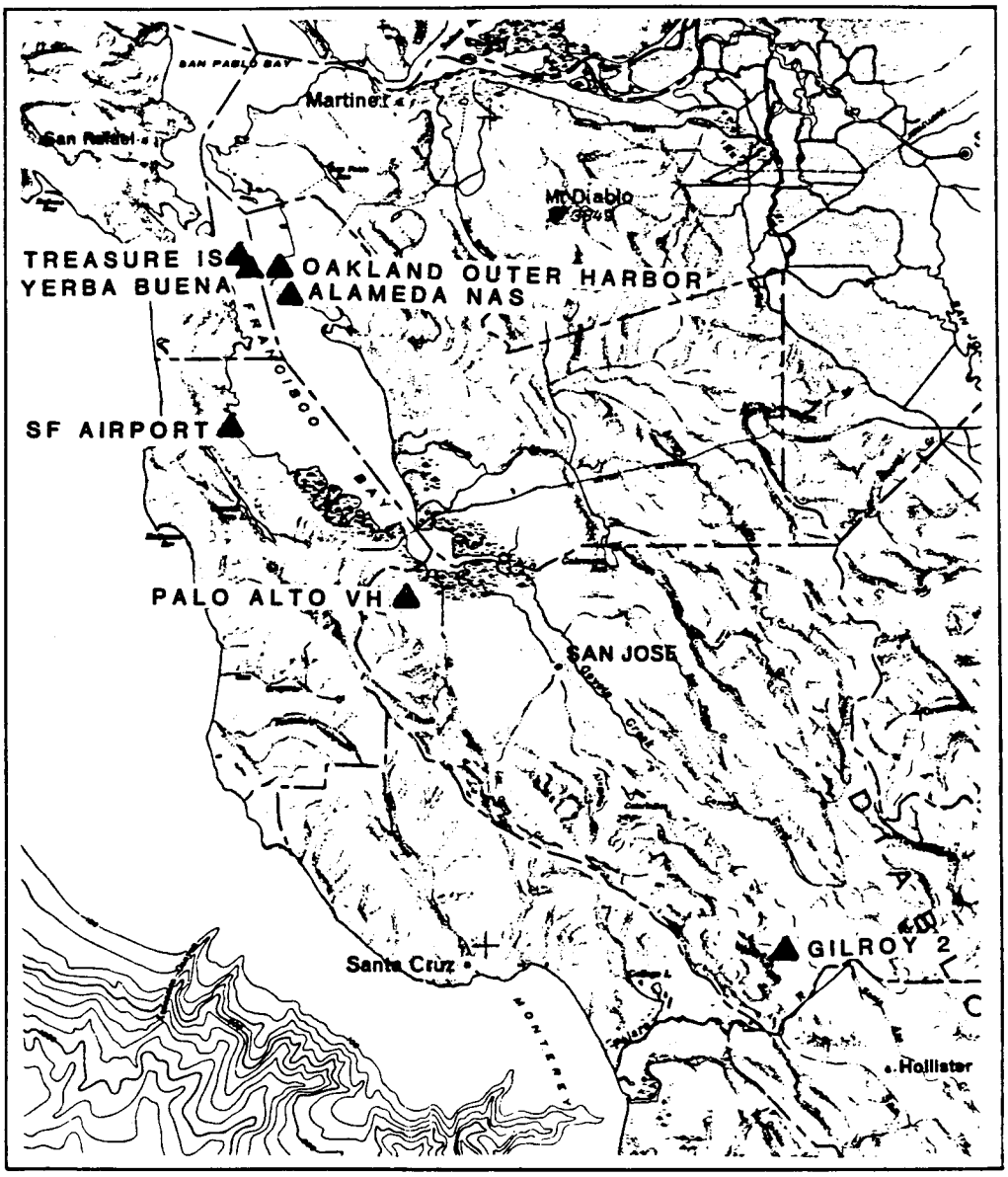

Figure 8-1. Location of Gilroy 2 and Treasure Island sites.

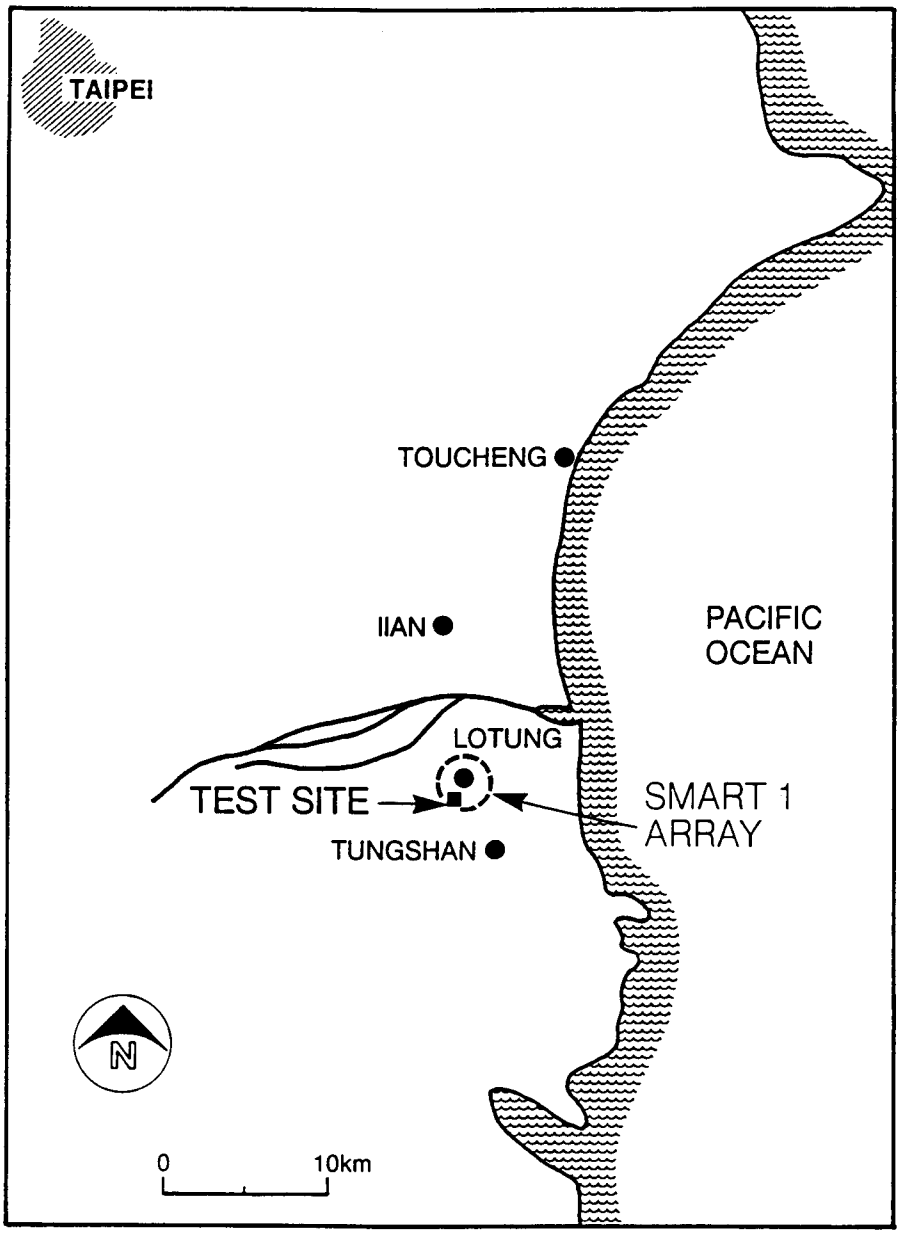

Figure 8-2. Location of Lotung site.

to define reasonable variations in shear modulus and material damping ratio. This information on soil property variation was then used in the analytical studies described in Section 6 to compare ground motion predictions based on derived dynamic properties with measured ground motions from seismic events. By using the most reliable soil property data, including their scatter, these comparisons allow an evaluation of the confidence in present predictive procedures and the effects of material property uncertainty on these confidence levels.

A third motivation for the field and laboratory investigations is to develop more reliable, in situ procedures for determining material damping. Site response analyses have demonstrated that ground response predictions can be sensitive to the value of material damping. Considerable variation can occur in the selection of material damping, depending on the experience and views of the person selecting or recommending the damping values. This situation is partly the result of having to rely on laboratory methods to determine material damping ratio. In contrast to the determination of shear modulus, where field seismic methods can be used to calibrate laboratory-derived modulus values, capabilities for estimating material damping in situ are limited, seldom applied, and subject to considerable uncertainty when they are used. Based on the comparison of shear modulus measured in the laboratory and in situ, differences between laboratory- and field-derived material damping values are expected, partly from unavoidable disturbance that is associated with laboratory testing of soil samples. However, in the absence of in situ measurements of material damping, personal judgment must be used in adjusting laboratory values of material damping. A key effort of this investigative program is, therefore, to develop procedures for measuring or interpreting material damping in situ.

The final motivation for the field and laboratory investigations at the reference sites is to collect information that will allow material properties to be extrapolated beyond the depths to which the actual site exploration and testing programs have been conducted. For both technical and cost reasons, most exploration and testing programs are limited to the upper several hundred feet of a soil profile. As ground response predictions have included the effects of soil properties at greater depths, the ability to determine soil properties to these depths has become an important consideration. One alternative has been to simulate within the laboratory testing equipment the effects of greater depths by imposing confining pressures consistent with the deeper depths. Since these confining pressures exceed those where laboratory tests are normally conducted by a factor of two or more, tests were conducted at higher pressures to evaluate whether any unusual requirements or behaviors would result from this approach.

8.1.2 Description of Reference Sites

Three reference sites were selected for this study. The selection of the three sites was based upon the following criteria:

- soil site with nearby rock outcrop (within 2–3 km) or a vertical accelerometer array
- recordings of both weak and strong motions at the site
- accessibility to drilling and testing
- soil stiffness and particle-size suitable for undisturbed sampling and dynamic soil testing in the laboratory, and
- soil conditions representing a broad range in consistency and type.

The three reference sites meeting these criteria are the Treasure Island site with a nearby rock outcrop at Yerba Buena Island, the Gilroy 2 site with Gilroy 1 as a nearby rock outcrop, and the Lotung site in Taiwan with a vertical array of three-component accelerometers. The Gilroy 2 and Treasure Island sites have earthquake records from the 1989 M 7 Loma Prieta earthquake. The epicenter for this event is approximately 15 km west of the Gilroy 2 site and approximately 80 km south of the Treasure Island site (Figure 8-1). The Lotung site is the location of a seismic test facility operated jointly by the Taiwan Power Company (Taipower) and EPRI (Tang, 1987). The facility includes two accelerometer arrays that extend 150 ft below the ground surface at the site. Each array has accelerometers located at multiple depths. The arrays have been in operation since 1986. Over 20 significant earthquake events have occurred in the vicinity of the site since startup in 1986. For many of these events, earthquake ground motions were recorded at multiple depths.

The three reference sites represent soil conditions, ranging from hard to soft. Gilroy 2 is a stiff, deep alluvial deposit, more similar in stiffness to potential nuclear power plant sites in the Eastern United States. Treasure Island consists of a relatively loose, liquefiable, hydraulic fill over stiff clays. In addition to meeting the criteria identified above, liquefaction occurred at some locations on Treasure Island within the hydraulic fill. This type of ground response represents one critical condition for testing the robustness of analytical predictive methods. Lotung is a soft, deep soil site comprised primarily of silty soil. It was selected as a reference site because of the abundance of ground motion and geotechnical data, and because of the silty nature of soil at the site. The dynamic response of such soil has not been studied adequately (EPRI/NSF, 1991), despite the widespread occurrence of this material type.

The remainder of this section provides a brief overview of explorations that have been carried out at each site, and the site characteristics revealed by these programs.

8.1.2.1 Gilroy 2

Gilroy, California is located east of Santa Cruz in the Santa Clara valley (Figure 8-1). The general locations of the Gilroy 2 site and the adjacent Gilroy 1 site, which is located on rock, are shown in Figure 8-3. A more detailed map of the Gilroy 2 site is shown in Figure 8-4. These sites are part of the Gilroy Array (1 to 7) of strong-motion accelerographs operated by the California Division of Mines and Geology (CDMG) Strong-Motion Instrumentation Program; the array extends across the southern end of the Santa Clara Valley.

A number of soil explorations have been conducted at the site. These include 130- and 600-foot deep holes drilled as part of a USGS program (Gibbs et al., 1992a), and four holes drilled to depths from 200 to 790 ft as part of this EPRI project. The locations of the six borings and the CDMG strong-motion accelerometer are shown in Figure 8-4. Pertinent information about these exploration programs is given in Table 8-1. Additional details of the drilling and sampling procedures used in the recent borings are given in Appendix 8.A5.

Nine seismic surveys have been conducted at the Gilroy 2 site for the determination of P- and S-wave velocities. Two were conducted by USGS (Joyner et al., 1981; Gibbs et al., 1992a), and the other seven were part of this EPRI project as outlined in Table 8-2. Details of the seismic and dynamic laboratory testing are provided in Sections 8.2 and 8.3 and in Appendices 8.A1 through 8.A5 and 8.B1 through 8.B3.

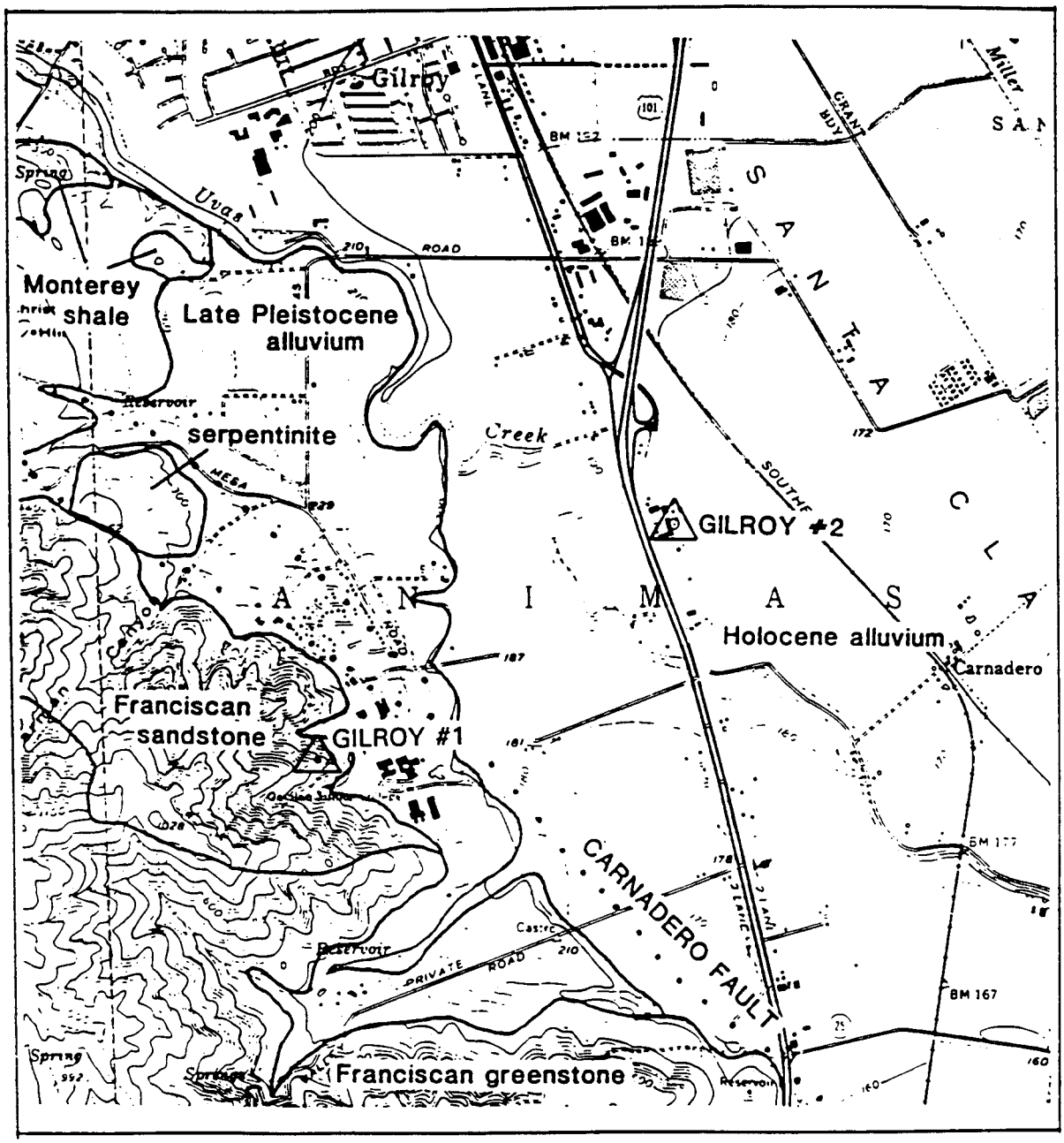

Figure 8-3. General site map for Gilroy 2.

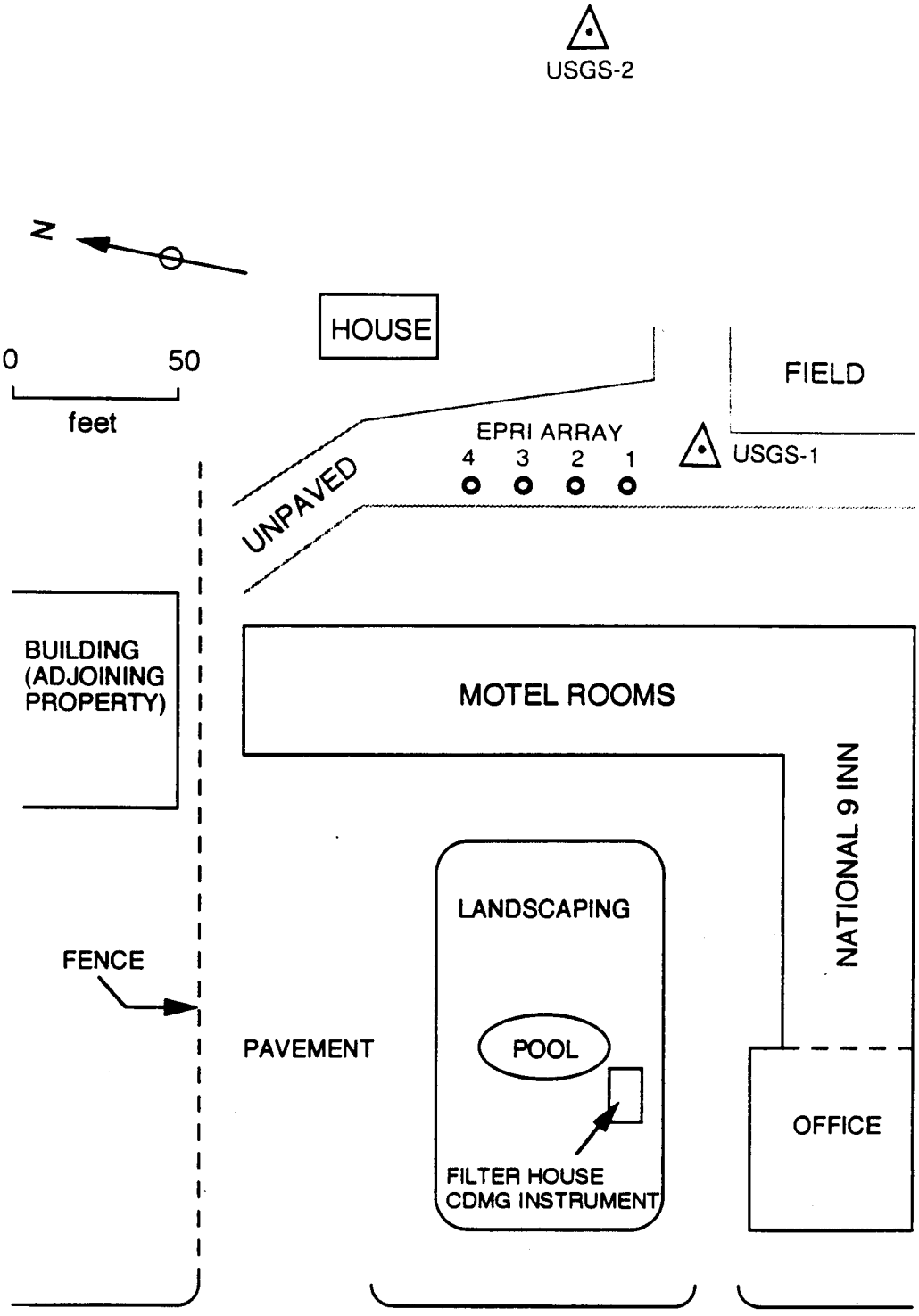

Figure 8-4. Exploration locations for Gilroy 2.

Table 8-1

Borings Drilled at Gilroy 2

Date	Boring	Depth	Casing	Samples	Reference	Comment
9/79	USGS-1	130 ft	4-in PVC	None	USGS (1982)[1]	Hole Lost
9/79	USGS-2	600 ft	4-in PVC	None	USGS (1982)	Hole Lost
9/90	EPRI-1	600 ft	4-in PVC	Shelby & STP	USGS (1992)[2]	Hole Open
10/91	EPRI-2	790 ft	4-in PVC	None	USGS (1992)	Hole Open
11/91	EPRI-3	200 ft	4-in PVC	None	USGS (1992)	Hole Open
11/91	EPRI-4	200 ft	4-in PVC	None	USGS (1992)	Hole Open

1. USGS OFR 82-407
2. USGS OFR 92-287

Table 8-2

Seismic Investigations Conducted at Gilroy 2

Date	Investigator	Measurement	Borehole	Reference
1979	USGS	Downhole—V_p & V_s	USGS-1	Joyner et al. (1981)[1]
1992	USGS	Downhole—V_p & V_s	USGS-2	Gibbs et al. (1992a)[2]
1992	USGS	Downhole—V_p & V_s	EPRI-1 & 2	USGS (1992)
1991	Redpath	Downhole—V_p & V_s	EPRI-1	Appendix 8.A4
1992	Agbabian	D & S[3]—V_p & V_s	EPRI-2	Appendix 8.A2
1992	Agbabian	Crosshole—V_p & V_s	EPRI-1,2,3	Appendix 8.A2
1992	Agbabian	In Situ Damping	EPRI-3	Appendix 8.A2
1992	U of Texas	Crosshole—V_p & V_s	EPRI-1,2,3,4	Appendix 8.A1
1992	U of Texas	In Situ Damping	EPRI-1,2,3,4	Appendix 8.A1

1. Also in USGS Bulletin 163
2. USGS OFR 92-287
3. Downhole and Suspension PS Logger

Based on the field exploration and laboratory testing programs, the soil at the Gilroy 2 site can be divided into five main strata. The surficial soil is a sandy Holocene alluvial fan deposit that extends to a depth of about 45 ft. This deposit is underlain by a gravelly, late Pleistocene alluvium and a clayey Pleistocene lake deposit to a depth of about 130 ft, beyond which there is a deep section of Pleistocene alluvium extending to bedrock which is found at a depth of about 540 ft. The Pleistocene alluvium is generally quite gravelly with the gravel apparently concentrated in lenses rather than continuous layers. The bedrock is reported to be a siltstone, serpentinite, and closely fractured shale and siltstone of the Franciscan assemblage (Gibbs et al., 1992a). The rock at Gilroy 1 is a hard sandstone, probably of the Franciscan assemblage. Figure 8-5 shows a geologic log for the upper 400 ft of the soil profile at Gilroy 2. Groundwater is located approximately 70 ft below the ground surface.

8.1.2.2 Treasure Island

Treasure Island is located in San Francisco Bay (Figure 8-1) just north of Yerba Buena Island. The locations of the Treasure Island strong-motion accelerometer site and the adjacent Yerba Buena Island site are shown in Figure 8-6 by the large triangles. The island is a man-made fill constructed by dredging and hydraulic placing of dredged material in the late 1930's as part of the 1939 World Fair. It currently serves as a major West Coast naval facility.

At least four geotechnical exploration programs have been conducted at the Treasure Island site since the Loma Prieta earthquake. Table 8-3 identifies these programs. These programs include one 340-foot hole, drilled as part of a previous USGS–EPRI cooperative program, and four other holes varying in depths from 24 to 145 ft, that were coordinated by the University of New Hampshire (UNH). Two explorations using cone penetrometer testing methods have also been coordinated by UNH. A summary of the UNH work is provided by de Alba et al. (1992). The locations of five borings drilled at this site are shown in Figure 8-7. [Dual numbers are shown for each boring. The B-series numbers are those used in Appendix 8.A1 of this report.] Details for the drilling and sampling procedures used in the EPRI-1 boring are given in Appendix 8.A5.

Six different seismic surveys have also been conducted to determine P- and S-wave velocities at Treasure Island as noted in Table 8-4. Three were sponsored by EPRI as part of this project. The other three were coordinated through UNH. These surveys were conducted in the same holes as shown in Figure 8-7. Details of the seismic and dynamic laboratory investigations carried out at the Treasure Island site by EPRI are included in Sections 8.2 and 8.3, respectively, and Appendices 8.A1, 8.A2, 8.B1, and 8.B2.

A description of the geologic setting of Treasure Island is provided by Rogers and Figuers (1991). Details of the construction of Treasure Island are described by Lee and Praszker (1969). Based on these references, as well as the results of recent explorations cited in Table 8-3, the soil at Treasure Island can be generally divided into three main strata as shown in Figure 8-8. The topmost stratum consists of a loose, hydraulically placed sand fill which overlies native shoal sand at some locations. The second stratum consists of Holocene-age Young Bay Mud which has a variable thickness due to earlier channeling at the site. The Young Bay Mud is underlain by Pleistocene-age old bay sediments which consist of both more sandy and more clayey materials with the more clayey materials corresponding to the Old Bay Clay designation that is used in San Francisco-area geotechnical practice. Groundwater occurs approximately 4 ft below the ground surface.

Of particular importance to the response of the old bay sediment is the degree of overconsolidation of the material. It tends to vary over short distances. Typically overconsolidation ratios (OCR) are about 2 rather than the higher numbers which are often reported in professional publications or geotechnical consulting reports. Consolidation tests conducted at the University of Texas at Austin on samples from Boring EPRI-1 (Appendix 8.B1) show OCR values of about 1.2 for a sample of the Young Bay Mud taken at a depth of 80 ft and about 2 for a sample of Old Bay Clay taken at a depth of 150 ft.

8.1.2.3 Lotung Site

The Lotung site is located approximately 30 miles southeast of Taipei, Taiwan (Figure 8-2) at a Taipower electric

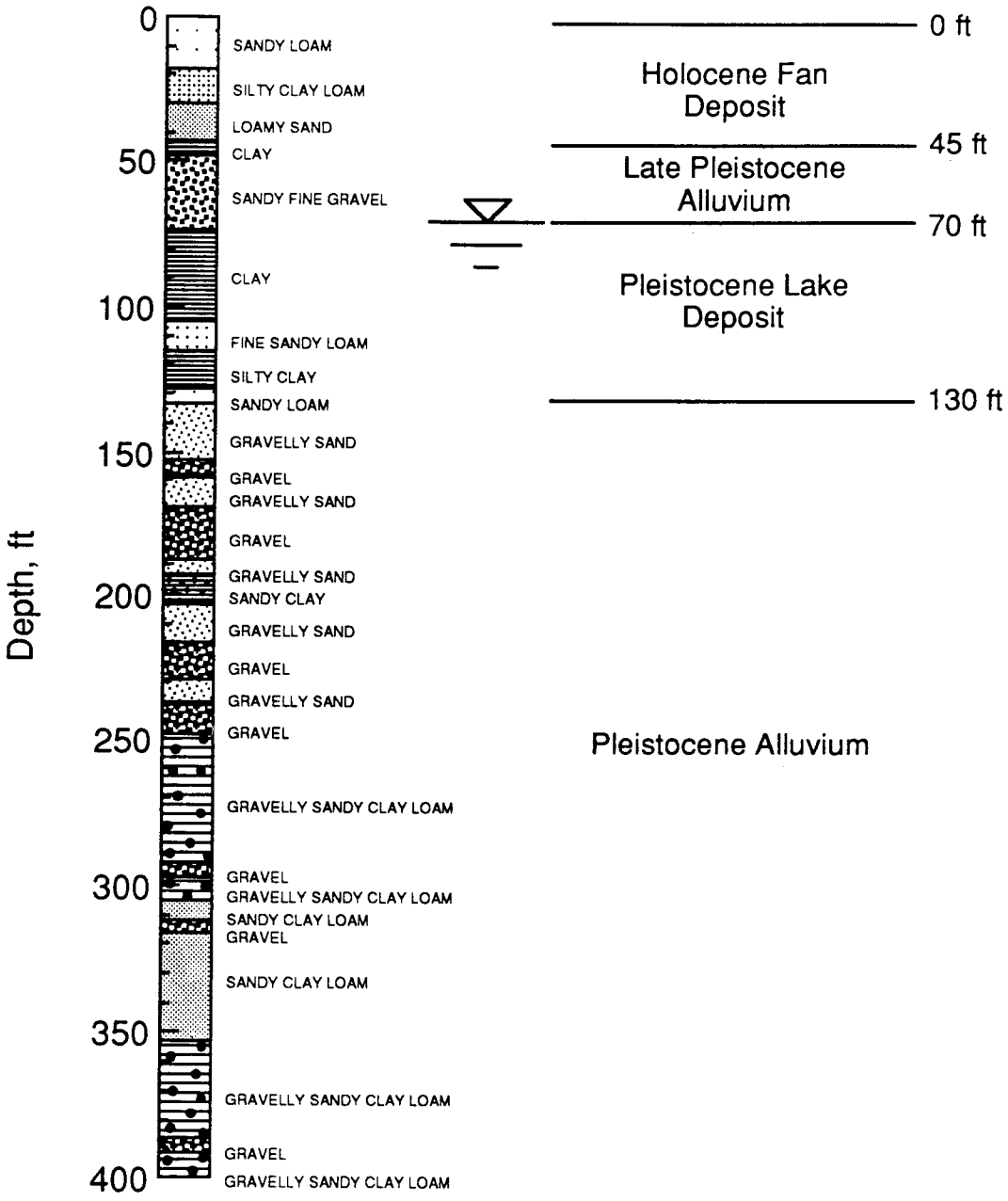

Figure 8-5. Geologic map based on boring EPRI-1 at Gilroy 2.

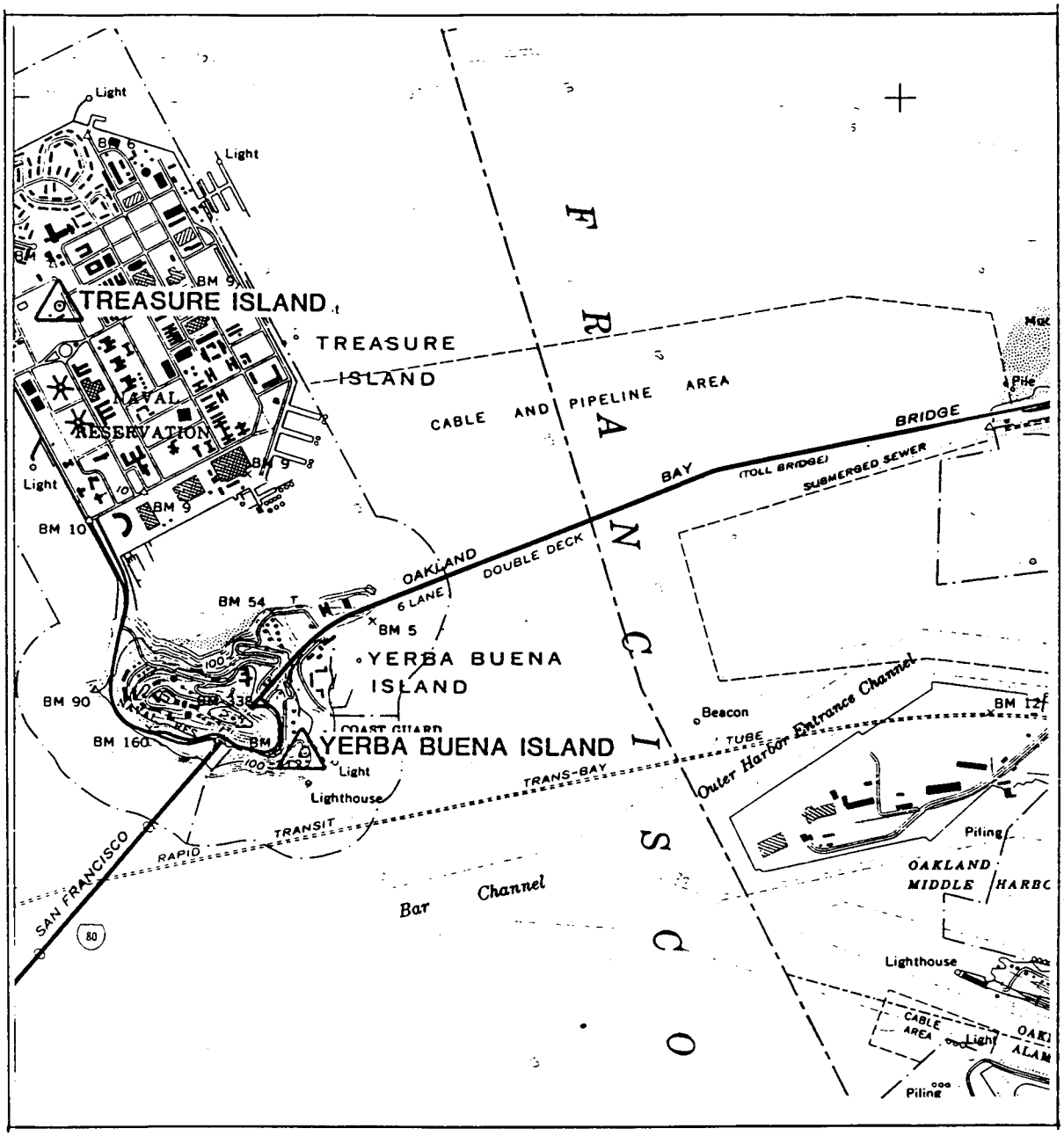

Figure 8-6. General site map for Treasure Island.

Table 8-3

Borings Drilled at Treasure Island

Date	Boring	Depth	Casing	Samples	Reference	Comment
1990	EPRI-1/B3	340 ft	5-in PVC	SPTs 3-in Shelby	Gibbs et al. (1992a)[1]	Hole Open
1991	UNH-1/B2	145 ft	5-in PVC	Yes	de Alba et al. (1992)	Hole Open
1991	UNH-2/B1	102 ft	5-in PVC	Yes	de Alba et al. (1992)	Hole Open
1991	UNH-3/B4	51 ft	5-in PVC	Yes	de Alba et al. (1992)	Hole Open
1991	UNH-4/B5	24 ft	5-in PVC	Yes	de Alba et al. (1992)	Hole Open
1991	CPT1-10	Various	CPT Soundings	—	de Alba et al. (1992)	—
1990	UM-10	90 ft	Seismic Cones & CPTs	—	Hryciw et al. (1991)	—

1. USGS OFR 92-287

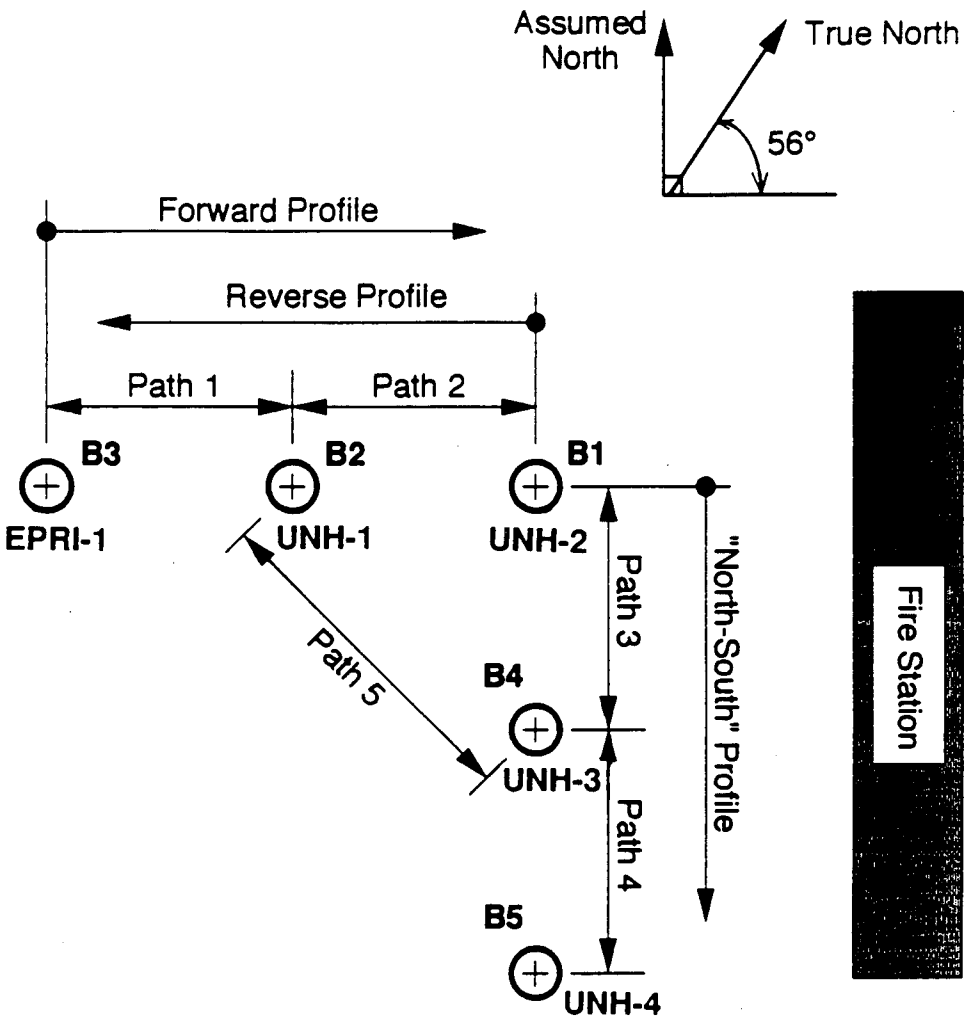

*Notes: Drawing For Layout Only
(Not to Scale)

Elevation Datum for Crosshole Tests is the Ground Surface at Borehole B3

Figure 8-7. Exploration locations at Treasure Island.

Table 8-4

Seismic Investigations Conducted at Treasure Island

Date	Investigator	Measurement	Borehole	Reference
1991	Redpath	Downhole—V_p & V_s	EPRI-1	Appendix 8.A4
1992	USGS	Downhole—V_p & V_s	EPRI-1	Gibbs et al. (1992a)[1]
1992	Agbabian	Crosshole—V_p & V_s & Damping	EPRI-1 UNH-1,3	Appendix 8.A2
1991	U of Michigan	Seismic Cone—V_s	UM-10	Hryciw et al. (1991)
1991	Earth Technology[2]	Crosshole—V_p & V_s	EPRI-1 UNH-1,3	de Alba et al. (1992)
1992	U of Texas	Crosshole—V_p & V_s & Damping	EPRI-1, UNH1,2,3,4	Appendix 8.A1

1. USGS OFR 92-287
2. Conducted for the University of New Hampshire

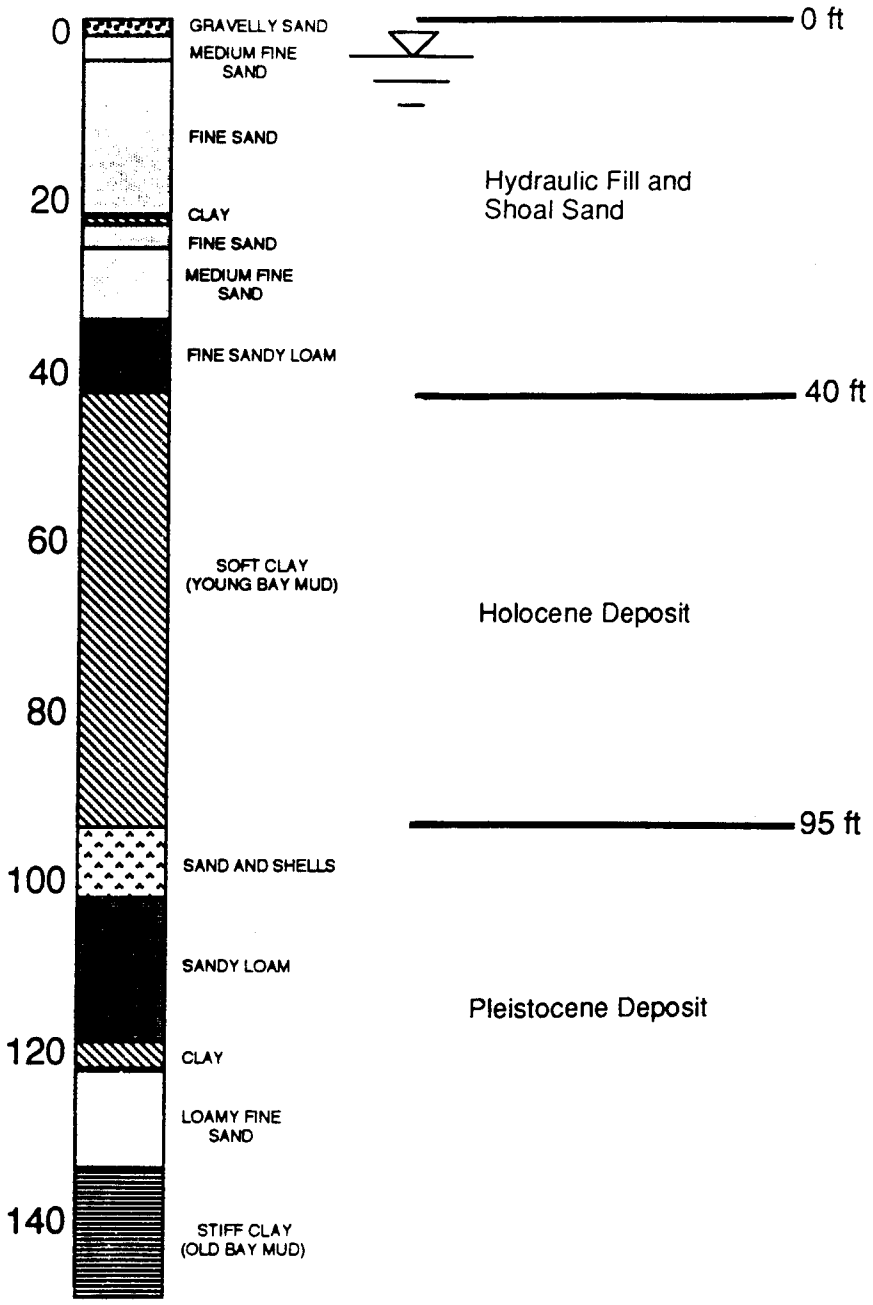

Figure 8-8. Geologic map based on boring EPRI-1 at Treasure Island.

substation. The site is the location of the Large-Scale Soil-Structure Test (LSST) facility, which was constructed in 1985 jointly by Taipower and EPRI. The LSST facility includes 1/12- and 1/4-scale concrete containment structures. The concrete structures are 10 ft and 35 ft in diameter and are embedded 4 ft and 15 ft, respectively. Each structure is instrumented with accelerometers at various levels within the structure and pressure cells on the side and base of the structures. Strong-motion accelerometers have been installed in the ground around the structure (Figure 8-9). Additional information about the Lotung site is provided by Tang (1987).

Five geotechnical exploration programs have been conducted at the Lotung site. These programs included four drilling and sampling programs and one cone penetration testing program. The most recent drilling and sampling program was conducted by EPRI as part of this project. Table 8-5 lists the borings drilled at the site. Figure 8-10 shows the location of the geotechnical explorations conducted at the site. Information about the previous field and laboratory testing programs is provided by Anderson (1993).

Two seismic surveys were conducted at the site, an extensive uphole and crosshole program and a S-wave refraction program. Table 8-6 summarizes key elements of these programs. Details regarding the geophysical surveys are presented by HCK (1986) and ORI (1989); Sections 8.2 summarizes data obtained during the programs. Results of dynamic laboratory tests on soil samples from the Lotung site are provided in Section 8.3 and Appendix 8.B3.

Results of these previous exploration programs indicate that Lotung is a relatively deep, soft soil site. The upper 100 to 120 ft consist of interbedded silty sand and sandy silt (Figure 8-11). Occasional deposits of gravel are encountered, particularly at depths of 60 to 70 ft. Below the upper cohesionless deposit is a thick layer of finer grained soil. This finer grained soil varies from silty clay to clayey silt. This layer is believed to extend to depths in excess of 1000 ft. The bedrock at the site is reported to occur at depths in excess of 1300 ft. Groundwater is located within a few feet of the ground surface. Artesian conditions occur at a depth of approximately 50 ft.

8.2 Seismic and Geophysical Testing at Reference Sites

As part of this study, seismic surveys were performed at the Gilroy 2 and Treasure Island sites by the University of Texas at Austin (Appendix 8.A1), Agbabian Associates (Appendix 8.A2), and Redpath Geophysics (Appendix 8.A4). The primary purpose of the seismic testing programs was to determine P- and S-wave velocities at each site. This information serves as a basis for site response analyses described in Section 6. Each of the groups also made estimates of material damping, or attenuation, at the Gilroy 2 and Treasure Island sites from the results of the seismic testing programs. The damping information was collected in an effort to establish the accuracy to which damping could be determined in situ, and the variability that could be expected between different investigators conducting damping measurements. Additional analyses of the University of Texas and Agbabian damping data were performed by the Massachusetts Institute of Technology (MIT) Earth Resources Laboratory (Appendix 8.A3).

8.2.1 Method

The soil exploration and seismic testing methods at the three reference sites were generally similar. Each program included a detailed site exploration as holes were being drilled for the seismic surveys. During the site exploration, information was collected about soil stratification, soil type, and basic engineering properties of the soil. Resistivity and natural gamma information was also collected at one of the sites, Gilroy 2. The seismic testing program at Gilroy 2 and Treasure Island involved the use of suspension logging tools, downhole testing methods, and crosshole testing methods. At the Lotung site the field exploration program was limited to two additional borings. The intent of the Lotung borings was to collect samples for dynamic laboratory testing and to install casing that could be used at a later date to conduct additional seismic testing. The additional seismic testing is planned to provide further in situ information about material damping.

8.2.1.1 Soil Borings and Resistivity/Natural Gamma Logging

Boreholes for the geophysical surveys were typically drilled with rotary mud drilling methods. A description

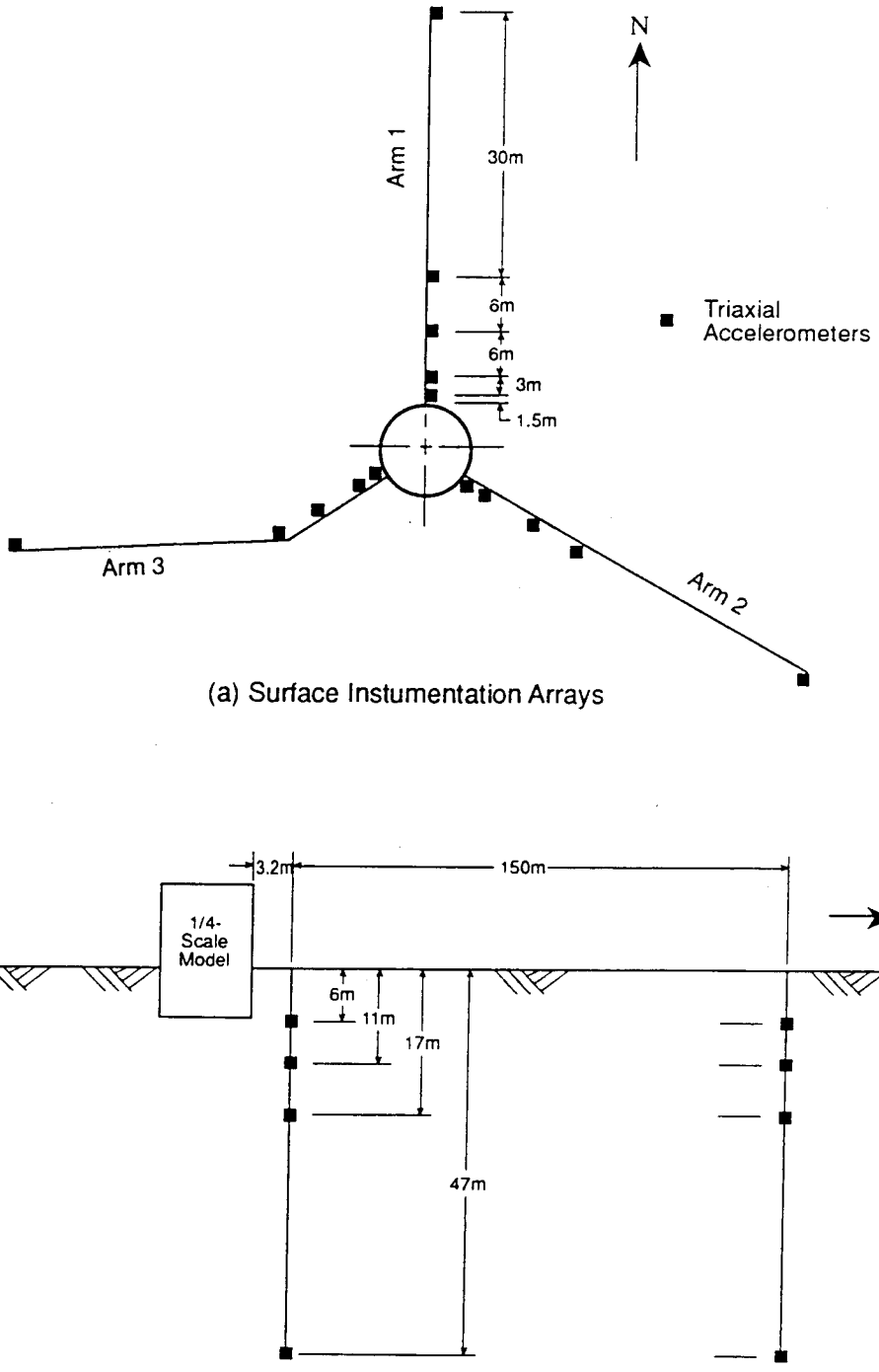

Figure 8-9. Schematic diagram of Lotung strong-motion arrays.

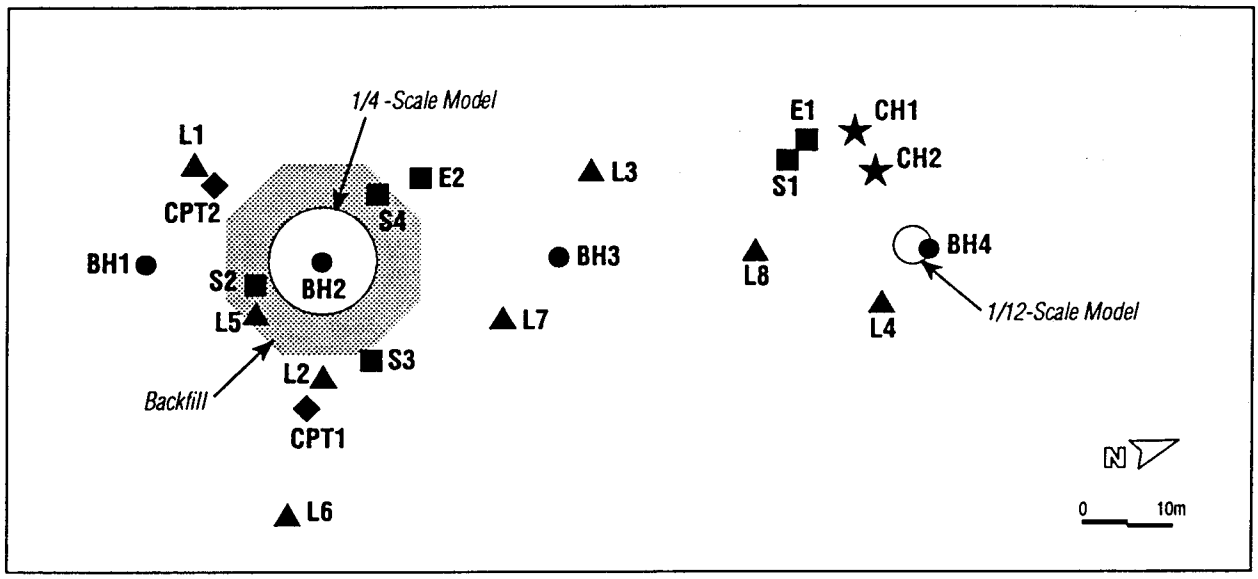

● Borehole drilled during JSBS (1984) Program
▲ Borehole drilled during WECC (1986) Program
◆ CPT sounding during UCD (1987) Program
■ Borehole drilled during MAA (1988) Program
★ Borehole drilled during MAA (1992) Program

Figure 8-10. Exploration locations at Lotung.

Table 8-5

Borings Drilled at Lotung

Date	Boring	Depth	Casing	Samples	Reference	Comment
1984	BH1—BH4	100 to 200 ft	Steel	SPTs 3-in Shelby	JSBS (1984)[1]	
1985	L1—L8	200 to 500 ft	PVC	SPTs 3-in Shelby	WECC (1986)	
1987	CPT1— CPT2	67 ft	—	SPTs 3-in Shelby	UCD (1987)	
1988	S1—S4 E1—E2	140 ft	—	SPTs 3-in Shelby	MAA (1988)	
1992	CH1—CH2	150 ft	4-in PVC	—	Appendix 8.A6	Holes Open

1. References for Lotung field explorations given in Anderson (1993)

Table 8-6

Seismic Investigations Conducted at Lotung

Date	Investigator	Measurement	Borehole	Reference	Comment
1985	HCK Geophysical	Uphole—V_p & V_s Crosshole—V_p & V_s	L1—L8	HCK (1986)	Explosive Source Long Travel Paths
1989	Ohsaki Research Institute	V_s Refraction		ORI (1989)	Very Near-Surface Information

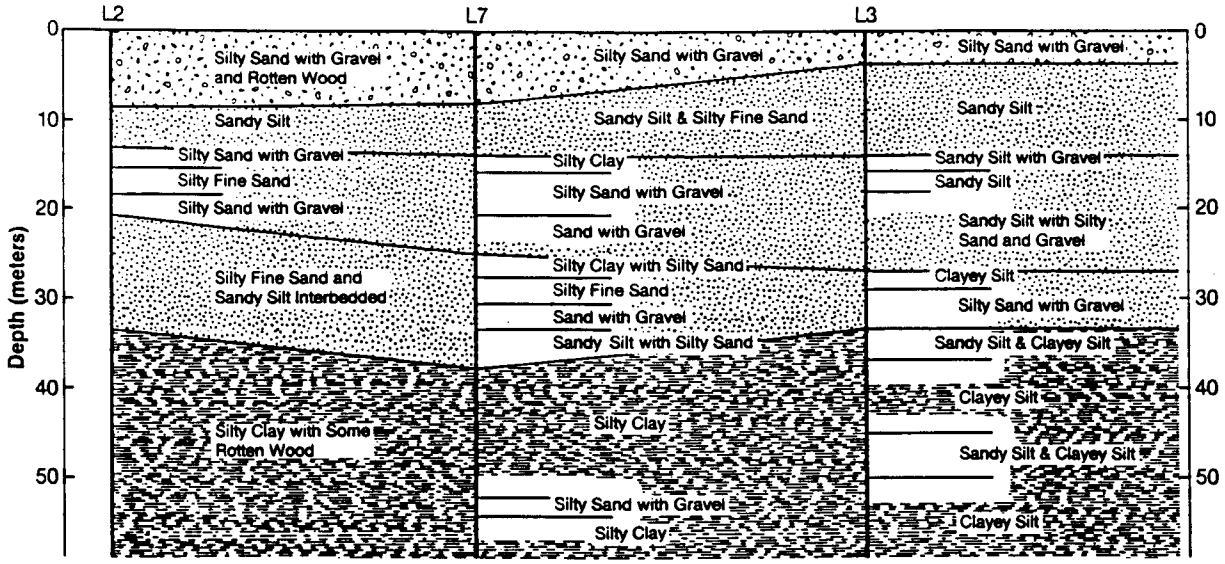

PROFILE I

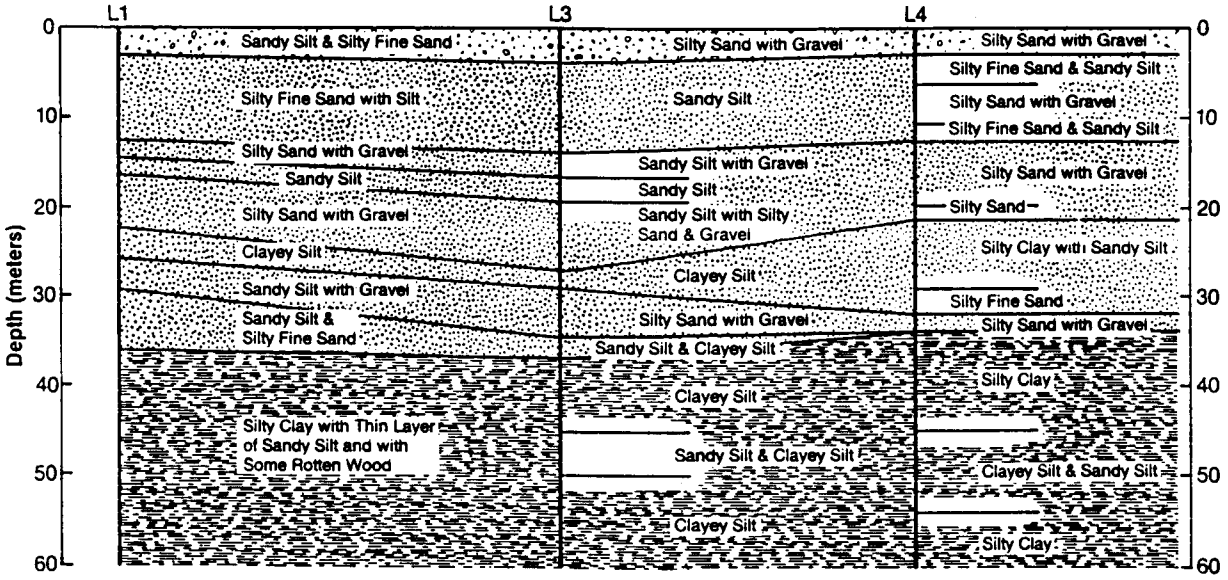

After NTU (4)

PROFILE II

Figure 8-11. Geologic cross-sections at Lotung.

of this drilling method is given in Winterkorn and Fang (1975). Samples were recovered from the boreholes using Standard Penetration Test (SPT) and thin-walled Shelby tube sampling methods. The SPT samples were used for soil classification information. Additionally, the blowcounts recorded during the SPT provided information about soil density and stiffness. The Shelby tube sampling method was used to obtain high-quality samples for laboratory testing. These samples had a nominal diameter of 3 inches and were pushed into the ground, rather than driven as in the case of the SPT sampler. At the Lotung site, fixed-piston Shelby tube samples were obtained. For loose, cohesionless soil the fixed-piston sampling procedure is believed to provide very high quality samples. Additional information about the EPRI drilling and sampling programs is provided in Appendices 8.A5 and 8.A6.

Soil drilling and sampling procedures were observed by experienced geotechnical/geological engineers at each site. These individuals provided visual descriptions of the samples as they were recovered, and oversaw the storing of the samples before shipping to the different laboratories for testing. Typically, cohesionless samples were drained of excess water before sealing and shipping the samples. This procedure was used to reduce the tendency of the samples to densify during transport. Cohesive soil samples were sealed immediately after recovery. During transport samples were protected from disturbance by cushioning the samples in foam rubber and styrofoam. The samples from Gilroy 2 and Treasure Island were transported by automobile to the University of Texas at Austin for testing. Lotung samples were shipped by air to the University of Texas

At one site, Gilroy 2, resistivity and natural gamma logging was completed by Agbabian Associates in late 1991. These measurements were made in borehole EPRI-2. The resistivity test involved inserting a resistivity probe into the uncased borehole and recording the variation in resistance between two electrodes with depth. Clay and organic deposits were identified by low resistivity (resistance per unit length), whereas sand, gravel and rock had high resistivity. The natural gamma measurement involved using a radiation counter in the probe. Clayey soil was identified from sandy soil by the higher natural radioactivity. Additional details about these logging efforts are provided in Appendix 8.A2.

8.2.1.2 Seismic Velocity Measurements

The general principle of seismic velocity measurements is to measure the travel time of seismic waves (P and S waves) between a source and geophone receiver or between two geophone receivers over a range of depths, from which seismic velocities can be derived. Figure 8-12 shows a sketch of the velocity measurement methods used in this study. Additional details about these methods are summarized below. These descriptions are generally common to all the programs completed. Specific details of data collection are given in Section 8.2.2.

Suspension Logging Measurements. The suspension measurement technique, although extensively used in the petroleum industry, is a relatively new method for measurement of both P- and S-wave velocities in geotechnical studies. The technique is normally used in an uncased borehole filled with drilling mud. Figure 8-13 shows a schematic diagram of the suspension logging device configuration. The probe is between 15 ft and 20 ft long, depending upon its configuration. The energy source is located near its bottom, and two biaxial geophone receivers are positioned near its top. It is suspended in the borehole by an armored cable. The energy source is a horizontal solenoid which produces an impulsive pressure wave in the borehole fluid. This pressure wave transmits energy to the borehole wall, producing both P and S waves in the soil or rock. The energy propagates through the soil and then couples through the borehole fluid to the geophones, which are spaced about 3 ft apart. Dominant frequencies are between 500 and

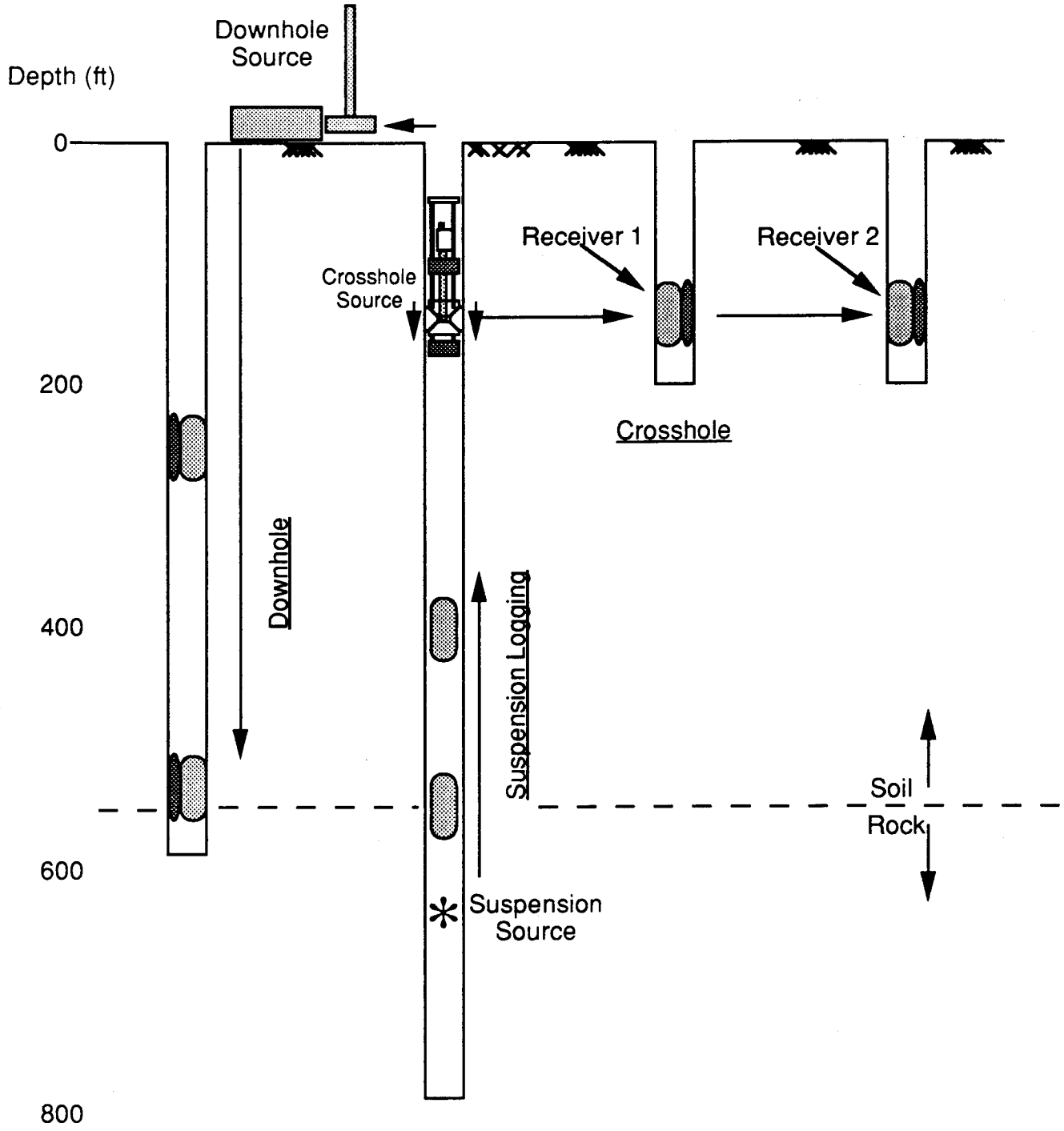

Figure 8-12. Seismic velocity measurement methods.

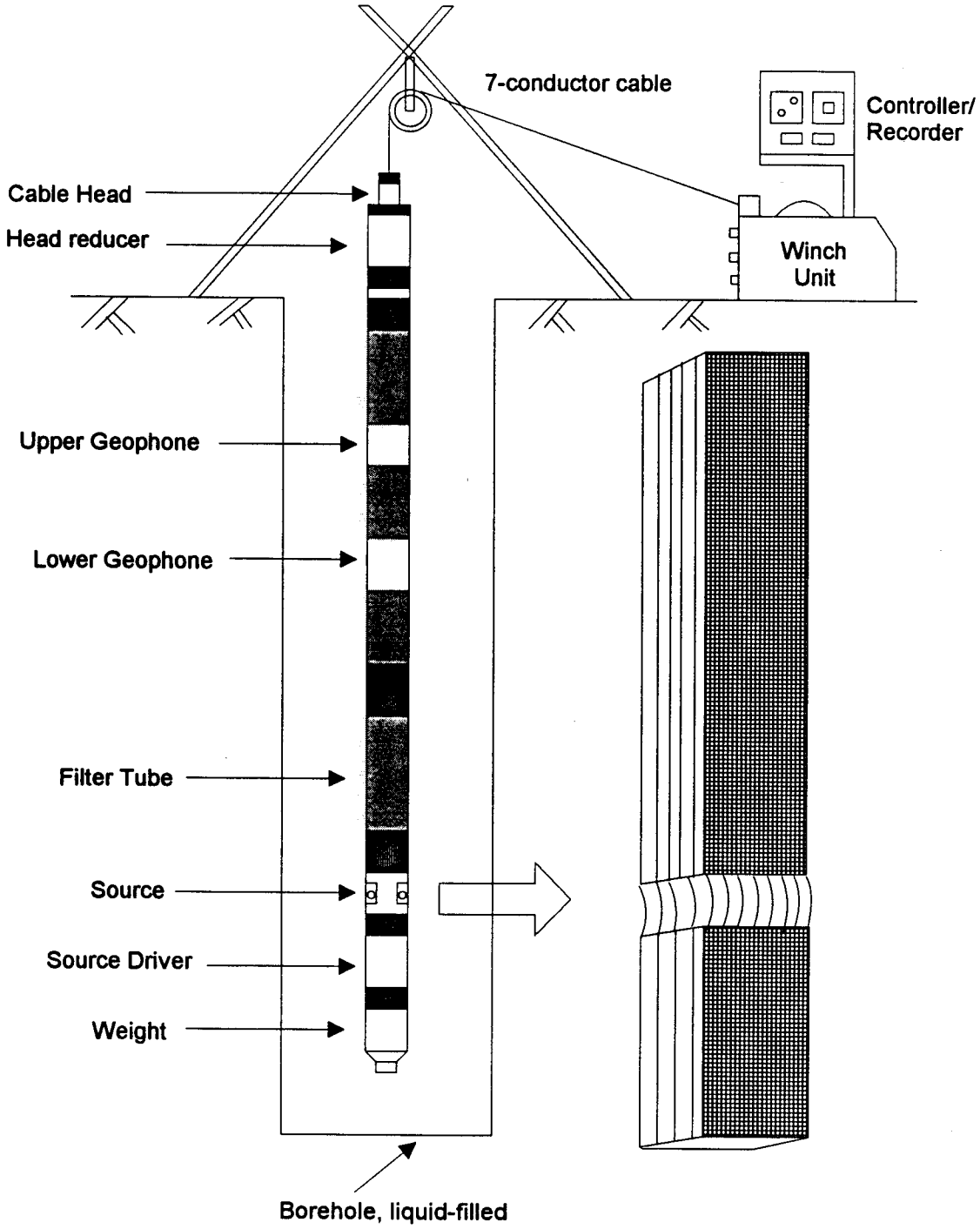

Figure 8-13. Suspension logging measurement configuration.

2,000 Hz for the S wave and between 1,000 and 3,000 Hz for the P wave. Table 8-7 shows a comparison of predominant frequencies of propagation for the suspension logging device versus other seismic testing methods.

Instrumentation at the surface controls the source and recording. A distinct, repeatable pattern of impulses is generated at a particular depth as follows: (1) the source is fired in one direction producing dominantly horizontal shear with some vertical compression, and the horizontal geophone signals are recorded; (2) the source is fired in the opposite direction and the horizontal geophone signals are recorded; and (3) the source is fired again and the vertical geophone signals are recorded. The repeated source pattern facilitates the picking of the P- and S-wave arrivals; reversal of the source changes the polarity of the S-wave pattern but not the P-wave pattern. Signals from the two geophones are recorded digitally at the surface for later analysis.

During computer analysis, an experienced operator picks the arrival times of both P and S waves at each geophone. Velocities are calculated from the measured difference in arrival times for each depth interval sampled, thereby defining an average material velocity between the two geophones.

The advantages of the suspension logging method are that interval measurements of velocities are obtained with minimum interpretation and from a single borehole. Furthermore, coupling with the borehole is not required so that data can be obtained from uncased boreholes. This has allowed measurements to be made to depths in excess of 1000 ft in stable borehole conditions. The disadvantages of the suspension logging method are that frequencies are much higher than earthquake frequency bands; there is typically large scatter in individual velocity measurements, corresponding to localized, small-scale variations in the soil or rock; it is sometimes difficult to maintain stability of a borehole without casing; and P-wave determination is difficult in unsaturated soil. Appendix 8.A2 contains further details regarding this method.

Downhole Velocity Measurements. This is the most widely used method for measurement of P- and S-wave velocities. Figure 8-14 is a schematic diagram of the measurement configuration. Generally a cased borehole is required, although it is possible to make these measurements in uncased boreholes if the consistency of the soil or rock allows the hole to remain open or if a thick drilling fluid is used to keep the hole open.

For the downhole test, an impulsive energy source at the surface near the top of the borehole generates waves which propagate radially from the source. The impulse can be produced manually by a hammer blow or by an automated source. Horizontal blows, coupled to the ground by a weighted plank or a post, will produce mainly S waves. Vertical blows will produce P waves. In

Table 8-7

Predominant Frequencies of Seismic Wave Propagation

Type of Source	Frequency of Compressional Waves (Hz)	Frequency of Shear Waves (Hz)
Suspension Logging Device	1,000 to 3,000	500 to 2,000
Downhole Velocity Method	50 to 100	20 to 40
Crosshole Velocity Method	100 to 500	60 to 300

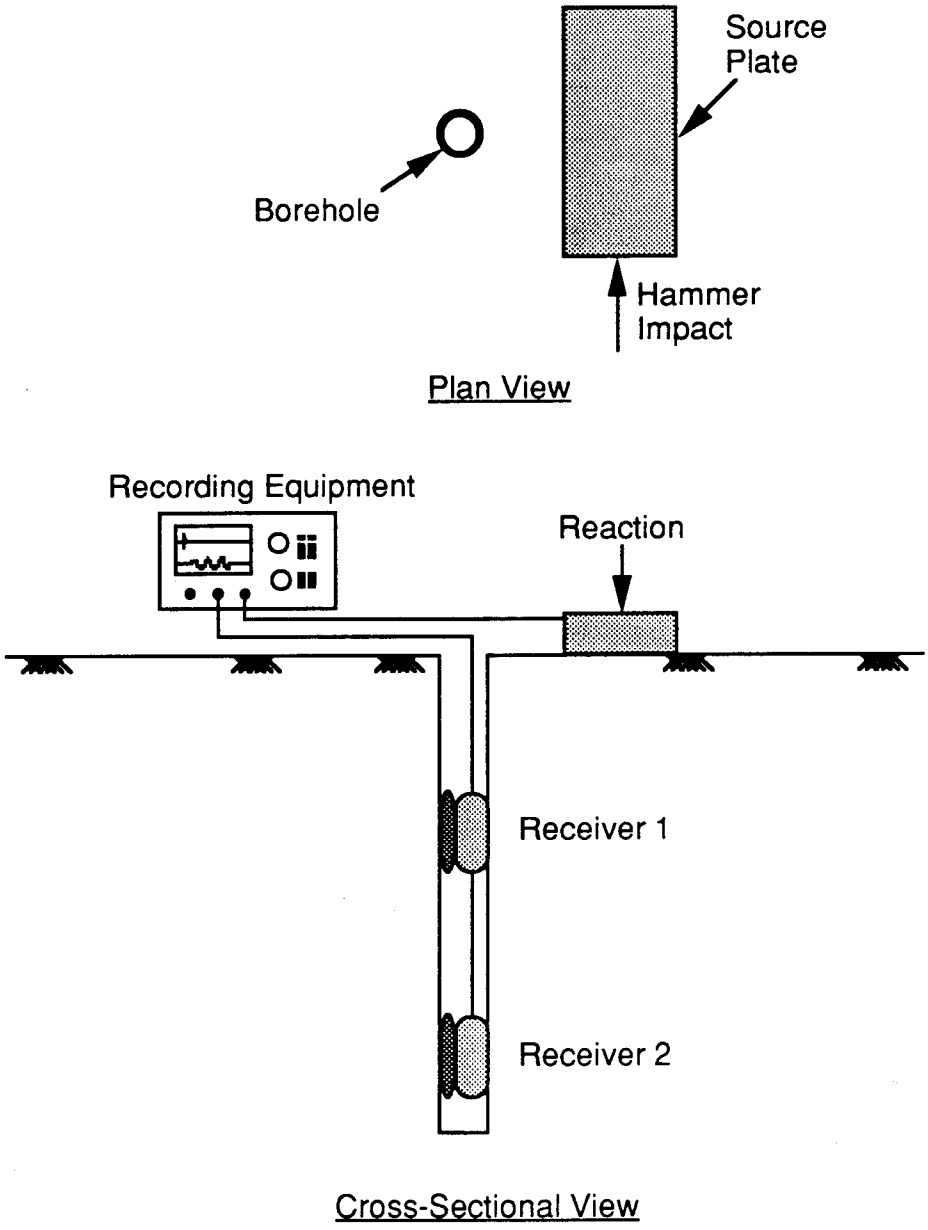

Figure 8-14. Downhole measurement configuration.

addition to the commonly-used manual hammer source, other types of sources are available. For example, an air-powered horizontal hammer was developed by USGS to produce repeatable shear waves (Gibbs et al., 1992a) and was used in some of the investigations at the reference sites. Explosive sources were used on many early downhole measurements. An explosive source is less desirable because it produces large amounts of P-wave energy, making the slower S-wave arrivals more difficult to detect.

One or more geophones are fixed at various depths in the borehole to measure the ground motion generated by the surface source. At each depth, the geophone signal(s) and a trigger signal from the impulsive source are recorded simultaneously. For S-wave measurements, the direction of the impulse is usually reversed. This reversal of the horizontal source assists the analyst in distinguishing the wave arrivals.

High-resolution digital seismographs (recorders) are usually used for data recording. One method of data analysis consists of picking the travel times (both P and S waves) for each measurement depth and constructing a travel time versus depth curve. The instantaneous slope of such a curve is inversely proportional to the wave velocity at the particular depth. Another method involves determining the travel times between geophones at various depths for the same input signal. This approach results in true interval measurements which generally improve velocity resolution (Mok, 1988). Inversion techniques can be also added to data analysis to further increase velocity resolution.

The conventional downhole velocity method has a limited depth range because of signal attenuation. This limitation is especially true for the manually-applied hammer source. In soil a maximum depth of reliable measurement is generally several hundred feet with a hammer-type source (energy concentrated between 10 Hz and 200 Hz) with signal attenuation more significant for S waves than P waves. The depth range and signal quality are greatly enhanced if the downhole geophones can be oriented in the same direction as the source; this is a critical aspect in many S-wave measurements. Use of signal enhancement seismographs, where several signals recorded at one depth are digitally added, also result in better quality records and greater depths.

The advantages of the downhole method are that it can be used to produce an overall, average velocity-depth profile or it can also be used with interval measurements to produce detailed profiles; the primary motion during the downhole test is vertically propagating SH waves; and the seismic energy is closer to the frequency band of earthquake motions. The disadvantages are that higher frequency components of the source signal tend to damp out, making wave arrivals difficult to determine at deeper depths; low velocity zones or thin layers may go undetected during the test unless careful interval measurements are made; orienting geophones for SH-wave velocity identification is difficult at deeper depths; and it is often difficult to determine P-wave velocities at soil sites where casing is used.

Redpath Geophysics and Agbabian Associates conducted downhole tests as part of this program. Further details on the specific methods and instrumentation used by these investigators are in Appendices 8.A2 and 8.A4. A variation of the downhole procedure, called the uphole test, was used at the Lotung site. For the uphole method the source and receiver were reversed from the normal downhole test; i.e., the source was located at depth and the receivers were located at the surface. Additional information about methods used during downhole tests conducted at the reference sites are included in Gibbs et al. (1992a) for Gilroy 2 and Treasure Island, Hryciw et al. (1991) for Treasure Island, de Alba et al. (1992) for Treasure Island, and HCK (1986) for Lotung.

Crosshole Velocity Measurements. Suspension and downhole velocity measurements produce a vertical velocity profile in a single boring. If two or three (collinear) boreholes are available at a site, the crosshole velocity technique allows direct measurement of velocities at a specific depth.

Figure 8-15 is an idealized crosshole velocity measurement configuration. A source is installed in one borehole at a given depth, and geophones are installed at the same depth in the adjacent boreholes. The source and geophones are aligned and securely coupled to the borehole by mechanical or pneumatic devices. Explosive sources are sometimes still used. However, as discussed previously, an explosive source is generally not recommended as P-wave arrivals often obscure the slower S-wave arrivals. In-hole mechanical sources are generally

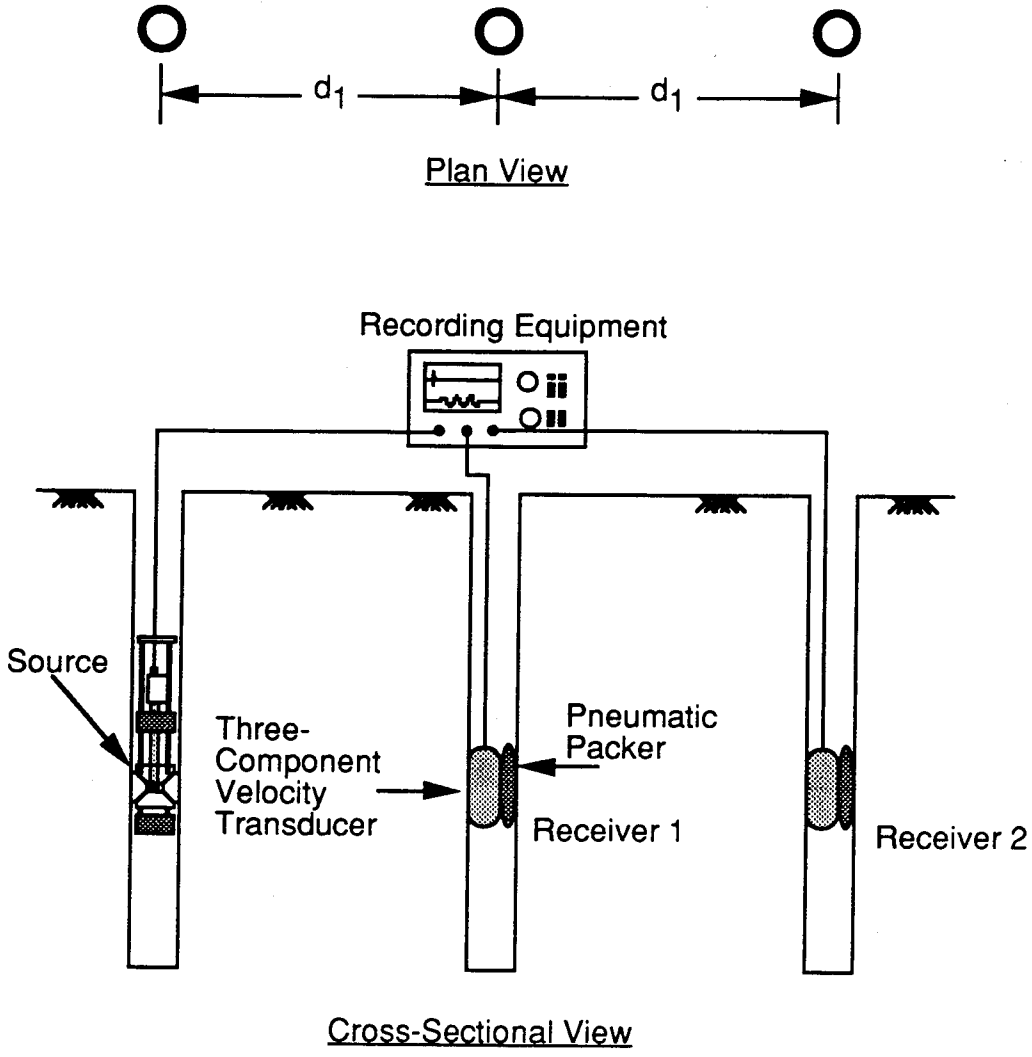

Figure 8-15. Crosshole measurement configuration.

employed. SH, SV, or P waves can be produced by in-hole sources. The common source types are a vertical hammer (producing SV and P waves) or a solenoid hammer (producing SH and P waves). As with the previous velocity measurement methods, identification of the S-wave arrival is enhanced if the impulse to the source is reversed.

Biaxial or triaxial geophones are used to record seismic wave arrivals. For high-quality velocity and damping measurements, it is necessary to orient the geophones in the borehole so that the two horizontal transducers are oriented parallel and perpendicular to the direction of wave propagation. For shallow depths, orientation can be performed using rigid orientation rods. At deeper depths, orientation is accomplished by installing an electronic compass (magnetometer) inside the geophone package and either manually or electronically rotating the sensors to correct alignment. It should be noted that alignment is only necessary for SH-wave arrivals because the SV-wave measurements are made using a vertical sensor, which is correctly oriented by the test configuration; i.e., geophone is locked vertically in a vertical borehole. P-wave measurements can be made using one or two horizontal sensors. If only one horizontal sensor is used, it should be oriented to best record P waves.

Geophone signals are recorded along with a reference signal from the source on a seismographic recorder. This is usually a high-resolution digital recorder. Data analysis is similar to that for the downhole and suspension logging methods. P- and S-wave arrival times are measured for each geophone. The average velocity is obtained by dividing the path length by the travel time. If three collinear boreholes are used for the crosshole measurements, velocities can be measured for three distinct paths: (1) source–near geophone, (2) source–far geophone, and (3) near geophone–far geophone. The near geophone–far geophone measurement is a true interval measurement and minimizes many of the variables that can enter all seismic measurements. If two boreholes are used, only the source–geophone path is measured.

The path length between source and geophone(s) must be accurately known for crosshole velocity measurements. Accurate calculation of path lengths at a given depth requires accurate measurement of the position of each borehole. This is typically measured using a special borehole probe containing both a biaxial tiltmeter and a magnetometer. The measured tilt and orientation of the borehole are integrated to provide the drift (deviation from vertical) as a function of depth. Such measurements were performed by Agbabian Associates at the Gilroy 2 and Treasure Island sites (see Appendix 8.A2) and by the Earth Technology Corporation at the Treasure Island site (de Alba et al., 1992).

Analysis of crosshole data is simple for relatively homogeneous soil deposits or within thick layers (layers whose thickness is equal to or greater than the source-receiver borehole spacing). However, it is more involved in thinly bedded or stratified materials. The wave pattern in such materials can be complicated due to multiple reflections at nearby interfaces, and the first arrival may not be the direct path due to refraction. The refraction issue was a particular problem in older crosshole surveys where distances between boreholes often exceeded 30 to 50 ft. Current standards require that the spacing be on the order of 10 to 15 ft. These shorter paths in combination with the larger amplitudes of the direct wave (Mok, 1988) have tended to minimize the concern with the refraction issue, unless very unusual soil conditions or very sharp velocity contrasts occur in proximity to the measurement depth.

The advantages of the crosshole method are that the velocities can be determined over small depth intervals; it is the only method in which both SH- and SV-wave velocities, inclined waves at depth [required to evaluate anisotropy (Lee, 1993)], and horizontally propagating P waves can be measured; and the method appears to provide the best approach for determining material damping. The disadvantages are that two and preferably three boreholes must be drilled consequently the costs are higher; accurate borehole deviation surveys must be conducted if hole depths exceed a few tens of feet; and data interpretations may be more difficult where thinly bedded materials occur or near layer boundaries with strong velocity contrasts.

Crosshole tests were conducted by Agbabian Associates and the University of Texas as part of this program. Further details on the specific methods and instrumentation are given in Appendices 8.A1 and 8.A2. Information about other crosshole tests conducted at the Treasure Island and Lotung reference sites is summarized by de Alba et al. (1992) and HCK (1986), respectively.

8.2.1.3 Attenuation Measurements

Low-strain attenuation of ground motion can be measured in situ concurrently with multiple-geophone downhole, suspension logging, or three-hole crosshole velocity measurements. In the velocity measurements, ground motion waveforms are recorded for analysis of P- and S-wave arrival times. These ground motion waveforms, if digitally recorded with sufficient resolution, also contain information regarding the attenuation of the motion over the distance between geophones. This attenuation information includes the effects of energy spreading and the effects of material energy absorption, with the adsorption part referred to in this project as material damping.

For the downhole attenuation method, a reference geophone is locked in the borehole at a fixed depth outside the near-field effects of the surface source, and a moving geophone is locked at various lower depths in the same or an adjacent borehole. Alternatively, if the source is highly repeatable the reference geophone may not be required (but this approach is discouraged). Waveforms are recorded as for velocity measurements, perhaps with more care in the setting of recorder gains and filters. Recorded waveforms at different depths are analyzed to extract material damping.

Attenuation can also be measured from crosshole velocity waveforms. As with the downhole velocity data, recorded crosshole data from the two geophones contains information regarding signal attenuation. However, there is a significant difference. Attenuation measured from downhole data is the effective attenuation for possibly many soil layers. This effective attenuation includes the effects of reflection and transmission, wave conversions, and scattering that often dominate in vertical propagation. With the crosshole method, the measured attenuation is that due to a single layer (assuming lateral homogeneity). With these two methods it is possible to separate intrinsic (or anelastic) attenuation effects, which dominate in a single layer, from additional geometric effects associated with wave propagation across boundaries.

Several methods are used for the interpreting the field attenuation data. These methods are discussed in more detail in Section 8.2.3. They include the spectral slope method and the similar spectral ratio method. Neither method is very robust when applied to actual field data, as shown in this project. This seems to be due to the effects of poor signal-to-noise ratios, layering effects, and to data contamination from reflections. More robust techniques have been developed by Toksoz and his colleagues at MIT (Appendix 8.A3) as part of this project for extraction of the intrinsic attenuation, or material damping, from downhole and crosshole data. These analysis techniques involve waveform fitting methods. They were applied to data from both the Gilroy 2 and Treasure Island site. Appendix 8.A3 contains detailed descriptions of these analyses.

8.2.1.4 Variability in Measurement Results

The different seismic testing methods provide information about wave propagation speed and attenuation within the media being sampled. Whereas the material properties within the media may be constant, differences in the measurement and interpretation methods described in the preceding subsections lead to variability amongst results obtained by the different methods. These factors include the following:

- **Resolution**. The suspension logger has the greatest depth resolution since velocities are measured between two geophones that are 1 to 3 ft apart. This is followed by the crosshole measurements, which in these studies were carried out at 2- to 10-ft depth intervals. Downhole measurements generally determined velocities over depth intervals of 10 ft or greater. Unless the soil is homogeneous, each method will give somewhat different velocities because of the different sampling intervals. This difference will be largest at very layered sites.
- **Accuracy**. Velocity measurements require the measurement of the travel time of the waves over a given distance. For low-velocity material travel times are longer, and velocities can be determined more accurately. For small reference distances, such as in the case of the suspension logging, small time variations due to borehole cave-ins and time delay measurements could contribute to velocity variations.
- **Depth Measurements**. Another cause of differences between velocity profiles can be due to inaccurate depth measurements in the borehole. It may be necessary to adjust depth scales by a few feet to obtain better correlation between, say, velocities measured by suspension logging and crosshole methods.

- **Soil and Stress Anisotropy.** Another cause of variation is material (and stress) anisotropy. When the medium is anisotropic, SV- and SH-wave velocities are not identical; therefore, horizontally and vertically traveling P waves are not the same. As a result, crosshole (horizontal wave propagation) and downhole (vertical propagation) could have different velocities, despite both measuring P- and S-wave velocities (Lee, 1993). Measurement variation between neighboring sites (such as an USGS hole and the an EPRI hole) and between different borehole combinations could be due in part to these effects of laterally heterogeneity.

Typically, these effects will introduce a 10 to 15% variation in velocity under the best conditions. As the soil profile becomes more varied or as the care and experience of the investigator decreases, the amount of variation is expected to increase.

8.2.2 Data Collection at Reference Sites

The field measurement methodologies described above were used at each of the three reference sites. This section provides further details regarding the actual data collection methods used during the seismic measurements. Information about the USGS program is included in the summary, as portions of this work were done cooperatively with EPRI. Details about the drilling and sampling programs are reported in Appendices 8.A5 and 8.A6; details about the seismic testing programs are provided in Appendices 8.A1, 8.A2, and 8.A4.

8.2.2.1 Gilroy 2

Three types of seismic measurements were made at Gilroy 2 as part of this project. These included suspension logging measurements, downhole measurements, and crosshole measurements. Table 8-2 summarizes key elements of these programs. The scope of activities for each program are summarized below.

- **Agbabian Suspension Velocity Measurements.** Suspension logging was done in borehole EPRI-2 immediately after drilling was completed in late 1991 and before the hole was cased. The suspension logging system, manufactured by OYO Corporation, was used for these measurements. P- and S-wave velocities were measured to a depth of 770 ft at intervals ranging from 3 ft to 10 ft.
- **USGS Downhole Velocity Measurements.** The USGS measured velocities in borehole USGS-1 in 1979 (Joyner et al., 1981) and 1989, and boreholes USGS-2 and EPRI-1 in 1989 and 1991, respectively. The 1979 measurements used a hammer source, and involved large depth increments (66-foot intervals). For the 1989 measurements an air-powered hammer source was used to measure P- and S-wave travel times (and derived velocities) to almost 400 ft. In 1991 the measurements were repeated in borehole EPRI-1. Interfering waves prevented S-wave measurements below 230 ft, but P waves were measured to 560 ft.
- **Redpath Downhole Velocity Measurements.** Redpath measured velocities in borehole EPRI-1 in 1991 using the downhole method and a hammer source. S-wave travel times were measured to a depth of 340 ft. P-wave travel times were measured to a depth of 600 ft.
- **University of Texas Crosshole Velocity Measurements.** Crosshole velocity measurements were made by the University of Texas in December 1991. All four EPRI boreholes were used. The source was a mechanical wedge borehole hammer. P and SV waves were determined to depths of 390 ft. A solenoid source was also used as an SH-wave source to depths of 120 ft. Three-component geophones in three receiver boreholes were used for these measurements; orientation of the geophones was controlled for measurement depths less than 200 ft. The geophones were custom-designed and each contained triaxial 4.5-Hz geophones. Coupling to the borehole was accomplished by pneumatic bladders. Data were recorded using a Hewlett-Packard two-channel dynamic signal analyzer. Borehole drift was measured by Agbabian Associates.
- **Agbabian Crosshole Velocity Measurements.** Agbabian Associates, with the help of Redpath Geophysics, measured crosshole velocities with a solenoid source in borehole EPRI-1 and two biaxial geophones in boreholes EPRI-2 and EPRI-3. The source was the OYO Suspension Logger source, modified for electronic compass orientation. The geophones were custom packages from Redpath Geophysics containing biaxial (horizontal and vertical) 4.5-Hz geophones, a pneumatic locking mechanism, and a magnetometer-based orientation

system. Source control and data recording were accomplished using the OYO Suspension Logger electronics package. P- and SH-wave travel times (and derived velocities) were measured to 200 ft, the bottom of borehole EPRI-3. Borehole drift measurements were made in each hole.

- **University of Texas Attenuation Measurements.** Some of the crosshole seismic data obtained by the University of Texas team was also used for estimation of attenuation. SV waveforms from depths of 15, 25, 115, and 125 ft were analyzed using the spectral slope and spectral ratio methods (see Appendix 8.A1). The MIT team also used the University of Texas crosshole data for attenuation analysis in the depth range of 10 ft to 200 ft (see Appendix 8.A3).
- **Agbabian Attenuation Measurements.** Agbabian Associates made additional downhole measurements at Gilroy 2 in 1992 specifically for the estimation of attenuation. Two shakers and a hammer source generated surface SH energy which propagated downwards. One of the shakers was a large counter-rotating eccentric mass shaker capable of producing a peak sinusoidal force in excess of 2,000 lbs; the other was a small electromagnetic shaker capable of producing 30 lbs peak force. Both were coupled to the soil by the weight of a large truck. Ground motion was measured by a fixed reference geophone at 50 ft in borehole EPRI-3 and by a second geophone in borehole EPRI-2. The second geophone was fixed at depths of 50, 100, 150, 200, 300, and 450 ft. The geophones were the Redpath Geophysics geophones used in the crosshole measurements. Waveform data were recorded using a Kinemetrics Model SSR-1 digital recorder, and on-site analysis was done using a Hewlett-Packard two-channel signal analyzer. At each depth, signals from both shakers and the hammer source were recorded. Data were analyzed both by Agbabian Associates (spectral slope method) and by the MIT team (waveform modeling).
- **USGS Attenuation Measurements.** USGS investigators (Gibbs et al., 1992b) made an independent study of the attenuation of SH waves in the depth range of 30 to 360 ft. They used downhole (VSP) waveforms generated by the air hammer source at the surface. Attenuation determinations were made using the spectral ratio and waveform modeling method in the frequency range of 15 to 60 Hz.

8.2.2.2 Treasure Island

Velocity measurements were made at the Treasure Island reference site using the suspension logging method, the downhole method, and the crosshole method. The following paragraphs provide further details about these velocity measurements. Specific details of the programs are provided in Appendices 8.A1, 8.A2, and 8.A4.

- **Agbabian Suspension Velocity Measurements.** Suspension logging was unsuccessfully attempted by Agbabian Associates in borehole EPRI-1 in 1991. The 5-inch diameter PVC casing did not allow good energy coupling between the casing and the soil.
- **USGS Downhole Velocity Measurements.** The USGS used the downhole method and their air-powered hammer system to measure P- and S-wave travel times (Gibbs et al., 1992a). These measurements were made in borehole EPRI-1. P and S waves were measured to depths of 330 ft.
- **Redpath Downhole Velocity Measurements.** Redpath Geophysics measured velocities in borehole EPRI-1 in 1991 using the downhole method and a hammer source. S-wave travel times were measured to a depth of 280 ft. P-wave travel times were measured to a depth of 320 ft.
- **University of Texas Crosshole Velocity Measurements.** Crosshole velocity measurements at Treasure Island were made by the University of Texas in January of 1992. Five of the boreholes were used in these measurements: EPRI-1, UNH-1, UNH-2, UNH-3, and UNH-4 (see Figure 8-7). A mechanical wedge borehole hammer was used as a source for both P and SV waves to depths of 140 ft. A solenoid source was also used as an SH source to depths of 100 ft. Three-component geophones properly oriented from the surface were used for these measurements. The geophones were custom-designed and each contained triaxial 4.5-Hz geophones. Coupling to the borehole was accomplished by pneumatic bladders. Data were recorded using a Hewlett-Packard two-channel dynamic signal analyzer.
- **Agbabian Crosshole Velocity Measurements.** Agbabian Associates, with the help of Redpath Geophysics, measured crosshole velocities with a solenoid source in borehole EPRI-1 and two biaxial geophones in boreholes UNH-1 and UNH-3. The source was the OYO Suspension Logger device,

modified for electronic compass orientation. The geophones were custom packages from Redpath Geophysics containing biaxial (horizontal and vertical) 4.5-Hz geophones, a pneumatic locking mechanism, and a magnetometer-based orientation system. Source control and data recording were accomplished using the OYO Suspension Logger electronics package. Geophone-to-geophone P- and SH-wave travel times (and derived velocities) were measured to 100 ft, the bottom of borehole NH-3. Source-to-geophone travel times were measured to 140 ft, the bottom of borehole NH-1.

- **University of Texas Attenuation Measurements.** Some of the crosshole seismic data obtained by the University of Texas team was also used for estimation of attenuation. Both spectral slope and spectral ratio methods were used to interpret attenuation values. MIT used some of these data in their interpretation of attenuation.
- **Agbabian Attenuation Measurements.** Agbabian Associates made additional downhole measurements at Treasure Island in 1992 specifically for the estimation of attenuation. These measurements were similar to those at Gilroy 2, where two shakers and a hammer source generated surface SH energy which propagated downwards. Both the reference geophones at 50 ft and the second moveable geophone were installed in borehole EPRI-1. The second geophone was fixed at depths of 55, 100, 150, 200, and 280 ft. Data were analyzed both by Agbabian Associates (spectral slope method) and by the MIT team (inverse waveform modeling).

8.2.2.3 Lotung

No seismic tests were conducted as part of the current EPRI study. However, seismic tests had been conducted previously at the Lotung site for EPRI and Taipower. General information about these tests is given below. Additional information about the seismic testing programs is found in HCK (1986) and ORI (1989).

- **Crosshole and Uphole Measurements.** Crosshole and uphole velocity measurements were conducted at the Lotung site by HCK Geophysical Company, Taipei, Taiwan, in December of 1985. These tests were conducted as part of the initial characterization of the Lotung test site. Two crosshole arrays were used by HCK. One was located at the 1/4-scale model structure site (see Figure 8-10); the other array was located at the 1/12-scale model structure site. The travel distances between the source and the geophone holes during the crosshole tests varied from 30 ft to nearly 70 ft. Maximum depth of crosshole testing was about 200 ft. Uphole tests were conducted to depths of 500 ft. The boreholes used during the seismic testing program were lined with PVC casing. All holes were surveyed for verticality using drift (deviation) logging. Blasting caps were used as the source during all tests. Seismic signals were detected with 7.5-Hz geophones manufactured by GeoSpace Corporation. A spring set was used to physically push the geophones against the casing. No attempt was made to orient the geophones. An OYO Corporation Model 1220 Oscillograph recorded the signals.
- **Shear-Wave Refraction Testing.** Shear-wave refraction tests were conducted at Lotung in January of 1989 by the Ohsaki Research Institute (ORI) of Tokyo, Japan. These tests involved conducting shallow S-wave refraction tests within and next to the backfill material around the 1/4-scale structure. The purpose of these measurements was to determine relative values of P- and S-wave velocities in the upper 10 ft of backfill material and of native materials.
- **Attenuation Measurements.** No attenuation measurements were made during the seismic testing at Lotung. Estimates of material damping from back analyses of ground motion records have been made for Lotung by Chang et al. (1990) and Zeghal and Elgamal (1992), as part of other EPRI programs.

8.2.3 Attenuation Data Analysis

Procedures for determining P- and S-wave velocities from the field measurements described above followed relatively conventional velocity interpretation methods. Details for these methods are provided in Appendices 8.A1 through 8.A4. The remainder of this subsection summarizes procedures used during interpretation of damping from field measurements. Additional details about the attenuation interpretations are given in Appendix 8.A3.

Attenuation of seismic waves, recorded at two or more distances from a given source, can be determined using the amplitudes or amplitude ratios. The most frequently used technique is the spectral ratio method (Toksoz et al., 1979; Redpath et al., 1982; Redpath and Lee, 1986;

Mok, 1988). Fourier amplitude spectra of waveforms recorded at two distances are used. The amplitudes are corrected for geometric spreading. Generally, amplitudes decrease due to geometrical spreading in proportional to 1/r, where r is the source to geophone distance. Then the natural log of the corrected amplitude ratio is plotted as a function of frequency. If attenuation (Q^{-1}) is independent of frequency, the plot of the natural log versus frequency should be a straight line of slope equal to (–1/QV), where V is wave velocity.

The applicability and accuracy of this method depends on the validity of the following assumptions: (1) the coupling and response of the two sensors (geophones) are the same for all frequencies; (2) the geometric spreading factor is independent of frequency; and (3) the attenuation Q^{-1} is independent of frequency in the spectral band of interest. The accuracy of the method improves when signal-to-noise ratio is high over a wide frequency band.

If there are waveform measurements at several (e.g., 10) distances from a given source, another method can be used to determine attenuation using amplitude versus distance. Fourier amplitude spectra are calculated for each pulse after correction for geometric spreading. At each frequency, amplitude ratios are calculated using a reference location, generally the instrument closest to the source. Then at each frequency the natural log of amplitude ratios is plotted versus distance. Ideally, at a given frequency Ä, the plot should be a straight line with the slope -1Ä/QV. The advantage of this method over the spectral ratio method is that the assumption that Q be independent of frequency is not needed, if one assumes that the geometrical spreading factor is frequency independent. Thus, the frequency dependence of Q may be determined from the data. This approach was used by Kudo and Shima (1970) for determining soil attenuation in the Tokyo metropolis, and Pujol and Smithson (1991) for determining rock attenuation in the northwestern United States.

A third method, based on waveform matching and inversion, was also used to determine attenuation from crosshole and downhole measurements at the Treasure Island and Gilroy 2 sites. This technique, described in Appendix 8.A3, uses the phase and amplitude match between the two waveforms recorded at different distances from a common source. The method was initially developed for determining attenuation in the laboratory (Tang et al., 1988; Tang, 1992) and was applied to the field data for the first time under this project. The method has the advantage of being robust by utilizing both the phase and amplitude information. However, it is computationally more intensive than the spectral ratio method. Despite this limitation, it was concluded from the results of this project that the waveform matching method is the best approach for determining damping, or attenuation, from velocity measurements.

In all methods once Q is extracted from the in situ measurements, the material damping ratio, D = 1/2Q, is computed. Within this document D is often shown in percent, which is equivalent to 100/2Q.

8.2.4 Results of Velocity and Attenuation Measurements

Detailed results for all seismic measurements and analyses carried out as part of this project are included in the Appendices (8.A1 through 8.A4). Additional information about site explorations and seismic testing is given by Gibbs et al. (1992a) and in de Alba et al. (1992). The following paragraphs provide a summary of velocity and attenuation information collected at the three reference sites.

8.2.4.1 Gilroy 2

Results of velocity and attenuation measurements at the Gilroy 2 site are summarized in Figures 8-16 through 8-23. Velocity results from different programs are shown together to provide a visual indication of velocity variations that occur for the different investigators.

P- and S-Wave Velocities. Figures 8-15 and 8-17 are composite plots of the S-wave velocities measured at the Gilroy 2 site using the suspension, downhole, and crosshole methods. Figures 8-18 through 8-21 are composite plots of the P-wave velocities measured using the three methods.

These results show that the average S-wave velocity increases from approximately 500 fps at the ground surface to as high as 6,500 fps in the bedrock at 770 ft. Both depth and geologic formation affect the average velocity, with a significant decrease in velocity occurring at 70 ft as the geologic formation changes from a gravelly sandy material to fine-grained lake deposits. At any single depth the S-wave velocity can vary with lateral location by several hundred feet per second, or about 5 to 10% of the average velocity. No single measurement

method appears to be consistently higher or lower than the average recorded value, although it is clear from the data that the crosshole and suspension logging method were more capable of detecting velocity variations with depth. The results suggest that the differences in velocity between methods are a random variation resulting from differences in testing methodology, data interpretation, and wave propagation path.

P-wave velocities range from 1,000 fps at the ground surface to nearly 12,000 fps at the bottom of the borehole. A nearly constant velocity of 5,000 to 7,000 fps occurs between depths of 70 ft and 540 ft, indicating saturated soil deposits. The variation in P-wave velocity with lateral location approaches several thousand feet per second, or nearly 30% of the average velocity. In the upper 70 ft of soil profile, the variation for the different measurements was nearly 100% at some depths. Much of this scatter can be attributed to the heterogeneous soil, particularly the alluvium deposits where gravels occur. The effects of heterogenous soil conditions are shown in Figures 8-20 and 8-21 by the range of values for different travel paths recorded by a single investigator, the University of Texas. These results clearly indicate the value of using more than one testing method and presenting results for all travel paths, rather than just average velocity values.

It is noted that the smallest variation in S-wave velocity occurred in the Pleistocene Lake Deposits where the variation was less than a 200 fps. Soil in this deposit is very uniform in consistency relative to the alluvium deposits above and below it. These results indicate that very good agreement can be obtained among different investigators if soil is uniform in consistency. As material becomes more heterogeneous, the scatter in results increases. At least part of the variation at deeper depths can be attributed to a combination of data sampling intervals and frequency effects.

Attenuation Values. An extensive study of S-wave damping was carried out at the Gilroy 2 site. This included downhole measurements by USGS (Gibbs et al., 1992a), downhole measurements by Agbabian Associates, crosshole measurements by the University of Texas, and laboratory resonant column measurements carried out by the University of Texas (see Section 8.2 for detailed discussion of these laboratory tests.) Figure 8-22 shows the composite results of all the damping measurements. These results show that in situ values of damping generally varied from 2 to 6% depending on the depth and the method of determination.

The damping values from crosshole data were obtained by spectral ratio and spectral slope methods at depths of 15, 25, 115, and 125 ft. Resonant column measurements were also made on samples from the four depths. From the University of Texas crosshole data, MIT investigators obtained damping values in the depth range of 10 to 190 ft using the waveform inversion method (Appendix 8.A3). In situ damping values obtained by the University of Texas and MIT agree well with each other. These values are higher, by a factor of two, than the laboratory results. The frequencies of testing during the resonant column tests were approximately 39 Hz for samples from 15 ft and 25 ft, and 92 Hz for samples from 115 ft and 125 ft. These values were generally less than the in situ tests and presumably contributed to the difference between field and laboratory values.

The downhole (VSP) test provided damping values averaged over 50 and 100 ft or greater depth intervals. As a result, these average over different soil layers (i.e., lithologic units). Furthermore, downhole damping values, unless corrected for wave propagation, velocity-dependent geometric spreading, and at lithologic boundaries, cannot be compared directly with crosshole and laboratory data that specifically give the damping values for a given lithologic unit. Four sets of downhole damping values are shown in Figure 8-22. The first is the Agbabian interval damping based on spectral slope. The second set is damping calculated from Agbabian data using the MIT waveform inversion and correcting for wave propagation and reflection effects. The other two sets of downhole damping are USGS measurements, one based on spectral ratios and the second based on wave propagation as described by Gibbs et al. (1992b).

Figure 8-23 shows the S-wave damping versus depth profile obtained by the MIT waveform inversion of the University of Texas crosshole data. Plotted on the same depth scale are the S-wave velocity profile determined by the University of Texas and the geologic log from USGS (Gibbs et al., 1992a). A comparison of the damping and velocity results in Figure 8-23 shows some surprising correlations. High damping is correlated with high shear-wave velocities at depths of about 60 and 180 ft. These zones are characterized as "sandy fine gravel" and "gravel," respectively. In clay, sand loam, and silty clay units, both damping and velocities are lower.

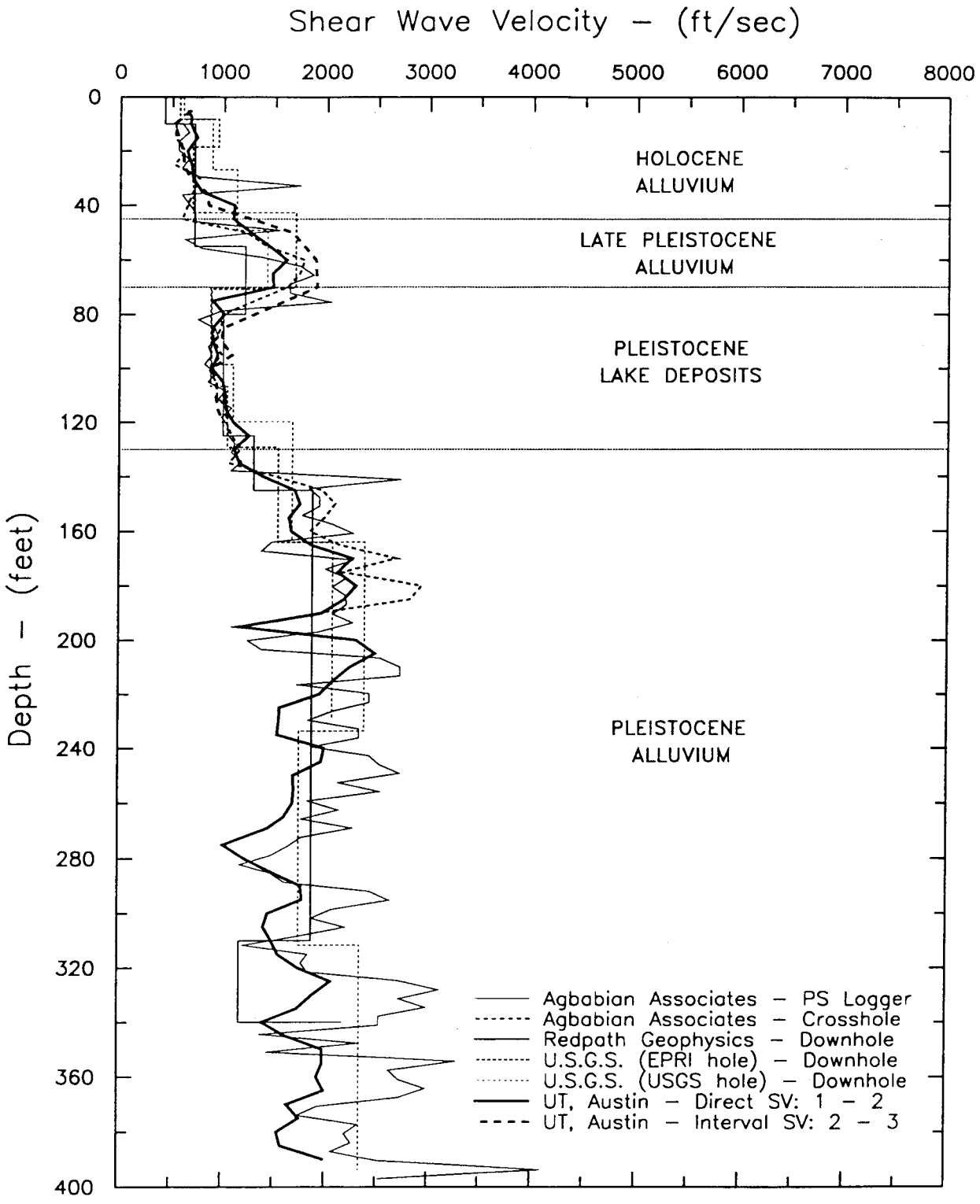

Figure 8-16. S-wave velocity measurements at Gilroy 2 (0 to 400 ft).

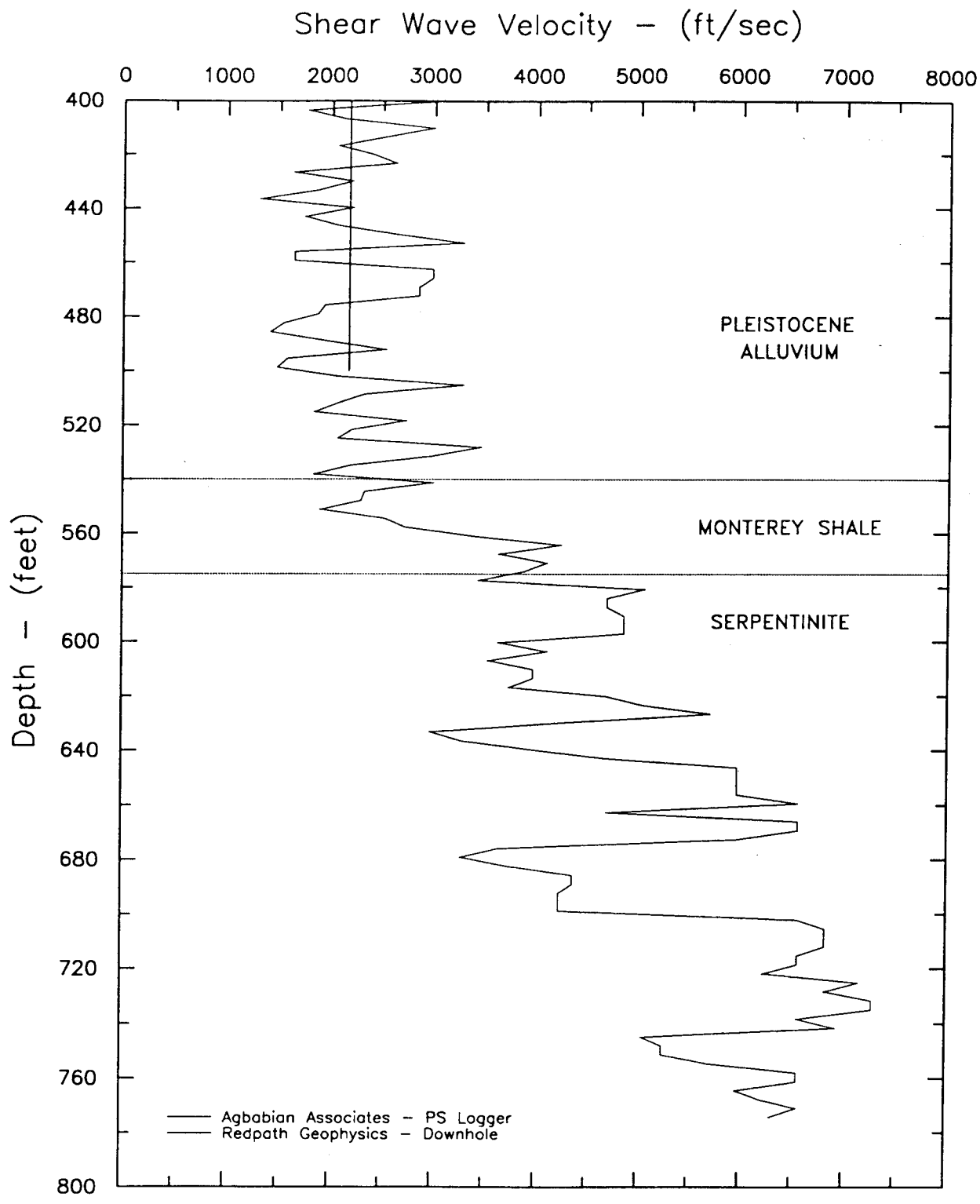

Figure 8-17. S-wave velocity measurements at Gilroy 2 (400 to 800 ft).

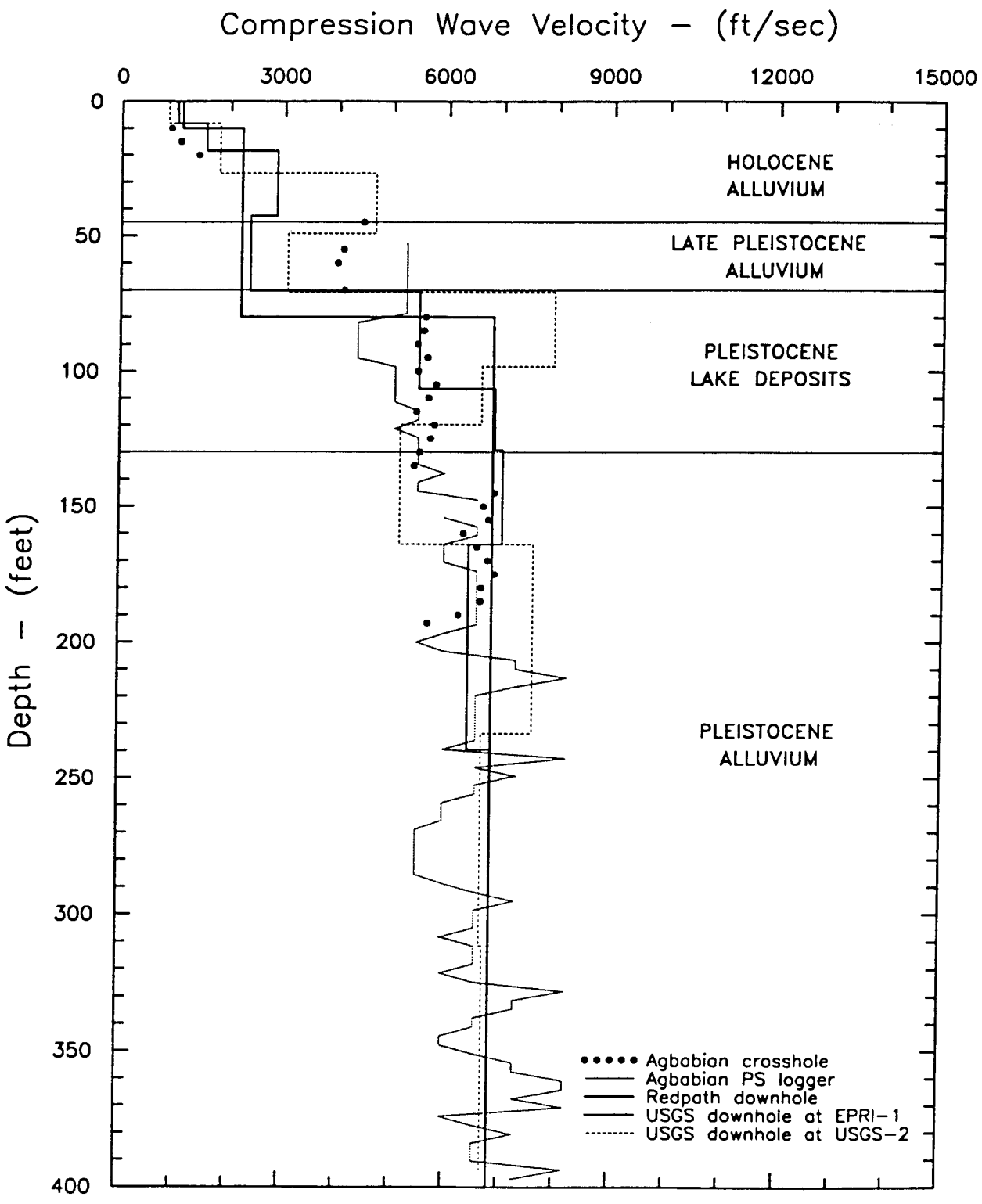

Figure 8-18. P-wave velocity measurements at Gilroy 2 (0 to 400 ft).

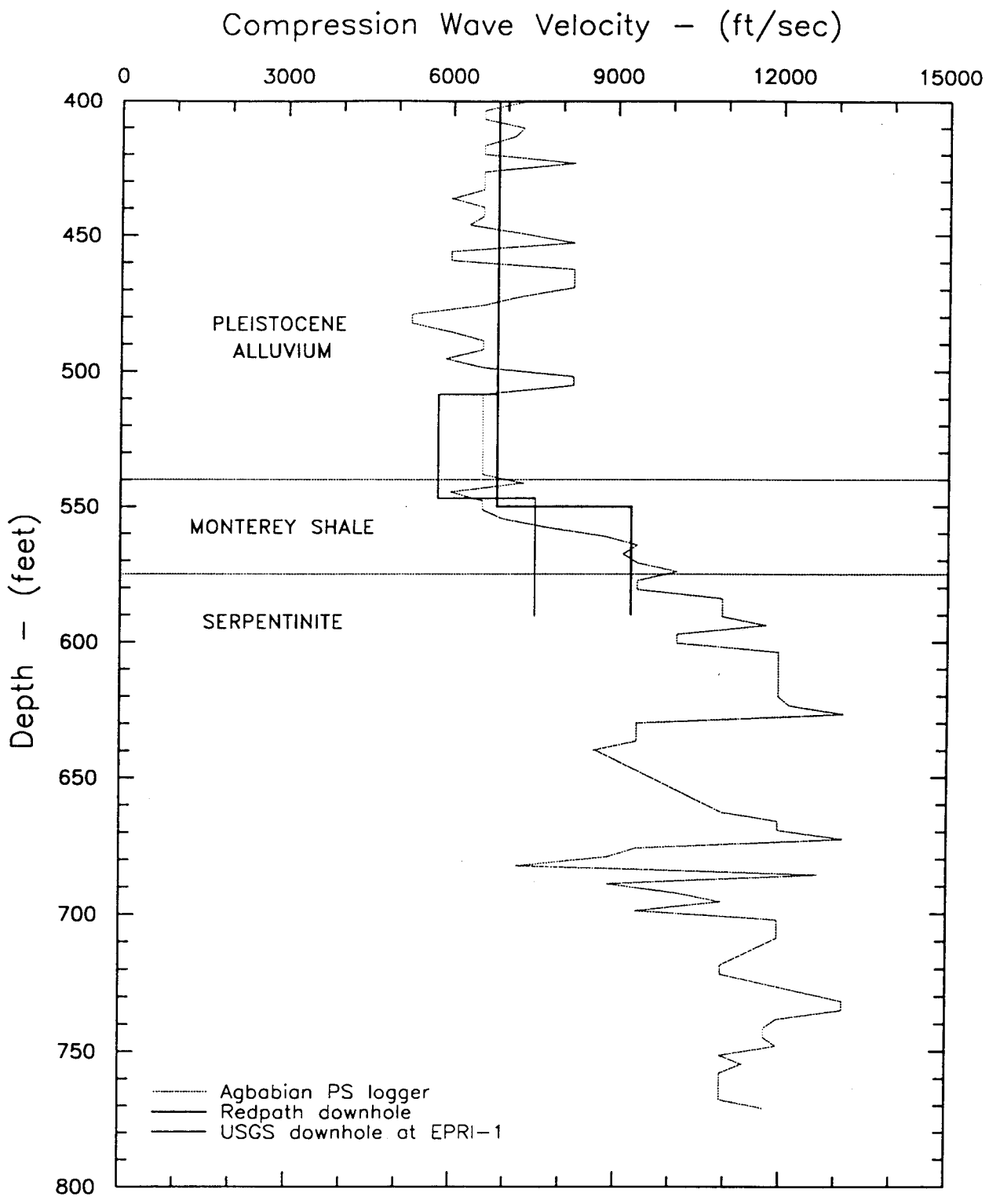

Figure 8-19. P-wave velocity measurements at Gilroy 2 (400 to 800 ft).

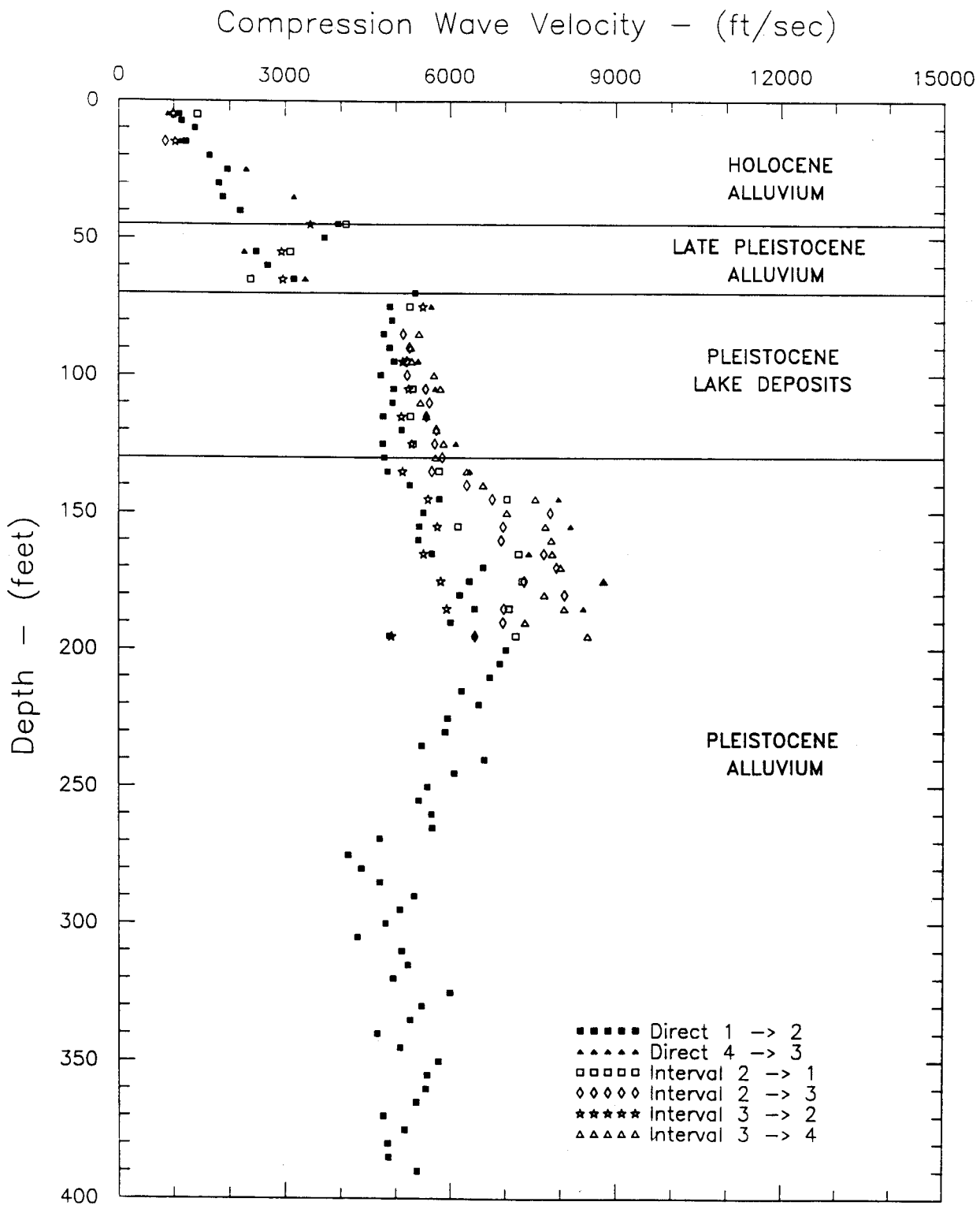

Figure 8-20. P-wave velocity measurements at Gilroy 2 (University of Texas—hammer source).

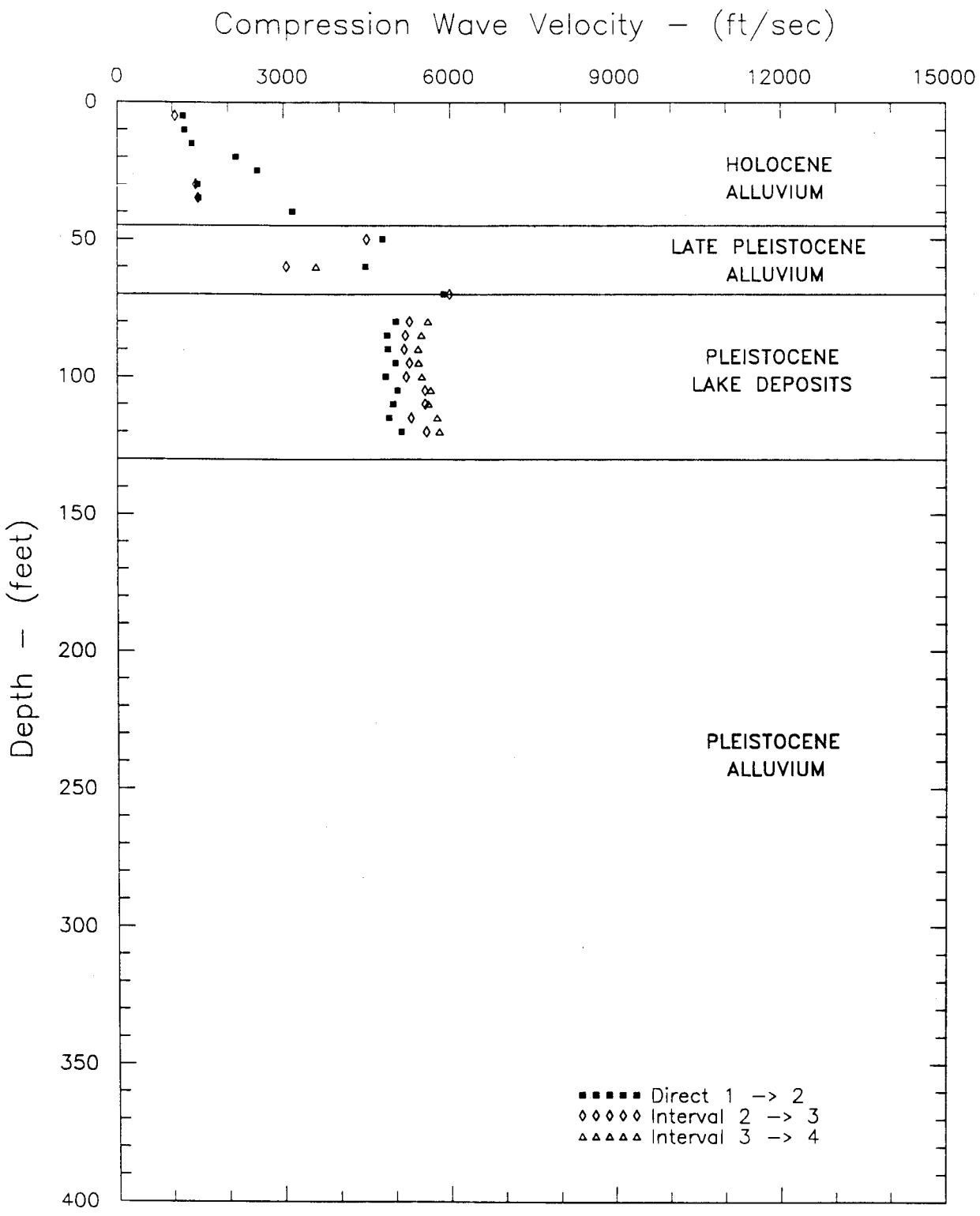

Figure 8-21. P-wave velocity measurements at Gilroy 2 (University of Texas—solenoid source).

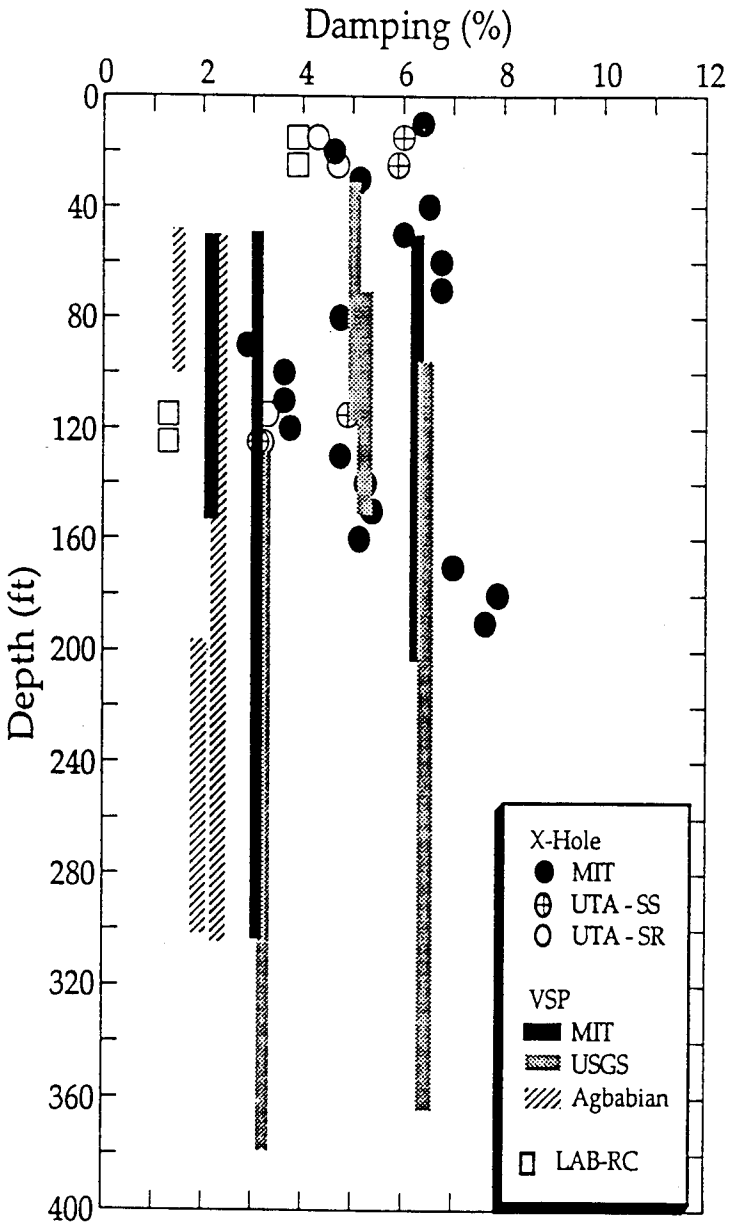

Figure 8-22. S-wave damping ratio measurements at Gilroy 2.

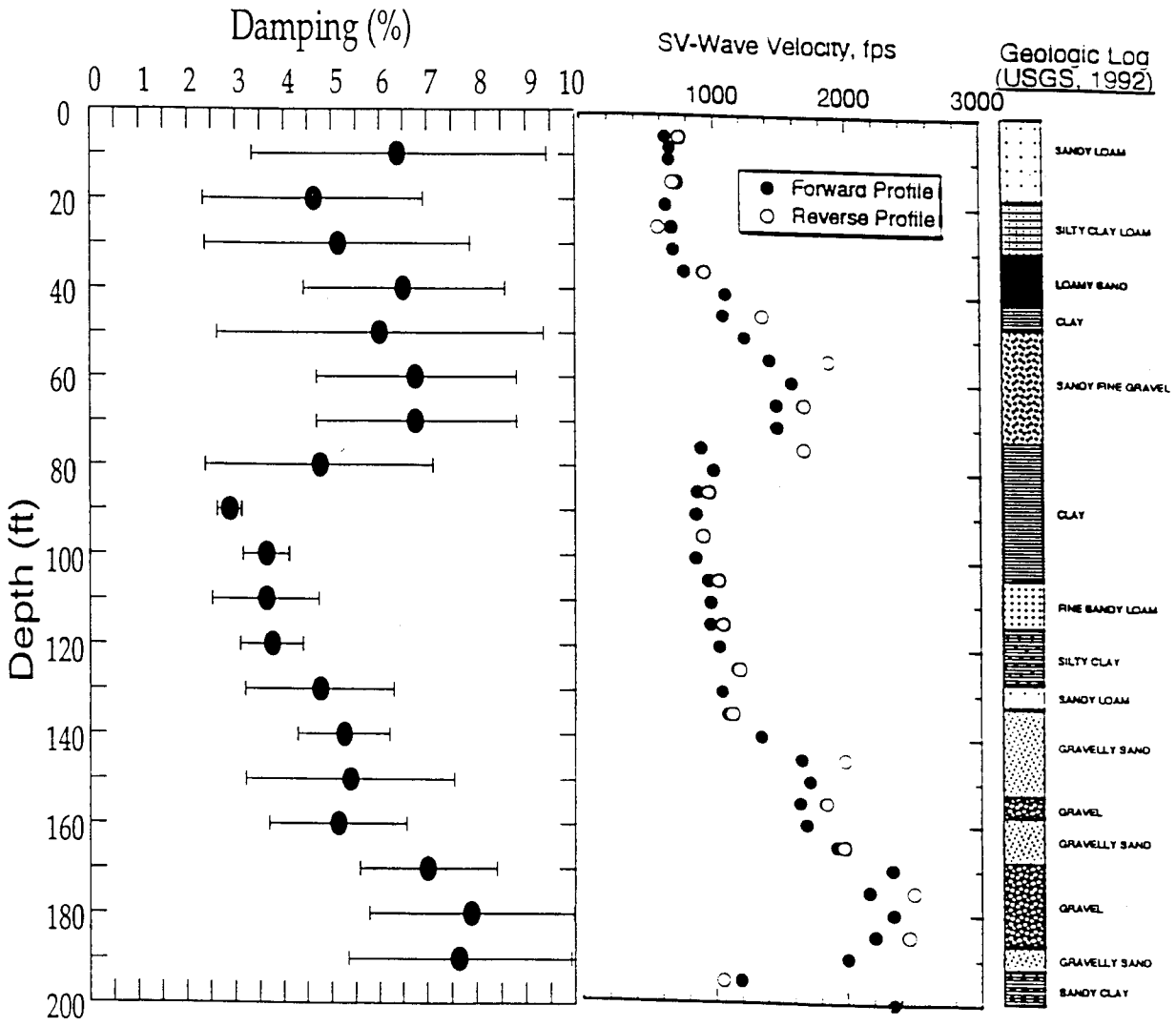

Figure 8-23. Average S-wave damping from crosshole data at Gilroy 2.

8.2.4.2 Treasure Island

Results of the velocity and attenuation measurements at the Treasure Island site are summarized in Figures 8-24 though 8-29. As with the presentation of the Gilroy 2 data, results of various investigators are shown on the same plot to indicate the range of velocities that can be expected.

P- and S-Wave Velocities. Figure 8-24 is a composite plot of the S-wave velocities measured at the Treasure Island site using the downhole, crosshole, and seismic cone methods. Figures 8-25 through 8-27 are composite plots of the P-wave velocities measured using the downhole and crosshole methods.

The S-wave results show that velocities increase from approximately 500 fps at the surface to slightly more than 2,000 fps at a depth of 300 ft. The velocities varied with both depth and geologic formation. Variation in results from different investigators was relatively small, typically ranging from less than 100 fps to a maximum of 300 fps. This variation represents approximately 20% of the measured average velocities. As with the Gilroy 2 data, no investigator was consistently high or low, suggesting that variations that do occur are due to subtle variations in soil conditions along travel paths and interpretation differences.

Figures 8-25 through 8-27 show variations in P-wave velocities. These results confirm that the groundwater is very near the ground surface, as evidenced by velocities increasing to approximately 5,000 fps in the upper 10 ft. P-wave velocities in the bedrock range from 6,000 to 10,000 fps, which is consistent with the low S-wave velocities. The variation in P-wave velocity at any depth can be as much as 50%. Similar to the Gilroy 2 data, much of this variation can be attributed to differences in soil conditions, as shown in Figure 8-26 and 8-27 where measurements were made by a single investigator.

The reduction in P-wave velocity within the Young Bay Mud layer between depths of 50 ft and 90 ft was consistently observed by all investigators. The very low P-wave velocities, less than 4,000 fps, suggest that the material is not fully saturated. This condition may be due to decomposition of organic materials, resulting in gas bubbles within the deposit. Similar results were obtained at Lotung.

Attenuation Values. Figure 8-28 plots the results of the attenuation measurements at the Treasure Island site. These results were determined from the field measurements by Agbabian and the University of Texas using the spectral slope, spectral ratio, and MIT waveform fitting methods. They show that the in situ values of material damping range from 1 to 3.5%. At any given depth the damping variation is typically several percent. For these results, the magnitude of damping is consistently less in the laboratory than determined by the in situ measurements, opposite that which was observed at Gilroy 2.

From Figure 8-28 it can be seen that down to 100-ft depth, there is an overlap between downhole (VSP), crosshole, and laboratory damping measurements. Laboratory-measured damping is lower than the crosshole in situ damping. Downhole damping values vary greatly. Based on both the Treasure Island and Gilroy experiments, it is difficult to determine damping from downhole data when receivers are 50 ft apart. To obtain reliable in situ damping from downhole data, it would be best to use about 10-ft vertical spacing of geophone receivers. This was done by the USGS at Gilroy 2.

Figure 8-29 shows the damping ratio versus depth obtained from the University of Texas crosshole data by the MIT waveform inversion method. Also shown in this figure is the University of Texas S-wave velocity profile and the USGS geologic log (Gibbs et al., 1992a). Comparison of the velocity and damping profiles shows that higher velocities at 30 ft and 70 ft are correlated with high damping values. The correlation at a depth of 70 ft is especially significant since the geologic log does not show a separate unit at this depth. Most probably there is a sand layer or a layer with shells at this depth.

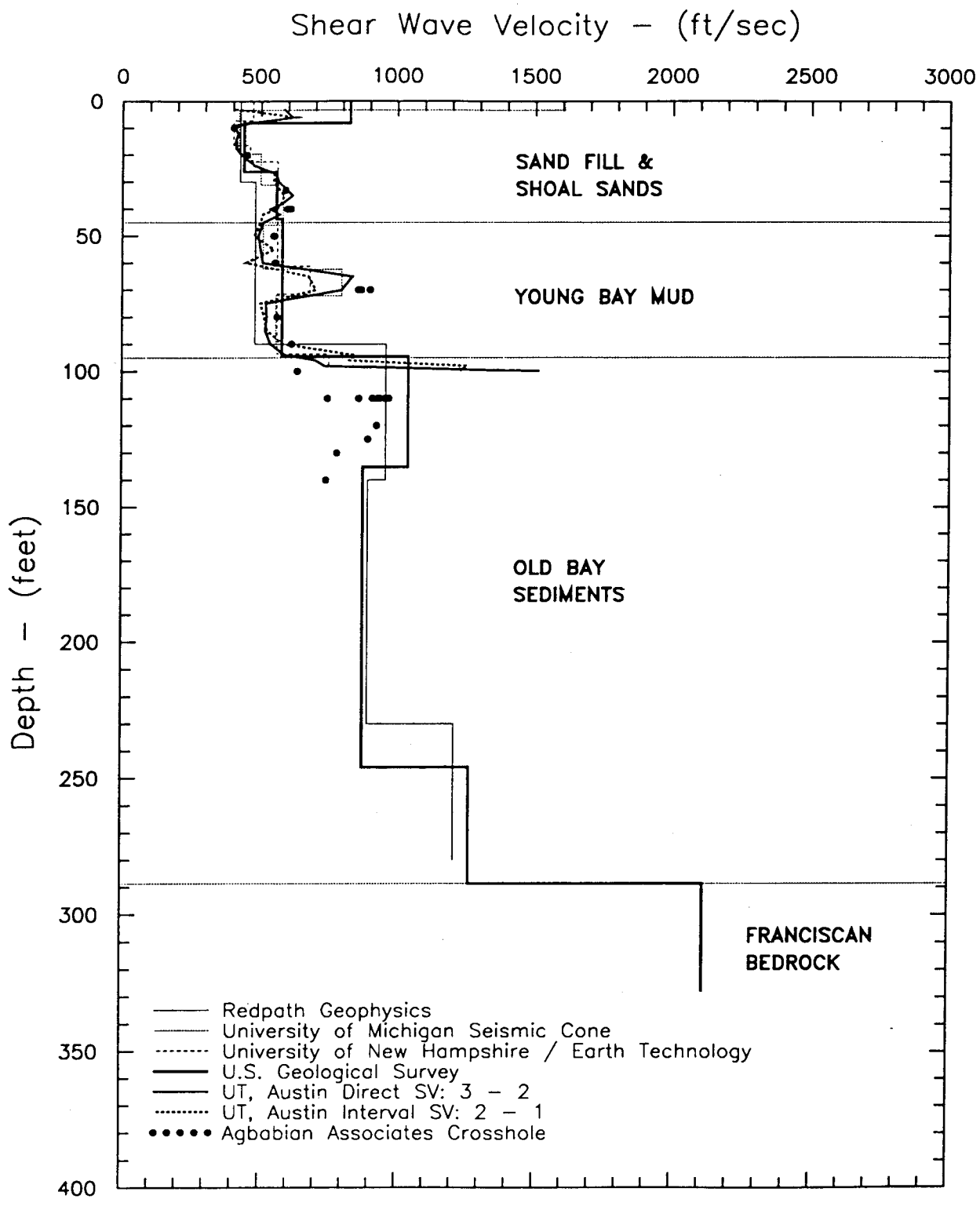

Figure 8-24. S-wave velocity measurements at Treasure Island.

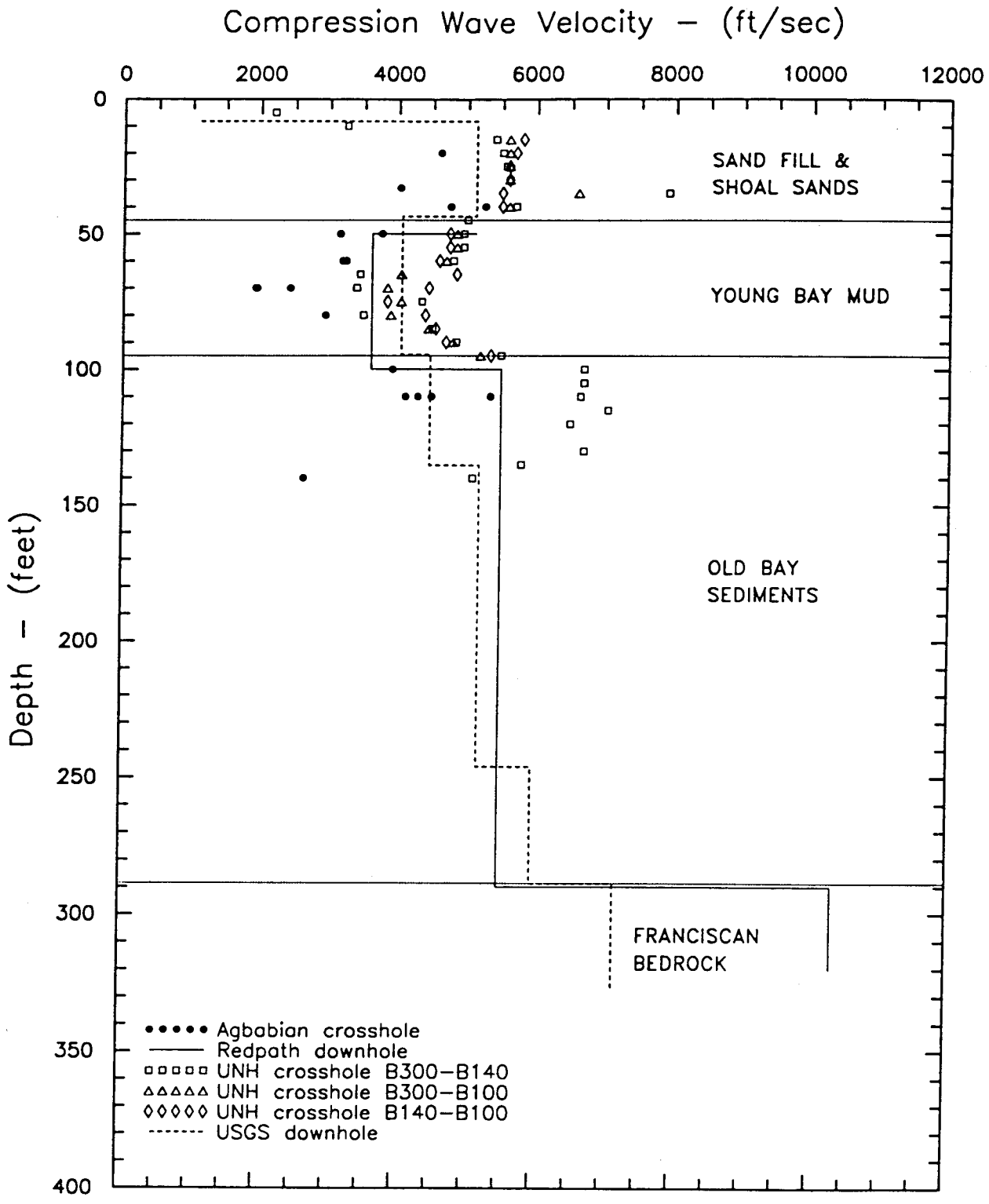

Figure 8-25. P-wave velocity measurements at Treasure Island.

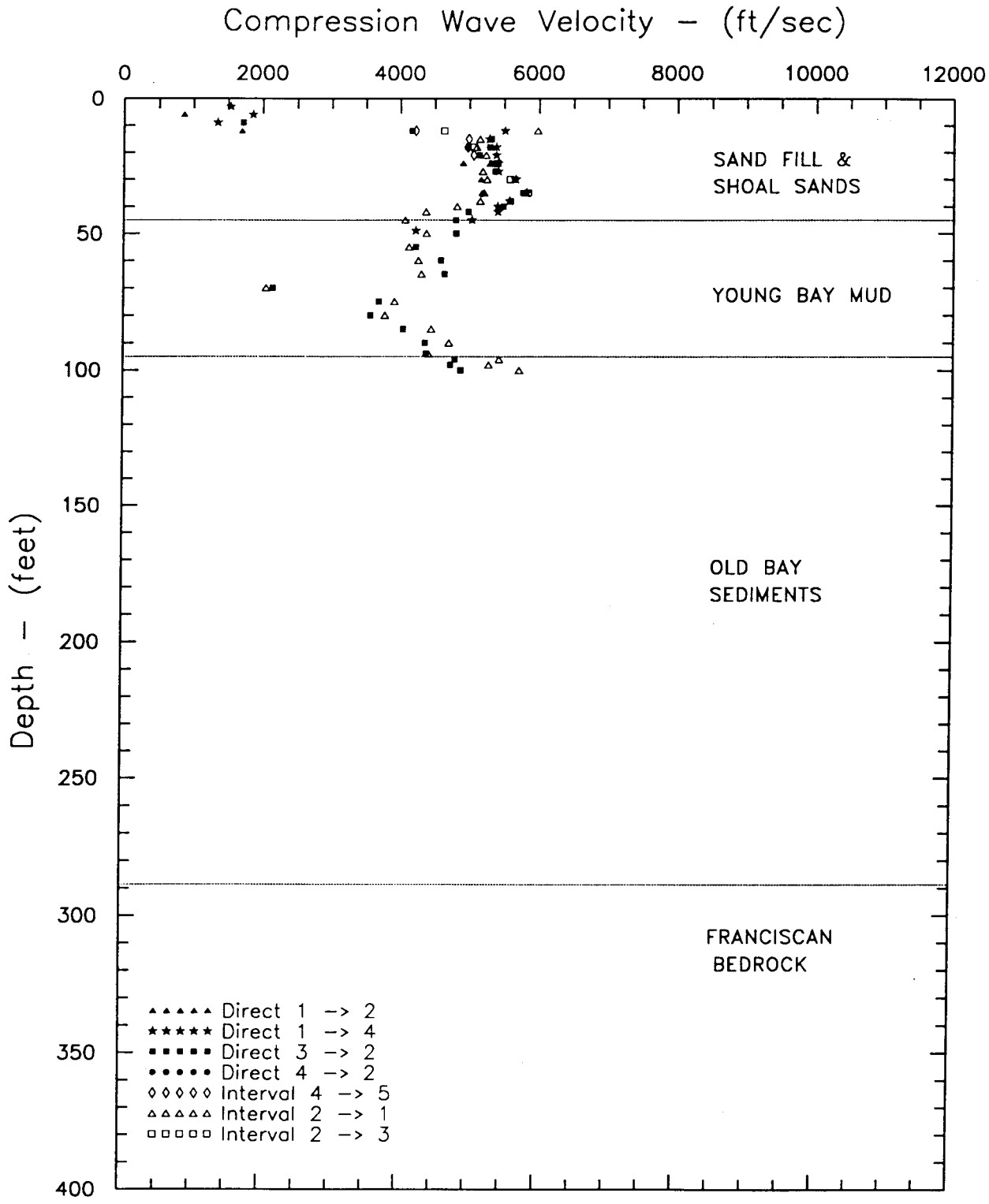

Figure 8-26. P-wave velocity measurements at Treasure Island (University of Texas—solenoid source).

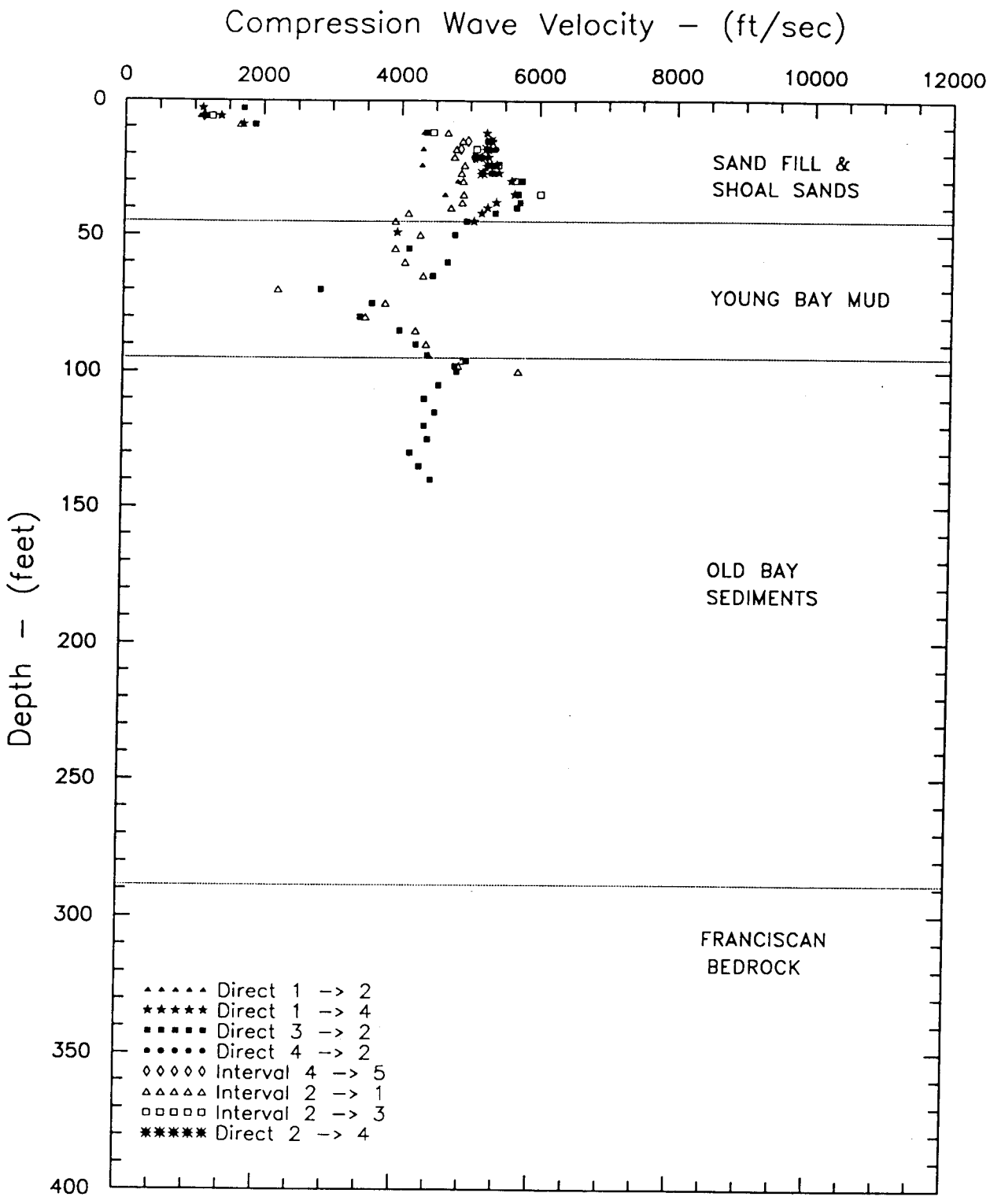

Figure 8-27. P-wave velocity measurements at Treasure Island (University of Texas—hammer source).

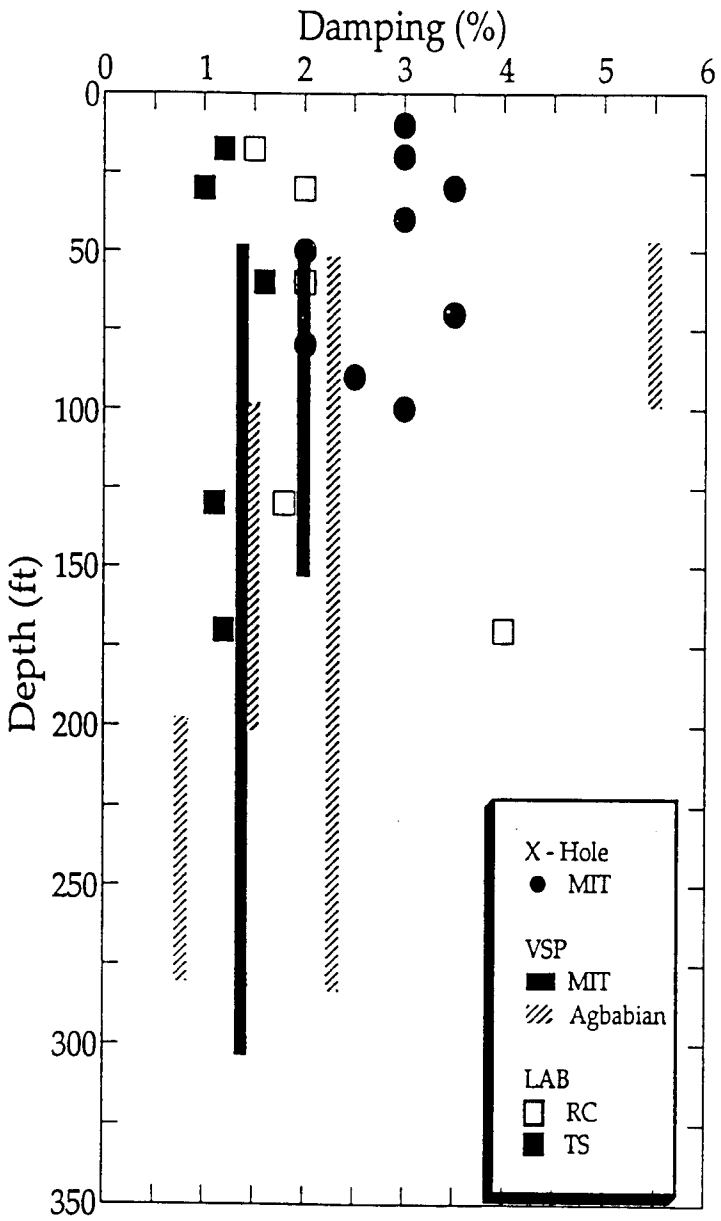

Figure 8-28. S-wave damping ratio measurements at Treasure Island.

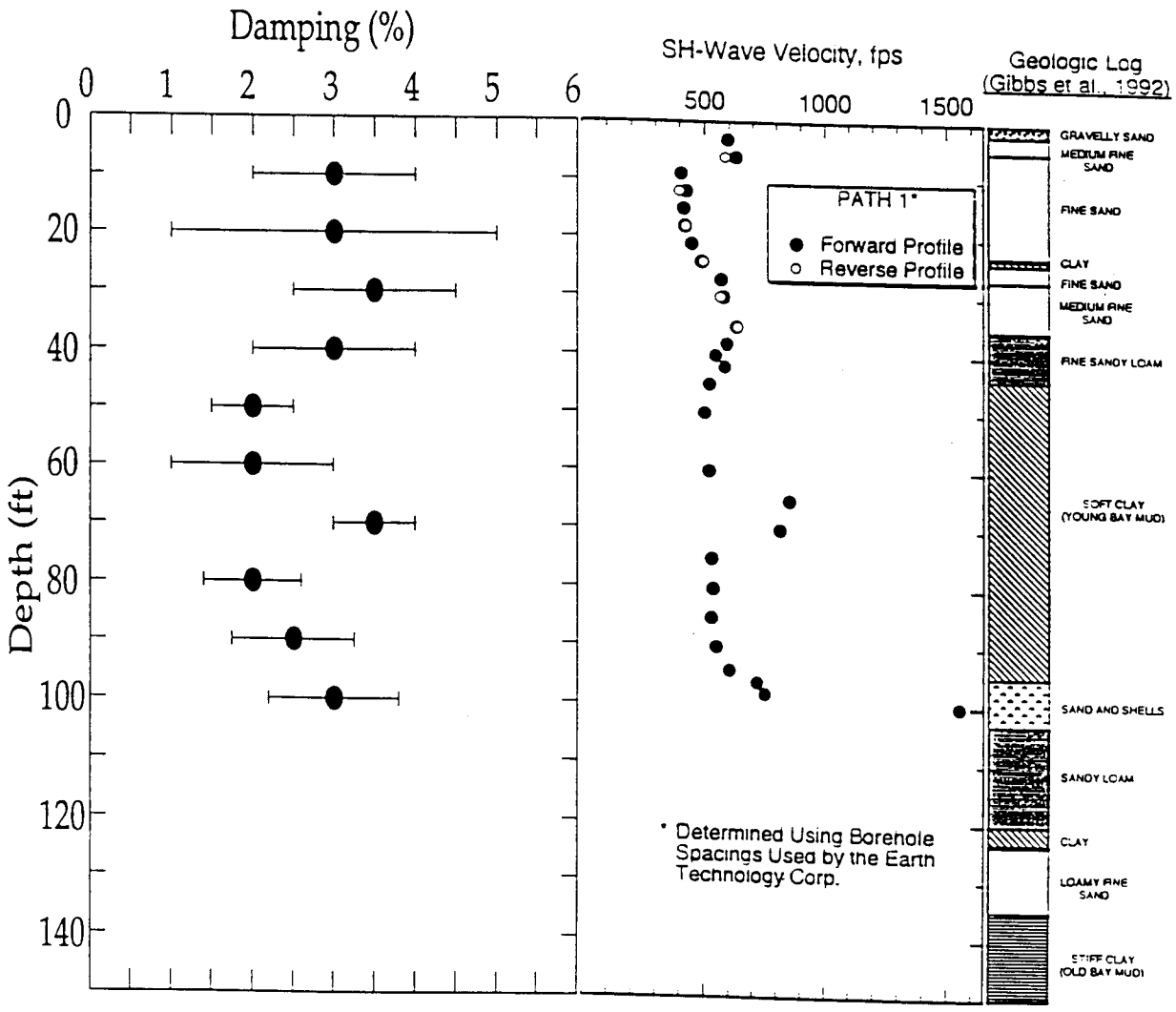

Figure 8-29. Average S-wave damping from crosshole data at Treasure Island.

8.2.4.3 Lotung

Result of the velocity measurements obtained during previous EPRI programs at Lotung are summarized below.

Seismic Reflection Results. Figure 8-30 shows P-wave velocities measured during deep seismic reflection studies at the site (Anderson, 1993). This figure indicates that P-wave velocities within the Pleistocene layer vary from 6,000 to 7,000 fps. P-wave velocities in the basement rock range from 10,000 to 13,000 fps.

P- and S-Wave Velocities. Figures 8-31 and 8-32 are composite plots of the S-wave and P-wave velocities, respectively, measured at the Lotung site using crosshole methods. Different symbols indicate velocities measured along different paths. Results of the uphole testing are summarized in Table 8-8.

These results indicate that S-wave velocities typically varied by 100 to 200 fps, or about 20%, while P-wave velocities varied by approximately 1,000 fps, or about 20% of the average velocity. The low P-wave velocities above a depth of 40 ft, despite the high groundwater level, suggest less than full saturation of the soil.

The ORI S-wave refraction tests provided an estimate of S-wave velocities in the upper few feet at the Lotung site. These velocities ranged from 330 to 600 fps. It can be observed from Figure 8-29 that these velocities are considerably higher than the results of the HCK crosshole tests. No explanation for this difference has been determined (Anderson, 1993).

8.3 Laboratory Investigations

A series of laboratory tests has been conducted on high-quality, undisturbed samples of soil obtained from the Gilroy 2, Treasure Island, and Lotung sites. The primary purpose of these tests was to establish the dynamic properties of the soil for use in site-specific ground response analyses (see Sections 6 and 9). Dynamic properties of primary interest included the soil shear modulus and material damping ratio (in shear), and their variations with:

- shearing strain amplitude
- effective confining pressure
- frequency of cyclic loading
- duration of loading at a sustained confining pressure, and
- number of repetitions of cyclic loading

In addition to the dynamic laboratory testing of the soil from the reference sites, two additional series of dynamic laboratory tests were conducted. The first involved a series of high-pressure resonant column tests on remolded dry sand samples and several undisturbed samples. These tests were conducted to evaluate the effects of confining pressures, above those normally used in laboratory testing, on shear modulus and material damping ratio. The second series of tests involved wave attenuation (damping) measurements in dry sand confined in a large-scale triaxial chamber (LSTC). These tests were specifically conducted to evaluate the use of wave attenuation methods in determining material damping for well-controlled soil conditions.

The laboratory testing program also included a series of classification tests. These tests were conducted to provide information regarding the specific types of soil being tested. The classification test information also provided a basis for checking measured properties against values predicted using published relationships and basic classification properties.

The laboratory tests described in this section were conducted at the University of Texas. Detailed results of the University of Texas test program are included in Appendix 8.B1 for Treasure Island, Appendix 8.B2 for Gilroy 2, Appendix 8.B3 for Lotung, Appendix 8.B4 for the high pressure testing, and Appendix 8.B5 for the LSTC testing.

8.3.1 Method

The University of Texas laboratory testing program involved the use of resonant column/torsional shear equipment, and a large-scale triaxial chamber for dynamic property measurement. The resonant column/torsional shear device was used because this equipment has the capabilities of combining different test methods in terms of shearing strain levels and rates of loading into one device. The LSTC was used because it provided a method for determining soil attenuation, or material damping, that closely approximates methods that would occur during field experiments (Section 8.2). However, these tests were conducted in the laboratory

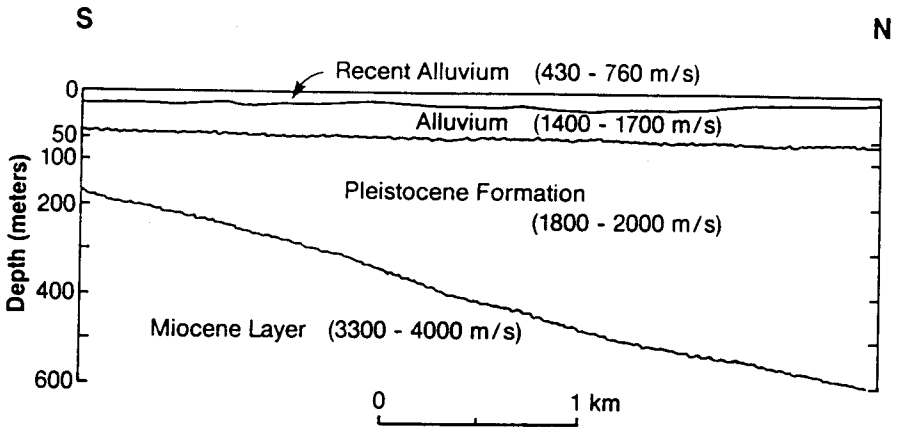

a) Geological Profile and Compressional Wave Velocity Along North-South Section

After Tang (1)

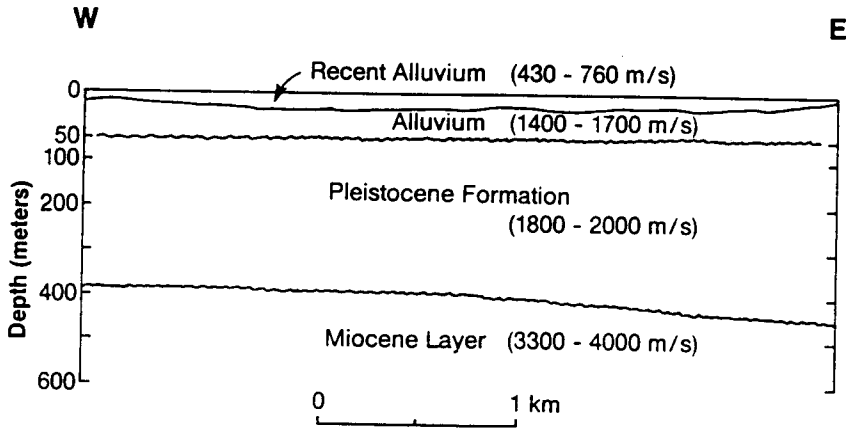

b) Geological Profile and Compressional Wave Velocity Along East-West Section

Figure 8-30. Deep P-wave velocities at Lotung.

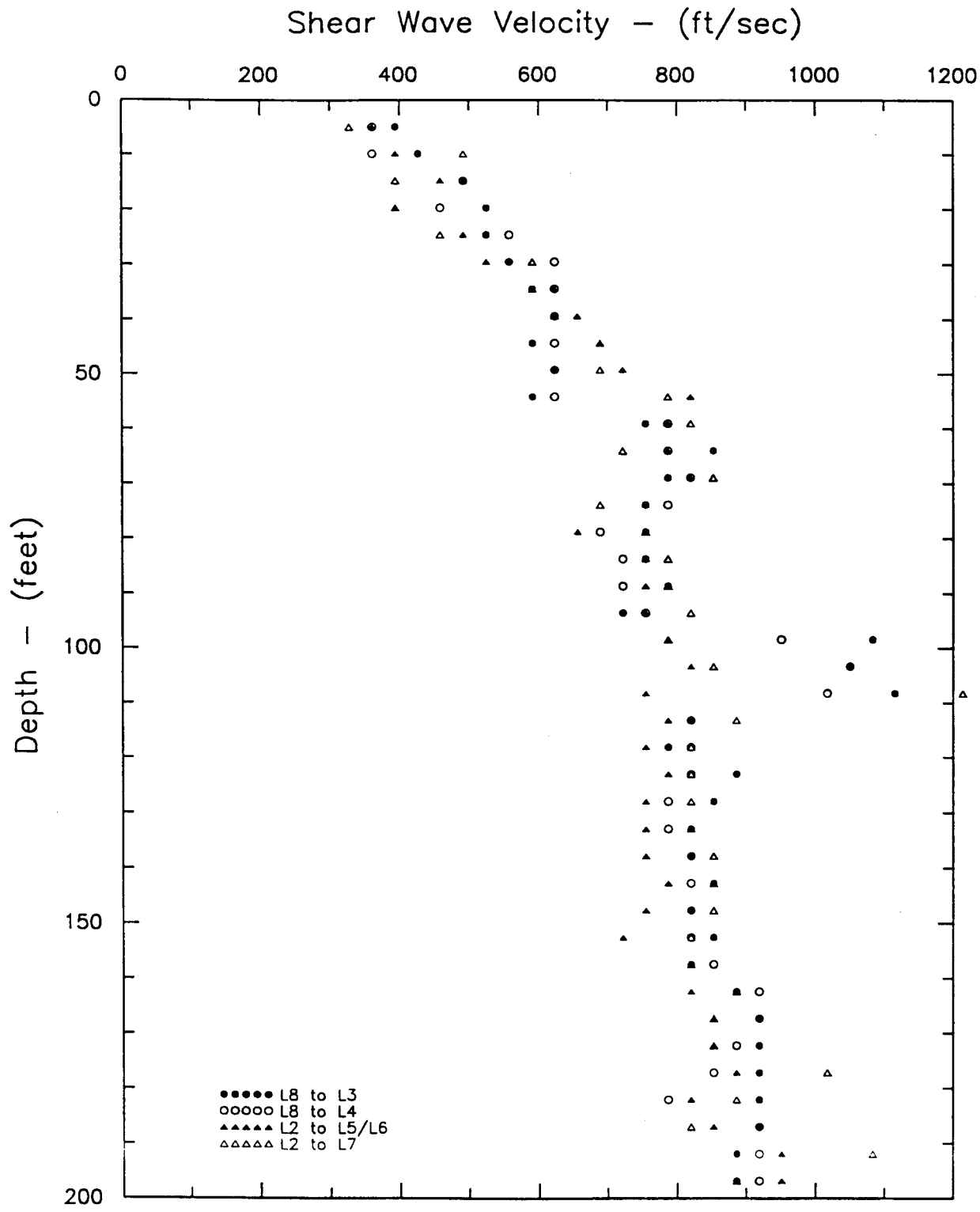

Figure 8-31. S-wave velocities at Lotung.

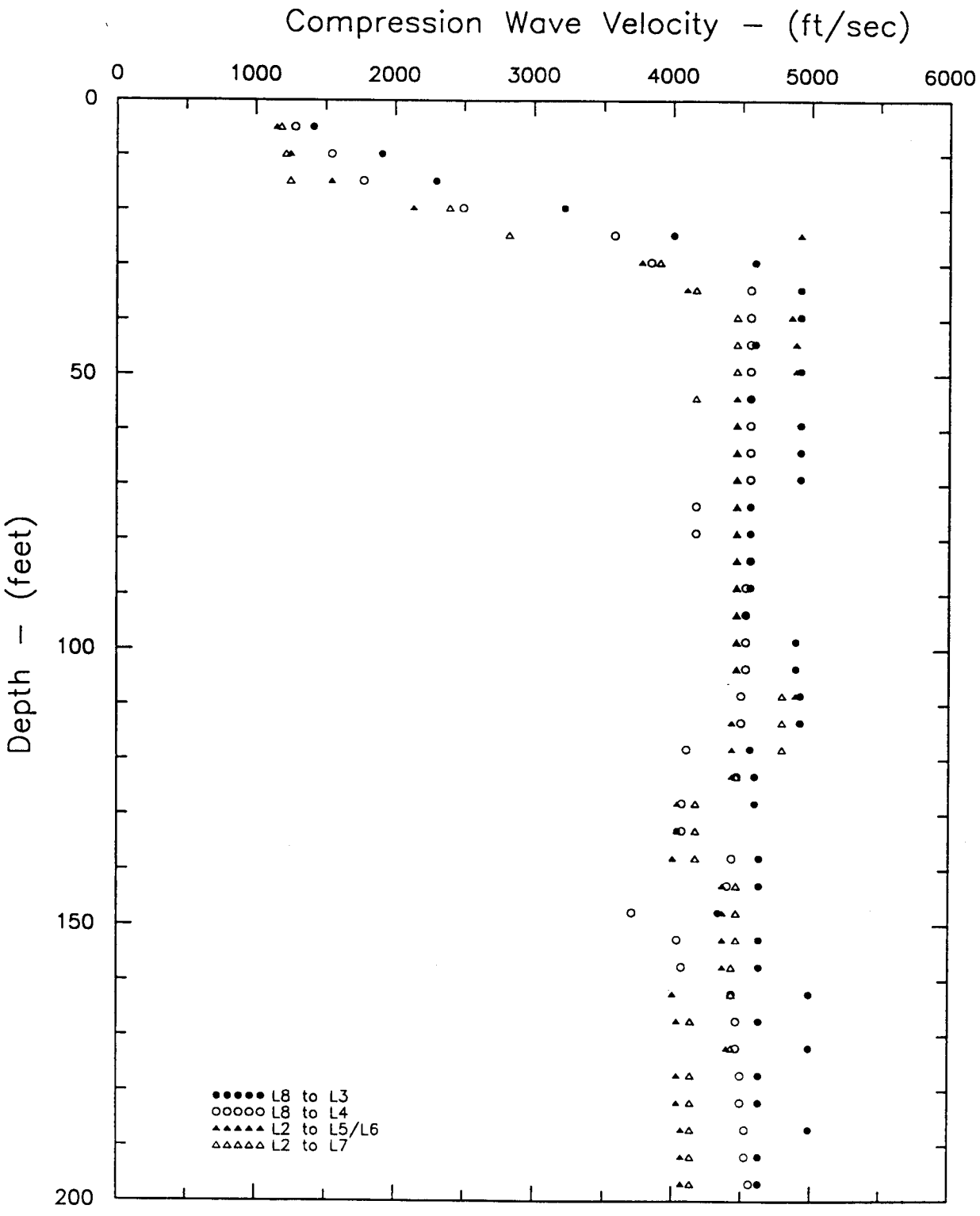

Figure 8-32. P-wave velocities at Lotung.

Table 8-8

Results of Uphole Seismic Testing at Lotung Site

Depth Interval (ft)	P-Wave Velocities (fps)			S-Wave Velocities (fps)
	L2	L3	L4	
0–16	920	950	886	—
16–26	1804	950	886	—
26–197	4822	4986	5248	—
197–262	4822	—	—	1050
262–492	5051	—	—	1574

where soil preparation methods, soil boundary conditions, and seismic wave generation and measurement systems could be closely controlled.

8.3.1.1 RCTS Equipment

The resonant column and torsional shear (RCTS) equipment has been developed at the University of Texas over the past two decades. The equipment is of the fixed-free type, with the bottom of the specimen fixed and torsional excitation applied to the top. The equipment is an outgrowth of the resonant column testing devices that were first used in the late 1960's. SW/AA (1972) provide a general discussion of resonant column and cyclic torsion testing methods. Richart et al. (1970) discuss the theory used during the resonant column tests. Numerous technical publications that deal with resonant column and cyclic torsion testing can be found in the ASCE geotechnical journal and the ASTM testing journal. An ASTM standard (D4015-81) has been prepared for resonant column testing.

The University of Texas RCTS apparatus is set up such that resonant column (RC) or torsional shear (TS) tests can be performed in a sequential series on the same specimen over a cyclic shearing strain range from about 10^{-4}% to more than 10^{-1}%. The primary difference between the two types of tests is the excitation frequency. In the RC test, frequencies above 20 Hz are required and inertia of the specimen and drive system are needed to analyze the measurements. The TS test involves slow cyclic loading with frequencies generally below 5 Hz, and inertia does not enter data analyses at frequencies below 1 Hz.

For the RC test the soil sample is vibrated in first-mode torsional motion by applying torsional excitation to the top of the specimen. First-mode resonance is established by varying the excitation frequency until the maximum response occurs. This frequency together with equipment characteristics and specimen size are used to calculate the S-wave velocity, from which shear modulus can be derived. By modifying the level of excitation, different levels of shearing strain can be achieved. Material damping is determined either from the width of the frequency response curve or from the free-vibration decay curve. The TS test also involves the application of torsional excitation to the top of the specimen. However, in this case the stress-strain hysteresis loop is determined by measuring the torque-twist response of the specimen. Shear modulus is calculated from the slope of a line through the end points of the hysteresis loop, and material damping is obtained from the area of the hysteresis loop. Details of these analysis methods are provided in the appendices to the laboratory testing reports (Appendices 8.B1 through 8.B4).

The basic components of the University of Texas RCTS equipment used during the program are as follows:

- a confining pressure chamber system capable of developing isotropic confining pressures to 500 psi. A fluid bath surrounds the specimen such that air pressure is applied to the fluid bath which in turn pressurizes a rubber membrane-encased test specimen.
- a coil-magnet drive system capable of applying up to 0.60 lb-ft of torque.
- a vertical height monitoring system capable of measuring changes in vertical specimen height during sample consolidation to less than 0.0001 inches.
- a horizontal motion monitoring system. In the RC device the motion monitoring system involves use of an accelerometer. The accelerometer is capable of measuring acceleration of the specimen-top cap system to less than 10^{-3}g. The TS test involves the use of proximity sensors. These sensors can record torsional motions to as small as 0.0001 radians.

Laboratory tests were carried out on undisturbed samples from the reference sites and on reconstituted samples of washed mortar sand for some of the high confining pressure tests. Undisturbed samples were extruded from short sections of the 3-inch diameter sampling tubes and hand trimmed to the final specimen dimensions. It was necessary to lightly freeze (not frozen throughout specimen) some fine silty samples from Lotung to facilitate set up in the test equipment.

The dimensions of the test specimens were nominally either 2 inches in diameter and 4 inches in height, or 1.5 inches in diameter and 3 inches in height. The smaller of the two specimen sizes was used to obtain the largest dynamic strain amplitudes.

Compliance tests were conducted on each RCTS device to enable accurate material damping determinations. These calibration tests were conducted on brass and aluminum tubes. Results of these tests (see Appendices 8.B1 through 8.B4 for details) indicate that no compliance adjustments were required at loading frequencies less than 0.5 Hz, but equipment damping values ranged from about 3.5% at 20 Hz to about 0.4% at 200 Hz.

8.3.1.2 LSTC Equipment

The LSTC is a cubical box with interior dimensions of 7 ft on a side. It was designed to confine dry sand under isotropic, biaxial, and true triaxial states of stress. The maximum confining stress is about 50 psi. Stress states can be controlled by applying different pressures to the six sides of the chamber. The sand in the LSTC was a washed mortar sand. This sand is uniform, medium-to-fine in grain size, and classifies as an SP according to the Unified Soil Classification system. Relative densities of the sand samples ranged from 50 to 79% and averaged 72%. The sample was prepared by a pluviation method.

The LSTC was developed to allow small-strain, wave propagation studies to be conducted in soil systems. Geophones were used to create the seismic wave in the LSTC. Signals were generated at frequencies from 0.25 to 4 kHz. Wave travel times and amplitudes were monitored with accelerometers and velocity transducers located in vertical and horizontal planes within the LSTC. In the case of S-wave propagation, this sensor configuration allowed both SH and SV waves to be recorded. Geophones were Mark Products, Model L40 devices, which have a natural frequency of 60 Hz. The accelerometers were Endevco Model 7701-100 devices, which have a resonant frequency of about 20 kHz. For both types of instrumentation the frequency range of the recorded motion was much different than the system resonant frequency.

Velocity and damping within the sand were determined using wave propagation analysis methods. For material damping determinations, three methods of analysis can be used to define damping: the waveform fitting, spectral ratio, and spectral slope methods. Details about these methods of analysis are provided in Appendix 8.B5. In these LSTC tests, only the spectral ratio method was used.

8.3.2 Laboratory Data Collection

Data collection for the RCTS tests involved determination of shear modulus and material damping for different values of shearing strain amplitude, confining pressure, time of confinement, number of cycles of loading, and excitation frequency. Data collection for the LSTC involved collecting wave propagation data as a function of confining pressure for different states of confinement at fixed frequencies ranging from 1 kHz to 4 kHz.

8.3.2.1 RCTS Testing

Each series of RCTS tests involved a similar sequence. In this sequence the influences of the following variables were evaluated:

- four to six isotropic pressures ranging from below to above the estimated in situ mean effective stress
- time of confinement ranging from 1 to about 3 days
- shearing strain levels ranging from less than 10^{-3}% to strains slightly above 0.2%
- numbers of cycles of loading ranging from 1 to 10 cycles in the TS test followed by 500 to 1,000 cycles in the RC test
- excitation frequencies ranging from 0.1 Hz to about 5 Hz in the TS test and from 20 to over 100 Hz in the RC test.

Values of shear modulus and material damping were typically determined at confining pressures equal to 0.25, 0.5, 1, 2 and 4 times the estimated in situ mean effective stress. Low-amplitude RC testing was performed at each confining pressure to determine the influence of time and confining pressure on the small-strain shear modulus, G_{max}, and small-strain material damping ratio, D_{min}. Low-amplitude dynamic tests were defined as those tests in which the resonant amplitude did not exceed 10^{-3}% and typically was considerably below that level. Increasing levels of shearing strain were then applied.

High-strain testing consisted of two series of tests. The first involved TS testing. This testing was performed under drained conditions and involved shearing strains from 10^{-3}% to about 0.05%. The majority of the measurements were made at 0.5 Hz and 1 to 10 cycles of loading were applied. At strains of 10^{-3}% and 10^{-2}%, the effect of frequency was evaluated with typically 1 to 4 cycles of loading applied at frequencies ranging from 0.1 to about 10 Hz. After the TS tests were completed, the sample was tested using the RC method. Checks of G_{max} were performed at various times to evaluate the effects of high-strain loading on the soil skeleton.

The high-pressure testing program involved the same testing sequence. All but two samples were conducted on reconstituted washed mortar sand. These reconstituted samples were prepared using the under-compaction method. All but one of the reconstituted test specimens was tested dry; one sample was tested in a saturated condition. During the test on the reconstituted saturated sample, drainage was permitted during the shearing strain sequence. The four high-pressure tests on undisturbed samples involved two samples from Treasure Island and two samples from Lotung. The maximum pressure during the high confining pressure tests was approximately 500 psi. Specific details about the laboratory testing programs are presented in Appendices 8.B1 through 8.B4.

8.3.2.2 LSTC Testing

The testing method for the LSTC program involved recording the propagation of body waves along various travel paths. These body waves were polarized along the principal stress directions and also propagated at oblique angles to the principal stress directions. Confining pressures from 4 to 37.4 psi were used in the test program. Both isotropic and anisotropic states of stress were used. Material damping values were estimated for P- and S-wave propagation in horizontal and vertical planes.

8.3.3 Laboratory Test Results

Detailed results for all of the laboratory measurements and analyses are included in Appendices 8.B1 through 8.B5. A summary of the laboratory investigation follows for each of the reference sites, the high confining pressure tests, and the LSTC tests. Appendix 7.A contains additional information about the use of these test results in the development of a generic material model, and specifically the reference strains for each set of tests.

8.3.3.1 Treasure Island

The results of the Treasure Island tests include plots showing the relationships between low-amplitude shear modulus (G_{max}) and confining pressure, low-amplitude material damping ratio (D_{min}) and effective confining pressure, shear modulus ratio (G/G_{max}) and shearing strain, and material damping ratio and shearing strain. Appendix 8.B1 presents these plots along with all the supporting data necessary to develop the plots.

Key results of the University of Texas tests are summarized in the shear modulus ratio and material damping ratio plots presented in Figure 8-33 for the fine-grained soils and Figure 8-34 for the sandy soils. These results show that the shear modulus ratio for sandy soil plots very close to the upper bound Seed-Idriss modulus ratio

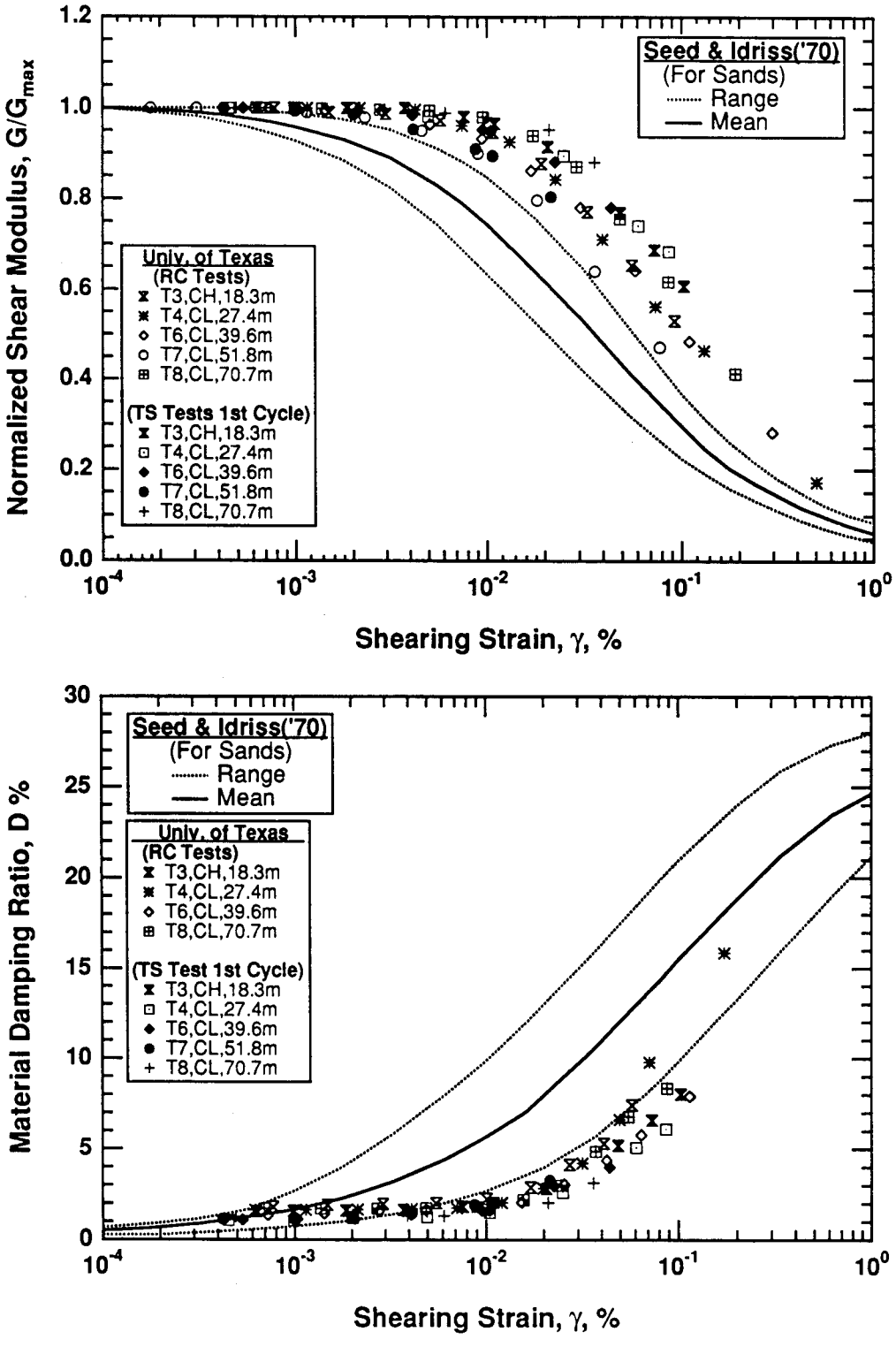

Figure 8-33. G/G_{max} and material damping results from Treasure Island—fine-grained soil.

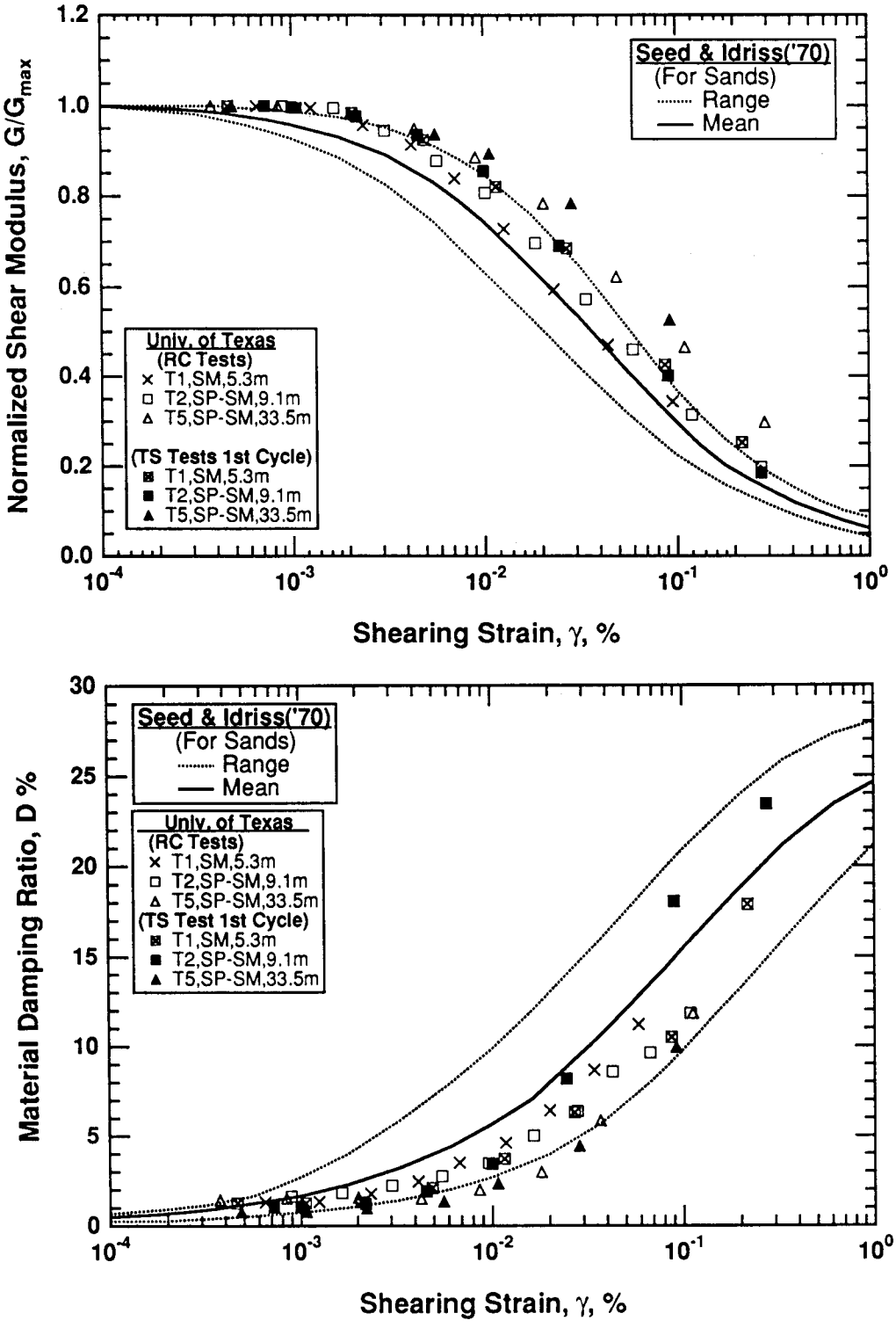

Figure 8-34. G/G_{max} and material damping results from Treasure Island—sandy soil.

plot (Seed and Idriss, 1970) for sand, while the fine-grained soils plot above the upper bound. For material damping, the sandy soil generally plots between the mean and lower bound curves for Seed-Idriss sand at strains > 10^{-3}%, while the fine-grained soil generally plots below the sandy soil at strains > 10^{-2}%. At strains less than 10^{-3}%, material damping in the fine-grained soil is slightly above that of the sandy soil and all values are less than 2%. The shear modulus ratio and material damping are both somewhat affected by the number of cycles of loading, with modulus and damping decreasing slightly as the number of cycles of constant shearing strain increases.

One of the key observations from Figures 8-33 and 8-34 is that the absolute scatter in data was minimal, despite the large range of depths from which the samples had been recovered. Typically the variation in shear modulus ratio at any shearing strain level was less than 0.1; the absolute variation in material damping ratio ranged from less than 1% at very low shearing strain amplitudes (e.g., <10^{-2}%) to several percent at higher shearing strain levels (i.e.,>10^{-1}%). This narrow range in property variation illustrates the critical benefits of accurate equipment calibration, extremely careful sample handling and testing, and careful data interpretation.

Laboratory results at very low shearing strain amplitudes (e.g., <10^{-4}%) were compared to in situ values of modulus and material damping discussed in Section 8.2. These comparisons indicate that the low-amplitude shear moduli from the laboratory tests are slightly less than the value determined from the field velocity measurement. This result was expected and is attributed to the effects of soil disturbance during sampling. Laboratory values of material damping are also less than the field-derived damping values, sometimes by a factor of two. Several explanations for this difference have been proposed, including different frequencies of loading in the laboratory and the field, the inability in the laboratory to duplicate field states of stress, and limitations associated with the field determination of material damping. The damping comparisons suggest that extreme care must be taken when using either field- or laboratory-derived values of material damping in any site-response analyses.

8.3.3.2 Gilroy 2

The results of the Gilroy 2 tests include the same set of plots as discussed above for Treasure Island. Appendix 8.B2 presents these plots along with all the supporting data necessary to develop the plots.

Key results of the University of Texas tests are summarized in the shear modulus ratio and material damping ratio plots presented in Figure 8-35 for fine-grained soil and Figure 8-36 for sandy soil. These results also show that the shear modulus ratio for fine-grained soil plots slightly above the upper bound Seed-Idriss modulus ratio plot for sand and that the material damping ratio compares closely with the lower bound Seed-Idriss plot for sand at strains > 10^{-3}%. The modulus ratio of undisturbed sandy soil is slightly above the Seed-Idriss average plot; the damping is above at low strains and approaches the average at higher strains. The shear modulus ratio appeared to be only slightly affected by the number of cycles of loading, while material damping ratio decreased slightly as the number of cycles of constant shearing strain increased.

As with the Treasure Island results, one of the key observations from Figures 8-35 and 8-36 is that the absolute scatter in data is minimal, despite the large range of depths from which the samples had been recovered. Typically the variation in shear modulus ratio at any shearing strain level is less than 0.2. The variation in material damping ratio for fine-grained soil ranges from less than 1% at very low shearing strain amplitudes (e.g., <10^{-2}%) to above 10% at higher shearing strain levels (>10^{-1}%). There is, however, considerable variation in D_{min}, ranging up to about 5%. The narrow range in modulus variation again illustrates the critical benefits of accurate equipment calibration, extremely careful sample handling and testing, and careful data interpretation. A larger variation occurs in damping, which highlights the importance of these measurements. This variation is attributed to differences in sample consistency.

Comparisons of low-amplitude values of shear modulus and material damping from the laboratory with similar results from the field (Section 8.2) lead to similar conclusions as those cited above for Treasure Island. In general low-amplitude modulus and material damping are lower in the laboratory than measured and interpreted in the field. The most significant of these differences occurs for material damping where the laboratory values are 50% of the field data. The explanation for the differences is the same as given for Treasure Island.

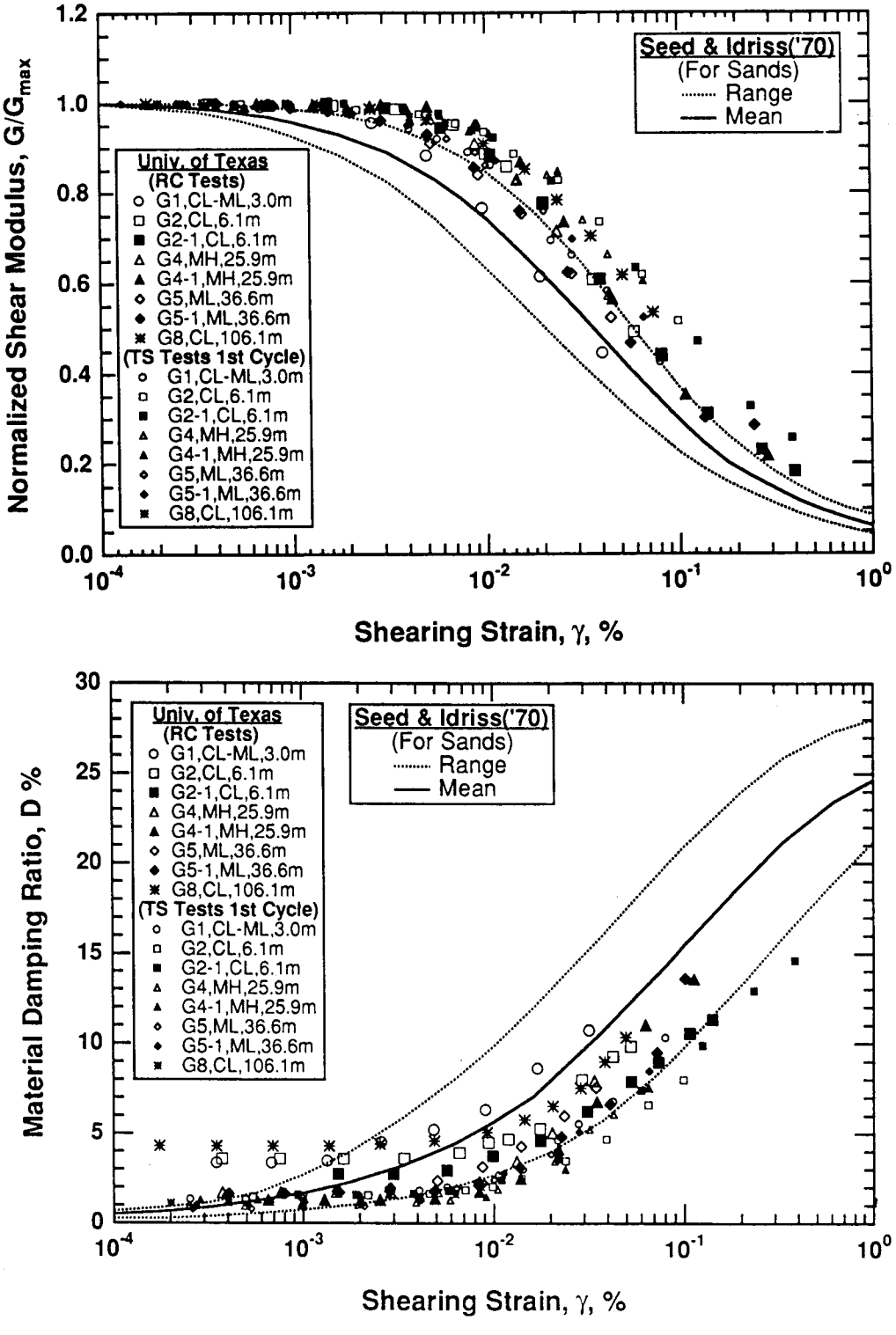

Figure 8-35. G/G_{max} and material damping results from Gilroy 2—fine-grained soil.

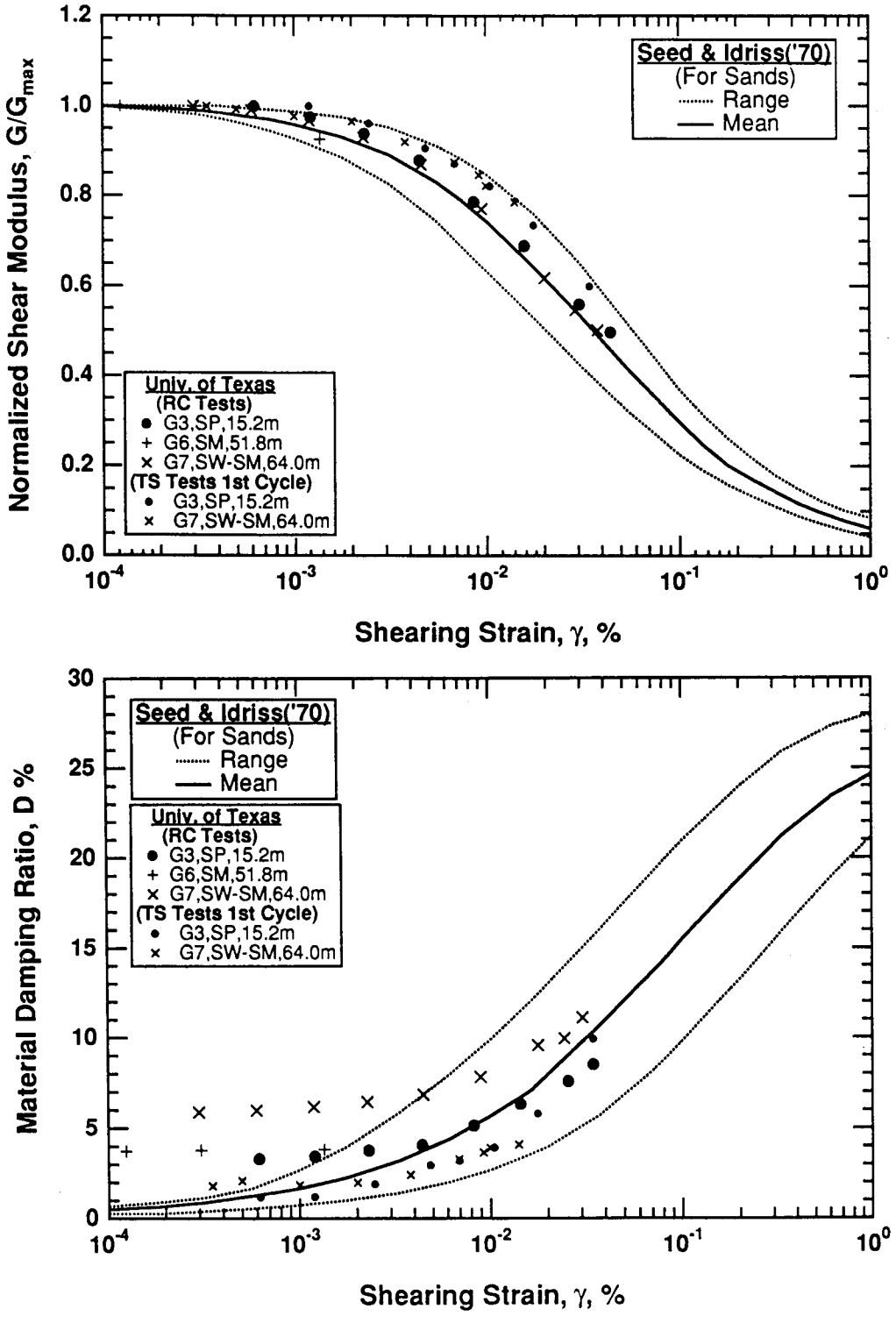

Figure 8-36. G/G_{max} and material damping results from Gilroy 2—sandy soil.

8.3.3.3 Lotung

The results of the Lotung tests include tests conducted at the University of Texas, as well as testing completed previously for the Lotung site. Appendix 8.B3 presents these plots along with all the supporting data necessary to develop the plots.

Key results of the University of Texas tests are summarized in the shear modulus ratio and material damping ratio plots presented in Figure 8-37. These results show that the shear modulus ratio plots very close to the upper bound Seed-Idriss modulus ratio plot for sand and that the material damping ratio compares closely with the lower bound Seed-Idriss plot for sand. The shear modulus ratio appeared to be essentially unaffected by the number of cycles of loading in these unsaturated tests, while material damping ratio decreased slightly as the number of cycles of constant shearing strain increased.

One of the key observations from Figure 8-37 is that the absolute scatter in data was minimal, despite the large range of depths from which the samples have been recovered. Typically the variation in shear modulus ratio at any shearing strain level was less than 0.1; the variation in material damping ratio ranged from less than 1% at very low shearing strain amplitudes (e.g., $<10^{-2}$%) to several percent at higher shearing strain levels (i.e.,$>10^{-1}$%). This level of data variation was far less than had been recorded during previous Lotung laboratory testing programs. For example, the variation in shear modulus ratio ranged from less than 0.1 (in absolute value) to as much as 0.4 while the variation in material damping ratio ranged from a few percent at low shearing strain levels to well over 10% at high shearing strain levels. The narrow range in property variation for this project relative to previous measurements is thought to illustrate the critical influence of accurate equipment calibration, extremely careful sample handling and testing, and careful data interpretation.

The comparison of field and laboratory values of shear modulus at low shearing strain amplitudes followed the same trends as discussed above. In the absence of field measurements of material damping in this project at the Lotung site, no comparisons were made between material damping measured in the laboratory and in the field.

8.3.3.4 High-Pressure Confining Pressure Tests

Typical high-pressure test results are plotted in Figures 8-38 and 8-39. The modulus results in Figure 8-38 show that all six remolded and four intact samples exhibited similar relationships between the logarithm of the low-amplitude shear modulus and the logarithm of the effective confining pressure [the samples ranged from poorly graded remolded sand (SP) to intact silty sand (SM) to sandy silt (ML)]. However, the small-strain damping values (Figure 8-39) are quite different. The dry remolded sands exhibited D_{min} values on the order of 0.2 to 0.3% at a confining pressure of 500 psi. When saturated, the value of D_{min} increased to about 0.4 to 0.5%. On the other hand, the four undisturbed samples had D_{min} equal to 0.7% and 1.5% for the ML and SP-SM samples, respectively.

The remolded sand specimens show somewhat more influence of effective confining pressure on shifting the G/G_{max} and D curves than the undisturbed specimens. Therefore, at high confining pressures, the modulus ratio is higher and material damping is lower for the remolded samples than for the intact samples.

8.3.3.5 LSTC Tests

The results from the LSTC test program dealt primarily with material damping measurements. These measurements were for small levels of shearing or lineal strain; they covered damping in shear as well as compression. Details about these results can be found in Appendix 8.B5.

The most significant observation was that considerable scatter occurs in material damping determined by the spectral ratio method, even under the most closely controlled conditions. The absolute magnitude of this variation was typically on the order of 1 to 2%; i.e., measured damping could range from 0.5 to 3.5% for a soil with a mean value of 2%. This variation occurred when measurements were combined for forward and reverse directions of wave propagation and was considerably larger if measurements were performed in only one propagation direction.

Results of the material damping determination confirmed that there is a reduction in material damping with increasing effective confining pressure, as was also noted in the laboratory RCTS tests. Values of material damping in shear were slightly less than those measured

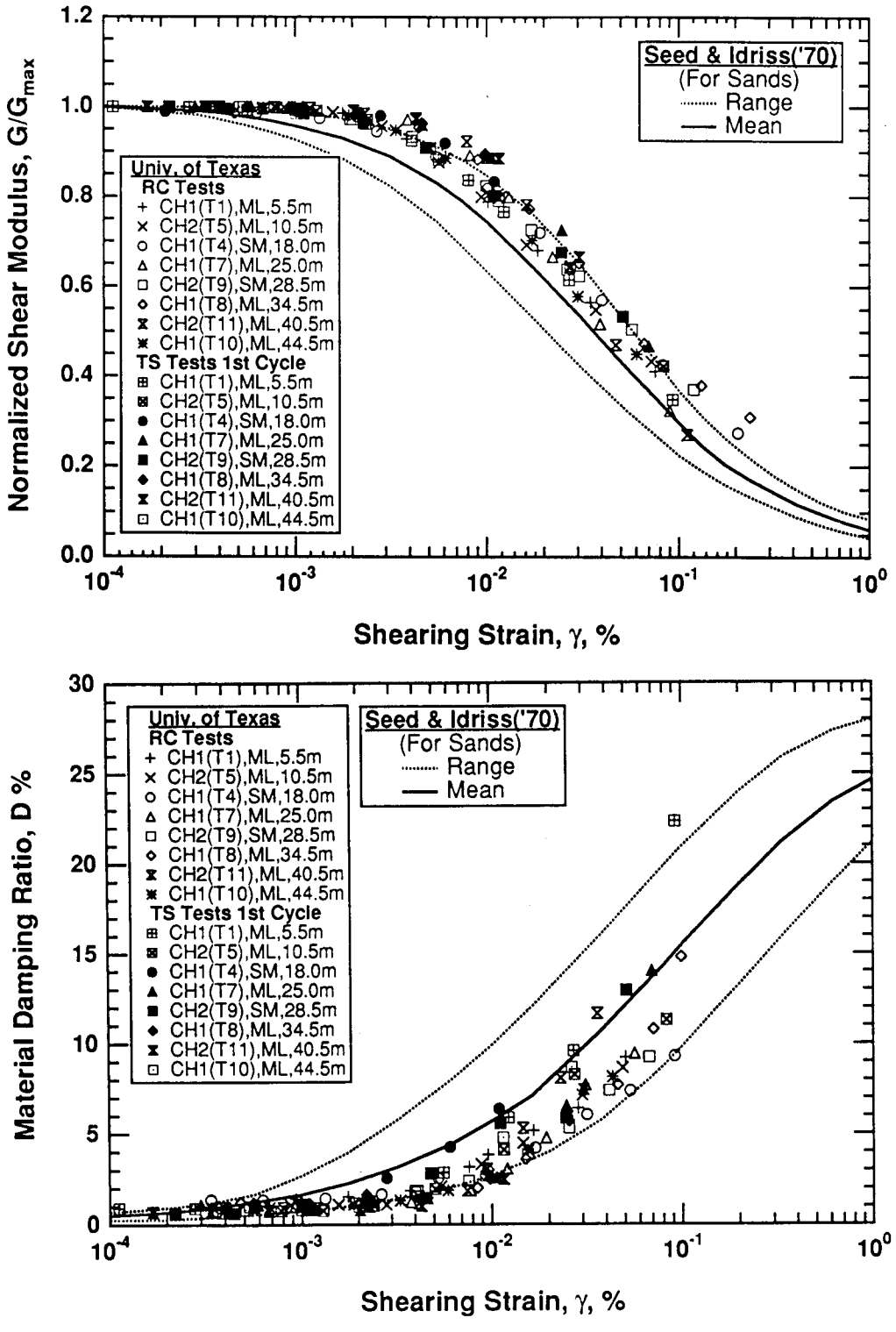

Figure 8-37. G/G_{max} and material damping results from Lotung.

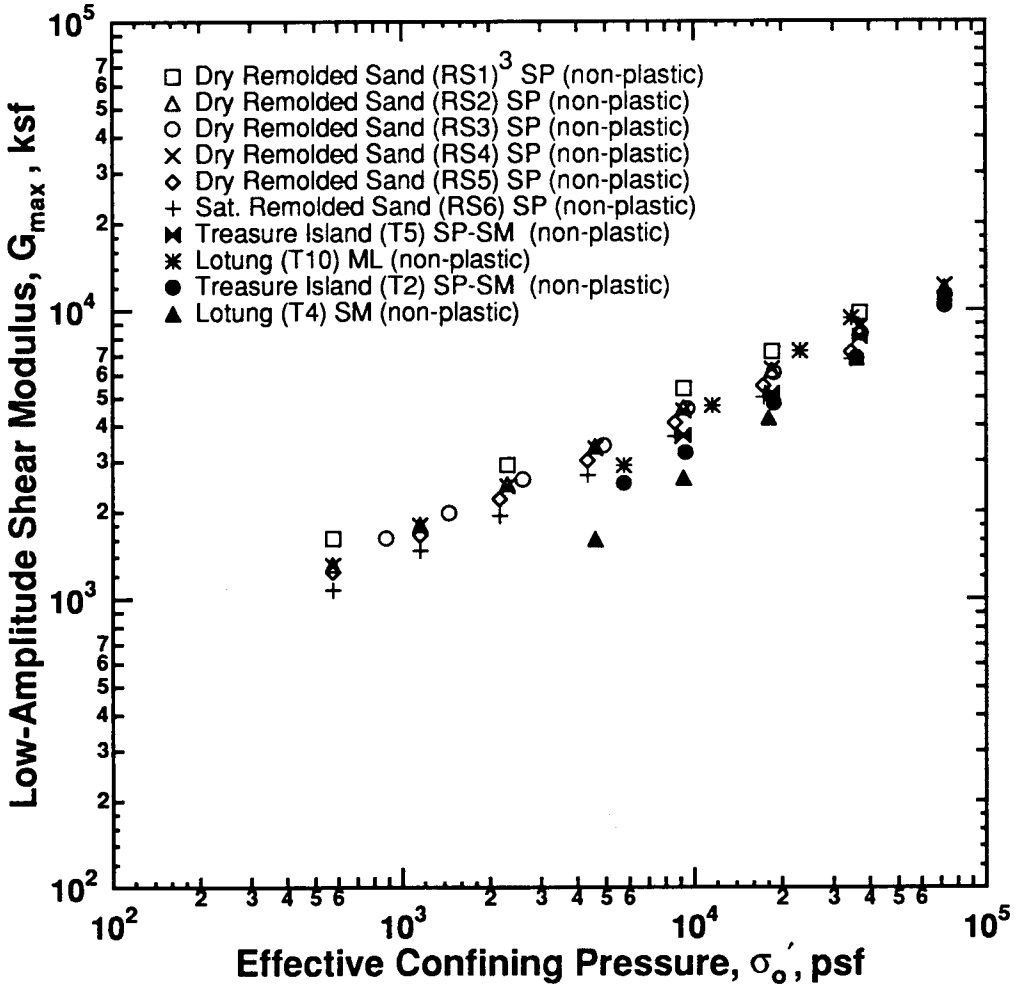

Notes:

1. G_{max} measured at t = 15-50 min. at each σ_o' for remolded samples of washed mortar sand.
2. G_{max} measured at t = 1000 min. at each $\sigma_o' \geq \sigma_m'$ for undisturbed samples from Treasure Island and Lotung.
3. Second Loading Cycle (B) is plotted.
4. σ_m' = estimated in situ mean effective stress using $k_o = 0.5$.

Figure 8-38. Typical high-pressure confining pressure results—shear modulus.

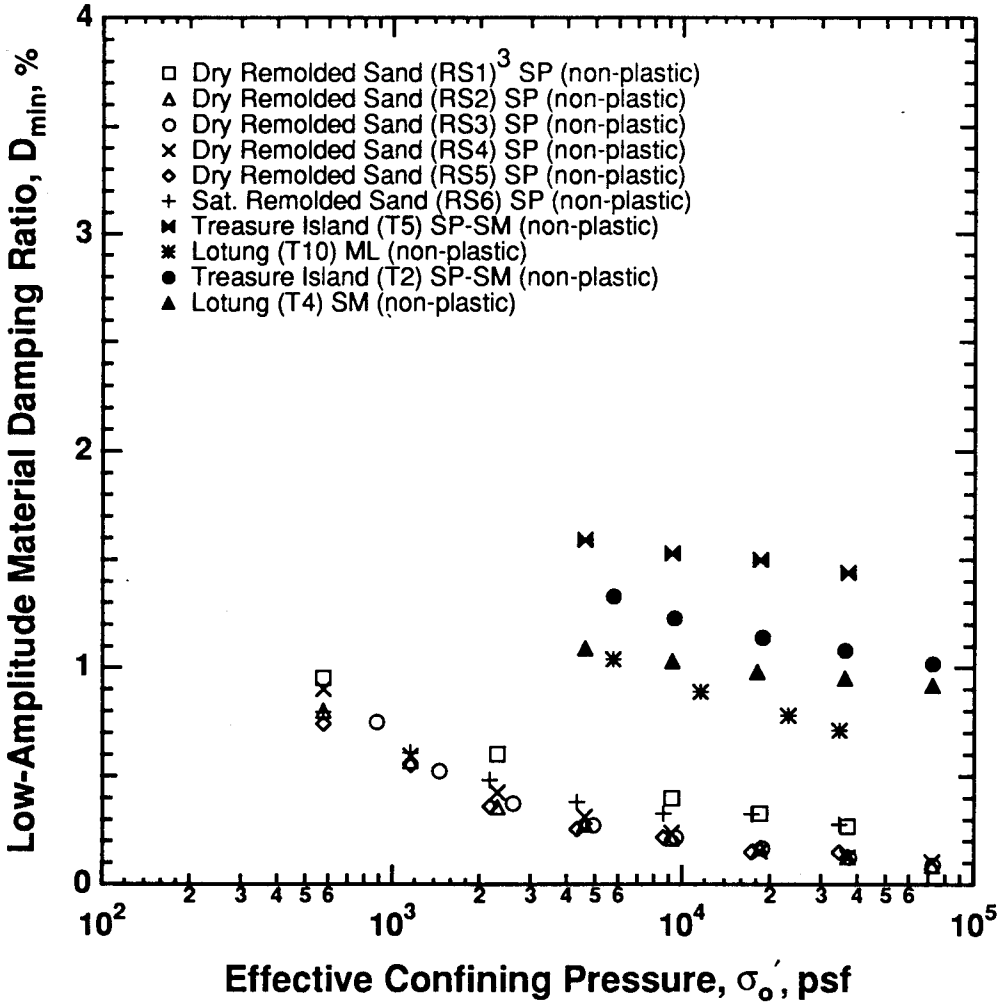

Notes:

1. D_{min} measured at t = 15-50 min. at each σ_o' for remolded samples of washed mortar sand.
2. D_{min} measured at t = 1000 min. at each $\sigma_o' \geq \sigma_m'$ for undisturbed samples from Treasure Island and Lotung.
3. Second Loading Cycle (B) is plotted.
4. σ_m' = estimated in situ mean effective stress using $k_o = 0.5$.

Figure 8-39. Typical high-pressure confining pressure results—material damping.

in compression under the same confining stress. The typical difference varied from 0.5 to 1% in absolute terms. The material damping observed in the LSTC was typically about 1 to 2% higher than material damping measured at similar confining pressures in the RCTS device. Part of this difference is possibly the result of the much higher frequencies of wave propagation in the LSTC device (e.g., 1 to 4 kHz) than in the RCTS device (100 Hz). Finally, on the whole, values of material damping calculated under a biaxial state of stress were comparable to those measured under the isotropic loading tests.

8.4 Conclusions

This project has included an extensive series of field and laboratory investigations. These investigations were conducted to evaluate the dynamic properties of soil at three reference sites. Two of the reference sites, Gilroy 2 and Treasure Island, are located in the San Francisco Bay area; the third site is located near Lotung, Taiwan. The primary purpose of these field and laboratory investigations was to establish a database for shear modulus and material damping ratio at each site for use in site-specific ground response studies. This shear modulus and material damping ratio database defined the manner in which shear modulus and material damping ratio varied with soil type, shearing strain amplitude, effective confining pressure, frequency of cyclic loading, duration of sustained confinement, and repetitions of cyclic loading at each site.

The project also had as a purpose to provide a forum for comparison of various methods of measurement and analysis in order to develop guidelines for the conduct of site-specific geotechnical investigations. The areas specifically requiring guidance include: procedures for determining material damping using in situ testing methods; quantification of the variability in material property determination that could be expected when the best available testing and interpretation methods are applied; and effects of high confining pressures on shear modulus and material damping ratio. Conclusions reached on the basis of these investigations are summarized below.

8.4.1 Shear Modulus and Material Damping Ratio Database

The shear modulus and material damping ratio database for the three reference sites is comprehensive. This database includes P- and S-wave velocities determined by crosshole, downhole, and inhole (suspension/interval) procedures. These velocity values extend from the ground surface to nearly 500 ft below the ground surface at some of the sites. At two of the sites, Treasure Island and Gilroy 2, the velocity profiles have been established by different investigators. Results of these measurements indicate that velocities vary significantly with local geologic conditions, but that with a reasonable level of care in the interpretation of data, very similar values of velocity are obtained by different investigators.

Complementing this field database is an extensive database defining the results of laboratory testing of soil from the three reference sites. The database provides information about the shear modulus and material damping ratio, and the variation of these properties with levels of shearing strain, effective confining pressure, frequency of cyclic loading, number of cycles of loading, and duration of confinement.

Results of the laboratory tests indicate that the shear modulus ratio and material damping ratio follow similar trends at all three sites. For all three sites the upper-bound Seed-Idriss sand modulus curve appears to fit the sandy and silty soil data very well, while the clayey sample data are somewhat above this relationship. This trend is consistent with what has been reported in the literature. The fit for the damping-strain relationship is somewhat more involved. At strains below 10^{-3}%, the data for sand are near the mean Seed-Idriss sand curve while the data for clayey soil are considerably above. At strains above 10^{-1}% the sand data fall between the mean Seed-Idriss curve and the lower bound. The damping ratio of clayey samples is generally below the lower bound Seed-Idriss curve in this strain range. This trend is also consistent with what has been reported in the literature. In the absence of detailed laboratory test information, the Seed-Idriss curves seem to provide an excellent basis for use in site response analyses of sandy sites. For clay site slightly higher modulus ratios and lower damping ratios such as reported by Vucetic and Dobry (1991) appear to be more appropriate.

Modulus ratio and material damping curves for the sandy and silty soil compare closely to curves derived using a reference strain (see Appendix 7.A) of about 0.1%, which approximates the upper bound of the Seed-Idriss modulus reduction curves and the lower bound

Seed-Idriss damping curves. The clayey soils at Treasure Island show relatively lower modulus reduction and damping curves corresponding to a reference strain on the order of 0.3%, and the gravelly soils at Gilroy show relatively greater modulus reduction and damping, corresponding to a reference strain on the order of 0.05%.

8.4.2 In Situ Determination of Material Damping

In situ estimates of material damping ratio were made using velocity measurement waveforms from two of the reference sites, Gilroy 2 and Treasure Island. The estimates used data from downhole and crosshole seismic wave propagation measurements. Several procedures for interpreting data, including spectral ratio and spectral slope methods, were used. It was concluded from these studies that estimates of material damping could be made from in situ wave propagation data; however, the determination was difficult and required extreme care during both the measurement itself and during the interpretation of the data. Both the spectral ratio and spectral slope methods were found not to be robust. Waveform fitting methods were found to give the most realistic estimates of material damping.

Typically the magnitude of material damping determined in situ ranged from about 1% to as high as 7%. The values of in situ damping ratio were normally higher than damping determined in the laboratory at similar effective confining pressures.

Special Large-Scale Triaxial Chamber (LSTC) tests were conducted to further evaluate material damping ratio of dry sand. By using the spectral ratio method in a well-controlled test facility, it was found that damping in shear was slightly less than damping in compression in the dry sand. However, scatter in the data and the lack of robustness of the method was clearly exhibited in these tests.

Resonant column measurements of shear damping ratios were lower than the LSTC results. Given this comparison, plus the fact that the in situ damping ratio measured at Gilroy 2 was higher than the damping determined in the laboratory, raises the possibility that some scaling law might apply to damping.

8.4.3 Dynamic Property Variation

Results of the field and laboratory tests for the reference sites show that dynamic properties of the soil vary throughout the soil profile. Some of this variation can be attributed to changes in the geology at the site; a small amount can be attributed to inaccuracies in the measurement or interpretation method.

The P- and S-wave velocity measurements from the in situ seismic tests indicate that the variation in velocity from all sources ranges from 10 to 15% for a reasonably well-defined soil profile. This magnitude of variation should be expected to increase as the complexity of geologic layering at a site increases, as the size of the site increases, and as the depth over which properties are averaged increases. Of the available seismic techniques, the crosshole and suspension logging methods appear to provide the most detail about velocity within a soil profile at any given location. Downhole procedures appear to provide less detailed velocity profile information but are more widely available. Furthermore, the downhole method tends to yield an unbiased, smoothed (low-pass filtered) version of the velocity-depth profile that can be used directly in site response analyses. The other two methods require careful smoothing in order to approximate the sensitivity of the actual response of earthquake-generated seismic waves. These conclusions suggest that, at important sites, combinations of all procedures offer the best opportunity for determining the spatial variation in velocity.

The laboratory information about shear modulus and material damping ratio indicate that both properties are relatively well-behaved in terms of data scatter. Tight bands in shear modulus ratio and material damping ratio as a function of shearing strain level were derived by using high-quality soil samples, well-calibrated laboratory testing equipment, careful testing techniques, and detailed data interpretations. Even under the best circumstances, some variation in data must be expected. For shear modulus ratio, the variation at shearing strains greater than 10^{-2}% should be 0.1 or less; for material damping ratio at similar strain levels, the variation should be less than 2%.

8.4.4 High Confining Pressure Effects

Laboratory tests conducted at confining pressures from 200 to 500 psi indicate that soil behaves in a very predictable manner within this range of confining pressures. The relationship between the logarithm of low-amplitude shear modulus and the logarithm of the effective confining pressure increases linearly throughout the pressure range. Likewise, the material damping ratio decreases with increases in confining pressure, and values of small-strain damping around 1% are measured for undisturbed granular samples.

These results suggest that laboratory testing methods can be used to extrapolate low-amplitude shear modulus and material damping ratios to depths of 1,000 ft or more below the ground surface in situations where specific in situ or laboratory test data are not available. In making any of these extrapolations, extreme care must be used in applying the extrapolation procedures. Specifically, any significant changes in soil type or geologic age could preclude use of the extrapolation procedure.

References

de Alba, P., Benoit, J., Youd, T.L., Shakal, A.F., Pass, D.G., and J.J. Carter (1992). Deep Instrumentation Array at Treasure Island Naval Station, USGS Professional Paper (in press).

Anderson, D.G. (1993). Geotechnical Synthesis for the Lotung Large-Scale Seismic Experiment, final report to EPRI (in press).

Chang, C-Y, Mok, C.M., Power, M.S., Tang, Y.K., Tang, H.T., and J.C. Stepp (1990). Equivalent Linear Versus Nonlinear Ground Response Analyses at Lotung Seismic Experiment Site, *Proc. 4th US National Conf. Earthquake Engr.*, 1, Palm Springs, May.

EPRI/NSF (1991). *Proceedings of the NSF/EPRI Workshop on Dynamic Soil Properties and Site Characterization*, Palo Alto, Calif.: Electric Power Research Institute, NP-7337.

Gibbs, J.F., T.E. Fumal, D.M. Boore, and W.B. Joyner (1992a). Seismic Velocities and Geologic Logs from Borehole Measurements at Seven Strong-Motion Stations that Recorded the Loma Prieta Earthquake, USGS Open File Report 92–287.

Gibbs, J.F., D.M. Boore, W.B. Joyner, and T.E. Fumal (1992b). The Attenuation of Seismic Waves in Quaternary Alluvium in Santa Clara Valley, California, *Bull. Seism. Soc. Am.*, (submitted).

HCK (1986). Geophysical Survey Report of Lo-Tung Project, submitted to Taiwan Power Company by HCK Geophysical Company.

Hryciw, R.D., K.M. Rollins, M. Homolka, S.E. Shewbridge, and M. McHood (1991). Soil Amplification at Treasure Island during the Loma Prieta Earthquake, *Proc. 2nd Int. Conf. on Recent Adv. in Earthquake Engr. and Soil Dyn.*, St. Louis, 1679–1685.

Joyner, W.B., R.E. Warrick, and T.E. Fumal (1981). The Effect of Quaternary Alluvium on Strong Ground Motion in the Coyote Lake, California Earthquake of 1979, *Bull. Seism. Soc. Am.* 71:1333–1350.

Kudo, K. and E. Shima (1970). Attenuation of Shear Waves in Soil, *Bull. Earthquake Res. Inst.*, 48:145–158.

Lee, C.H. and M. Praszker (1969). Bay Mud Developments and Related Structural Foundations, included in Special Report 97, California Division of Mines & Geology.

Lee, J.N-K (1993). Experimental Study of Body Wave Velocities in Sand under Anisotropic Conditions, Ph.D. Dissertation, University of Texas at Austin, 503 p.

Mok, Y.J. (1987). *Analytical and Experimental Studies of Borehole Seismic Methods*, Ph.D. Dissertation, University of Texas at Austin, 272 p.

ORI (1989). Geophysical Test Report of Backfill for Lotung Project (DRAFT), submitted to Tokyo Electric Company by Ohsaki Research Institute.

Pujol, J. and S. Smithson (1991). Seismic Wave Attenuation from VSP Experiments, *Geophysics*, 56:1441–1455

Redpath, B.B., R.B. Edwards, R.J. Hale, and F.C. Kinpzer (1982). *Development of Field Techniques to Measure Damping Values for Near-Surface Rocks and Soils*, URS/John A. Blume & Associates, NSF Grant PFR-7900192.

Redpath, B. and R.C. Lee (1986). *In Situ Measurements of Shear-Wave Attenuation at a Strong-Motion Recording Site*, URS/John A. Blume & Associates, USGS Contract 14-08-001-21823.

Richart, F.E., Hall, J.R., and R.D. Woods (1970). *Vibrations of Soils and Foundations*, Prentice-Hall, Englewood, 414p.

Rogers, J.D. and S.H. Figuers (1991). *Engineering Geologic Site Characterization of the Greater Oakland-Alameda Area*, Alameda and San Francisco Counties, California, a report to NSF.

Seed, H.B. and I.M. Idriss (1970). *Soil Moduli and Damping Factors for Dynamic Analyses*, Report No. EERC 10-10, Earthquake Engineering Research Center, University of California, Berkeley.

SW/AA (1972). Soil Behavior Under Earthquake Loading Conditions, prepared by Shannon & Wilson and Agbabian Associates, USAEC Contract W-7405-eng-26.

Tang, H.T. (1987). *Large-Scale Soil Structure Interaction*, Palo Alto, Calif.: Electric Power Research Institute, NP-5513-SR

Tang, X.M. (1992). A Waveform Inversion Technique for Measuring Elastic Wave Attenuation in a Cylindrical Bar, *Geophysics*, 57:854–859.

Tang, X.M., Toksoz, M.N., Tarif, P., and R.H. Wilkens (1988). A Method of Measuring Acoustic Wave Attenuation in the Laboratory, *J. Acoust. Soc. Am.*, 83:453–462.

Toksoz, M.N., Johnston, D.H., and A. Timur (1979). Attenuation of Seismic Waves in Dry and Saturated Rocks, *Geophysics*, 44:681–690.

Vucetic, M., and R. Dobry (1991). Effects of Soil Plasticity on Cyclic Response, *J. Geotech Engr*, ASCE, 117-1:89–107.

Winterkorn, H.F. and H-Y Fang (1975). *Foundation Engineering Handbook*, Van Nostrand, New York, 751p.

Zeghal, M., and A-W Elgamal (1992). Analysis of Site Amplification Using the Lotung Seismic Array, report submitted to EPRI (draft).

9

ENGINEERING MODEL OF STRONG GROUND MOTIONS

9.1 Summary of Models, Parameters, and Uncertainties

The ground motions used for the developing the engineering model of ground motion attenuation are simulated ground motions computed using the stochastic model described in Section 3.1. The frequency band, distance range, and magnitude range of interest for this study are 1 to 35 Hz, 1 to 500 km, and magnitude 5 to 8. For these distance, frequency, and magnitude ranges, the stochastic model using an equivalent point-source distance (Section 3.1) and region specific geometrical spreading terms (Appendix 3A) is used.

The stochastic model was tested against recorded motions for several large magnitude events (Section 3) and shown to adequately match the recorded ground motions for the frequency, distance, and magnitude range of interest. In these comparisons, the equivalent point-source distance is the distance from the site to the closest point on the rupture surface at the depth of the main slip. The effect of an extended source on this equivalent point-source distance was described in Section 4.3 for use in forward predictions of ground motion.

The key parameters for the stochastic model are magnitude, distance, stress-drop, crustal velocity structure, Q, kappa, and focal depth, variabilities of these parameters are described below.

9.1.1 Treatment of Physical Uncertainties

The variability of the model parameter values is separated into randomness and uncertainty. Randomness represents variability that is inherent to the parameter; uncertainty represents variability that is due to our lack of knowledge of the parameter. Therefore, randomness can be refined but not reduced, whereas uncertainty may be reduced in the future with additional information.

9.1.1.1 Stress-Drop

The randomness and uncertainty of stress-drop are given in Eq. 4-6 and 4-7 (Section 4.2.3). The weights for stress-drop are proportional to the density function for a log-normal distribution.

9.1.1.2 Focal Depth

For a given focal depth distribution, the variability in focal depth represents randomness. The differences among the various focal depth distributions represent uncertainty (see Section 5.2.3 and Appendix 5B for details on these distributions). Differences between the depth distributions for margins and "other than margins" do not lead to statistically significant differences in median ground motions (using criteria analogous to those used in Section 5). These two data sets (see Figure 5-22) are then combined and used to construct the depth distribution that is used to derive the engineering model. Because the two distributions are combined into one, all of the variability in depth is treated as randomness.

9.1.1.3 Kappa

As shown in Section 5.4.2, a kappa of 0.006 provides an adequate match to the spectral shape of ENA hard rock ground motions. In section 5.4.2, WUS kappa values are described as log-normally distributed with a standard error of 0.4. This variability of kappa is the variability from site to site and represents randomness. In the engineering model, three kappa values are used: 0.003, 0.006, and 0.012. These three kappa values are given equal weight. The variability of kappa represented by these

weights and values exceeds the variability implied by a lognormal distribution with a standard error of 0.4, but is used in the engineering model as a conservative approach.

9.1.1.4 Q

The variability of the Q models for each region is given by the median, high, and low Q models described in Section 5.6. This variability represents variability of Q within a group of crustal regions and represents randomness. In the engineering model, the three Q models for each region are given equal weight based on the range of Q from previous studies.

9.1.1.5 Crustal Velocity Structure

A crustal velocity structure for each of the two distinct attenuation regions given in Section 5.5 are used in the engineering model. The variability of ground motion is quantified in (Section 5.3). However, this variability is included in the total variability as modeling variability (Section 3). Therefore, the crustal structure variability is not explicitly represented.

9.1.1.6 Modeling

The modeling variability is determined from the misfit of modeled ground motion data with recorded data (Section 3). The variability in the D terms (Tables 3-2 to 3-5 and the model bias) represent the uncertainty of the model. That is, in the future, the model could be improved such that the D terms and bias are reduced. The randomness is represented by the standard error of the model misfit allowing the D terms to be different from 1. The modeling uncertainty and randomness are shown in Section 3 and are given below.

Modeling Randomness:

$$\sigma_{r,\,\text{modeling}}(f) = 0.32 \qquad f \geq 9 \text{ Hz}$$

$$\sigma_{r,\,\text{modeling}}(f) = 0.63 - 0.14\ln(f) \qquad 1 \leq f < 9 \text{ Hz}$$

Modeling Uncertainty:

$$\sigma_{U,\,\text{modeling}} = 0.27$$

where σ is in natural log units.

Thus, randomness in the predicted ground motions comes from parametric randomness in stress drop, focal depth, kappa and Q, and from modeling randomness. Uncertainty in the predicted ground motions comes from parametric uncertainty in stress drop and from modeling uncertainty.

9.2 Development of Predictive Equations

9.2.1 Functional Form of Predictive Equations

Practical considerations dictate that the ground-motion predictions for engineering applications must be in the form of relatively simple equations in terms of magnitude and distance (we will call this set of attenuation functions the Engineering Model). The functional form and number of terms in these equations must, however, be sufficient to match the main features of the ground motions predicted by the physical models described in Sections 3 through 5, over the entire range of magnitudes, distances, and frequencies of engineering interest.

The functional form adopted here is the following:

$$\ln Y = C_1 + C_2(M-6) + C_3(M-6)^2 - C_4 \ln R_M - (C_5 - C_4)\max\left[\ln\left(\frac{R_M}{100}\right), 0\right] - C_6 R_M + \varepsilon_U + \varepsilon_r \qquad \text{(Eq. 9-1)}$$

$$R_M = \sqrt{R^2 + C_7^2} \qquad \text{(Eq. 9-2)}$$

where Y is spectral acceleration or peak ground acceleration (in units of g), C_1 through C_7 are constants to be determined from the modeling results (see next section), M is either Lg magnitude (m_{Lg}) or moment magnitude (**M**), and R is the closest horizontal distance to the rupture surface (km).

The quadratic magnitude term is needed in order to provide a better fit to the model predictions for low-frequency ground motions. The magnitude terms are of the form $(M-6)^n$ for the sake of numerical stability in the values of C_2 and C_3. The term in C_3 is not always present (it is not required for frequencies of 5 Hz or higher). The terms in C_4 and C_5 represent geometrical spreading with slopes C_4 (R_M < 100 km) and C_5 (R_M > 100 km). The model with two slopes provides a better fit to the crustal effects predicted by the ground-motion model in Section 3.

Table 9-1

Parameter Variations

Category	Quantity	Number	Values	Median
Dependent Variables	Ground-Motion Amplitude	15	PGA, PGV, spectral acceleration 1, 2.5, 5., 10., 25., 35.	
Independent Variables	Magnitude (**M**)	5	4.5, 5.5, 6.5, 7.5, 8.0	
	Horizontal Distance (km)	13	1, 2, 5, 10, 20, 50, 75, 100,125, 150, 200, 300, 500	
	Crustal Province	2	Midcontinent, Gulf	
Random Parameters	Stress Drop (bars)	8	20, 50, 75, 100, 150, 200, 400, 600	120
	Asperity Depth (km)	6	5, 10, 15, 20, 25, 30	10
	$Q=Q_0 f^{\eta}$ (Q_o, η)	3	Midcontinent: (400, 0.4), (670, 0.33), (1000, 0.3)	Midcontinent: (670, 0.33)
			Gulf: (200, 0.3), (300, 0.3), (500, 0.3)	Gulf: (300,0.3)
	Near-site attenuation, κ (sec)	3	0.003, 0.006, 0.012	0.06
Total number of runs		842,400		

Variability about these equations is represented by the quantities ε_r (randomness) and ε_U (uncertainty), which are assumed to follow normal distributions. The associated standard deviations are, in general, dependent on magnitude and distance. Randomness and uncertainty are presented in Section 9.3.3.

The functional form in Equation 9-1 represents a compromise between simplicity and goodness of fit. This particular functional form was obtained after extensive experimentation with more complex, as well as more simple, functional forms. In particular, tri-linear forms were considered for the geometric-attenuation terms, as well as different transition distances between the slopes of C_4 and C_5. All these functional forms fit the simulated ground motions equally well, because the variability in source depth tends to smooth out the effect of critical reflections.

9.2.2 Fit to Model Predictions

The stochastic ground-motion model was used to calculate peak ground-motion amplitudes for a large number of ground-motion measures, and for magnitudes, distances, and model parameters, covering the range of engineering interest. Table 9-1 summarizes all the parameter variations considered. Ground-motion amplitudes were obtained for all parameter combinations. This large set of results embodies all ground-motion predictions by the models of wave propagation, seismic source, and crustal structure, for all parameters of interest.

Each combination of the random parameters in Table 9-1 is assigned a weight, based on the distributions for those parameters as determined in Sections 4 and 5 (see Section 9.1.1 for a summary). Because all random parameters are probabilistically independent among themselves and do

Table 9-2

Coefficients of Attenuation Functions for Midcontinent Region (using moment magnitude)

Freq. (Hz)	C_1	C_2	C_3	C_4	C_5	C_6	C_7
1.0	0.09	1.41	–0.20	0.90	0.49	0.0023	6.8
2.5	1.07	1.04	–0.10	0.93	0.56	0.0033	7.1
5.0	1.72	0.84	0	0.98	0.66	0.0042	7.5
10.0	2.37	0.81	0	1.10	1.02	0.0040	8.3
25.0	3.68	0.80	0	1.46	1.77	0.0013	10.5
35.0	4.00	0.79	0	1.57	1.82	0.0008	11.1
Peak Accel.	2.20	0.81	0	1.27	1.15	0.0021	9.3

not depend on the independent variables, this weight is simply the product of weights for the individual random parameters.

Depth is the only random quantity that requires special treatment in the calculation of weights. Asperity depth, which is the depth quantity used as a parameter for the ground-motion simulations, must be converted to hypocentral depth. Then, a weight is assigned based on the distribution of hypocentral depth. Details of this transformation are provided in Section 4.3.

The ground-motion amplitudes and associated weights are used to fit the attenuation equation in Equation 9-1 using non-linear weighted least squares. One fit (i.e., one set of coefficients) is obtained for each combination of ground-motion measure, crustal region, and choice of magnitude scale (**M** or m_{Lg}).

The fit for m_{Lg} requires one additional step. For each combination of independent variables and random parameters, **M** is converted to m_{Lg} using Equations 4-1 and 4-4. The random term δ in Equation 4-4 is handled by Monte Carlo simulations drawing one independent value of δ each time this conversion is performed. The resulting m_{Lg} values are then used as the magnitude variable in the regression.

9.3 Results

Tables 9-2 through 9-5 list the coefficients C_1 through C_7 of the Engineering Model, which were obtained by fitting Equations 9-1 to the modeling results described above. Separate sets of coefficients are provided for the Midcontinent[1] and Gulf regions and for the two choices of magnitude variable.

For high-frequency ground-motion measures, a satisfactory fit is obtained while fixing C_3=0; these results are preferred for the sake of parsimony. For low frequencies, the terms in C_3 are required for an adequate fit at all magnitudes of interest.

Figures 9-1 through 9-12 show representative predictions by the Engineering Model for the two groups of crustal regions, for one high frequency (10 Hz), one low frequency (1 Hz) and PGA, and for the two magnitude representations considered in this study. Figures 9-13 through 9-16 show the predicted response spectra for magnitudes 5 and 7 a distance of 25 km.

Figures 9-1 through 9-12 indicate only a minor discontinuity in slope at 100 km as a result of crustal reflections. This discontinuities is smoothed out by the distribution of hypocentral depth (causes increased variability near 100 km, as will be shown in Section 3.3.3).

1. We refer to the Midcontinent as a "region," although it is a group of crustal regions.

Table 9-3

Coefficients of Attenuation Functions for Midcontinent Region (using Lg magnitude)

Freq. (Hz)	C_1	C_2	C_3	C_4	C_5	C_6	C_7
1.0	–0.12	2.05	–0.34	0.90	0.59	0.0019	6.8
2.5	0.90	1.70	–0.26	0.94	0.65	0.0029	7.2
5.0	1.60	1.24	0	0.98	0.74	0.0039	7.5
10.0	2.36	1.23	0	1.12	1.05	0.0043	8.5
25.0	3.54	1.19	0	1.46	1.84	0.0010	10.5
35.0	3.87	1.19	0	1.57	1.90	0.0005	11.1
Peak Accel.	2.07	1.20	0	1.28	1.23	0.0018	9.3

Table 9-4

Coefficients of Attenuation Equations for Gulf Region (using moment magnitude)

Freq. (Hz)	C_1	C_2	C_3	C_4	C_5	C_6	C_7
1.0	0.24	1.31	–0.15	0.79	0.82	0.0034	7.2
2.5	1.64	1.06	–0.08	0.99	1.27	0.0036	8.9
5.0	3.10	0.92	0	1.34	1.95	0.0017	11.4
10.0	5.08	1.00	0	1.87	2.52	0.0002	14.1
25.0	5.19	0.91	0	1.96	1.96	0.0004	12.9
35.0	4.81	0.91	0	1.89	1.80	0.0008	11.9
Peak Accel.	2.91	0.92	0	1.49	1.61	0.0014	10.9

Table 9-5

Coefficients of Attenuation Equations for Gulf Region (using Lg magnitude)

Freq. (Hz)	C_1	C_2	C_3	C_4	C_5	C_6	C_7
1.0	0.06	1.97	–0.32	0.80	0.92	0.0030	7.3
2.5	1.49	1.74	–0.26	1.00	1.36	0.0032	9.0
5.0	3.00	1.31	0	1.35	2.03	0.0014	11.4
10.0	4.65	1.30	0	1.78	2.41	0	13.8
25.0	5.08	1.29	0	1.97	2.04	0	12.9
35.0	4.68	1.30	0	1.89	1.88	0.0005	11.9
Peak Accel.	2.80	1.31	0	1.49	1.68	0.0017	10.9

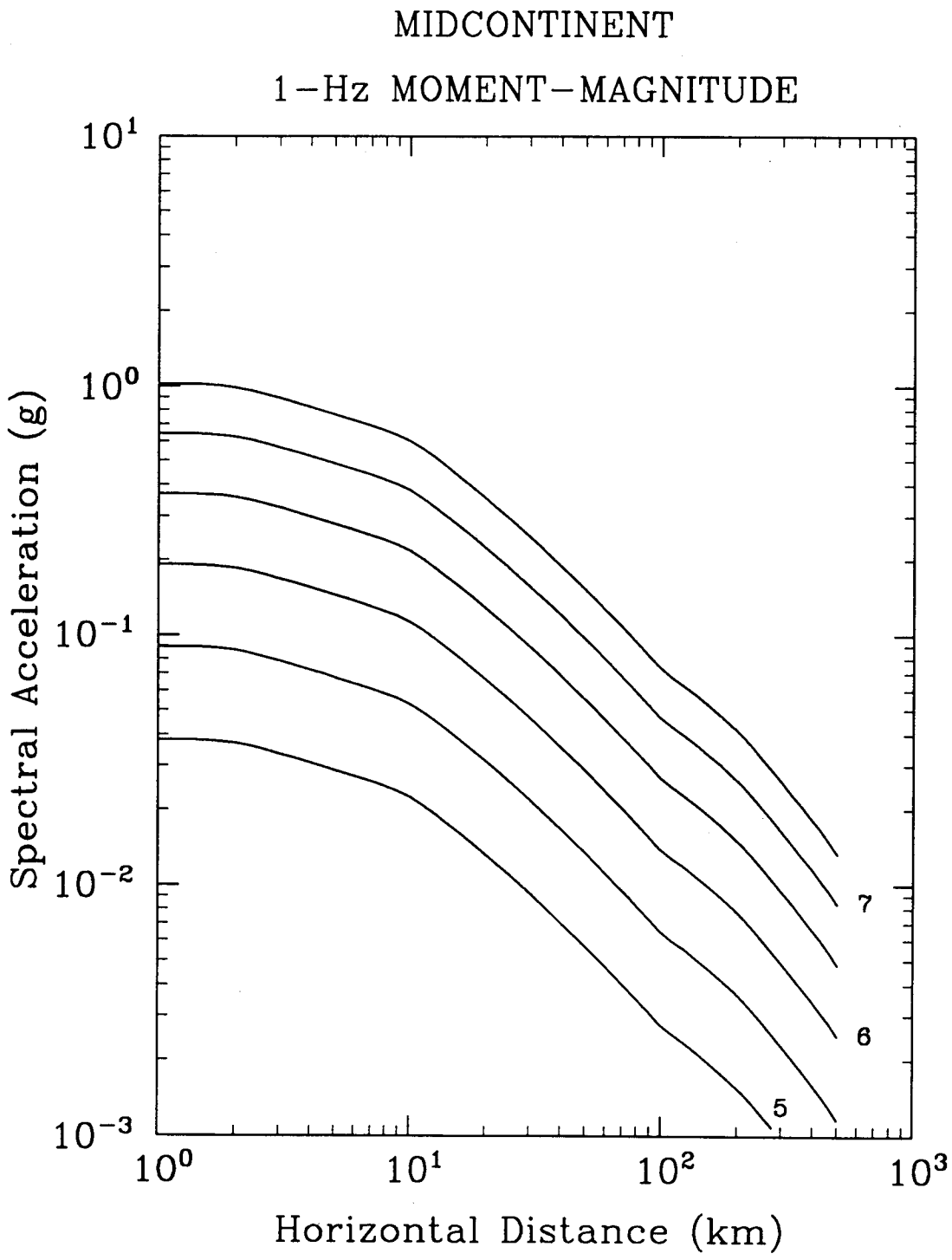

Figure 9-1. Attenuation equation for 1-Hz spectral acceleration in the Midcontinent region; equation in terms of M.

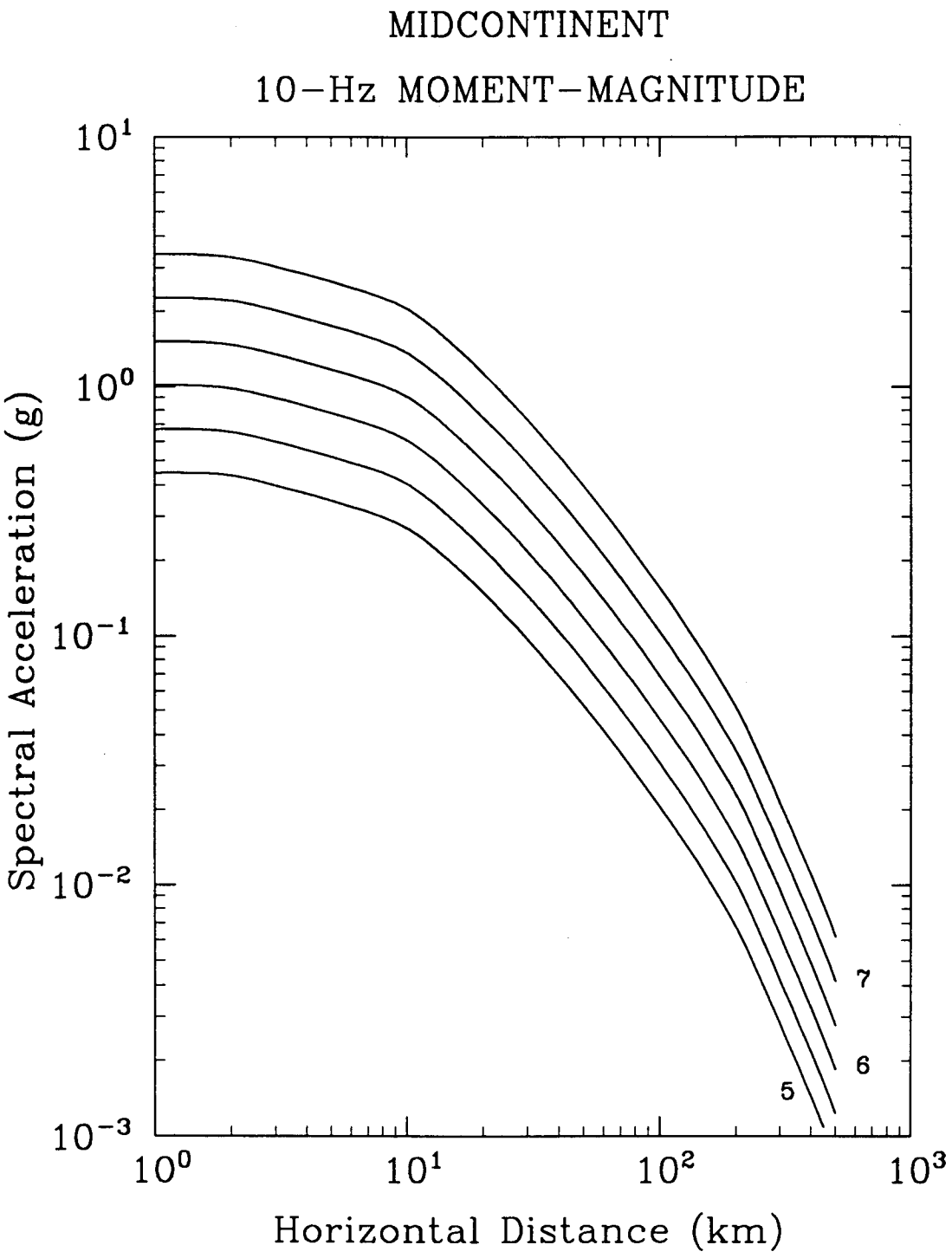

Figure 9-2. Attenuation equation for 10-Hz spectral acceleration in the Midcontinent region; equation in terms of M.

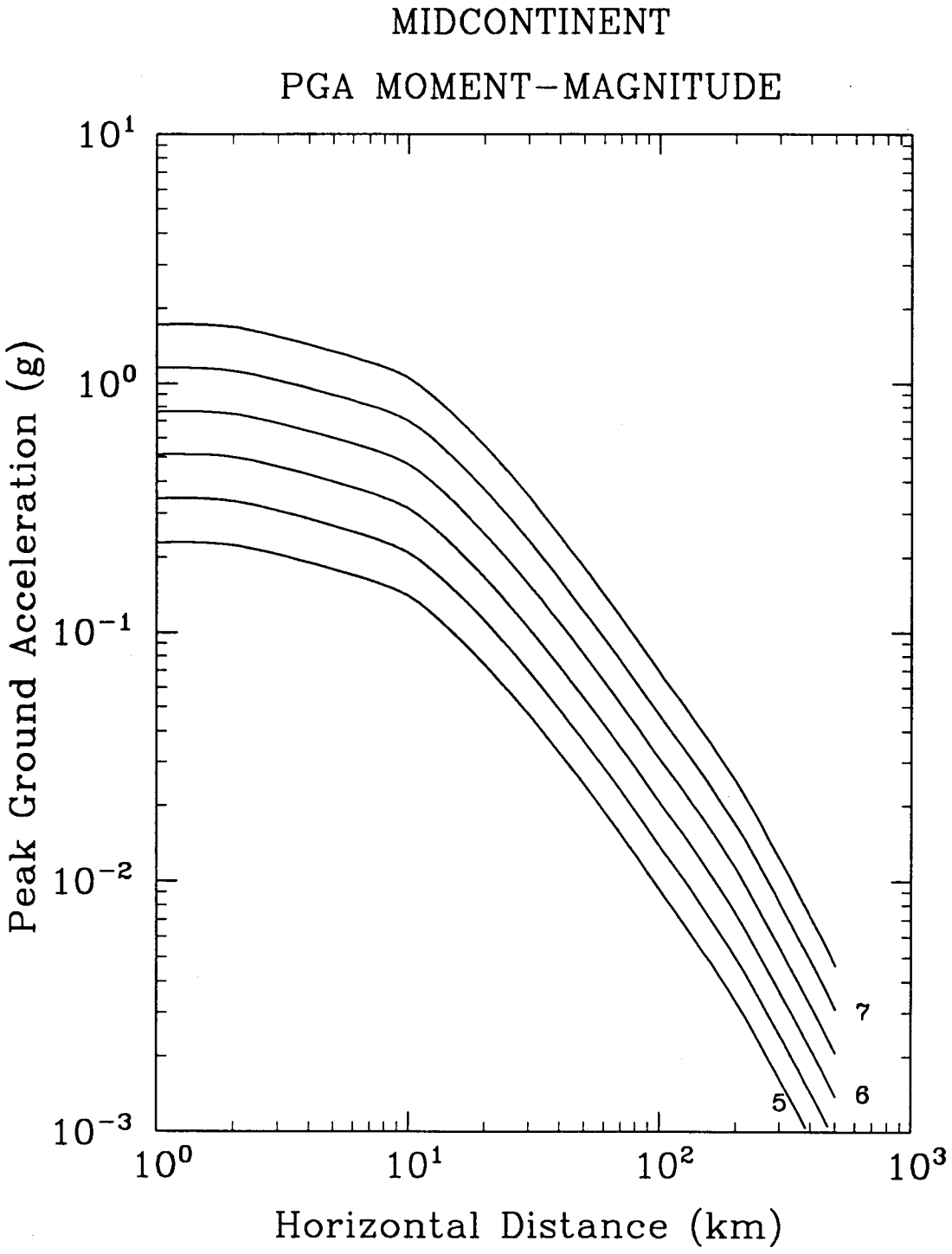

Figure 9-3. Attenuation equation for peak ground acceleration in the Midcontinent region; equation in terms of M.

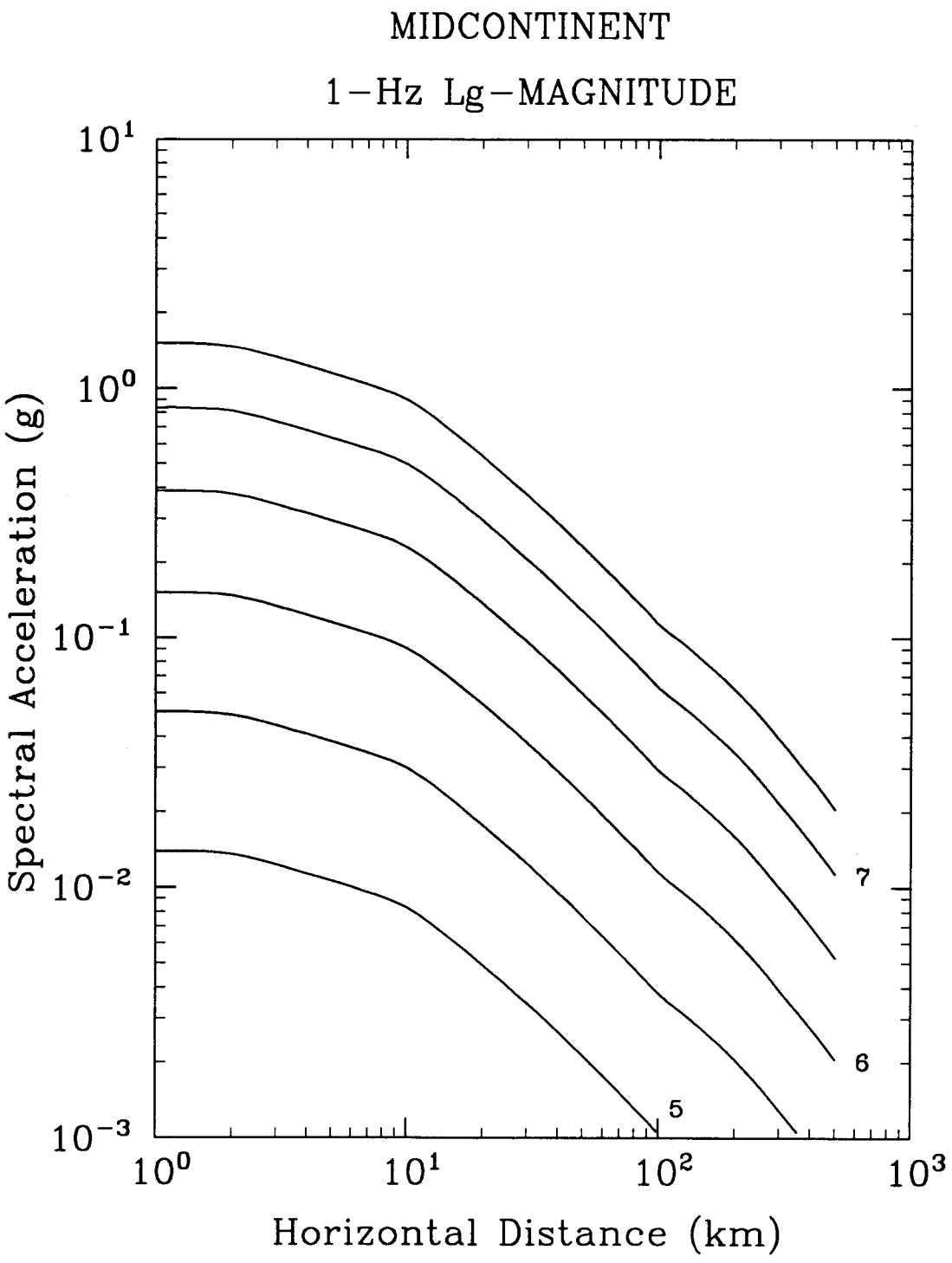

Figure 9-4. Attenuation equation for 1-Hz spectral acceleration in the Midcontinent region; equation in terms of m_{Lg}.

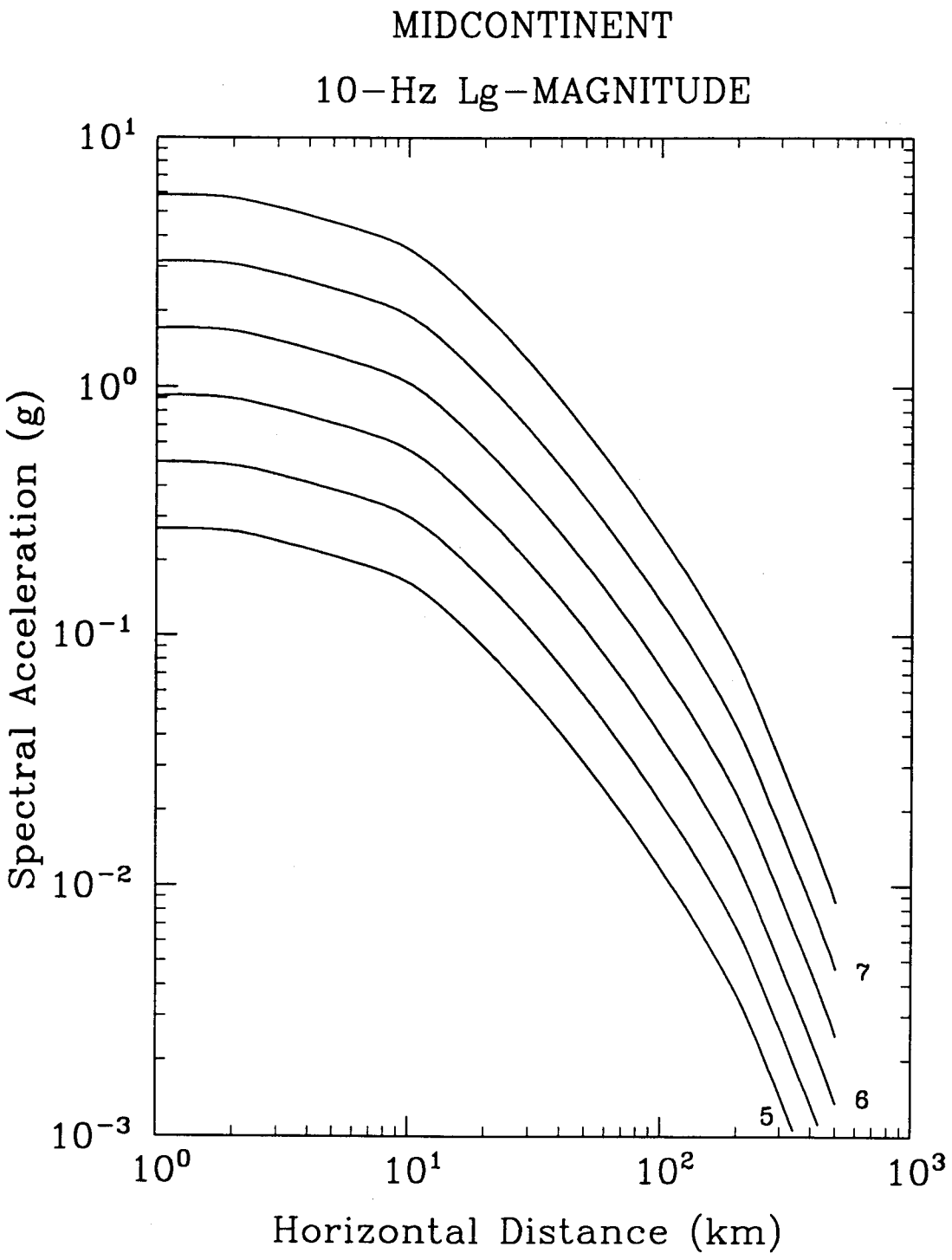

Figure 9-5. Attenuation equation for 10-Hz spectral acceleration in the Midcontinent region; equation in terms of m_{Lg}.

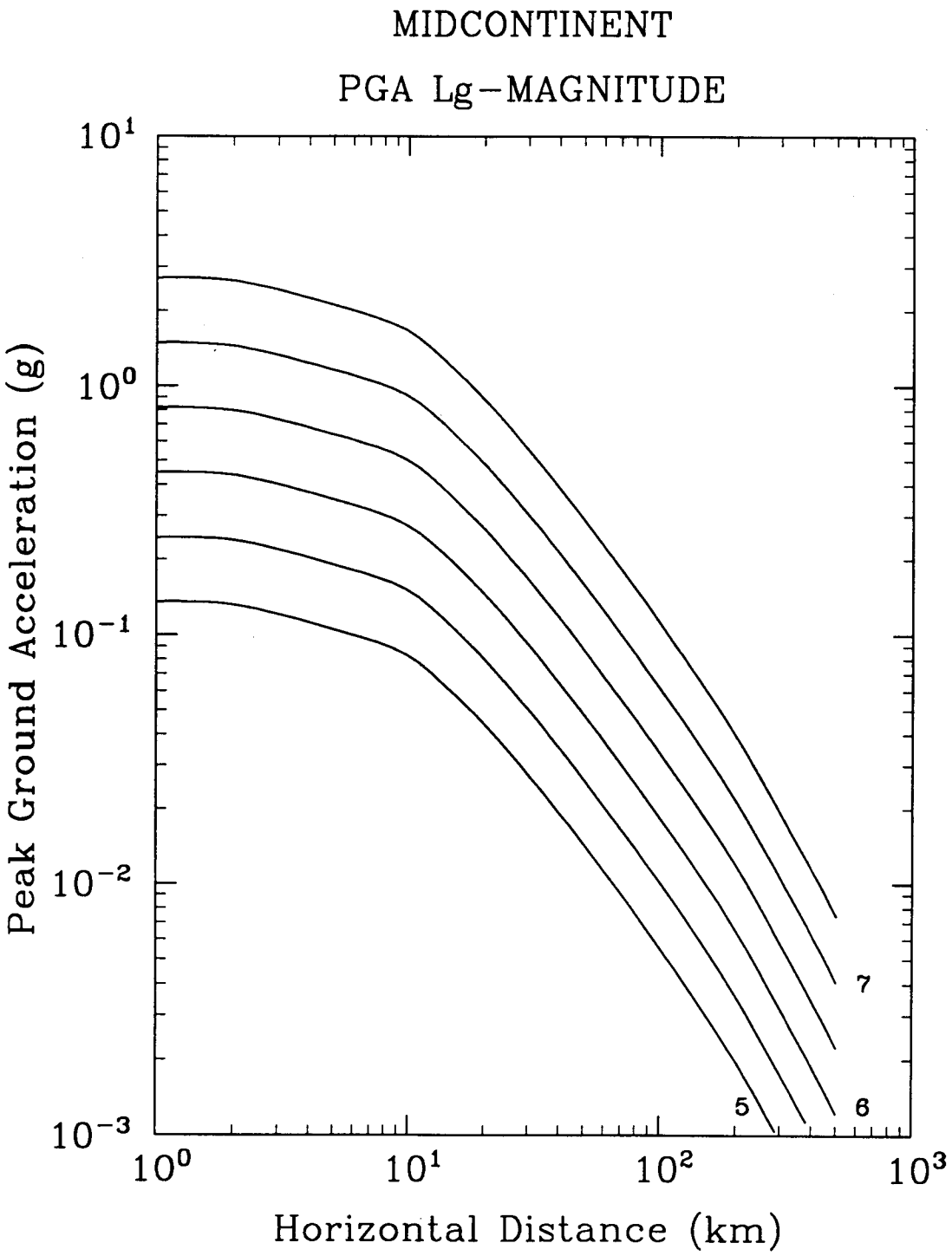

Figure 9-6. Attenuation equation for peak ground acceleration in the Midcontinent region; equation in terms of m_{Lg}.

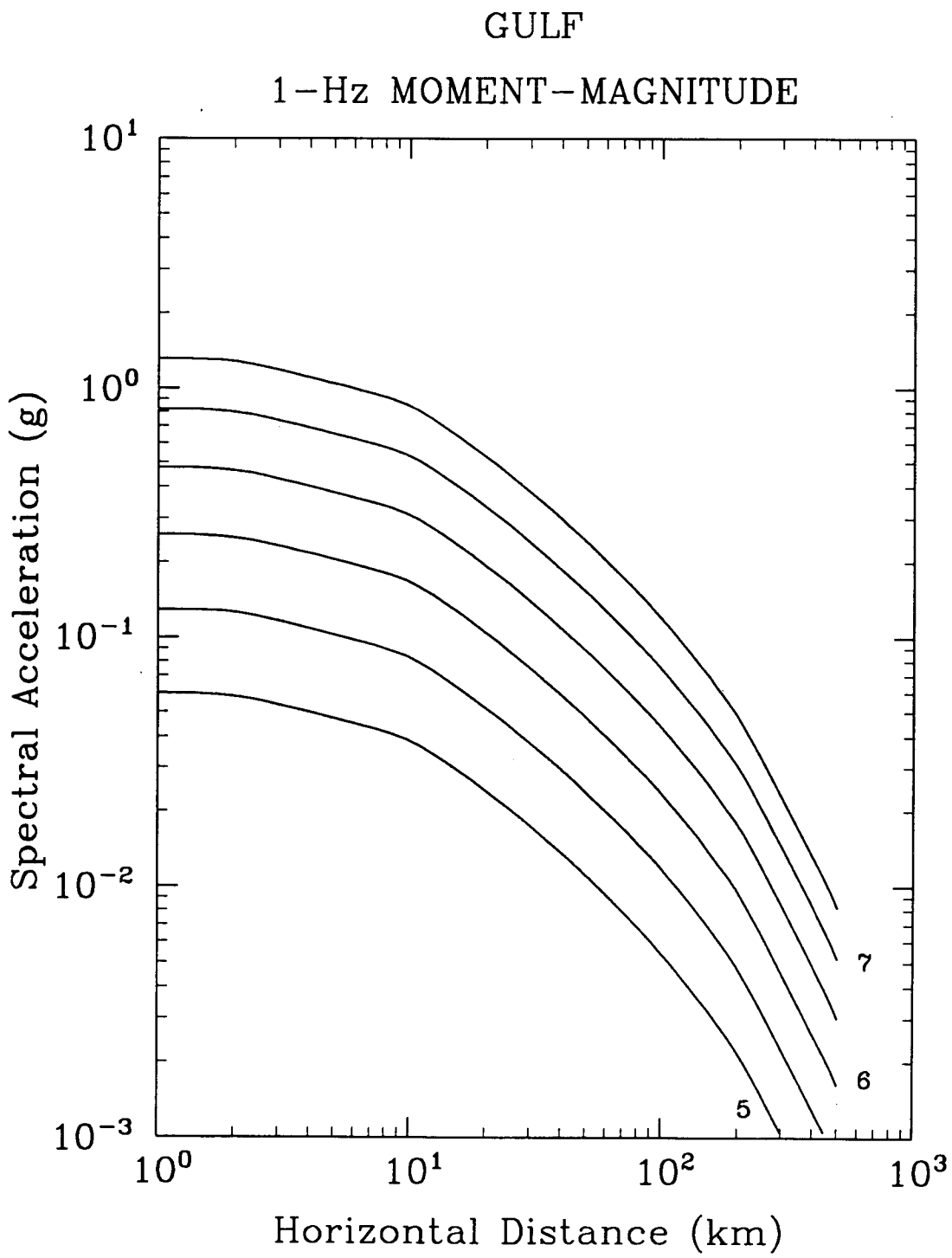

Figure 9-7. Attenuation equation for 1-Hz spectral acceleration in the Gulf region; equation in terms of M.

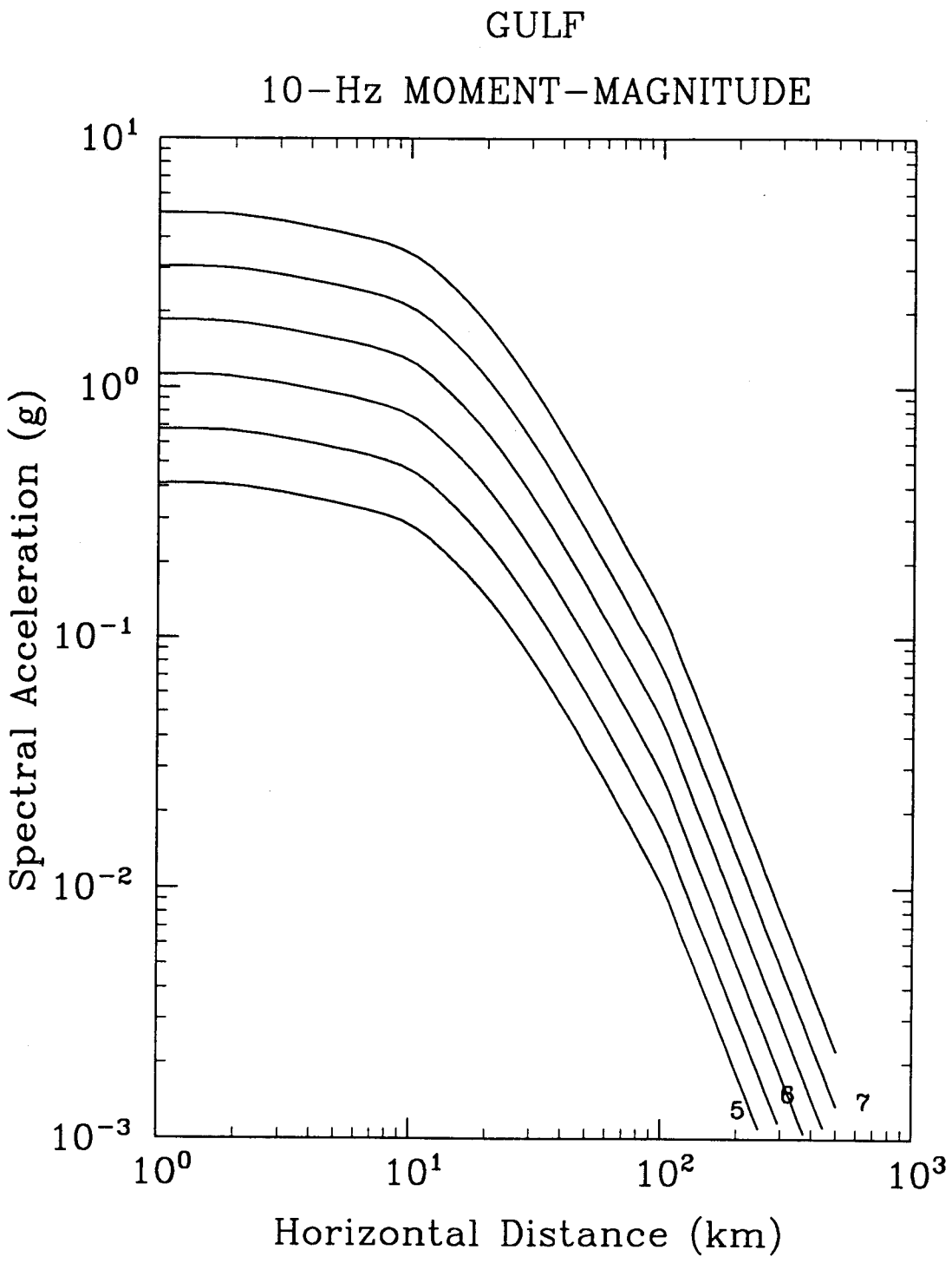

Figure 9-8. Attenuation equation for 10-Hz spectral acceleration in the Gulf region; equation in terms of M.

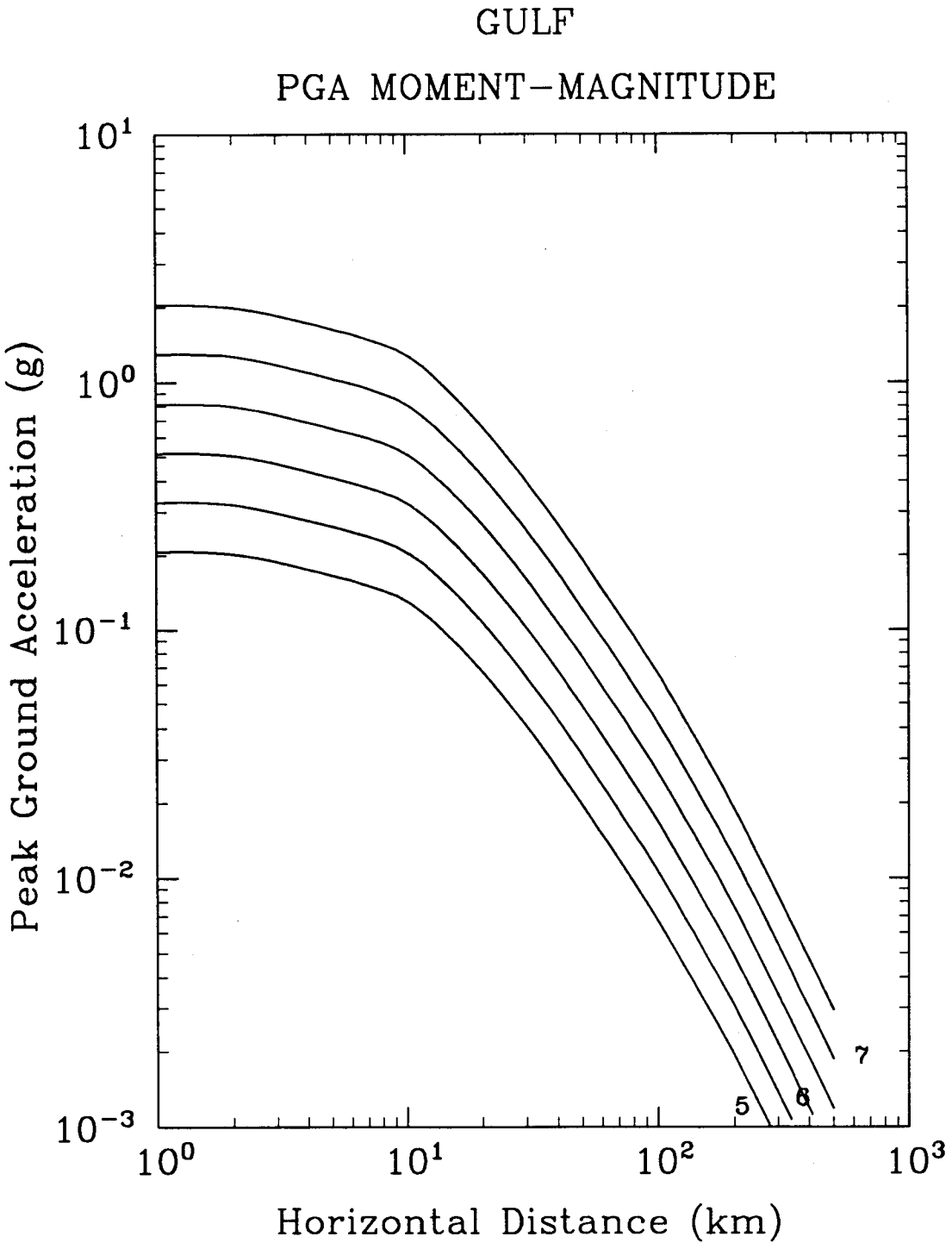

Figure 9-9. Attenuation equation for peak ground acceleration in the Gulf region; equation in terms of M.

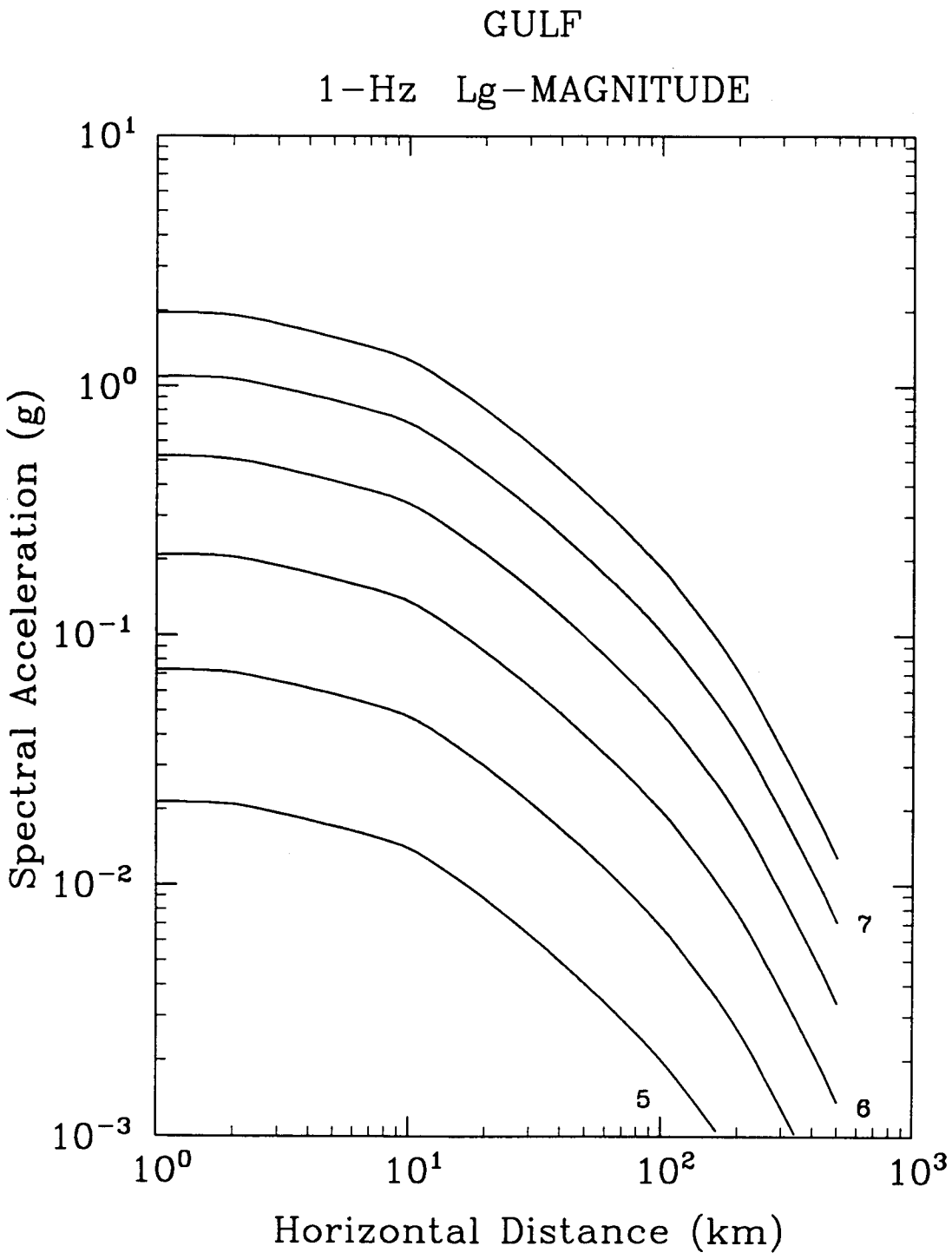

Figure 9-10. Attenuation equation for 1-Hz spectral acceleration in the Gulf region; equation in terms of m_{Lg}.

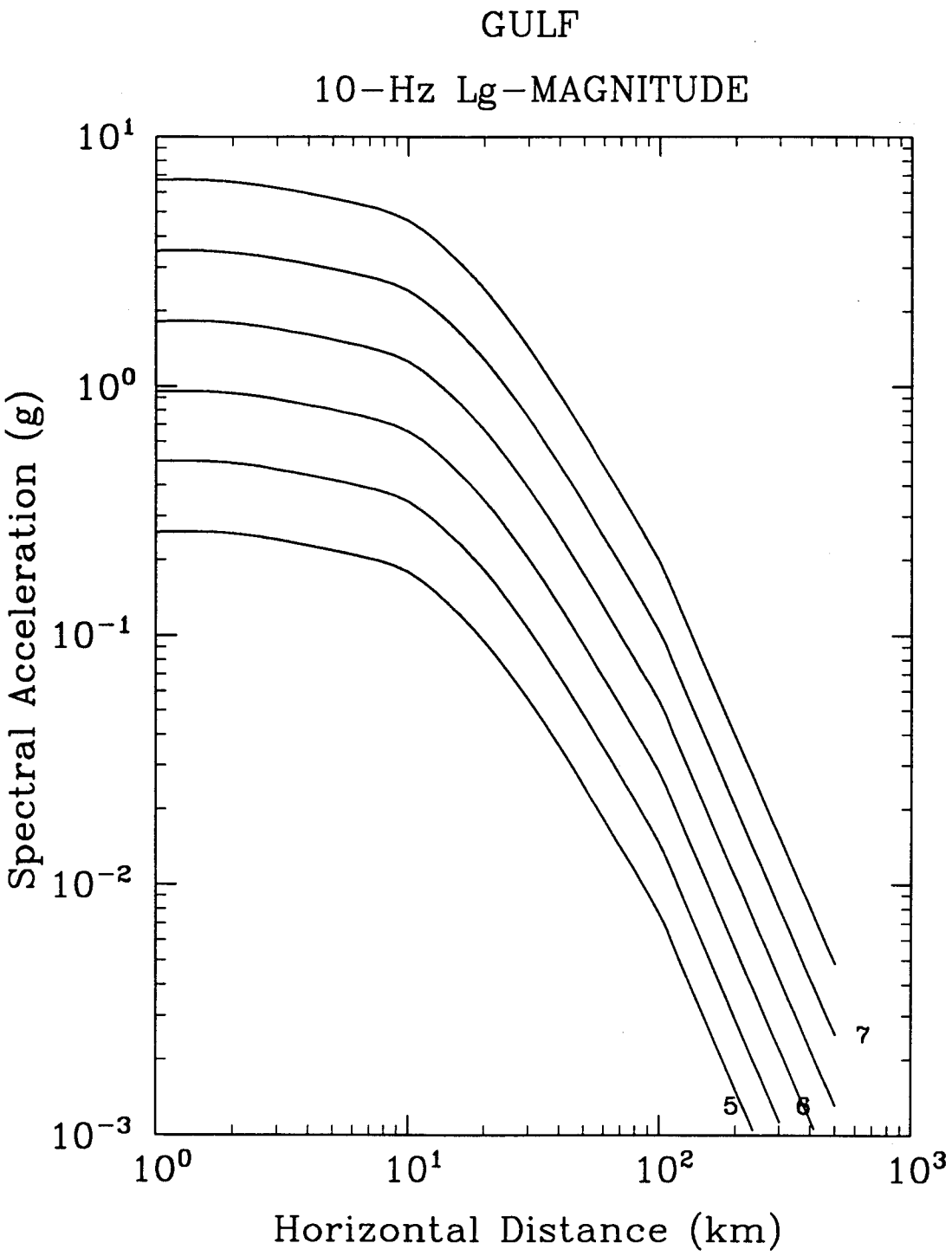

Figure 9-11. Attenuation equation for 10-Hz spectral acceleration in the Gulf region; equation in terms of m_{Lg}.

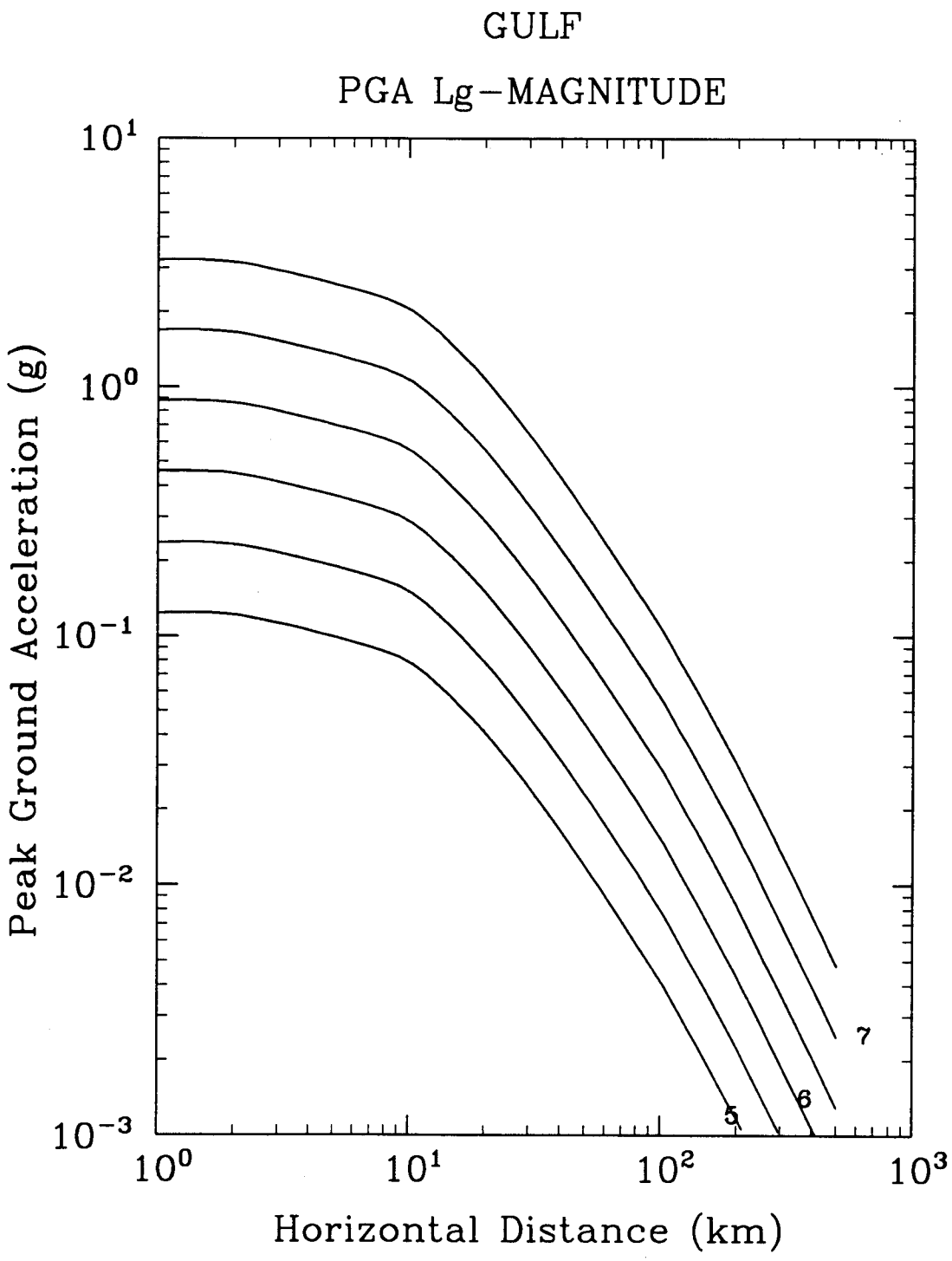

Figure 9-12. Attenuation equation for peak ground acceleration in the Gulf region; equation in terms of m_{Lg}.

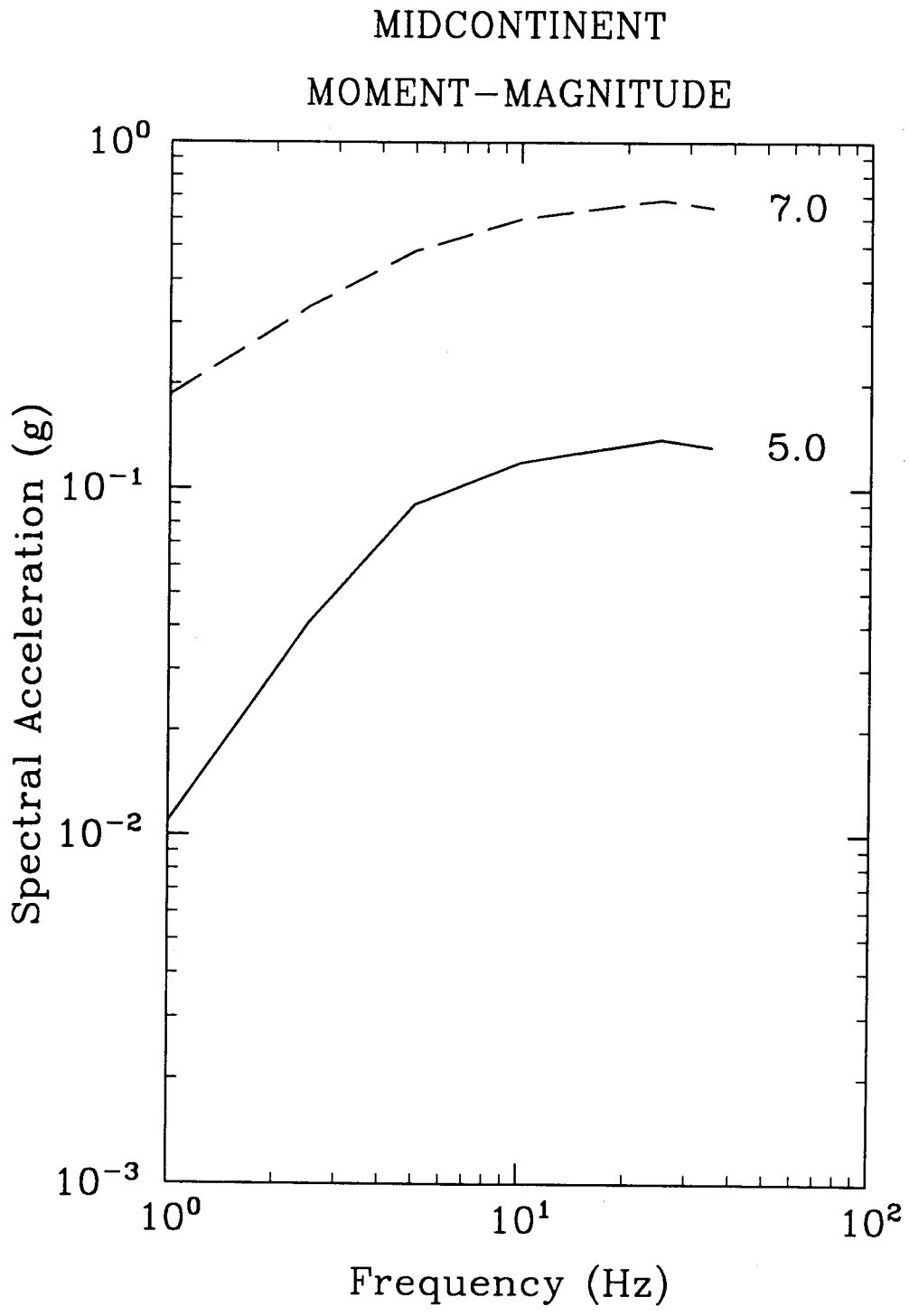

Figure 9-13. Pseudoacceleration spectra for magnitudes 5 and 7 at a distance of 20 km; Midcontinent region, equation in terms of M.

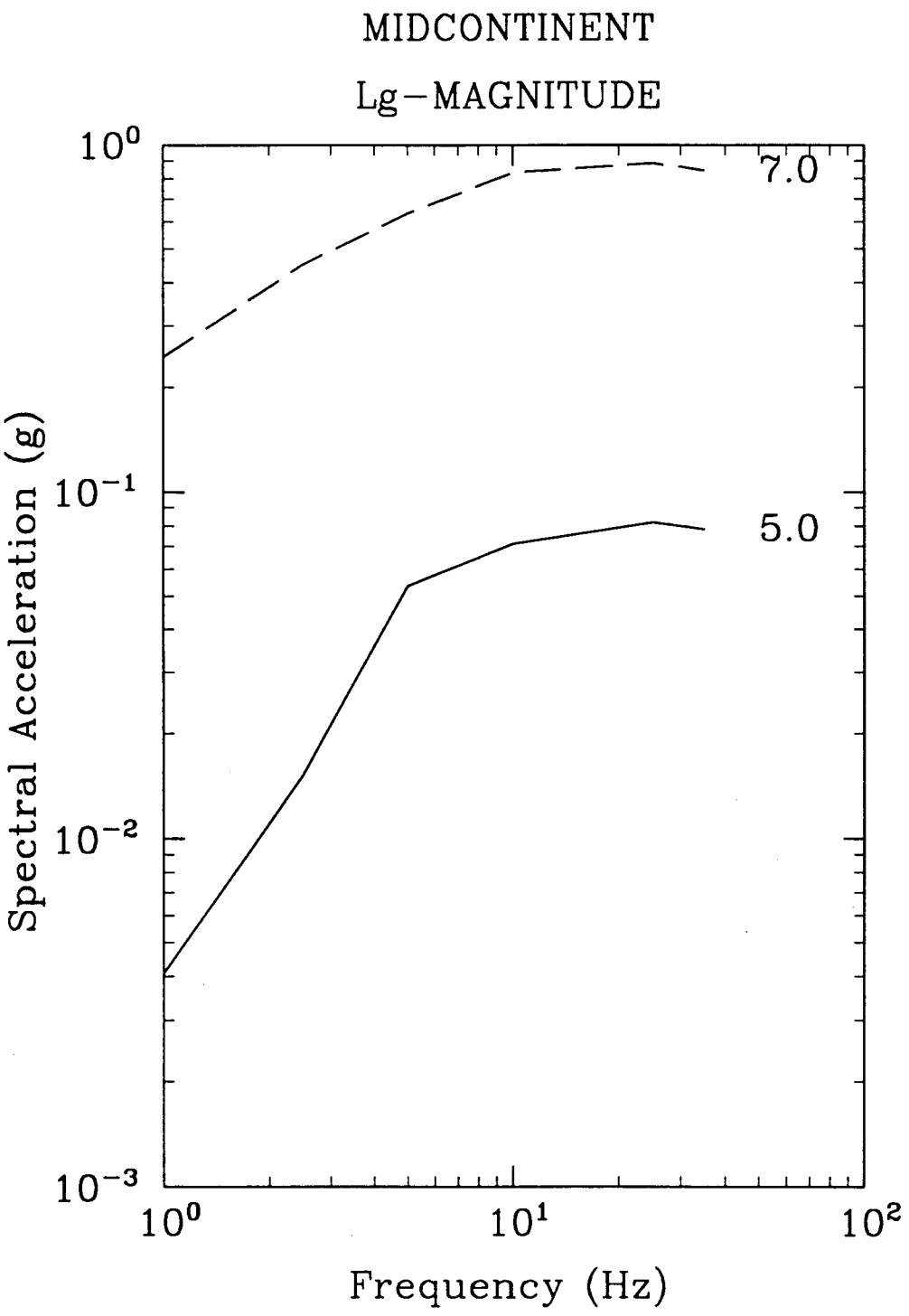

Figure 9-14. Pseudoacceleration spectra for magnitudes 5 and 7 at a distance of 20 km; Midcontinent region, equation in terms of m_{Lg}.

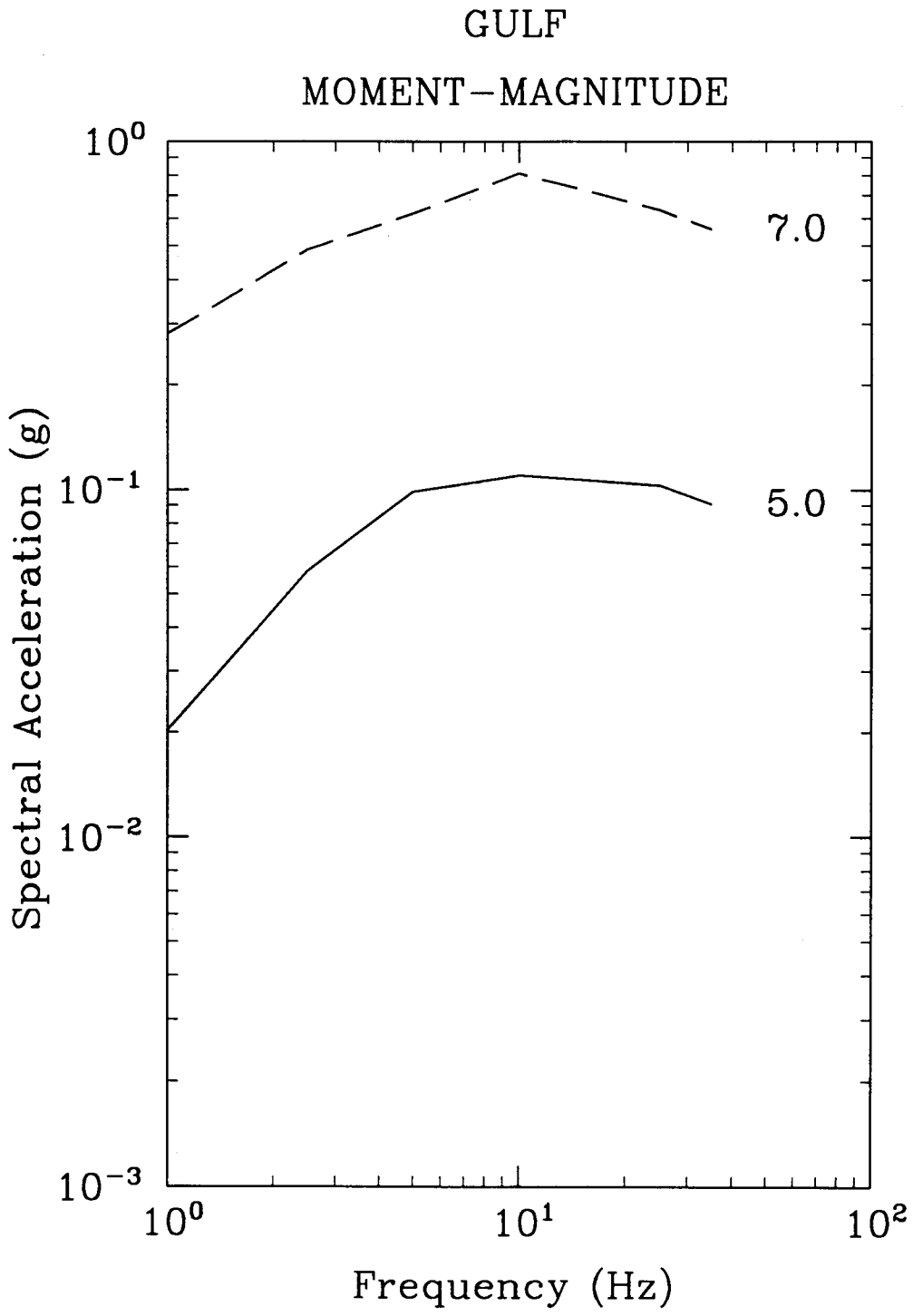

Figure 9-15. Pseudoacceleration spectra for magnitudes 5 and 7 at a distance of 20 km; Gulf region, equation in terms of M.

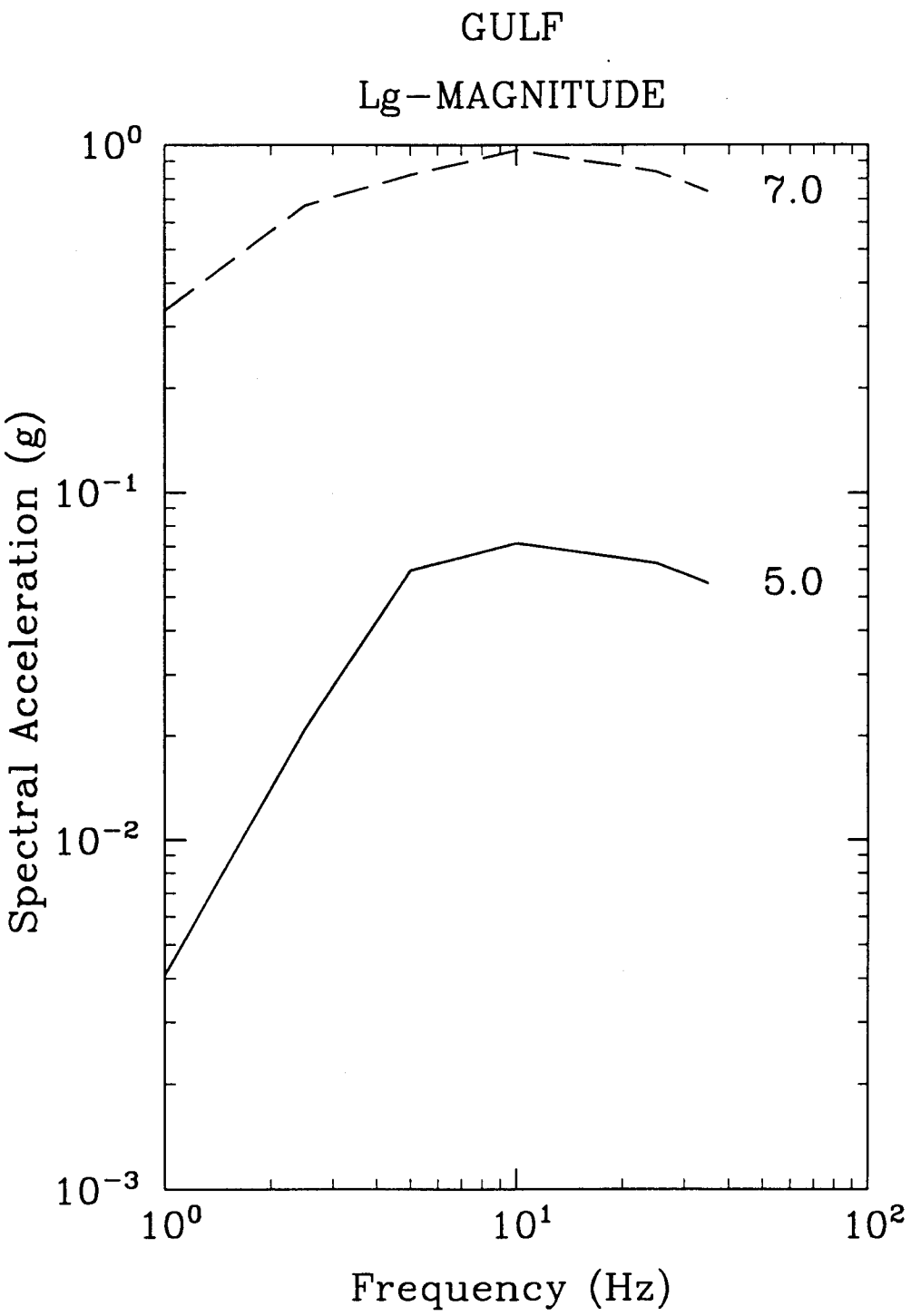

Figure 9-16. Pseudoacceleration spectra for magnitudes 5 and 7 at a distance of 20 km; Gulf region, equation in terms of m_{Lg}.

9.3.2 Special Cases: Paths Crossing Crustal Group Boundaries

If the path from a seismic source to the site crosses the boundary between the two crustal regions considered here, the question arises as to which equations to use and whether to consider increased variability.

Data and modeling results relating to paths that cross region boundaries were reviewed in Section 5.2.2.3. Due to the complexity of this problem, the most practical engineering solution is to compare the attenuation equations for the two crustal groups, and use the one that predicts the highest amplitude. The associated variability should be taken as the variability corresponding to that crustal group.

9.3.3 Treatment of Variability

Variability is separated into randomness and uncertainty, but it is sometimes useful to separate it into parametric and modeling variabilities. The combined effect of all parametric variabilities is obtained by examining the residuals from the least-squares fit to model predictions. The modeling variability, which is obtained from comparisons of predictions to data, is added as a separate term.

The parametric variability is made up of variabilities in stress drop, hypocentral depth, Q, and κ. The variability in stress drop is part randomness and part uncertainty, with their proportions varying as a function of magnitude. The variabilities in hypocentral depth, Q, and κ are considered all randomness (see Section 9.1). Their effects are distance- and frequency-dependent, as will be shown below.

The modeling variability is part randomness and part uncertainty. The randomness being frequency-dependent; the uncertainty is constant (see Section 9.1.1.6).

Figures 9-17 and 9-18 illustrate the various components of randomness and their dependence on distance for **M** 6.5 in the Midcontinent. These figures show that depth is a very important contributor to randomness at short distances, stress drop and modeling error are important contributors at all distances, and Q is an important contributor at long distances (particularly for high frequencies).

The tables and equations that follow provide a simplified representation of how randomness and uncertainty vary as a function of magnitude and distance for the various ground-motion measures. The focus is on the magnitude-distance-frequency combinations of engineering interest, and little attention is paid to unimportant combinations such as high frequencies at long distances.

The expressions for the total randomness and uncertainty can be obtained using the following equations:

$$\sigma_r(\mathrm{M},\mathrm{R},f) = \sqrt{\alpha^2(f)\,\sigma^2_{r,\Delta\sigma}(\mathrm{M}) + \sigma^2_{r,dist}(\mathrm{R}) + \sigma^2_{r,modeling}(f)}$$

$$\sigma_u(\mathrm{M},f) = \sqrt{\alpha^2(f)\,\sigma^2_{U,\Delta\sigma}(\mathrm{M}) + \sigma^2_{U,modeling}}$$

(Eq. 9-3)

where σ_r and σ_U are randomness and uncertainty, α(f) denotes the sensitivity of spectral acceleration to stress drop, $\sigma_{r,\Delta\sigma}$ and $\sigma_{U,\Delta\sigma}$ are the randomness and uncertainty in stress drop, $\sigma_{r,dist}$ is the distance-dependent randomness (associated with depth, Q, and κ). Finally, $\sigma_{r,modeling}$ and $\sigma_{U,modeling}$, are the modeling randomness and uncertainty, respectively.

Values of α(f) are given in Table 9-6, where separate values are given for both **M** and m_{Lg}. $\sigma_{r,\Delta\sigma}$ and $\sigma_{U,\Delta\sigma}$ are given by the following equations (see also Section 4.2.3):[2]

$$\sigma_{r,\Delta\sigma}(\mathbf{M}) = \begin{cases} 0.684 & \mathbf{M} < 6 \\ \sqrt{(0.684)^2 - 0.436\,(\mathbf{M}-6)} & 6 < \mathbf{M} < 6.5 \\ 0.50 & \mathbf{M} \geq 6.5 \end{cases}$$

(Eq. 9-4)

$$\sigma_{U,\Delta\sigma}(\mathbf{M}) = \begin{cases} 0.15 & \mathbf{M} < 6 \\ \sqrt{(0.15)^2 - 0.455\,(\mathrm{M}-6)} & 6 < \mathbf{M} < 6.5 \\ 0.50 & \mathbf{M} \geq 6.5 \end{cases}$$

(Eq. 9-5)

The distance-dependent randomness $\sigma_{r,dist}$ is defined in terms of its values for distances of 5 and 20 km.[3] These

2. For the attenuation equations in terms of m_{Lg}, the moment-magnitude values of 6 and 6.5 in these equations are replaced by the equivalent m_{Lg} values of 6.2 and 6.6.
3. Values of $\sigma_{r,dist}$ for distances between 5 and 20 km are obtained by interpolation. Values for distances shorter than 5 km or longer than 20 km are equal to the values for 5 and 20 km, respectively.

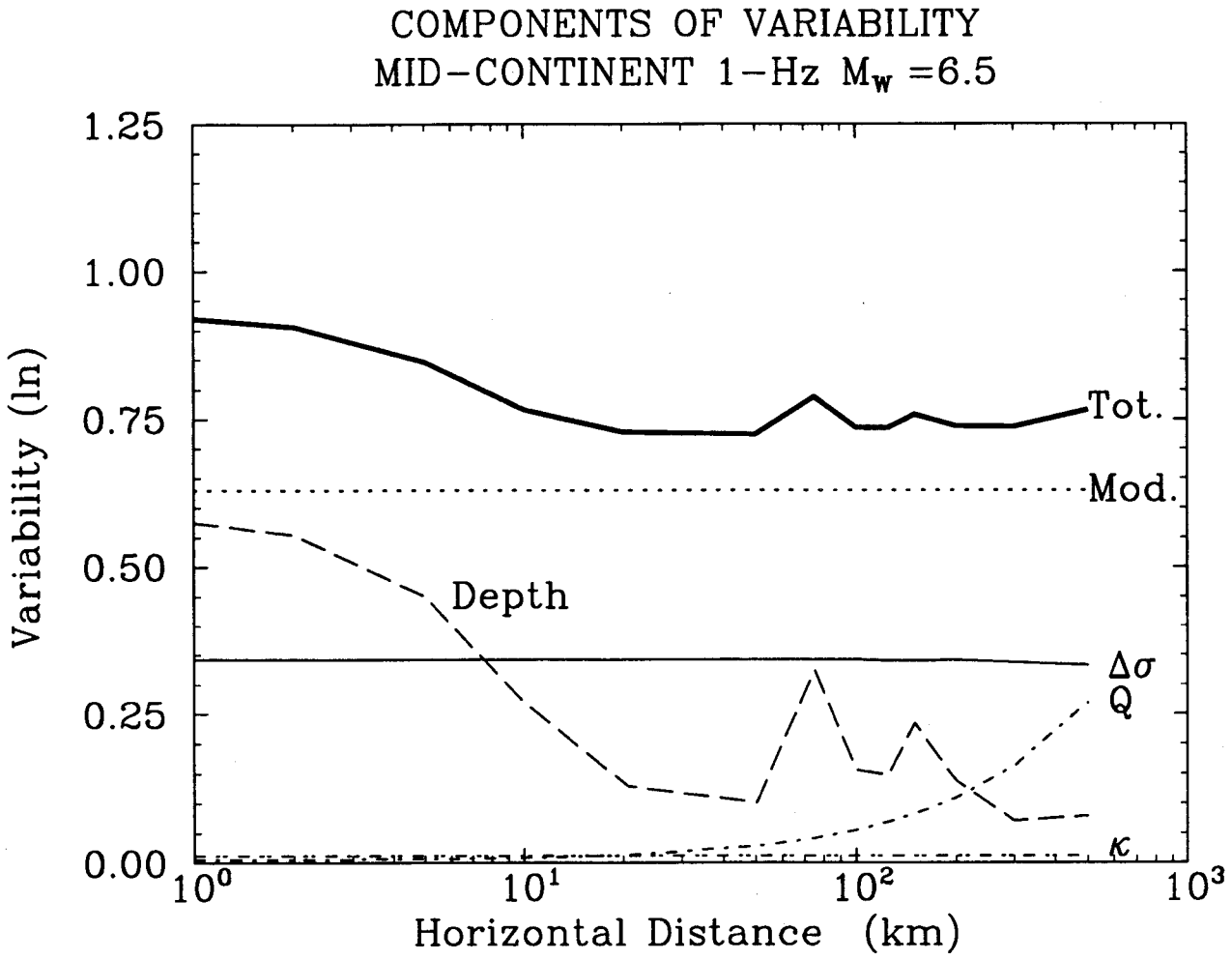

Figure 9-17. Contributors to randomness and their dependence on distance; 1-Hz spectral acceleration for M 6.5 in the Midcontinent region.

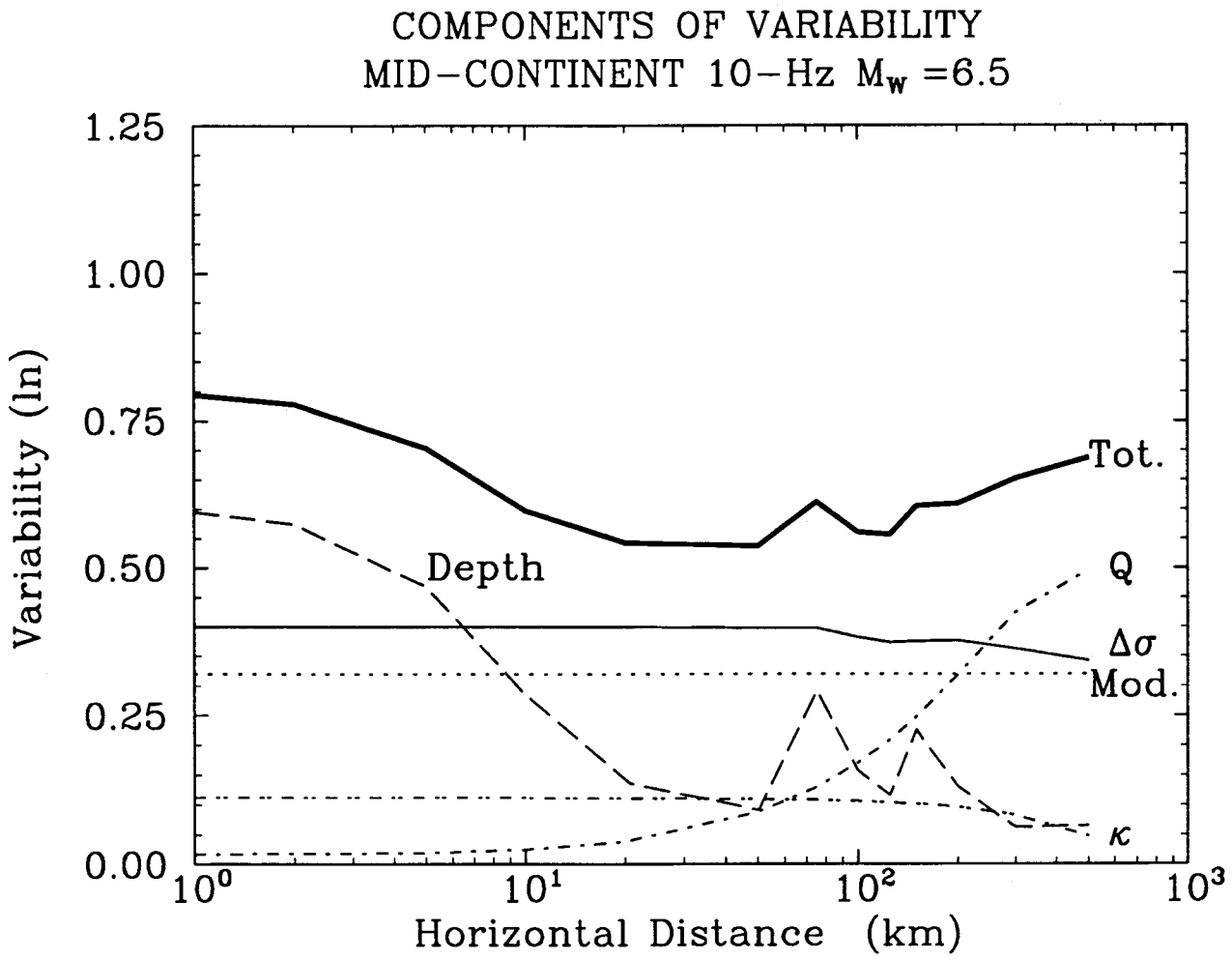

Figure 9-18. Contributors to randomness and their dependence on distance; 10-Hz spectral acceleration for M 6.5 in the Midcontinent region.

Table 9-6

Parameters Controlling Randomness and Uncertainty

	Midcontinent				Gulf	
Freq.(Hz)	α (M)	α (m_{Lg})	$\sigma_{r,dist}$ (5 km)	$\sigma_{r,dist}$ (20 km)	$\sigma_{r,dist}$ (5 km)	$\sigma_{r,dist}$ (20 km)
1.0	0.69	0.94	0.45	0.12	0.51	0.39
2.5	0.76	0.77	0.45	0.12	0.50	0.34
5.0	0.79	0.75	0.45	0.12	0.50	0.33
10.0	0.80	0.73	0.50	0.17	0.53	0.38
25.0	0.81	0.72	0.57	0.29	0.63	0.47
35.0	0.81	0.72	0.62	0.35	0.68	0.47
Peak Accel.	0.81	0.72	0.54	0.20	0.48	0.30

values are calculated by examination of the regression residuals and are given in Table 9-6. The modeling variabilities $\sigma_{r,modeling}$ and $\sigma_{U,modeling}$ are given by the equations presented in Section 9.1.1.6 (see also Table 3-2), i.e.,

$$\sigma_{r,\,modeling}(f) = \begin{cases} 0.32 & f \geq 9\text{Hz} \\ 0.63 - 0.14 \ln(f) & 1 \leq f < 9\text{Hz} \end{cases} \qquad \text{(Eq. 9-6)}$$

$$\sigma_{\dot{U},\,modeling} = 0.27 \qquad \text{(Eq. 9-7)}$$

Figures 9-19 through 9-26 show the total randomness as a function of magnitude and distance. Randomness is higher at short distances due to the effect of random focal depth. Randomness is lower at high magnitudes because randomness in stress drop is lower for high magnitudes. Randomness is higher for low-frequency ground motions due to higher model randomness (see Equation 9.3.4). The attenuation equations for m_{Lg} have higher randomness than the equations for M for low frequencies and slightly lower randomness for high frequencies.

Table 9-7 shows the uncertainty for magnitudes smaller than 6 and larger than 6.5. The uncertainty is smaller at lower magnitudes and larger at high magnitudes. This is caused by the uncertainty in stress drop, which is higher for higher magnitudes due to the limited availability of data.

9.3.3.1 Discretization of Uncertainty for Seismic Hazard Analysis

In seismic hazard analysis, uncertainty is typically represented by considering multiple attenuation equations with weights related to their credibilities. This approach is natural when using attenuation equations developed by different authors or under a discrete set of alternative assumptions, and is convenient because it lends itself to a logic-tree analysis and to the display of sensitivity. Randomness, on the other hand, is represented by a continuous random variable and is integrated over during the first step (i.e., the conditional analysis step) of the seismic-hazard calculations.

The median predictions by the Engineering Model (represented by Equation 9-1 and Tables 9-2 through 9-5) and the uncertainty represented by σ_U may be transformed into a discrete set of attenuation equations. This is accomplished by replacing the normal distribution of the uncertainty term ε_U with a discrete distribution. The discrete distribution consists of n values

$$\varepsilon_{U,i} = U_i \sigma_U(M, R), \qquad i = 1, n \qquad \text{(Eq. 9-8)}$$

and their associated weights W_i, where U_i represents a value from a discrete approximation to a standard normal

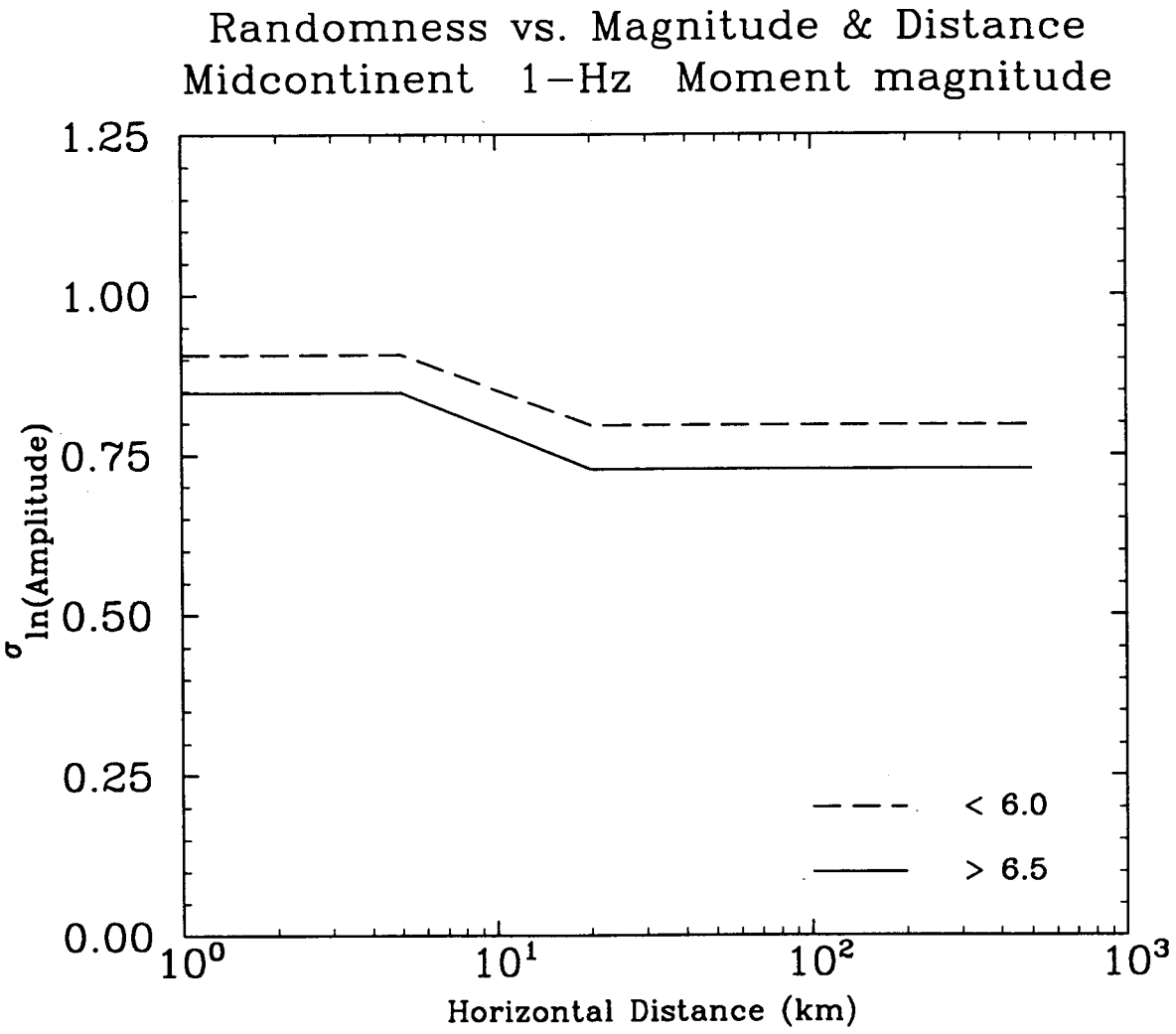

Figure 9-19. Variation of randomness as a function of magnitude and distance for 1-Hz spectral acceleration; Midcontinent region, equation in terms of M. Solid, M>6.5; dashed, M<6.

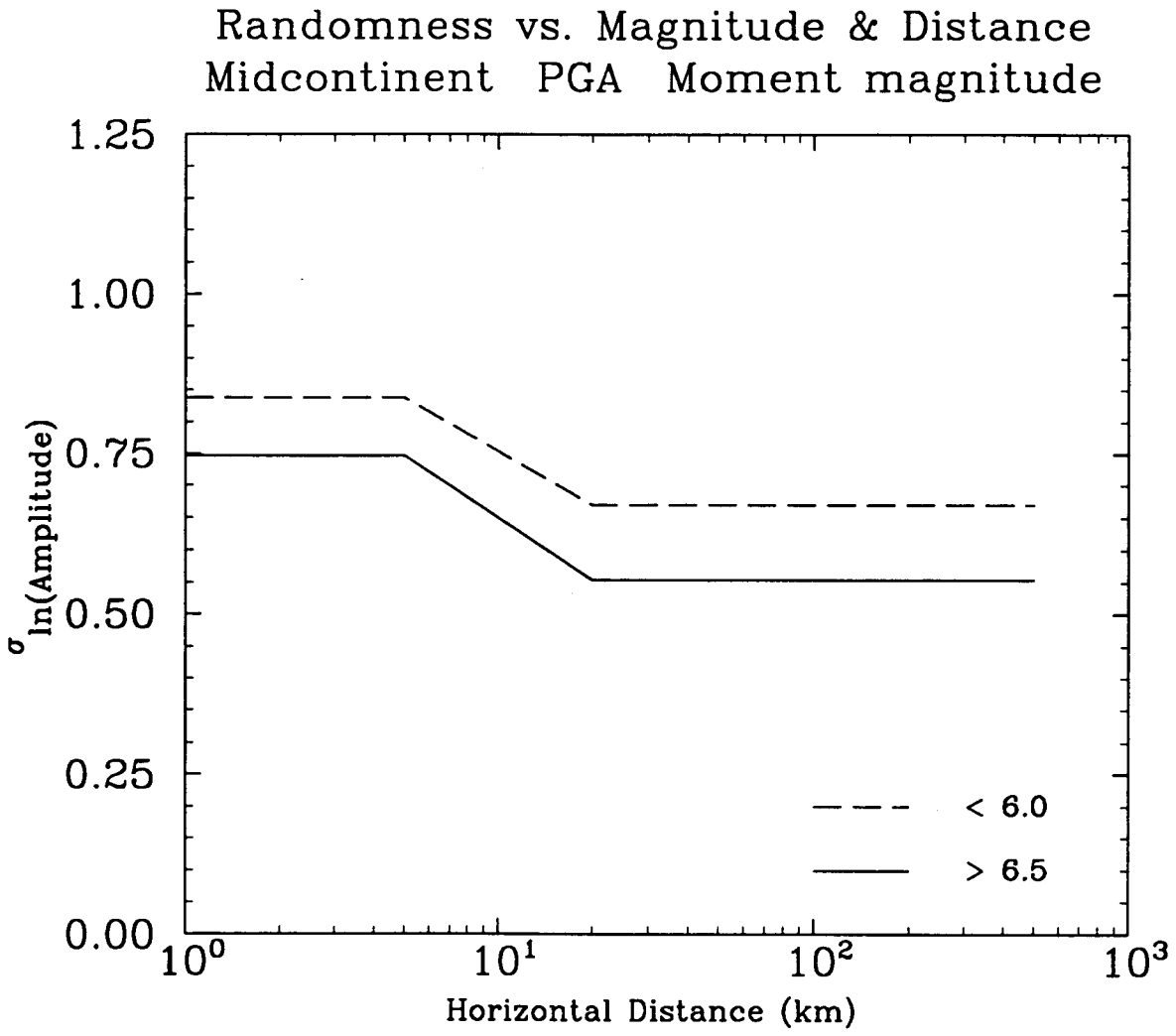

Figure 9-20. Variation of randomness as a function of magnitude and distance for peak ground acceleration; Midcontinent region, equation in terms of M. Solid, M>6.5; dashed, M<6.

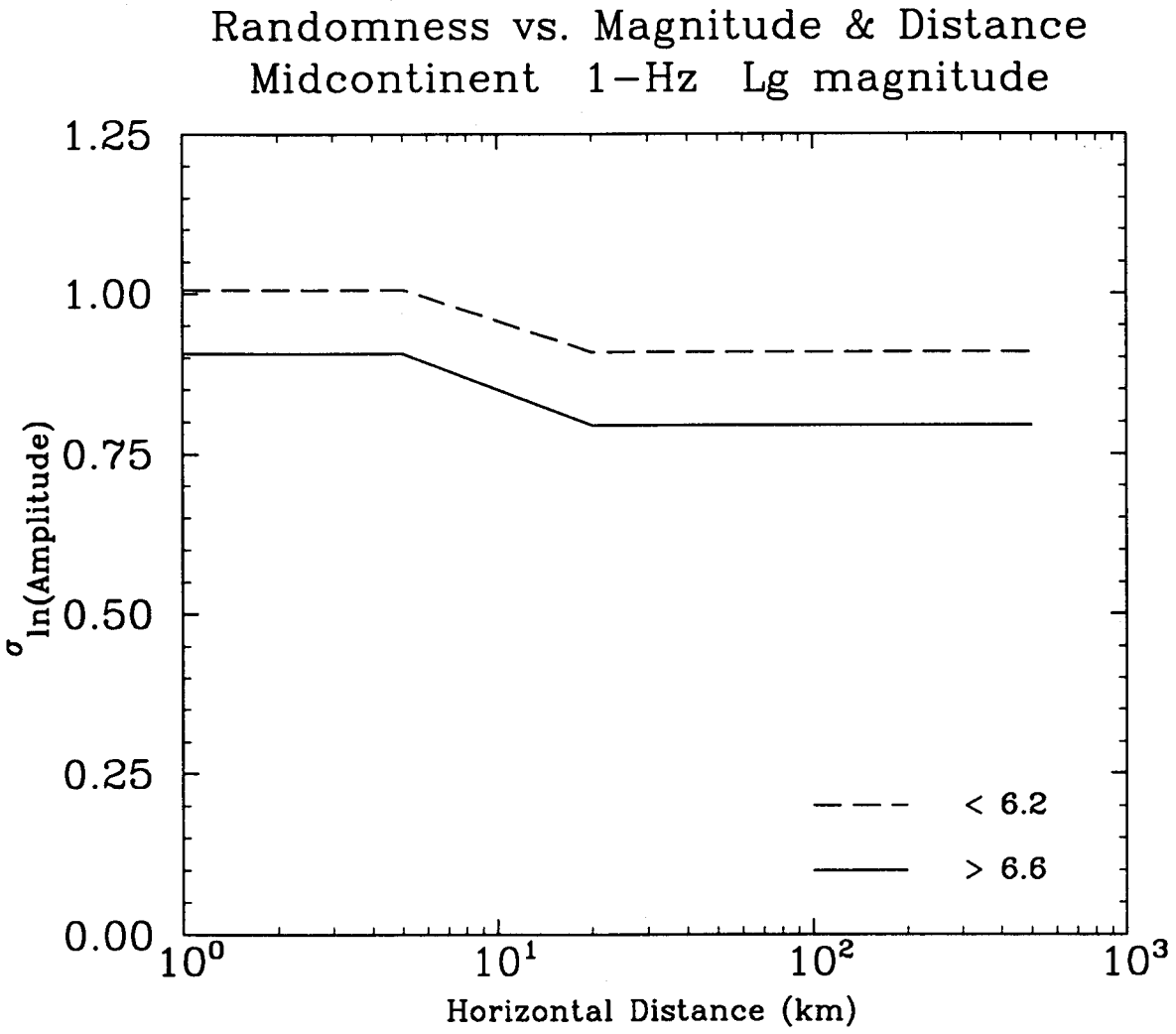

Figure 9-21. Variation of randomness as a function of magnitude and distance for 1-Hz spectral acceleration; Midcontinent region, equation in terms of m_{Lg}. Solid, M>6.5; dashed, M<6.

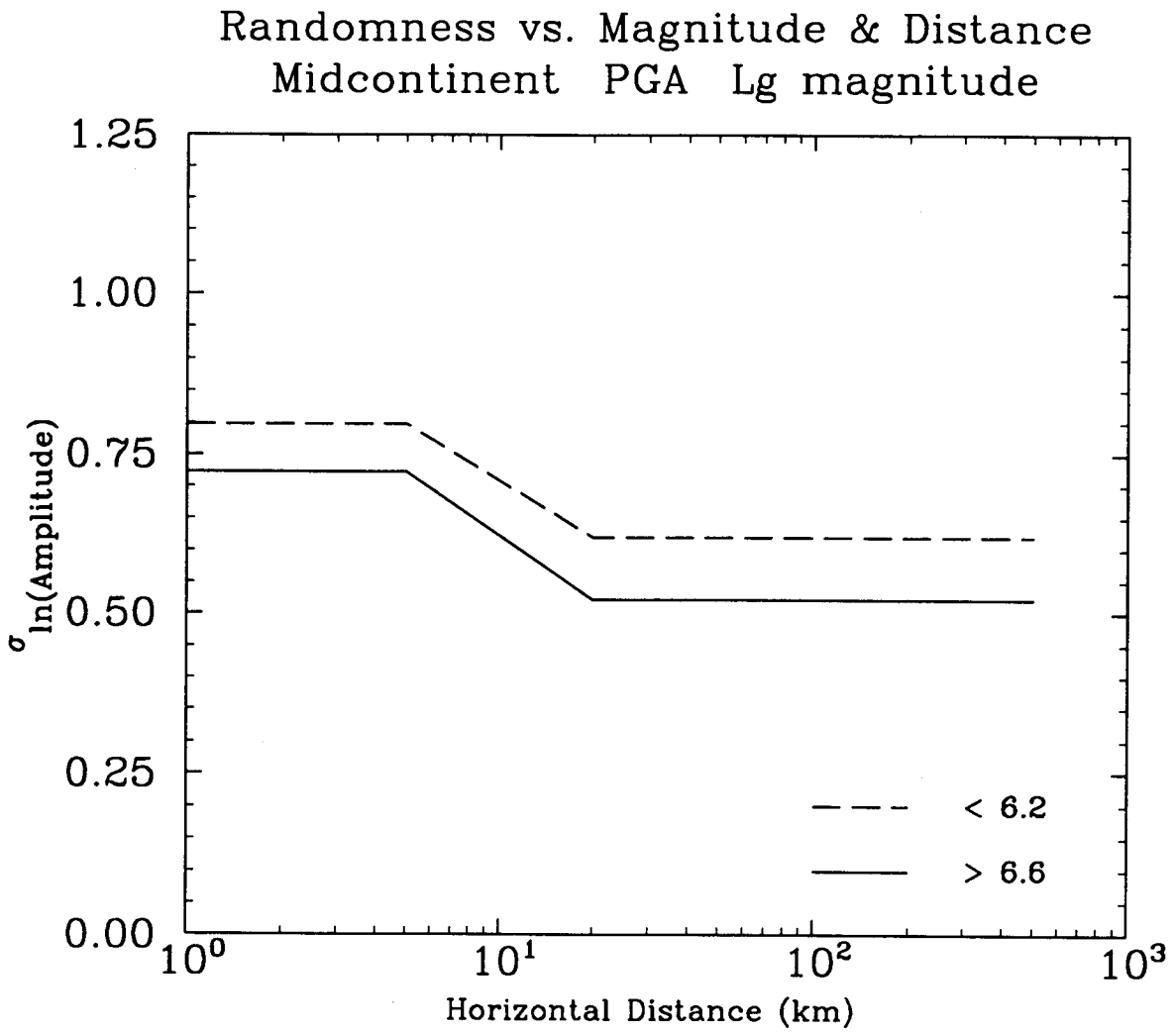

Figure 9-22. Variation of randomness as a function of magnitude and distance for peak ground acceleration; Midcontinent region, equation in terms of m_{Lg}. Solid, M>6.5; dashed, M<6.

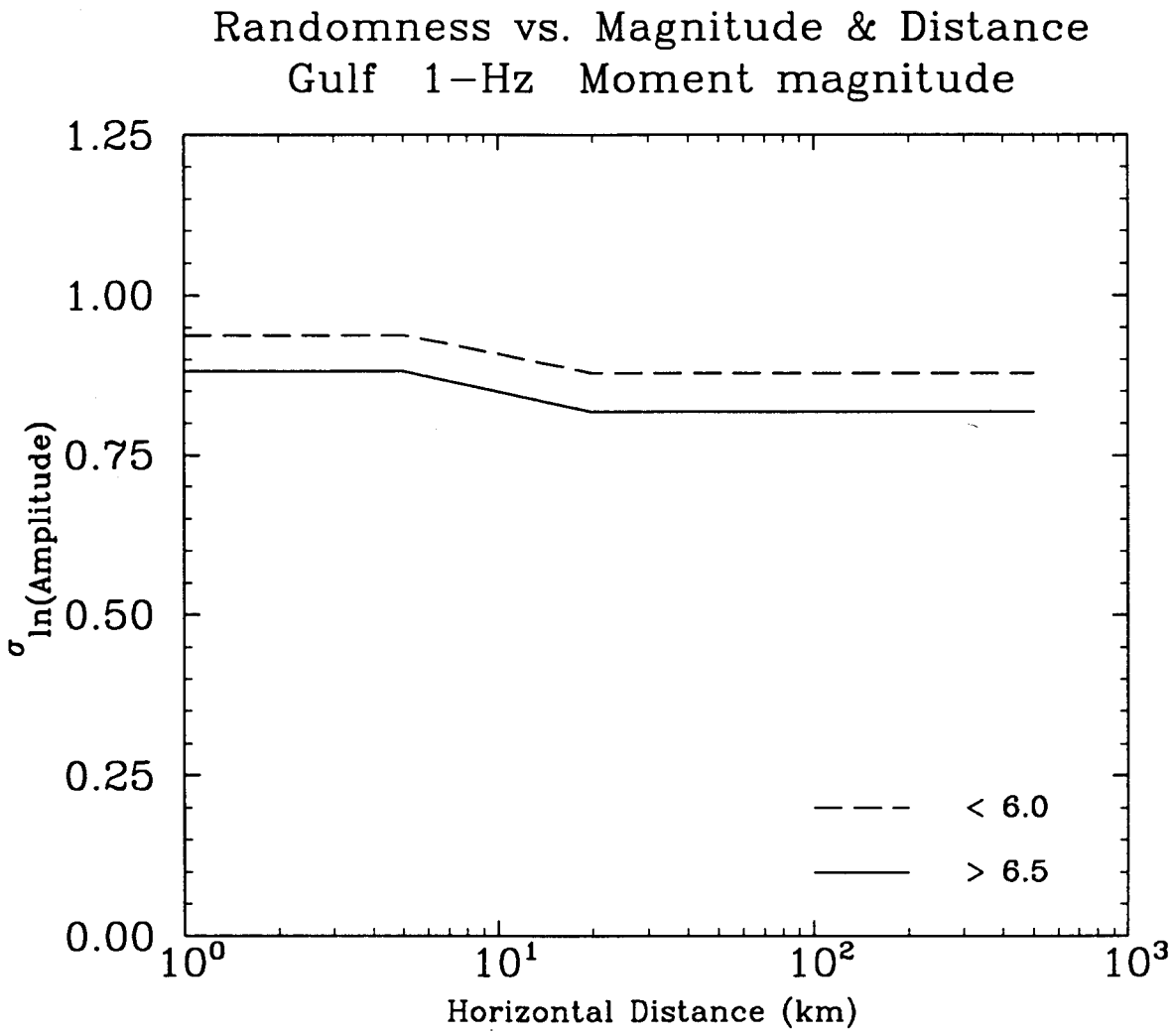

Figure 9-23. Variation of randomness as a function of magnitude and distance for 1-Hz spectral acceleration; Gulf region, equation in terms of M. Solid, M>6.5; dashed, M<6.

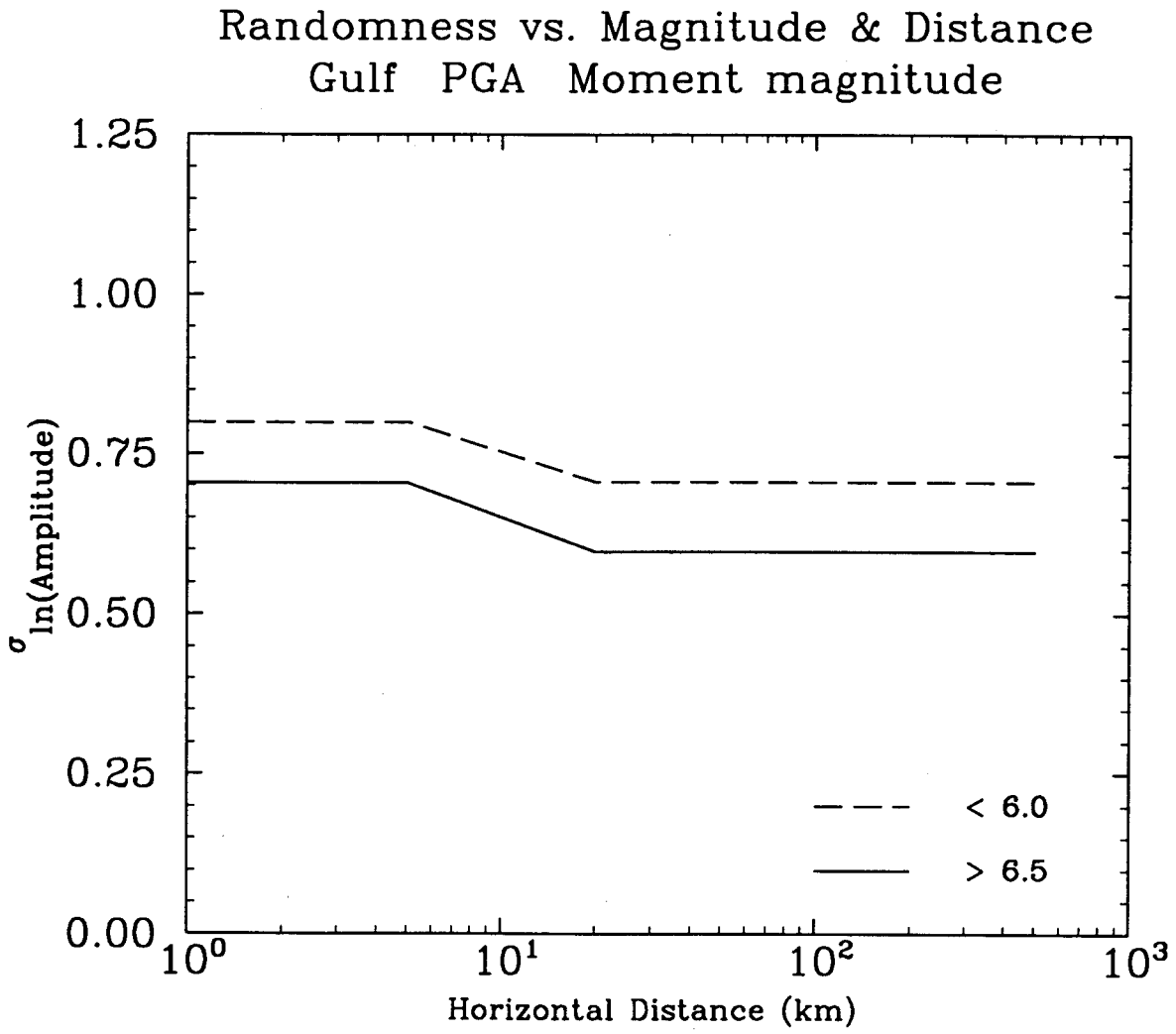

Figure 9-24. Variation of randomness as a function of magnitude and distance for peak ground acceleration; Gulf region, equation in terms of M. Solid, M>6.5; dashed, M<6.

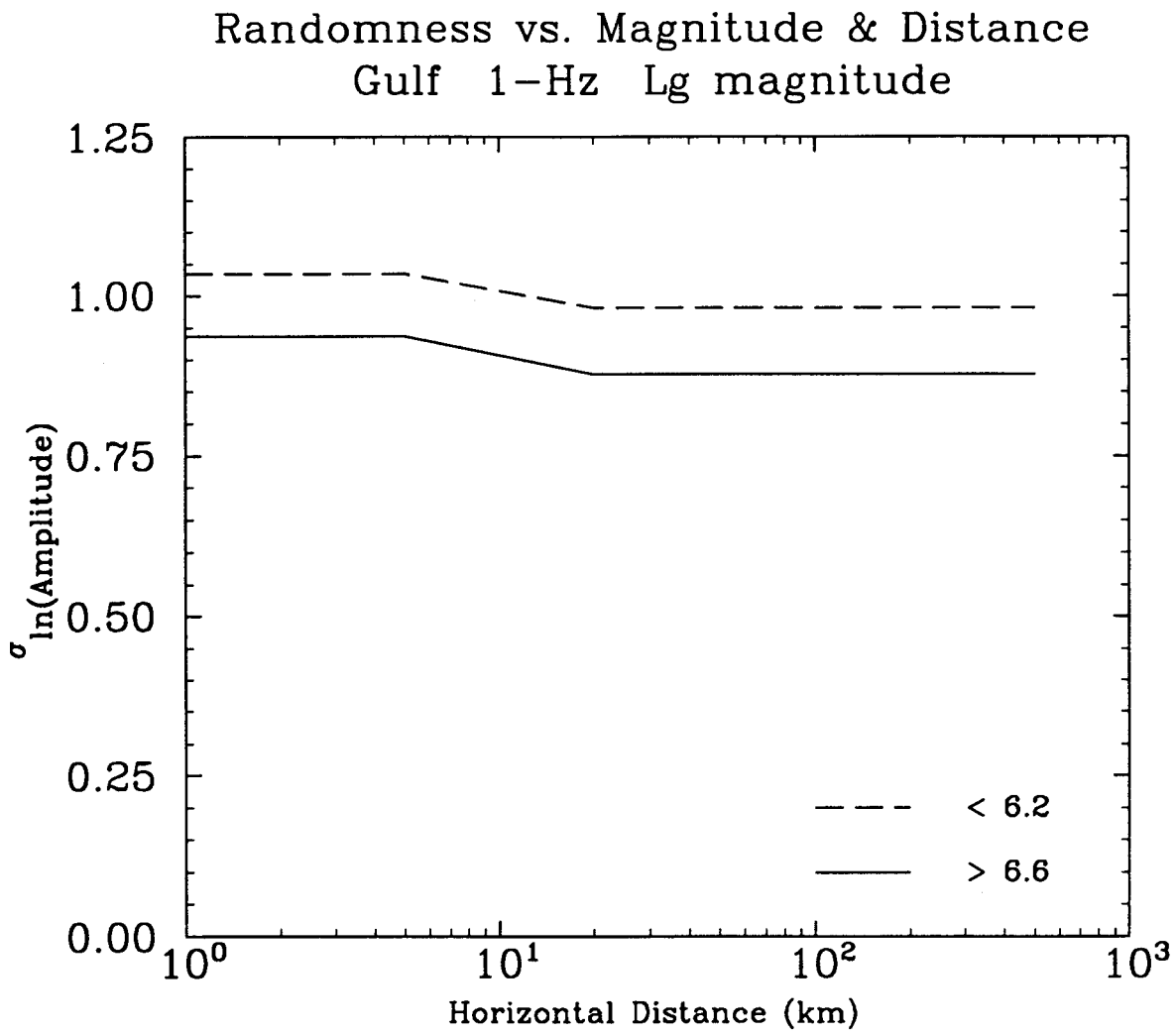

Figure 9-25. Variation of randomness as a function of magnitude and distance for 1-Hz spectral acceleration; Gulf region, equation in terms of m_{Lg}. Solid, M>6.5; dashed, M<6.

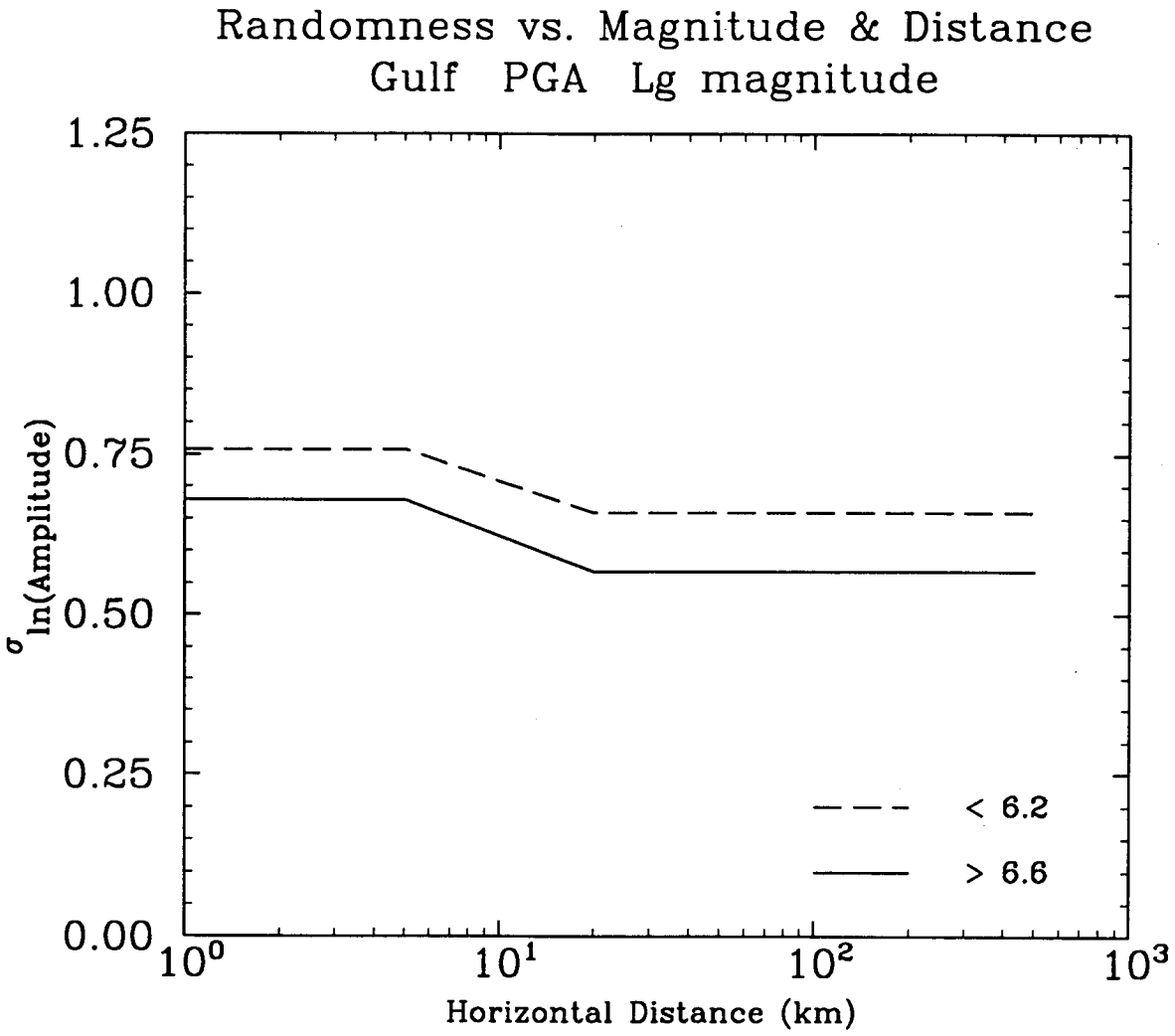

Figure 9-26. Variation of randomness as a function of magnitude and distance for peak ground acceleration; Gulf region, equation in terms of m_{Lg}. Solid, M>6.5; dashed, M<6.

Table 9-7
Uncertainty in Attenuation Equations (Midcontinent and Gulf)

	Moment Magnitude		Lg Magnitude	
Freq. (Hz)	**M<6**	**M>6.5**	**m_{Lg}<6.2**	**m_{Lg}>6.6**
1.0	0.29	0.44	0.30	0.54
2.5	0.29	0.47	0.29	0.47
5.0	0.29	0.48	0.29	0.46
10.0	0.30	0.48	0.29	0.45
25.0	0.30	0.49	0.29	0.45
35.0	0.30	0.49	0.29	0.45
Peak Accel.	0.30	0.49	0.29	0.45

distribution. For n=4, the values of U_i and W_i in Table 9-8 have been chosen so that the probabilistic moments up to order six of the four-point discrete distribution are equal to the corresponding moments of the standard normal distribution. The resulting four attenuation equations are of the form

$$\ln Y_i = C_1 + C_2(M-6) + C_3(M-6)^2 - C_4 \ln R_M - (C_5 - C_4)\max\left[\ln\left(\frac{R_M}{100}\right), 0\right] - C_6 R_M + U_i \sigma_U(M, R) + \varepsilon_r \quad \text{(Eq. 9-9)}$$

with the values of U_i (i=1 to 4), and their associated weights W_i, as given in Table 9-8. Because σ_U depends on magnitude and distance, the uncertainty term does not simply translate into a new value of coefficient C_1.

Table 9-8

Discrete Approximation to Standard Normal Distribution (Used to Discretize the Uncertainty)

i	Distance U_i	Weight W_i
1	–2.33	0.046
2	–0.74	0.454
3	0.74	0.454
4	2.33	0.046

9.3.4 Use of Site-Specific Information

The characterization of parameter variability that was presented in Section 9.1.1 treats intra-region variation of a parameter as randomness. This was done because the available data make it difficult to differentiate intra-region variability from other, less predictable, forms of randomness. If one takes the perspective of a given site, the intra-region variability becomes uncertainty and can be reduced with the collection and analysis of data at a more local scale. These new data would be anticipated to yield parameter distributions that are tighter than the generic distributions in Section 9.1.1 and have median values within the one-sigma ranges of the generic medians. These site-specific distributions would result in lower randomness and in median attenuation equations that are somewhat different from the generic Engineering Model developed here.

The parameters that are more amenable to site-specific investigation are κ, Q, hypocentral depth, and crustal structure. Figures 9-17 and 9-18 the contributions of the various parameters to randomness in ground-motion amplitudes (recall that the effect of crustal structure is included as part of modeling randomness). These figures indicate the relative importance of the contributions from the various parameters. This information, coupled with knowledge about the seismic source zones that are important to seismic hazard at the site, are useful in deciding the type and scope of the site-specific studies. Some of these studies would use truly site-specific data (i.e., for κ), while others would use data from within a few hundred kilometers of the site.

Site-specific investigations of κ would focus on the local geology of the site and should include any possible local variations among locations (buildings) within the site. Information might be obtained from local recordings obtained with a temporary seismograph network, site-response studies using local measurements of near-surface shear-wave velocity and Q, or analogies with other sites with similar geology. A tighter distribution of κ would have an effect on the variability of high-frequency (> 10 Hz) ground motions and peak ground acceleration.

Site-specific investigations of Q would focus on a radius of 100 to 500 km around the site, with the choice of radius being dictated by the distances to the seismic source zones that contribute to seismic hazard at the site (see Section 1.3). The regionalization by Gupta et al. (1989; see also Section 5.2.2) provides a starting point for the development of region-specific values of Q.

Site-specific investigations of hypocentral depth would focus on the tectonic province where the site is located. Section 5.2.3 discusses several relevant data sets on hypocentral depth; these would provide a starting point for the development of a regional distribution of depth. A tighter distribution of hypocentral-depth would have the largest effect on the seismic hazard coming from distances less than 20 km, which is often a major contributor to seismic hazard. It would also have some effect on the seismic hazard coming from distances near 100 km, due to crustal reflections.

Analysis of regional data on κ, Q, or hypocentral depth would result on site-specific distributions for these parameters. Because the sizes of the site-specific samples will likely be smaller than the sample sizes considered in Section 5, care must be taken in quantifying statistical uncertainties and propagating them through the calculations. The updating of the Engineering Model would consist of re-weighting the simulation results using the new parameter distributions, repeating the regressions (using the same functional form of Section 9.2), and re-calculating randomness and uncertainty.

The treatment of crustal structure is somewhat different from the parameters considered above because the variability in crustal structure is captured by modeling (as opposed to parametric) variability. Thus, it is not easy to quantify the reduction in variability that is achieved by better knowledge of the crustal structure near the site. It is possible, however to modify the median attenuation equations to reflect differences in the geometric attenuation of the site-specific and generic crustal models.

The uncertainty in stress drop and the modeling uncertainty are not amenable to site-specific re-evaluation. The necessary data are not available at a site-specific or small-region scale, especially if attention is focused on earthquakes with magnitudes of engineering interest.

9.4 Comparison to Eastern North America Ground-Motion Data

The ENA ground-motion data documented in Section 2 are used for comparison to the Engineering ground-motion model developed here. In order to remove complications such as site effects and to limit the comparison to magnitudes and distances not too removed from the range of engineering interest, the following criteria are used for the selection of records for this comparison: (1) magnitudes $M \geq 4$, (2) distances less than 200 km, (3) horizontal components, (4) rock site conditions, (5) instruments located in shelters or at the lower level of buildings at most four stories high, and (6) estimate of stress drop available from Table 4-1. Table 9-9 lists the records that meet these criteria. Figures 9-27 through 9-34 compare the observed spectral accelerations at 1 and 10 Hz to the predictions by the Engineering Model (using both the attenuation equations for **M** and for m_{Lg}). The data are partitioned into two groups ($M \leq 5$ and $M > 5$). Predictions are shown as median curve, median $\times \exp(\pm\sigma_r)$, and median $\times \exp[\pm(\sigma_r^2+\sigma_U^2)^{1/2}]$. The reference magnitudes for the two groups of data are **M** 4.5 and 5.9, and m_{Lg} 5.0 and 6.5 (the reference magnitude for the large-magnitude group is chosen as the magnitude of the 1988 Saguenay earthquake). All observations are scaled to the corresponding reference magnitude. These figures show that the ground-motion amplitudes predicted by the Engineering Model are generally consistent with observations. The only discrepancy relates to the 1988 Saguenay earthquake. The observed 10-Hz amplitudes for Saguenay lay, on average, two standard deviations above the median (1.5 standard deviations for the m_{Lg} attenuation equations). This discrepancy is explained by the higher stress drop of this event. This stress drop is high, but is not inconsistent with the stress-drop distribution obtained in Sections 4.2.3 and used here.

Table 9-9

Earthquake Records Used in Comparisons

Event Name	Date	m_{Lg}	M	Site Name	R (km)	No. of Compo-nents	Code	Stress Drop (bars)
New Madrid, Mo	04/27/89	4.7	4.7	Old Appleton, Missouri	8.0	2	2	229
New Madrid, Mo	05/04/91	4.6	4.4	Old Appleton, Missouri	160	2	3	39
Saguenay, Can.	11/23/88	4.8	4.5	Dickey, Maine	198	2	4	53
New Brunswick (A)	03/31/82	4.8	4.0	Indian Brook II, N.B. (IB2)	0.8	2	1	96
New Brunswick (A)	03/31/82	4.8	4.0	Mitchell Lake Rd., N.B. (ML, Temp.)	4.0	2	1	96
New Brunswick (A)	03/31/82	4.8	4.0	Hickey Lake, N.B. (HL, Temp.)	4.1	2	1	96
Nahanni, Can.	12/23/85	6.4	6.7	Nahanni, NWT, Station 2	7.4	2	5	86
Nahanni, Can.	12/23/85	6.4	6.7	Nahanni, NWT Station 1	7.6	2	5	86
Nahanni, Can.	12/23/85	6.4	6.7	Nahanni, NWT Station 3	22.6	2	5	86
Saguenay, Can.	11/25/88	6.5	5.9	GSC Site 17—St-Andre-Du-Lac, Que	64.1	2	6	655
Saguenay, Can.	11/25/88	6.5	5.9	GSC Site 20—Les Eboulements, Que	90	2	6	655
Saguenay, Can.	11/25/88	6.5	5.9	GSC Site 8—La Malbaie, Que	93	2	6	655
Saguenay, Can.	11/25/88	6.5	5.9	GSC Site 14—St. Lucie de Beaur., Que	101	2	6	655
Saguenay, Can.	11/25/88	6.5	5.9	GSC Site 5—Tadoussac, Que	113	1	6	655
Saguenay, Can.	11/25/88	6.5	5.9	GSC Site 10—Riviere Quelle	118	2	6	655
Saguenay, Can.	11/25/88	6.5	5.9	GSC Site 1—St. Ferreol, Que	117	2	6	655
Saguenay, Can.	11/25/88	6.5	5.9	GSC Site 9—Pascal, Que	132	2	6	655
Saguenay, Can.	11/25/88	6.5	5.9	Dickey, Maine	197	2	6	655

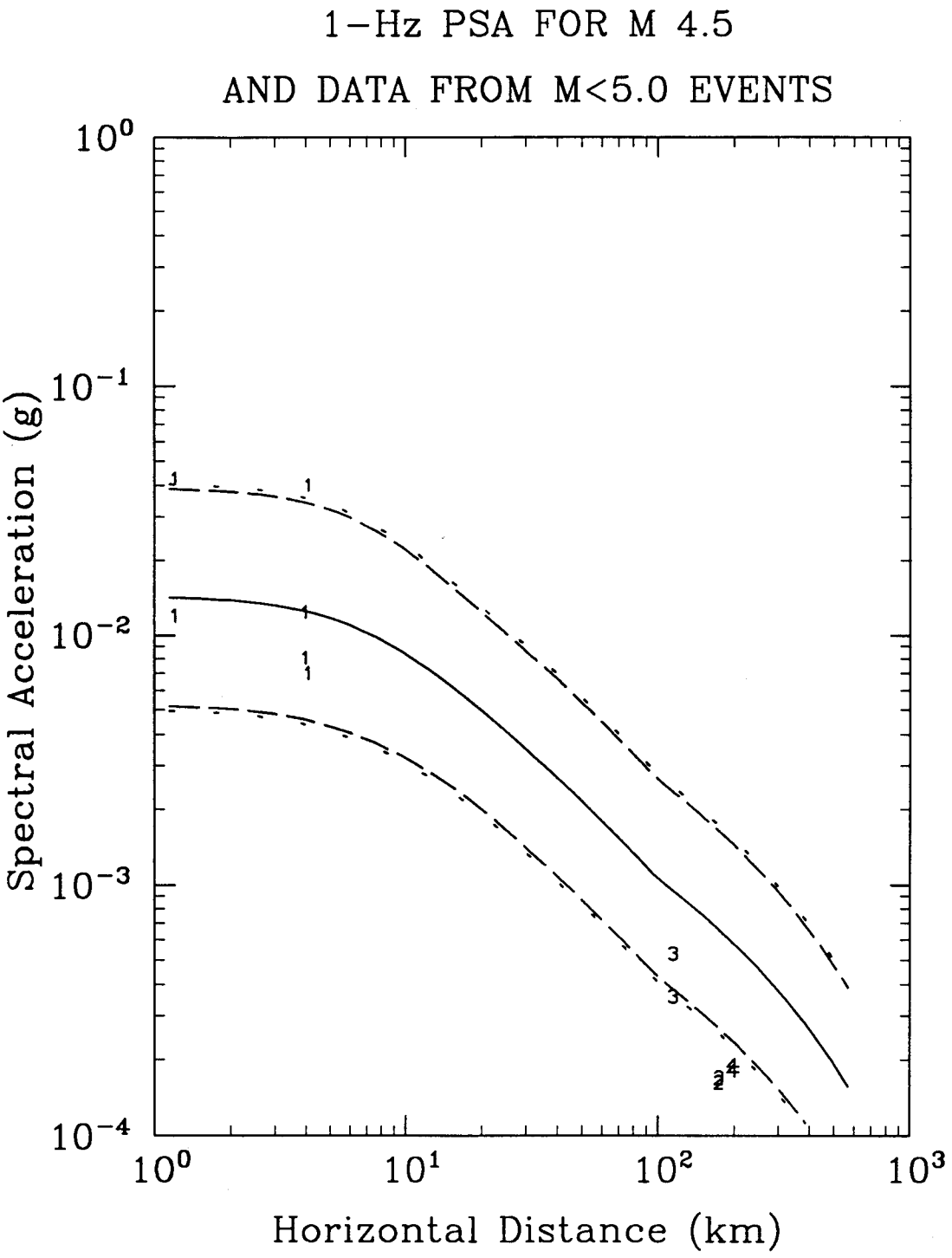

Figure 9-27. Comparison of 1-Hz spectral acceleration data (M<5, scaled to M 4.5) to the attenuation functions developed in this study. Predictions shown for M 4.5.

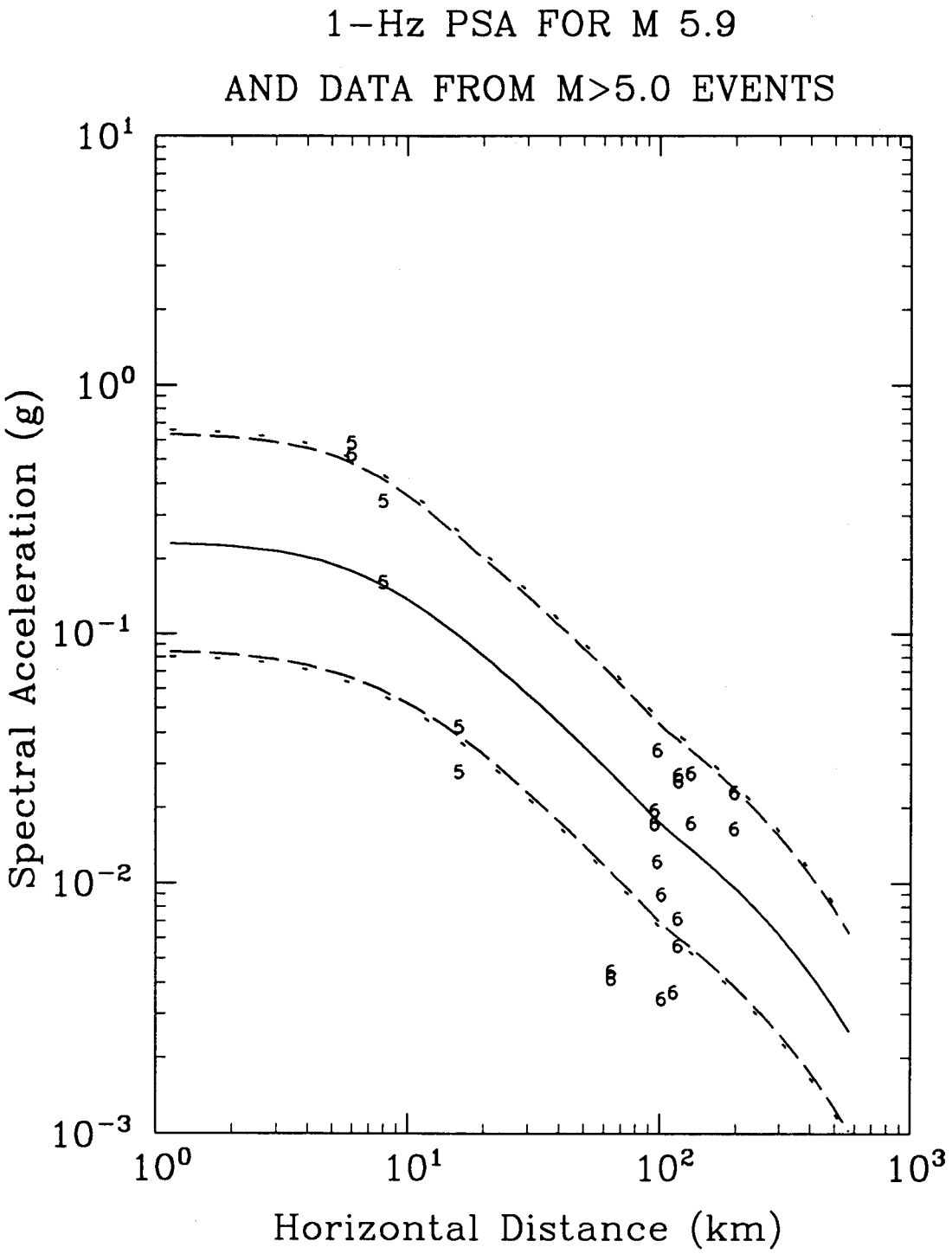

Figure 9-28. Comparison of 1-Hz spectral acceleration data (M<5, scaled to M 5.9) to the attenuation functions developed in this study. Predictions shown for M 5.9.

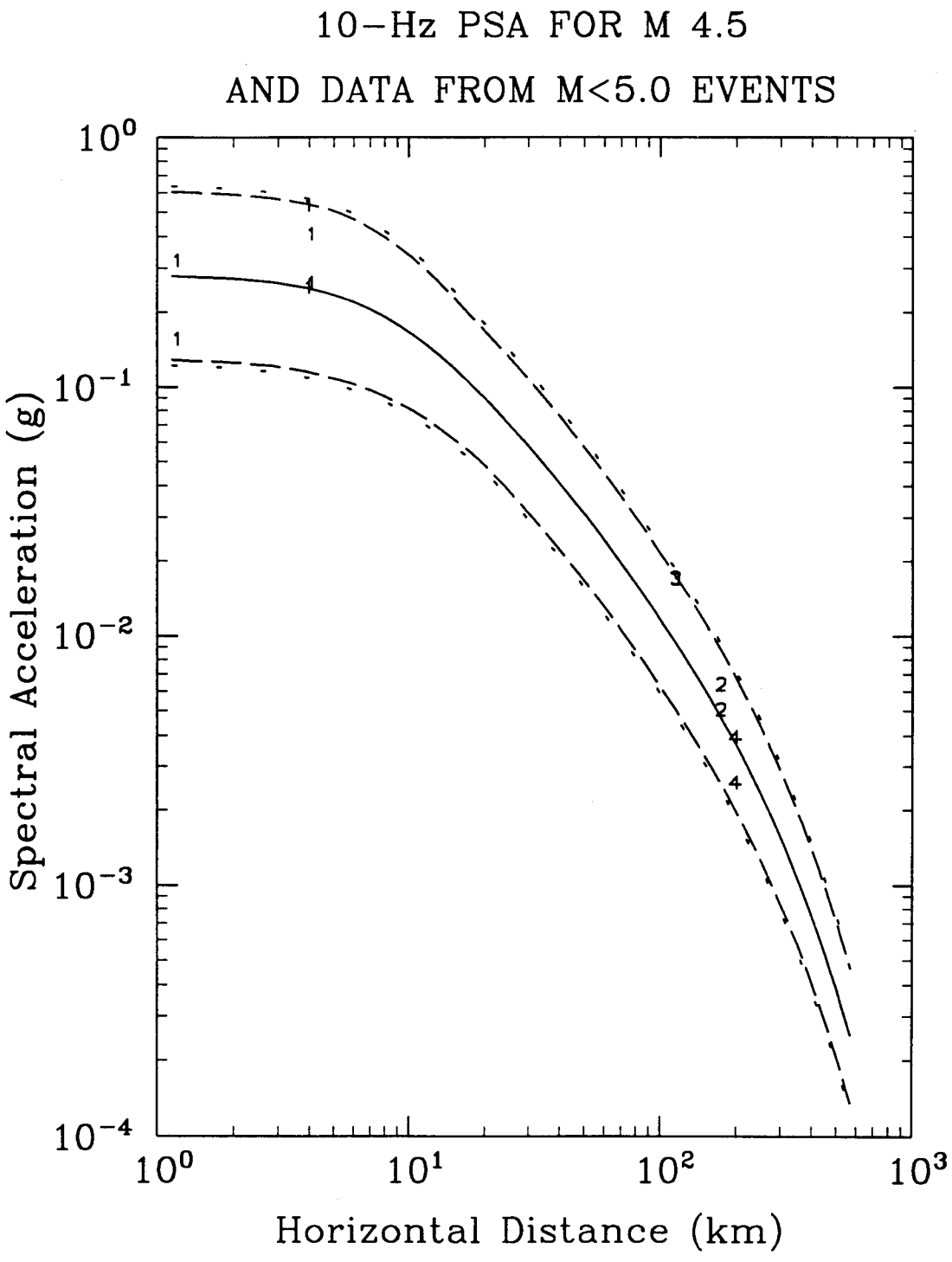

Figure 9-29. Comparison of 10-Hz spectral acceleration data (M<5, scaled to M 4.5) to the attenuation functions developed in this study. Predictions shown for M 4.5.

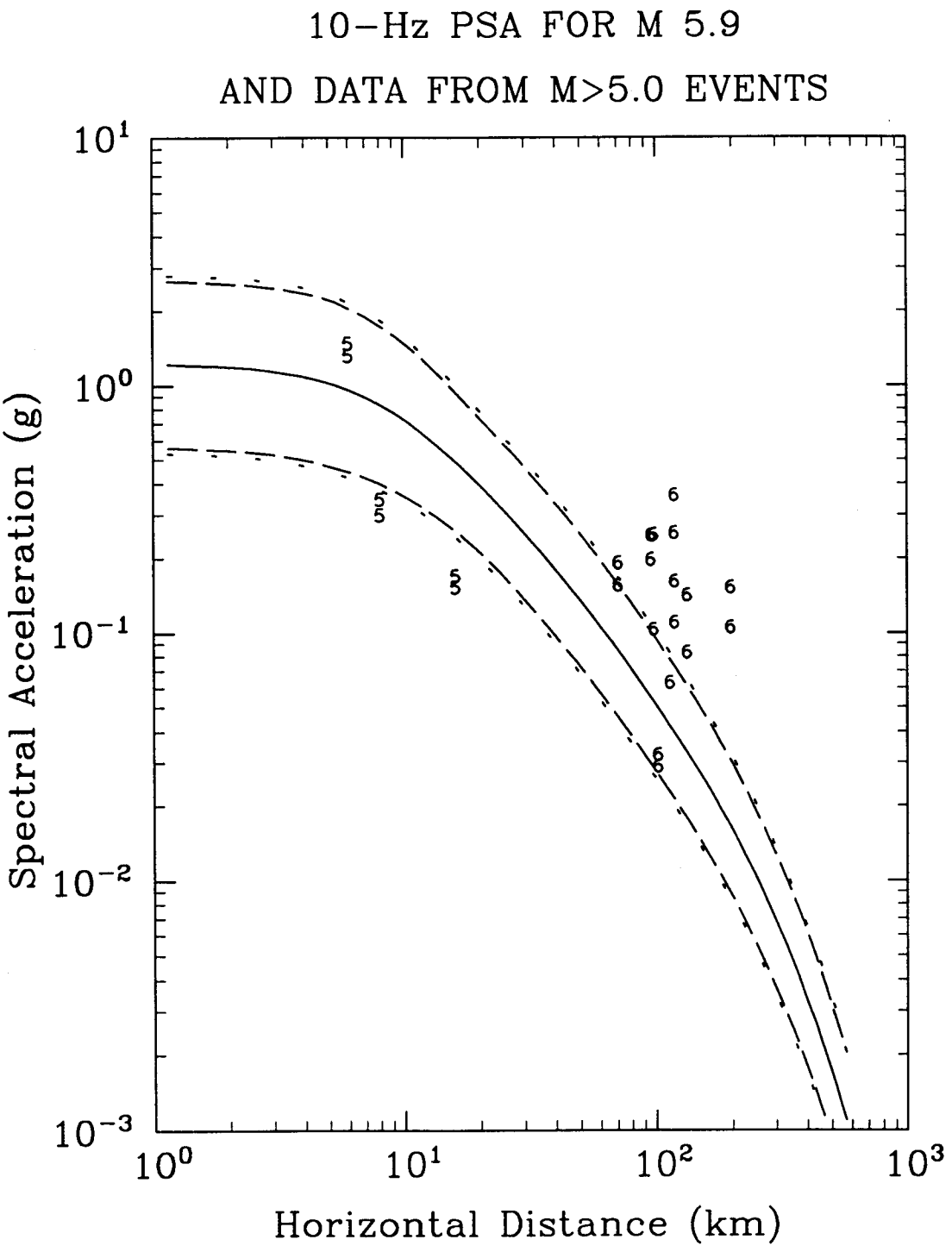

Figure 9-30. Comparison of 10-Hz spectral acceleration data (M<5, scaled to M 5.9) to the attenuation functions developed in this study. Predictions shown for M 5.9.

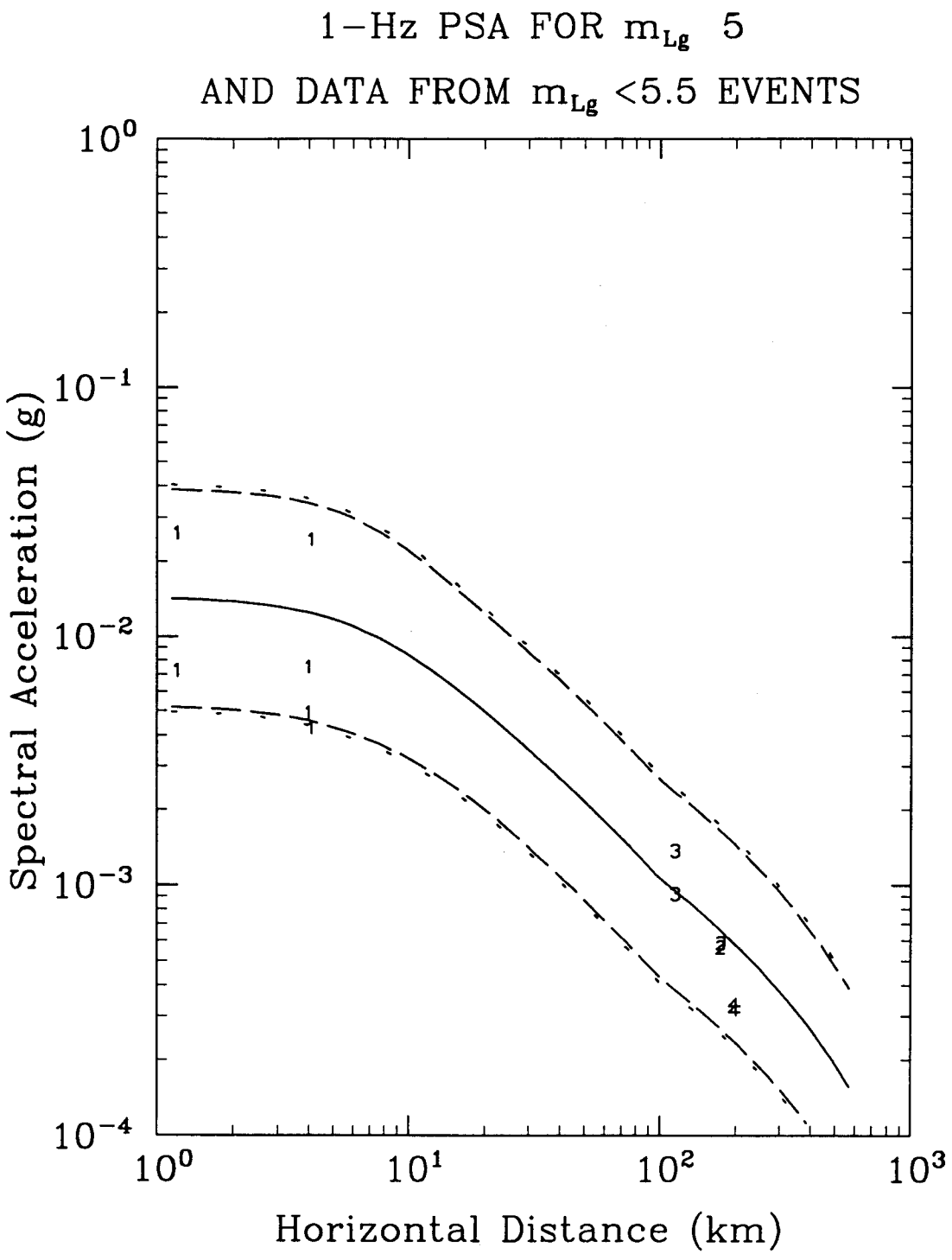

Figure 9-31. Comparison of 1-Hz spectral acceleration data (M<5, scaled to m_{Lg} 5) to the attenuation functions developed in this study. Predictions shown for m_{Lg} 5.

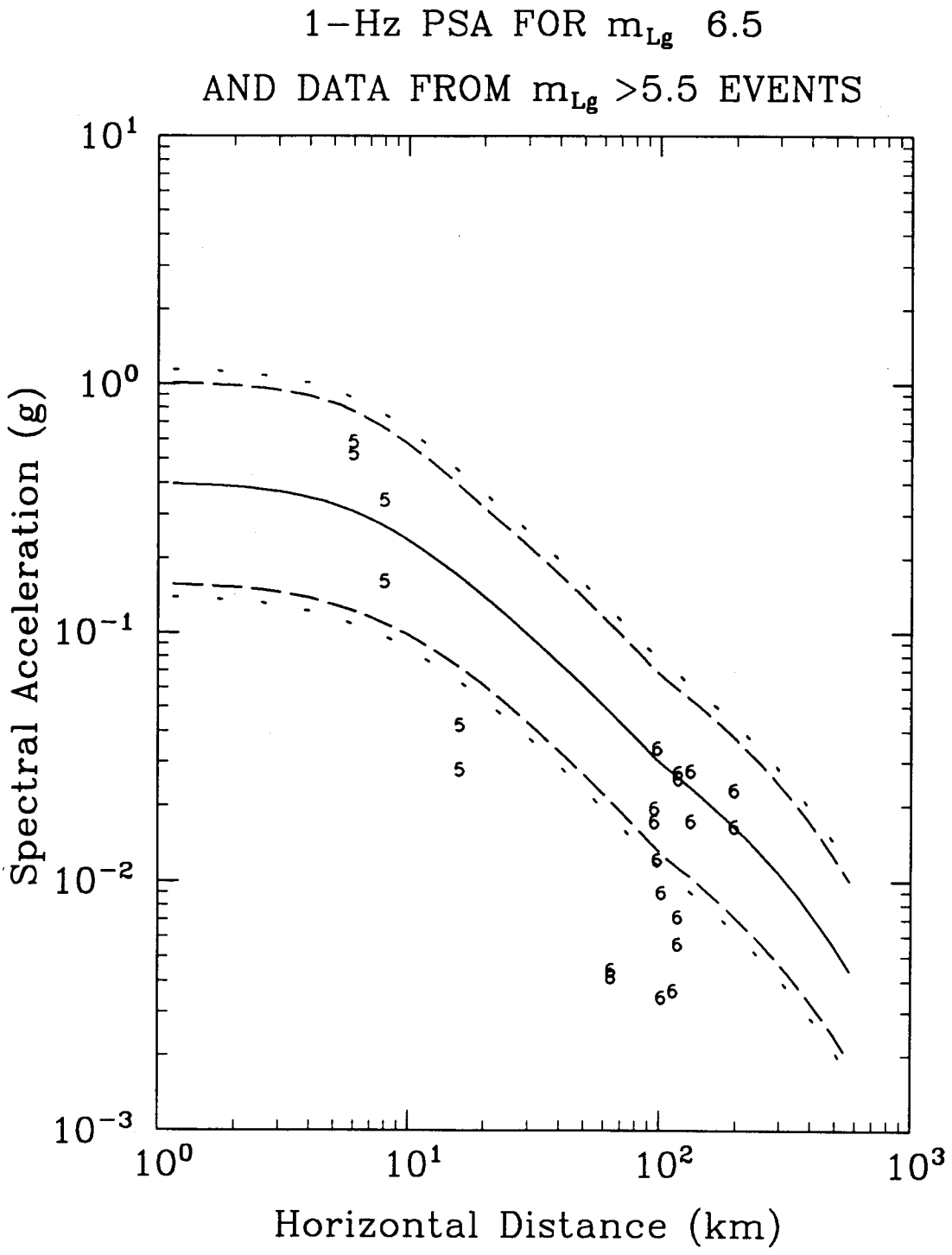

Figure 9-32. Comparison of 1-Hz spectral acceleration data (M<5, scaled to m_{Lg} 6.5) to the attenuation functions developed in this study. Predictions shown for m_{Lg} 6.5.

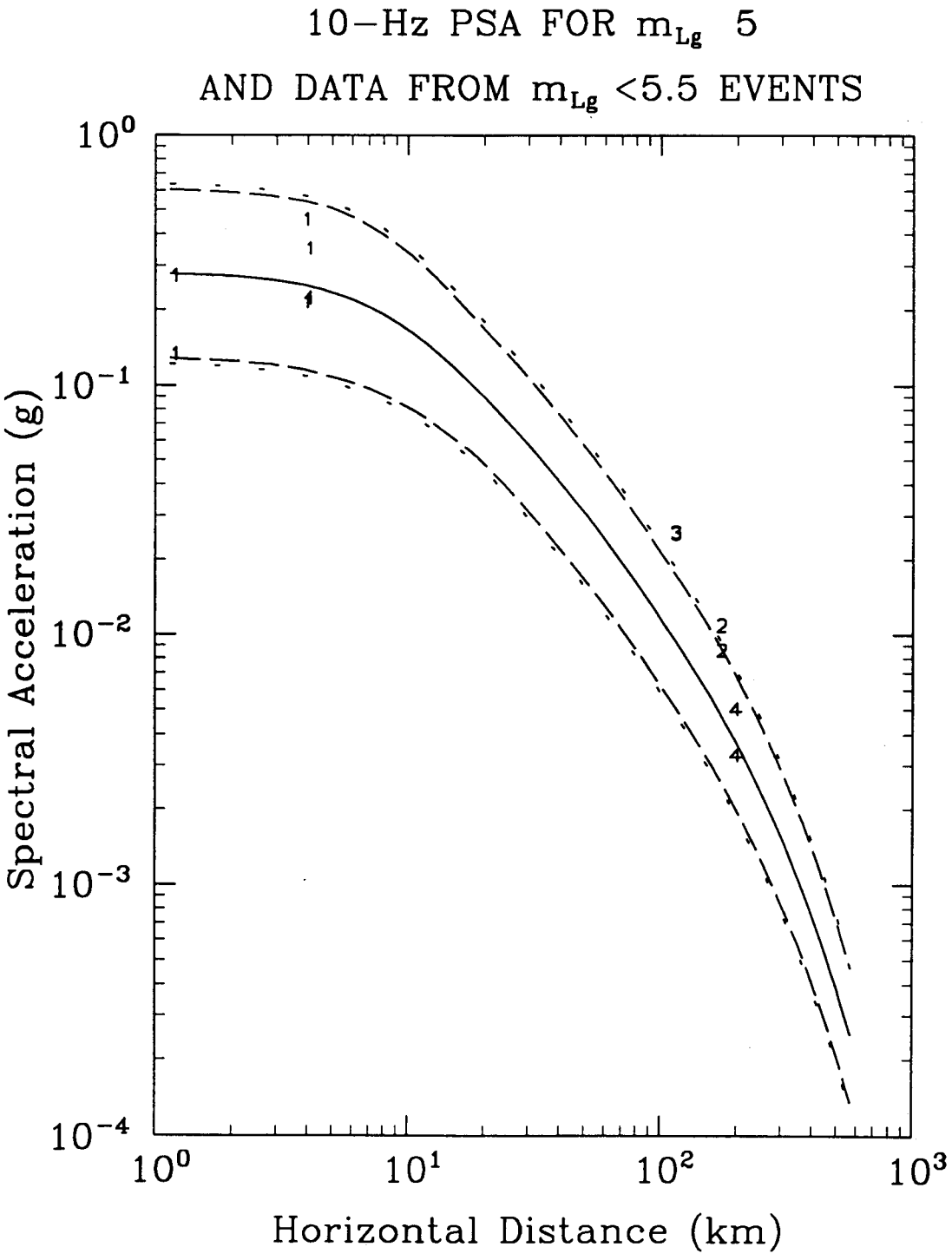

Figure 9-33. Comparison of 10-Hz spectral acceleration data (M<5, scaled to m_{Lg} 5) to the attenuation functions developed in this study. Predictions shown for m_{Lg} 5.

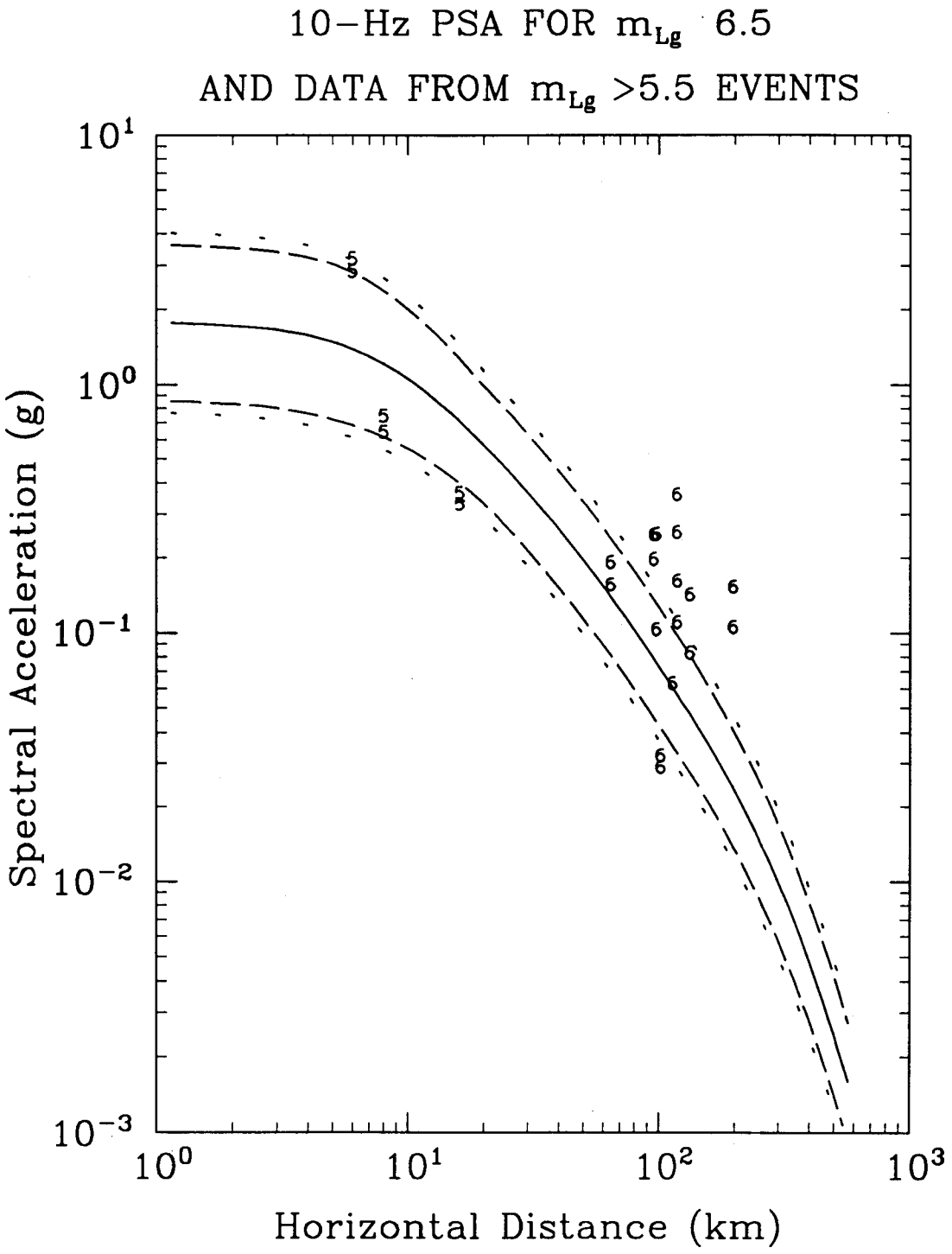

Figure 9-34. Comparison of 10-Hz spectral acceleration data (M<5, scaled to m_{Lg} 6.5) to the attenuation functions developed in this study. Predictions shown for m_{Lg} 6.5.

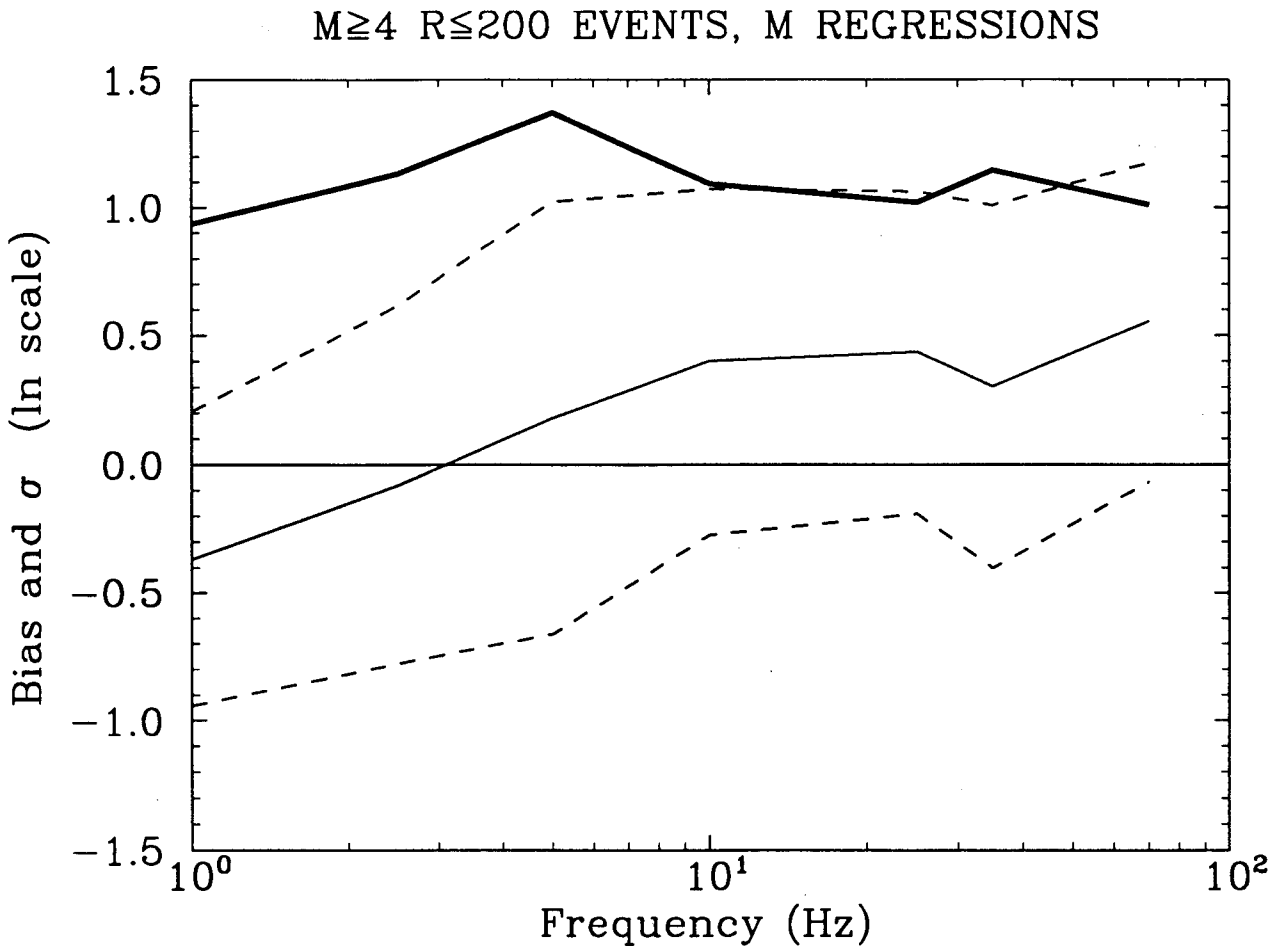

Figure 9-35. Bias and standard error of attenuation equations in terms of moment magnitude with respect to selected ENA ground-motion data. Thin lines: bias and its associated 90% confidence bounds: thick line: standard error.

One can quantify the closeness of fit between observations and predictions by calculating the bias and standard error of the predictions (Abrahamson et al., 1990), i.e.,

$$\text{Bias} = \frac{1}{n}\sum_i \{\ln[Y_{obs,i}] - \ln[Y_{pred}(M_i, R_i)]\} \qquad \text{(Eq. 9-10)}$$

$$\text{Std. Err.}^2 = \frac{1}{n-1}\sum_i \{\ln[Y_{obs,i}] - \ln[Y_{pred}(M_i, R_i)] - \text{Bias}\}^2 \qquad \text{(Eq. 9-11)}$$

where the summation extends over all selected records, n is the number of such records, $Y_{obs,i}$ is the observed value of spectral acceleration or peak ground acceleration for record i, and $Y_{pred}(M_i,R_i)$ is the value predicted by the corresponding attenuation equation (given magnitude M_i and horizontal distance R_i).[4] The bias and standard error are calculated for each frequency, as well as for peak acceleration. Comparisons are performed separately for the attenuation equations in terms of moment magnitude and Lg magnitude.

Figures 9-35 and 9-36 show the calculated bias and standard error as a function of frequency for the attenuation

4. For the New Brunswick records, we calculate the predicted ground motions using the actual hypocentral depth (4km) in place of the "depth-like" coefficient C_7, instead of using the values for C_7 from Tables 9-2 through 9-5. This is done because our data have a poor sampling of the depth distribution for short-distance records.

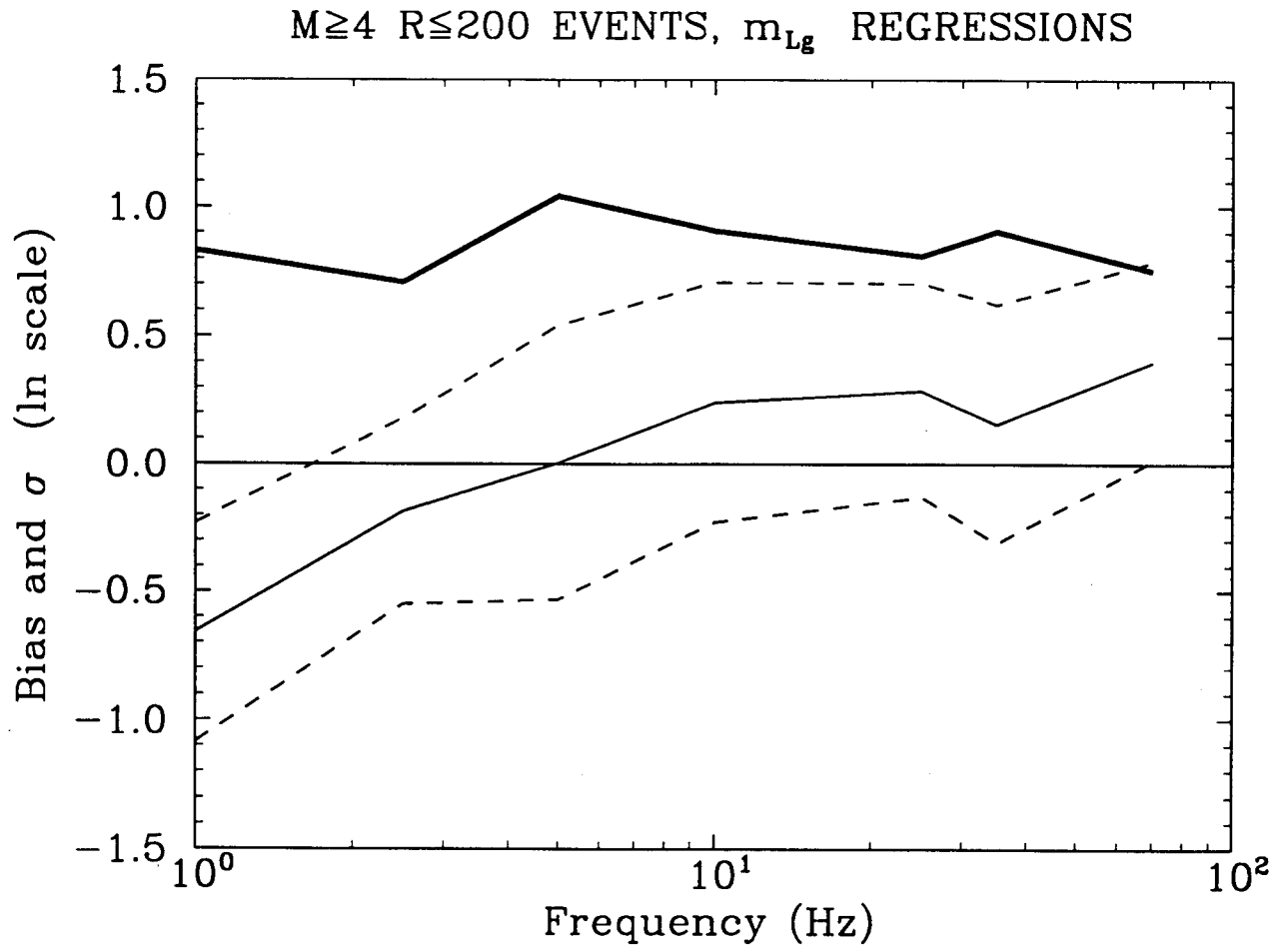

Figure 9-36. Bias and standard error of attenuation equations in terms of Lg magnitude with respect to selected ENA ground-motion data. Thin lines: bias and its associated 90% confidence bounds; thick line: standard error.

equations in terms of M and m_{Lg}, respectively.[5] Results for peak acceleration are shown as corresponding to 70 Hz. These figures show that the Engineering Model is in reasonable agreement with the limited data. The Engineering Model has a statistically significant tendency to over-predict ground-motions at 1 and Hz. At all other frequencies, the differences between observations and the Engineering Model are not statistically significant. The trend with frequency is a consequence of the high average stress drop in this sample (230 bars), which is caused mainly by the 1988 Saguenay earthquake. The observed variability is roughly consistent with the variability obtained in Section 9.3. Note that the attenuation equations in terms of m_{Lg} have slightly higher variability at low frequencies and slightly lower variability at high frequencies, as obtained in Section 9-3.

Figure 9-37 shows similar plots for each event in Table 9-8 having four or more records. These figures confirm that the aforementioned tendency to over-predict low frequencies is driven mainly by the Saguenay records. The slight tendency to over-predict low frequencies is more consistent among events, but it is small and it is on the conservative side.

5. The confidence bounds on the bias are calculated considering inter-event correlation (using the ratios of inter-event to total variability that were observed in Section 2), but without considering correlation among the two horizontal components recorded at the same station. Thus, the true bounds are somewhat wider.

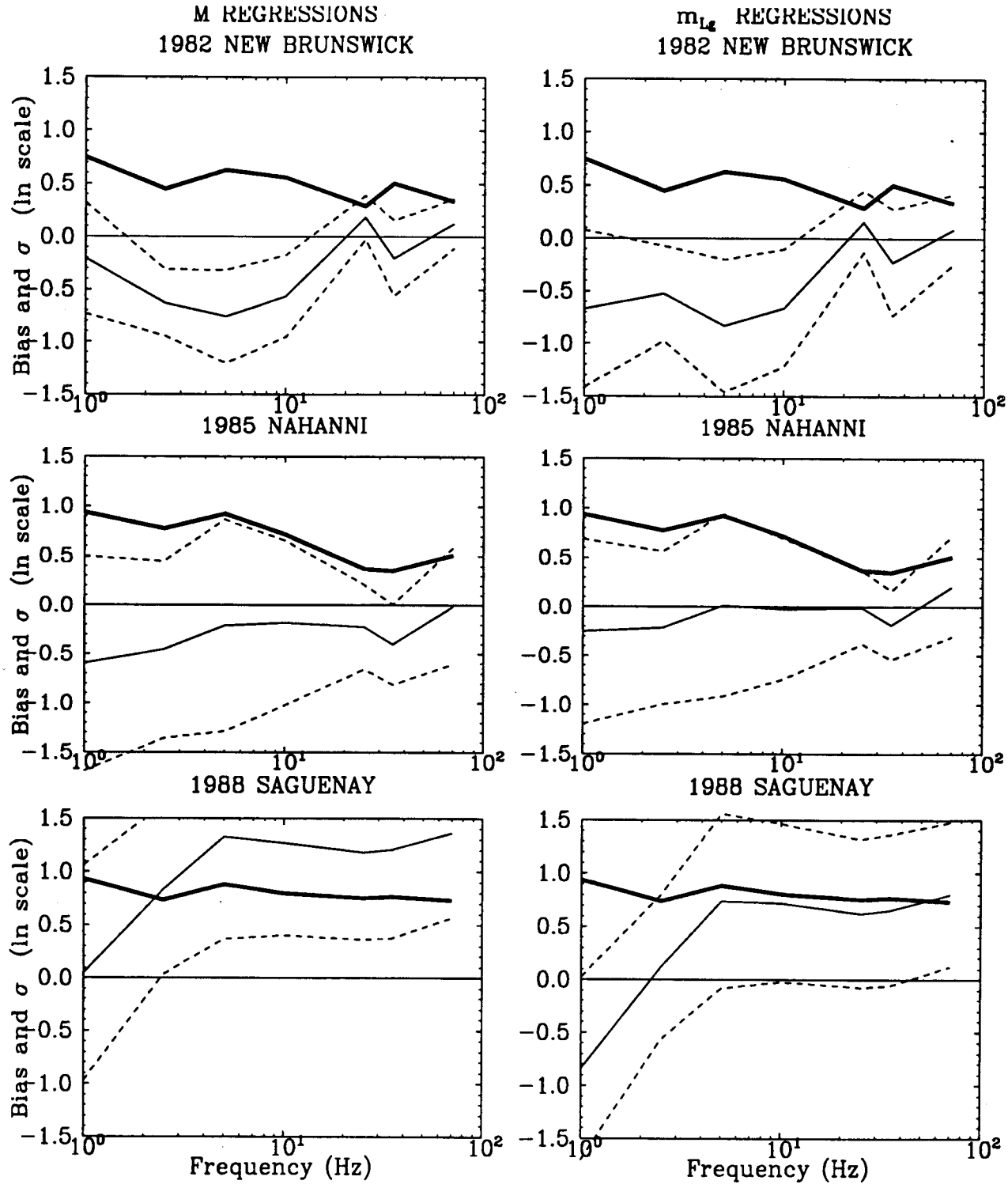

Figure 9-37. Bias and standard error of attenuation equations (in terms of moment magnitude and m_{Lg}) with respect to data from important ENA events.

In conclusion, comparisons of the Engineering Model to data indicate no inconsistencies. The limited sample size (especially as it relates the small number of events), is manifested by the wide confidence bands. The more important differences relate to the 1988 Saguenay earthquake and are explained by the high stress drop of this earthquake.

The above statement about the Saguenay earthquake having significantly higher than average stress drop does not imply that this earthquake should be disregarded. Saguenay should not be taken as typical, but it should not be explained away as an "odd event." The differences between Saguenay and other events should be taken as an indication of randomness in seismic-source parameters, as has been done in this study (see Section 4.2.3).

9.5 Comparison to Other Models

Figures 9-38 and 9-39 compare the predictions by the Engineering Model in terms of m_{Lg} for the Midcontinent region to predictions by the attenuation equations of Boore and Atkinson (1987) and McGuire et al. (1988). Figures 9-40 and 9-41 compare the predictions by the Engineering Model in terms of **M** to predictions by the attenuation equations of Boore and Atkinson (1987) and ground motions calculated using the model by Atkinson (1993) and Atkinson and Mereu (1992). We refer to the latter as the Atkinson (1993) ground-motion model.

The differences between predictions by the Engineering Model developed here and by the earlier attenuation equations are comparable to the uncertainties obtained in the previous Section. This indicates general consistency between the new model and the earlier models. The differences at high frequencies are due to differences in ground-motion duration. The larger differences at low frequencies are due to the combined effect of duration and spectral shape. The only significant difference is that with the Atkinson (1993) ground-motion model at 1 Hz and is due to differences in the assumed shape of the power spectrum of large earthquakes at low frequencies.

9.6 Application

The Engineering Model has been used to calculate the seismic hazard at two EUS sites, for the purpose of comparing to the results obtained with the attenuation equations used in the EPRI/SOG study (McGuire et al., 1989, Appendix A). One site is located in New England and is typical of sites in the Northeast, with high activity rates and maximum magnitudes typically less than m_{Lg} 7. The other site is located in the Midwest, in an area of low local seismicity. The New Madrid Seismic source zone is located within a 500 km radius of the site.

The source-zone geometries, magnitude-recurrence models, and maximum magnitudes for these calculations are taken from the EPRI/SOG study. Because activity rates are in terms of m_{Lg}, we consider only the Engineering Model predictions in terms of m_{Lg}.

Figures 9-42 and 9-43 show the median and mean uniform-hazard spectra obtained using the Engineering Model (Sections 9.2 and 9.3) and the EPRI/SOG attenuation equations, for an annual exceedance probability of 10^{-4}. Comparing the median spectra, the Engineering Model leads to higher amplitudes at low frequencies, similar amplitudes at intermediate frequencies, and slightly lower amplitudes at high frequencies. The differences at low frequencies are mainly due to higher randomness (the EPRI/SOG calculations assumed a standard deviation of 0.5 for randomness, for all frequencies). Comparing the mean hazard curves, the differences between the two sets of attenuation equations are smaller. The higher randomness of the Engineering Model is offset by the higher uncertainty of the EPRI/SOG attenuation equations.

The results from this exercise confirm that the predictions by the Engineering Model developed here are in general agreement with attenuation equations in current use. The only important source of differences with the attenuation equations in current use is the higher randomness at low frequencies, which causes an increase in the median uniform-hazard spectrum at 1 Hz (but not in the mean uniform-hazard spectrum).

When comparing the randomness obtained here to estimates of randomness associated with empirical attenuation equations, it must be noted that the latter do not include the effect of random depth on ground motions at short distances, because of limited data at short distances.

9.7 Ground Motion Variability for Soil Sites

Intuitively, the variability of ground motion at soil sites would be estimated by adding the variability of the site response to the variability of the input rock ground motion. The variability of the input rock ground motion would be estimated by the variability of the rock attenuation relation. Although intuitively appealing, this procedure would significantly overestimate the variability

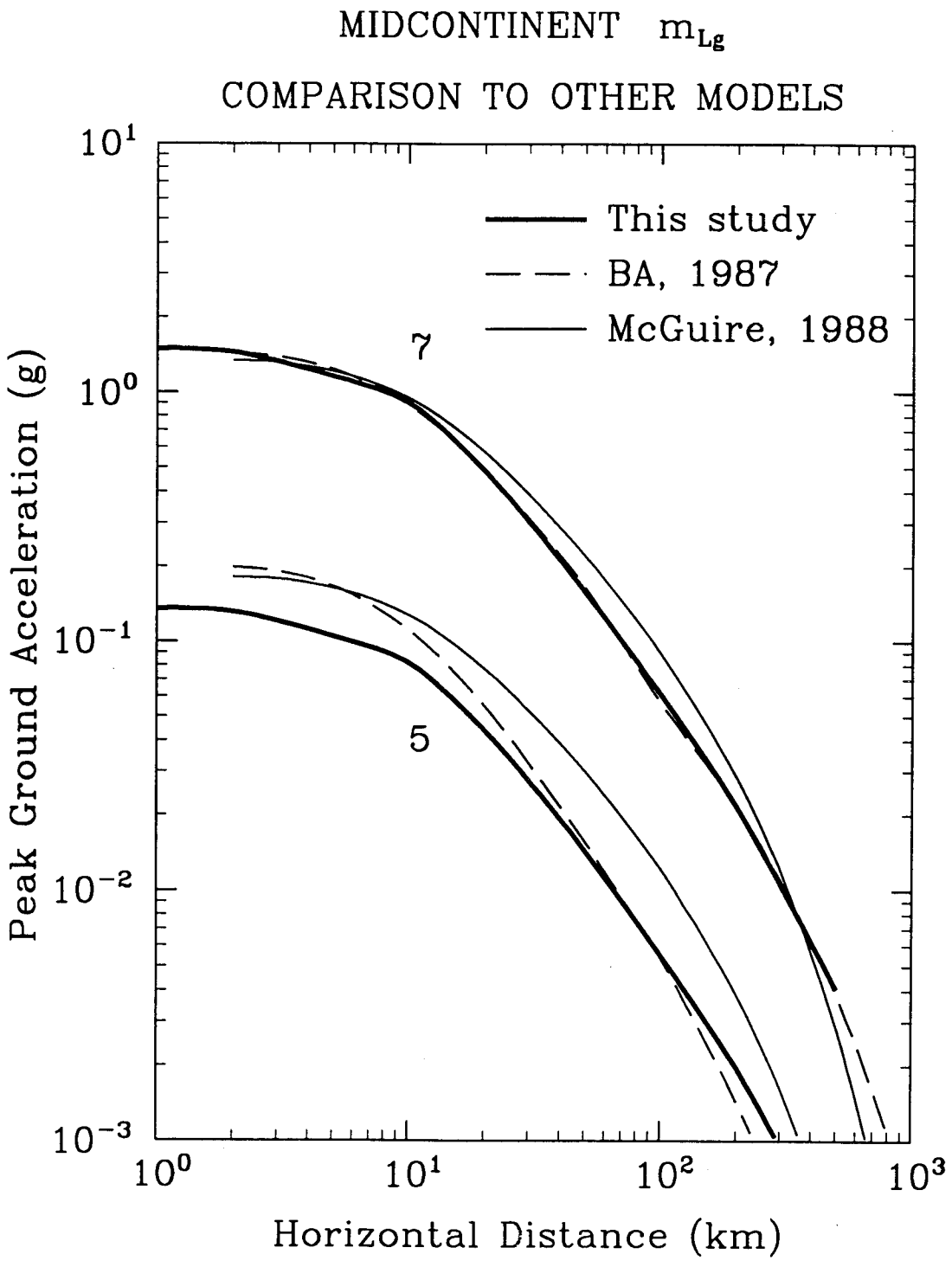

Figure 9-38. Comparison of attenuation equations for peak ground acceleration in the Midcontinent (Lg magnitude; thick solid line) to predictions by the attenuation equations of Boore and Atkinson (1987) and McGuire et. al. (1988).

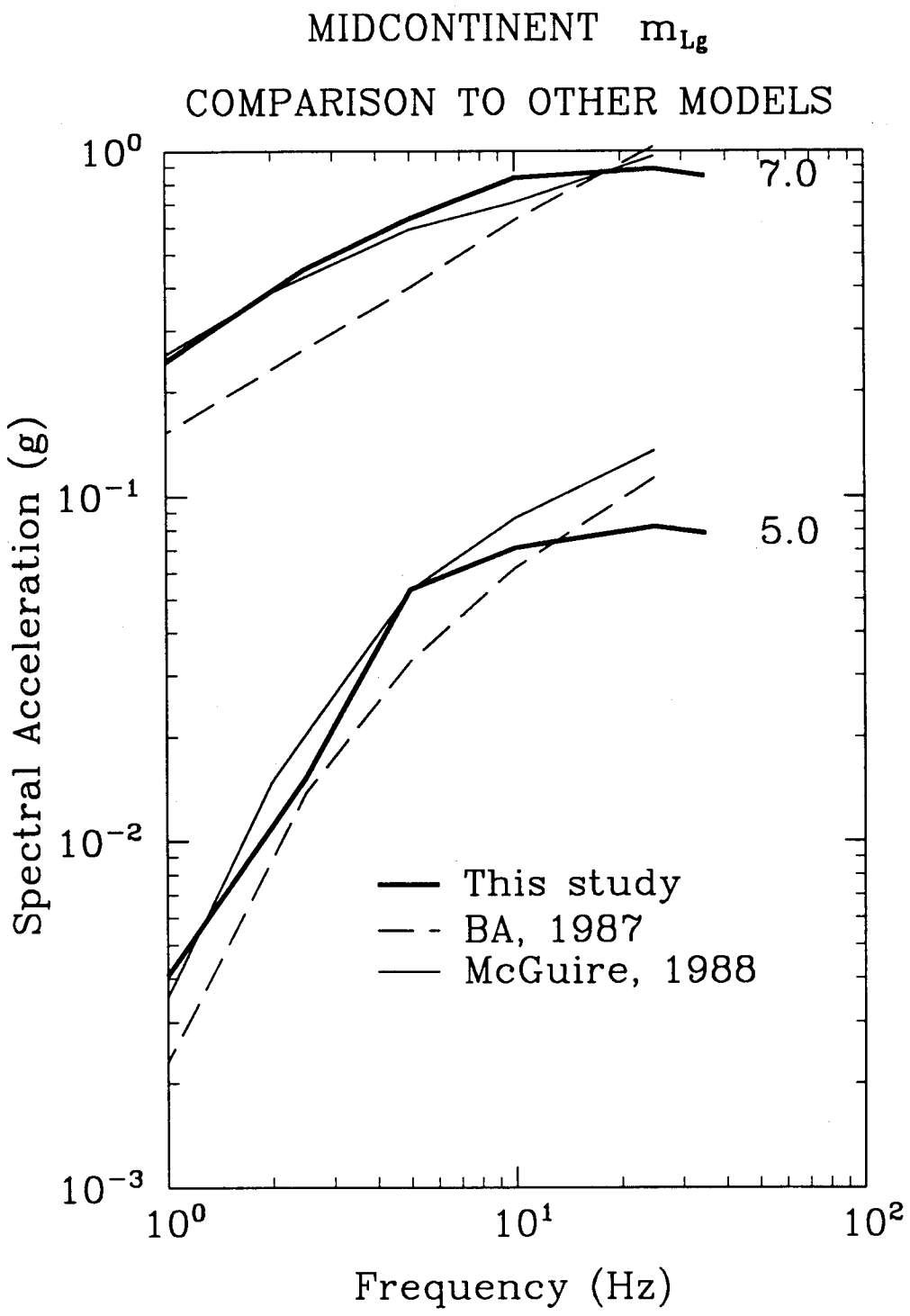

Figure 9-39. Comparison of spectra predicted by the attenuation equations for the Midcontinent (Lg magnitude; thick solid line) to predictions by the attenuation equations of Boore and Atkinson (1987) and McGuire et. al. (1988).

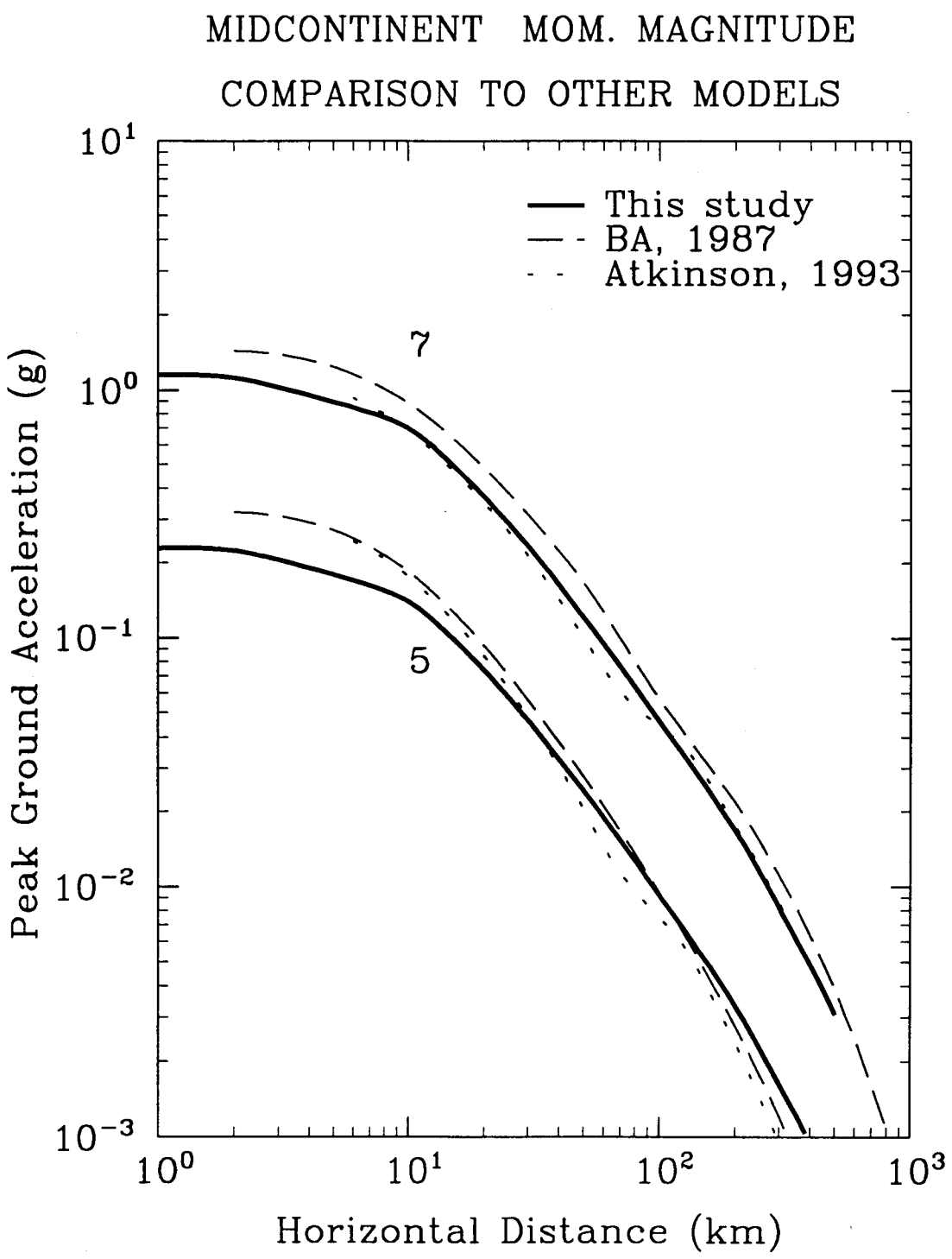

Figure 9-40. Comparison of spectra predicted by the attenuation equations for the Midcontinent (moment magnitude) to predictions by the attenuation equations of Boore and Atkinson (1987) and Atkinson (1993).

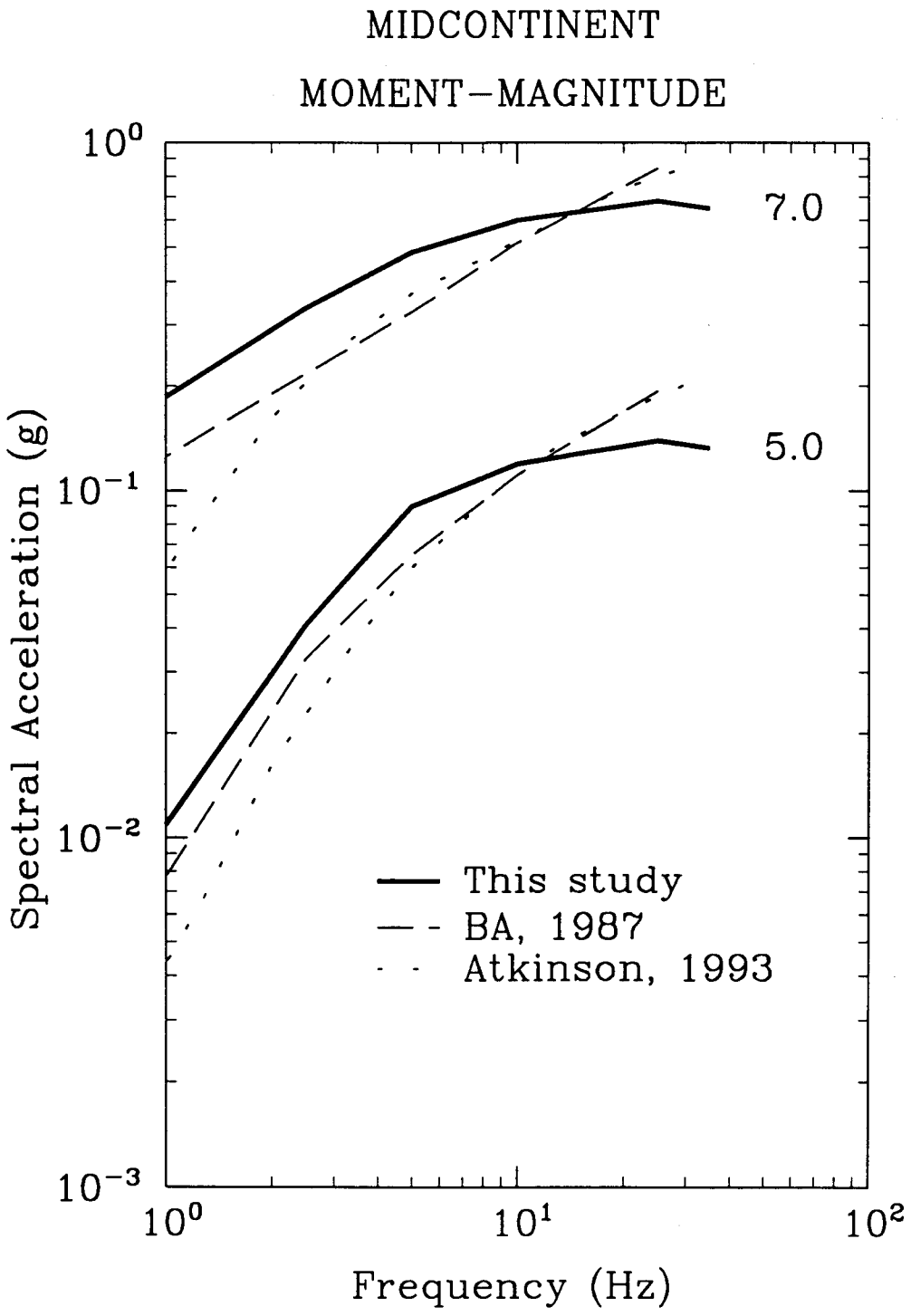

Figure 9-41. Comparison of spectra predicted by the attenuation equations for the Midcontinent (moment magnitude) to predictions by Boore and Atkinson (1987) and Atkinson (1993).

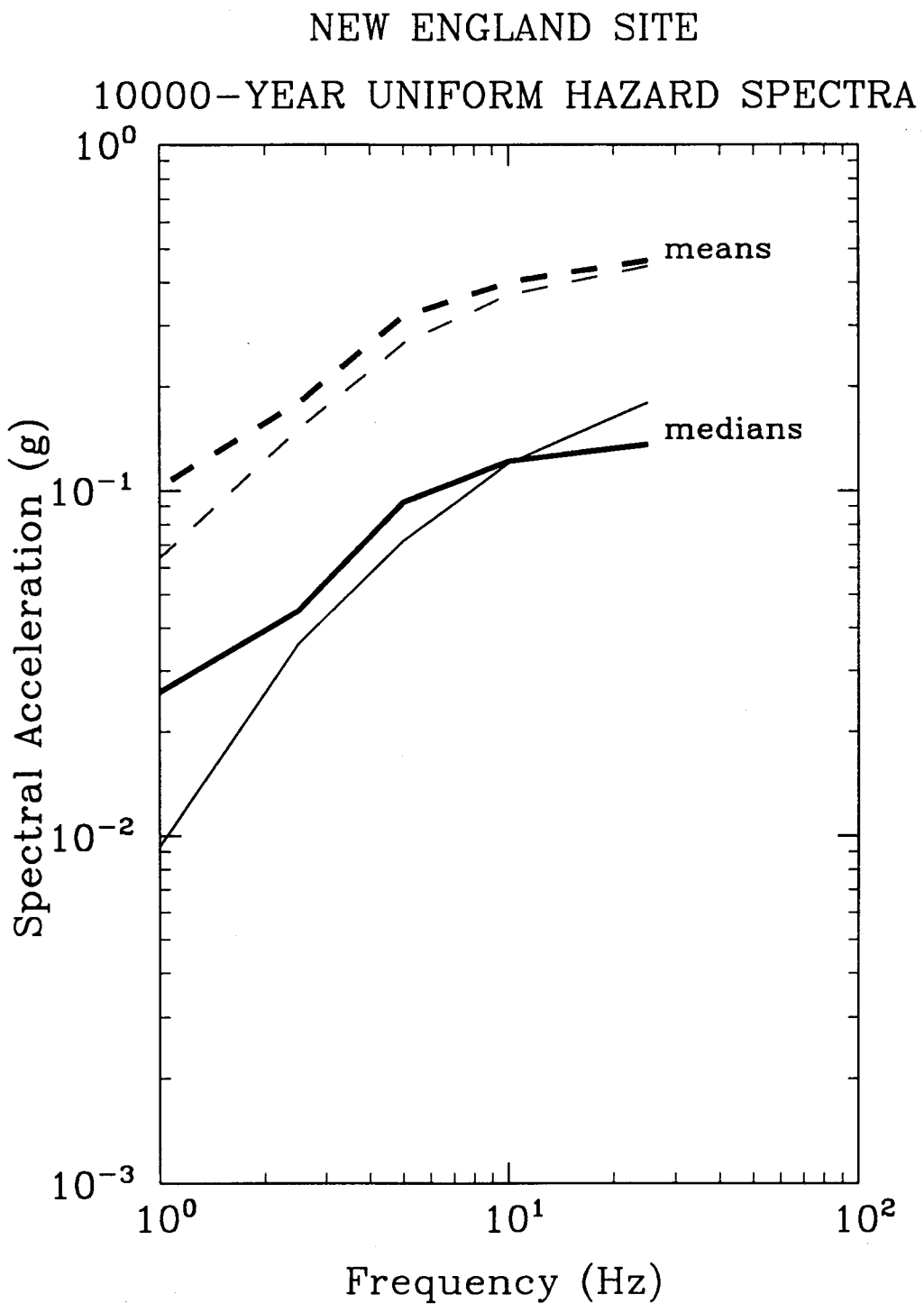

Figure 9-42. Uniform-hazard spectra with an annual exceedance probability of 10^{-4}; New England site. Thick lines: attenuation equations developed in this study; thin lines EPRI/SOG attenuation equations.

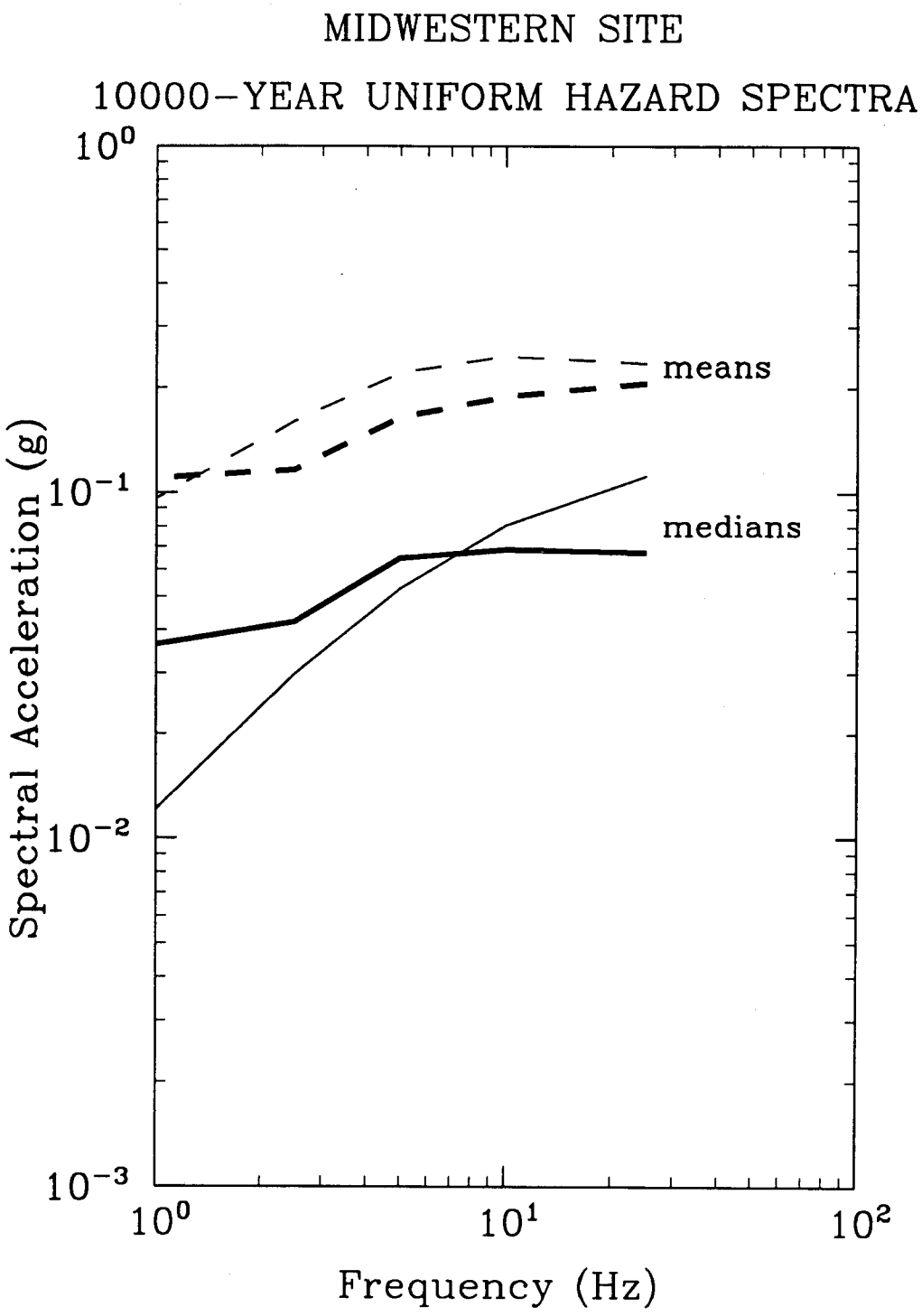

Figure 9-43. Uniform-hazard spectra with an annual exceedance probability of 10^{-4}; Midwest site. Thick lines: attenuation equations developed in this study; thin lines EPRI/SOG attenuation equations.

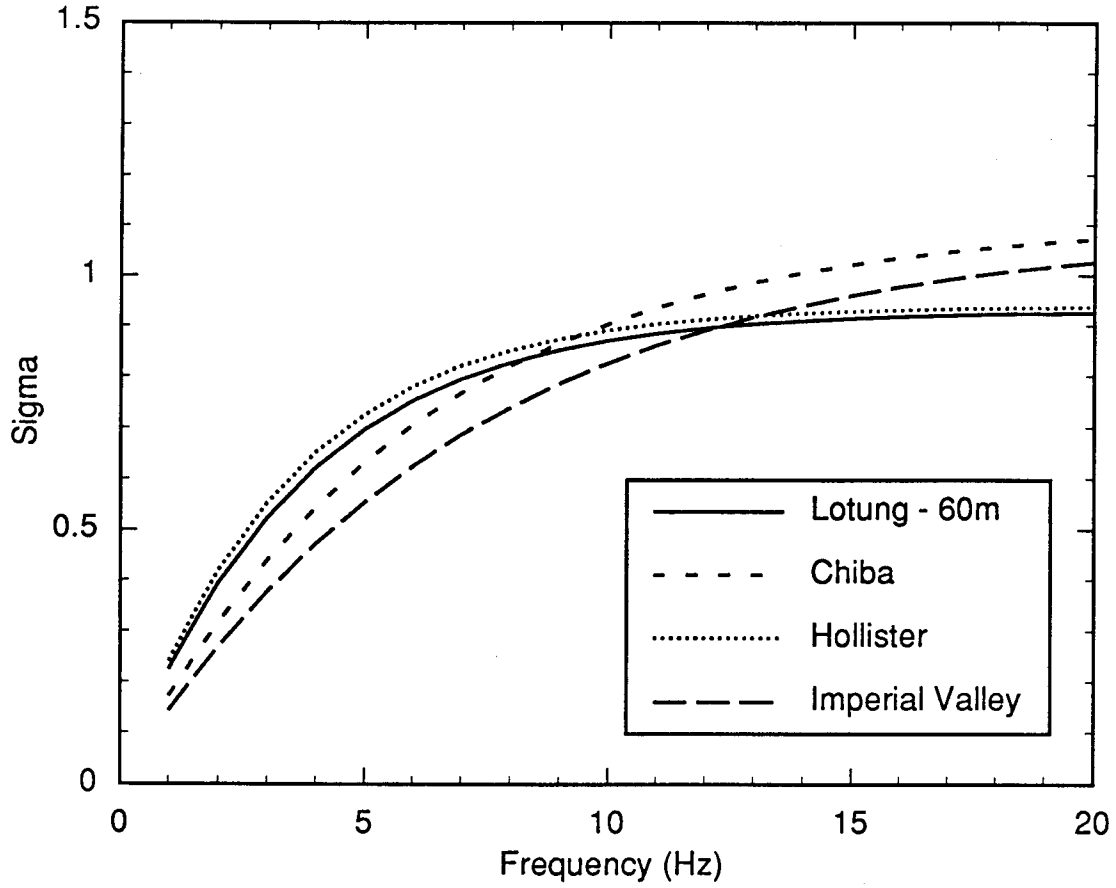

Figure 9-44a. Median variation of Fourier Amplitude at a separation distance of 60m for individual soil sites from dense array recordings. Sigma is the standard deviation.

of ground motions. In this subsection, we show that the variability of ground motions for a given soil site category is less than for rock sites. We recommend using the rock site variability as a conservative estimate of the soil site variability.

There are two main issues to consider in comparing the variability of soil site and rock site ground motions. The first is the variability of the site response for low to moderate levels of shaking and the second is the variability of non-linear site response for high levels of shaking.

For low to moderate levels of shaking, the variability of ground motion on soil and rock sites can be compared using recordings from dense arrays of seismometers. Schneider et al. (1992) examined the distance and frequency dependence of the Fourier amplitude variation from 9 dense arrays. Five of the arrays were located on rock sites and 4 arrays were located on soil sites. The amplitude variation for each array was fit to the functional form:

$$\sigma(f,\xi) = c_1(1-\exp(c_2 f + c_3 f\xi)) \qquad \text{(Eq. 9-12)}$$

where σ is the standard deviation of the difference in natural-log Fourier amplitude between two sites separated by a distance ξ, and c_1, c_2, and c_3 are coefficients estimated by maximum likelihood. The resulting amplitude variation models are shown in Figures 9-44a and 9-44b for soil and rock sites, respectively. The amplitude

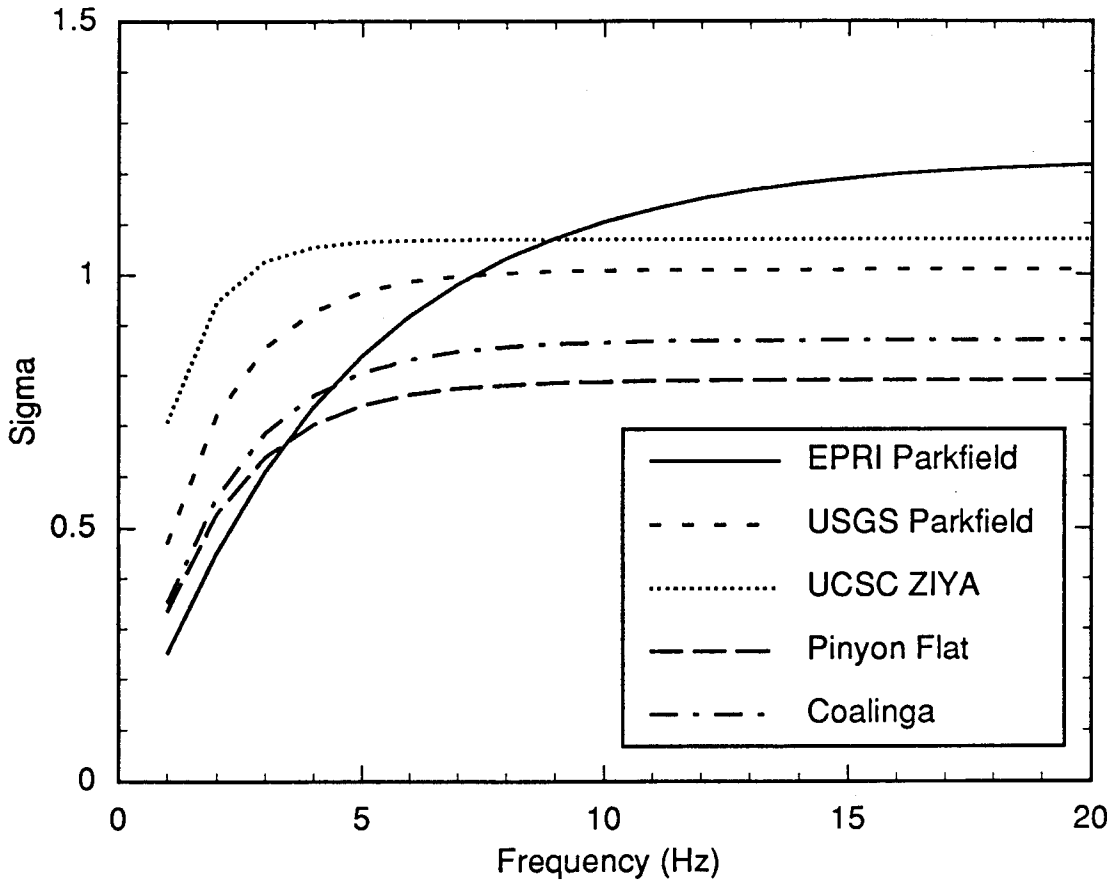

Figure 9-44b. Median variation of Fourier Amplitude at a separation distance of 60m for individual rock sites from dense array recordings. Sigma is the standard deviation.

variations for soil sites are similar to one another, whereas the amplitude variations for rock sites are more varied. On average, the amplitude variations for rock sites are larger than for soil sites (Figure 9-45).

A second concern is whether the variability in nonlinear response of soil sites should increase the total variability of soil site ground motions for large ground motion levels. This issue was examined by modeling site response using a range of soil properties for site category 4 using the equivalent linear procedure described in Section 6. The variability of the resulting surface ground motion was computed for a site a 5 km from events with magnitudes ranging from 5.5 to 7.5. The results are shown in Figure 9-46. As the level of shaking increases, the variability of the ground motion decreases slightly. We conclude that the effect of nonlinear response is to reduce the variability of surface ground motions such that it counteracts the additional variability due to variations of the soil properties.

These results imply that the variability computed for rock sites is an upper bound for the variability on soil sites. Therefore, we recommend using the variability of ground motion for rock site given in Section 9.3 as a conservative estimate of the variability of ground motion for soil sites.

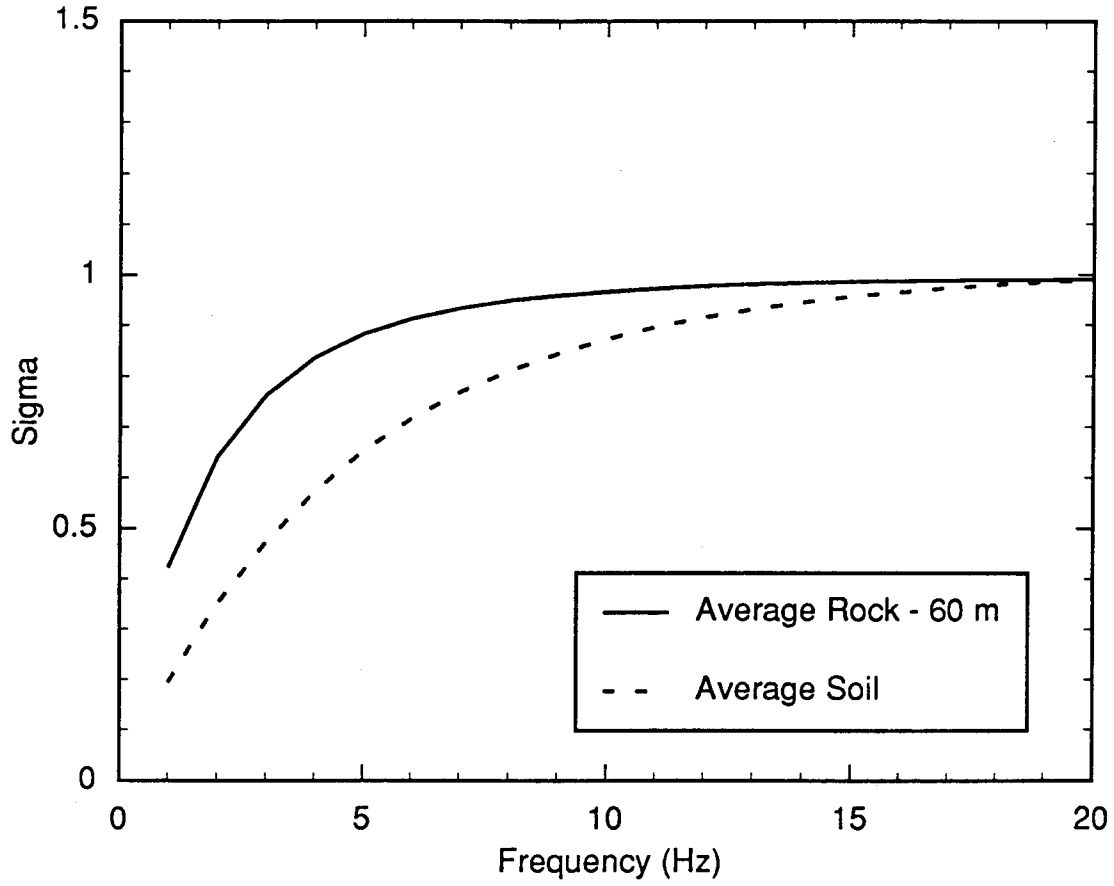

Figure 9-45. Comparison of the average rock site and soil site variation of Fourier Amplitude at a separation distance of 60m from dense array recordings. The variation of individual rock site response is greater than variation of individual soil site response.

9.8 Discussion

The Engineering Model of ground motion, and the associated models of randomness and uncertainty, developed here embody the ground motions predicted using the models and parameters presented in Sections 3, 4, and 5. Though slightly more complicated than most attenuation equations in current use, these attenuation equations are in a form suitable for the determination of design ground motions and for seismic hazard evaluations.

Predictions by the Engineering Model for the Midcontinent and Gulf crustal regions are comparable to predictions by earlier models that use omega-square representations of the source spectra. Predictions by the Engineering Model are generally consistent with available records from ENA. The associated randomness and uncertainty are similar to the values in current use for some cases (i.e., high frequencies and moderate distances) and higher in other cases (i.e., low frequencies or short distances). The causes for the higher randomness at low frequencies and short distances are higher modeling uncertainty and randomness in focal depth, respectively.

What sets this study apart from the previous studies cited earlier is the much larger amount of data that was collected and used to estimate model parameters, the more realistic modeling of crustal effects, and the rational, quantitative process used to derive the median predictions and associated variabilities. These characteristics make the predictions by the Engineering Model, and associated measures of variability, much more robust than earlier results.

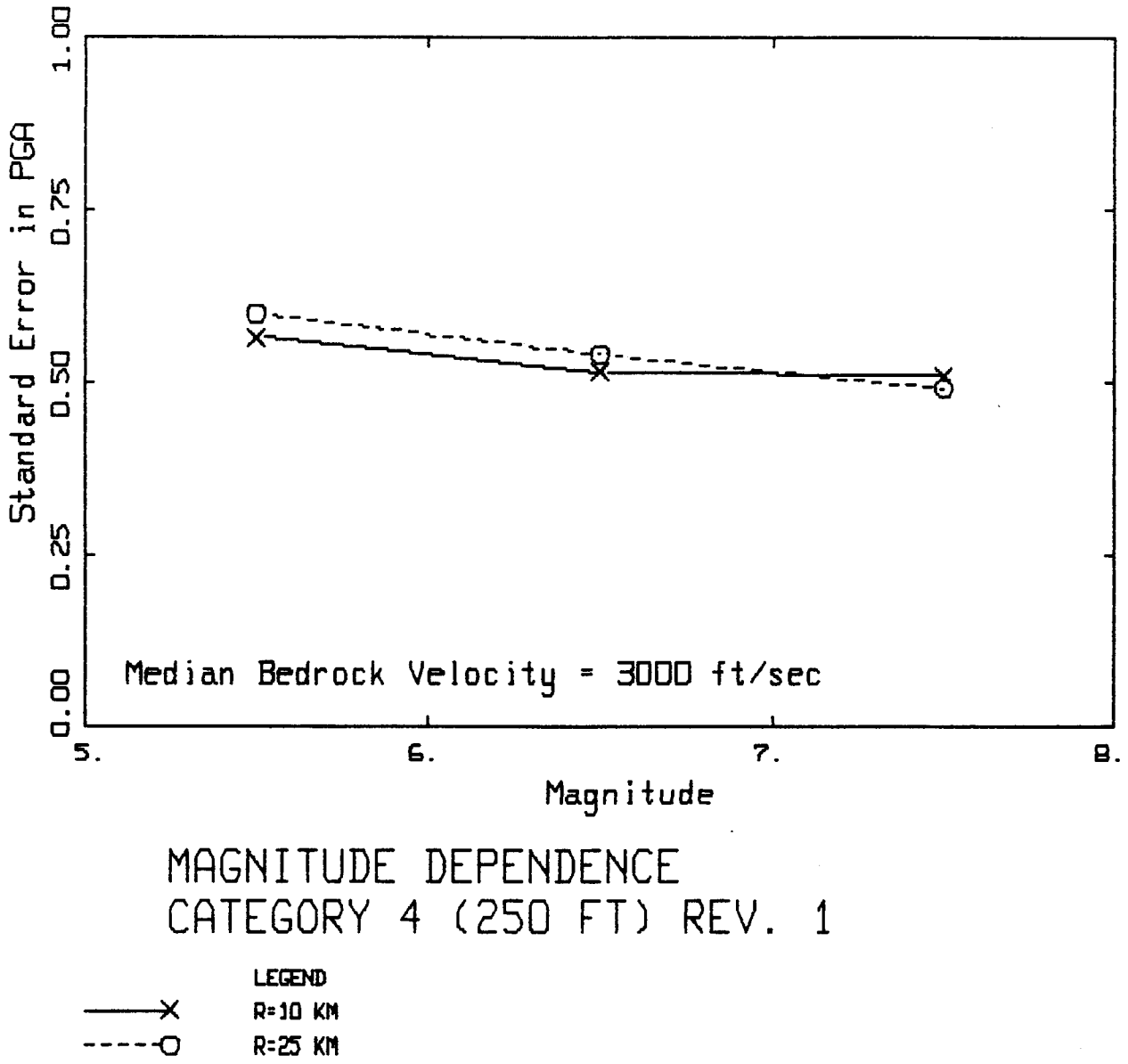

Figure 9-46. Magnitude dependence of variability of ground motion on a soil site (category 4) at a horizontal distance of 5 km from the source. The computed variability includes effects of variability in stress-drop and soil properties. For higher levels of ground motion (larger magnitude) the total variability remains fairly constant even though there is a larger variability in the site-response.

It must be pointed out that the Engineering Model was derived using mainly point-source modeling assumptions (the only exception being the conversion of asperity depth to hypocentral depth). As a consequence, these results may overestimate ground motions at sites near the rupture of a large earthquake, because we have not included other geometric and potential source-scaling effects associated with extended ruptures. Therefore, caution should be exercised if these results are used to predict ground motions at distances shorter than one or two source dimensions. This limitation is of little significance for most sites in the Central and Eastern United States.

References

Abrahamson, N. A., P. G. Somerville, and C. Allin Cornell (1990). "Goodness of fit for numerical strong motion simulations and uncertainty in numerical strong motion predictions," *Proceedings of the 4th U. S. National Conference on Earthquake Engineering.*

Atkinson, G. M. (1993). "Earthquake Source Spectra in Eastern North America." Submitted to the Bulletin, Seismological Society of America, 1993.

Atkinson, G. M., and D. M. Boore. (1987) "Stochastic Prediction of Ground Motion and Spectral Response Parameters at Hard-Rock Sites in Eastern North America." *Bulletin, Seismological Society of America,* Vol. 77, No. 2, 1987, pp. 440–467.

Atkinson, G. M., and R. F. Mereu (1992). The Shape of Ground Motion Attenuation Curves in southeastern Canada. *Bulletin, Seismological Society of America,* Vol. 82, No. 5, pp. 2014–2031.

Gupta, I. N., K. L. McLaughlin, R. A. Wagner, R. S. Ji, and T. W. McElfresh (1989). *Seismic Wave Attenuation in Eastern North America.* Palo Alto, California: Electric Power Research Institute, October 1989. N-6304.

McGuire, R. K., G. R. Toro, and W. J. Silva (1989). *Engineering Model of Earthquake Ground Motion for Eastern North America.* Palo Alto, California: Electric Power Research Institute, October 1988. N-6074.

McGuire, R. K., G. R. Toro, T. P. O'Hara, J. P. Jacobson, and Walter J. Silva (1989). *Probabilistic Seismic Hazard Evaluations at Nuclear Plant Sites in the Central and Eastern United States: Resolution of the Charleston Earthquake Issue.* Palo Alto, California: Electric Power Research Institute, April 1989. N-6395-D.

Schneider, J. F., J. C. Stepp, and N. A. Abrahamson (1992). "The Spatial Variability of Earthquake Ground Motions and Effects of Local Site Conditions." *Proceedings, 10th World Conference of Earthquake Engineering,* Madrid, Spain, pp. 967–972.

10

SUMMARY AND CONCLUSIONS

This study has developed and applied a methodology for the estimation of strong earthquake ground motion. An earthquake's ground motion is a function of the earthquake's magnitude, and the physical properties of the earth through which the seismic waves travel from the earthquake fault to the site of interest. The emphasis of this study is on ground motion estimation in Eastern North America (east of the Rocky Mountains), with particular emphasis on the Eastern United States and southeastern Canada.

The physical phenomena that affect earthquake shaking are the characteristics of earthquake energy release ("source effects"), the way in which seismic waves propagate through the earth to bedrock beneath a site ("path effects"), and the way in which seismic waves are modified as they travel through surficial soils to the earth's surface ("site effects"). These topics are addressed by determining mean parameters and variability, and by quantifying these in a way that can be used for ground motion estimation. An important part of this estimation methodology is the explicit quantification of the two components of variability—randomness and uncertainty. These reflect the variability in earthquake ground shaking from earthquake to earthquake, from region to region, and from site to site.

The focus of this report is on the attributes of ground motion in Eastern North America (ENA) that are of interest for the design of facilities such as nuclear power plants. Specifically considered are magnitudes M from 5 to 8, distances from 0 to 500 km, and frequencies from 1 to 35 Hz. The information contained in this report may be used for site screening as well as for the detailed site ground motion characterization that is needed to assess the seismic safety of a structural design. The results of this report can be used to determine seismic hazards at a site, provided the magnitudes and distances of potential earthquakes are predetermined.

The major products of this work are an engineering ground motion model for rock sites in Eastern North America (Section 9), soil amplification factors (relative to rock) for Eastern North America (Section 6), and a geotechnical guideline for conduct of site-specific investigations (Section 7).

A summary and major conclusions of the report are given in Section 10.1. Recommendations for use of the products of this report are given in Section 10.2.

10.1 Summary of Sections 1 to 9

10.1.1 Section 1: Introduction

This section develops the motivation for the report and the significant ground motion issues to be resolved. It is recognized that regulatory guidance is needed for ground motion estimation on a generic as well as site-specific basis. A new engineering ground motion model together with geotechnical guidelines are intended to provide the basis for improved regulatory guidance for application to site licensing. The following observations are made:

- A fundamental basis for this work is that earthquake ground motion is a product of source, path and site effects that can be quantified and expressed in an engineering model.
- Ground motion estimation for application to ENA is a fundamentally different problem than it is for

Western North America (WNA). In ENA, where observed data are sparse, well-calibrated theoretical models provide the most reasonable approach to the estimation of ground motion.

- It is desirable to have a single consensus model of ground motion and its variability in order to eliminate the need for comparing various individual models, none of which presently treats the ground motion issues in a comprehensive manner.
- A careful process involving data compilation, analytical modeling and site-specific investigations is essential to provide the background information needed to develop an engineering ground motion model and geotechnical guidelines for application to ENA.

10.1.2 Section 2: Empirical Ground Motion Data in Eastern North America

This section develops a database of strong motion data appropriate for assessing the reasonableness of the engineering ground motion model (Section 9) and soil amplification factors (Section 6). Data are examined with regression models to identify the constraints implied by the data for magnitude and distance scaling and on ground motion variability. The examination of variance in recorded motions provides one measure of variability in estimating ground motions from individual events in ENA. In addition, statistical analyses of strong motion data from active tectonic environments such as California aid in evaluating model scaling results. The following conclusions are drawn:

- ENA ground motions indicate similar scaling and attenuation trends to those observed in WNA. The peak spectral acceleration scaling parameters estimated from the data have values consistent with WNA data and predictions made from theoretical models.
- While the data are limited, they do provide broad constraints on the form and parameters of appropriate ground motion relationships for evaluating seismic hazard in ENA.
- The examinations of both strong ground motion and seismographic network amplitude data indicate comparable levels of variability for ENA and WNA data when the effects of earthquake size on ground motion variability are taken into account.

10.1.3 Section 3: Theoretical Ground Motion Modeling

This section discusses the two ground motion models that are used in the project. The first, the stochastic model, is a simple, physically-based model of ground motion, which includes source, path and site terms. A basic assumption of the model is that ground motion in the frequency range of interest (1–35 Hz) may be well-described stochastically. The model assumes that the seismic source can be adequately represented by an equivalent point dislocation, where the point-source distance is modified at close distances to large magnitude earthquakes to account for the finite extent of the seismic source. In addition, seismic site response is directly incorporated through a one-dimensional equivalent-linear approach. Distributions are given for model parameter values that are needed to realistically describe the range of earthquake behavior expected in ENA. This model and the range of parameter values are used to generate synthetic ground motions that are used in developing the engineering model in Section 9.

The second model described is the semi-empirical model. In this approach, near-source recordings of small earthquakes are used as empirical source functions to provide a realistic representation of source effects that combines more stochastic behavior at high frequencies with more deterministic behavior at low frequencies. Wave propagation effects are modeled using simplified transfer functions or Green's functions that are designed to transfer empirical source functions from their recording sites to those required for use in simulations at a specific site. This model is used in Section 5 to explore regional variations in the ground motion due to variations in the crustal structure and source depth.

A model validation is conducted wherein ground motions are simulated using the stochastic and semi-empirical ground motion models and compared to empirical observations. Recordings of two WNA earthquakes (M 6.9 Loma Prieta and M 5.8 Whittier Narrows) and two ENA earthquakes (M 6.8 Nahanni and M 5.9 Saguenay) are modeled to demonstrate the adequacy of both models for simulations of ENA earthquakes. The main results of this validation exercise are as follows:

- The differences between observed and calculated response spectra for the average of horizontal components yields an estimate of modeling variability.

The modeling variability is partitioned into randomness and uncertainty for input to the total variability developed for the engineering model.

- Calculations from both models accurately represent observed response spectra of the data. The stochastic model provides lower variability at high frequency due to the explicit inclusion of the site-specific damping factor, κ.

10.1.4 Section 4: Quantification of Source Effects

There are three main parameters of the seismic source for the stochastic ground motion simulation procedure described in Section 3.2. These parameters are magnitude, stress drop (corner frequency), and the relation between source distance and equivalent point-source distance (accounts for effect of extended sources). The major developments in this section are given below:

- Both m_{Lg} and moment magnitude, **M**, are used to characterize earthquake size for the development of the engineering model in Section 9. The use of m_{Lg} provides a link to ENA earthquake catalogs and to current and past practice. The use of **M** provides a more direct and physically based estimate of ground motion. A relation between m_{Lg} and **M** including the effect of stress drop is developed here using a hybrid approach in which the stochastic ground motion model is used to develop an average **M**-m_{Lg} relationship. Empirical data are then used to validate this relationship and to quantify the variability in m_{Lg} given **M** and the dependence of m_{Lg} on stress drop.
- In the stochastic ground motion model, stress drop directly scales the relationship between magnitude **M** and the level of high frequency ground motion. Two representations of stress drop are considered: the Brune stress drop and the high frequency stress parameter. While the differences in measured stress drops using the two definitions are not significant, the high frequency stress parameter provides slightly more conservatism in estimated ground motion. Part of this conservatism may be due to the existence of a double corner in the source spectrum. The distribution of stress drop values is therefore constrained by values of the high-frequency stress parameter in developing the engineering model in Section 9. Stress drops ranging from 20 to 600 bars have been considered, and this variability is partitioned between randomness and uncertainty. The median stress drop for ENA is determined to be 120 bars.
- The source depth distributions for ENA events developed in Section 5.2 are based on the locations of earthquake hypocenters (i.e., the point of initiation of source rupture). However, the stochastic ground motion model yields simulations of ground motions relative to an asperity (i.e., a zone of greatest slip and greatest high-frequency radiation). Moreover, because the stochastic model used here considers source radiation from a point, geometrical effects of an extended fault that are significant at close distances are not explicitly considered in the simulations. Therefore, a conversion from hypocentral depth to asperity depth that accounts approximately for the extended source effect is derived. In addition, geometrical constraints on the spatial extent of the source are developed in terms of the probability that a large magnitude event will occur at shallow focal depths.

10.1.5 Section 5: Quantification of Crustal Path Effects

In this section, an objective was to determine if there are significant variations in the ground motion attenuation in ENA, especially the Eastern United States (EUS), that would warrant sub-dividing the area into multiple distinct ground motion attenuation regions. A second objective was to determine the overall variability of ground motion contributed by the seismic path. The approach was to first divide the EUS into sixteen distinct regions based upon a literature review of seismological and geological factors. The main factors considered were vertical variation in seismic velocity with depth, seismic attenuation, and depth distribution of earthquake sources. Numerical simulations were then performed using the semi-empirical ground motion model. Earthquake path effects were then examined by modeling the propagation of seismic shear waves through the earth's crust, including the contributions of reflected waves to motion at a site. The simulated ground motions for each region were then compared to one another to determine if the seismological and/or geological differences resulted in significantly different estimates of ground motion for a range of frequencies and distances. The major conclusions from this section are as follows:

- Two crustal models were determined to be sufficiently different to warrant inclusion in the engineering model. The two crustal models correspond to the Gulf coast region and a composite of regions characterized by the Midcontinent region crustal model.
- In Eastern North America, the depths of earthquakes range from about 3 to 32 km, as determined from a global database of earthquake characteristics from stable continental regions.
- Depth distributions within two tectonic domains (i.e., continental margins and non-margins) differ in a statistically significant manner. In Section 9 it is shown that these differences in depth distribution, while statistically significant, do not significantly alter the estimates of ground motion in the engineering model. Therefore the combined depth distribution from all tectonic domains is used in the development of the engineering model.
- Source depth distribution contributes much more significantly to the variation in ground motion at close distances (i.e., < 100 km) than does variation in crustal structure.
- The contribution to ground motion variability from crustal structure variation within each of the two groups of crustal structures is adequately accommodated by the combined variability in source depth and attenuation parameters Q and κ.

10.1.6 Section 6: Quantification of Site Effects

This section develops a set of site amplification parameters for representative soil site conditions in ENA. Equivalent-linear site response analyses were used to develop the soil amplification factors for 5% damped response spectra, peak accelerations, and peak particle velocities. The amplification factors were computed for control motions with ENA characteristics, specifically peak outcrop accelerations for a wide range of accelerations (i.e., from 0.05 to 1.25g). A model was also developed to express vertical-to-horizontal (V/H) spectral ratios at both rock and soil sites. From these results the following conclusions are drawn.

- Results of empirical and analytical studies at three reference sites clearly demonstrate that nonlinear response occurs in soil, even at relatively low to moderate levels of ground shaking. These nonlinear effects can be accounted for using either equivalent linear or nonlinear modeling methods coupled with high quality soil property information. Site response analyses for ENA site categories also demonstrate nonlinear site response.
- Site response can be adequately modeled with one-dimensional, vertically propagating S waves. For the frequency range of interest, the effects of two- and three-dimensional wave propagation are generally minor.
- The spectral amplification factors [5% damped S_a(soil)/S_a(rock)] for ENA differ from those in WNA. Based on comparisons to analytical and empirical results, the amplification factors given Table 6-4 can be used for ENA.
- Increases in bedrock velocity have minor effects on spectral amplification factors; e.g., an increase in the S-wave velocity of bedrock from 6,000 ft/sec to 9,000 ft/sec results in less than a 10% increase in spectral amplification factor. As the mean bedrock velocity decreases from 6,000 fps to 3,000 fps, a 30% reduction in amplification factors can occur near the soil profile resonance. Other variables such as the magnitude of control motion and the bedrock velocity gradient have relatively minor effects on the spectral amplification factors.
- The vertical to horizontal spectral ratio (V/H) varies with geologic characteristics (soil versus rock), source distance, control motion acceleration, and frequency. For rock sites typical V/H values will range from 0.7 for source distances greater than 20 km, to values of 1.2 for a source within 10 km and frequencies greater than about 20 Hz. For soil sites the V/H ratio varies from 0.7 to 1.5 for control motions of 0.5g and frequencies from 10 to 20 Hz.

10.1.7 Section 7: Guidelines for Site Investigations and Response Analyses

Guidelines for the determination and use of dynamic soil properties in ground response studies were developed. These guidelines are based on a review of recent literature and the results of field and laboratory tests presented in Section 8. The guidelines are intended to serve as the basis for regulatory guidance in the conduct of geotechnical site characterization and site response analyses. From these guidelines the following key conclusions can be made.

- The quality of field and laboratory results depends closely on the attention given to the setup and conduct of the tests. In the absence of individuals with appropriate experience and financial support to implement an adequate program, results of field and laboratory testing can be erratic and misleading.
- Uncertainties inherent to both field and laboratory testing methods must be anticipated in any site-specific response study. Different testing methods involving different boundary and loading conditions, as well as redundant tests, should be used to establish both the average and range of dynamic properties for any specific soil layer.
- A consistent family of modulus reduction and material damping curves for soils ranging from clay to gravel is presented in Appendix 7.A. Procedures are suggested for obtaining a better fit in nonlinear models to measured material damping data at low to high levels of strain.

10.1.8 Section 8: Field and Laboratory Investigations

Three reference sites were used to evaluate current procedures for determining dynamic properties of soil, and their variability. Two of the reference sites, Gilroy 2 and Treasure Island, are located in the San Francisco Bay area; the third site is located in Lotung, Taiwan. Each site has weak- and strong-seismic ground motion records. S- and P-wave velocity versus depth profiles from suspension logging, downhole testing, and crosshole testing are given for the Treasure Island and Gilroy 2 site. Attenuation results obtained from waveform interpretations of the Treasure Island and Gilroy 2 sites are also presented. Complementing this field information is a large laboratory-derived database of shear modulus and material damping information, showing the effects of confining pressure, shearing strain amplitude, and cycles of loading for soil at the three reference sites. From these field and laboratory tests the following conclusions are made.

- Different seismic methods give similar average S- and P-wave velocities at the reference sites. The variation at any depth typically ranges from 10 to 20% of the average velocity for both the S- and P-wave velocities. Greater variation appears to occur where heterogeneous soil, such as gravelly sand and sandy gravel, occurs.
- Results of waveform fitting indicate that in situ values of low-strain material damping range from 2% to nearly 7%. The largest damping occurs in gravelly soil, the least in relatively uniform clay deposits. Other methods of interpreting material damping, specifically spectral ratio and spectral amplitude methods, result in more data scatter.
- High-quality laboratory damping measurements on undisturbed samples from the reference sites indicate that damping at low shearing strain is very low, typically being less than 2 or 3%. For accurate damping measurements in the resonant column test, it is necessary to account for equipment compliance in the device. Although laboratory values of damping are typically less than field measurements, the laboratory and field measurements are consistent in their variation (e.g., lower laboratory measurements correspond to lower field measurements). This difference between laboratory and field measurements may be the result of frequency of loading effects, as well as wave scattering effects during in situ measurements.
- Results of laboratory dynamic tests define modulus-strain and material damping-strain relationships that are very well behaved when high-quality, undisturbed samples are tested in resonant column and cyclic torsional testing equipment. The form of the modulus-strain and damping-strain relationships is generally consistent with hyperbolic relationships described in Appendix 7.A with reference strains from 0.05 to 0.3%.

10.1.9 Section 9: Engineering Model of Strong Ground Motions

The ground motion relations presented in Section 9 describe the predictions obtained from the source and path-effects models, integrated over the distributions of all model parameters. The approach and results in Section 9 demonstrate how earthquake shaking can be estimated in a practical way. The functions require only a specification of the earthquake magnitude (either **M** or m_{Lg}) and horizontal distance from the source (epicenter or surface projection of a fault). Terms describing randomness and uncertainty are included so that the variability around the median estimate can be calculated. This variability is important in determining the range of ground motions that might occur for a given earthquake, either for

probability studies or for representations of ground motions of deterministically specified events. The main attributes of this model are summarized as follows:

- The total variability in ground motion is generally larger for the low frequencies and less for high frequencies, because the stochastic simulation procedure has larger modeling variability for the low frequencies.
- At any frequency, the total variability is lowest in the distance range 20 to 50 km. It is higher at short distances because of randomness associated with the depth at which earthquakes occur, and it is higher at longer distances because of the contributions of reflected waves (depth randomness contributes to this effect) and the randomness in crustal attenuation.
- The equations for ground motion estimation are generally consistent with instrumental observations of earthquake ground shaking in ENA, and are consistent with previous attenuation functions. Differences with observations are not statistically significant (except at low frequencies where they over estimate ground response) and are attributable to the limited sample of earthquakes with magnitudes and distances of engineering interest. In particular, the average stress drop in this sample is dominated by one event with a high stress drop.
- It is anticipated that the results of this study will be useful for some years. The distinction between randomness and uncertainty means that as more is learned about the earthquake process, the uncertainty terms can be refined and reduced. The resulting estimates of median ground motion may be higher or lower than those from Section 9, but they will have reduced uncertainty as a result of the new knowledge.

10.2 Application of Results

The results of extensive seismological, geotechnical and seismic engineering analyses have yielded a comprehensive engineering ground motion model for the EUS and guidelines for site-specific investigations. Key products of the report and their attributes are briefly described.

The engineering model is applicable to a wide variety of site conditions, especially potential sites of future nuclear power plants. The engineering model is also appropriate for use in either a probabilistic or a deterministic development of site-specific design spectra. The basic ground motion attenuation relations are developed in Section 9. These relations are directly applicable to rock sites for site screening or to the determination of rock-outcrop motions needed for input to soil sites. Ground motion is given in terms of 5% damped response spectra as a function of frequency for a wide range of magnitudes and distances.

For site screening at soil sites, generic soil models are developed in Section 6. From these categories are developed a series of soil amplification factors that can be directly applied to the rock-outcrop motions given in Section 9. These factors consider the differences in amplification with soil depth, frequency and level of input motion.

For site-specific application, the geotechnical guideline in Section 7 provides general guidance for a user to carry out a systematic and thorough site geotechnical investigation and site response analysis appropriate for NRC licensing consideration. These guidelines are intended to serve as a basis for a new regulatory guide on site-specific geotechnical investigations. The results of investigations at reference sites (Section 8), together with appendices to Sections 6, 7 and 8 provide the basis for this guideline. This guideline is generally applicable to siting issues at stiff soil sites in ENA, WNA or elsewhere.

1.A

GLOSSARY

1.A.1 Seismological/Geotechnical Glossary of Terms

Term	Use[1]	Symbol[2]	Units	Explanation
Acceleration	S, G	a	g	Ground acceleration in the path of a seismic wave expressed in g, the vertical acceleration of gravity at the earth's surface (9.80665 m/sec^2).
Acceleration, Peak Ground	S, G	PGA	g	Maximum acceleration of the ground from an earthquake.
Acceleration, Spectral	S, G	PSa	g	Pseudo-absolute response spectral acceleration, given as a function of period or frequency.
Accelerogram	S, G			A seismogram where ground motion is expressed in terms of ground acceleration. (See "Seismogram.")
Accelerograph	S, G			A seismograph that records ground motion in terms of ground acceleration. (See "Seismograph.")
Accelerometer	S, G			A transducer that produces a signal proportional to acceleration or force over a given bandwidth. Accelerometers are used in earthquake engineering to record strong motion from earthquakes. (See "Seismometer.")
Asperity	S			A zone of relatively high slip (displacement) on a fault surface. In the Brune source model, asperities have high stress drop, and hence yield dominant high-frequency energy.
Attenuation Equation	S, G			An equation that estimates a certain characteristic of ground shaking (e.g., peak acceleration or spectral velocity at a given period and damping) as a function of earthquake source, path and site parameters.
Attenuation, Anelastic	S	Q		Attenuation caused by absorption of seismic energy in the earth. Ratio of energy lost per seismic wave cycle to the energy stored in that cycle is $2\pi/Q$. Also $1/Q = 2D/\text{sqrt}(1 - D^2)$. (See "Damping Ratio.")

1. Refers to primary usage of term in Geotechnical Engineering (G) or Seismology (S).
2. In some cases there may be different symbols and units used in Geotechnical Engineering and Seismology.

Term	Use[1]	Symbol[2]	Units	Explanation
Attenuation, Ground Motion	S, G			Decrease in severity (or amplitude) of ground shaking with increasing distance from the earthquake source.
B Parameter	G	B	%	Pore pressure parameter indicating degree of saturation of soil sample [$B = \Delta\mu/\Delta\sigma$].
Bandwidth	S, G			A range of frequencies or periods.
Coda (P or S)	S			The seismic energy in a seismogram that arrives after the primary waves (P, S or Surface waves), typically associated with energy scattered throughout the source-site region.
Coherency	S			A complex number representing a quantitative measure of spatial variation of the phase spectrum of a seismic wavefield. Qualitatively, a measure of the degree of similarity of two time series (e.g., seismograms).
Cohesion Intercept	G	c'	lb/ft^2	Shearing strength intercept at zero confining stress for a Mohr-Coulomb Failure Law.
Compression Index	G	C_c		Slope of the line relating change in void ratio per logarithmic change in stress.
Control Motion	S, G			The input time history to a seismic site response analysis. (See "Seismogram" and "Accelerogram.")
Control Point	S, G			The location in the soil profile where the control motion is specified.
Convolution	S, G			Complex multiplication in the frequency domain. Used in site response analysis to take the ground motion at a given depth and "propagate" it upward through the soil column. (See Section 1.A.2.1 below.)
Damping Ratio	G	D	%	Amount of energy absorbed by hysteretic or viscous action of soil. (See "Attenuation.")
Density	S	ρ	gm/cm^3	The mass per unit volume of a substance. Densities for rock in the crust range from about 2.5 at the surface to 3.5 at the base of the crust. (See "Unit Weight, Total.")
Density, Relative	G	D_r	%	Procedure used to characterize the density of natural granular soil $[(e_{max} - e)/(e_{max} - e_{min}) \times 100\%$
Dip	S, G		degrees	The angle by which a stratum (or plane) deviates from the horizontal, measured in a plane perpendicular to the strike.
Discontinuity, Conrad	S			The division between the upper and lower continental crust, marked by an increase in P-wave velocity of about 10–15%, but not universally observed in the ENA.
Discontinuity, Mohorovicic	S			Boundary between the crust and mantle, marked by a rapid increase in P-wave velocity ($V_P \geq 8$ km/sec). In the ENA, the "Moho" is located at 30–50 km depth.

1. Refers to primary usage of term in Geotechnical Engineering (G) or Seismology (S).
2. In some cases there may be different symbols and units used in Geotechnical Engineering and Seismology.

Term	Use[1]	Symbol[2]	Units	Explanation
Distance, Epicentral	S	R_E	km	Distance from the epicenter to the receiver.
Distance, Fault	S	R_F	km	Shortest distance from the fault to the receiver.
Distance, Hypocentral	S	R_H	km	Distance from the hypocenter to the receiver.
Distance, JB	S	R_{JB}	km	Shortest distance from the surface projection of the fault to the receiver (after Joyner and Boore, 1981).
Earth Pressure, at Rest	G	K_o		Ratio between normal stress on a vertical section and normal stress on a horizontal section at a given point in a mass of soil.
Earthquake, Aftershock	S			An earthquake that occurs after the mainshock, and is correlated in space and time and smaller in magnitude than the mainshock. (See "Earthquake, Mainshock.")
Earthquake, Characteristic	S			One of a series of earthquakes that repeatedly rupture the same segment of the fault zone with similarly sized events.
Earthquake, Foreshock	S			An earthquake that occurs before the mainshock, and is correlated in space and time and smaller in magnitude than the mainshock. (See "Earthquake, Mainshock.")
Earthquake, Mainshock	S			The largest magnitude earthquake within a sequence of earthquakes that are correlated in space and time. (See "Earthquake, Aftershock" and "Earthquake, Foreshock.")
Eastern North America	S	ENA		The region of North America east of the Rocky Mountains, and characterized as a stable continental region. (See "Stable Continental Region").
Eastern United States	S	EUS		The portion of the United States east of the Rocky Mountains, and characterized as part of the stable continental region of the ENA. (See "Stable Continental Region" and "Eastern North America").
Epicenter	S, G			The point on the earth's surface directly above the focus or hypocenter of an earthquake.
Fault	S, G			A planar or gently curved fracture surface or zone in the earth across which there has been relative displacement.
Fault, Active	S, G			A fault along which tectonic displacement is expected to occur under current tectonic conditions based upon historical, geological, or seismological evidence.
Fault, Dip-Slip	S, G			A fault in which the relative displacement is along the direction of the dip of the fault plane; either down-dip (normal fault) or up-dip (reverse fault).
Fault, Normal	S, G			A dip-slip fault in which the block above the fault has moved downward relative to the block below. This type of fault represents crustal extension.

1. Refers to primary usage of term in Geotechnical Engineering (G) or Seismology (S).
2. In some cases there may be different symbols and units used in Geotechnical Engineering and Seismology.

Term	Use[1]	Symbol[2]	Units	Explanation
Fault, Reverse	S, G			A dip-slip fault in which the block above the fault has moved upward relative to the block below, and the fault dip ≥ 45°. (See also "Fault, Reverse.")
Fault, Strike-Slip	S, G			A fault in which the relative displacement is along the strike of the fault plane, either right- or left-lateral.
Fault, Thrust	S, G			A dip-slip fault in which the block above the fault has moved upward relative to the block below, and the fault dip < 45°. This type of fault represents crustal compression.
Focal Mechanism	S			The combination of the dip angle of the fault and the direction of slip across the fault; faults are classified as strike-slip, normal or reverse. (See "Fault.")
Fourier Spectrum	S, G			See "Spectrum, Fourier."
Frequency	S, G	f	Hz	Rate of oscillation of a wave. (Hz = cycles/sec.)
Frequency, Circular	S, G	ω	radians/ sec	Rate of oscillation of a wave in radians ($2\pi f = \omega$).
Frequency, Corner	S	f_c	Hz	Frequency at which the amplitude spectrum of an earthquake transitions from a low-frequency level controlled by the seismic moment, to a high-frequency level controlled by the stress drop. $1/f_c$ is approximately the duration of the earthquake rupture.
Frequency, Damped	G	f_d	Hz	$f_d = f_n(1 - D^2)^{0.5}$
Frequency, Natural	G	f_n	Hz	Frequency of a system without damping
Friction angle	G	ϕ	degrees	Material constant that relates frictional resistance to normal stress on a plane.
Geometrical Spreading	S			The dissipation of seismic energy due to elastic propagation of energy within a medium. In a whole space the rate of geometrical spreading is distance^{-1} from the source, while in a half space it is distance$^{-1/2}$. (See also "Attenuation, Anelastic.")
Hypocenter	S			The point in the earth at which an earthquake is initiated, the focus.
Kappa	S	κ	sec	Attenuation in the upper 1–2 km of the earth's surface, expressed as H/V_SQ (where H is depth and V_S is average S-wave velocity of the attenuating layers).
Kips	G	Kips		Weight equal to 1000 pounds (lb).
Liquid Limit	G	w_l	%	Water content of fined-grained soil at boundary between liquid and plastic states.
Logarithmic Decrement	G	δ		Natural logarithm of two successive peaks of sinusoidal motion [$\delta = 2\ D/(1 - D^2)^{0.5}$].

1. Refers to primary usage of term in Geotechnical Engineering (G) or Seismology (S).
2. In some cases there may be different symbols and units used in Geotechnical Engineering and Seismology.

Term	Use[1]	Symbol[2]	Units	Explanation
Low-Velocity Zone	S, G			A region in the earth, especially a planar layer, that has lower seismic-wave velocities than the region immediately above and below it.
Magnitude	S	M		A measure of earthquake size, determined by taking the common logarithm (base 10) of the largest ground motion observed during the arrival of the P-wave or seismic surface wave and applying a standard correction for distance to the epicenter.
Magnitude, Body-Wave	S	M_b		Magnitude derived from the largest displacement amplitude of body waves (P or S).
Magnitude, Coda-Wave	S	M_C		Magnitude derived from the amplitude and duration of the seismic coda.
Magnitude, Lg	S	M_{Lg}, M_{bLg}		Magnitude derived from the displacement amplitude of Lg waves; often used in ENA because it can be accurately measured from typical low-gain seismographs at long distances from the source.
Magnitude, Moment	S	**M**		Earthquake magnitude derived from the seismic moment.
Magnitude, Surface-Wave	S	M_S		Earthquake magnitude determined from the maximum amplitude of 20-sec period surface waves.
Margin	S			A rift in which extension progressed to the stage of continental separation and generation of oceanic crust. Margins typically include broad zones of continental stretching. (See "Rift").
Mass	G	m	lb-sec^2/ft	Weight divided by acceleration of gravity (m = W/g)
Mass Density	G	ρ	lb-sec^2/ft^4	Unit weight of soil divided by acceleration of gravity ($\rho = \gamma/g$).
Modulus, Bulk	G	k	lb/ft^2	Ratio of volumetric stress to volumetric strain. Bulk modulus of water is approximately 4.47 X 10^7 lb/ft^2. Related to Young's modulus and Poisson's ratio by $k = E/3(1-2\nu)$.
Modulus, Bulk	S	k	bar	$k = E/3(1-2\sigma)$.
Modulus, Constrained	G	M	lb/ft^2	Ratio of axial stress to axial strain with lateral deformation constrained. Related to bulk modulus and shear modulus by $M = k + 4/3\ G$.
Modulus, Constrained	S	M	bar	$M = k + 4/3\ \mu$
Modulus, Shear	G	G	lb/ft^2	Ratio of shearing stress to shearing strain. For elastic material $G = E/2(1 + \nu)$; G = 0 in a perfect fluid.
Modulus, Shear	S	μ	bar	$= E/2(1 + \sigma)$
Modulus, Young's	G	E	lb/ft^2	Ratio of axial stress to axial strain. For elastic material $E = 2G(1 + \nu)$.
Modulus, Young's	S	E	bar	$E = 2\ \mu\ (1 + \sigma)$

1. Refers to primary usage of term in Geotechnical Engineering (G) or Seismology (S).
2. In some cases there may be different symbols and units used in Geotechnical Engineering and Seismology.

Term	Use[1]	Symbol[2]	Units	Explanation
One-Dimensional Analysis	S, G			A soil-column or shear-beam analysis in which material properties are assumed to vary only in one dimension. (See Section 1.A.2.2 below.)
Outcrop Motion	S, G			Motion specified at the free surface of either soil or rock. (See Section 1.A.2.3 below.)
Overconsolidation Ratio	G	OCR		Ratio of maximum past vertical effective stress to present vertical effective stress.
Period (Wave)	S, G	T	sec	The time interval between the arrival of successive crests of a wave ($T = 1/f$).
Plastic Limit	G	w_p	%	Water content of fine-grained soil at boundary between plastic and semisolid states.
Plasticity Index	G	PI	%	Difference between liquid limit and plastic limit within soil.
Poisson's Ratio	G	ν		Ratio of transverse strain to lateral strain of elastic media under lateral stress.
Poisson's Ratio	S	σ		$\sigma \sim .25$ in most of the crust, such that $V_p \sim 1.7\ V_s$.
Porosity	G	n		Volume of soil voids divided by total volume of soil [$n = e/(1 + e)$].
Preconsolidation Pressure	G	p_c	lb/ft^2	Largest pressure experienced by a soil during its lifetime.
Pressure	G	P	lb/ft^2	Force per unit area.
Quality Factor	S	Q		See "Attenuation, Anelastic."
Response Spectrum	S, G			See "Spectrum, Response."
Rift	S			A portion of the earth's crust that has experienced extension that resulted in crustal thinning and surface faulting, often accompanied by mantle upwelling. (See also "Margin").
Saturation, Degree of	G	S	%	Ratio of volume of water to volume of voids [$S = V_w/V_v$]. Complete saturation occurs when all voids are filled with water.
Seismic Hazard	S, G			The outcome of the combination of earthquake occurrences and their resulting ground motion. It is expressed for a given region or site of interest either as maximum values of a ground motion parameter or as the probability of exceeding values of a ground motion parameter per unit time.
Seismic Moment	S	M_0	dyne-cm	A measure of the size of an earthquake based on interpretations of how much stress was relieved over the area of the fault or rupture surface. It is defined by the product of the rupture area, the average slip, and the crustal rigidity.
Seismicity	S			The distribution of earthquakes in space and time.

1. Refers to primary usage of term in Geotechnical Engineering (G) or Seismology (S).
2. In some cases there may be different symbols and units used in Geotechnical Engineering and Seismology.

Term	Use[1]	Symbol[2]	Units	Explanation
Seismogram	S, G			A time history recording of ground motion. A single seismogram expresses motion in terms of ground acceleration, velocity or displacement for one component (one axis). The complete ground motion at a point requires three seismograms, typically a vertical component and two horizontal components oriented N–S and E–W.
Seismograph	S			An instrument used to record ground motion on visible or electronic media. (See "Seismogram.")
Seismometer	S			An instrument used to convert vibratory ground or structural motion to a signal appropriate to be recorded by a seismograph. Seismometers amplify motions relative to displacement, velocity or acceleration and have characteristic bandwidths and dynamic ranges. (See "Seismograph.")
Signal-to-noise Ratio	S, G			In ground motion observations, the ratio between the seismic waves of interest and the combination of earth noise and/or instrument noise. (See Section 1.A.2.4 below.)
Site Response (Amplification)	S, G			The amplification (increase or decrease) of earthquake ground motion by rock and soil near the earth's surface in the vicinity of the site of interest.
Source, Finite	S			A representation of the earthquake rupture process whereby seismic energy is modeled as originating across a two-dimensional surface.
Source, Point	S			A representation of the earthquake rupture process whereby seismic energy is modeled as originating from a single point in space.
Specific Gravity	G	G_s		Total unit weight of soil divided by unit weight of water at 4°C (= 1 gram/cm^3).
Spectrum, Fourier	S, G			A representation of the energy in ground motion as a function of frequency. The spectrum is derived from the composition of sine and cosine waves of varying periods and amplitudes that make up a seismogram or accelerogram. (See Section 1.A.2.5 below.)
Spectrum, Response	S, G			Spectrum derived from the maximum responses to ground motion of a series of single degree-of-freedom oscillators with a range of frequencies and a specified damping. The response may be in units of acceleration, velocity or displacement. (See Section 1.A.2.6 below.)
Stable Continental Region	S	SCR		A region of continental crust characterized by the lack of significant tectonic activity since the early Cretaceous Period (~ 130 M yrs). Eastern North America is considered to be an SCR. (See "Eastern North America").
Strain (general)	S, G	e		The measure of deformation expressed as the ratio of the change in dimension to the original dimension.

1. Refers to primary usage of term in Geotechnical Engineering (G) or Seismology (S).
2. In some cases there may be different symbols and units used in Geotechnical Engineering and Seismology.

Term	Use[1]	Symbol[2]	Units	Explanation
Strain, Axial	G	ε_a	%	Change in axial length per unit length.
Strain, Shearing	G	γ	%	Distortion per unit length. For elastic material shearing strain is the ratio of shearing stress to shear modulus.
Stress (general)	G, S	σ	lb/ft^2 bar	The force per unit area acting on a body.
Stress Drop	S	$\Delta\sigma$	bar	The average stress released across a rupture surface during an earthquake. (1 bar = 1.013 x 10^6 dyne/cm^2.)
Stress, Axial	G	σ_a	lb/ft^2	Axial force per unit area
Stress, Horizontal	G	σ_h	lb/ft^2	Horizontal force per unit area
Stress, Octahedral	G	$\sigma\Delta$	lb/ft^2	Average of the three principal stresses [$\sigma_\Delta = 1/3(\sigma_1 + \sigma_2 + \sigma_3)$].
Stress, Shearing	G	τ	lb/ft^2	Shearing force per unit area.
Unit Weight, Buoyant	G	γ_b	lb/ft^3	Total unit weight of soil minus total unit weight of water.
Unit Weight, Dry	G	γ_d	lb/ft^3	Weight of soil solids divided by total volume. (See "Density.")
Unit Weight, Total	G	γ_t	lb/ft^3	Total soil weight per unit volume.
Unit Weight, Water	G	γ_w	lb/ft^3	Total weight of water per unit volume (62.4 lb/ft^3).
Velocity, Longitudinal	G	V_c	ft/sec	Velocity of longitudinal or rod wave [$V_c = (E/\rho)^{0.5}$].
Velocity, P-Wave	G	V_P	ft/sec	Velocity of compressional or dilatational wave [$V_p = (M/\rho)^{0.5}$]. For saturated soil V_p equals approximately 4800 ft/sec.
Velocity, P-Wave	S		km/sec	$V_p = [(K + 4/3\ \mu)/\rho)]^{1/2}$ in a homogeneous, isotropic medium. P-waves travel at 3–6 km/sec in rocks at the earth's surface and up to 7.5 km/sec in the lower crust.
Velocity, S-Wave	G	V_S	ft/sec	$V_S = (G/\rho)^{1/2}$.
Velocity, S-Wave	S	V_S	km/sec	Velocity of shear wave or distortional wave [$V_S = (\mu/\rho)^{1/2}$] in a homogeneous, isotropic medium. S-waves travel at 1–3 km/sec in rocks at the earth's surface and up to 4.5 km /sec in the lower crust. SV-wave has motion in a plane perpendicular to the plane of the interface; SH-wave has motion in a plane parallel to the interface.
Void ratio	G	e		Volume of soil voids divided by volume of soil solids [e = n/(1 – n)].

1. Refers to primary usage of term in Geotechnical Engineering (G) or Seismology (S).
2. In some cases there may be different symbols and units used in Geotechnical Engineering and Seismology.

Term	Use[1]	Symbol[2]	Units	Explanation
Void ratio, Maximum	G	e_{max}		Void ratio of soil in loosest condition.
Void ratio, Minimum	G	e_{min}		Void ratio of soil in densest condition.
Water content	G	w	%	Weight of water divided by weight of soil solids per unit volume.
Wave Length	G S	L	ft km	Distance between peaks of a sinusoidal wave form [L = V/f].
Wave, Body				Seismic waves that travel through the earth; there are two types: P waves and S waves.
Wave, Lg	S	Lg		Intermediate-period (.5–6 sec), large-amplitude seismic waves with predominantly transverse motion, which propagate to 1000 km or more in the continental crust. These waves are comprised mainly of S-waves multiply reflected (or guided) near the earth's surface.
Wave, P	S, G	P		The primary or fastest wave traveling away from a seismic event, consisting of a train of compressions and dilations of the material. The sense of motion is typically parallel to the direction of wave propagation.
Wave, Pn (Sn)	S	P_n, S_n		P (S) wave refracted from the top of the mantle, typically arriving in the distance range 100–200 km.
Wave, S	S, G	S		The secondary seismic wave, traveling slower than the P-wave, consisting of shear vibrations, transverse to the direction of wave propagation. These waves typically dominate ground motion of engineering interest.
Wave, S_cs	S	S_CS		S wave reflected from the Conrad discontinuity, typically observed in the distance range 60–100 km in the ENA.
Wave, S_ms	S	S_MS		S wave reflected from the Mohorovicic discontinuity (or base of the crust), typically observed in the distance range 80–120 km in the ENA.
Wave, Surface	S			A seismic wave that propagates along the earth's surface, with a speed less than that of S-waves. These waves are often used to estimate magnitude, particularly for shallow earthquakes, because their long-period characteristics travel long distances and are relatively insensitive to near-surface heterogeneities.
Waves, Teleseismic	S			Seismic waves that are identifiable on seismographs at long distances (e.g., > 1000 km) from their source.
Western North America	S	WNA		The region of North America west of and including the Rocky Mountains, and characterized as tectonically active.
Western United States	S	WUS		The portion of the United States west of and including the Rocky Mountains, and characterized as tectonically active. (See "Western North America").

1. Refers to primary usage of term in Geotechnical Engineering (G) or Seismology (S).
2. In some cases there may be different symbols and units used in Geotechnical Engineering and Seismology.

1.A.2 Expanded Definitions

1.A.2.1 Convolution

A term arising from linear filter theory. To compute ground motion at the surface (for small strains) given a specified control motion and control point at some depth, the transfer function ($H(\omega)$) between the surface and the prescribed depth is computed using an appropriate formulation. The Fourier transform of the computed surface motion ($A(\omega)$) is then the transfer function multiplied by the Fourier transform of the control motion ($C(\omega)$).

$$A(\omega) = H(\omega)\, C(\omega) \qquad \text{(Eq. 1.A-1)}$$

If this is transformed into the time domain, the computed surface acceleration time history is given by

$$a(t) = h(t) * c(t) \qquad \text{(Eq. 1.A-2)}$$

where * denotes a convolution operator which is defined by

$$a(t) = \int_{-\infty}^{\tau} h(t-\tau)\, c(\tau)\, d\tau \qquad \text{(Eq. 1.A-3)}$$

and h(t) is the inverse Fourier transform of the transfer function (or filter).

To propagate motion through [motion through] (or up) a profile then implies convolution of a filter with the control motion. Conversely, if the control point is specified at the surface, propagation down implies removal of a filter or deconvolution.

Convolutions are used in many other fields as well. In probability theory, the probability density function of the sum of two independent random variables is equal to the convolution of the probability density functions of the two random variables.

1.A.2.2 Analysis

It is important to clarify this term as it has a different interpretation to engineers and seismologists. Strictly speaking, an engineering interpretation of one-dimensional site response analysis implies a soil column or shear beam analysis and is therefore confined to vertically propagating compressional- or shear-waves. However, from a wave propagation point of view, the term one-dimensional material model implies only that the material properties (velocity, density, and material damping) vary in a vertical direction. The wave-field may vary horizontally as well as vertically and thus one-dimensional site response analysis, in a seismological context, may include vertical and inclined body waves (compressional and shear) as well as surface waves (Rayleigh and Love).

1.A.2.3 Outcrop Motion

Motion specified at the free surface of either soil or rock. The amplitude of this motion is exactly double that of the upgoing waves if material damping is neglected and there are no converted waves. This is not to be confused with the *total* motion at some depth. The total motion includes contribution from the upgoing and downgoing fields. In a linear system, the amplitudes of the upgoing and downgoing fields are simply summed to give the total motion.

1.A.2.4 Signal-to-Noise Ratio

In strong motion recordings, there are two sources of noise: instrument and earth. Instrumental noise may simply be regarded as distortions in the measurement process. Contributions to this noise are both electrical and mechanical and are usually small. Earth noise is actual ground motion that is not associated with the earthquake of interest. This ambient seismic noise has a relatively predictable Fourier spectral shape (Aki and Richards, 1980) although for frequencies greater than 1 Hz, the shape is highly variable due to the nature of cultural sources. In order to determine the frequency range over which the motion from the earthquake of interest is greater than the noise levels, the following procedure is followed. If sufficient pre-event record is available, this portion of the record is windowed and the Fourier spectrum is computed. A section of the earthquake ground motion is then also windowed (ideally both windows should be of the same length) and the Fourier spectrum computed. The ratio of these spectra, earthquake to pre-event windows, is then taken to approximate the signal-to-noise ratio. The regions where this exceeds 2 (6 dB) is generally accepted as the useful or reliable bandwidth for analyses.

1.A.2.5 Fourier Spectrum

The Fourier transform is defined as

$$F(\omega) = \int_{-\infty}^{\infty} f(t) e^{-i\omega t} dt \qquad \text{(Eq. 1.A-4)}$$

and is a complex variable with a real and imaginary part at each frequency (ω). The inverse Fourier transform is defined by

$$f(t) = \frac{1}{2\pi}\int_{-\infty}^{\infty} F(\omega)e^{-i\omega t}d\omega \qquad \text{(Eq. 1.A-5)}$$

If $f(t)$ represents an acceleration time history scaled to gravity, then F(ω) has the dimensions of g-sec or g/Hz and the Fourier transform represents acceleration per Hz or a density. Writing the Fourier transform in real and imaginary parts we have

$$H(\omega) = H_R(\omega) + iH_I(\omega) \qquad \text{(Eq. 1.A-6)}$$

which may be rewritten

$$H(\omega) = \|H(\omega)\| e^{i\phi(\omega)} \qquad \text{(Eq. 1.A-7)}$$

where the modulus and phase are given by

$$\|H(\omega)\| = \left(H_R^2(\omega) + H_I^2(\omega)\right)^{1/2} \qquad \text{(Eq. 1.A-8)}$$

$$\phi(\omega) = \tan^{-1}\frac{H_I(\omega)}{H_R(\omega)} \qquad \text{(Eq. 1.A-9)}$$

The modulus of the Fourier transform is sometimes called the Fourier spectrum and represents the contribution of a sinusoid of frequency ω to the total motion given by f(t). The Fourier spectrum then shows the relative contributions of different spectra components to the time history. The phase spectrum, ø(ω), although being a function of frequency, actually controls the distribution of energy in time. That is, the phase spectrum controls the shape of f(t). There is a direct correspondence between the time associated with the 5 to 95% Arias Intensity of f(t) and the phase of $f(t)$.

1.A.2.6 Response Spectrum

To demonstrate the relationships between the two spectral representations, the following development will introduce response spectra in terms of the time-domain response of simple harmonic oscillators. Following that, the Fourier spectrum will be introduced by showing how the frequency-domain approach can be applied to calculate the oscillator response. This results in a very clear picture of the relationship between the two types of spectra. From this perspective it is easy to see why the two possess certain similarities and also why they can exhibit marked differences.

The equation of a simple harmonic oscillator subjected to a forcing function of ground acceleration may be written as

$$\ddot{x} + 2\omega_j\eta\dot{x} + \omega_j^2 x = -a_s \qquad \text{(Eq. 1.A-10)}$$

where

x = oscillator displacement relative to the ground, a function of t, ω_j, and η

ω_j = j^{th} oscillator resonant frequency

η = fraction of critical damping

a_s = ground surface acceleration time history.

The relative displacement response spectrum is defined by

$$R(\omega_j, \eta) = \max_t \left\|x(t, \omega_j, \eta)\right\| \qquad \text{(Eq. 1.A-11)}$$

for a suite of ω_j.

The general solution for x (t, ω_j, η) is given by the Du Hamel integral:

$$x(t) = \frac{1}{\omega_j\sqrt{(1-\eta^2)}}\int_o^t a_s(\tau)e^{-\omega_j\eta(t-\tau)} \times \sin\omega_j\sqrt{(1-\eta^2)}(t-\tau)d\tau \qquad \text{(Eq. 1.A-12)}$$

(Hudson, 1979). The integral may be evaluated using numerical integration techniques such as the Runge-Kutta scheme (Jennings, 1962) or analytically by assuming linear segments in acceleration between time steps and solving an arithmetical relation at each time step (Nigam and Jennings, 1968).

An alternate approach to solving equation (1.A-10) for the response (x) is to assume that x and as may be expressed as:

$$x(t) = \frac{1}{\sqrt{(2\pi)}}\int_{-\infty}^{\infty}\bar{X}(\omega)e^{i\omega t}d\omega$$

$$\alpha_s(t) = \frac{1}{\sqrt{2\pi}}\int_{-\infty}^{\infty}\bar{A}_s(\omega)e^{-i\omega t}d\omega \qquad \text{(Eq. 1.A-13)}$$

where

$$\bar{X}(\omega) = \frac{1}{\sqrt{2\pi}} \int_{-\infty}^{\infty} x(t)\, e^{i\omega t} dt$$

and

$$\bar{X}(\omega) = \frac{1}{\sqrt{2\pi}} \int_{-\infty}^{\infty} x(t)\, e^{i\omega t} dt$$

The frequency-domain (complex) functions $\bar{X}(\omega)$ and $\bar{A}_s(\omega)$ are the Fourier transforms of x(t) and $a_s(t)$; their absolute values, $\|\bar{X}(\omega)\|$ and $\|\bar{A}_s(\omega)\|$ are the Fourier spectra of x(t) and $a_s(t)$.

The value of the Fourier spectrum at frequency ω is a direct measure of the amount of power in the time history at that frequency.

Rewriting equation (1.A-10) in terms of the Fourier transforms,

$$\left(-\omega^2 + 2i\omega_j \omega\eta + \omega_j^2\right)\bar{X}(\omega) = -\bar{A}_s(\omega) \qquad \text{(Eq. 1.A-14)}$$

we obtain for $\bar{X}(\omega)$

$$\bar{X}(\omega) = \frac{1}{\omega_j^2 - \omega^2 - 2i\omega\omega_j\eta} \bar{A}_s(\omega) \qquad \text{(Eq. 1.A-15)}$$

$$= \bar{O}\left(\omega, \omega_j, \eta\right)\bar{A}_s(\omega) \qquad \text{(Eq. 1.A-16)}$$

where $\bar{O}\left(\omega, \omega_j, \eta\right)$ is the oscillator transfer function or filter. The Fourier transform of the response is the product of the oscillator transfer function and the Fourier transform of the input acceleration time history. The modulus or absolute value of the transfer function is the amplification or gain of the oscillator. Figure 1.A-1 shows a plot of an oscillator amplification function (multiplied by ω_j^2 to represent acceleration response) for 5% damping and a natural frequency of 3 Hz. The oscillator response in this case simply passes the ground surface acceleration spectra unchanged up to about 1 Hz, greatly amplifies around 3 Hz, and then rapidly truncates beyond.

In the time domain, equation (1.A-16) is expressed as

$$x\left(t, \omega_j, \eta\right) = o\left(t, \omega_j, \eta\right) * a_s(t) \qquad \text{(Eq. 1.A-17)}$$

where $o\left(t, \omega_j, \eta\right)$ is the impulse response of the oscillator—the inverse Fourier transform of the oscillator transfer function. The impulse response is the time-domain response of the free simple harmonic oscillator to a delta function (impulse) of acceleration. The * symbol represents a convolution operator and is defined by the integral relation

$$x\left(t, \omega_j, \eta\right) = \int_{-\infty}^{t} o\left(\tau, \omega_j, \eta\right) a_s(t - \tau) d\tau \qquad \text{(Eq. 1.A-18)}$$

which is another way of expressing equation (1.A-12).

The response spectrum can then be expressed in terms of convolutions by combining equations (1.A-11) and (1.A-17):

$$R\left(\omega_j, \eta\right) = \max_t \left\| o\left(t, \omega_j, \eta\right) * a_s(t) \right\| \qquad \text{(Eq. 1.A-19)}$$

Vertical and Horizontal Transfer Functions. To illustrate the theoretical differences in the response spectra and Fourier spectra, it is instructive to examine the effects of site operators (or transfer functions) on equation (1.A-19).

If we consider $\bar{A}_s(\omega)$ the Fourier transform of a rock outcrop acceleration time history, then a reasonable far-field model of this process may be written as

$$A_s(\omega) = 2\overset{*}{S}(\omega)\bar{P}(\omega) \qquad \text{(Eq. 1.A-20)}$$

where

$\overset{*}{S}(\omega)$ = Fourier transform of doubly differentiated far-field source time history

$\bar{P}(\omega)$ = propagation path operator

and the factor 2 represents the free surface effect. To consider motion at depth z, the surface Fourier transform is multiplied by a transfer function which accounts for the sum of the upgoing and downgoing vertically propagating

$$\bar{A}_z(\omega) = 2\overset{*}{S}(\omega)\bar{P}(\omega)\bar{S}(\omega, z)$$

where

$$\bar{S}(\omega, z) = \cos kz \qquad \text{(Eq. 1.A-22)}$$

and

$$k = \frac{\omega}{v_s}(1 - i2\beta),$$

β = material critical damping ratio.

The response spectra for the surface motion and the at-depth motion are

$$R_s(\omega_j,\eta) = 2\max_t \| o(t,\omega_j,\eta) * \ddot{s}(t) * P(t) \| \quad \text{(Eq. 1.A-23)}$$

$$R_z(\omega_j,\eta) = 2\max_t \| o(t,\omega_j,\eta) * \ddot{s}(t) * P(t) * S(t,z) \| \quad \text{(Eq. 1.A-24)}$$

In order to isolate the vertical transfer function and examine the effects of depth, ratios are taken of the surface motion divided by the at-depth motion. For Fourier spectra, this ratio results in

$$\frac{\|\bar{A}_s(\omega)\|}{\|\bar{A}_z(\omega)\|} = \frac{1}{\|\bar{S}(\omega,z)\|} = \frac{1}{\cos kz} \quad \text{(Eq. 1.A-25)}$$

which shows cancellation of source and path operators. On the other hand, ratios of the response spectra, because they each are represented as time domain convolutions, do not, in general, result in exact cancellations of source and path operators:

$$\frac{R_s(\omega_j,\eta)}{R_z(\omega_j,\eta)} = \frac{\max_t \| o(t,\omega_j,\eta) * \ddot{s}(t) * P(t) \|}{\max_t \| o(t,\omega_j,\eta) * \ddot{s}(t) * P(t) * S(t,z) \|} \quad \text{(Eq. 1.A-26)}$$

Similar arguments may also be presented for horizontal transfer functions represented by motion at nearby soil sites divided by rock outcrop motion. For a simple single layer site of thickness (d) overlying a rock halfspace, the transfer function may be expressed as

$$\bar{S}(\omega,d) = \frac{2}{\cos kd + i\frac{\rho_1 V_{s_1}}{\rho_2 V_{s_2}} \sin kd} \quad \text{(Eq. 1.A-27)}$$

where

d = depth to bedrock

ρ_1 = density of layer i

V_{s_i} = shear wave velocity of layer i.

Substituting this transfer function into equation (1.A-21) to simulate the site effect on the rock outcrop motion we have

$$\bar{A}_{site}(\omega) = \bar{A}_s(\omega)\bar{S}(\omega,d) \quad \text{(Eq. 1.A-28)}$$

The ratio of the Fourier spectrum at the surface of the site to the Fourier spectrum of the outcrop motion is simply

$$\frac{\|\bar{A}_{site}(\omega)\|}{\|\bar{A}_s(\omega)\|} = \|\bar{S}(\omega,d)\| \quad \text{(Eq. 1.A-29)}$$

while the ratio of response spectra is given by

$$\frac{R_{site}(\omega_j,\eta)}{R_s(\omega_j,\eta)} = \frac{\max_t \| o(t,\omega_j,\eta) * \ddot{s}(t) * P(t) * S(t,d) \|}{\max_t \| o(t,\omega_j,\eta) * \ddot{s}(t) * P(t) \|} \quad \text{(Eq. 1.A-30)}$$

As with the vertical ratios, the Fourier spectral ratios show complete cancellation of all operators (filters) from the source to the site while ratios of the response spectra do not.

In reality, the situation for the Fourier spectral ratios is more complicated than the theoretical results presented above. This arises because the calculation of Fourier spectral values for a stochastic time history results in nearly independent spectral estimates for different frequencies with associated resolution and variances (Otnes and Enochson, 1978). Because the spectral estimates are nearly independent, the associated variance is high and the resulting instability produces large oscillations or an erratic spectrum. For a deterministic process, increasing the sample length will decrease the variance and the spectrum will become less erratic and converge to the true spectrum. However, for a stochastic process, increasing the sample length will not cause the spectral estimates to converge to stable values. The actual measurement or statistical estimation of the amplification function may be modeled as a system with additive noise.

$$\bar{T}_n(\omega,d) = E\left\{ \frac{\|\bar{A}_{site}(\omega)\|}{\|\bar{A}_s(\omega)\|} \right\} + n(\omega) \quad \text{(Eq. 1.A-31)}$$

where

$\bar{T}_n(\omega,d)$ = measured value of the site amplification function.

$n(\omega)$ = noise model

and E{ } = expected value

In order to increase the stability of the amplification function estimate, the variance of the individual Fourier

spectral values are reduced by appropriate smoothing techniques (Otnes and Enochson, 1978). There is an accompanying decrease in resolution; and this tradeoff, along with the noise contamination, ultimately controls the degree of reliability of the amplification function estimate at each frequency.

The response spectral estimates for a stochastic process are also statistical in nature (Udwadia and Trifunac, 1974); however, the spectral estimates at different frequencies are not independent. This arises because, from equation (1.A-15), the response $\overline{X}(\omega)$ for a given ω_j is a weighted integration (sum) of the nearly independent Fourier spectral estimates $\overline{A}_s(\omega)$. The degree of dependence between the response spectral estimates depends upon the damping and, to some extent, the shape of the acceleration power spectrum. If the damping is increased, the width of the acceleration amplification function shown in Figure A.2-1 increases and more Fourier spectral estimates are given relatively higher weighting. Also if the power spectrum of the acceleration time history is strongly peaked (monochromatic time history), it may influence the weighting of the amplification function.

To summarize, the response spectral ratios, due to the possibility of non-cancellation of source and path processes, may present an inaccurate picture of site response. Conversely, ratios of Fourier spectra have more complete cancellation of source and path operators, but they are limited in that the Fourier spectral estimates are erratic and the spectrum must be smoothed in order to reduce its variance.

1.A.3 References

Abrahamson, N.A. (1985). Estimation of seismic wave coherency and rupture velocity using the SMART 1 strong motion array recordings, Univ. California Berkeley, EERC Report No. EERC/UCB/85-02.

Aki, K. and P. G. Richards, 1980. *Quantitative Seismology, Theory and Methods*, San Francisco, CA: W. H. Freeman and Co.

Hudson, D.E. (1979). Reading and Interpreting Strong Motion Accelerograms., Berkeley, California: Earthquake Engineering Research Institute.

Jennings, P.G. (1962). Velocity Spectra of the Mexican Earthquakes of 11 May and 19 May 1962, Earthquake Engineering Laboratory, California Institute of Technology, Pasadena, California, December.

Nigam, N.C. and P.C. Jennings (1968). *Digital Calculation of Response Spectra from Strong-Motion Earthquake Records.* Earthquake Engineering Research Laboratory, California Institute of Technology, Pasadena, California, June, 1968.

Otnes, R.K., and L. Enochson (1978). *Applied Time Series Analysis*, Vol. 1, New York: John Wiley and Sons.

Udwadia, F. E. and M. D. Trifunac (1974). Characterization of Response Spectra Through the Statistics of Oscillator Response., *Bull. Seis. Soc. Am.*, Vol. 64, 205–219.

WARNING: This Document contains information classified under U.S. Export Control regulations as restricted from export outside the United States. You are under an obligation to ensure that you have a legal right to obtain access to this information and to ensure that you obtain an export license prior to any re-export of this information. Special restrictions apply to access by anyone that is not a United States citizen or a Permanent United States resident. For further information regarding your obligations, please see the information contained below in the section titled "Export Control Restrictions."

Export Control Restrictions

Access to and use of EPRI Intellectual Property is granted with the specific understanding and requirement that responsibility for ensuring full compliance with all applicable U.S. and foreign export laws and regulations is being undertaken by you and your company. This includes an obligation to ensure that any individual receiving access hereunder who is not a U.S. citizen or permanent U.S. resident is permitted access under applicable U.S. and foreign export laws and regulations. In the event you are uncertain whether you or your company may lawfully obtain access to this EPRI Intellectual Property, you acknowledge that it is your obligation to consult with your company's legal counsel to determine whether this access is lawful. Although EPRI may make available on a case by case basis an informal assessment of the applicable U.S. export classification for specific EPRI Intellectual Property, you and your company acknowledge that this assessment is solely for informational purposes and not for reliance purposes. You and your company acknowledge that it is still the obligation of you and your company to make your own assessment of the applicable U.S. export classification and ensure compliance accordingly. You and your company understand and acknowledge your obligations to make a prompt report to EPRI and the appropriate authorities regarding any access to or use of EPRI Intellectual Property hereunder that may be in violation of applicable U.S. or foreign export laws or regulations.

About EPRI

EPRI creates science and technology solutions for the global energy and energy services industry. U.S. electric utilities established the Electric Power Research Institute in 1973 as a nonprofit research consortium for the benefit of utility members, their customers, and society. Now known simply as EPRI, the company provides a wide range of innovative products and services to more than 1000 energy-related organizations in 40 countries. EPRI's multidisciplinary team of scientists and engineers draws on a worldwide network of technical and business expertise to help solve today's toughest energy and environmental problems.

EPRI. Electrify the World

TR-102293-V1

EPRI • 3412 Hillview Avenue, Palo Alto, California 94304 • PO Box 10412, Palo Alto, California 94303 • USA
800.313.3774 • 650.855.2121 • askepri@epri.com • www.epri.com